

Critical Explorations

Ophthalmology

Breakthroughs in Research and Practice

Copyright 2018. Medical Information Science Reference. All rights reserved. May not be reproduced in any form without permission from the publisher, except fair uses permitted under U.S. or applicable copyright law.

EBSCO Publishing : eBook Collection
(EBSCOhost) - printed on 2/11/2023 1:24 AM
via
AN: 1662542 ; Information Resources
Management Association.; Ophthal
Information Resources Management Association
Breakthroughs in Research and Practice
Account: ns335141



Ophthalmology: Breakthroughs in Research and Practice

Information Resources Management Association
USA



Published in the United States of America by

IGI Global

Medical Information Science Reference (an imprint of IGI Global)

701 E. Chocolate Avenue

Hershey PA, USA 17033

Tel: 717-533-8845

Fax: 717-533-8661

E-mail: cust@igi-global.com

Web site: <http://www.igi-global.com>

Copyright © 2018 by IGI Global. All rights reserved. No part of this publication may be reproduced, stored or distributed in any form or by any means, electronic or mechanical, including photocopying, without written permission from the publisher. Product or company names used in this set are for identification purposes only. Inclusion of the names of the products or companies does not indicate a claim of ownership by IGI Global of the trademark or registered trademark.

Library of Congress Cataloging-in-Publication Data

Names: Information Resources Management Association, editor.

Title: Ophthalmology : breakthroughs in research and practice / Information

Resources Management Association, editor.

Other titles: Ophthalmology (Information Resources Management Association)

Description: Hershey PA : Medical Information Science Reference (an imprint of IGI Global), [2018] | Includes bibliographical references.

Identifiers: LCCN 2017038145 | ISBN 9781522551959 (hardcover) | ISBN 9781522551966 (ebook)

Subjects: | MESH: Eye Diseases | Case Reports

Classification: LCC RE46 | NLM WW 140 | DDC 617.7--dc23 LC record available at <https://lcn.loc.gov/2017038145>

British Cataloguing in Publication Data

A Cataloguing in Publication record for this book is available from the British Library.

All work contributed to this book is new, previously-unpublished material. The views expressed in this book are those of the authors, but not necessarily of the publisher.

For electronic access to this publication, please contact: eresources@igi-global.com.

Editor-in-Chief

Mehdi Khosrow-Pour, DBA
Information Resources Management Association, USA

Associate Editors

Steve Clarke, *University of Hull, UK*
Murray E. Jennex, *San Diego State University, USA*
Annie Becker, *Florida Institute of Technology, USA*
Ari-Veikko Anttiroiko, *University of Tampere, Finland*

Editorial Advisory Board

Sherif Kamel, *American University in Cairo, Egypt*
In Lee, *Western Illinois University, USA*
Jerzy Kisielnicki, *Warsaw University, Poland*
Amar Gupta, *Arizona University, USA*
Craig van Slyke, *University of Central Florida, USA*
John Wang, *Montclair State University, USA*
Vishanth Weerakkody, *Brunel University, UK*

List of Contributors

Aruna, P. / <i>Annamalai University, India</i>	153
Banerjee, Anwesha / <i>Jadavpur University, India</i>	98
Bidgoli, Azam Asilian / <i>University of Kashan, Iran</i>	122
D., Gladis / <i>Presidency College, Chennai, India</i>	69
Devaraajan, N. Praveen / <i>Pondicherry Engineering College, India</i>	217
Dong, Hao / <i>University of Massachusetts, Amherst, USA</i>	317
Dutta, Malay Kishore / <i>Amity University, Noida, India</i>	172,189
Ebrahimpour-Komleh, Hossein / <i>University of Kashan, Iran</i>	122
Elbalaoui, Abderrahmane / <i>Sultan Moulay Slimane University, Beni Mellal, Morocco</i>	18
Ezhilarasan, M. / <i>Pondicherry Engineering College, India</i>	217
Fakir, Mohamed / <i>Sultan Moulay Slimane University, Beni Mellal, Morocco</i>	18
Ganz, Aura / <i>University of Massachusetts, Amherst, USA</i>	317
Ghosh, Poulami / <i>Jadavpur University, India</i>	98
Grover, Aditya / <i>University of South Florida, USA</i>	283
Gupta, Swarna Biseria / <i>L.N. Medical College, Bhopal, India</i>	115,211
Hariharan, R. / <i>Pondicherry Engineering College, India</i>	217
Hassan, Gehad / <i>Fayoum University, Egypt & Scientific Research Group in Egypt (SRGE), Egypt</i> ...	1
Hassanien, Aboul Ella / <i>Cairo University, Egypt & Scientific Research Group in Egypt (SRGE), Egypt</i>	1
Hirani, Anjali / <i>University of South Florida, USA & Virginia Tech-Wake Forest University, USA</i> .	283
Hossain, Gahangir / <i>Texas A&M University-Kingsville, USA</i>	300
J., Shiny Priyadarshini / <i>Madras Christian College, India</i>	69
Kandan, Priya / <i>Annamalai University, India</i>	153
Kang, Jieqi / <i>University of Massachusetts, Amherst, USA</i>	317
khaddouj, Taifi / <i>Sultan Moulay Slimane University, Beni Mellal, Morocco</i>	18
Kim, Pyung Soo / <i>Korea Polytechnic University, South Korea</i>	189
Kumar, Upendra / <i>Dr. A. P. J. Abdul Kalam Technical University, India</i>	53
Lee, Yong Woo / <i>Virginia Tech-Wake Forest University, USA</i>	283
Mazumder, Ankita / <i>Jadavpur University, India</i>	98
Medhi, Jyoti Prakash / <i>Gauhati University, India</i>	241
Mehta, Garima / <i>Amity University, Noida, India</i>	189
MERBOUHA, Abdelkarim / <i>Sultan Moulay Slimane University, Beni Mellal, Morocco</i>	18
Mousavirad, Seyed Jalaleddin / <i>University of Kashan, Iran</i>	122
N, Poonguzhali / <i>Pondicherry Engineering College, India</i>	217
Nithya, V. / <i>Alagappa University, India</i>	268

Ogram, Geoff / <i>Stereoscopic Society, UK</i>	78
Pathak, Yashwant / <i>University of South Florida, USA</i>	283
Sah, Puspallata / <i>Centre of Plasma Physics, Institute for Plasma Research, India</i>	34
Sarma, Kandarpa Kumar / <i>Gauhati University, India</i>	34
Schafer, James / <i>University of Massachusetts, Amherst, USA</i>	317
Singh, Abhilasha / <i>Amity University, Noida, India</i>	172
Singh, D. P. / <i>L.N. Medical College, Bhopal, India</i>	115,211
Sutariya, Vijaykumar / <i>University of South Florida, USA</i>	283
Tibarewala, D. N. / <i>Jadavpur University, India</i>	98
Verma, Divya / <i>L.N. Medical College, Bhopal, India</i>	115,211

Table of Contents

Preface	ix
----------------------	----

Section 1 **Diagnostics and Imaging**

Chapter 1

A Review of Vessel Segmentation Methodologies and Algorithms: Comprehensive Review.....	1
<i>Gehad Hassan, Fayoum University, Egypt & Scientific Research Group in Egypt (SRGE), Egypt</i>	
<i>Aboul Ella Hassanien, Cairo University, Egypt & Scientific Research Group in Egypt (SRGE), Egypt</i>	

Chapter 2

Automatic Detection of Blood Vessel in Retinal Images Using Vesselness Enhancement Filter and Adaptive Thresholding.....	18
<i>Abderrahmane Elbalaoui, Sultan Moulay Slimane University, Beni Mellal, Morocco</i>	
<i>Mohamed Fakir, Sultan Moulay Slimane University, Beni Mellal, Morocco</i>	
<i>Taifi khaddouj, Sultan Moulay Slimane University, Beni Mellal, Morocco</i>	
<i>Abdelkarim MERBOUHA, Sultan Moulay Slimane University, Beni Mellal, Morocco</i>	

Chapter 3

Bloodless Technique to Detect Diabetes using Soft Computational Tool	34
<i>Puspalata Sah, Centre of Plasma Physics, Institute for Plasma Research, India</i>	
<i>Kandarpa Kumar Sarma, Gauhati University, India</i>	

Chapter 4

Significant Enhancement of Segmentation Efficiency of Retinal Images Using Texture-Based Gabor Filter Approach Followed by Optimization Algorithm	53
<i>Upendra Kumar, Dr. A. P. J. Abdul Kalam Technical University, India</i>	

Chapter 5

Analogizing the Thinning Algorithm and Elicitation of Vascular Landmark in Retinal Images	69
<i>Shiny Priyadarshini J., Madras Christian College, India</i>	
<i>Gladis D., Presidency College, Chennai, India</i>	

Chapter 6

- Principles of Binocular Stereoscopic Imaging..... 78
Geoff Ogram, Stereoscopic Society, UK

Chapter 7

- Visual Perception from Object Scanning as Revealed by Electrooculography 98
Anwsha Banerjee, Jadavpur University, India
Ankita Mazumder, Jadavpur University, India
Poulami Ghosh, Jadavpur University, India
D. N. Tibarewala, Jadavpur University, India

Chapter 8

- Case Study: Resolving Diagnostic Uncertainties in the Clinical Presentation of Ocular Tuberculosis 115
Swarna Biseria Gupta, L.N. Medical College, Bhopal, India
Divya Verma, L.N. Medical College, Bhopal, India
D. P. Singh, L.N. Medical College, Bhopal, India

Chapter 9

- A Comparative Study on Diabetic Retinopathy Detection Using Texture-Based Feature Extraction Techniques 122
Azam Asilian Bidgoli, University of Kashan, Iran
Hossein Ebrahimipour-Komleh, University of Kashan, Iran
Seyed Jalaeddin Mousavirad, University of Kashan, Iran

Chapter 10

- A New EYENET Model for Diagnosis of Age-Related Macular Degeneration: Diagnosis of Age-Related Macular Degeneration..... 153
Priya Kandan, Annamalai University, India
P. Aruna, Annamalai University, India

Chapter 11

- A Reversible Data Hiding Scheme for Efficient Management of Tele-Ophthalmological Data 172
Abhilasha Singh, Amity University, Noida, India
Malay Kishore Dutta, Amity University, Noida, India

Chapter 12

- An Efficient and Lossless Cryptosystem for Security in Tele-Ophthalmology Applications Using Chaotic Theory 189
Garima Mehta, Amity University, Noida, India
Malay Kishore Dutta, Amity University, Noida, India
Pyung Soo Kim, Korea Polytechnic University, South Korea

Chapter 13

- Case Study: Glaucoma and Epidemic Dropsy - A Past Possible Association Revisited 211
Swarna Biseria Gupta, L.N. Medical College, Bhopal, India
Divya Verma, L.N. Medical College, Bhopal, India
D. P. Singh, L.N. Medical College, Bhopal, India

Chapter 14

Human Health Diagnosis System Based on Iris Features..... 217

Poonguzhali N, Pondicherry Engineering College, India

M. Ezhilarasan, Pondicherry Engineering College, India

R. Hariharan, Pondicherry Engineering College, India

N. Praveen Devaraajan, Pondicherry Engineering College, India

Chapter 15

An Approach for Automatic Detection and Grading of Macular Edema 241

Jyoti Prakash Medhi, Gauhati University, India

Section 2

Drug Delivery and Design

Chapter 16

Bioactive Compound Analysis of Coriandrum Sativum L Against Microbial Keratitis 268

V. Nithya, Alagappa University, India

Chapter 17

Nanotechnology for Omics-Based Ocular Drug Delivery 283

Anjali Hirani, University of South Florida, USA & Virginia Tech-Wake Forest University, USA

Aditya Grover, University of South Florida, USA

Yong Woo Lee, Virginia Tech-Wake Forest University, USA

Yashwant Pathak, University of South Florida, USA

Vijaykumar Sutariya, University of South Florida, USA

Section 3

Visual Impairment

Chapter 18

Design Analytics of Complex Communication Systems Involving Two Different Sensory

Disabilities 300

Gahangir Hossain, Texas A&M University-Kingsville, USA

Chapter 19

Android-Based Visual Tag Detection for Visually Impaired Users: System Design and Testing 317

Hao Dong, University of Massachusetts, Amherst, USA

Jieqi Kang, University of Massachusetts, Amherst, USA

James Schafer, University of Massachusetts, Amherst, USA

Aura Ganz, University of Massachusetts, Amherst, USA

Index..... 335

Preface

The constantly changing landscape surrounding ophthalmology makes it challenging for experts and practitioners to stay informed of the field's most up-to-date research. That is why IGI Global is pleased to offer this one-volume comprehensive reference collection that will empower students, researchers, and academicians with a strong understanding of these critical issues by providing both broad and detailed perspectives on cutting-edge theories and developments. This compilation is designed to act as a single reference source on conceptual, methodological, and technical aspects, as well as to provide insight into emerging trends and future opportunities within the discipline.

Ophthalmology: Breakthroughs in Research and Practice is organized into three sections that provide comprehensive coverage of important topics. The sections are:

1. Diagnostics and Imaging
2. Drug Delivery and Design
3. Visual Impairment

The following paragraphs provide a summary of what to expect from this invaluable reference source:

Section 1, "Diagnostics and Imaging," opens this extensive reference source by highlighting the latest trends in computer-aided diagnosis systems and teleophthalmology. Through perspectives on retinal vessel segmentation, diabetic retinopathy, and age-related macular degeneration, this section demonstrates the importance of developing new methods and techniques to treat ocular diseases. The presented research facilitates a better understanding of ocular diagnostics and imaging to promote ocular health and vitality.

Section 2, "Drug Delivery and Design," includes chapters on emerging innovations in ocular drug delivery. Including discussions on glaucoma, uveal melanoma, and monocular blindness, this section presents research on the impact of antibacterials, antifungals, and coriandrum sativum on ocular disease treatment. This inclusive information assists in advancing current practices in the use of medication in ocular diseases.

Section 3, "Visual Impairment," presents coverage on strategies and devices to assist the visually impaired. Through innovative discussions on collaborative sense making, android-based visual tag detection, and sensory disabilities, this section highlights the changing landscape of disability communication. These inclusive perspectives contribute to the available knowledge on deaf-blind communication systems.

Although the primary organization of the contents in this work is based on its three sections, offering a progression of coverage of the important concepts, methodologies, technologies, applications, social issues, and emerging trends, the reader can also identify specific contents by utilizing the extensive indexing system listed at the end.

As a comprehensive collection of research on the latest findings related to ophthalmology, this publication provides researchers, practitioners, and all audiences with a complete understanding of the development of applications and concepts surrounding these critical issues.

Section 1

Diagnostics and Imaging

Chapter 1

A Review of Vessel Segmentation Methodologies and Algorithms: Comprehensive Review

Gehad Hassan

Fayoum University, Egypt & Scientific Research Group in Egypt (SRGE), Egypt

About Ella Hassanien

Cairo University, Egypt & Scientific Research Group in Egypt (SRGE), Egypt

ABSTRACT

“Prevention is better than cure”, true statement which all of us neglect. One of the most reasons which cause speedy recovery from any diseases is to discover it in advanced stages. From here come the importance of computer systems which preserve time and achieve accurate results in knowing the diseases and its first symptoms. One of these systems is retinal image analysis system which considered as a key role and the first step of Computer Aided Diagnosis Systems (CAD). In addition to monitor the patient health status under different treatment methods to ensure How it effects on the disease.. In this chapter the authors examine most of approaches that are used for vessel segmentation for retinal images, and a review of techniques is presented comparing between their quality and accessibility, analyzing and catgrizing them. This chapter gives a description and highlights the key points and the performance measures of each one.

INTRODUCTION

Retinal image analysis is one of systems which help on diagnosing almost of diseases in advanced stages like (hypertension, diabetic retinopathy, hemorrhages, macular degeneration, glaucoma, neo-vascularization and vein occlusion), in addition to achieving accurate result and saving time (Bernardes, Serranho, & Lobo, 2011). It is the main first step of Computer Aided Diagnosis (CAD) systems and registration of patient images. This diagnosis done by detection of some morphological features and attributes of the

DOI: 10.4018/978-1-5225-5195-9.ch001

retinal vasculature like width, length, branching pattern or tortuosity and angles. And on another level, manually detection of retinal vasculature is very difficult because of the complexity and the low contrast of blood vessels in retinal image (Asad, Azar, & Hassanien, 2014). Here come the importance of vessel segmentation as a pre-step in most of medical applications .

No specific method is existed which segments the vasculature from each retinal image modality. So on classifying the segmentation methods, we should put in our mind some important factors such as application domain, method being automated or semi-automated, imagining modality, and other factors (Miri & Mahloojifar, 2011; Fraz, Remagnino, Hoppe, & Barman, 2013) . And also not lose sight of the amount of effort and time which taken in the manual manner of the retinal blood vessel segmentation, in addition to our need for training and skill.

Sometimes we may need a preprocessing step before the actual algorithm of segmentation method is executed; this is due to other factors such as noise or bad acquisition that effect on the quality of image. In the opposite some methods perform post-processing in order to treat some problems which happened after segmentation method. And there are methods which not to do neither this nor that.

In this chapter, the authors present a review about the most methodologies of blood vessel segmentation; to provide the algorithms which employed for vessel segmentation to researchers to be considered as ready reference; to discuss the advantages and limitations of these approaches; to discuss the current trends and future challenges to be opened for solving, then it discusses the proposed approach for vessel segmentation which will be completely explained in the next sections.

BACKGROUND

Retinal Image Processing

Retinal Photography

Creating photograph of the interior surface of the eye containing the retina, macula, optic disc, and posterior pole is called fundus photography (also called fundography) (Lee, et al., 2000). A fundus camera is used in performing this fundus photograph; it consists of a specialized low power microscope with an attaching camera (Cassin & Solomon, 1990b; Saine, 2011).

Three modes the fundus camera basically operates in:

1. **Color Photography:** Examining the retina with full color under white light illumination.
2. **Red Free Photography:** Improving contrast of the vessels and other structures where the imaging light is filtered to remove red colors.
3. **Angiography Photography:** Where the vessels are brought into high contrast by intravenous injection of a fluorescent dye. The retina is illuminated with an excitation color which fluoresces light of another color where the dye is present. By filtering to exclude the excitation color and pass the fluorescent color, a very high-contrast image of the vessels is produced. Shooting a timed sequence of photographs of the progression of the dye into the vessels reveals the flow dynamics and related pathologies. Specific methods include sodiumfluorescein angiography (abbreviated FA or FAG) and indocyanine green (abbreviated ICG) angiography (Cassin & Solomon, 1990a).

Medical Image Analysis

The medical field is a source of interest of images. Large amount of image information is generated Because of the multiplicity of imaging modalities like MRI (Magnetic Resonance Imaging), as CT (Computed Tomography), PET (Positron Emission Tomography) etc. Not only the image's resolution and size grow with new improved technology, but also the image's number of dimensions increase. In the previous, only two dimensional images in medical staff were studied which produced by X-ray. But now there is image with three dimension volumes which is common in usual practice (Läthén, 2010). In addition to four dimensional data (three dimensional images which changed with time changing) is also used. So the key technical challenges are introduced because of this huge increasing of size and dimensionality.

We really need to store, transmit, look at and find relational information between all this data. Here, we find automatic or semi-automatic algorithms as kind of interest. We want algorithms which automatically detect lesions, diseases and tumors and stand out their locations in the huge heap of images. But another problem presents itself, we also must trust in these algorithms results. This is special important issue in medical applications; we don't need to algorithms with missing fatal diseases or algorithms with false alarms. So, it is important issue to perform validation studies to make the algorithms results for medical image analysis usable. Another dimension is added to the research process which includes communication between two non-similar worlds- the medical world which focus on patient, and the technical world which focus on computer. Coexistence between these two worlds rarely found and both sides must join to make great efforts achieving a common goal.

Retinal Vessel Segmentation

One of the most popular problems of computer vision is the image segmentation (Terzopoulos, 1984). Containment effects in general images like shadows, highlights, object occlusion, and transparency is considered as so difficult problem. Segmentation may be easy task and difficult task in the same time depending on its characteristics. On the one hand, an anatomic region is the most popular thing which the imaging is focused on (Asad, Azar, & Hassanien, 2012). Context may be provide some scope in general images segmenting (e.g., indoor vs. outdoor, people vs. animals, city vs. nature), it is more accurate in a medical imaging task where method, conditions, and organ identity of the imaging is known. In addition, there are limitations in the pose variations, and a prior knowledge of the Region of Interest (ROI) and tissue's number (Deserno & Thomas, 2010).

On the other hand, producing the images in the medical field is one of the challenges because of the imaging poor quality, based on that; we find it is difficult to segment the anatomical region from the background. To discriminate between the foreground and background, we depend on not only the intensity variations but also additional cues to isolate ROIs. Summarizing for the above, in medical imaging, segmentation is used as essential tool for many reasons, one of them is detection process or diagnosis such as segmentation of anatomical surfaces for blood vessels and this what we will discuss in the next paragraph in more details about the anatomic of the retina.

The retinal vasculature consists of both arteries and veins which appearing as outspread features, with visible tributaries within the retinal medical image. Vessel widths vary depending on both the image resolution and the vessel's width ranging from one pixel to twenty pixels. Ocular fundus image shown other structures including the optic disc, the retina boundary, and pathologies which take the form of bright and dark lesions, cotton wool spots, and exudates. If we take a cross-sectional intensity of vessel

retinal medical image, we will note approximation to gaussian shape. The intensity of the grey level and orientation of a vessel is gradually changing along their lengths. From other aspect about vessels shape it seems to take the structure of connected treelike (Emary E., Zawbaa, Hassanien, Tolba, & Sansel, 2014). However, there are huge varying in the shape, local grey level, and size. However, there are huge varying in the shape, local grey level, and size and, on the other hand some features of background may have similar attributes to vessels.

Vessel crossing and branching can further complicate the profile model. As with the processing of most medical images, signal noise, drift in image intensity and lack of image contrast pose significant challenges to the extraction of blood vessels. A central vessel reflex which is considered as indicator of a presence of strongly reflection along retinal vessels centerline, this reflection is more clear in arteries than veins, we can see it more stronger at images which taken at long wave-lengths in the retinal images of younger patients.

There are some characteristics of vessel segmentation depending on different aims, contrary to classical segmentation, such as:

1. Complex topologies and branches which should be correctly detected,
2. Vessels should be detected with different thickness (ranging from very thick to very thin),
3. Small occlusions should be repaired (false disconnections),
4. Noise which is incorrectly segmented should be removed, and
5. The vessel's minimum thickness should be put under control. Moreover, it must take into account robust, automatic, and efficient methods when we use vessel segmentation in a medical real-time environment (Emary E., Zawbaa, Hassanien, Schaefer, & Azar, 2014), so we find very challenging problems in this domain in return for all these requirements.

CLASSIFICATION OF RETINAL VESSEL SEGMENTATION APPROACHES

The authors have divided the retinal vessel segmentation algorithms into seven main categories:

- Pattern recognition techniques.
- Matched filtering.
- Vessel tracking/tracing.
- Mathematical morphology.
- Multiscale approaches.
- Model based approaches.
- Parallel/hardware based approaches.

Some of these categories are further divided into subcategories.

PATTERN CLASSIFICATION AND MACHINE LEARNING

Pattern recognition algorithms handle with the automatic detection or blood vessel features which classified on retinal images and other non-vessel objects one main object of them is background. To perform

pattern recognition tasks, humans are adapted. There are two main vessel segmentation categories of pattern recognition techniques:

1. **Supervised Approaches:** In this method it should be decided if a pixel is a vessel or non-vessel depending on some prior labeling information which is exploited to make this decision.
2. **Unsupervised Approaches:** The vessel segmentation is performed with no any prior labeling knowledge.

Supervised Approaches

The gold standard of vessel extraction in this method is about the training set basis of reference images which is manually processed and segmented. Ophthalmologist is doing this by precisely marking the gold standard images. In a supervised method, the algorithm performs its classification according to a given features. Therefore the classified ground truth data have to be available because in some real life applications, it is not available and this is the main condition of the classification. Usually In healthy retinal images, a supervised method produce good results more than unsupervised method because of its dependability on pre-classified data.

As we said before that supervised method classify each pixel if it is vessel or not. In (Niemeijer, Staal, Van Ginneken, Loog, & Abramoff, 2004) 31- feature sets are extracted by Gaussians and their derivatives through the k-Nearest Neighbor (kNN) classifier. Then in (Staal, Abramoff, Niemeijer, Viergever, & Van Ginneken, 2004) the algorithm was improved using ridge-based detection. The image should be partitioned by assigning each pixel to its nearest ridge element. So a 27 feature set is computed for each pixel which KNN classifier uses. But these methods have two main disadvantages. Firstly the large size of the features sets and thus the algorithm becomes slow down, and secondly the dependency of the training data and its sensitivity to false edges. Another method presented in (Soares, Leandro, Cesar, Jelinek, & Cree, 2006) performs Gaussian Mixture Model (GMM) classifier which extracts a 6-feature set using Gabor-wavelets. This method also is characterized by the dependency of its training data and requires more hours to train GMM models with a mixture of 20 Gaussians.

Table 1. Performance measures for supervised methods

Test Data	Drive Test			Stare Test		
	Acc	Specificity	Sensitivity	Acc	Specificity	Sensitivity
(Niemeijer, Staal, Van Ginneken, Loog, & Abramoff, 2004)	0.942	0.969	0.689	–	–	–
(Staal, Abramoff, Niemeijer, Viergever, & Van Ginneken, 2004)	0.944	0.977	0.719	0.952	0.981	0.697
(Soares, Leandro, Cesar, Jelinek, & Cree, 2006)	0.946	0.978	0.733	0.948	0.975	0.72
(Ricci & Perfetti, 2007)	0.959	0.972	0.775	0.965	0.939	0.903
(Fraz, et al., 2012b)	0.948	0.981	0.74	0.953	0.976	0.755
(Marin, Aquino, Gegundez-Arias, & Bra, 2011)	0.945	0.98	0.706	0.952	0.982	0.694
(Lam, Gao, & Liew, 2010)	0.947	–	–	0.957	–	–
(Roychowdhury, Koozekanani, & Parhi, 2014)	0.952	0.983	0.725	0.951	0.973	0.772

The method in (Ricci & Perfetti, 2007) performs line operators and support vector machine (SVM) classifier, a 3-feature set is extracted per each pixel. But this method characterized by its sensitivity to the training data, and it's intensively computation because it uses the SVM classifier. Boosting and bagging strategies is applied in (Fraz, et al., 2012b) with vessel classification of 200 decision trees with Gabor filters which extracts 9-feature set. And because of using boosting strategy, this method has high computational complexity. And about method that has independent training data set is produced in (Marin, Aquino, Gegundez-Arias, & Bra, 2011). It extracts 7-features set using moment invariants-based method and neighborhood parameters with neural network as classifier. The motivation of this method is to design an algorithm with low dependence on training data and with quickly computation.

The part of computational complexity has been proposed in (Perfetti, Ricci, Casali, & Costantin, 2007) and (Lam, Gao, & Liew, 2010). In (Roychowdhury, Koozekanani, & Parhi, 2014) Gaussian Mixture Model (GMM) classifier is used with 8-features which extracted using pixel neighborhood with first and second-order gradient images. This method has good consistency in the accuracy of vessel segmentation because it reduces the number of pixels which classified and identifies an optimal feature set, but on the other hand it has low computational complexity. The performance measures adopted for evaluating the efficiency of supervised classification of retinal vessels are illustrated in Table 1.

Unsupervised Approaches

Unsupervised classification approaches aim to find inherent patterns of blood vessels, and then uses these patterns to determine if a particular pixel is classified as a vessel or not. The training data do not directly contribute to the design of the algorithm in these unsupervised approaches.

An unsupervised approach, presented in (Kande, Subbaiah, & Savithri, 2010), corrects non-uniform illumination of color fundus images by using the intensity information of red and green channels on the same retinal image. Then matched filtering is used to enhance blood vessels contrast against the background. Finally, identifying the vascular tree structure of the retinal images by applying connected component labeling after weighted fuzzy C-means clustering is performed. In (Ng, Clay, Barman, & Feilde, 2010) a vessel detection system presented using the idea of maximum likelihood inversion of a model of image formation. Second derivative Gaussian filters are applied on images at several scales, and from the outputs of these filters, it is inferred the presence of vessels and their properties. For blood vessels detection, a generative model is proposed using a Gaussian-profiled valley and their corresponding filter outputs are calculated. The Gaussian model of noise is performed, and then the filter outputs covariance is calculated to the isotropic. To estimate the image and noise models parameters, these models are incorporated into a maximum likelihood estimator. The contrast, width, and direction of the blood vessel at every point in the image are estimated by the system. It also produces likelihoods of the model with additive noise. Likelihoods with additive noise are produced. Then the vessel centerline is detected by using these likelihoods in conjunction with vessel parameters which were estimated previously. Finally the model marks the vessel by combining the estimated width parameter and this centerline.

The Gray-Level Co-occurrence Matrix (GLCM) in combination with The local entropy information is performed in (Castaldi, Fabiola, & River, 2010) for vessel segmentation. To enhance the vessels structure, a matched filter is performed, then GLCM is computed, from the calculations of a statistical feature, and this calculated value is considered as threshold. Another method is presented in (Zhang, Cui, Jiang, & Wang, 2015), it aims to construct multidimensional feature vector with the green channel intensity as first step. Also the vessel intensity is enhanced using morphological operation. As second

step, they perform pixel clustering by constructing Self-Organizing Map (SOM) which considered as unsupervised neural network. In the last stage by using Otsu's method, each neuron is classified as neuron or non-vessel neuron in the output layer of SOM. Finally, in order to segment the vessel network, local entropy thresholding is applied. The performance measures adopted for evaluating the efficiency of unsupervised classification of retinal vessels are illustrated in Table 2.

MATCHED FILTERING

In this approach, 2-D kernel is convolved with the retinal image to detect the vasculature. A feature in the image is modeled by the kernel at some orientation and position, and also the matched filter response (MFR) is used as indicator of the presence of the feature (Sreejini & Govindan, 2015). The following properties are used to design the matched filter kernel:

1. Vessels usually characterized by a limiting on its curvature and it may be approached by piecewise linear segments.
2. The farther the vessels move radially outward from the optic disc, the less the diameter of the vessels.
3. The line segment on its cross-sectional intensity of the pixel approximately takes a Gaussian curve shape.

The convolution kernel is large and should be applied in a computational head at several rotations resulting. and also to confirm investigating the optimal responding for the kernel, the underlying Gaussian function which specified by the kernel must be have the same standard deviation for most vessels. So it is possible that the kernel do not respond to the vessels with a different profile. Another reason for false response, it is the variation of background and existence of pathologies. in the retinal image, this in turn increase the number of false responses because the pathologies and the vessels may have the same local attributes. A matched filter achieves good effective response when it applied with other processing techniques.

Matched filter approach is used in (Cinsdikici & Aydin, 2009), firstly the image is preprocessed, and then the matched filter and ANT algorithm is performed on the image in parallel manner. To completely extract the vasculature, the results are combined followed by length filtering. In (Zhang, Zhang, Zhang, & karray, 2010) the method exploits that the classical matched filter is generalized and extended with the first-order derivative of the Gaussian (MF-FDOG) to exploit the property of the blood vessel which

Table 2. Performance measures for unsupervised methods

Test Data	Drive Test			Stare Test		
	Acc	Specificity	Sensitivity	Acc	Specificity	Sensitivity
(Kande, Subbaiah, & Savithri, 2010)	0.891	–	–	0.898	–	–
(Ng, Clay, Barman, & Feilde, 2010)	–	0.953	0.700	–	–	–
(Castaldi, Fabiola, & River, 2010)	0.976	0.948	0.9648	0.948	0.975	0.72
(Zhang, Cui, Jiang, & Wang, 2015)	0.940	–	–	–	–	–

is the symmetric Gaussian shaped cross section with respect to its peak position, on the other hand the nonvessel edges - e.g. the step edge for lesions- are asymmetric. For detecting the vessels in this method, the zero-mean Gaussian filter (MF) and the first-order derivative of the Gaussian (FDOG) are used. For vessel structure, there will be a high response for the MF around shape's peak position, while the value of the local mean to the FDOG will be close to zero around position of the peak. In contrast, for non-vessel, the response of both the MF and the local mean to the FDOG will be high. The advantage of this method is that many vessels which are missed by MF are fine detected, so in this methodology, the false detections produced by the original MF are reduced.

Phase congruency is used in (Amin & Yan, 2011) to detect the retinal blood vessels. Firstly phase congruency is performed on the retinal image. This classification features by its soft and invariant because both luminosity and contrast of the image change. Then to measure phase congruency, a log-Gabor filters are applied, finally binary vessel tree is extracted by thresholding. The performance measures adopted for evaluating the efficiency of unsupervised classification of retinal vessels are illustrated in Table 3.

MORPHOLOGICAL PREPROCESSING

The term morphology is a branch of biology, its basics are the structures and the form of animals and plants. As for the mathematical morphology, it is a tool which extracts the image components that are forms a good data in the description and representation of region shapes such as boundaries, features, skeletons and convex hulls. The mathematical morphology produces a powerful and unified approach to a huge image processing problems. Morphological image processing (Serra, 1982), (Hassan, Elbendary, Hassanien, Shoeb, & Snasel, 2015) is a collection of techniques for digital image processing based on mathematical morphology. Structuring elements (SE) are applied to images by morphological operators, and specially are applied to binary images or to gray level images. There are two main operators (dilation and erosion). In dilation, objects are expanded by a structuring element, holes will be filled, and the disjoint regions will be connected. In erosion the objects are shrunk by a structuring element. There are two other compound operations which are closing and opening. Closing is a combination of dilation and erosion respectively, opening is a combination of erosion and dilation, respectively.

In medical image segmentation, there are two algorithms that used as enhancement tool. Top-hat transformation performs morphology opening operation to estimate the local background, and then subtracts it from the original image, this in turn leads to enhance in vessels to perform high results later in segmentation process. If we look at the vasculature from the point of view the morphology, it will show that the vasculature is a collection of linear segments which are connected together to form the final shape. If we reviewed the advantages and disadvantages of identifying shapes with morphological

Table 3. Performance measures for matched filtering methods

Test Data	Drive Test			Stare Test		
	Acc	Specificity	Sensitivity	Acc	Specificity	Sensitivity
(Cinsdikici & Aydin, 2009)	0.929	–	–	–	–	–
(Zhang, Zhang, Zhang, & karray, 2010)	0.938	0.972	0.712	0.948	0.975	0.718
(Amin & Yan, 2011)	0.920	–	–	–	–	–

processing, we will find that noise resistance and speed are from its main advantages. From the other hand morphological processing use long structure element which makes fitting highly tortuous vessels difficult, also the known vessel cross-sectional shape isn't exploited in this method.

Mathematical morphology and a fuzzy clustering algorithm are proposed in (Yang, Huang, & Rao, 2008). Top-hat morphological operation enhances the blood vessels and removes the background, then by using fuzzy clustering, the vessels are extracted. Morphological multi-scale enhancement method is also presented in (Sun, Chen, Jiang, & Wang, 2011). For the extraction of the blood vessels in the angiogram, fuzzy filter and watershed transformation are used. Multi-scale non-linear morphology opening operators with structuring element which vary in size is used to estimate the background, and then the background is subtracted from the image to achieve the contrast normalization. A combined fuzzy morphological operation is applied on the normalized angiogram with twelve linear structuring elements with nine pixels length, the structuring element rotated every 15° between zero and 180° . Thresholding the filtered image to obtain the vessel region, then for approximating the vessels centerlines, thinning operation is applied. Finally watershed techniques are applied on vessel centerline to detect the vessel boundaries.

Another method is presented in (Fraz, et al., 2012a) which is a combined unique vessel centerlines detection with morphological bit plane slicing. The first order derivative of a Gaussian filter is used in four directions to extract the centerlines, and then performing an average derivative and derivative signs with the extracted centerlines. Mathematical morphology has proven their worth as a brilliant technique for the blood vessels segmentation in the retina. Morphological multidirectional top-hat operation is applied on blood vessels gray-scale image with linear structure element to obtain the orientation map and shape, and then the enhanced vessels are subject to bit plane slicing. For obtaining the vessel tree, these maps are combined with the centerlines.

In (Miri & Mahloojifar, 2011) fast discrete curvelet transform with multi-structure mathematical morphology is proposed. For contrast enhancement, FDCT is performed. For detecting the blood vessels edges, multi-structure morphological transformation is applied. Then morphological opening is applied on the result image to remove the false edges. Finally for obtaining the complete final vascular tree, a connected adaptive component analysis is applied.

Another automated enhancement and segmentation method for blood vessels is presented in (Hou, 2014). This method decreases the optic disc influence and emphasizes the vessels by applying a morphological multidirectional top-hat transform with rotating structuring elements to the background of the retinal image. For producing a vessel response image and the final blood vessel tree, an improved multi-scale line detector is applied. As line detectors in the multi-scale detector have different line responses, the longer line detectors produce more vessel responses than the shorter line detectors. To set different weights for different scales, all the responses are combined by the improved multi-scale detector at different scales. The performance measures adopted for evaluating the efficiency of morphological processing methods of retinal vessels are illustrated in Table 4.

MULTI-SCALE APPROACHES

The width of a vessel decreases as it travels radially outward from the optic disk and such a change in vessel caliber is a gradual one. The farther the vessel travels from the optic disc, the smaller the vessels width will be. Depending on this property, we can define a vessel as contrasted pattern with a Gaussian

such as piecewise connected, shape cross-section profile, and locally linear, with a decreasing gradually vessel width. So to extract the complete vascular of retinal image in this method, some information which is related to the blood vessels with varying different scales is separated out.

A proposed supervised method for red-free vessel segmentation retinal images is presented in (Anzalone, Bizzarri, Parodi, & Storace, 2008). Normalization of the background of retinal image is performed for uneven illumination, and then enhancement of the vessels via scale space theory. For determining the optimal scale factor and also the threshold to binarize the segmented image, an optimization supervised algorithm is performed, and then cleaning operation is done to ensure completely super removal.

Another blood vessel segmentation method is investigated in (Farnell, et al., 2008) whose idea depends on the multi-scale line operator (MSLO). By using Gaussian sampling on a series of images at respectively coarser length scales with respect to the original image, sub-sampled images Gaussian pyramid- are constructed. Then the line operator is performed to the images on every level of this Gaussian pyramid in a separate manner. By using a cubic spline, the result image of the previous stage was mapped to the original level of scale. The final image is the addition of all images of the Gaussian pyramid. For each length scale in the MSLO image, the weight is obtained, and then a threshold is calculated to produce a binary segmented image. Finally By using a region simple growing algorithm, all remaining noise should be removed.

In (Vlachos & Dermatas, 2010) a multi-scale line tracking algorithm for blood vessel segmentation is proposed. Firstly both contrast normalization and luminosity are performed, and then based on normalized histogram; brightness selection rule is obtained to derive the seeds of the line tracking. We get varying widths of the vessel via initialization of the line tracking at multiple scaled. Many cross sectional conditions are constructed as a termination condition of line tracking. The result of all multi-scale line tracking is combined to get the confidence image map which quantized in order to derive the initial vessel network. And because of the disconnected vessel lines and the remaining noise, Median filter is performed for restoration. Finally by performing morphological reconstruction, the fault artifacts are removed.

In (Hou, 2014) another proposed vascular segmentation is presented as we explain before in section 3 morphological processing. This method combines between morphological processing to enhance the influence of optic disc and the multi-scale line detector to produce the final vascular tree of the retinal image. The performance measures adopted for evaluating the efficiency of multi-scale approaches of retinal vessels are illustrated in Table 5.

Table 4. Performance measures for morphological processing methods

Test Data	Drive Test			Stare Test		
	Acc	Specificity	Sensitivity	Acc	Specificity	Sensitivity
(Fraz, et al., 2012a)	0.943	0.977	0.715	0.944	0.968	0.731
(Miri & Mahloojifar, 2011)	0.946	0.979	0.735	–	–	–
(Hou, 2014)	0.942	0.969	0.735	0.934	0.965	0.735

Table 5. Performance measures for multiscale approaches

Test Data	Drive Test			Stare Test		
	Acc	Specificity	Sensitivity	Acc	Specificity	Sensitivity
(Anzalone, Bizzarri, Parodi et al., 2008)	0.942	–	–	–	–	–
(Vlachos & Dermatas, 2010)	0.929	0.955	0.747	–	–	–
(Hou, 2014)	0.942	0.969	0.735	0.934	0.965	0.735

MODEL BASED APPROACHES

In these approaches, an explicit vessel models are applied in order to extract the vascular. In (Vermeer, Vos, Lemij, & Vossepoel, 2004) a proposed segmentation method is presented which extracts the blood vessels by convolving with a Laplacian kernel, and then a threshold is calculated to segment the vessels. Finally the broken lines are connected. In (Lam & Yan, 2008) some improvement is performed on the previous methodology. The Laplacian operator is used to extract the vascular and pruning is performed for objects with noise according to center lines. Some advantage of this methodology is that it can extract the vessels from images with bright abnormalities, but in contrast it can't work with red lesions in retinal images (like microaneurysms or hemorrhages).

The method in (Lam, Gao, & Liew, 2010) proposed perceptive transformation approaches for segmenting vascular in retinal images with both bright and red lesions. A model-based method in (Jiang & Mojon, 2003) performs adaptive locally thresholding. In the verification process, vessel information is integrated. And because this method has an overall low accuracy, it is more generalizable than matched filter methods. Another approach for vessel segmentation presented in (Al-Diri, Hunter, & Steel, 2009). Active contour models are used, but it has computational complexity. The performance measures adopted for evaluating the efficiency of model based methods of retinal vessels are illustrated in Table 6.

PARALLEL HARDWARE BASED IMPLEMENTATIONS

The Parallel hardware based implementation addresses the high computational cost of vascular segmentation algorithms, and also addresses the real-time performance requirements. Cellular neural networks represent one appealing paradigm for image processing of parallel real-time (Manganaro, Arena, & Fortuna, 1999), (Roska & Chua, 1993), which VLSI chips are used to implement on. For parallel implementation for vascular segmentation algorithms, the registration ToolKit and insight segmentation are also used in high resolution images (Ibanez, Schroeder, Ng, & Cates, 2003). An approach is presented in (Alonso-Montes, Vilario, Dudek, & Penedo, 2008) which is pixel-parallel based method to confirm fast vascular extraction. In fact this method is an improvement of the original proposal (Alonso-Montes, Vilarino, & Penedo, CNN-based automatic retinal vascular tree extraction, 2005) which implements and tests morphological operations and local dynamic convolutions together with logical and arithmetic operations in parallel processor array (a fine-grain single instruction multiple data (SIMD)).

ITK parallel based implementation is presented in (Palomera-perez, Martinez-Peez, Benitez-Perez, & Ortega-Arhona, 2010). It ensures achieving accuracy similar to its serial counterpart. In addition to its quick processing time (8-10 times faster), and that make it possible to handle high resolution images

Table 6. Performance measures for model based approaches

Test Data	Drive Test			Stare Test		
	Acc	Specificity	Sensitivity	Acc	Specificity	Sensitivity
(Vermeer, Vos, Lemij, & Vossepoel, 2004)	0.929	–	–	–	–	–
(Lam & Yan, 2008)	–	–	–	0.965	–	–
(Lam, Gao, & Liew, 2010)	0.947	–	–	0.957	–	–
(Jiang & Mojon, 2003)	0.891	0.900	0.830	0.901	0.900	0.857
(Al-Diri, Hunter, & Steel, 2009)	–	0.955	0.728	–	0.968	0.752

and large datasets. The image should be divided into sub-images which have overlapped regions. Then these sub images is distributed across computers. Each computer calculates the feature extraction and region growing and finally combining the segmentation results from different computers. But there are no guidelines to tune its design parameters (the neighborhood size, scaling factors of variance and local mean, and the structuring element for morphological operations), so they must be empirically tuned. In addition, for local variance estimation in the image, nonlinear CNN templates are required. (Costantini, Casali, & Todisco, 2010) overcomes the drawbacks of previous approach by exploiting the blood vessels geometrical properties. The line strength measures is calculated for the blood vessels on the level of green plane in the colored retinal image. Linear space-invariant 3×3 templates are required for the CNN algorithm, so by using one existing CNN chips, it could be implemented. The performance measures adopted for evaluating the efficiency of Parallel hardware based implementations of retinal vessels are illustrated in Table 7.

FUTURE RESEARCH DIRECTIONS

The future direction of vessel segmentation research is to develop more accurate, faster automatic techniques. The segmentation accuracy is a critical and essential point in the research because of the nature of work that dealing with a part of human which is dealing with a part of the human body which must stop in front of him and do the best of ours. In order to achieve high accuracy we must focus on two important factors which are the acquisition phase to get images with high resolution with perfect brightness and these will help in the processing phase, and developing hybrid approach with optimization techniques which achieve faster and accurate results. In the end, we must not forget that we are dealing with human nature, so we must investigate precision to handle with.

Table 7. Performance measures for parallel hardware implementation based methods

Test Data	Drive Test			Stare Test		
	Acc	Specificity	Sensitivity	Acc	Specificity	Sensitivity
(Alonso-Montes, Vilario, Dudek, & Penedo, 2008)	0.919	–	–	–	–	–
(Palomera-perez, Martinez-Peez, Benitez-Perez, & Ortega-Arhone, 2010)	0.925	0.967	0.64	0.926	0.945	0.769

CONCLUSION

Segmentation algorithms are the heart of medical image applications like multimodal image registration, radiological diagnostic systems, visualization, creating anatomical atlases, and computer-aided diagnosis systems. There is different and large number of techniques on this area, however it is still having an areas which needs more research. In the future, the authors aim to develop more accurate automated segmentation techniques. The quick progress in radiological imaging systems lead to increase in volume patient images. Based on that, image processing in radiological diagnostic systems will require more fast segmentation algorithms. Developing parallel algorithms is one of the ways of achieving faster segmentation results. Cronemeyer is one of the people who relied on the exploitation of the nature of parallel hardware to achieve faster skeleton algorithm. Also from other approaches which achieve faster segmentation is neural network-based approaches because of their parallel nature. Also multi-scale approach is considered as faster segmentation approach because it can extract major structures in low resolution images and fine structures in high resolution images. The authors proposed a survey of current vessel segmentation algorithms. The authors tried to cover both old and new researches related to vessel segmentation approaches and techniques. The authors aimed to introduce the current vessel segmentation methods and also to give the researcher a base line and a framework for the existing research.

REFERENCES

- Al-Diri, B., Hunter, A., & Steel, D. (2009). An active contour model for segmenting and measuring retinal vessels. *IEEE Transactions on Medical Imaging*, 28(9), 1488–1497.
- Alonso-Montes, C., Vilarino, D., & Penedo, M. (2005). CNN-based automatic retinal vascular tree extraction. *Proceedings of the 2005 9th International Workshop on Cellular Neural Networks and their Applications* (pp. 61-64).
- Alonso-Montes, C., Vilario, D., Dudek, P., & Penedo, M. (2008). Fast retinal vessel tree extraction: A pixel parallel approach. *International Journal of Circuit Theory and Applications*, 36(5-6), 641–651. doi:10.1002/cta.512
- Amin, M., & Yan, H. (2011). High speed detection of retinal blood vessels in fundus image using phase congruency. *Soft Computing*, 15(6), 1217–1230. doi:10.1007/s00500-010-0574-2
- Anzalone, A., Bizzarri, F., Parodi, M., & Storace, M. (2008). A modular supervised algorithm for vessel segmentation in red-free retinal images. *Computers in Biology and Medicine*, 38(8), 913–922. doi:10.1016/j.compbiomed.2008.05.006 PMID:18619588
- Asad, A., Azar, A., & Hassanien, A. (2012). Integrated Features Based on Gray-Level and Hu Moment-Invariants with Ant Colony System for Retinal Blood Vessels Segmentation. *International Journal of Systems Biology and Biomedical Technologies*, 1(4), 61–74. doi:10.4018/ijssbt.2012100105
- Asad, A., Azar, A., & Hassanien, A. (2014). A New Heuristic Function of Ant Colony System for Retinal Vessel Segmentation. *International Journal of Rough Sets and Data Analysis*, 1(2), 14–31. doi:10.4018/ijrdsda.2014070102

- Bernardes, R., Serranho, P., & Lobo, C. (2011). Digital ocular fundus imaging: A review. *Ophthalmologica*, 226(4), 161–181. doi:10.1159/000329597 PMID:21952522
- Cassin, B., & Solomon, S. (1990a). Dictionary of Eye Terminology (2nd ed.). Gainesville, Florida: Triad Publishing Company.
- Cassin, B., & Solomon, S. (1990b). Dictionary of Eye Terminology (1st ed.). Gainesville, Florida: Triad Publishing Company.
- Castaldi, V., Fabiola, M., & River, F. (2010). A fast, efficient and automated method to extract vessels from fundus images. *Journal of Visualization*, 13(3), 263–270. doi:10.1007/s12650-010-0037-y
- Cinsdikici, M., & Aydin, D. (2009). Detection of blood vessels in ophthalmoscope images using MF/ant (matched filter/ant colony) algorithm. *Computer Methods and Programs in Biomedicine*, 96(2), 85–95. doi:10.1016/j.cmpb.2009.04.005 PMID:19419790
- Costantini, G., Casali, D., & Todisco, M. (2010). A hardware-implementable system for retinal vessel segmentation. *Proceedings of the 14th WSEAS international conference on Computers: part of the 14th WSEAS CSCC multiconference (Vol. 2, pp. 568-573)*.
- Deserno, T., & Thomas, M. (2010). Fundamentals of Biomedical Image Processing. In Biological and Medical Physics, Biomedical Engineering (pp. 1-51). Verlag, Berlin, Heidelberg: Springer. doi:10.1007/978-3-642-15816-2_1
- Emary, E., Zawbaa, H., Hassanien, A., Schaefer, G., & Azar, A. (2014). Retinal Blood Vessel Segmentation using Bee Colony Optimisation and Pattern Search. *Proceedings of the annual IEEE International Joint Conference on Neural Networks (IJCNN)*, Beijing, China (pp. 1001-1006).
- Emary, E., Zawbaa, H., Hassanien, A., Tolba, M., & Sansel, V. (2014). Retinal vessel segmentation based on flower pollination search algorithm. *Proceedings of the 5th International Conference on Innovations in Bio-Inspired Computing and Applications*, Ostrava, Czech Republic (pp. 93-100).
- Farnell, D., Hatfield, F., Knox, P., Reakes, M., Spencer, S., Parry, D., & Harding, S. P. (2008). Enhancement of blood vessels in digital fundus photographs via the application of multiscale line operators. *Journal of the Franklin Institute*, 345(8), 748–765. doi:10.1016/j.jfranklin.2008.04.009
- Fraz, M., Barman, S., Remagnino, P., Hoppe, A., Basit, A., Uyyanonvara, B., & Owen, C. G. et al. (2012a). An approach to localize the retinal blood vessels using bit planes and centerline detection. *Computer Methods and Programs in Biomedicine*, 108(2), 600–616. doi:10.1016/j.cmpb.2011.08.009 PMID:21963241
- Fraz, M., Remagnino, P., Hoppe, A., & Barman, S. (2013). Retinal image analysis aimed at extraction of vascular structure using linear discriminant classifier. *Proceedings of the International Conference on Computer Medical Applications*, Sousse, Tunisia. doi:10.1109/ICCMA.2013.6506180
- Fraz, M., Remagnino, P., Hoppe, A., Uyyanonvara, B., Rudnicka, A., Owen, C., & Barman, S. A. (2012b). An ensemble classification-based approach applied to retinal blood vessel segmentation. *IEEE Transactions on Bio-Medical Engineering*, 59(9), 2538–2548. doi:10.1109/TBME.2012.2205687 PMID:22736688

- Hassan, G., Elbendary, N., Hassanien, A., Shueb, A., & Snasel, V. (2015). Retinal Blood Vessel Segmentation Approach Based on Mathematical Morphology. *Procedia Computer Science*, 62, 612–622. doi:10.1016/j.procs.2015.09.005
- Hou, Y. (2014). Automatic Segmentation of Retinal Blood Vessels Based on Improved Multiscale Line Detection. *Journal of Computing Science and Engineering*, 8(2), 119–128. doi:10.5626/JCSE.2014.8.2.119
- Ibanez, L., Schroeder, W., Ng, L., & Cates, J. (2003, August 21). *The itk software guide*. Kitware, Inc.
- Jiang, X., & Mojon, D. (2003). Adaptive local thresholding by verification-based multithreshold probing with application to vessel detection in retinal images. *Pattern Analysis and Machine Intelligence. IEEE Transactions on*, 25(1), 131–137.
- Kande, G., Subbaiah, P., & Savithri, T. (2010). Unsupervised fuzzy based vessel segmentation in pathological digital fundus images. *Journal of Medical Systems*, 34(5), 849–858. doi:10.1007/s10916-009-9299-0 PMID:20703624
- Lam, B., Gao, Y., & Liew, A. (2010). General retinal vessel segmentation using regularization-based multiconcavity modeling. *IEEE Transactions on Medical Imaging*, 29(7), 1369–1381. doi:10.1109/TMI.2010.2043259 PMID:20304729
- Lam, B., & Yan, H. (2008). A novel vessel segmentation algorithm for pathological retina images based on the divergence of vector fields. *IEEE Transactions on Medical Imaging*, 27(2), 237–246.
- Läthén, G. (2010). *Segmentation Methods for Medical Image Analysis Blood vessels, multi-scale filtering and level set methods* [Thesis]. Center for Medical Image Science and Visualization (CMIV) Linköping University Institute of Technology, Sweden.
- Lee, Y., Lin, R., Sung, C., Yang, C., Chien, K., Chen, W., & Huang, Y.-C. et al. (2000). Chin-Shan Community Cardiovascular Cohort in Taiwan-baseline data and five-year follow-up morbidity and mortality. *Journal of Clinical Epidemiology*, 53(8), 838–846. doi:10.1016/S0895-4356(00)00198-0 PMID:10942867
- Manganaro, G., Arena, G., & Fortuna, L. (1999). *Cellular Neural Networks: Chaos, Complexity and VLSI Processing*. Springer-Verlag New York, Inc. doi:10.1007/978-3-642-60044-9
- Marin, D., Aquino, A., Gegundez-Arias, M., & Bra, J. (2011). A new supervised method for blood vessel segmentation in retinal images by using gray-level and moment invariants-based features. *IEEE Transactions on Medical Imaging*, 30(1), 146–158. doi:10.1109/TMI.2010.2064333 PMID:20699207
- Miri, M., & Mahloojifar, A. (2011). Retinal image analysis using curvelet transform and multistructure elements morphology by reconstruction. *IEEE Transactions on Biomedical Engineering*, 58(5), 1183–1192.
- Ng, J., Clay, S., Barman, S., & Feilde, A. (2010). Maximum likelihood estimation of vessel parameters from scale space analysis. *Image and Vision Computing*, 28(1), 55–63. doi:10.1016/j.imavis.2009.04.019
- Niemeijer, M., Staal, J., Van Ginneken, B., Loog, M., & Abramoff, M. D. (2004). Comparative study of retinal vessel segmentation methods on a new publicly available database. In *Medical Imaging 2004* (pp. 648–656). doi:10.1117/12.535349

- Palomera-perez, M., Martinez-Peez, M., Benitez-Perez, H., & Ortega-Arhona, J. (2010). Parallel multiscale feature extraction and region growing: Application in retinal blood vessel detection. *IEEE Transactions on Information Technology in Biomedicine*, 14(2), 500–506.
- Perfetti, R., Ricci, E., Casali, D., & Costantin, G. (2007). Cellular neural networks with virtual template expansion for retinal vessel segmentation. *IEEE Transactions on Circuits and Wystems. II, Express Briefs*, 54(2), 141–145. doi:10.1109/TCSII.2006.886244
- Ricci, E., & Perfetti, R. (2007). Retinal blood vessel segmentation using line operators and support vector classification. *IEEE Transactions on Medical Imaging*, 26(10), 1357–1365. doi:10.1109/TMI.2007.898551 PMID:17948726
- Roletschek, R. (2010, 12 7). Retrieved from Image Texture. Wikipedia. Retrieved from <http://en.wikipedia.org/wiki/File:2010-12-07-funduskamera-by-RalfR-02.jpg>
- Roska, T., & Chua, L. (1993). The CNN universal machine: an analogic array computer. *IEEE Transactions on Circuits and Systems II: Analog and Digital Signal Processing*, 40(3), 163–173.
- Roychowdhury, S., Koozekanani, D., & Parhi, K. (2014). Blood Vessel Segmentation of Fundus Images by major Vessel Extraction and Sub-Image Classification. *IEEE Journal of Biomedical and Health Informatics*, 19(3), 2168–2194.
- Saine, P. (2011). Fundus Imaging. *Ophthalmic photographers Socity OPS*. Retrieved from <http://www.opsweb.org/page/fundusimaging>
- Serra, J. (1982). *Image analysis and mathematical morphology* (1st ed.). Academic press.
- Soares, J., Leandro, J., Cesar, R., Jelinek, H., & Cree, M. (2006). Retinal vessel segmentation using the 2-D Gabor wavelet and supervised classification. *IEEE Transactions on Medical Imaging*, 25(9), 1214–1222. doi:10.1109/TMI.2006.879967 PMID:16967806
- Sreejini, K., & Govindan, V. (2015). Improved multiscale matched filter for retina vessel segmentation using PSO algorithm. *Egyptian Informatics Journal*, 16(3), 253–260. doi:10.1016/j.eij.2015.06.004
- Staal, J., Abramoff, M., Niemeijer, M., Viergever, M., & Van Ginneken, B. (2004). Ridge-based vessel segmentation in color images of the retina. *IEEE Transactions on Medical Imaging*, 23(4), 501–509. doi:10.1109/TMI.2004.825627 PMID:15084075
- Sun, K., Chen, Z., Jiang, S., & Wang, Y. (2011). Morphological multiscale enhancement, fuzzy filter and watershed for vascular tree extraction in angiogram. *Journal of Medical Systems*, 35(5), 811–824. doi:10.1007/s10916-010-9466-3 PMID:20703728
- Terzopoulos, D. (1984). *Multiresolution Computation of Visible-Surface Representation*. Massachusetts Institute of Technology. Dept. of Electrical Engineering and Computer Science. Massachusetts Institute of Technology.
- Vermeer, K., Vos, F., Lemij, H., & Vossepoel, A. (2004). A model based method for retinal blood vessel detection. *Computers in Biology and Medicine*, 34(3), 209–219. doi:10.1016/S0010-4825(03)00055-6 PMID:15047433

Vlachos, M., & Dermatas, E. (2010). Multi-scale retinal vessel segmentation using line tracking. *Computerized Medical Imaging and Graphics*, 34(3), 213–227. doi:10.1016/j.compmedimag.2009.09.006 PMID:19892522

Yang, Y., Huang, S., & Rao, N. (2008). An automatic hybrid method for retinal blood vessel extraction. *International Journal of Applied Mathematics and Computer Science*, 18(3), 399–407. doi:10.2478/v10006-008-0036-5

Zhang, B., Zhang, L., Zhang, L., & Karray, F. (2010). Retinal vessel extraction by matched filter with first-order derivative of Gaussian. *Computers in Biology and Medicine*, 40(4), 438–445. doi:10.1016/j.compbiomed.2010.02.008 PMID:20202631

Zhang, J., Cui, Y., Jiang, W., & Wang, L. (2015). Blood Vessel Segmentation of Retinal Images Based on Neural Network. In *Image and Graphics, LNCS* (Vol. 9218, pp. 11–17). Springer International Publishing. doi:10.1007/978-3-319-21963-9_2

KEY TERMS AND DEFINITIONS

Blood Vessel: A tubular channel that is characterized as flexible like a vein, an artery, and a capillary, and the blood passes through it to the eye.

Blood Vessel Extraction: An automatic processing step to extract vessels away from image to investigate the existence on some disease.

Hemorrhages: Secretions and ample blood as a result of a ruptured blood vessel.

Lesions: A pathologic change in the tissues and individual points of multifocal disease.

Macular Degeneration: A disease happened in the eye, especially destroys the macula and causes blindness because it effects on the center of vision.

Magnetic Resonance Imaging: A method which used to obtain images of the interiors of objects, as humans and animals, it uses radio-frequency waves on its caption.

Neural Network: A Deep learning technology depends on simulating the nature of brain to solve pattern recognition problems.

This research was previously published in the Handbook of Research on Machine Learning Innovations and Trends edited by Aboul Ella Hassanien and Tarek Gaber, pages 187-203, copyright year 2017 by Information Science Reference (an imprint of IGI Global).

Chapter 2

Automatic Detection of Blood Vessel in Retinal Images Using Vesselness Enhancement Filter and Adaptive Thresholding

Abderrahmane Elbalaoui

Sultan Moulay Slimane University, Beni Mellal, Morocco

Mohamed Fakir

Sultan Moulay Slimane University, Beni Mellal, Morocco

Taifi khaddouj

Sultan Moulay Slimane University, Beni Mellal, Morocco

Abdelkarim MERBOUHA

Sultan Moulay Slimane University, Beni Mellal, Morocco

ABSTRACT

Retinal blood vessels detection and measurement of morphological attributes, such as length, width, sinuosity and corners are very much important for the diagnosis and treatment of different ocular diseases including diabetic retinopathy (DR), glaucoma, and hypertension. This paper presents a integration method for blood vessels detection in fundus retinal images. The proposed method consists of two main steps. The first step is pre-processing of retinal image to improve the retinal images by evaluation of several image enhancement techniques. The second step is vessels detection, the vesselness filter is usually used to enhance the blood vessels. The enhancement filter is designed from the adaptive thresholding of the output of the vesselness filter for vessels detection. The algorithms performance is compared and analyzed on three publicly available databases (DRIVE, STARE and CHASE_DB) of retinal images using a number of measures, which include accuracy, sensitivity, and specificity.

DOI: 10.4018/978-1-5225-5195-9.ch002

1. INTRODUCTION

A new study finds that certain morphological changes of the retinal blood vessels in retinal images are important indicators for diseases like diabetes, hypertension and glaucoma. However, the length, width, diameter of the blood vessels may change as indications of various ophthalmologic diseases (Mendonça, 2006). For example, vessel occlusion that makes veins longer, abnormal narrowing of retinal blood vessels may indicate the earlier stages of glaucoma or DR that creates new blood vessels (neovascularization) which are tiny, thin, fragile and abnormal in nature and cause frequent minor bleeding that may lead to permanent vision loss (Gonzalez, 2014). Automatic extraction of retinal blood vessels is very important for the diagnosis and the treatment of different diseases such as hypertension (Leung, 2003), obesity, glaucoma (Wang, 2006) and diabetic retinopathy (Morello, 2007). Diabetic retinopathy is an increasingly growing public health problem and the leading cause of blindness in the world (Elbalaoui, 2014). In all cases, correct detection of retinal blood vessel is crucial. In most of the retinal screening programs, blood vessels are extracted manually. Figure 1 shows the eyeball structure and retinal image captured through a retinal imaging device.

Many methods can be found in the literature for segmentation of blood vessels, which can be divided into the following major categories: supervised and unsupervised methods.

Supervised methods require a feature vector for each pixel and manually labeled images in order to discriminate between vessel and non-vessel pixels. Soares et al. (Soares, 2006) used a Bayesian classifier with class-conditional probability density functions (likelihoods) described as Gaussian mixtures, yielding a classification to model complex decision surfaces. The probability distributions are estimated based on training set of labeled pixels obtained from manual segmentations. Xu et al. (Xu, 2011) proposed a method to segment retinal blood vessels to overcome the variations in contrast of large and thin vessels. This method uses adaptive local thresholding to produce a binary image then extract large connected components as large vessels. The residual fragments in the binary image including some thin vessel segments (or pixels), are classified by Support Vector Machine (SVM). The tracking growth is applied to the thin vessel segments to form the whole vascular network. Fraz et al. (Fraz, 2012) employed a classification system based on an ensemble of bagged and boosted decision trees and utilizes a feature vector based on the orientation analysis of gradient vector field, morphological transformation, line strength measures, and Gabor filter responses. Marin et al. (Marin, 2011) used a neural network (NN) scheme for pixel classification and computes a 7-D vector composed of gray-level and moment invariants-based features for pixel representation.

Unsupervised methods in the literature comprise the matched filter responses, grouping of edge pixels, adaptive thresholding, vessel tracking and morphology based techniques. Mendonça et al. (Mendonça, 2006) proposed an algorithm starts with the extraction of vessel centerlines, which are used as guidelines for the subsequent vessel filling phase. For this purpose, the outputs of four directional differential operators are processed in order to select connected sets of candidate points to be further classified as centerline pixels using vessel derived features.

The final segmentation is obtained using an iterative region growing method that integrates the contents of several binary images resulting from vessel width dependent morphological filters. Gonzalez et al. (Gonzalez, 2014) presented a method to segment blood vessels and optic disk in the fundus retinal images. The method takes as first step the extraction of the retina vascular tree using the graph cut technique. The blood vessel information is then used to estimate the location of the optic disk. The optic disk segmentation is performed using two alternative methods. The Markov random field (MRF)

Figure 1. (a) Anatomy of the eye, (b) Fundus image

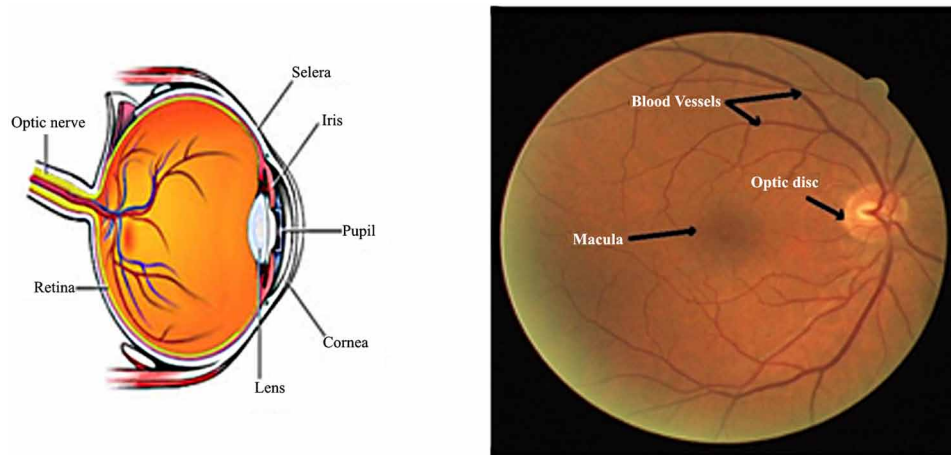


image reconstruction method segments the optic disk by removing vessels from the optic disk region, and the compensation factor method segments the optic disk using the prior local intensity knowledge of the vessels. R.M. Rangayyan et al. (Rangayyan, 2008) proposed a Model based also include the use of directionally sensitive Gabor filters with tunable scale and elongation parameters. Al-Rawi et al. (Al-Rawi, 2007) used the matched filter response to the detection of blood vessels is increased by proposing better filter parameters. These filter parameters are found by using an optimization procedure on 20 retina images of the DRIVE database. Lam et al. (Lam, 2010) proposed a multiconcavity modeling approach with differentiable concavity measure to handle both healthy and unhealthy retinal images simultaneously and handle bright lesions in a perceptive space. These concavity measures are combined together according to their statistical distributions to detect vessels in general retinal images. Martinez-Pérez et al. (Martinez-Pérez, 2007) proposed a method based on multiscale analysis to obtain vessels widths, lengths and orientations information. The local maxima over scales of the magnitude of the gradient and the maximum principal curvature of the Hessian tensor are used in a multiple pass region growing procedure. The growth progressively segments the blood vessels using feature information together with spatial information. Azzopardi et al. (Azzopardi, 2015) proposed a filter that selectively responds to vessels and which he called B-COSFIRE with B standing for bar which is an abstraction for a vessel. It is based on the existing COSFIRE (Combination Of Shifted Filter Responses) approach. A B-COSFIRE filter achieves orientation selectivity by computing the weighted geometric mean of the output of a pool of Difference-of-Gaussians filters, whose supports are aligned in a collinear manner.

The rest of the paper is organized as follows: in Section 2 we explain the proposed method and implementation details are presented to detect blood vessels. We provide the results and discussion in Section 3. Finally, we conclude the paper in Section 4.

2. METHODOLOGY

Actually, automatic detection of the blood vessels in retinal images is a challenging task. The bloc diagram of proposed method is shown in Figure 2, consists of two phases, namely (1) preprocessing and (2) vessels Detection.

2.1. Datasets

In this work, extensive experimentations are performed on all three publicly available retinal image databases, namely, DRIVE, STARE and CHASE for evaluation of the proposed methods which will be explained in this section.

2.1.1. DRIVE Database

DRIVE (Digital Retinal Images for Vessel Extraction) database, consists of 40 color images, 33 do not show any sign of diabetic retinopathy and 7 show signs of mild early diabetic retinopathy, these images are of size 565×584 pixels, with a field of view of 45° and an approximate spatial resolution of 20 µm/pixel (Staal, 2004).

2.1.2. STARE Database

STARE (STructured Analysis of the Retina) dataset, contains 81 fundus images, 31 images of healthy retinas and 50 images of retinas with disease, and subsequently digitized at 605×700 pixels in resolution, 24 bits per pixel (standard RGB) (Hoover, 2000).

2.1.3. CHASE_DB1 Database

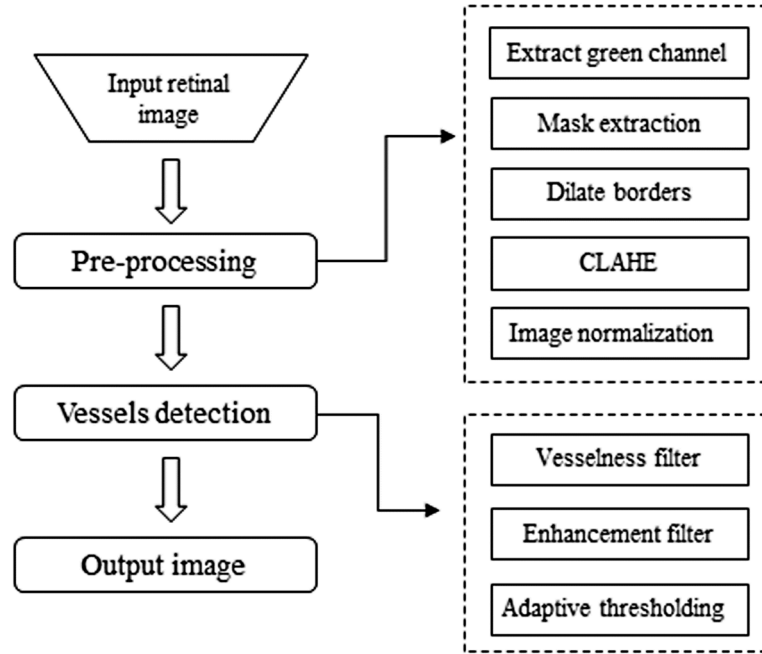
CHASE_DB1 data set contains 28 colour images of retinal fundus from 14 patients in the program Child Heart and Health Study in England. The images were captured at 30 field of view a resolution of 1280x960 pixels (Owen, 2010).

2.2. Preprocessing

Before segmentation of blood vessels, the first attempt is at improving the retinal images by evaluation of several image enhancement techniques. Image enhancement is an important step in this method since the contrast of blood vessels in the retinal images are initially very low.

According to red, green, and blue histogram shown in Figure 3, green channel exhibits the best contrast between the vessels and background while the red and blue ones tend to be more noise. So we work on the gray image from green channel and the retinal blood vessels appear darker in the gray image and invert it to appear the vessels brighter than non-vessel background. Next, the Contrast-Limited Adaptive Histogram Equalization (CLAHE) is used because it can increase the contrast between contours (El-balaoui, 2016). When enhancing the contrast of images, the two factors must be considered to complete the task, because of their speed and efficiency. The technique has been utilized in the spatial domain.

Figure 2. Blood vessel detection



Normalizing the image based on its size takes the following course: first, the size of the processed image is determined. Then the enhancement variable (S) is computed using the subsequent equation:

$$S = \frac{\sum_{i=1}^n \sum_{j=1}^m I(i, j)}{m * n} \quad (1)$$

where I is the original image and (n*m) is the size of image. Finally, the image is enhanced using the following equation:

$$C = \frac{(I - \min(I))e^S}{\max(I) - \min(I)} \quad (2)$$

where I is the original image, (min, max) are the minimum and maximum pixel values of the processed image, (S) is the enhancement variable, and (C) is the contrast improved image. Thereby blood vessels are brighter than the background after normalization. In Figure 4, we illustrate all the preprocessing steps.

2.3. Vessel Detection

Frangi et al. (Frangi, 1998) designed a multiscale algorithm for identifying vascular structures by studying the eigenvalues of the hessian matrix after convolving the image with a Gaussian kernel which can be defined by equation (3).

Figure 3. (a) Original RGB retinal image, (b) Red, green, and blue histogram of the (a)

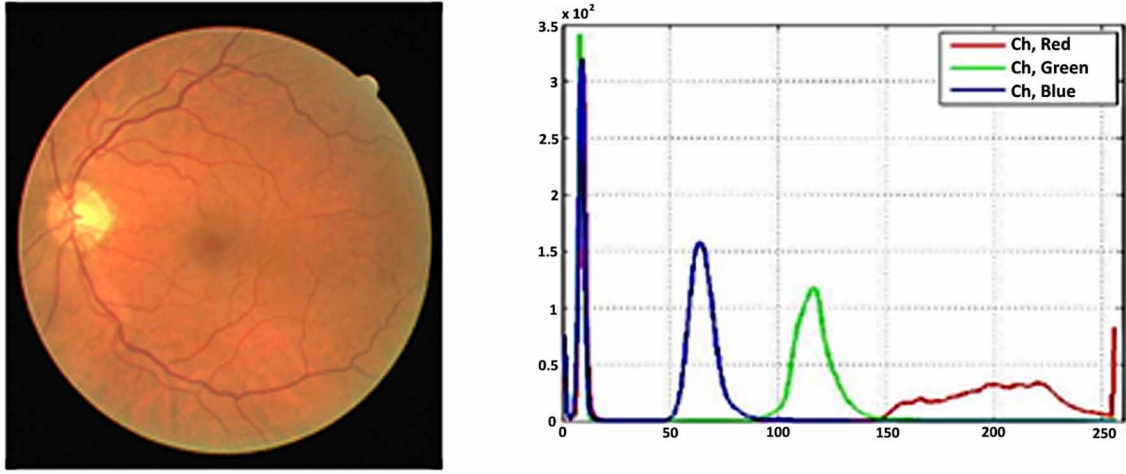
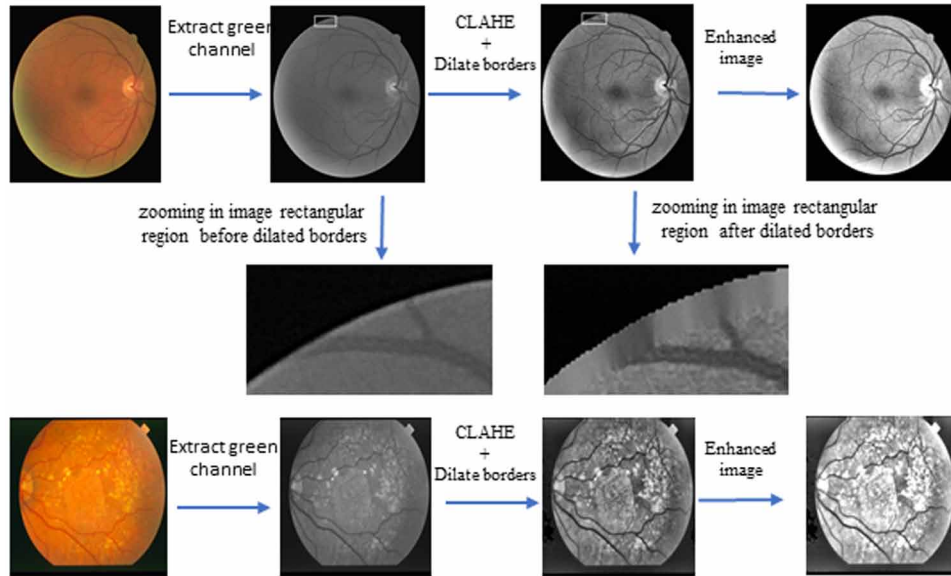


Figure 4. Preprocessing steps. (a) Original RGB retinal image (DRIVE and STARE dataset). (b) Extract green Channel. (c) Image after CLAHE and dilate borders. (d) Enhanced image (e) zooming in rectangular region before dilate borders. (f) Zooming in rectangular region after dilated borders.



$$G_{2D}(x, y) = \frac{1}{2\pi\sigma^2} e^{-\frac{x^2+y^2}{2\sigma^2}} \quad (3)$$

where σ is the standard deviation of the Gaussian distribution.

It is known from differential geometry that the second order derivatives of an image can be geometrically interpreted by evaluating the eigenvalues at each point. The Hessian matrix $H(x, y)$ for a volume $I(x, y)$ is given by:

$$H(x, y) = \begin{bmatrix} h_{xx} & h_{xy} \\ h_{yx} & h_{yy} \end{bmatrix} \quad (4)$$

The elements of the Hessian matrix are expressed as:

$$h_{yy} = I(x, y) \odot \frac{\partial^2 G_{2D}(x, y)}{\partial^2 y} \quad (5)$$

$$h_{xx} = I(x, y) \odot \frac{\partial^2 G_{2D}(x, y)}{\partial^2 x} \quad (6)$$

$$h_{xy} = h_{yx} = I(x, y) \odot \frac{\partial^2 G_{2D}(x, y)}{\partial x \partial y} \quad (7)$$

where \odot is the convolution operator.

The Hessian matrix is used to obtain vessel features that have two eigenvalues λ_1 and λ_2 in a 2D image. In this study, a dark vessel structure in a bright background has a high positive eigenvalue λ_2 and a low eigenvalue λ_1 . For a vessel structure in a 2D image, the condition can be regarded as $|\lambda_2| > |\lambda_1|$ and $|\lambda_1| \approx 0$. The higher positive eigenvalue λ_2 is used as our vessel feature.

The symbols λ_1 and λ_2 are determined by the relations between vessels object and the background: When the vessels bright and the background are dark, the two eigenvalues are negative and they are positive for the opposite condition. Typically, blood vessels are bright whereas the background is dark in retinal images. The 2D vesselness function defined in traditional Hessian multiscale filtering:

$$\Gamma(\lambda) = \begin{cases} 0 & \text{if } \lambda_2 > 0 \\ \frac{-R^2}{(e^{2\beta^2})} \left(1 - e^{\frac{-S^2}{2c^2}} \right) & \text{otherwise} \end{cases} \quad (8)$$

where: $R = \frac{|\lambda_1|}{|\lambda_2|}$, $S = \sqrt{\lambda_1^2 + \lambda_2^2}$, and the values of β & c are chosen manually, in our case: $\beta = 0.5$, $c=15$.

The value of $\Gamma(\lambda)$ is between 0 and 1. If a pixel belongs to a vessel structure, the value of the vesselness function is closed to 1. Otherwise, it is closed to 0. In this way, the vascular structure can be enhanced.

The improved Hessian multiscale enhancement filter, which combines the global grayscale information with the local geometric features. This improved filter can effectively reduce the number of the pseudo vessel structures and isolated noise points in the process of blood vessel enhancement. Therefore, the gray scale factor K added to Hessian multiscale filter is defined by:

$$K = \frac{1}{2} + \frac{1}{\pi} \arctan(\alpha X) \quad (9)$$

$$X = \frac{I(x, y) - Th}{\max(I(x, y))} \quad (10)$$

where $\alpha = 2$ is the smoothness factor of K . The parameter Th is a global adaptive threshold to determine whether $I(x, y)$ is the vessel or not.

The threshold techniques, which make decisions based on local pixel information, are effective when the intensity levels of the objects fall squarely outside the range of levels in the background. Thresholding is a pixel classification process to identify the pixels of a given image into two classes: those pertaining to objects and those pertaining to background. Firstly, it calculates the average image gray value; then, it is used to segment the original image into foreground and background. This is represented by a mathematical expression as follows.

$$Th = \frac{\sum_{j=0}^{n-1} f_j \cdot j}{2 \sum_{j=0}^{n-1} f_j} \quad (11)$$

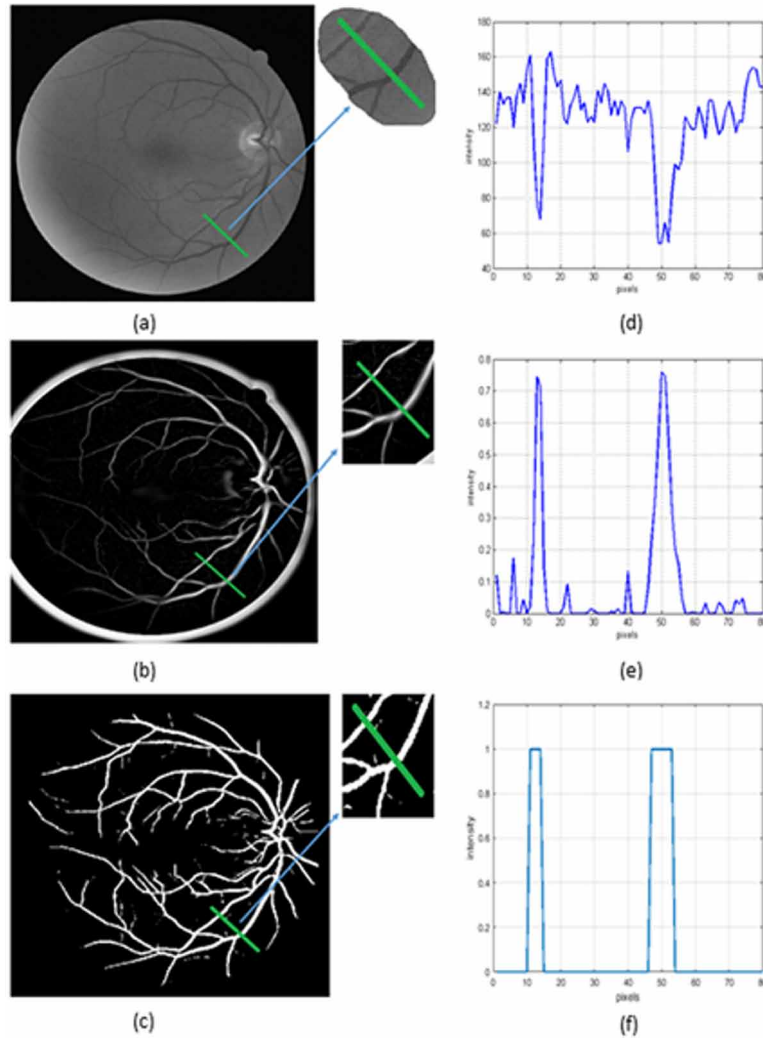
where L is the number of gray scales, and f_j is the number of pixels with gray j .

The improved Hessian enhancement filtering is represented as shown in the flowing equation:

$$\Gamma(\lambda) = \begin{cases} 0 & \text{if } \lambda_2 > 0 \\ e^{\frac{-R^2}{2\beta^2}} \left(1 - e^{\frac{-S^2}{2c^2}} \right) & \text{otherwise} \end{cases} \cdot K \quad (12)$$

Figure 5(a) is the amplified fragment of the original retinal image in the green channel containing thin vessels. Figure 5(b) and (c) is the enhanced results of Figure 5(a) using the Vesselness filter and Hessian multiscale enhancement filter, respectively. To further compare to the enhanced performance between the above two steps, 1D cross sections is plotted for the intensity difference between the gray scale value of each pixel of the middle rows (green lines in Figure 5(a)) and the minimal gray scale value of the correspond in grow.

Figure 5. Comparison of the different steps for vessel enhancement: (a) original image DRIVE database. (b) output of vesselness filter, (c) final output. (d), (e) and (f) the intensity distribution of a cross section marked in (a), (b) and (c) respectively.



3. RESULTS AND DISCUSSIONS

In this work, extensive experimentations are performed on all three publicly available retinal image databases, namely, DRIVE, STARE and CHASE. Thorough qualitative as well as quantitative comparisons are done (Figure 6).

In the retinal blood vessels detection process, the outcome is a pixel-based classification result. Any pixel is classified either as vessel or non-vessel. Then, every resulting binary image is compared to the corresponding ground truth by computing the following four performance measurements: the pixels that belong to a vessel in the ground truth image and that are classified as vessels are counted as true positives (TP), otherwise they are counted as false negatives (FN). The pixels that belong to the background

Automatic Detection of Blood Vessel in Retinal Images

Figure 6. Performance measures on images from (a) DRIVE database, (b) STARE database and (c) CHASE_DB1 database

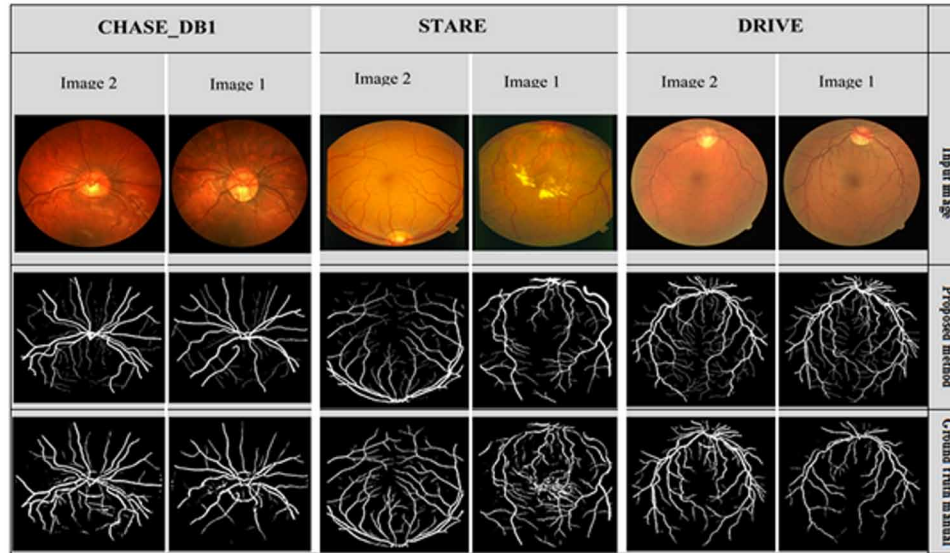


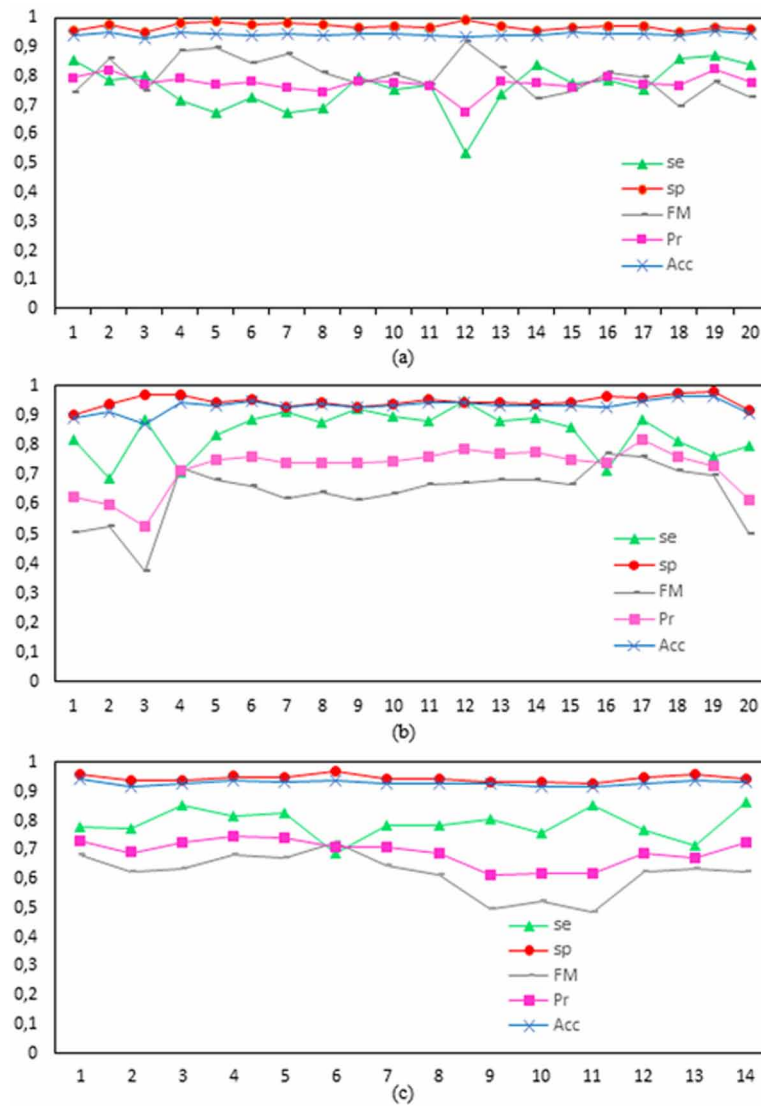
Table 1. Performance parameters for retinal blood vessel

Sensitivity	$\frac{TP}{TP + FN}$
Specificity	$\frac{TN}{TN + FP}$
Accuracy	$\frac{TP + TN}{TP + TN + FP + FN}$
Precision	$\frac{TP}{TP + FP}$
F-measure	$\frac{2*TP}{2*TP + FN + FP}$

and that are classified as non-vessels, are counted as true negatives (TN), otherwise they are counted as false positives (FP).

In order to compare the performance of the proposed method with other state-of-the-art algorithms, we compute the sensitivity (Se), specificity (Sp), accuracy (Acc), precision (Pr) and F-measure (Fm). Table 1 summaries the performance parameters used by retinal vessel detection algorithms. Figure 7 illustrated the plot of selected performance measures for every image in the DRIVE, STARE and CHASE_DB1 databases. In Figure 6, two images from the DRIVE, two from the STARE and two from CHASE_DB1

Figure 7. Results of the proposed method for DRIVE, STARE and CHABE_DB1 databases



datasets are shown along with the results of the proposed vessel detection method and the manually segmented images from the human observer which is considered as the ground truth.

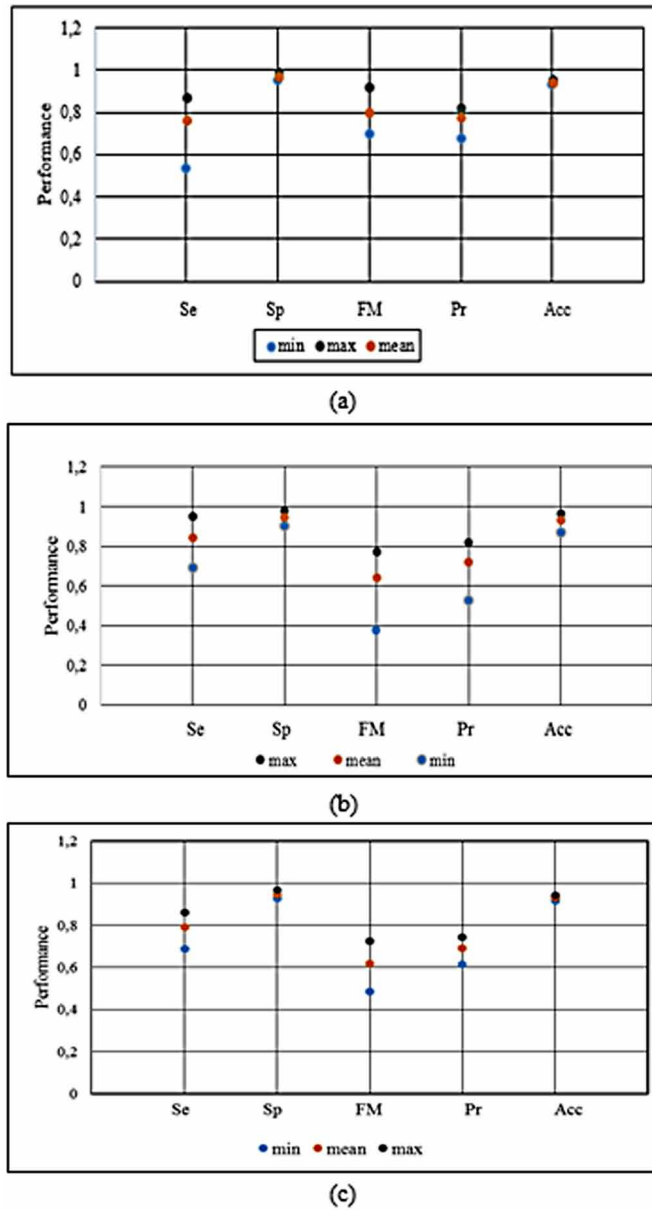
The proposed method achieved an average accuracy of $(94.43 \pm 0.14)\%$ on DRIVE dataset, $(93.26 \pm 4.53)\%$ on STARE dataset and $(92.98 \pm 0.21)\%$ on CHASE_DB1 dataset is illustrated in Figure 8.

Using the manual labeled set as a reference, Se, Sp and the average accuracy are (DRIVE: Se=0.7630, Sp=0.9764 and Acc=0.9463), (STARE: Se=0.8440, Sp=0.9476 and Acc=0.9326) and (CHASE_DB1: Se=0.7896, Sp=0.9455 and Acc=0.9298). For comparison purpose, the performance results that have been achieved on the test set of each of the databases are better than many state-of-the-art unsupervised and supervised algorithms are shown in Tables 2, 3 and 4.

A receiver operating characteristic (ROC) curve plots the fraction of vessel pixels correctly classified as vessel, namely the TPR), versus the fraction of non-vessel pixels wrongly classified as vessel,

Automatic Detection of Blood Vessel in Retinal Images

Figure 8. Summary of performance parameters for proposed method: (a) performance evaluation for DRIVE dataset, (b) performance evaluation for STARE dataset and (c) performance evaluation for CHASE_DB1 dataset.



namely the FPR). The closer the curve approaches the top left corner; the better is the performance of the system. The most frequently used performance measure extracted from the ROC curve is the value of the area under the curve (AUC) which is 1 for an optimal system. For retinal images, the TPR and FPR are computed considering only pixels inside the FOV (Fawcett, 2006).

Table 2. Performance comparison of vessel segmentation methods on DRIVE images

DRIVE	Method	Se	Sp	Acc
Supervised methods	Soares et al. (2006)	0.7332	0.9782	0.9466
	Xu et al.	0.7760	-	0.9328
	Fraz et al. (2012)	0.7406	0.9807	0.9480
	Marin et al. (2011)	0.7067	0.9801	0.9452
Unsupervised methods	Mendonça et al. (2006)	0.7344	0.9764	0.9463
	Gonzalez et al. 2014	0.7512	0.9684	0.9412
	Rangayyan et al.	-	-	-
	Al-Rawi et al. (2007)	-	-	0.9510
	Martinez-Pérez et al. (2007)	0.7246	0.9655	0.9344
	Lam et al. (2010)	-	-	0.9472
	Azzopardi at al. (2014)	0.7655	0.9704	0.9442
	Proposed method	0.7630	0.9713	0.9443

Table 3. Performance comparison of vessel segmentation methods on STARE images

STARE	Method	Se	Sp	Acc
Supervised methods	Soares et al. (2006)	-	-	0.9516
	Xu et al. (2010)	-	-	-
	Fraz et al. (2012)	0.7548	0.9763	0.9534
	Marin et al. (2011)	0.6944	0.9801	0.9452
Unsupervised methods	Mendonça et al. (2006)	0.6966	0.9730	0.9479
	Gonzalez et al. (2014)	0.7887	0.9633	0.9441
	Rangayyan et al. (2008)	-	-	-
	Al-Rawi et al. (2007)	-	-	0.9090
	Martinez-Pérez et al. (2007)	0.7506	0.9569	0.9410
	Lam et al. (2010)	-	-	0.9567
	Azzopardi at al. (2014)	0.7716	0.9701	0.9497
	Proposed method	0.8440	0.9476	0.9326

Table 4. Performance comparison of vessel segmentation methods on CHASE_DB1 images

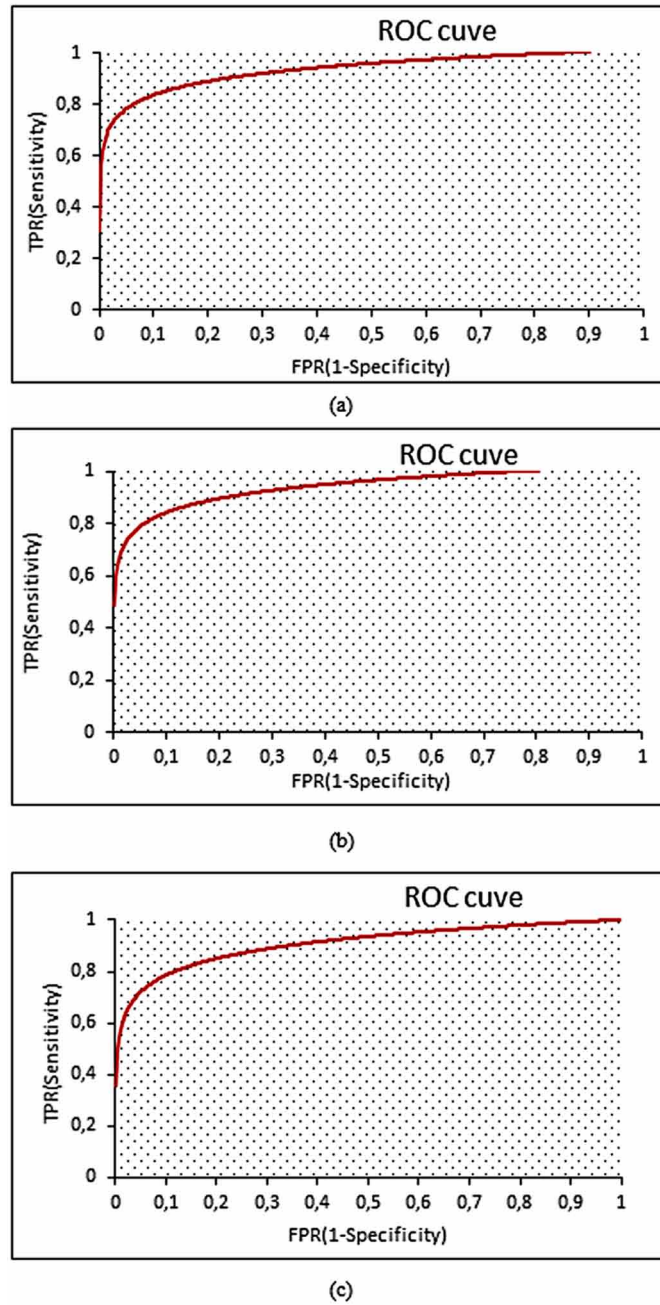
CHASE_DB1	Method	Se	Sp	Acc
Supervised methods	Fraz et al. (2012)	0.7224	0.9711	0.9469
Unsupervised methods	Azzopardi at al. (2014)	0.7585	0.9587	0.9387
	Proposed method	0.7896	0.9455	0.9298

Therefore, to justify the effectiveness of proposed approach, the ROC curve is plotted by using the TPR and FPR for both the DRIVE, STARE and CHASE_DB1 database as shown in Figure 9 (a), (b) and (c) respectively.

4. CONCLUSION

In this paper, we presented an integrated method for detection of retinal blood vessels. This technique tested on the DRIVE, STARE and CHASE_DB1 databases. The results that been achieved on three benchmark data sets, (DRIVE: Se = 0.7630, Sp = 0.9713; STARE: Se = 0.8440, Sp = 0.9476. CHASE_DB1: Se =

Figure 9. ROC curve for (a) DRIVE, (b) STRAE and (c) CHASE_DB1



0.7896, $Sp = 0.9455$) are higher than many of the state-of-the-art methods. Compared to the approaches by other researchers, our algorithm for detection of blood vessels has the advantage that it is applicable to all types of retinal images, healthy as well as abnormal.

REFERENCES

- Al-Rawi, M., Qutaishat, M., & Arrar, M. (2007). An improved matched filter for blood vessel detection of digital retinal images. *Computers in Biology and Medicine*, 37(2), 262–267. doi:10.1016/j.compbiomed.2006.03.003 PMID:16697363
- Azzopardi, G., Strisciuglio, N., Vento, M., & Petkov, N. (2015). Trainable COSFIRE filters for vessel delineation with application to retinal images. *Med. Image Anal.*, 19(1), 46–57.
- Elbalaoui, A., Boutaounte, M., Faouzi, H., Fakir, M., & Merbouha, A. (2014). Segmentation and detection of diabetic retinopathy exudates. *Proceedings of the 2014 International Conference on Multimedia Computing and Systems (ICMCS)*, Marrakech (pp. 171–178). doi:10.1109/ICMCS.2014.6911368
- Elbalaoui, A., & Mohamed Fakir, M. (2015). Boutaounte and A. Merbouha. “Automatic Localization of the Optic Disc Center in Retinal Images based on Angle Detection in Curvature Scale Space. *Journal of Electronic Commerce in Organizations*, 13(2), 1–13. doi:10.4018/JECO.2015040101
- Fawcett, T. (2006). An introduction to roc analysis. *Pattern Recognition Letters*, 27(8), 861–874. doi:10.1016/j.patrec.2005.10.010
- Frangi, A. F., Niessen, W. J., Vincken, K. L., & Viergever, M. A. (1998). Multiscale vessel enhancement filtering. *Proceedings of Medical Image Computing and Computer-Assisted Interventions MICCAI '98*, LNCS (Vol. 1496, pp. 130–137). Berlin, Germany: Springer-Verlag. doi:10.1007/BFb0056195
- Fraz, M., Remagnino, P., Hoppe, A., Uyyanonvara, B., Rudnicka, B., Owen, C., & Barman, S. (2012). An ensemble classification-based approach applied to retinal blood vessel segmentation. *IEEE Transactions on Bio-Medical Engineering*, 59(9), 2538–2548. doi:10.1109/TBME.2012.2205687 PMID:22736688
- Hoover, A., Kouznetsova, V., & Goldbaum, M. (2000, March). Locating blood vessels in retinal images by piecewise threshold probing of a matched filter response. *IEEE Transactions on Medical Imaging*, 19(3), 203–210. doi:10.1109/42.845178 PMID:10875704
- Lam, B., Gao, Y., & Liew, A.C. (2010). General retinal vessel segmentation using regularization-based multiconcavity modeling. *IEEE Trans. Med. Imag.*, 29(7), 1369–1381.
- Leung, H., Wang, J. J., Rochtchina, E., Wong, T. Y., Klein, R., & Mitchell, P. (2003). Impact of current and past blood pressure on retinal arteriolar diameter in older population. *Journal of Hypertension*, 2003, 1543–1549.
- Marin, D., Aquino, A., Emilio Gegundez-Arias, M., & Manuel Bravo, J. (2011). A new supervised method for blood vessel segmentation in retinal images by using gray-level and moment invariants-based features. *IEEE Transactions on Medical Imaging*, 30(1), 146–158. doi:10.1109/TMI.2010.2064333 PMID:20699207
- Martinez-Pérez, M. E., Hughes, A. D., Thom, S. A., Bharath, A. A., & Parker, K. H. (2007). Segmentation of blood vessels from red-free and fluorescein retinal images. *Medical Image Analysis*, 11(1), 47–61. doi:10.1016/j.media.2006.11.004 PMID:17204445

- Mendonca, A. M., & Campilho, A. (2006). Segmentation of retinal blood vessels by combining the detection of centerlines and morphological reconstruction. *IEEE Transactions on Medical Imaging*, 25(9), 1200–1213. doi:10.1109/TMI.2006.879955 PMID:16967805
- Morello, C. M. (2007). Etiology and natural history of diabetic retinopathy: An overview. (2007). *American Journal of Health-System Pharmacy*, 64(17, Suppl. 12), S3–S7. doi:10.2146/ajhp070330 PMID:17720892
- Owen, C. G., Rudnicka, A. R., Mullen, R., Barman, S. A., Monekosso, D., Whincup, P. H., & Paterson, C. et al. (2009). Measuring retinal vessel tortuosity in 10-year-old children: Validation of the computer-assisted image analysis of the retina (CAIAR) program. *Investigative Ophthalmology & Visual Science*, 50(5), 2004–2010. doi:10.1167/iops.08-3018 PMID:19324866
- Rangayyan, R. M., Ayres, F. J., Oloumi, F., & Eshghzadeh-Zanjani, P. (2008). Detection of blood vessels in the retina with multiscale gabor filters. *Journal of Electronic Imaging*, 17(2), 023018. doi:10.1117/1.2907209
- Salazar-Gonzalez, A., Kaba, D., Yongmin, L., & Xiaohui, L. (2014). Segmentation of the Blood Vessels and Optic Disk in Retinal Images,” *IEEE J. Biomedical and Health Informatics*, 18(6), 1874–1886. doi:10.1109/JBHI.2014.2302749 PMID:25265617
- Soares, J. V., Leandro, J. J., Cesar, R. M., Jelinek, H. F., & Cree, M. J. (2006, September). Retinal vessel segmentation using the 2-D gabor wavelet and supervised classification. *IEEE Transactions on Medical Imaging*, 25(9), 1214–1222. doi:10.1109/TMI.2006.879967 PMID:16967806
- Staal, J. J., Abramoff, M. D., Niemeijer, M., Viergever, M. A., & van Ginneken, B. (2004). Ridge based vessel segmentation in color images of the retina. *IEEE Transactions on Medical Imaging*, 23(4), 501–509. doi:10.1109/TMI.2004.825627 PMID:15084075
- Wang, J. J., Taylor, B., Wong, T. Y., Chua, B., Rochtchina, E., Klein, R., & Mitchell, P. (2006). Retinal vessel diameters and obesity: A population- based study in older persons. *Obesity Research*, 14(2), 206–214. doi:10.1038/oby.2006.27 PMID:16571845
- Xu, L., & Luo, S. (2010). A novel method for blood vessel detection from retinal images. *Biomedical Engineering Online*, 9(1), 14. doi:10.1186/1475-925X-9-14 PMID:20187975

Chapter 3

Bloodless Technique to Detect Diabetes using Soft Computational Tool

Puspalata Sah

Centre of Plasma Physics, Institute for Plasma Research, India

Kandarpa Kumar Sarma

Gauhati University, India

ABSTRACT

Detection of diabetes using bloodless technique is an important research issue in the area of machine learning and artificial intelligence (AI). Here we present the working of a system designed to detect the abnormality of the eye with pain and blood free method. The typical features for diabetic retinopathy (DR) are used along with certain soft computing techniques to design such a system. The essential components of DR are blood vessels, red lesions visible as microaneurysms, hemorrhages and whitish lesions i.e., lipid exudates and cotton wool spots. The chapter reports the use of a unique feature set derived from the retinal image of the eye. The feature set is applied to a Support Vector Machine (SVM) which provides the decision regarding the state of infection of the eye. The classification ability of the proposed system for blood vessel and exudate is 91.67% and for optic disc and microaneurysm is 83.33%.

INTRODUCTION

Diabetic retinopathy is the commonest cause of blindness and one of the commonest cause of vision defects in both developing and developed countries (Chaudhuri, Chatterjee, Katz, Nelson & Goldman, 1989). The World Health Organization (WHO) has estimated that, the number of adults with diabetes increasing alarmingly: from 135 million in 1995 to 300 million in 2025 (Premi, 2015). In India, this increases is expected to be greatest; 195 from 18 million in 1995 to 54 million in 2025. Studies done by the ICMR in the early 1970s had shown the prevalence of diabetes in India to be 2.5 and 1.5% in the rural population. However recent reports have shown the prevalence to be in the range of 12% to 14% in the

DOI: 10.4018/978-1-5225-5195-9.ch003

urban population. Of these patients with diabetes, over 20% are expected to be suffering from diabetic retinopathy. The prevalence of diabetes in the rural population is expected to be about 5%.

Diabetes is a disorder of metabolism. The energy required by the body is obtained from glucose which is produced as a result of food digestion (Chaudhuri, Chatterjee, Katz, Nelson & Goldman, 1989). Digested food enters the body stream with the aid of a hormone called insulin that is produced by the pancreas, an organ that lies near the stomach. During eating, the pancreas automatically produces the correct amount of insulin needed for allowing glucose absorption from the blood into the cells. In individuals with diabetes, the pancreas either produces too little or no insulin or the cells do not react properly to the insulin or the cells don't react properly to the insulin that is produced (Bevilacqua, Cambo, Cariello & Mastronardi, 2005). The buildup of glucose in the blood, overflows into the urine and then passes out of the body. Therefore, the body loses its main source of fuel even though the blood contains large amount of glucose. Basically there are three types of diabetes:

1. Diabetes caused as a result of auto immune problem. The immune system of the body destroys the insulin producing beta cells in the pancreas leading to no or less production of required insulin by the pancreas.
2. Diabetes due to malfunctioning of beta cell itself. This malfunction includes non production of insulin or situation known as insulin resistance (Wang, Hsu, Goh & Lee, 2000).
3. Third type is known as gestational diabetes. During this stage, the body resists the effect of insulin produced.

The effect of diabetes on the eye is called Diabetic Retinopathy (DR). It is known to damage the small blood vessel of the retina and this might lead to loss of vision. The disease is classified into three stages viz. Background Diabetic Retinopathy (BDR), Proliferate Diabetic Retinopathy (PDR) and Severe Diabetic Retinopathy (SDR). In BDR phase, the arteries in the retina become weakened and leak, forming small, dot like haemorrhages. These leaking vessels often lead to swelling or edema in the retina and decreased vision. In the PDR phase, circulation problems cause areas of the retina to become oxygen deprived or ischemic. New fragile, vessels develop as the circulatory system attempts to maintain adequate oxygen levels within the retina. This phenomenon is called neovascularisation. Blood may leak into the retina and vitreous, causing spots or floaters, along with decreased vision. In the SDR phase of the disease, there is continued abnormal vessel growth and scar tissue, which may cause serious problems such as retinal detachment and glaucoma and gradual loss of vision.

Diabetes is a major disease affecting a sizable portion of the humanity. Hence, detection of diabetes and its subsequent is a major challenge faced by the medical fraternity. Traditional methods of detection of diabetes involves pain and necessity of blood which has certain constraints including the possibility of contamination and related health hazards. Hence, there is a necessity to develop systems which are painless and also don't require blood samples. Detection of diabetes using bloodless technique is an issue which is in the limelight of research in the field of machine learning and artificial intelligence (AI). It primarily intends to contribute towards faster and efficient means of detection and subsequent diagnosis of diabetes. Here, we present the working of a system designed to detect the abnormality of the eye with pain- and blood-free method. The typical features for diabetic retinopathy (DR) are used along with certain soft computing techniques to design such a system. The essential components of DR are blood vessels, red lesions visible as microaneurysms, hemorrhages and whitish lesions i.e., lipid exudates and cotton wool spots. We formulate a framework for bloodless diagnosis of diabetes using a unique feature

set derived from the retinal image of the eye. The feature set is applied to a soft computational tool Support Vector Machine (SVM) which provides us the decision regarding the state of infection of the eye. The classification ability of the proposed system for blood vessel and exudate is 91.67% and for optic disc and microaneurysm is 83.33%.

DIABETIC RETINOPATHY

Diabetic can affect the eye in a number of ways. It affects the retina, mainly the network of blood vessel lying within it. The name of this condition is diabetic retinopathy. There are four stages of diabetic retinopathy:

1. Mild nonproliferative retinopathy: At this early stage microaneurysms occurs. They are small areas of balloon like swelling in the retina's tiny blood vessels.
2. Moderate nonproliferative retinopathy: As the disease progress, some blood vessels that nourish the retina are blocked.
3. Severe nonproliferative retinopathy: Many more blood vessels are blocked, depriving several areas of the retina send signals to the body to grow new blood vessels for nourishment.
4. Proliferative retinopathy: At this advance stage, the signals sent by the retina for the nourishment trigger the growth of new blood vessels. This condition is called proliferative retinopathy. These new blood vessels are abnormal and fragile. These blood vessels have thin fragile walls. If they leak blood severe vision loss and even blindness can result.

There are two ways in which one's vision may be affected due to diabetic retinopathy.

1. Fragile, abnormal blood vessels can develop and leak blood into the centre of the eye, blurring vision. This is proliferative retinopathy and is the most advance stage of the disease.
2. Fluid can leak into the centre of the macula, part of the eye where sharp and straightahead vision occurs. The fluid makes the macula swell, blurring vision. This condition is called macular edema. It can occur in the any stage of diabetic retinopathy.

ABNORMALITIES ASSOCIATED WITH THE EYE

Abnormalities associated with the eye can be divided into two main classes, the first being disease of the eye, such as cataract, conjunctivitis, blepharitis and glaucoma. The second group is categorized as life style related disease such as life style related disease such as hypertension, arteriosclerosis and diabetes (Gardenr, Abcouwer, Barber & Jackson, 2011). When the retina is been affected as a result of diabetes, this type of disease is called Diabetic retinopathy (DR). DR occurrence have been generally categorise into three main form viz. BDR, PDR, SDR as discussed above. These three classes can occur in any of the form described below:

Microanurysms: These are the first clinical abnormality to be noticed in the eye. They may appear in isolation or in clusters as tiny, dark red spots or looking like tiny haemorrhages within the light sensitive

Bloodless Technique to Detect Diabetes using Soft Computational Tool

retina. Their sizes ranges from 10-100 microns i.e. less than $1/12^{\text{th}}$ the diameter of an average optics disc and are circular in shape (Sah & Sarma, 2013) at this stage, the disease is not eye threatening.

Haemorrhages: Occurs in the deeper layers of the retina and are often called plot haemorrhages because of their round shape.

Hard Exudates: These are one of the main characteristics of diabetic retinopathy and can vary in size from tiny specks to large patches with clear edges. As well as blood, fluid that is rich in fat and protein is contained in the eye and this is what leaks out to form the exudates. These can impair vision by preventing light from reaching the retina.

Soft Exudates: These are often called cotton wool spots and are more often seen in advance retinopathy.

Neovascularisation: This can be described as abnormal growth of blood vessels in areas of the eye including the retina and is associated with vision loss. This occurs in response to ischemia, or diminished blood flow to ocular tissues. If these abnormal blood vessels grow around the pupil, glaucoma can result from the increasing pressure within the eye. These new blood vessels have weaker walls and may break and bleed, or cause scar tissue to grow that can pull the retina away from the back of the eye. When the retina is pulled away it is called a retinal detachment can cause severe vision loss, including blindness. Leaking blood can cloud the vitreous (the clear, jelly like substance that fills the eye) and block the light passing through the pupil to the retina, causing blurred and distorted images. In more advanced proliferate retinopathy, diabetic fibrous or scar tissue can form on retina (Lochan, Sah & Sarma, 2012).

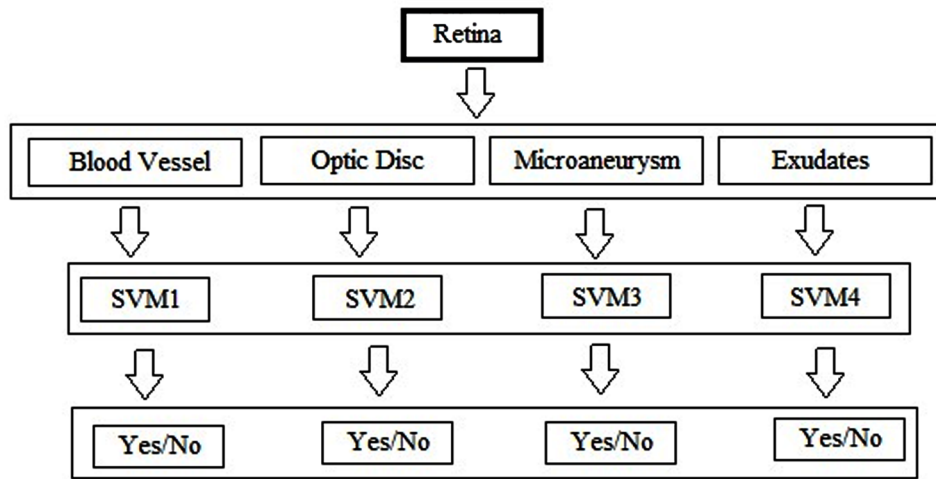
The algorithm used in our case is classified in terms of five basic image processing and decision making categories. The associated primary subdivision are as follows:

- Preprocessing stages
 1. Correction of non-uniform illumination
 2. Color normalization
 3. Contrast enhancement
- Localization and Segmentation of Optic Disc
 1. Characteristics of the optic Disc
 2. Optic Disc localization
 3. Optic disc segmentation
- Localization of Macula Fovea
 1. Characteristics of the macula and fovea
 2. Methods for localizing the macula and fovea
- Segmentation of retinal vasculature
 1. Characteristics of the vasculature
 2. Method for segmenting the vasculature
- Localization and Segmentation of retinopathy
 1. Microaneurysms/ haemorrhages
 2. Exudates/ cotton wool spots

OVERVIEW OF THE DETECTION

The proposed system in a conceptualized form is depicted in Figure 1. It has several stages which are discussed in the subsequent sections.

Figure 1. System Model



Detection of Blood Vessel

Information about retinal blood vessels is important for the diagnosis, treatment, evaluation, and clinical study of many diseases such as diabetes and hypertension (Ming, 2009). Changes in vessel morphology can indicate the current state and progression of a disease. For example, the diameter, shape, and colour of retinal arteries and veins can be used for grading the severity and progression of a number of diseases. Figure 2 shows the block diagram of the system adopted to detect the blood vessel (Vallabha, Dorairaj, Namuduri & Thompson, 2004).

Blood vessels are extracted in our work for the identification of diabetic retinopathy. The contrast of the fundus image tends to be bright in the centre and diminish at the side, hence pre-processing is essential to minimize this effect and have a more uniform image. After which, the green channel of the image is applied with morphological image processing to remove the optical disc. Image segmentation is then performed to adjust the contrast intensity and small pixels considered to be noise are removed. The obtained image would represent the blood vessel of the original image as indicated in Figure 3.

Figure 2. Block diagram to detect the blood vessel

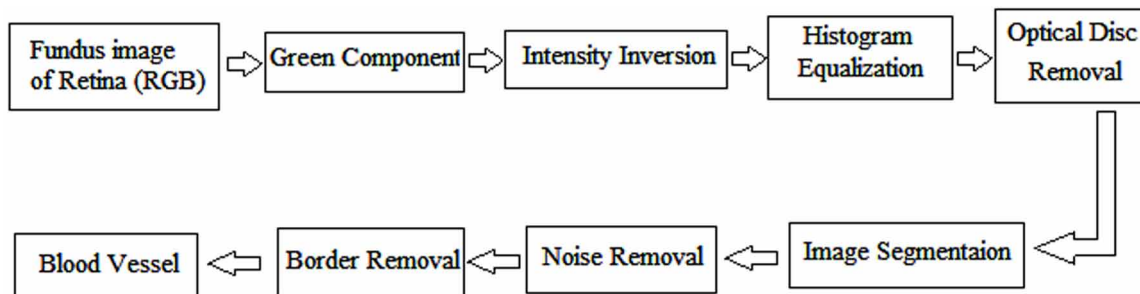
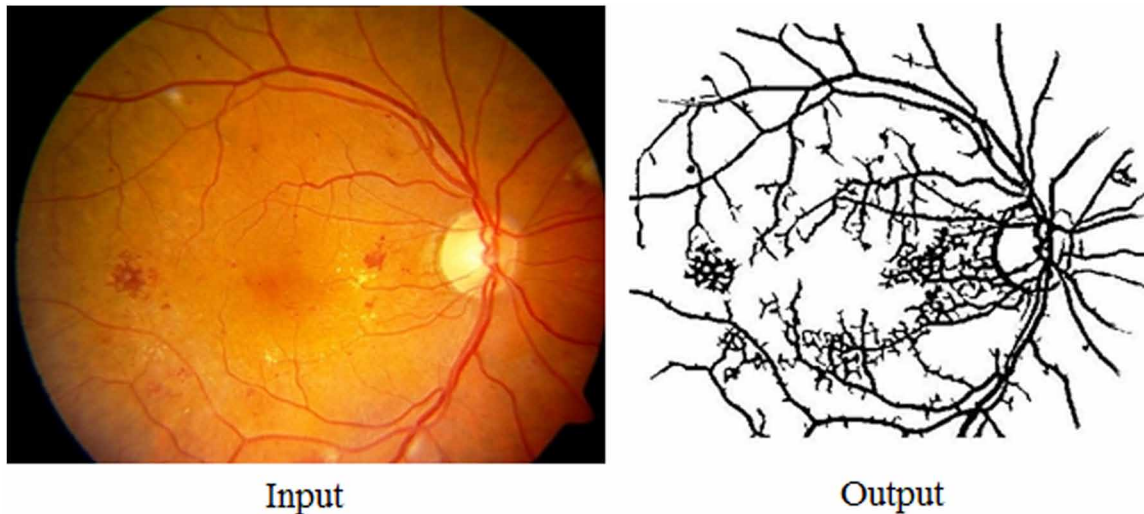


Figure 3. Input image with the extracted blood vessel



Detection of Microaneurysm

These are the first clinical abnormality to be noticed in the eye. They may appear in isolation or in clusters as tiny, dark red spots or looking like tiny haemorrhages within the light sensitive retina. Their sizes ranges from 10-100 microns i.e. less than 1/12th the diameter of an average optics disc and are circular in shape (Ahmad, Mansoor, Mumtaz, Khan, & Mirza, 2014), at this stage, the disease is not eye threatening. Figure 4 shows the block diagram to detect the microaneurysm. The grayscale image is used to detect the circular border and optical disc mask. The green channel of the images first finds the edges using the Canny operator before removing the circular border to fill the enclosed small area. The image is contrast is stretched by applying adaptive histogram equalization before using edge detection to detect the outlines of the image. The larger area are then removed and applied with the AND logic to remove the exudates. The output is the microaneurysm Figure 5.

Detection of Optic Disc

As the optical disc is made up of a group of bright spots, it is not suitable to use loops and locate the largest value. This would only point to one spot and most likely to be on the side of the optical disk. The mask required to cover the optical disc would be inefficient as it would be much larger and covers more details. Mask creation is used in the detection of blood vessels, exudates and microaneurysms. Gray scale image instead of the green channel is used as it is more efficient in the detection (Wang, Hsu, Goh & Lee, 2000). The above lines would first and the maximum value for each of the 720 columns of the image before locating the largest value. The co-ordinates (row and column) of all brightness point (s) are than one point. After locating the optical disc, a mask needs to be created. The radius of the mask is given by:

$$R^2 = (x - h)^2 + (y - k)^2$$

Figure 4. Block diagram to detect microaneurysm

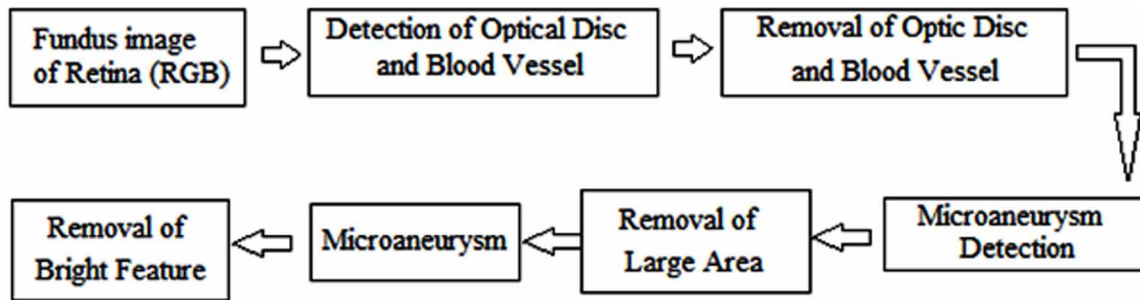


Figure 5. Input image with the detected microaneurysm

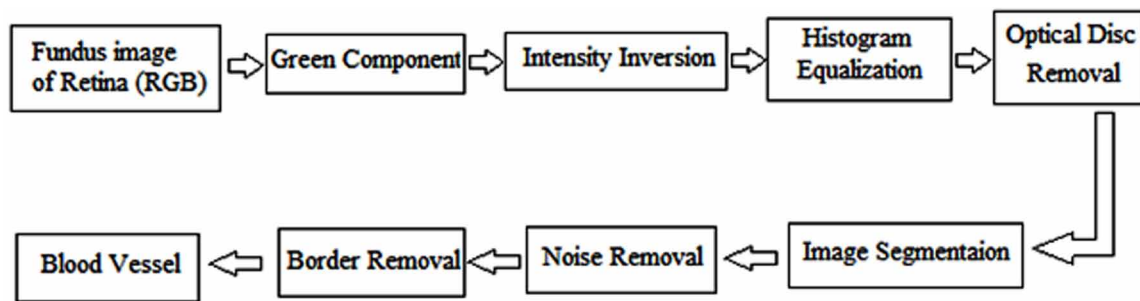
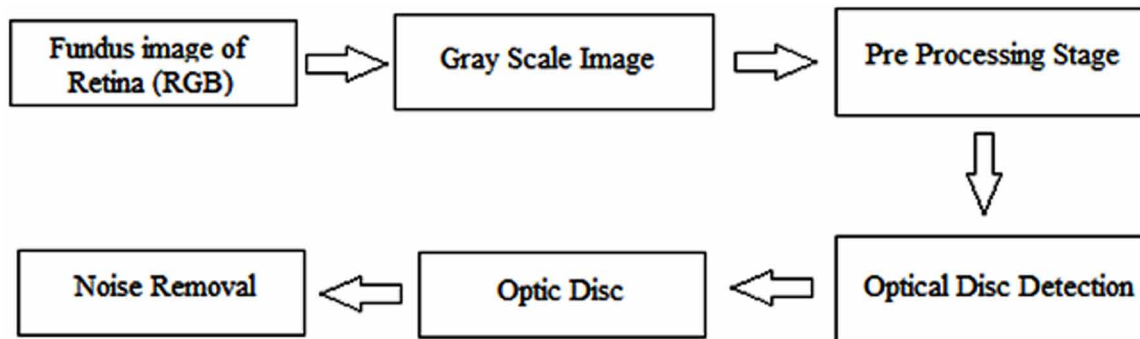


Figure 6. Block diagram to detect optic disc

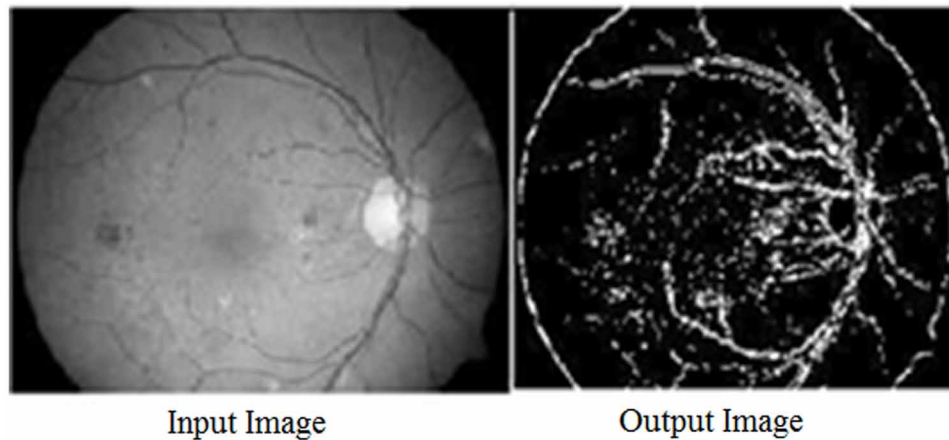


where h and k are the coordinates (row and columns), x and y are the matrices. Figure 6 shows the block diagram for the detection of optic disc and Figure 7 shows extracted optic disc.

Detection of Exudates

Exudates appeared as bright yellow - white deposits on the retina due to the leakage blood from abnormal vessels. Their shape and size will vary with the different retinopathy stages. The grayscale image is first pre processed for uniformity before the morphological image processing is applied to remove the blood

Figure 7. Input image with extracted optic disc



vessels and identify the exudates region (Vapnik, 1998). The exudates are detected after removing the border, optical disc and non exudates area. Figure 8 shows the block diagram to detect exudates. In Fig 9, we can see the extracted exudates from the input image.

PROPOSED SYSTEM

The proposed system is based on SVM which uses a feature set. The system provides us the decision regarding the state of infection of the eye for a range of samples considered for the purpose. In the recent years, SVM classifiers have demonstrated excellent performance as a soft computational tool in a variety of pattern recognition problem (Xu, Chan, 2003).

In a system based on SVM, the input space is mapped into a high dimensional feature space. Then, the hyper plane that maximizes the margin of separation between classes is constructed. The points that lie closest to the decision surface are called support vectors and directly affect its location (Gonzalez & Woods, 2002). When the classes are non-separable, the optimal hyperplane is the one that minimizes the probability of classification error as indicated in Figure 10.

Figure 8. Block diagram to detect Exudates

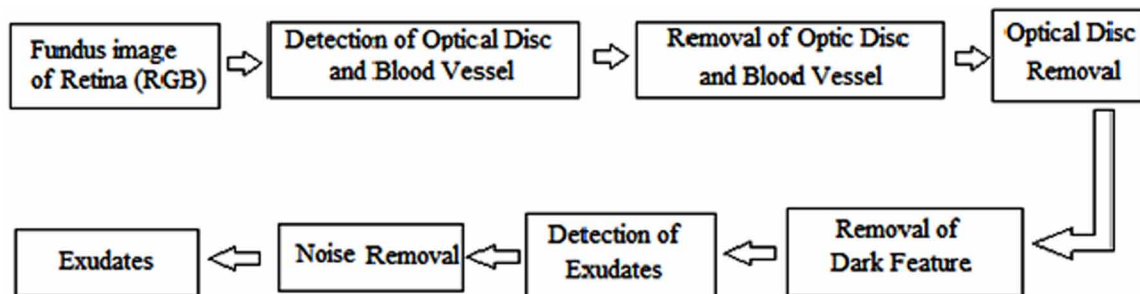


Figure 9. Input image with extracted exudates

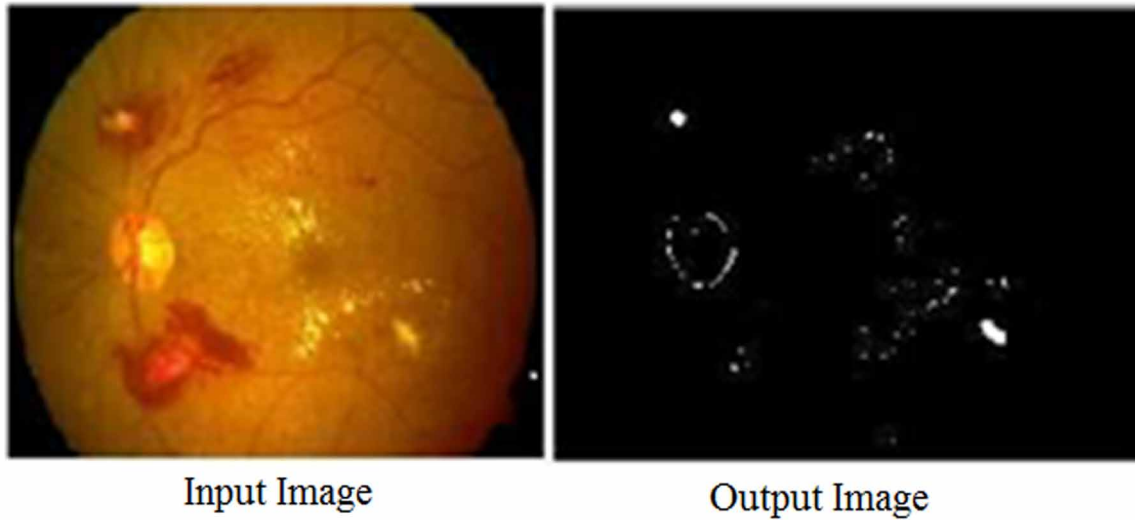
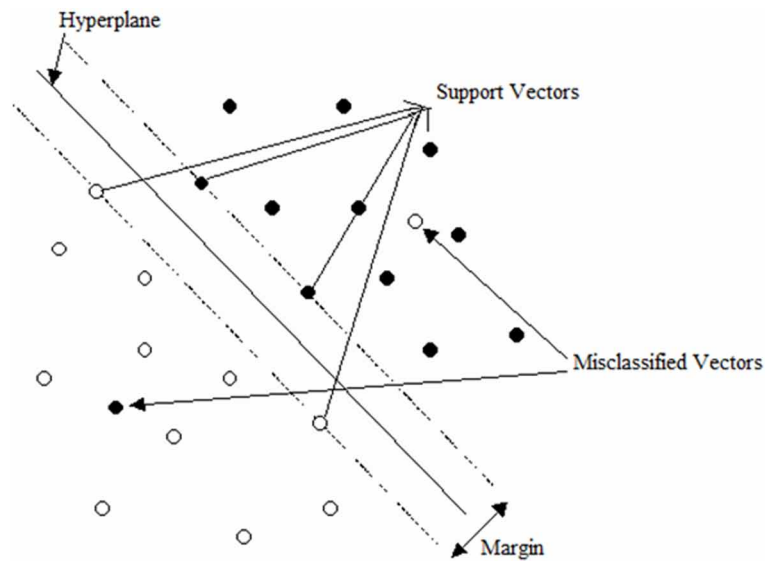


Figure 10. Optimal hyperplane, margin and support vectors



The general method of construction of the Optimal Hyperplane (HO) which separates from the data belonging to two different classes linearly separable is as follows: Let, $H : (w \cdot x) + b$ be the hyperplane, which satisfies the following condition:

$$y_i(w \cdot x_i + b) \geq 1 \dots \dots \dots i = 1, \dots, m$$

To find the optimal hyperplane amounts to maximizing the margin

$$M = \frac{2}{\|w\|}.$$

This is equivalent to minimize

$$\frac{\|w\|^2}{2}$$

under the constraint. This is a problem of minimization of a quadratic objective function with linear constraints

$$\min \frac{1}{2} \|w\|^2 \quad \forall i, y_i(w \cdot x_i + b) \geq 1$$

By applying the principle of Lagrange, one obtains the quadratic problem of programming of dimension m (a number of examples) according to

$$\max \sum_{i=1}^m \alpha_i - \frac{1}{2} \sum_{i,j} \alpha_i \alpha_j y_i y_j (x_i \cdot x_j) \quad \forall i, \alpha_i \geq 0$$

where, α_i are the coefficients of Lagrange.

The solution for the optimum boundary w_0 is a linear combination of subset of the training data, $s \in \{1, \dots, N\}$: the support vectors. These support vectors define the margin edges and satisfy the equality $y_i[(w_0 \cdot x_i) + b_0] = 1$, what is equivalent to:

$$VS = \{x_i | \alpha_i > 0\} \dots \dots \dots i = 1, \dots, m$$

The function of classification $class(x)$ is defined by:

$$\begin{aligned} class(x) &= sign[(w_0 \cdot x) + b_0] \\ &= sign \left[\sum_{x_i \in VS} \alpha_i y_i (x_i \cdot x) + b_0 \right] \end{aligned}$$

If $class(x)$ is lower than 0, X is in the class “-1” if not it is in the class 1. The typical kernel functions are listed below:

- Linear, $k(x, x') = x \cdot x'$
- Polynomial, $k(x, x') = (x \cdot x' + c)^d$

- Gaussian, $k(x, x') = e^{(-\|x-x'\|^2)/\sigma}$
- Sigmoid, $k(x, x') = \tanh(\alpha_0(x.x') + \beta_0)$

With the origin, the SVM were conceived primarily for the problems with 2 classes, however several approaches making it possible to extend this algorithm to the cases N classes were proposed. Generalization in the case multi-classes can be done in three different ways. In this paper, SVM is used as binary classifier.

EXPERIMENTAL DETAILS AND RESULTS

As discussed above, we take different fundus image of retina of both normal and diabetic effected. The different features (blood Vessel, microaneurysm, optic disc, exudates) extracted using the proposed algorithm (Ahmad et al., 2014) (Wang et al., 2000) and then these extracted features (Figures 3, 5, 7 and 9) are applied to the SVM classifier for classification. Next, we used 3 abnormal (abnormal1, abnormal2, abnormal3) samples and 3 normal (normal1, normal2, normal3) samples of retina. Thus, a total of nine combination of retina for training are obtained. Each sample is tested for twelve to fifteen times. The overall block diagram for our system is already shown in Figure 1. Tables 1, 3, 5 and 7 show testing data for features related to blood vessel, microaneurysm, optic disc and exudates respectively.

We tested our classifier system for different feature combination of normal and abnormal samples of retina (Table 9) and it shows that designed SVM classifier is able to classify from 87.49% to 91.67% (Tables 2, 4, 6 and 8) for different features and combination of different feature sets.

Table 1. Testing data for blood vessel

Test Sample	Correct Classification	Classification (%)
12	11	91.67
12	10	83.33
12	9	75
12	12	100
12	12	100
12	9	75
12	12	100
12	12	100
12	12	100

Table 2. Results of SVM classification for blood vessel

No.of training	No. Of Testing	No. Of Correctly Classified	Classification (%)
9	12	11	91.66

Bloodless Technique to Detect Diabetes using Soft Computational Tool

Table 3. Testing data for microaneurysm

Test Sample	Correct Classification	Classification (%)
12	10	83.33
12	8	83.33
12	12	100
12	11	91.67
12	9	75
12	9	75
12	10	83.33
12	10	83.33
12	11	91.67

Table 4. Results of SVM classification for microaneurysm

No.of training	No. Of Testing	No. Of Correctly Classified	Classification (%)
9	12	10	83.33

Table 5. Testing data for optic disc

Test Sample	Correct Classification	Classification (%)
12	12	100
12	8	66.67
12	10	83.33
12	9	75
12	11	91.67
12	11	91.67
12	10	83.33
12	9	75
12	10	83.33

Table 6. Results of SVM classification for optic disc

No.of training	No. Of Testing	No. Of Correctly Classified	Classification (%)
9	12	10	83.33

Table 7. Testing data for exudates

Test Sample	Correct Classification	Classification (%)
12	9	75
12	11	91.67
12	12	100
12	9	75
12	8	66.67
12	10	83.33
12	10	83.33
12	11	91.67
12	10	83.33

Table 8. Results of SVM classification for exudates

No.of training	No. Of Testing	No. Of Correctly Classified	Classification (%)
9	12	11	91.66

The outputs of the SVM classifier are shown in Tables 10, 11, 12 and 13 where, the blue arrow represents the weight vector and red is decision boundary. The experiment is performed for each Feature with threshold value: 0.735 and weight vectors (2.789 and -2.054) for blood vessel with threshold value: -0.691 and weight vectors (2.786 and -2.095) for optical disc, microaneurysm and exudates. The shadow around the decision boundary represent the minimum margin on the training data (the SVM algorithm finds the largest possible minimum margin). Circles and green lines indicate the support vectors of the classifier. The perpendicular distance of the decision boundary from the origin is $(-\theta / \|w\|)$, where θ the threshold is and w is the weight vector.

Finally, the performance graph of the proposed system for different features of retina are shown in Figures 11, 12, 13 and 14 using bar diagram.

Table 9. Comparison of classification ability of SVM according to feature combination of Retina for DR

Combination of Features	Classification ability of SVM classifier (%)				
Blood Vessel and Optic Disc	8	7	.	4	9
Blood Vessel and Microaneurysm	8	7	.	4	9
Blood Vessel and Exudates	9	1	.	6	6
Optic Disc and Microaneurysm	8	3	.	3	3
Optic Disc and Exudates	8	7	.	4	9
Microaneurysm and Exudates	8	7	.	4	9

Table 10. SVM output

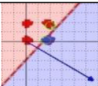
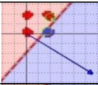
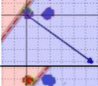
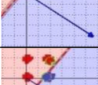
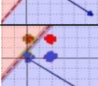
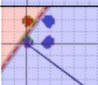

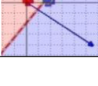

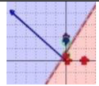
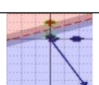
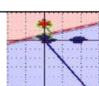
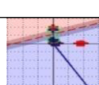
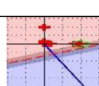
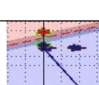
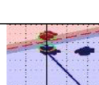
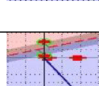
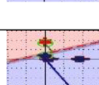
Weight vectors: 2.789 and -2.054, Threshold value: 0.735	
Combination	Output
Normal1 +Abnormal1	
Normal1 +Abnormal2	
Normal1 +Abnormal3	
Normal2 +Abnormal1	
Normal2 +Abnormal2	
Normal2 +Abnormal3	
Normal3 +Abnormal1	
Normal3 +Abnormal2	
Normal3 +Abnormal3	

Table 11. Output of SVM for Microaneurysm

Weight vectors: 2.786 and -2.095, Threshold value: -.0691	
Combination	Output
Normal1 +Abnormal1	
Normal1 +Abnormal2	
Normal1 +Abnormal3	
Normal2 +Abnormal1	
Normal2 +Abnormal2	
Normal2 +Abnormal3	
Normal3 +Abnormal1	
Normal3 +Abnormal2	
Normal3 +Abnormal3	

Our results show that the classifier is able to identify their class up to 91.67% for Blood vessel. For microaneurysm, optic disc and exudates percentage of classification ability of SVM classifier are 83.33%, 83.33% and 91.67% respectively. And for combined feature set classification ability of our system is from 87.49% to 91.67% (Table 9).

Table 12. Output of SVM for Optic Disc

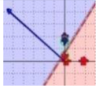
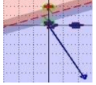
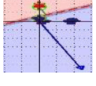
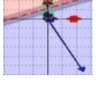
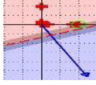
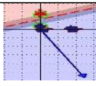
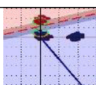
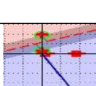
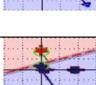
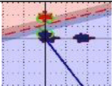
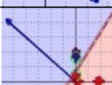
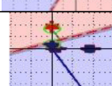
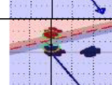
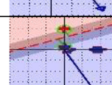
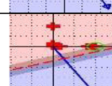
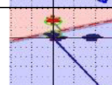
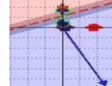
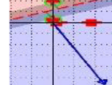
Weight vectors: 2.786 and -2.095, Threshold value: -.0691	
Combination	Output
Normal1 +Abnormal1	
Normal1 +Abnormal2	
Normal1 +Abnormal3	
Normal2 +Abnormal1	
Normal2 +Abnormal2	
Normal2 +Abnormal3	
Normal3 +Abnormal1	
Normal3 +Abnormal2	
Normal3 +Abnormal3	

Table 13. Output of SVM for Exudates

Weight vectors: 2.786 and -2.095, Threshold value: -.0691	
Combination	Output
Normal1 +Abnormal1	
Normal1 +Abnormal2	
Normal1 +Abnormal3	
Normal2 +Abnormal1	
Normal2 +Abnormal2	
Normal2 +Abnormal3	
Normal3 +Abnormal1	
Normal3 +Abnormal2	
Normal3 +Abnormal3	

CONCLUSION

In this chapter, we presented a system to detect the abnormality (due to diabetes) of the eye with the focus to show the application of machine learning approaches for pain and blood-free method. Here, we designed a soft computational tool which can be trained with samples of the retina image and prior knowledge provided regarding the condition of diabetes as is indicated by the eye. The trained SVM classifier can be used repeatedly with samples of the retina image and decision regarding the state of diabetes can be generated. It has the capacity to deal with a decision making process regarding diabetes using retina image. The proposed system shows classification ability from 83.33% up to 91.66% for dif-

Figure 11. Performance graph of our system for Blood vessel (9 different trials)

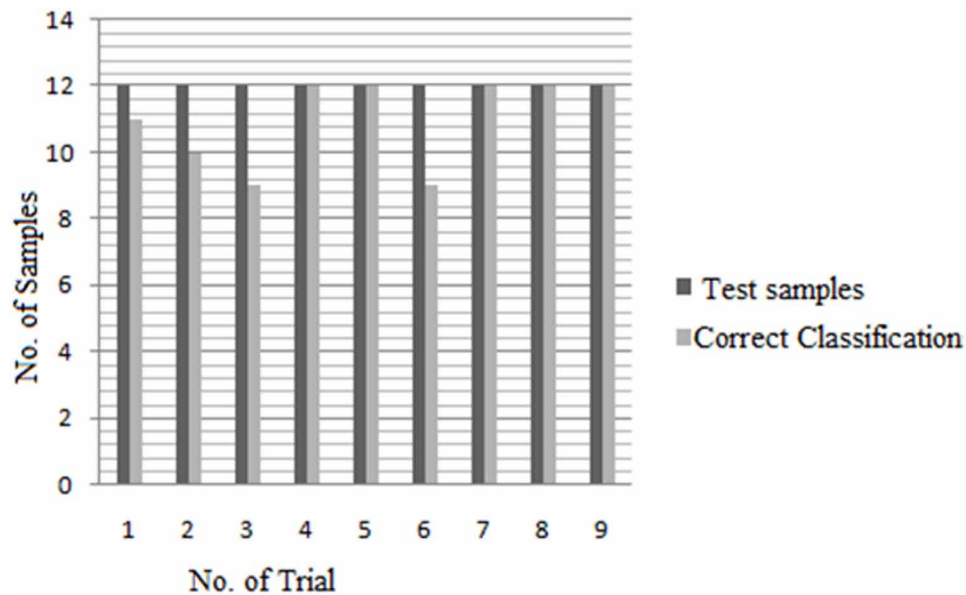
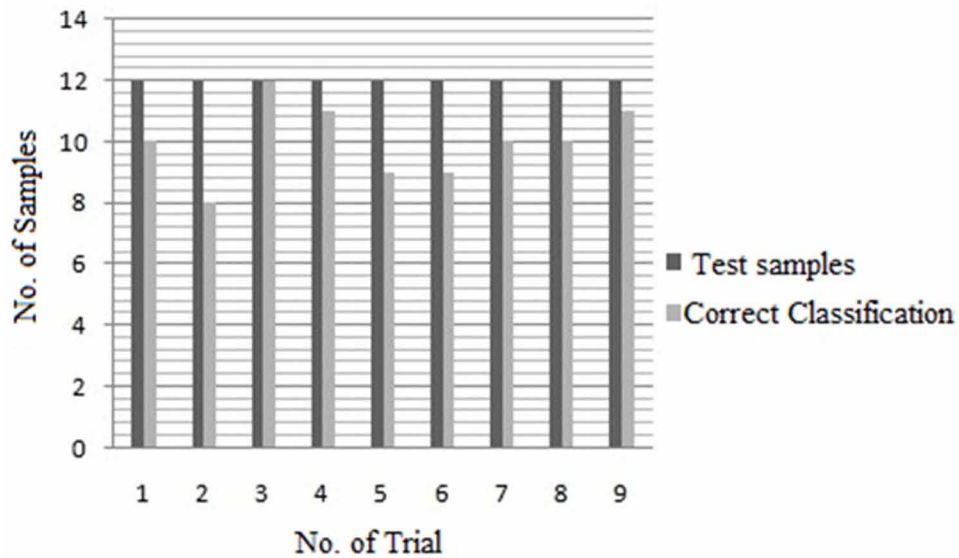


Figure 12. Performance graph of our system for microaneurysm (9 different trials)



ferent features (blood vessel, microaneurysm, optic disc and exudates) and different feature combination set of retina. The advantage of such system shall be the speed of information processing, blood-less diagnosis, re-usability and help for subsequent advice/ suggestion for related treatment.

Some more advantages of our system are:

- Since we detect different features of diabetic effected retina, which help us to classify the diabetic effected and not effected retina. Which will also help us to know the different stages of diabetes

Figure 13. Performance graph of our system for Optic Disc (9 different trials)

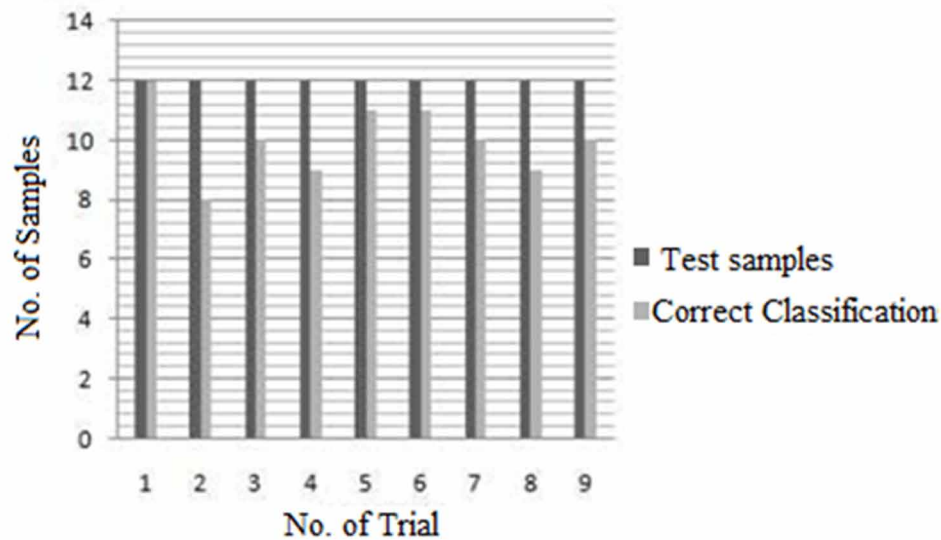
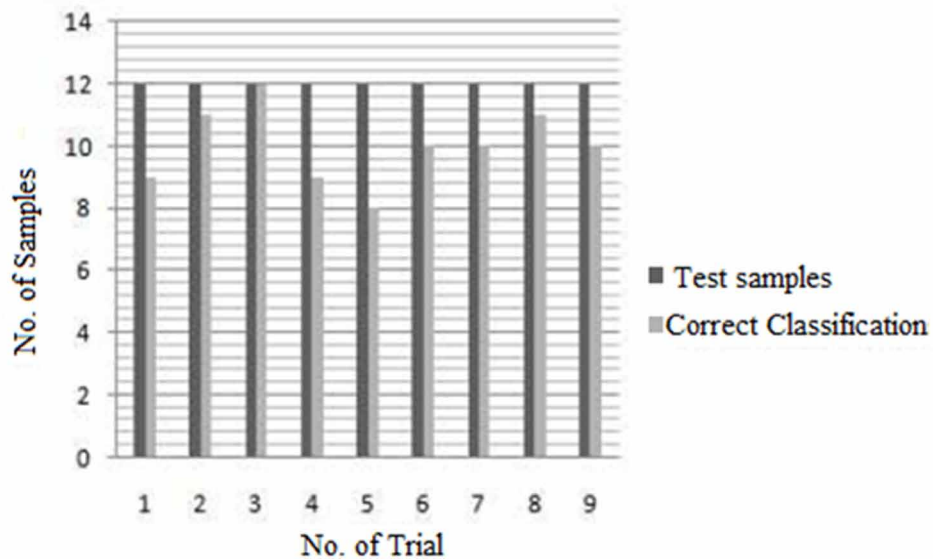


Figure 14. Performance graph of the proposed system for exudates (9 different trials)



- Equalization of uneven illumination of the set of provided fundus image is one of the key success of this work. The quality of the images provided and used in the hospital is very low and very difficult for visual manual grading by the ophthalmologist. The quality of which is firstly improved by our method of illumination equalization.

In addition we can extend the work to crossover point classification which will help to classify more accurately.

REFERENCES

- Ahmad, A., Mansoor, A., Mumtaz, R., Khan, M., & Mirza, S. (2014). Image processing and classification in diabetic retinopathy: A Review. *Proceedings of the 5th European workshop on visual information Processing (EUVIP 2014)* (pp 1-6). France. IEEE
- Bevilacqua, V., Cambo, S., Cariello, L., & Mastronardi, G. (2005), A combined method to detect Retinal Fundus Features. *Proceedings of European Conference on Data Analysis*.
- Chaudhuri, G. S., Chatterjee, S., Katz, N., Nelson, M., & Goldman, M. (1989). Detection of blood vessels in retinal images using two dimensional matched filters. *IEEE Transactions on Medical Imaging*, 8(3), 263–269. doi:10.1109/42.34715 PMID:18230524
- Gardenr, T. W., Abcouwer, S. F., Barber, A. J., & Jackson, G. R. (2011). An Integrated approach to diabetic retinopathy research. *Arch. Ophthalmol.*, 129(2), 230–235. PMID:21320973
- Gonzalez, R. C., & Woods, R. E. (2002). *Digital Image Processing using MATLAB. 2nd edition*. New Delhi: Prentice Hall.
- Lochan, K., Sah, P., & Sarma, K. K. (2012). Innovative Feature Set for Retinopathic Analysis of Diabetes and its Detection. *Proceeding of 2nd IEEE National Conference on Emerging Trends and Applications in Computer Science*, Shillong, India.
- Ming, Y. F. (2009). Identification of diabetic retinopathy stages using digital fundus images using imaging [Master's thesis]. SIM University.
- Premi, M.S. G. (2015). Novel approach for retinal blood vessels extraction and exudates segmentation. *Journal of Chemical and pharmaceutical Research*, 7(1), 792-797.
- Sah, P., & Sarma, K. K. (2013). Detection of Blood Vessel and its application for Classifying Diabetic Retinopathy. *Journal of the Instrument Society of India*, 43, 72–74.
- Vallabha, D. R. Dorairaj, Namuduri, K., Thompson, H. (2004). Automated Detection and Classification of Vascular Abnormalities in Diabetic Retinopathy. *Proceedings of 38th Asilomar Conference on Signals, Systems and Computers*.
- Vapnik, V. (1998). *Statistical learning theory*. New York: Wiley.
- Wang, H. H., Goh, W., K.G. & Lee, M. L. (2000). An effective approach to detect lesions in color retinal images. *Proceedings of IEEE Conference on engineering in medicine and biology Society*.
- Wang, H., Hsu, W., Goh, K. G., & Lee, M. L. (2000). An effective approach to detect lesions in color retinal images. *Proceedings of IEEE Conference on Computer Vision and Pattern Recognition* (pp. 1-6).
- Xu, P., & Chan, A. K. (2003). Support vector machine for multi-class signal classification with unbalanced samples. *Proceedings of the International Joint Conference on Neural Networks* (pp. 1116-1119). Portland, USA.

KEY TERMS AND DEFINITIONS

Canny Operator: Canny operator is an edge detector operator that uses a multi stage algorithm to detect a wide range of edges in images. It was developed by John F. Canny in 1986.

Diabetic Retinopathy: *Diabetic retinopathy* is a common complication of diabetes. It occurs when high blood sugar levels damage the cells at the back of the eye (known as the retina).

Hemorrhages: Hemorrhaging is the loss of blood escaping from the circulatory system.

Hyperplane: Hyperplane is the linear classifier with the maximum margin for a given finite set of learning patterns. A *Support Vector Machine (SVM)* performs classification by finding the *hyperplane*.

Kernel Function: In machine learning method, Kernel function is a class of algorithm for pattern analysis, whose best known member is the Support Vector Machine (SVM). The general task of pattern analysis is to find and study general types of relations (for example clusters, principle components, correlations, classifications) in datasets.

Machine Learning Method: Machine learning is a subfield of computer science that evolved from the study of pattern recognition and computational learning theory in artificial intelligence. Machine learning explores the construction and study of algorithms that can learn from and make predictions on data. Such algorithms operate by building a model from example inputs in order to make data driven predictions or decisions.

Microaneurysms: Microaneurysm is a small swelling that forms on the side of tiny blood vessels. These small swellings may break and bleed into nearby tissue.

Optic Disc: Optic disc is a round area in the back of the eye where retinal nerve fibres collect to form the optic nerve.

Support Vector Machine: Support Vector Machine is a machine learning method for data classification. These type of machines are based on the concept of decision planes that define decision boundaries.

This research was previously published in Intelligent Applications for Heterogeneous System Modeling and Design edited by Kandarpa Kumar Sarma, Manash Pratim Sarma, and Mousmita Sarma, pages 139-158, copyright year 2015 by Information Science Reference (an imprint of IGI Global).

Chapter 4

Significant Enhancement of Segmentation Efficiency of Retinal Images Using Texture-Based Gabor Filter Approach Followed by Optimization Algorithm

Upendra Kumar

Dr. A. P. J. Abdul Kalam Technical University, India

ABSTRACT

Considering Retinal image as textured image, its texture based segmentation is required to identify the presence of retinal diseases. This pre-processing is important in automatic detection system for recognizing the abnormality present in the retinal images. Likewise, the proposed system mainly focused on diabetic retinopathy disease caused into eye –retina, generally leads to eye-blindness. Inspired from robust human's texture based segmentation capability, a mathematical model of the eye was formulated. A texture based Gabor filter was applied to get the output feature helping in detecting the abnormality and deriving statistical properties, further used in segmentation and classification. This work deals with the better separation of various clusters of Gabor filter output features, in order to get better segmentation efficiency. This was also followed by formalizing an objective function to tune filter parameters with Gradient descent and further Genetic Algorithm. This paper showed both qualitative and quantitative segmentation results with improved efficiency.

INTRODUCTION

Segmentation is an important step which is required in many image processing applications to extract useful information. In medical imaging field, segmentation is required to identify the disease embedded in particular organ, e.g. it helps in early diagnosis of diseases like glaucoma, diabetic retinopathy and

DOI: 10.4018/978-1-5225-5195-9.ch004

macular degeneration by segmenting retinal images (Sinthanayothin et al., 2002; Ahmed et al., 2008; Dey et al., 2012). Glaucoma is one of the most common diseases and if it is not early detected, may have serious cost, can even lead to eye blindness. Most of the existing detection and assessment methods of diabetic retinopathy are manual, costly affair and also require trained ophthalmologists (Teng et al., 2002; Olson et al., 2003).

Morphological feature of retinal blood vessel may be utilized as a vital sign for various retinal diseases such as diabetes, arteriosclerosis and hypertension. The geometrical changes in veins and arteries of the retinal images can be measured and applied to a variety of clinical studies to develop automatic diagnostic system for early detection of diseases (Palomera-Perez et al., 2010). Segmentation of retinal blood vessels suffers from two kinds of problems, one is the presence of a wide variety of vessel widths and the other is heterogeneous retinal background (Hol & Pail, 2011). Many research works on segmentation of retinal images were done by various researchers and shown its importance in medical diagnosis system (Huang et al., 2006). Huang et al. applied maximal entropy thresholding to segment out the retinal blood vessels and got moderate results. They have not shown any quantitative results for comparative study with this paper work. Medhane and Shukla (2016) worked on automated approach for artery–vein classification by analyzing graphical vasculature tree and also intensity based features extracted from DRIVE retinal image database. Osareh and Shadgar (2010) worked on segmentation of retinal images to classify the retinal pixels as vascular and non-vascular. They applied various machine learning algorithms as classifiers to obtain moderate segmentation and classification results. The study done by Lili and Shuqian (2010) showed that morphological changes occurred in retinal images towards blood vessels are important indicators for diseases like hypertension, diabetes and glaucoma and concluded that the accurate segmentation of blood vessel has significant diagnostic value for the purpose of implementation of diagnosis system. The proposed model was applied and tested on DRIVE database (used in this work also), and showed average sensitivity as 77% while the average accuracy as 93.2%. Zhen et al. (2014) worked on automatically identifying retinal vessels from fundus images using multi-scale directional contrast quantification (MDCQ) strategy and obtained moderate segmentation results on various retinal image databases.

The analysis of retinal image based on computer-aided techniques, plays a key role in diagnostic procedures. However, automatic retinal segmentation process suffers from various drawbacks, i.e. the retinal images are often poorly contrasted, noisy and also the widths of retinal vessels may vary from very large scale to very small value. Therefore, in this work the images were preprocessed using adaptive thresholding and contrast enhancement techniques. Detection and assessment of blood vessels has been the area of research in medical imaging for the past few years. This work includes some algorithms that usually use some kind of vessel enhancement before applying segmentation techniques. The current methods producing high accuracy for retinal image with thick vessels requires high computational cost. The use of proposed methods in this work makes it possible to detect these vessels faster, while preserving a high accuracy.

This work proposed a texture based segmentation method inspired from texture based segmentation capabilities of human beings. Following this an attempt was made to formulate a mathematical model of the human beings' eye, leading discovery of the band-pass filter-bank characteristics of the eye. The transfer function used by these filters is formulated by the Gabor elementary functions. The outputs produced by Gabor filters applied on differently textured images are significantly distinct for the differently textured regions. Utilizing the discontinuities present in the outputs of filters used and their statistical properties obtained from mathematical formulation help in segmentation and classification of a given

image. Previous works were done on designing and modeling Gabor filters to obtain the maximum discrimination of different textured regions present (Dunn et al., 1994 and 1995). Most of the previous work done on designing Gabor filters were based on incorporation of such decision theoretic framework which in turn minimize the probability of misclassification for bi-partite images having two different textured regions (Bovik et al., 1990). However, the approach proposed in this work mainly deals with a more general problem of classifying multi-textured images by applying clustering on output features obtained from above-mentioned filters. This followed the concept of getting better classification results, which inherently requires moving the clusters far apart from each other. In this work, this concept was utilized in formulating as an objective function to design the Gabor filter by tuning its parameters using evolutionary genetic algorithms. It has been observed that genetic algorithms are very efficient in various optimization problems which are convolved with discontinuous and non-differentiable objective functions. This work proposed a model to implement a filter bank using Gabor filters and a classification scheme to get an efficient segmentation and classification results for differently textured images.

The word texture can be described by characteristics of surface and appearance of an object given by the shape, size, component composition, density, arrangement and proportion of its elementary parts. The human visual system has the ability to pre-attentively segment out different textured regions in an efficient manner. Motivated from this realization, owing to already existing concept and by extensive study on this has lead to utilize promising theory of human texture perception. This human texture based concept is also supported by many psycho physical and Neuro-physiological data, which has shown that some form of analysis based on local spatial frequency is performed by human visual system by utilizing a bank of tuned band pass filters (Dennis et al., 1994). Earlier, many years back this concept of local spatial frequency was already discussed by Gabor in the context of communication systems. In classical concept, an image is considered as either a collection of pixels in spatial domain and in frequency domain, it is expressed as sum of sinusoids of infinite extent. However, it was observed by Gabor that the both representations, spatial and frequency based belong to opposite extremes in a joint space-spatial frequency representation. Frequency representation is viewed as a local phenomenon (i.e., as a local frequency) and its value may vary along with position throughout the varying textured-image. Utilizing the above paradigm under the human vision framework, the significant texture differences observed perceptually, are most-likely correspond to the differences present in the form of local spatial frequency content. Following this, texture segmentation may be considered as decomposition of a textured image in the form of a joint space-spatial frequency representation, by designing a bank of band-pass filters and this information can be utilized to locate regions comprising similar content of local spatial frequency. Furthermore, based on the known fact that Gabor filter is able to produce different outputs corresponding to distinct textured regions present in an image, many studies have been done to design texture based segmentation models using Gabor filters. The work done by (Das et al., 1998) has shown the better segmentation results using 1-D Gabor instead of using 2-D Gabor filter. Inspiring from this result, in this work, an attempt was done to design an optimal 1-D Gabor filters incorporating evolutionary genetic algorithm to get improved segmentation results for the complex natured retinal images. The application of matched filters is also discussed in (Chaudhuri et al., 1989).

MATERIAL AND METHODS

DRIVE database was used for this study. 20 retinal images were used for training (standard manual segmented images) and 20 images (un-segmented images corresponding to training dataset) for testing purpose.

Extracting Gabor Filter Features from Retinal Images

The study done by (Kulikowski et al., 1982) on mathematical modeling of visual cortical cells proposed a formalism of a structure of tuned band pass filter bank. It has been found that, in the frequency domain, these filters comprise Gaussian transfer functions. Furthermore, filter characteristics can be obtained by taking the inverse Fourier transform of this transfer function which closely resembles to the Gabor filters. However, the Gabor filter is viewed as a composition of Gaussian function modulated by a complex sinusoidal function. The Gabor filter can be described by the following equation:

$$f_g(x,y) = \frac{1}{2\pi\sigma_x\sigma_y} e^{-\frac{1}{2}\left[\left(\frac{x-x_0}{\sigma_x}\right)^2 + \left(\frac{y-y_0}{\sigma_y}\right)^2\right] + 2\pi j(U_x x + V_y y)} \quad (1)$$

where, σ_x and σ_y are variances along x and y axes respectively and U_x and V_y are center frequencies along x and y-axes respectively and x_0 and y_0 are center coordinates. However, 2D Gabor filter comprises Gaussian term, which has smoothing effect; it has been found that if 2D Gabor filter is applied to the image, the edges present in all direction in the image are smoothened out. This smoothing operation leads to the loss of important edge information, resulting lower segmentation efficiency. Therefore, instead of applying 2D Gabor filter, being a separable one, 1D Gabor filter can be applied in order to retain the important edge information. In this approach, edges are smoothened out along only those directions, where 1D Gabor filter is applied, leaving the edges intact in all other directions. If 1D Gabor filters are applied in both horizontal and vertical directions separately, their outputs can be combined to get better texture signature map. Moreover, the computational complexity gets lower in the application of 1D Gabor filter ($O(MN^2)$) in comparison to 2D Gabor filter ($O(M^2N^2)$), where MXN is the size of an image. After applying 1D Gabor filter on image $I(x,y)$, yields output texture signature map $I'(x,y)$, described by following equations:

$$f_g(x) = \frac{1}{2\pi\sigma_x} e^{-\frac{1}{2}\left(\frac{x}{\sigma_x}\right)^2 + 2\pi j U_x x} \quad (2)$$

$$f_g(y) = \frac{1}{2\pi\sigma_y} e^{-\frac{1}{2}\left(\frac{y}{\sigma_y}\right)^2 + 2\pi j V_y y} \quad (3)$$

$$I_h(x,y) = I(x,y) \otimes f_g(y) \quad (4)$$

$$I_v(x,y) = I(x,y) \otimes f_g(x) \quad (5)$$

$$I' (x,y) = \sqrt{\left(I_h (x,y)\right)^2 + \left(I_v (x,y)\right)^2} \quad (6)$$

Equations 2 and 3 represents 1D Gabor filter along x and y-axes respectively. Equations 4 and 5 represents convolution of 1D Gabor filter with image along with x and y-axes respectively. However, the noise present in output texture signature map was decided to smoothen out by again passing it through Gaussian post filter. 2D Gaussian Filters being as separable one, again 1D Gaussian Filters were applied on this output texture signature map to smoothen noise and thus retaining the important edge information and also reduces the required number of filter operations. The output obtained from applying Gaussian Post Filter has reduced noise and its distribution is smoother more close to Gaussian as shown in Figure 1. This nearly equivalent Gaussian distribution leads to make the task of texture-based classification easier in feature space, where it is formulated by combining the parameters of Gaussian distribution both mean and standard deviation.

Optimizing Gabor Filter Parameters Using Local Optimization Tool (Gradient Descent Approach)

In this work, gradient descent method was used for first order optimization and genetic algorithm was used to globally optimize the Gabor filter parameters. In gradient descent approach searching performs proportional to the negative of the gradient of the function at the current point to find the local minimum result and positive gradient for local maximum. If the function representation in feature space of the image is $F(x)$ and it is defined and differentiable nearby point p , then its value gets decreases fastest along the direction of negative gradient, similarly its value gets increases fastest along the direction of positive gradient. The negative gradient of $F(x)$ at point p is defined as $-\Delta F(p)$.

For next point q , if it follows as $q = p - \gamma \Delta F(p)$ for a given very small value of γ , then $F(q) \leq F(p)$. In this approach, one guess x_0 is considered as a point for initial local minimum of $F(x)$ to start and then for sequence of points $x_0, x_1, x_2, x_3, \dots$ and follows the condition such that:

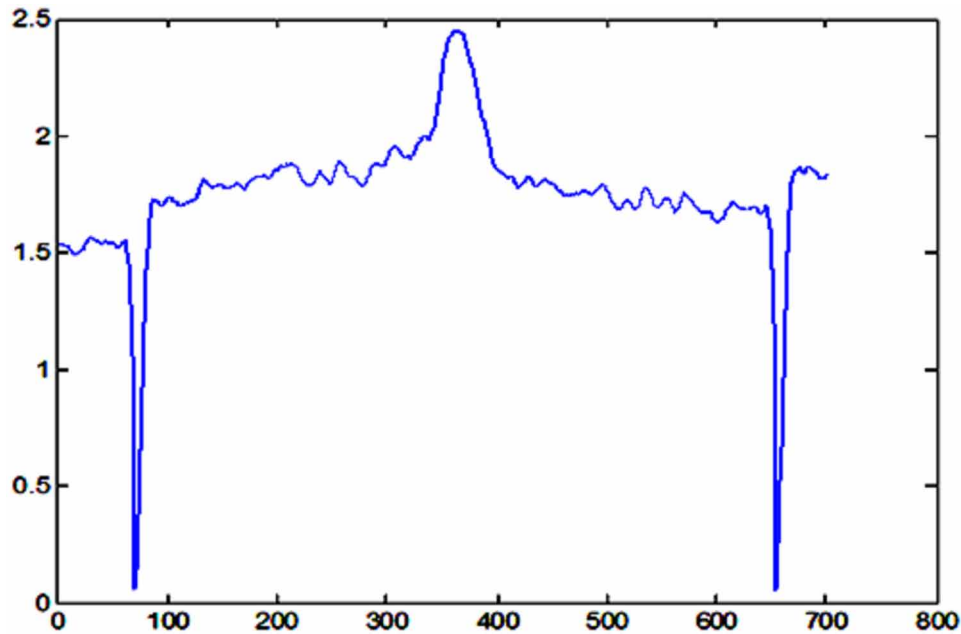
$$x_{i+1} = x_i - \gamma_i \Delta F(x_i), i \geq 0$$

The local minimum convergence for the above sequence can be hopefully obtained if the following relation is satisfied:

$$F(x_0) \geq F(x_1) \geq F(x_2) \geq F(x_3) \dots$$

The Gabor filter parameters were first order optimized using above-mentioned gradient descent method, resulting improved segmentation result. These Gabor filter parameters are σ_x, σ_y, U, V , where σ_x ,

Figure 1. 'Almost Gaussian distribution' of output texture signature of Gabor filter applied on a retinal image



σ_x and σ_y are variances along x and y-axes respectively and U and V are center frequencies along x and y-axes respectively. In this method, at first the Gabor 2D and post filter features are fed into objective function for initial guess of Gabor filter parameters and thereafter using gradient descent method, it tries to find the optimized set of values to obtain better segmentation results.

Optimizing Gabor Filter Parameters Using Global Optimization Tool (Genetic Algorithm)

Genetic algorithm (GA) is an evolutionary algorithm which follows biological processes of natural selection and reproduction to find the solution for fittest. This can be used to find the global optimum solution for a given problem which computes the successive maximum and minimum value of a function. However, many of the processes of genetic algorithm involved in biological evolution are random, still the level of randomization and level of control can be fixed in this optimization technique (Goldberg, 1989). The power and efficiency of these evolutionary algorithms are much better than other searching algorithms like random search and exhaustive search (Kinnear, 1994), as no extra information is required by them in advance about the given problem. Owing to this feature, Genetic algorithm has the ability to find the solution to those kinds of problems, which cannot be handled by other optimization techniques because of lack of differentiability, continuity, linearity or other characteristics.

Algorithm starts with generating initial population by randomly selecting parameters in search space. The genetic operators i.e. mutation, crossover, are applied to generate new population. The new individual is created based on bits and pieces of the fittest old individuals in every next generation. Though the genetic algorithms follow some random choices, but actually they are not simple random walk. However,

the historical information is exploited by these algorithms in efficient manner to guess new search points expecting lead to get better performance. Each individual is evaluated applying fitness function and the newly created individual with improved fitness value is selected for success. These algorithms do not work on parameters as such, but first encode these parameters and then apply genetic operators. This encoding transforms the natural parameters of the optimization problem into a finite length string composed of some alphabets only. Searching is performed among a set of population points, not from a single point, resulting achievement of optimized value. The information about fitness value of the individual using fitness or objective function is being used by this algorithm rather using some other information i.e. derivatives or other auxiliary knowledge. This feature is exploited by GA, to solve those optimization problems having objective (fitness) functions which are non-continuous and non-differentiable. These Gabor filter parameters are σ_x , σ_y , U and V , where σ_x , σ_y are variances along x and y-axes respectively and U and V are center frequencies along x and y-axes respectively.

Design of Segmentation Model Based on Gabor Filters

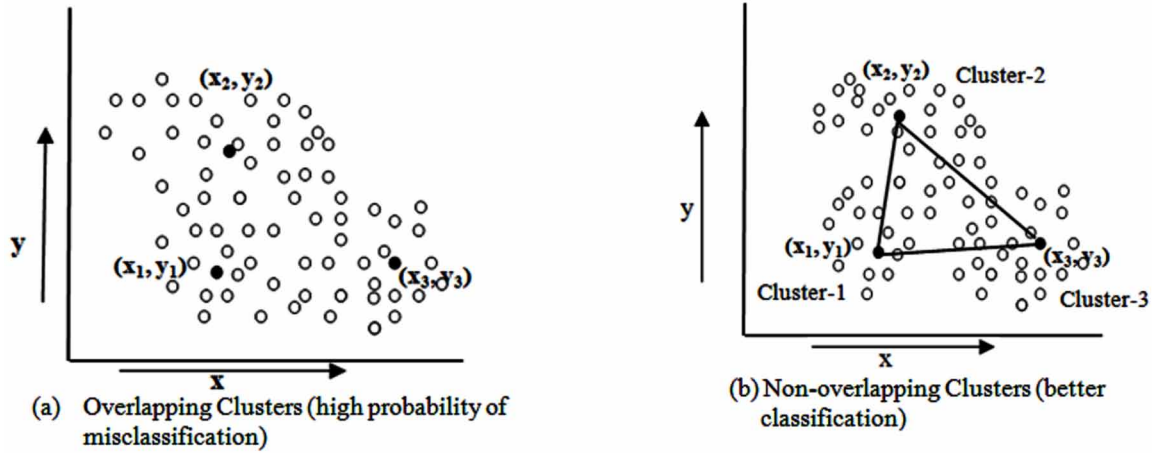
This work is based on application of a combination of Gabor and Gaussian filters on retinal images. The output images obtained from these filters are analyzed by taking window frames of certain dimension (odd length) as samples. The statistical features, mean and standard deviation were extracted from each sample window and that window block was classified as a certain class of textured region by Nearest Neighbor classifier (NN) which follows minimum distance criteria. For this classifier, it is supposed that the textures present in the database can only appear in the images and the feature points corresponding to a particular texture are already known in advance for classification. This classifier needs to calculate the distance metric of a feature point corresponding to sample window block from all N feature points present in the feature database (N is total number of textures) and then it assigns a class (texture) number to the window block by texture number from which is closest. For better classification, this algorithm needs minimizing the overlap of different clusters formed based on distance metric corresponding to different classes of textures present in the database. In this work, this was achieved by tuning the filters. To obtain maximum discrimination between heterogeneous textured regions, filters were tunes in such a way that centroids of all the clusters should move away from each other, as shown in Figure 2(b).

The correct classification of any feature point to a cluster is only possible if all the clusters are maximally separated (Non-overlapping) from each other. If the clusters are overlapping, it is not an easy task to assign a feature point to a cluster accurately, may get stuck in high probability of misclassification as shown in Figure 2(a). The case shown in Figure 2(b) is for non-overlapping arrangement of clusters. The second case is not always possible for all the cases, still it is better to minimize the extent of overlap for most of the problems.

In Figure 2, (x_i, y_i) is the centroids of the i -th cluster (texture class) and (x_j, y_j) is the centroids of the j -th cluster of feature points in feature space (in this case x_i is mean and y_i is standard deviation feature), the Euclidean distance d_{ij} ($i \neq j$) is calculated by the formula:

$$d_{ij} = \sqrt{(x_i - x_j)^2 + (y_i - y_j)^2} \quad (7)$$

Figure 2. Non-overlapping clusters based criteria for maximum discrimination



For non-overlapping clusters, in order to move away each other, the value of d_{ij} should be maximized. This goal can be achieved by maximizing only the minimum value among all d_{ij} , automatically lead to maximize others. Therefore, the criteria for objective function to be used in this works are as follows:

$$F_{obj} = \text{MIN} (d_{ij}), \forall i, j \text{ and } i \neq j \quad (8)$$

The main goal of filter design is choose the Gabor filter parameters such that objective function F_{obj} is maximized in order to move all clusters away from each other. However, this objective function is non-differentiable and discontinuous, deterministic optimization methods i.e. gradient descent method, Newton-Raphson, etc. cannot be able to solve these problems efficiently. Evolutionary based stochastic methods are found highly efficient for those kinds of optimization problems where the objective functions are non-differentiable. The scale of Gabor filter is designed as per the size of Texel of the texture class. The criteria to derive the standard deviation (σ) were selected from the scale (s) of Gabor filter as shown in Equation 9:

$$2 * \sigma + 1 = s \quad (9)$$

The scale of post filter operation was also considered as scale of Gabor filter.

Procedure to Optimize Gabor Parameters (U, V) Using Genetic Algorithm

The Gabor filter parameters are σ_x , σ_y , U, V, where σ_x , σ_y are variances along x and y-axes respectively and U and V are center frequencies along x and y-axes respectively. These parameters (U, V) were tried to be optimized using Genetic algorithm, in order to maximize the objective function (F_{obj}). In this approach, these parameters were represented into bit string using GA tool, then after the evolutionary rules and operators were applied. Thereafter, the best individual (with best score) are chosen for next generations and consequently the objective function evaluates maximize in each generation. Sufficient

number of generations was provided as stopping criteria to algorithm to run. Expecting that one may be able to get better result of the problem as the number of generations specified to the algorithm increases.

Overall Structure of Texture Based Filter and Classification Model

The model used in this work for texture based filtering and classification is discussed in Figure 3. The segmented image is obtained by inputting a sample image to the filtering and classification model through various phases. First, input image is passed through Gabor Filters ($F_{g1}(x, y)$ to $F_{gn}(x, y)$); thereafter their outputs are tuned by magnitude operators (MOP_1 to MOP_n) and finally passed through Gaussian Post Filters ($F_{p1}(x, y)$ to $F_{pn}(x, y)$). These outputs are inputted into various intermediate classifier stages (CS_1 to CS_n) as shown in Figure 3. These classifier stages use the Nearest Neighbor algorithm, which inherently work on minimum distance to find the closest class matching. Based on minimum distance, this classifier assigns a number to a pixel corresponding to a particular textured region to which it has highest matching (minimum distance). Finally, these outputs of intermediate classifiers are fed into final classifier block to get segmented output image. The algorithm used in final classifier takes pixel wise information from all the images and classifies each pixel to that texture class to which the filter-bank classifier stage combination model has classified maximum number of times.

However, the pixel which is classified maximum number of times does not represent unique classification, is marked as unclassified and assigned a value zero. Thereafter, all the unclassified pixels are selected to find their NXN neighborhood (N is taken as an odd number to capture equal distributive texture feature through all directions) and is assigned to that textured region (class) to which maximum number of classified pixels of that neighborhood belong. This neighborhood based classification technique minimizes probability of misclassification. Edge detection technique was used to find edges by convolving $[-1 \ 0 \ 1]$ and its transpose with the above mentioned classified image, resulting a completely segmented and classified image as an output. The accuracy of filter and classification model used was evaluated by defining a metric, "CA" to represent classification accuracy. It is calculated in the form of ratio of correctly classified pixels to the total number of pixels (expressed in percentage). The sample set of test images were used to evaluate this metric, whose classification results are known in advance as named ground truth.

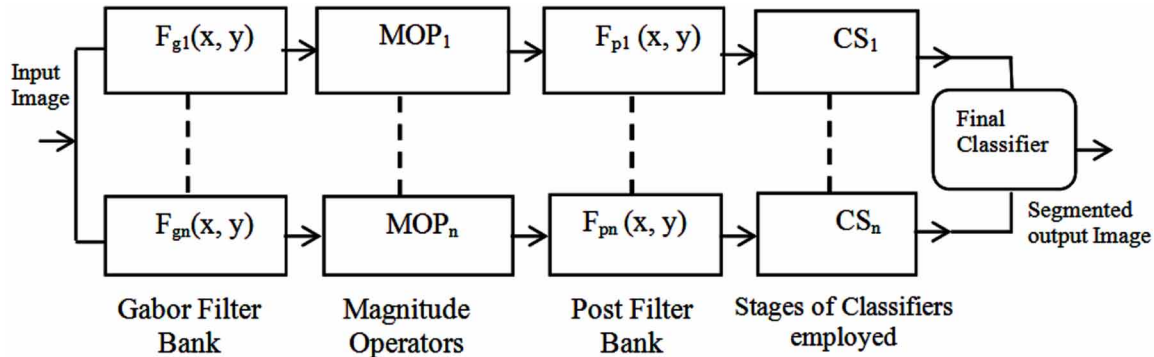
EXPERIMENTAL RESULTS

Data Collection

To illustrate the behavior of the methodology proposed in this work, medical image database DRIVE was downloaded from website (isi.uu.nl/Research/Databases/DRIVE/download.php), comprising 20 test and 20 training retinal fundus images. Test and training both set also comprises the manual segmented retinal images. These manual segmented retinal fundus images were considered to find the ground truth data (required to be known apriori) required to calculate the classification (segmentation) accuracy of filterbank-classification model.

The task of segmentation and classification, if retinal fundus images are considered as bi-partite images, such that it contains only two different textured regions, only one Gabor filter-Post filter cascade is required. In this approach, our objective is to form only two clusters and make them as far apart as

Figure 3. Block diagram of structure of filter and classification model



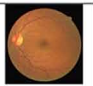
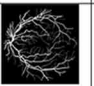
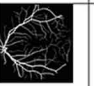

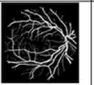

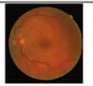
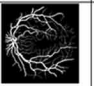
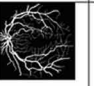

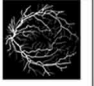
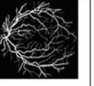

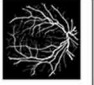
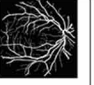

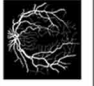
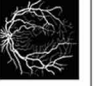

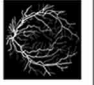
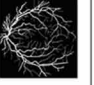

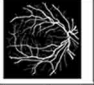
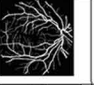



possible. Thus, to accomplish it the Euclidian distance between their cluster center points needs to be maximized. However, in this case, the Gabor filter employed needs only local optimization technique i.e. Gradient descent method to tune its filter parameters, as the objective function used here is differentiable and continuous. The classification and segmentation results are shown along with segmentation accuracy and filter parameters as shown in Table 1.

The qualitative and quantitative results shown in Table 1 were obtained by optimizing the Gabor filter parameters using gradient descent method considering the presence of only two different textured regions in the image. However, considering the complexity of the retinal images, it appears that it may have more than two different textured regions. For this case, the objective function is neither continuous nor differentiable. Therefore, it needs global optimization technique, i.e. Genetic Algorithm. Table 2 shows some selective qualitative and quantitative segmentation and classification results by optimizing filter parameters using Genetic Algorithm.

The results shown in Table 3 shows the sensitivity and specificity of the proposed segmentation model using hybrid Gabor filter and local optimization tool for various sets, whereas the results shown in Table 4 shows the sensitivity and specificity of the proposed segmentation model using hybrid Gabor filter and global optimization tool. In first case, retinal image was considered as bi-partite image (i.e. it may have two different textures), for that nature of objective function to optimize Gabor filter parameters would be differentiable and continuous. Therefore, local optimization tool was incorporated in the model. Thereafter, to check the presence of more than two different textures, non-differentiable and non-continuous objective function is required to optimize Gabor filter parameters. Therefore, a global optimization tool was also incorporated in Gabor texture based segmentation model, in order to obtain improved sensitivity and specificity. The results in Table 3 and 4 also show the false positive and false negative classification results of our proposed model, which may be further improved by incorporating Artificial Neural Network classification model. Our proposed segmentation model outperforms the classification results for such highly complex natural images as supported by results shown as Sensitivity and Specificity in Table 3 and 4 with less false positive and negative results.

Significant Enhancement of Segmentation Efficiency of Retinal Images

Table 1. Qualitative and quantitative results with classification accuracy using Gabor filter by optimizing filter parameters with gradient descent method



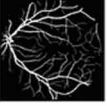






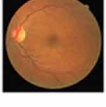










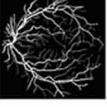



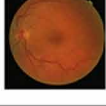


Result set-1: Gabor Parameters: $g_x = 7, g_y = 7, U = -0.030008, V = 0.030008$			
Original Image	Ground Truth Classification (standard Manual segmentation)	Classified Image using our protocol	Classification Accuracy (CA) (%)
			82.309977
			81.149685
			81.003152
Result set-2: Gabor Parameters: $g_x = 7, g_y = 7, U = 0.001888, V = -0.001888$			
			82.985362
			82.116469
			82.079494
Result set-3: Gabor Parameters: $\sigma_x = 10, \sigma_y = 10, U = -0.018934, V = 0.018934$			
			83.519214
			82.536823
			82.930810
Overall Classification Accuracy (Accuracy \pm standard deviation) = 82.2923 ± 0.8289			

CONCLUSION

The segmentation of blood vessels is highly required process in diagnosis of diabetic retinopathy. This paper proposed a new method to automate the process of segmenting out the blood vessels from retinal images. The results obtained in this work provides mathematical and experimental evidence to promote applying Gabor filters on textured images, like retinal images, producing a crucial output characteristic signature, which helps in segmenting and classifying the images with better accuracy. As it is evident, the filters employed in an ideal autonomous texture segmentation tool, cannot be customized for single type of textures. Therefore, to capture the spreading and different orientation and frequency domain of the textures of interest, a bank of filters is required to implement the filter and classification model

Significant Enhancement of Segmentation Efficiency of Retinal Images

Table 2. Qualitative and quantitative results with classification accuracy using Gabor filter by optimizing filter parameters with genetic algorithm

Result set-1: Gabor Parameters: $\sigma_x = 7$, $\sigma_y = 7$, $U = -0.020004$, $V = 0.020004$			
Original Image	Ground Truth Classification (standard Manual segmentation)	Classified Image using our protocol	Classification Accuracy (CA) (%)
			83.808977
			82.459685
			82.024152
Result set-2: Gabor Parameters: $\sigma_x = 7$, $\sigma_y = 7$, $U=0.002767$ and $V=-0.002767$			
			83.175362
			83.118469
			83.389494
Result set-3: Gabor Parameters: $\sigma_x = 10$, $\sigma_y = 10$, $U=-0.018934$, $V=0.018934$			
			83.979214
			83.337823
			83.430810
Overall Classification Accuracy (Accuracy \pm standard deviation) = <u>83.1916 \pm 0.6148</u>			

Significant Enhancement of Segmentation Efficiency of Retinal Images

Table 3. Sensitivity and specificity of segmentation model using Gabor filter by optimizing filter parameters with gradient descent method

Image No.	Total No. of Pixels in each Image	Pixels Correctly Classified in each Image	Sensitivity %	Specificity %	False Positive %	False Negative %
Result Set-1: Gabor Parameters: $\sigma_x = 7, \sigma_y = 7, U = -0.030008, V = 0.030008$						
1	659920	543180	82.31	81.08	18.92	17.69
2	659920	535523	81.15	81.66	18.34	18.85
3	659920	534556	81.00	81.73	18.27	19.00
Result Set-2: Gabor Parameters: $\sigma_x = 7, \sigma_y = 7, U = 0.001888, V = -0.001888$						
1	659920	547637	82.99	82.10	17.90	17.01
2	659920	541903	82.12	82.53	17.47	17.88
3	659920	541659	82.08	82.55	17.45	17.92
Result Set-3: Gabor Parameters: $\sigma_x = 10, \sigma_y = 10, U = -0.018934, V = 0.018934$						
1	659920	551160	83.52	82.73	17.27	16.48
2	659920	544677	82.54	83.23	16.77	17.46
3	659920	547277	82.93	83.03	16.97	17.07
Average Results			82.29	82.29	17.70	17.70

Table 4. Sensitivity and specificity of segmentation model using Gabor filter by optimizing filter parameters with genetic algorithm

Image No.	Total No. of Pixels in each Image	Pixels Correctly Classified in each Image	Sensitivity %	Specificity %	False Positive %	False Negative %
Result Set-1: Gabor Parameters: $\sigma_x = 7, \sigma_y = 7, U = -0.020004, V = 0.020004$						
1	659920	553072	83.81	82.24	17.76	16.19
2	659920	544168	82.46	82.92	17.08	17.54
3	659920	541294	82.02	83.13	16.87	17.98
Result Set-2: Gabor Parameters: $\sigma_x = 7, \sigma_y = 7, U = 0.002767, V = -0.002767$						
1	659920	548891	83.18	83.25	16.75	16.82
2	659920	548515	83.12	83.28	16.72	16.88
3	659920	550304	83.39	83.15	16.85	16.61
Result Set-3: Gabor Parameters: $\sigma_x = 10, \sigma_y = 10, U = -0.018934, V = 0.018934$						
1	659920	554196	83.98	83.38	16.62	16.02
2	659920	549963	83.34	83.71	16.29	16.66
3	659920	550577	83.43	83.66	16.34	16.57
Average Results			83.19	83.19	16.80	16.80

(Dunn et. al, 1995). This work showed the segmentation and classification of retinal images by applying Gabor and post Gaussian filter bank optimizing filter parameters firstly by Gradient descent method and finally by Genetic algorithm. The comparative results are shown in Table 1 and 2 with improved

classification accuracy. Sensitivity and Specificity shown in Table 3 and 4 show the robustness of our proposed segmentation model with less false positive and negative results. As Genetic Algorithm (GA) is an evolutionary algorithm provides efficient global search in parameter space, employing GA only a few Gabor filter can be designed efficiently to obtain efficient classification and segmentation of multi-textured images. It is not always required the number of textures present in the image to be equal to number filters in filter-bank. It has been observed that for some cases, a smaller filter-bank (lesser number of filters than number of textures) produces more efficient discrimination for a given set of textures. However, the algorithm used in final classifier block (as shown in Figure 3) uses pixel-wise information for processing, consequently slow in speed in its inherent nature.

The classification work in this paper can also be extended to simulate the whole process of classification by an Artificial Neural Network (ANN). The standard manual segmented retinal images (prepared by trained medical expert) available in standard database (DRIVE) can be used to train ANN. Once ANN is trained properly, it will ready to take input data from the feature space and will assign a class (textured region) accordingly. The problem associated with the classification of overlapping clusters formed in some higher dimension can also be resolved using ANN as classifier. In such applications, the properly trained ANNs are found very efficient and fast in classification. The hybrid of trained ANN and tuned Filter-bank may be utilized in implementing a stand-alone automated system for real time multi-textured image processing applications.

This research was previously published in the International Journal of Computer Vision and Image Processing (IJCVIP), 7(1); edited by Jose Garcia-Rodriguez, pages 44-58, copyright year 2017 by IGI Publishing (an imprint of IGI Global).

ACKNOWLEDGMENT

The authors would like to give thanks to the owners of the retinal image database (DRIVE) that was used in this paper and also thanks to Prof. (Dr.) Tapobrata Lahiri, Professor, IIIT Allahabad, India for giving valuable suggestions during study of this paper's work.

REFERENCES

- Ahmed, W. R., Eswaran, C., & Subhas, H. (2008). Diabetic Retinopathy: A Quadtree Based Blood Vessel Detection Algorithm Using RGB Components in Fundus Images. *Journal of Medical Systems*, 2008, 147–155. PMID:18461818
- Bovik, A. C., Clark, M., & Geisler, W. S. (1990). Multichannel Texture Analysis using localised spatial filters. *IEEE Transactions on Pattern Analysis and Machine Intelligence*, 12(1), 55–73. doi:10.1109/34.41384
- Chaudhuri, S., Chatterjee, S., Katz, N., Nelson, M., & Goldbaum, M. (1989). Detection of blood vessels in retinal images using two dimensional matched filters. *IEEE Transactions on Medical Imaging*, 8(3), 263–269. doi:10.1109/42.34715 PMID:18230524

Significant Enhancement of Segmentation Efficiency of Retinal Images

Das, S. and Kumar, G.P. and Yegnanarayana, B. (1998). One Dimensional Gabor Filtering for Texture Edge Detection. In *Computer Vision, and book-title: Graphics and Image Processing - Recent Advances* (pp. 231 – 237).

Dennis, D., William, E. H., & Joseph, W. (1994). Texture Segmentation Using 2-D Gabor Elementary Functions. *IEEE Transactions on Pattern Analysis and Machine Intelligence*, 16(2), 130–149. doi:10.1109/34.273736

Dey, N., Roy, A. B., Pal, M., & Das, A. (2012). FCM Based Blood Vessel Segmentation Method for Retinal Images. *International Journal of Computer Science and Network*, 1(3), 148–152.

DRIVE- Retinal Image Database. (n. d.). Retrieved from <http://www.isi.uu.nl/Research/Databases/DRIVE/download.php>

Dunn, D., & Higgins, W. E. (1995). Optimal Gabor Filters for Texture Segmentation. *IEEE Transactions on Image Processing*, 4(7), 947–964. doi:10.1109/83.392336 PMID:18290045

Goldberg, D. E. (1989). *Genetic Algorithms in Search, Optimization, and Machine Learning*. Reading: Addison-Wesley.

Ho, C.-Y. & Pai, T.-W. (2011). An automatic fundus image analysis system for clinical diagnosis of glaucoma. *Proceedings of the International Conference on Complex, Intelligent, and Software Intensive Systems*, Seoul (pp. 559-564).

Huang, S., Yang, Y., & Xia, Y. (2006), Segmentation of Retinal Image Vessels with a Novel Automated Approach. *Proceedings of the Sixth International Conference on Intelligent Systems Design and Applications (ISDA'06)* (Vol. 2, pp. 488-492). IEEE. doi:10.1109/ISDA.2006.253885

Kinney, K. E. Jr. (1994). A Perspective on the Work in this Book. In K. E. Kinney (Ed.), *Advances in Genetic Programming* (pp. 3–17). Cambridge: MIT Press.

Kulikowski, J. J., Marcelja, S., & Bishop, P. (1982). Theory of spatial position and spatial frequency relations in the receptive fields of simple cells in the visual cortex. *Biological Cybernetics*, 43(3), 187–198. doi:10.1007/BF00319978 PMID:7093361

Lili, X., & Shuqian, L. (2010). A novel method for blood vessel detection from retinal images. *Biomedical Engineering Online*, 9, 9–14. PMID:20163724

Lingel, N. J. (n. d.). Care of the patient with diabetic retinopathy. Pacific On-Line Optometry Education.

Medhane, D., & Shukla, A. (2016), An Automatic Approach to Segment Retinal Blood Vessels and Its Separation into Arteries/Veins. *Proceedings of the International Conference on Data Engineering and Communication Technology, AISC* (Vol. 468, pp. 191-199). doi:10.1007/978-981-10-1675-2_21

Olson, J. A., Strachana, F. M., & Hipwell, J. H. (2003). A comparative evaluation of digital imaging, retinal Photography and optometrist examination in screening for diabetic retinopathy. *Diabetic Medicine*, 20(7), 528–534. doi:10.1046/j.1464-5491.2003.00969.x PMID:12823232

Osareh, A., & Shadgar, B. (2010). An Automated Tracking Approach for Extraction of Retinal Vascularity in Fundus Images. *J Ophthalmic Vis Res*, 5(1), 20–26. PMID:22737322

Palomera-Perez, M. A., Martinez-Perez, M. E., Benitez-Perez, H., & Ortega-Arjona, J. L. (2010). Parallel multiscale feature extraction and region growing: Application in retinal blood vessel detection. *IEEE Transactions on Information Technology in Biomedicine*, 14(2), 500–506. doi:10.1109/TITB.2009.2036604 PMID:20007040

Sinthanayothin, C., Boyce, J. F., Williamson, T. H., Cook, H. L., Mensah, E., Lal, S., & Usher, D. (2002). Automated detection of diabetic retinopathy on digital fundus images. *Diabetic Medicine*, 19(2), 105–112. doi:10.1046/j.1464-5491.2002.00613.x PMID:11874425

Teng, T., Lefley, M., & Claremont, D. (2002). Progress towards automated diabetic ocular screening: A review of image analysis and intelligent systems for diabetic retinopathy. *Medical & Biological Engineering & Computing*, 40(1), 2–13. doi:10.1007/BF02347689 PMID:11954703

Zhen, Y., Gu, S., Meng, X., Zhang, X., Zheng, B., Wang, N., & Pu, J. (2014). Automated identification of retinal vessels using a multiscale directional contrast quantification (MDCQ) strategy. *Medical Physics*, 41(9), 092702. doi:10.1118/1.4893500 PMID:25186416

Chapter 5

Analogizing the Thinning Algorithm and Elicitation of Vascular Landmark in Retinal Images

Shiny Priyadarshini J.
Madras Christian College, India

Gladis D.
Presidency College, Chennai, India

ABSTRACT

The retinal tissue is composed of network of blood vessels forming a unique biometric pattern. Feature extraction in retinal blood vessel is becoming an emerging trend in the field of personal identification. Because of its unique identity and less vulnerability to noise and distortion it has become one of the most secured biometric identities. The paper highlights the segmentation of blood vessel and the extraction of feature points such as termination and bifurcation points using Zhang Suen's thinning algorithm in retinal images. A comparison has been made and results are analyzed and tabulated between Zhang Suen and Morphological thinning. The count has been taken for both termination and bifurcation markings as spurious and non-spurious minutiae. The spurious minutiae are removed by using the crossing number method. The results clearly depict that the Zhang Suen's thinning algorithm gives better result when compared to morphological thinning.

1. INTRODUCTION

Retinal pattern is a unique biometric identification which forms the inner layer of the eye where even identical twins do not share the same pattern. The pattern remains unchanged from birth to death. The retinal blood vessel pattern plays a vital role as a secured personal identification mark. The fundus image obtained from the retina scanners can be accessed only from living human beings because the retina decays soon after the death. So it is mainly used in military bases and governments where very high

DOI: 10.4018/978-1-5225-5195-9.ch005

secured identifications are required. In the article by Kataryzna and Adam (2004) the authors say that the retinal blood vessels are the land mark of fundus images. A typical fundus image and the important parts of retina are shown in Figure 1.

The retina is found in the posterior region of an eye which forms a tissue like substance mainly composed of Optic nerve, blood vessels and Macula. In the article by Fabiola and Edgardo (2009) the authors says that the blood vessel pattern forms a unique structure for each individual and are analyzed which results in tiny characteristics points.

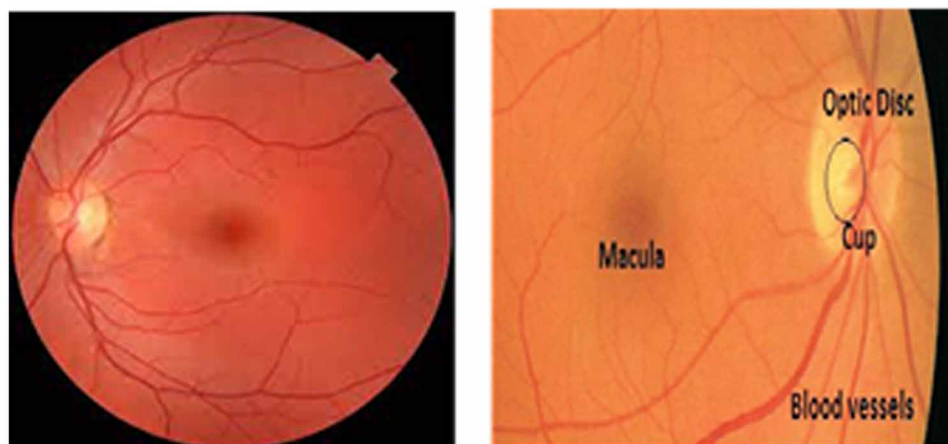
2. EXISTING WORK

Stapor and Switonski (2004) presented Segmentation using Mathematical morphology such as top hat transform in retinal images. Villalobos-Castaldi and Felipe-Riveron (2009) presented segmentation steps and minutiae retrieval in retina. Fraz, Remagnino and Hoppe (2012) presented the segmentation methodologies on retinal images. Divya and Shantala (2013) presented the blood vessel extraction using optic disc in retina. Ahmad and Butt (2013) presented segmentation using thresholding and filtering techniques in retina. Sivakumar and Chitra (2014) presented the improvised line detection and entropy thresholding in retinal images. Akhavan and Faez (2014) presented the centre line detection and segmentation using morphological operations and combined the two results to obtain the segmented image in retian. Monisha and Seldevchristopher (2015) presented segmentation in retina and also feature extraction along with matching.

3. PROPOSED METHODOLOGY

This paper focuses on the thinning methods for the retinal image. The retinal characteristics are obtained and compared by applying Zhang suen and morphological thinning algorithm. The different stages used in Retinal minutiae extraction are shown in Figure 2

Figure 1. Sample retinal image



4. RETINA PRE-PROCESSING

4.1. Segmentation

Segmentation is a pre-processing step to extract the blood vessel pattern in human retina. The fundus image captured from a fundus camera is given as an input and the binarized skeleton image is obtained as the output. The pre-processing stage is an essential step to have uniform appearance in the output image.

The fundus image is first converted into gray scale and the green channel is chosen as proposed in the article by authors Sivakumar and Chitra (2014) for further processing, since the green channel exhibits great contrast in blood vessels pattern. In image, the background pixels are black and the foreground pixels are white. The contrast between blood vessels (foreground) and the retinal tissue (background) is generally poor or has non – uniform lighting condition. In the article by Razieh and Karim (2014) the authors have proposed double thresholding for background exclusion. Therefore, it is necessary to deepen the contrast of these images to provide better transform representation for subsequent image analysis steps. Adaptive Histogram Equalization function is used for enhancing the contrast of an image. To analyze shapes within the image and to estimate the background, morphological operations are also used.

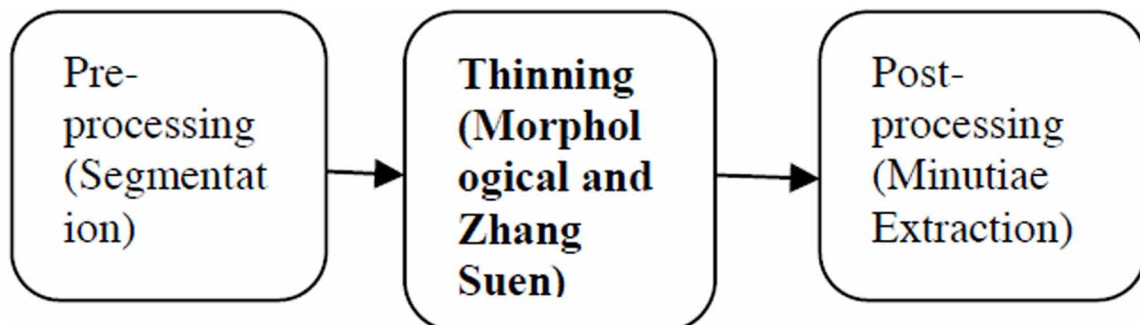
Structuring element is applied to the image. The number of pixels being added or removed from the object in the image is affected by the size and shape of the structuring element. The morphological open function is used for thickening the retinal blood vessels. The Morphological operation such as erosion followed by dilation is also done by using structuring element. To get more uniform background, the background image is subtracted from the processed image.

Filters are also used here to highlight and improve contrast in vessel identification which was also proposed in the article as Gaussian filter by authors Asloob and Saira (2013). The crucial step is to eliminate background and focus on foreground so that foreground objects can be easily analyzed. The segmented image is shown in Figure 3(b).

4.2. Thresholding

It is a process where the segmented image is binarized using thresholding. In the article by Divya and Shantala (2013), the segmentation using thresholding has been proposed. The global threshold value

Figure 2. Stages in retinal feature extraction



is computed automatically based on the intensity of an image. The binary image has only two possible values, zero's and one's and are normally displayed as black and white.

5. THINNING

The retinal image is thinned using Zhang-Suen thinning algorithm. Thinning is a process to eliminate redundant pixels where the pixels are just one pixel wide. A sample of thinned image using Zhang -suen thinning is shown in Figure 4(b). Algorithm 1 has the following two iterations.

6. RETINA POST-PROCESSING

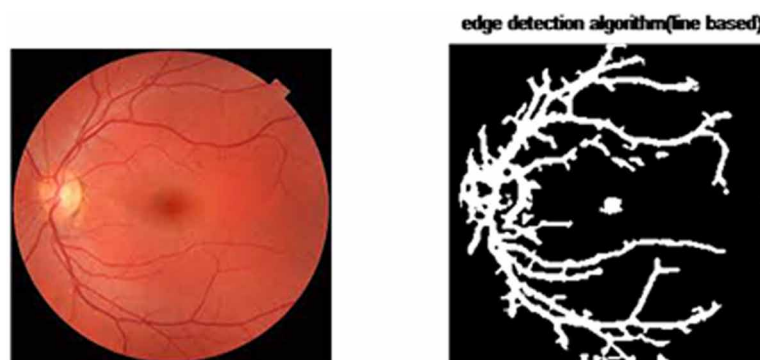
6.1. Bifurcations and Terminations Marking

It is a process to mark the terminations and bifurcations. In the article by Lincy and Seldevchristopher (2015) the authors have extracted the minutiae points called Termination and Bifurcation. Termination is the immediate ending whereas bifurcation refers to branches. The retinal image is divided into a 3x3 window. For each window the crossing number concept is applied. If the central pixel is 1 and has exactly 3 one-value neighbours then it represents a bifurcation. If the central pixel is 1 and has only one-value neighbour then it represents a termination. Figure 5 (a) depicts retinal image with spurious markings.

6.2. Spurious Minutiae Removal

To maintain the image identity, spurious bifurcations and terminations points are removed. This is done by calculating the average inter ridge distance D . The average inter-ridge width D refers to the average distance between two neighbouring lines for each row. Inter-ridge distance (D) is calculated as Sum of all pixels with value 1 divided by the row length. The spurious points are eliminated if the distance between two bifurcations and two terminations is less than six and also if the distance between terminations and bifurcations is less than six. Figure 5(b) depicts retinal image with non- spurious markings.

Figure 3. (a) Original images & (b) Blood Vessel Segmented image



Analogizing the Thinning Algorithm and Elicitation of Vascular Landmark in Retinal Images

Algorithm 1

1. Input image of size $m \times n$

2. Divide the image into 3×3 matrix

3. For each 3×3 matrix arrange the eight neighbors in clockwise manner

4. $N(P1)$ = the number of non-zero pixel neighbors of $P1 (= \sum(P2..P9))$

$S(P1)$ = the number of transitions from 0 to 1, (0 \rightarrow 1) in the sequence $P2, P3, \dots, P8, P9, P2$.

5. Iteration 1:

For all $N(i, j)$ do,

All pixels are set to 0 when,

Condition 0: The pixel is 1 and has eight neighbors

Condition 1: $2 \leq N(P1) \leq 6$

Condition 2: $S(P1) = 1$

Condition 3: $P2 * P4 * P6 = 0$

Condition 4: $P4 * P6 * P8 = 0$

6. Iteration 2:

For all $N(i, j)$ do,

All pixels are set to 0 when,

Condition 0: The pixel is 1 and has eight neighbors

Condition 1: $2 \leq N(P1) \leq 6$

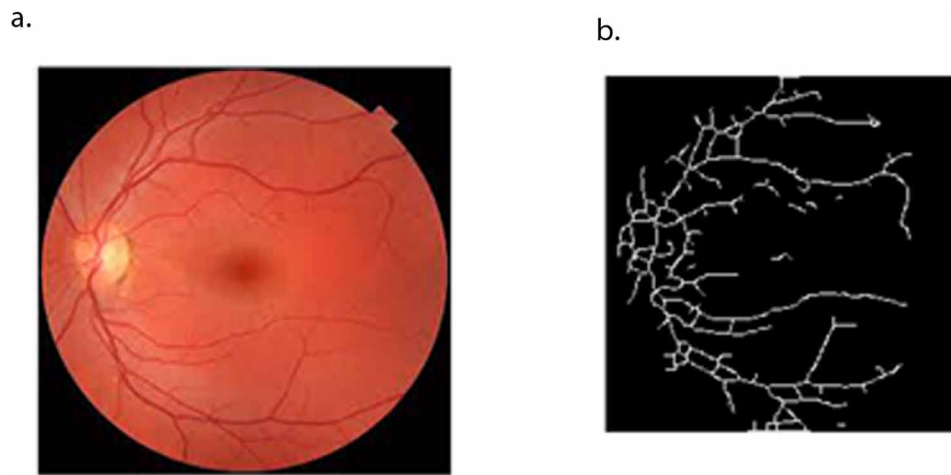
Condition 2: $S(P1) = 1$

Condition 3: $P2 * P4 * P8 = 0$

Condition 4: $P2 * P6 * P8 = 0$

7. Delete pixel $N(i, j)$

Figure 4. (a) Original images & (b) Zhang Suen's thinned image



7. SIMULATION RESULTS

In pre-processing stage, the blood vessels are segmented and thinned from the original image to extract the feature points. Samples of five retinal images are taken randomly from the DRIVE database which were also used by authors Frarz et.al (2012) and tested for Zhang-Suen thinning algorithm. Table 1 represents five retinal sample images which depicts its segmented blood vessel image along with its Zhang-Suen's thinned image.

Table 2 depicts the same five sample images with morphological thinning. The last two columns represent the termination and bifurcation count taken separately for Zhang-Suen and morphological thinning. The images are shown with extraction taken after spurious point removal. It clearly shows that the termination and bifurcation count is less for Zhang- Suen when compared to morphological thinning.

Figure 5. (a) Bifurcations and Terminations with Spurious Markings (b). Bifurcations and Terminations with spurious removal

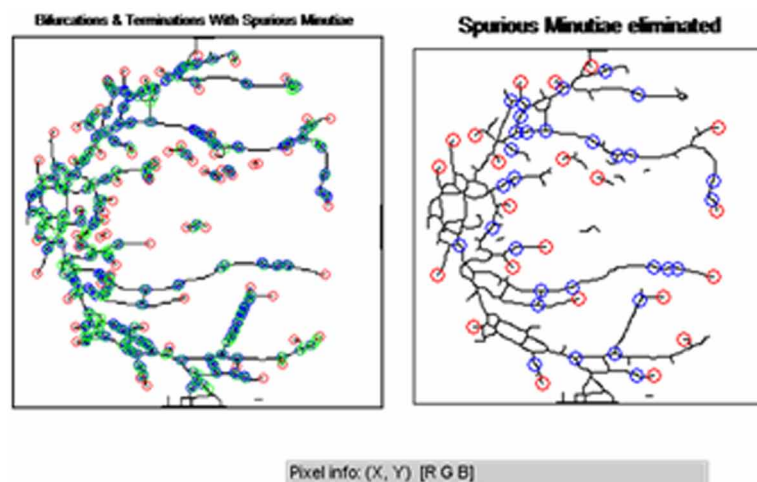


Table 1. Five retinal sample images- Original image, Segmented image, Zhang-Suen thinned image



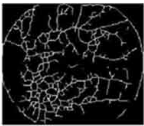
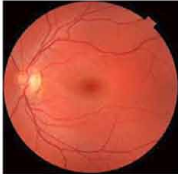

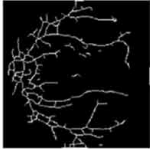






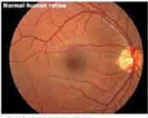


	Original image	Segmented image	Zhang suen thinned image
R1		edge detection algorithm(line based) 	
R2		edge detection algorithm(line based) 	
R3		edge detection algorithm(line based) 	
R4		edge detection algorithm(line based) 	
R5		edge detection algorithm(line based) 	

Table 3 shows the typical count taken for termination and bifurcation points for Zhang-Suen and Morphological thinning after spurious removal. It was found that the results remain the same for all five images with less count for Zhang-Suen when compared to morphological thinning.

8. CONCLUSION

The results show that the Zhang Suen thinning algorithm gives better result when compared to morphological thinning in terms of terminations and bifurcation count thus the scope of the work in developing a unique personal identification using retinal images has been achieved. The results show less terminations and bifurcations count which makes the pattern matching easier and faster.

Analogizing the Thinning Algorithm and Elicitation of Vascular Landmark in Retinal Images

Table 2. Five retinal sample images- Morphological thinning, Non spurious- Zhang-Suen, Non spurious- Morphological

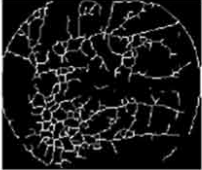
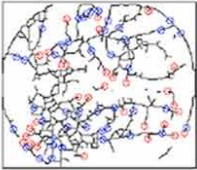
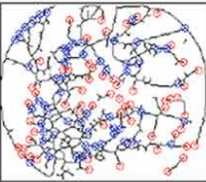
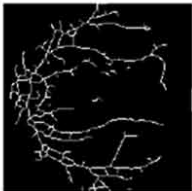
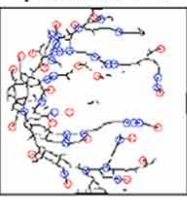
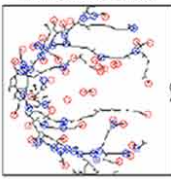

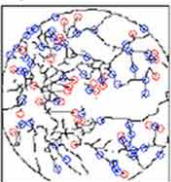
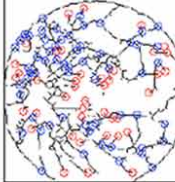

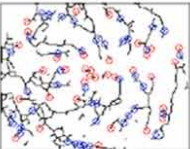
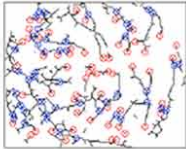

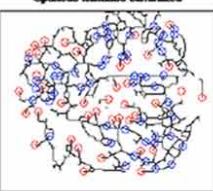
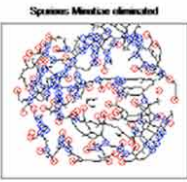
	Morphological thinning	Non spurious- Zhang suen	Non spurious- Morphological
R1		<p>Spurious: Noise eliminated</p>  <p>Real info: (10, 130) [1 1 1]</p>	<p>Spurious: Noise eliminated</p>  <p>Real info: (X, Y) [R G B]</p>
R2		<p>Spurious: Noise eliminated</p>  <p>Real info: (2, 140) [1 1 1]</p>	<p>Spurious: Noise eliminated</p>  <p>Real info: (X, Y) [R G B]</p>
R3		<p>Spurious: Noise eliminated</p>  <p>Real info: (X, Y) [R G B]</p>	<p>Spurious: Noise eliminated</p>  <p>Real info: (X, Y) [R G B]</p>
R4		<p>Spurious: Noise eliminated</p>  <p>Real info: (21, 120) [1 1 1]</p>	<p>Spurious: Noise eliminated</p>  <p>Real info: (X, Y) [R G B]</p>
R5		<p>Spurious: Noise eliminated</p>  <p>Real info: (X, Y) [R G B]</p>	<p>Spurious: Noise eliminated</p>  <p>Real info: (3, 136) [1 1 1]</p>

Table 3. Typical count taken for termination and bifurcation points for Zhang-Suen and Morphological thinning after spurious removal

Retina Names	Zhang Suen		Morphological	
	Non-Spur		Non-Spur	
	T	B	T	B
R1	31	43	60	58
R2	22	31	39	34
R3	31	54	41	60
R4	34	42	58	48
R5	40	50	62	79

REFERENCES

- Ahmad, A., & Butt, S. (2013). Extraction of blood vessels in Retinal images using four different techniques. Hidawi publication.
- Akhavan, R., & Faez, K. (2014). Two Novel Retinal Blood vessel Segmentation Algorithms. *International Journal of Electrical and Computer Engineering*, 4(3), 398.
- Divya, C., & Shantala, C. P. (2013). *Automated Localization od Optic disc and blood vessel Extraction in Retinal images*. Elsevier publications.
- Fraz, M. M., Remagnino, P., & Hoppe, A. (2012). *Blood vessel Segmentation methodologies in retinal images*. Elsevier.
- Monisha, L.S.L., & Seldevchristopher, C. (2015). Biometric identification using Retina scan. *International Journal of Advanced Research Trends in Engineering and Technology*, 2(23).
- Sivakumar, J., & Chitra, K. (2014). Segmentation of Blood Vessels using improve Line detection and entropy based Thresholding. *Journal of Theoretical & Applied Information Technology*, 63(2), 233-239.
- Stapor, K., & Switonski, A. (2004). Blood vessel segmentation from fundus eye images using mathematical morphology. *Studia Informatica*, 25(3), 41-48.
- Villalobos-Castaldi, F.M., & Felipe-Riveron, E.M. (2009). Fast Automatic Retinal Vessel Segmentation and Vascular Landmarks extraction method for Biometric applications.

This research was previously published in the International Journal of Cognitive Informatics and Natural Intelligence (IJCINI), 10(3); edited by Yingxu Wang, pages 29-37, copyright year 2016 by IGI Publishing (an imprint of IGI Global).

Chapter 6

Principles of Binocular Stereoscopic Imaging

Geoff Ogram
Stereoscopic Society, UK

ABSTRACT

The relation between visual perception and the recorded image is discussed in this chapter, emphasising the historical growth of the understanding of depth perception and its visual cues. The stereoscopic principle is explained in detail, and figures are given for comfortable viewing of stereoscopic images.

SPACE: MAPPING OUR SURROUNDINGS

Our world is three-dimensional. We were born into this three-dimensional space, we grew up in it and we handle it as part of our daily lives without conscious effort. We rarely contemplate its characteristics in detail or philosophise on its significance; we take it for granted. Nevertheless, if we wish to understand the principles underlying 3-D vision (stereopsis) or 3-D imaging (stereoscopy), we need to examine three-dimensional space in detail.

The word ‘space’ is not easy to define, although we may use it freely in common parlance. A typical dictionary definition is ‘Space, noun: that in which bodies have extension; a portion of extension; room; intervening distance; an interval; an open or empty place.’ A more helpful interpretation of ‘space’ can be achieved by mathematics. One of the many functions of mathematics is to describe the physical world in a succinct and accurate way. The dictionary definition covers both 2-D and 3-D space, but this chapter concentrates only on the latter. Using mathematical techniques we can map out our space to locate key points and show the relationships between various features within that space, such as the distance between two points or the angle between two lines. All such mapping enables us to understand the structure of that space in terms of the objects within it, their sizes, orientations and locations. These details can be established accurately with reference to some fixed point or scale. This principle will be familiar to anyone conversant with map-reading. Britain, for example, can be mapped onto flat sheets of paper despite the curvature of the Earth and the topography of the landscape. The space is two-dimensional and the reference lines are the N-S and E-W axes on which the Ordnance Survey references are based.

DOI: 10.4018/978-1-5225-5195-9.ch006

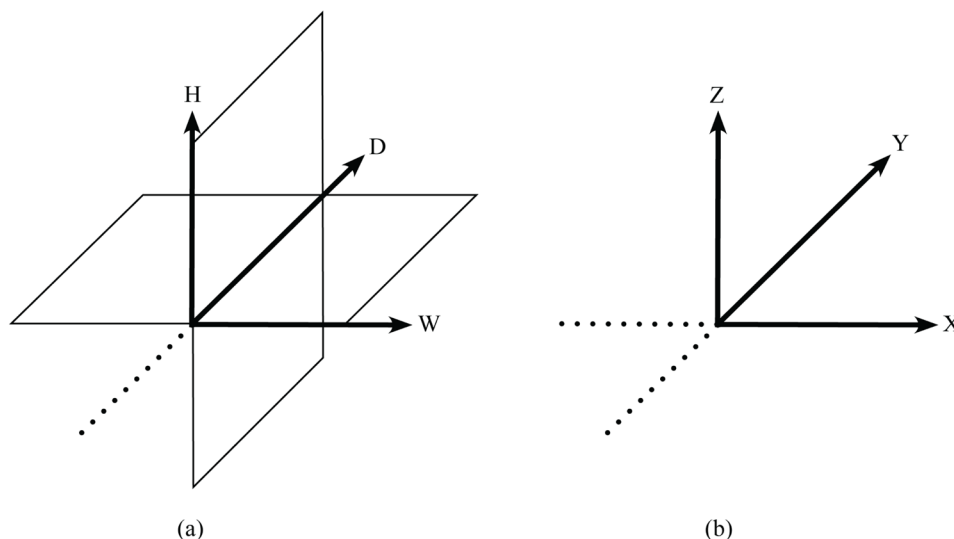
Thus the map reader can locate places and estimate distances from the scale of the map. Such maps are based upon the principle of a Cartesian graph plotted on a flat sheet with orthogonal x - and y -axes. Flat objects can be mapped in terms of width and depth (x - and y - coordinates). In a three-dimensional world we can apply the same principles, but we need an extra axis, the z -axis, perpendicular to both the x - and y - axes (Figure 1).

Whereas in 2-D representations the y -axis represents depth and the x -axis width, in 3-D space height is now represented by the z -axis. In this convention, distances in the y -direction are measured away from the observer. (Note, however, that in many mathematics textbooks the convention is to have the y -axis pointing out of the page.)

VISION: SEEING OUR SURROUNDINGS

Sight is arguably the most valuable of the senses, because it enables us to explore and understand our three-dimensional world to a greater extent than do hearing, taste, smell and touch. From the effects of visible light entering the eyes we are able to interpret information about our surroundings. The result of looking at our environment is usually described as 'creating an image' of that environment. The term 'image' is also applied to photographs and to what we see on a cinema or TV screen. An image matches what we see; it is an echo of reality. But the image we 'see' is not like that projected onto a screen or printed on paper. Light passes through the cornea and lens of the eye, then falls on the retina, and light-sensitive molecules within the rods and cones of the retina absorb the energy, resulting in a change in electrical potential. The detected signal is sent to the brain via the numerous nerve fibres. These signals are processed by the brain to produce what we call the 'image'. Like all real images produced by a convex lens, the retinal image is inverted, though the brain interprets it as being erect. The physiology of vision was discussed in Chapter 2.

Figure 1. (a) Three axes (x , y & z) mutually at 90° , representing width, depth, and height; (b) one of the conventional labelling methods for axes



RECORDING IMAGES

The images produced on the retina and processed by the brain are transitory, changing continuously as we look around and move about. Humankind seems to have longed to produce permanent images for thousands of years, from cave paintings to present-day sophisticated art forms. For centuries before this the principles of light propagation and image formation had been known, even in ancient Greece: as early as the fourth century BC Aristotle noted that sunlight passing through small apertures produced discs of light on the ground. This phenomenon was probably first described by the Chinese philosopher Mo-Ti in the fifth century BC, according to the sinologist Joseph Needham (1986).

The earliest demonstration of the projection of an entire outdoor image onto a screen indoors by a pinhole is attributed to Abu Ali Al-Hasan Ibn al-Haytham, known in the West as Alhazen, who described his work in his Book of Optics in 1021 (Crombie, 1990). He is credited as being the first person to appreciate that light passing through a small aperture produces an image of whatever is in front of it. A box with a pinhole aperture at one end and a translucent screen at the other, would project an inverted image of the view on the screen. This discovery marked an important contribution to the understanding of the way images formed in the eye, and demonstrated that light travelled in straight lines.

The image quality in a pinhole camera depends upon the size of the aperture: as its diameter is reduced the image becomes sharper (and less bright). But at a certain point the image begins to become unsharp again, this time owing to diffraction, a spreading of the light rays due to the wave nature of light. The principle of the pinhole camera was eventually scaled up using a darkened room with a larger aperture and a focusing lens. (Later workers included a mirror to render the image erect.) This construction became known as a *camera obscura*, which means literally 'dark chamber'. It has been shown that several artists, notably some of the Dutch Masters, including Vermeer, must have used portable versions of the camera obscura to produce images that could be traced in order to achieve accurate detail and convincing perspective, the rules of which were only imperfectly understood at the time. However, evidence of extensive use of the device is not conclusive. No doubt the artists who made use of the device wished that the beautiful images it produced could be made permanent; and there were many attempts to achieve this using materials known to be affected by light. But it was only in the early nineteenth century that scientific (and amateur) research at last led to the invention of photography.

THE PERCEPTION OF DEPTH

The disadvantage of these images was that while they represented the three-dimensional world they were themselves only two-dimensional. They were the equivalent of a one-eyed view, whereas most of us see the world through two eyes. This binocular vision gives us an enhanced ability to perceive the depths of objects and their spatial relationships in our immediate environment. The scientific name for this phenomenon is stereoscopy, ('seeing solid' from the Greek), and it signifies the ability to perceive depth as well as height and width. A more formal definition, by Chibisov (Valyus, 1966) was 'the science of the visual perception of the three-dimensional space surrounding us'. Valyus (1966) also states that the word 'is usually used to convey appreciation of relief, plasticity, roundness or spatial qualities of the visual images of the objects viewed.' Pinker (1997) discusses the interpretation of two-dimensional images in his book *How The Mind Works*. He points out initially that there is an element of illusion about various kinds of image and cites an example of the Victorian novelty in which a peephole in a door reveals a

Principles of Binocular Stereoscopic Imaging

well-furnished room, but when the door is opened the room is seen to be empty. The furnished room is a doll's house nailed over the peephole. Pinker also describes the work of Adelbert Ames Jr., a painter who turned to psychology. He hung rods and slabs from the ceiling of a room apparently at random. However, when seen through a peephole in the door there appeared to be a kitchen chair present. In his discussion of two-dimensional images, Pinker states:

Now, a picture is nothing but a more convenient way of arranging matter so that it projects a pattern identical to real objects. The mimicking matter sits on a flat surface, rather than in a dollhouse (sic) or suspended by wires, and it is formed by smearing pigments rather than cutting shapes out of wood. The shapes of the smears can be determined without the twisted ingenuity of an Ames.

The trick, Pinker said, had been stated succinctly by Leonardo da Vinci, who asserted that the perception of perspective was the same as would be obtained by a flat drawing seen behind a glass pane. It is our experience of the real world that enables us to view a flat (2-D) picture and from it gain a sense of the missing third dimension. In most photographs there will be visual clues that aid our understanding of the relative locations in space of the various objects within the picture. Some of these are to be seen in Figure 2.

We subconsciously compare this view with images of real landscapes stored in our memory, and conclude that the scene stretches into the distance from our vantage point. We deduce this from the following observations:

1. Various objects are partly obscured by others (one mountain by another, or part of the wall by a standing figure), so in each case the obscured object must lie farther away than the one that obscures it. A distant object cannot mask a closer one.

Figure 2. Illustrating visual clues to gauge depth (Great Wall of China)



2. The pathway appears to get narrower as it reaches the tower near the centre of the picture. We know that parallel lines appear to converge as they recede so we assume that the path leads away from us and that the tower is some way distant.
3. The size of the people in the photograph varies greatly. We know most adults are 1.6–2 m tall, so we deduce that the ‘larger’ man on the right is nearer to us than the ‘smaller’ man in shorts on the left. The same reasoning applies to other figures.
4. The mountains have a gradation of colours, some being very pale. We see this effect in life as a result of haze; the phenomenon is referred to as ‘aerial perspective’. The mountains that are paler (and bluer) in colour are more distant, and the fact that in this scene the darker ones partly obscure them confirms this.
5. The patterns of light and shade on objects reinforce the impression of solidity.
6. The closest objects are usually located near the bottom edge of the picture and the most distant ones nearer to the top (though there may be exceptions).

From the above observations and others we can compile a list of visual clues that help us to interpret the spatial aspects of the 2-D images. Not all such clues are necessarily present in every image, but they certainly exist in various combinations. In summary they are:

- **Masking (or Occlusion):** Nearer objects partially or wholly mask more distant ones, but not vice versa.
- **Perspective:** Parallel lines appear to converge in a direction away from the observer towards a point on the horizon (the vanishing point).
- **Relative Size:** If two objects of the same size are at different distances from the observer the farther one appears smaller as the distance increases.
- **Aerial Perspective:** The presence of haze in a landscape lowers the contrast of distant objects less distinct and produces a bluish hue.
- **Lighting and Shadows:** Side lighting produces shadows on objects and suggests their shape and solidity. Thus we can distinguish between a flat disc and a sphere of similar diameter and colour. If we view a photograph taken with the sunlight to one side of the camera, we may see an object such as a pole or tree casting a shadow along the ground and onto the front wall of a building.
- **Colour:** So-called aerial perspective is partly associated with colour, as mentioned above.
- **Relative Movement (Dynamic Parallax):** A classic example can be seen in the cinema when a scene is filmed (in 2-D) through the window of a moving train with the camera aimed at right angles to the direction of travel. Nearby objects such as trees appear to pass by rapidly; those farther away pass more slowly, while objects on the horizon appear to be almost stationary. Dynamic parallax is a key factor in depth perception. We rarely look at any real scene without some small involuntary head movements. Such movements change the relative positions of objects in the image we see, giving an immediate impression of depth.

There is also a psychological phenomenon associated with colour that may have some influence on depth perception of a 2-D image. It is that hues towards the red end of the spectrum, especially if saturated, can seem to stand out, whereas those towards the blue end, and desaturated colours, seem to recede. This effect can best be observed in projected images: bold lettering in a title, especially when seen against a plain blue or dark grey background, can often appear to float in front of the screen, while the background

recedes into it. The effect resembles that of looking into an empty box with words painted on a window in front. It may enhance the appearance of depth in a 2-D picture if the bright colours are on the nearer objects, but it can sometimes be disturbing if distant objects are in bolder colours than nearer ones.

All the above visual clues are important in judging spatial distribution of the various components in a flat image such as a photograph, painting or the image on a TV or cinema screen. They are the only factors that contribute to our relating of the perceived image to the real spatial world in which we live, and this ability develops in early childhood. The visual image alone is insufficient; it has to be assessed in conjunction with other stimuli. The classic scenario of the infant reaching out to grasp the moon is a valid one. Over the first few years of life, the child, by touching and feeling objects and by moving around the real world, will gain the experience required to relate the visual data to real space. A little later it learns to interpret the images representing that space more fully. In addition the child is all the time learning these spatial skills with two eyes, each with a slightly differing viewpoint. Now, the visual depth cues discussed above are relevant to our perception of three-dimensional images as to two-dimensional ones. But with binocular (two-eyed) vision we have the ability to gain additional information that would be denied to us if we were restricted to a view through one eye only. Stereoscopy enables us to recreate a visual experience of the real world with uncanny accuracy, provided we follow certain rules. Stepping too far outside these rules may introduce distortions to mar the illusion, as we shall see later. Fortunately, the eye-brain combination is fairly tolerant, and may ignore these distortions.

BINOCULAR VISION AND THE PERCEPTION OF DEPTH

If you move your head slightly when viewing a scene, the apparent movement of objects relative to one another gives the essential clue to true stereoscopy, the ability to perceive the depth of a scene by being aware of the third dimension, the y-axis of Figure 1. Moving the head laterally from one position to another causes the view of the scene to be changed because our viewpoint has shifted. When you view a scene with, say, your right eye closed, your left eye simply sees a flat image. If you now move your head about 65 mm to the right, so that your left eye now occupies the point previously occupied by your right eye, your eye will see a slightly different flat image, the 'parallax' described earlier. In this case you see the two images one after the other; but if you now view the same scene with your head still and both of your eyes open, you see the two flat images simultaneously, one with your left eye and the other with your right eye. The receptors in your cerebral cortex combine these images to provide you with a sense of depth that is lacking in a monocular image. The distance between the two viewpoints, i.e. your eye separation, is the stereo base. It differs from one person to another, but of course remains constant for any individual. In making stereoscopic images by photographic or other means the stereo base can sometimes be greater or less than this 'interocular distance', as long as this is appropriate for the conditions. In normal vision we are not usually aware of two separate images. Instead we seem to be looking out as if from a single eye positioned at the bridge of the nose. This is the so-called cyclopean image (Julesz, 1960), named after a race of giants in Greek mythology, who possessed only a single eye in the centre of their foreheads.

A simple experiment to illustrate parallax is as follows. Close your right eye and hold a pencil or similar object upright at arm's length and, viewing with your left eye alone, align the pencil with a vertical line such as the edge of a window frame, about 3 m or more away. Without moving the pencil or your head, close your left eye and open your right eye. The pencil will appear to have jumped to the left

relative to the window frame. If you repeat the experiment with the pencil closer to you, the apparent leftward movement of the pencil will be greater. Your left and right eye images make up what is termed a stereoscopic pair, and the pair of drawings in Figure 3 is a representation of what you have seen. It shows the difference between your left and right eye images. (Note that in this diagram the eyes are assumed to be focused on the pencil.)

In this experiment, the images are formed on the retinas of your eyes and interpreted by your brain; but we can create similar images as drawings or as photographs made from the two viewpoints occupied by the eyes. If these drawings or photographs are viewed in such a way that the left image is seen only by the left eye and the right image by the right eye, your brain combines them to reproduce the scene in depth as a three-dimensional sketch or, with colour photographs, a full-colour three-dimensional replica of the original scene. This is the basis of stereoscopy, and there are many techniques for accomplishing it. It is a simple concept, but to achieve the best results it requires a deep understanding of the subject.

LATERAL DISPLACEMENTS IN STEREO PAIRS

The pencil experiment described above employs a simple arrangement of two objects in which the nearer one (the pencil) appears to be laterally displaced leftwards relative to the background. With the left and right views placed side by side as in Figure 3, the window frame images are seen to have moved relative to the pencil images. As both of your eyes are focused on the pencil, it will not itself appear to have moved. When your eyes are focused on a near object any far object will appear to have a greater separation between the two images. These separations between corresponding points in the two images of any one object are known as homologous points or homologues.

Figure 3. A pencil-and-window experiment

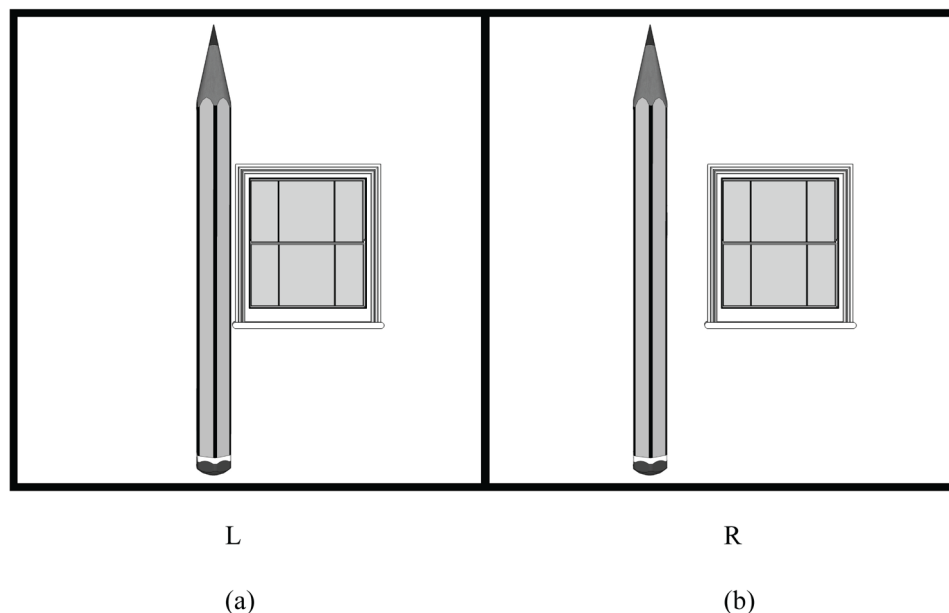
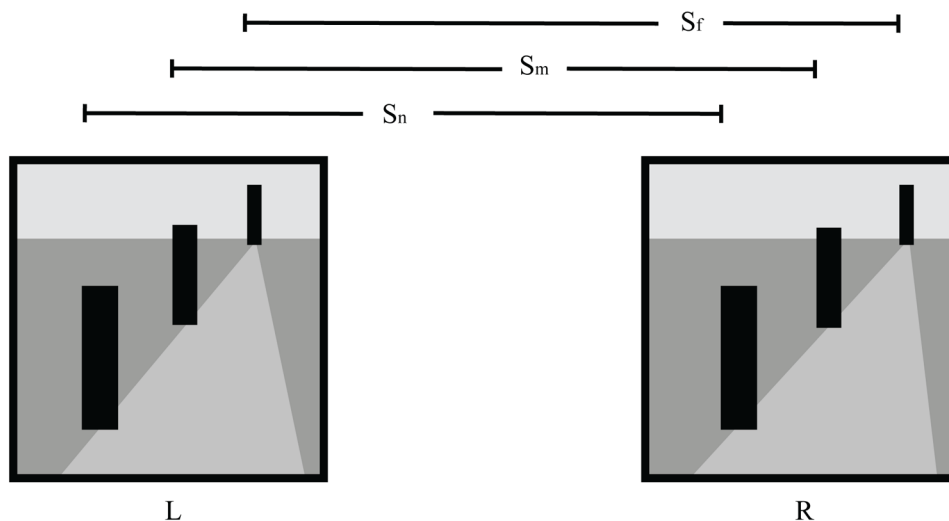


Figure 4 shows three post-like objects at different distances, the one on the left being closest and the one on the top right farthest away. In this diagram $s_f > s_m > s_n$. This illustration forms a true stereoscopic pair and can be viewed as such, verifying the relative locations of the objects as described. These separations are not true parameters because their absolute values depend upon how far apart the two images have been placed in whatever format is to be used for viewing them as a stereoscopic pair. The measurements are the differences $(s_f - s_m)$, $(s_f - s_n)$ and the like; these are independent of the left and right image spacing. Even so, the left and right images of a stereoscopic pair have to be a distance apart that suits whatever device is to be used for viewing, if the result is to be satisfactory.

If these differences in separation are to be of any practical use, they need to be compared against an appropriate reference value. The way in which your eyes function in normal vision provides a logical one. If you view any real scene, your eyes adjust in two ways: they re-focus (accommodation) and they rotate towards each other (convergence) as they focus on closer objects. In normal perceptual situations accommodation and convergence work together. However, the physiological mechanisms of accommodation and convergence are not fully linked, and can function independently. In viewing stereograms in a typical viewer they do so. Your eyes have to be focused on the surface of the photograph for every part of the image, but they converge as normal for objects at different distances, just as they would in a real scene. Thus, your eyes converge while maintaining a constant focus on the plane of the photograph; this does not occur in normal vision. (The eyes can even be made to diverge, but this is not a natural action and may result in eyestrain.)

The sense of depth resulting from binocular vision is not an absolute one. It enables us to understand the relative positions of objects but it does not tell us the precise distances; our eyes are continually adjusting their convergence by various amounts as we survey a photographed scene; but since we are not consciously aware of such movements or their magnitudes we do not relate these variations in convergence to actual distances. Nevertheless, with practice one can develop a certain degree of skill in estimating distances, using convergence as a subconscious clue.

Figure 4. Image separations for three objects at different distances



In theory, the axes of the eyes would be parallel when viewing an object at infinity, and when you view distant objects your sight-lines are so nearly parallel that for practical purposes they can be regarded as parallel. It therefore seems logical to take the separation of infinity homologues as a convenient standard, as it is essentially a natural limit. So, in defining the differences in separations of homologues, we can use the terms $(s_{\infty} - s_m)$, $(s_{\infty} - s_n)$, and so on, where s_{∞} is the separation of infinity homologues. The differences are now referred to as parallax deviations or simply deviations.

PERSPECTIVE DIFFERENCES IN STEREO PAIRS

So far this chapter has treated objects as consisting simply of a number of points (or flat cardboard cut-outs) situated at various distances from the observer. In reality, most objects are themselves three-dimensional and this will give rise to other differences in a stereo pair. Whereas in a flat object, photographed head on, the left and right images in a stereo pair are identical, for an object with depth the left eye sees more of its left side and the right eye sees more of its right side. Consequently each eye sees part of the object that is not visible to the other eye. Figure 5, representing a plan view of a cylinder, illustrates this point. L and R represent the eyes. In Figure 5 (a) both eyes can see the portion BC, but AC is visible only to the left eye and CD only to the right. For the same object seen at a greater distance as in Figure 5 (b), the portions AB and CD are both smaller, but BC and AD are both larger. While more of the object is seen with both eyes together the object does, of course, appear smaller because it is farther away. A further difference, which appears when you view an object such as a cube is in the shape that your two eyes perceive. Figure 6, another stereo pair, shows left and right images of a cube, each drawn in correct perspective. Consider the left face marked as HKLM in each image. The edge HK is farther away than the edge ML, and from our discussions of parallax deviations it follows that s_r is greater than s_n . So the shape of the face HKLM is different in the two images: in the right image, it is slightly narrower, so the lines HM and KL are slightly steeper. When viewed stereoscopically this left face of the cube appears as a receding plane, giving visual depth to the image of the cube.

ACCEPTABLE RANGE OF DEPTH

The pencil and window experiment described above provides another important aspect of depth perception. Try setting up the experiment as before, aligning the pencil with the edge of the window frame, but now view the result with both eyes. First focus on the window frame, and then refocus on the pencil. In the first instance you can become aware of two images of the pencil (somewhat out of focus), while in the second the pencil will be in focus but you will see two out-of-focus window frames in the background. This effect may be noticeable once you have become aware of it, although it should not normally be disturbing.

Now try a variation on the experiment, which may be enlightening. First, still holding the pencil at arm's length and viewing with both eyes, gradually move closer to the window frame. Then fix the pencil in some kind of holder and place it successively in several positions closer to the window frame, each time viewing with both eyes from your original vantage point. In each case, as the distance between the pencil and window frame decreases, the lateral distance between the relevant double images decreases, and eventually the double vision effect seems to disappear. In fact it is still present, but at some point

Principles of Binocular Stereoscopic Imaging

Figure 5. Perspective differences in stereo pairs: (a) near view, (b) far view

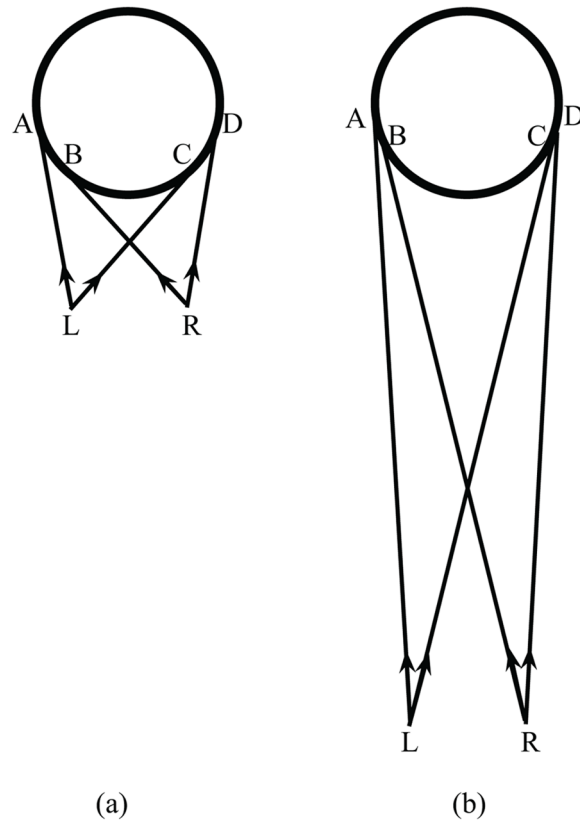
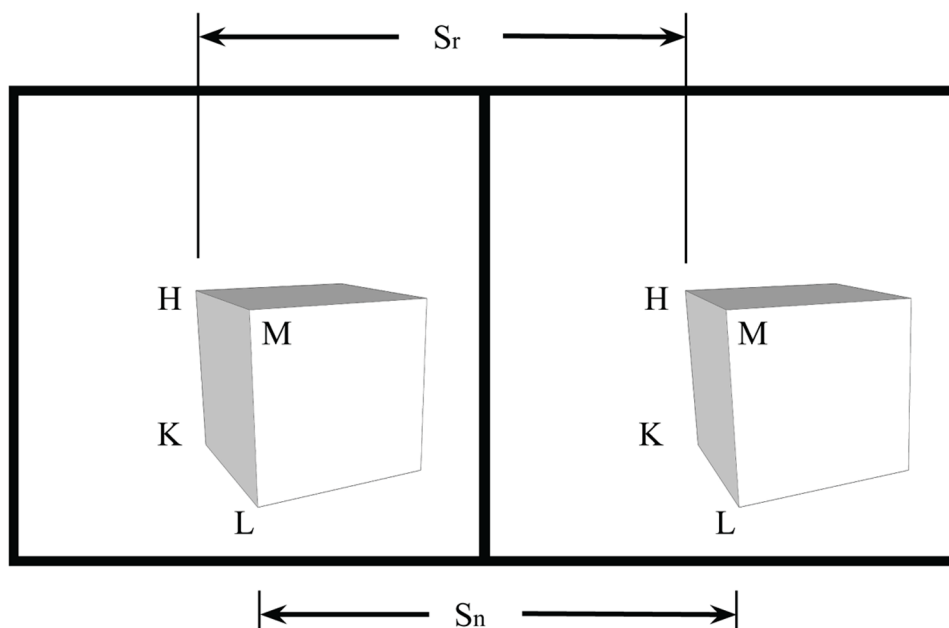


Figure 6. Left and right images of a cube



your eyes change focus repeatedly between the pencil to window frame and back without your being aware of it. This suggests that if the distance between the nearest and farthest objects in a scene is excessive, then the double imaging effect becomes too prominent for comfortable vision, and the image is described as having too much depth. There is thus a limited range of depth in a 3-D image that allows it to be viewed comfortably.

There is another difference between viewing reality and a viewing a 3-D photographic image. In a real scene, when an object is so close that it leads to double imaging, it is usually a simple matter to move away to a more favourable position. But when a still 3-D image includes too much depth there is no way of avoiding the discomfort. In the cinema or on 3-D TV the effect may be tolerable as long as it is short-lived, as when objects move swiftly across the screen and out of sight, or if the camera pans around a particular location.

It is generally agreed that the eye-brain combination will accept the view of an outdoor scene containing items ranging from the far distance to about two metres with no obvious double imaging, as long as the nearest object is no closer than this. This is not a precise physical law, but is a fair description of the acceptable depth range for comfortable viewing. By the same reasoning it follows that subjects for stereoscopic imagery should not exceed this range. Consider the geometry of Figure 7, which represents an overhead view of the eyes (marked L and R) looking at a scene that stretches to infinity, with a near object situated at N. For simplicity N is located on the left eye's direct line of sight.

The optic axes of the eyes are effectively parallel when they are focused on infinity; but when the focus is changed to the nearest object N at a distance D_N from the observer, the right eye swings through an angle θ . In adult humans the interocular distance (eye spacing) varies between some 55–75 mm. Taking a mean value of 65 mm (the dimension b in the diagram) we can calculate the value of θ . Plainly, angle LNR is equal to θ , so $\tan \theta = b/D_N$.

Since $D_N = 2000$ mm and $b = 65$ mm, $\tan \theta = 65/2000 = 0.03$, giving $\theta = 1.87^\circ$.

For convenience, we can round this value up to 2° . This angle represents approximately the maximum eye convergence that avoids obtrusive double imaging. As long as the nearest object is at 2 m distance it can be anywhere in the scene, and need not be confined to the line of sight of either eye. If it is located more centrally, say, then both eyes will turn inwards. The total eye convergence will not have exactly the same value, but for our purposes the difference will be negligible.

This 2 m-to-infinity restriction does not mean that we cannot view objects that are closer than 2 m; that would be absurd. We can view closer objects perfectly well, but in so doing we have to be aware of having too much depth for comfort. This suggests that some other restriction has to be imposed to prevent this occurring. The 2° eye convergence limit provides the answer. To avoid too much depth we must ensure that the permissible far point must be only so far from the nearest point that the 2° eye convergence difference is not exceeded. Thus if the nearest object is closer than 2 m then clearly we may not include in our view any objects at infinity. Instead, for every near point closer than 2 m we can calculate a corresponding permissible far-point distance based on this angle. Table 1 gives some values. Notice that there is a reduction in the acceptable depth range as the near-point distance becomes less. We are already familiar with the 2 m–infinity depth range, but for a near point just 1 m closer, i.e. at 1 m distance, the permissible far-point distance is reduced to as little as 2 m.

Another way to represent this information is to calculate the total permissible depth range ΔD that extends beyond the given near point distance D_N , i.e. $\Delta D = D_F - D_N$. Using the distances given in Table 1 we obtain Table 2.

Figure 7. Maximum depth range (2m to infinity) for comfortable viewing

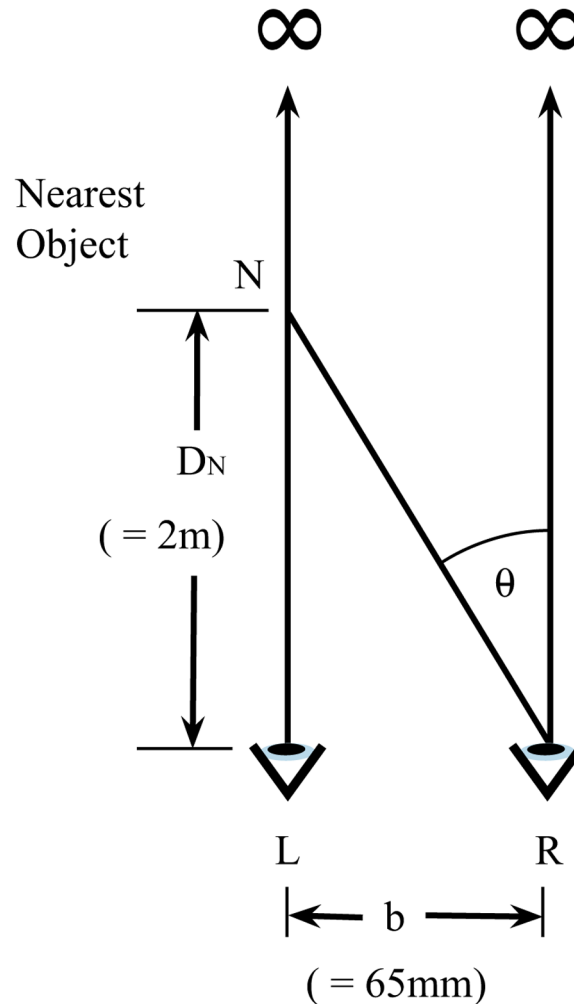


Table 1. Permissible far point distance D_F for a given near point D_N

Near distance D_N	200 mm	400 mm	600 mm	800 mm	1m	1.2m	1.4m	1.6m	1.8m	2m
Far distance D_F	222 mm	500 mm	857 mm	1333 mm	2m	3m	4.67m	8m	18m	inf

This information is useful when recording images by photography as camera viewpoints can be selected on the basis of the near point/depth range combinations so that the final stereoscopic image can be viewed comfortably. In a scene too much depth can lead to eyestrain. These acceptable depth ranges can be expressed as deviation values in images. Consider the two objects M and N in Figure 8, which lie on the axis of the left lens of a stereoscopic camera. From any object, light rays that pass through the optical centre of a lens are undeviated, enabling us to define in the simplest way where their images are

Figure 8. Parallax deviations d_m and d_n produced on film by point objects M and N , respectively

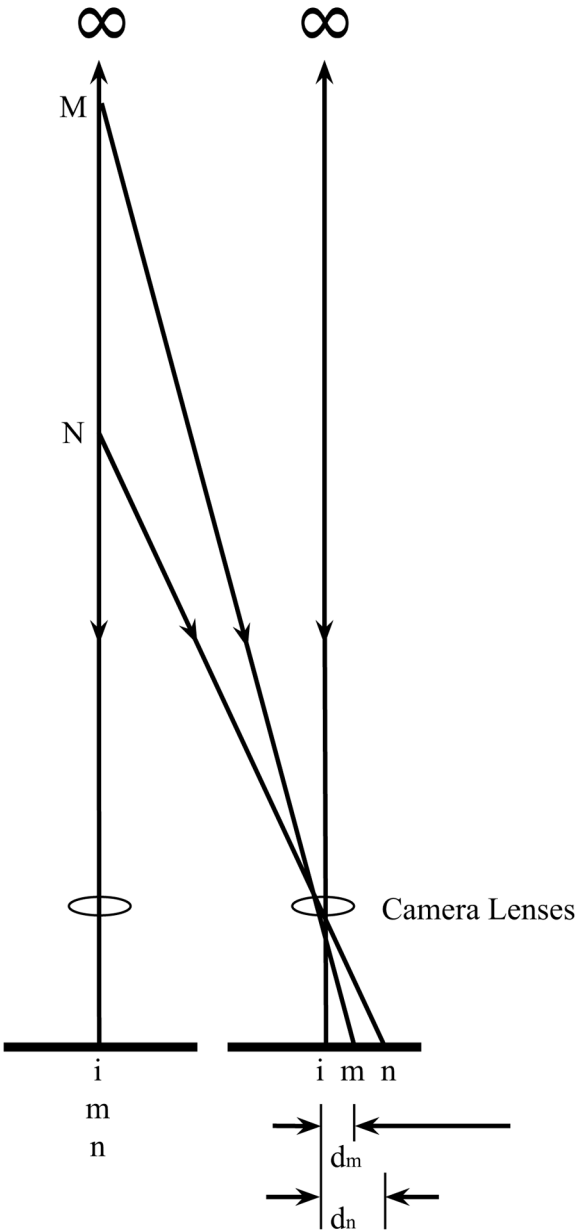


Table 2. Permissible depth range ΔD for a given near point distance D_N

D_N	200 mm	400 mm	600 mm	800 mm	1m	1.2m	1.4m	1.6m	1.8m	2m
ΔD	22 mm	100 mm	257 mm	533 mm	1m	1.8m	3.27m	6.4m	16.2m	inf

formed. Thus, the points m , n and i on the film are the images of M , N and an object at infinity respectively. The on-film deviations are shown as d_m for object M and d_n for N , measured as the separation differences between pairs of homologues ($mm - ii$) and ($nn - ii$). These are identical to the lengths $im (=d_m)$ and $in (=d_n)$ both on the right image.

Note: In the diagram the separations mm and nn are greater than the infinity separation ii , which is at odds with what is stated above, namely that separations of near points are smaller than infinity point separations. However, because the two optical images are inverted, when the uncut processed film is viewed from the non-emulsion side with the images the right way up, the left image will be on the right of the right image, so they have to be cut from the film, separated and transposed for correct viewing as a stereo pair. Thus the true values of the separations will be restored.

If point N represents the nearest permissible object (at 2 m in this example, which includes infinity) then d_n becomes the largest permissible on-film deviation. The same maximum deviation value will apply to any acceptable depth range, such as the examples given in Tables 1 and 2. Nevertheless, the value of maximum deviation as defined here is not fixed. If the camera lenses in Figure 8 were of longer focal length, the lens–film distance would be larger in order to achieve correct focus, and the deviation values would consequently be greater in magnitude.

For objects that do not lie on one of the lens axes the deviation will be split between the two film images. For example, if N were to be to the right of its position in Figure 8, exactly midway between the two parallel sight lines, there would be a deviation of $d_n/2$ on each of the left and right film images, so the value of the total deviation would be unchanged. The same value of total deviation will apply to any other object lying on a line through N parallel to the film plane, but it will be divided unequally between the two film frames. For objects left of centre, the greater portion of the deviation will appear on the right film frame, and vice versa. The same applies to the deviations of all points lying on a line through M parallel to the film plane, in this instance with a smaller total value of d_m rather than d_n . And the same principle applies to all points along any other similar line parallel to those through N and M ; the more distant the line, the smaller will be the value of the total deviation.

EXTENT OF BINOCULAR VISION AND DEPTH PERCEPTION

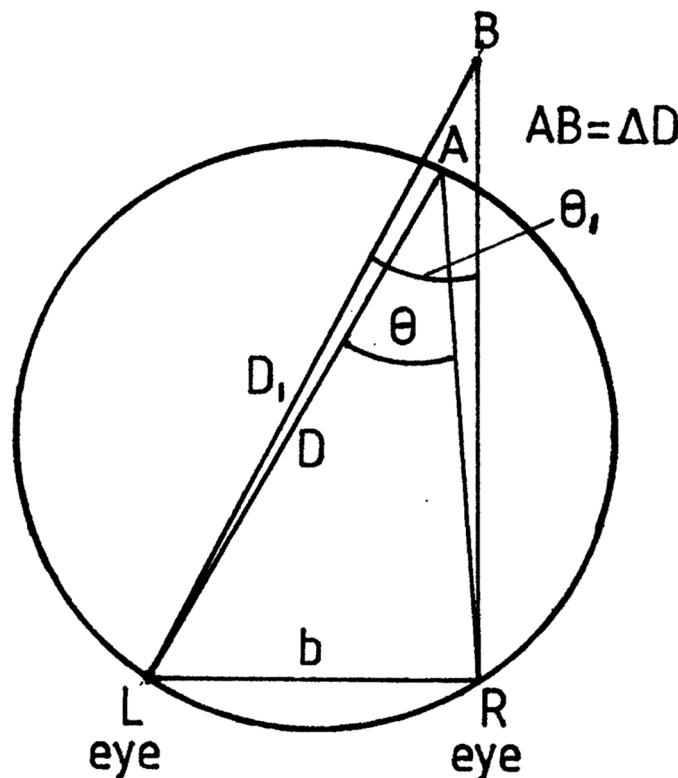
The clue to stereoscopic vision lies in the way in which nerve fibres connect the retinal rod and cone cells to cells within the cerebral cortex of the brain. In a simplified model, we can think of each brain cell being connected to two visual nerve fibres, the impulses in which have come from two corresponding eye areas, one in each retina. These are referred to as corresponding points. When the gaze is fixed on a stationary object, the impression of a single object is generated. Strictly, this applies only to an individual point on the object; the whole object is perceived by a replication of this effect as the eye scans the scene. However, returning to the fixed-gaze situation, the part of the object on which the eyes are focused forms images on corresponding points of the two retinas. Other objects either in front of or behind the primary object will form retinal images in different locations in the two eyes (Ackermann, 1992). Certain nerve cells in the brain, known as binocular disparity neurons, are activated only when this image difference occurs. Such interpretative skill is for a static scene gained through experience. The brain estimates distance using two main clues, namely the differences in retinal images and the size of the image, and if either the content of the scene or the viewer's head moves, the dynamic parallax becomes important.

Two parameters are relevant in defining the ability of the individual to distinguish depth clues and establish object locations in space. The first of these is known as stereo acuity, and represents the smallest depth difference that can be resolved by the eyes of the observer. It is also referred to as the stereopsis threshold or stereo definition. The second factor is the maximum distance at which any depth differences can be identified, what might be regarded as a limit to stereoscopic vision, or stereo infinity. The two are linked.

In Figure 9 the two eyes are shown fixated on a point A situated at a distance D . If A is off centre, the lengths LA and RA will differ, but provided they are much larger than the eye spacing b they can be taken as equal. The circle passing through L, R, and A represents the section of the horopter in the plane of the diagram. This horopter is the locus of points in space that form images on corresponding points in the retinas, and is spherical. The geometric properties of the circle are such that the angle subtended by a chord (LR.) at the perimeter, angle θ , is constant for all points on the perimeter. If the eyes are focused on a more distant point B, then there will be a similar horopter of greater diameter, representing other object points that produce images on corresponding retinal points, and a smaller angle θ_1 . In other words, each horopter relates to a particular eye convergence.

Referring to Figure 9, which shows the eyes focused at A, consider point B, lying just outside the horopter. The retinal images formed by B will not lie on corresponding points in the eye, and the image disparity will trigger the brain into registering the image of B as farther away than point A, provided ΔD

Figure 9. Horopter: Point A, on which the eyes are focused, gives retinal images on corresponding points in the two eyes



is large enough. However, if B is too close to A, the two points will be seen as one. For the observer to be able to distinguish the depth difference between A and B, and to see two separate points, the difference between the two angles LBR and LAR has to be sufficiently large. For angles LAR and LBR (θ and θ_1 respectively), the parallax angle is given by $\Delta\theta = \theta - \theta_1$.

Stereoscopic acuity is defined by the minimum discernible parallax angle $\Delta\theta_0$. Assigning a value to this is not straightforward, as it varies between individuals, and depends on external factors such as subject brightness and duration of observation. A value as low as 2 arcseconds has been reported (Klooswijk, 1978); but Valyus (1966) earlier suggested that 30 arcseconds was a representative value for use in calculations. Assuming that $D > b$ (Figure 9), then all parallax angles can be written in the form $\theta = b/D$ in radian measure. Accordingly, the expression can be used to determine the limit of stereoscopic vision. Rearranging and taking $b = 65$ mm and $\Delta\theta_0 = 30$ arcseconds or 0.000145 radians (i.e. 30 arcseconds or 1/120 degree) then

$$D = b/\Delta\theta_0 = 65/0.000145 = 448256 \text{ mm or just over } 448 \text{ m.}$$

The value of 30 arc seconds for stereo acuity takes into account the various factors that may diminish an individual's ability to detect small depth increments. The stereo acuity of most people is in practice better than this, in the region of 5–10 arc seconds, which suggests that the limit of stereoscopic vision is likely to be greater in magnitude. If the value 0.000048 radians is used in the calculation, we have $D = 65/0.000048 \text{ mm} = 1354 \text{ m}$ or just over 0.8 miles.

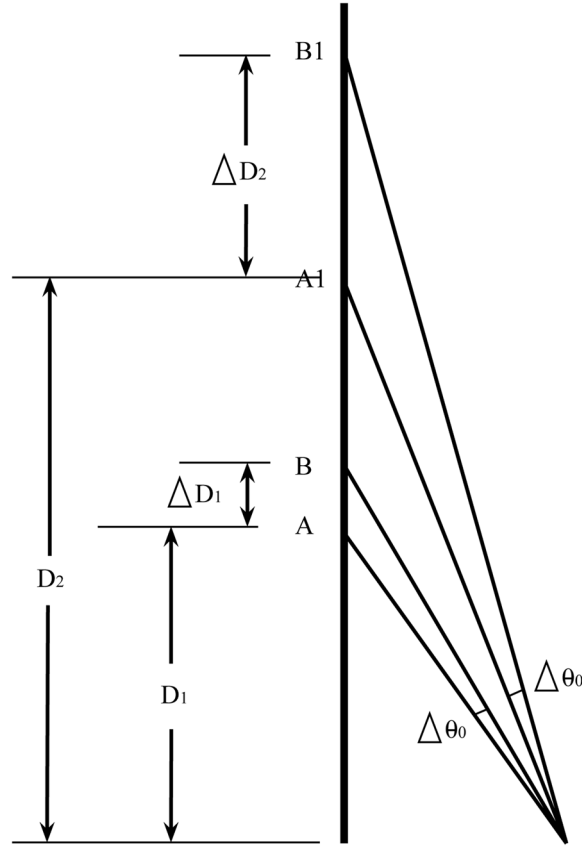
It should now be apparent that one cannot be dogmatic about the extent of binocular vision as it depends upon so many factors. 1.35 km is probably as good a value as any other quoted distance, though in many circumstances this figure is perhaps optimistic. On the other hand, figures as low as 200 m, which are sometimes quoted, seem pessimistic. Stereo acuity is undoubtedly likely to be better in an actual location (in a good light) than when viewing a stereoscopic picture of the same scene through a viewer. Under projection conditions stereo acuity will be probably be even lower.

To recapitulate, stereo acuity is defined as the parallax angle that just enables an observer to see that two objects lie at different distances. In Figure 10, A and B are two such points as determined by the stereo acuity angle $\Delta\theta_0$ as shown. The length AB is the detectable depth step, labelled as ΔD_1 . When the eyes focus onto a more distant point A1, the nearest point that can be detected as farther away is now B1. Because of the change of viewing angle the depth step is greater, with a value ΔD_2 . It should be clear that the smaller the stereo acuity value, the smaller is the depth step that can be detected for a given set of circumstances.

The conditions that affect the value of stereo acuity referred to above when outdoors include such factors as the quality of lighting (sunny or cloudy) and the presence of haze or rain; when viewing stereograms indoors variables such as the brightness and lens quality of viewers or projectors, and the quality of the photographic image itself, will be important. But, for a particular observer in specific conditions the stereo acuity will be fixed for the whole scene being viewed, and we can analyse the variation of depth step with distance more quantitatively. The exact relationship between object distance and the size of the minimum depth step can be determined from Figure 9. The distance AB normal to the horopter is given by

$$\Delta D = D_1 - D$$

Figure 10. Variation of depth step ΔD with distance



Since in practice D and D_1 are very much greater than b , the angles are very small. For the same reason we can assume that the sides of the triangles LA and RA are equal, as are LB and RB equal to D and D_1 respectively, so

$$D_1 = b/\theta_1 \text{ and } D = b/\theta.$$

hence

$$\Delta D = b(1/\theta_1 - 1/\theta) = b(\theta - \theta_1)/\theta_1\theta$$

$$\text{i.e. } \Delta D = D^2\Delta\theta/(b - D\Delta\theta)$$

The minimum depth step ΔD_0 is the value of ΔD when $\Delta\theta$ is equal to the stereo acuity $\Delta\theta_0$.
Thus

$$\Delta D_0 = D^2\Delta\theta_0/(b - D\Delta\theta_0)$$

Principles of Binocular Stereoscopic Imaging

This expression, which follows the analysis by Valyus (1966), shows that the minimum discernible depth step is roughly proportional to the square of the object distance, measured from the observer. The significance is that our perception of depth falls off rapidly for distant objects and that the stereoscopic effect is more pronounced at relatively close range. As a general guide, the photographer should ensure that the important elements of a stereoscopic image lie within the 2–200 m range, though more distant objects need not necessarily be excluded. It is worthwhile to calculate the number of discernible depth steps that occur with various distance ranges. For the purposes of this exercise the stereo acuity is taken as 30 arcseconds (0.000145 radians). An observer will thus just be able to discern two objects as lying at different depths if the parallax of one is 30 arcseconds greater than that of the other.

This can be seen from the following, where $b = 65$ mm and $\Delta\theta_0 = 0.000145$ radians.

From the above equation the minimum discernible depth step at $D = 10$ m will be given by

$$\Delta D_0 = (10^2 \times 0.000145) / [0.065 - (10 \times 0.000145)] \text{ m} = 0.228 \text{ m or } 228 \text{ mm}$$

So, if an object is located at a distance of 10 m, a second object will just be distinguished as lying farther away than the first if it lies at 10.228 m, but not if it lies at, say, 10.2 m. The 228 mm depth step value is shown in Table 3 together with those calculated for object distances of 2 m and 200 m.

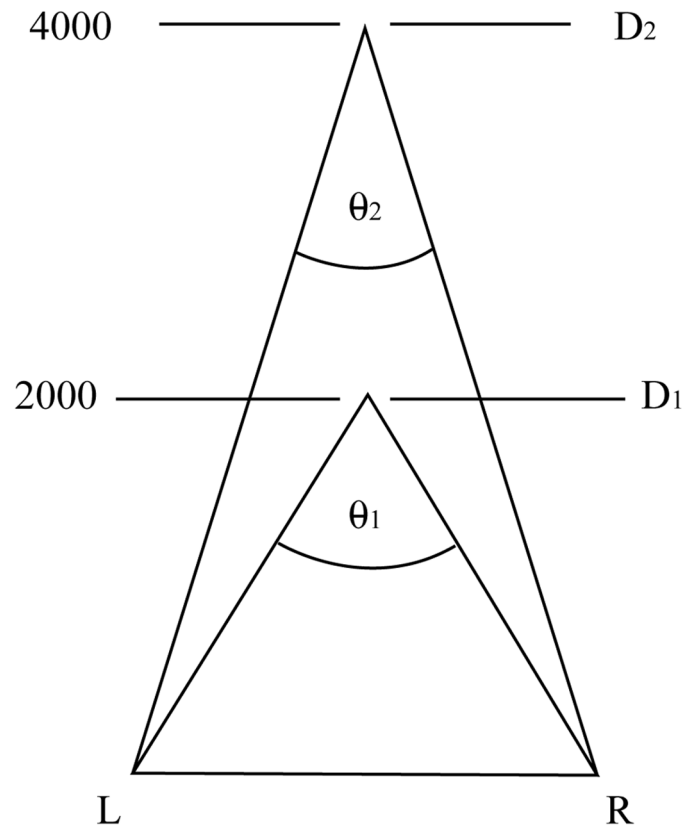
We can now calculate the number of depth steps that lie between two points at different distances from the observer. To do so, we need to consider the parallax angles as illustrated in Figure 11. The calculation simply involves determining the parallax angles θ_1 and θ_2 for the relevant distances D_1 and D_2 . The angular difference $(\theta_1 - \theta_2)$ divided by the stereo acuity gives the number of depth steps. Of course,

Table 3. Depth step values

Object Distance (metres)	Parallax (minutes arc)	Number of Depth Steps	Size of depth step (metres)
0.3	742		0.0002 (0.2mm)
1	224	1036	0.002 (2mm)
2	112	224	0.009 (9mm)
4	56	112	0.036 (36mm)
8	28	56	0.145 (145mm)
16	14	28	0.592 (592mm)
50	4.5	19	6.227
100	2.2	4.6	28.71
400 [#]	0.56	3.28	3314

[#] With a stereo acuity of 30", the limit of stereo perception is calculated to be 448m

Figure 11. Variation of parallax angle with distance



within a given distance range the step size is not constant but increases with distance, as shown in Table 3. For example, the parallax angle for 1 m distance, as seen by the eyes, is 224 arcminutes, and that for 2 m is 112 arcminutes. Since the stereo acuity of 30 arcseconds can be written as 0.5 arcminutes, the number of depth steps between 1 m and 2 m will be $(224 - 112) / 0.5 = 224$ steps.

Table 4 gives the results of similar calculations for object distances from 0.3 m (representing approximately the nearest distance of distinct vision) to 400 m, just short of the stereo infinity value of 448 m for the chosen stereo acuity value of 30 arcseconds. The table shows the number of depth steps in each distance range, and the size of the step at each key distance.

Table 4. Variation of depth steps with distance

D	ΔD_0 for $\Delta\theta_0 = 30''$	ΔD_0 for $\Delta\theta_0 = 10''$
2 m	8.65 mm	2.96 mm
10 m	228 mm	74.4 mm
200 m	160 m	34.7 m

The significance of this brief analysis is that the human eye can discern finer depth detail at close range, and that successful stereoscopic image making is likely to gain the maximum effect with the inclusion of objects in the foreground.

REFERENCES

- Ackermann, U. (1992). *Essentials of human physiology*. St Louis, MO: Mosby Yearbook.
- Crombie, A. C. (1990). *Science, optics, and music in medieval and early modern thought*. New York: Continuum International Publishing Group.
- Julesz, B. (1960). Binocular depth perception of computer-generated images. *The Bell System Technical Journal*, 39(5), 1125–1163. doi:10.1002/j.1538-7305.1960.tb03954.x
- Klooswijk, A. I. J. (1978). Natural and photographic stereo acuity. *Stereoscopy*, 5.
- Needham, J. (1986). *Science and civilization in China: Physics and physical technology*. Taipei, Taiwan: Caves Books Ltd.
- Pinker, S. (1997). *How the mind works*. London: Penguin Books.
- Valyus, N. A. (1966). *Stereoscopy*. London: Focal Press.

This research was previously published in Techniques and Principles in Three-Dimensional Imaging edited by Martin Richardson, pages 38-58, copyright year 2014 by Information Science Reference (an imprint of IGI Global).

Chapter 7

Visual Perception from Object Scanning as Revealed by Electrooculography

Anwesha Banerjee
Jadavpur University, India

Ankita Mazumder
Jadavpur University, India

Poulami Ghosh
Jadavpur University, India

D. N. Tibarewala
Jadavpur University, India

ABSTRACT

We the human beings are blessed by the nature to become well competent for performing highly precise and copious visual processes with how ever a restricted field of view. Howbeit, this process of visual perception is, to a great extent, controlled by the saccades or more commonly the eye movements. The positioning and accommodation of eyes allows an image to be placed (or fixed) in the fovea centralis of the eyes but although we do so to fix our gaze at a particular object, our eyes continuously move. Even though these fixational eye movements includes magnitude that should make them visible to us yet we remain oblivious to them. Microsacades, drifts and tremors that occurs frequently during fixational eye movements, contribute largely to the visual perception. We use saccades several times per second to move the fovea between points of interest and build an understanding of our visual environment.

INTRODUCTION

Visual perception can be defined as the ability to of the brain to detect and interpret visible light thus enabling a living being to perceive the image of something he has seen (Gompel, Fischer, Murry & Hill, 2007). Vision, as a sensory system, has always been entitled of paramount importance as the whole world

DOI: 10.4018/978-1-5225-5195-9.ch007

contains a huge deal of visual information (A.L. Yarbus, 1967). The sense organ, solely responsible, alongside brain, for creating a visual perception is eye, the light sensitive organ of human body (Leigh & Zee, 1999). Amongst several parts of the eye the few which play the most crucial role are the rod and cone cells at the back of the eye that actually responds to visible light rays and relay those signals via optical nerve to the brain which finally interprets it i.e. creates the perception (E. Kowler, 2011). The entry of the light inside the eyes is controlled by the pupil that dilates or contracts to adjust the amount of light rays entering (C. Araujo et. al., 2001).

The processes that are involved in visual perception are not only physiological but also psychological to a great extent; while the physiological process deals with the formation of image from the visual inputs the psychological aspect actually make sense out of that image (G.T. Buswell, 1935).

Vision Perception is the ability to interpret, analyze, and give meaning to what we see (A. Brouwer et. al., 2009). These skills help us recognize and integrate visual stimuli with previously stored data to form a stable, predictable, familiar world. In other words, vision perception allows us to understand, not just see (Rolfs, 2009).

In school, visual perceptual skills are particularly important. Without good perceptual skills, we could not recognize words we've already seen, tell the difference between a p and q, sequence the order of letters when spelling, visualize reading content for comprehension, determine left from right, scan a busy worksheet, mentally manipulate objects in math, conceptualize relationships in science, and connect other sensory stimuli to our visual construct, such as the sound of a keyboard to a piano (Cerf, Frady & Koch, 2009).

Visual perception skills are generally broken down into distinctive subcategories based on their analytical function (C. Araujo et. al., 2001). These subsets of skills do not work in isolation but operate in combination with each other for efficient visual function. Whether considered separately or collectively, these skills are critical to learning.

There are different aspects related to visual perception, such as

- **Visual Discrimination:** The ability to determine exact characteristics and distinctive features among similar objects (G.T. Buswell, 1935). In reading, this skill helps children distinguish between similarly spelled words, such as was/saw or then/when. Children with poor visual discrimination will often confuse words.
- **Visual Memory:** The ability to remember for immediate recall the characteristics of a given object or form. Children with poor visual memory may struggle with comprehension. They often subvocalize as they read because they must rely on auditory input to help them compensate. They may have difficulty remembering what a word looks like or fail to recognize the same word on a different page (Cerf, Frady & Koch, 2009). They may also take longer copying assignments because they can't retain information long enough to transfer it from the board to their page.
- **Visual Sequential Memory:** The ability to remember forms or characters in correct order. This skill is particularly important in spelling (Trommershäuser, Glimcher & Gegenfurtner, 2009). Letter omissions, additions, or transpositions within words are common for children who struggle with this skill. They often sub vocalize as they write. Recognizing and remembering patterns may also be a problem (Ross, Morrone, Goldberg & Burr, 2001).
- **Visual Spatial Relations:** The ability to perceive the position of objects in space, both in relation of object to each other and to one's own self (Castet & Masson, 2000). Two important considerations in spatial relationships are laterality, understanding left and right on one's own body, and di-

rectionality, understanding left and right on other objects. Children with poor spatial development can have difficulty with spatial concepts such as left and right or up and down. They may struggle with following a line of print left to right during reading and evidence frequent letter reversals and poor spacing during writing. If they don't have a good understanding of their body's position within space, they may struggle with gross motor function, often misjudging distances, bumping into things, having poor ball skills, and exhibiting a general awkwardness in their movements.

- **Visual Figure Ground:** The ability to perceive and locate an object within a busy field without getting confused by the background or surrounding images. This skill keeps children from getting lost in details (Tavassoli & Ringach, 2009). Children with poor figure-ground become easily confused with too much print on the page, affecting their concentration and attention. They may also have difficulty scanning text to locate specific information.
- **Visual Closure:** The ability to visualize a complete whole when given incomplete information or a partial picture. This skill helps children read and comprehend quickly; their eyes don't have to individually process every letter in every word for them to quickly recognize the word by sight. They may also confuse similar objects or words, especially words with close beginning or endings (Tatler, 2009). This skill can also help children recognize inferences and predict outcomes.
- **Visual Form Constancy:** The ability to mentally manipulate forms and visualize the resulting outcomes. This skill also helps children recognize an object in different contexts regardless of changes in size, shape, and orientation (Stone, Beutter & Lorenceau, 2000). Children with poor form-constancy may struggle to recognize objects when turned a different direction or viewed from a different vantage point. They can fail to recognize words they know that are presented in a different manner, i.e., written on paper, in a book, or on the board.

Tracking is the ability to control where we aim our eyes. Technically, the control of our eye movements is called oculomotor skills. This skill is critical for everything from sports to reading. Good tracking skills allow us to hit a baseball or follow a line of print without losing our place (Royden, Banks & Crowell, 1992). In school, if a child cannot track from word to word smoothly, accurately, and efficiently, reading suffers and comprehension drops as words jump around and meaning becomes muddled (Cerf, Frady & Koch, 2009). Tell-tale signs of tracking problems in school include frequent loss of place, skipping or transposing words, omitting entire lines, using a finger to follow print, moving the head rather than just the eyes, and poor comprehension because of scrambled text.

There are three basic types of eye movements:

- **Fixations:** Ability to hold eyes steady without moving off target
- **Saccades:** The ability of our eyes to make accurate jumps as we change targets
- **Pursuits:** The ability of our eyes to follow a moving target

Fixation

Fixation is the most basic eye movement skill from which other skills grow (A. Brouwer et. al., 2009). Good fixation skills allow us to maintain a steady gaze without our eyes moving involuntarily off target. This allows images entering the eye to be centered on the fovea, the part of the retina that gives us our clearest vision. Without the ability to fixate, images will be blurry and confusing. In school, comprehension suffers as our eyes involuntarily move off the print and words jumble or jump around. Inadequate fixation

skills must be addressed early in a treatment program before other oculomotor techniques are attempted because it is the foundation skill upon which others build (Martinez-Conde, Macknik & Hubel, 2004).

Saccades

Saccades are eye jumps—the sudden, quick voluntary change in fixation from one object to another (Castet & Masson, 2000). Saccades involve any shift in gaze, such as from road sign to speedometer, board to paper, notes to computer screen. During reading, accurate saccadic movements are critical. The eyes must move left to right along a straight line without deviating up or down to the lines above or below. In addition, when we reach the end of a line, our eyes must make a difficult reverse sweep back to the beginning of the next line. If a child cannot control these eye movements, he'll lose his place and comprehension becomes a problem. The ability to make accurate saccades involves a very precise coordination between our central and peripheral visual systems. Our central vision processes what we're looking at in clear detail and defines what we're seeing ("What is it?") while our peripheral vision simultaneously locates the next target to let us know where to aim our eyes during the next saccade ("Where is it?"). If there is not a continuous, fluid, simultaneous integration between the two systems, saccadic eye movements will be poor (Castet & Masson, 2000).

Pursuits

Pursuit eye movements are used to follow a moving target. Accurate, smooth pursuit eye movements allow us to make spatial judgments as to the speed and position of the moving target (D. Braun et. al., 2008). Pursuit eye movements are especially important in driving and sports. To evaluate pursuit movements, parents can randomly move a small target about 20 inches in front of the child's eyes and observe the following: Does the head move with the eyes? How accurate are left-right, up-down, z-axis movements, and rotations? (Spering & Montagnini, 2011) Does the patient falter at certain positions of gaze? How quickly do he/she correct? Is the patient tense, rigid, wiggly, or needing encouragement to complete the task, indicating the effort they must exert? Does accuracy degenerate with time? (Schütz, Braun & Gegenfurtner, 2011)

Eye movement detection can be done using many techniques such as Infrared Video System (IRVS), Infrared Oculography (IROG), Search Coil (SC), Optical-type Eye Tracking System, Purkinje dual-Purkinje image (DPI) and Electroculography (EOG) (Robinson, 1963). EOG is the simplest method among all of them. Moreover, an EOG system is fairly easy to construct using surface electrodes that are placed around the eye socket and is simple to work with in real time.

EOG signal is a measure of the potential difference between the front and back of the eye ball. Experiments reveal that there exists a linear relation between eye movement and EOG amplitude up to a certain degree. EOG can thus be used for detection of eye movements and blinks (A Bulling et. al., 2011). Detection and assessment of many ophthalmological diseases such as Retinitis Pigmentosa (Stavrou et. al., 1996) and Best's disease (R.G. Weleber, 1989) are the known application of EOG signal in ophthalmology. The progress of degenerative muscular disorders and neural diseases (e.g. Parkinson's, Alzheimer's etc.) can also be tracked from EOG (Rascol, 1989). There are different applications of EOG analysis drowsiness detection and cognitive process modeling (Magosso et. al., 2007). Eye movement controlled human computer interfaces based on EOG is recent area of interest. Traces of EOG-based control of neuro-prosthetic devices are found in the literature (Deng, 2010 & Lanez, Ubeda and Azorin

2011), controlling motion of computer cursor (Banerjee et. al., 2015) and controlling wheelchair system for rehabilitation (Barea et. al., 2000). There have been different strategies of analyzing (Wissel & Palaniappan, 2011) and implementing EOG in the field of robotics (Valbuena et. al., 2007 & Cinar and Sahin, 2009). In our previous experiments, we have analyzed EOG signal and found its application in eye dystonia prevention, reading speed analysis and also in assisting autistic children (Banerjee et. al., 2015, 2015, and 2014).

BACKGROUND

Visual Perception and Eye Movements

To study visual perception eye movement has always been considered to be the most important tool. There had been many studies relating eye movement to visual perception of which studies by J.M. Henderson, (2003), stand out for their research works relation fixational eye movement to visual realism using Markov models. All these studies had the similar aim to model visual perception during certain set of tasks discovering the relation between visual perception and eye movements. A study revealed that even in newborns visual perception is influenced by eye movements (Najemnik & Geisler, 2005). That study showed that infants showed lesser dispersion in scanning in any heterogeneous field scene rather than homogeneous field scene. Eye movements are used to survey perceptual span of effective vision, preview benefits and also for constructing visual perception models that helps in realizing real world tasks (Rayner, 1998). Eye movements are also used to investigate visual spatial attention. Studies revealed that superior target detection occurs at saccade location whatever may be the attention instruction is. Thus it indicates that a person is incapable of moving eyes to one location and attends a different one. Hence it is established from this fact that spatial visual attention is an important mechanism for generating voluntary eye movements (O'Regan, 1992).

Also it has been significant from research works that visual scan path eye movements reflects the content of the imagined diagrammatic pictures which a person visualizes i.e. the movements of the eye-ball are just not random ones (Ringach, Hawken & Shapley, 1996). Thus, Visual perception is a kind of cognitive process that controls the eye movement.

Electrooclogram

Our eyes are homologous to battery cells since there exists a standing electrical potential across them that usually maintains a voltage difference of about +0.40 to + 1.0 mili volts. This electrical potential difference is created due to the presence of huge numbers of electrically active neurons in the retinal region with respect to those present in the cornea. EOG (electrooculogram) is defined to be these standing potential differences that can be detected by skin electrodes when they are placed around the socket of eyes.

Some typical characteristic features of EOG signals are as follows:

- The magnitude of EOG signal usually ranges from 5 to 20 fl V per degree of eye ball movement.
- When we look upwards the positive cornea becomes closer to the upper electrode and hence becomes more positive with respect to the potential of the electrode placed just beneath the eye.

This is valid for the other way round as well and hence both negative and positive voltages can be obtained from the respective configurations.

- During the measurement of vertical movement the horizontal movement driven potential is found to be less as compared to that generated by vertical movement.
- Depending on the direction in which the eye moves, it is found whether the amplitude has a positive or a negative value.
- The pulse produced by upward and downward movement is almost equivalent in case of both pulse direction and amplitude duration. Closed eyes also yielded the same potential.
- Blinks are found to have short duration pulse and high amplitude value. They are not influenced by any kind of head movement.

EOG system used for this research work is a very robust eyeball tracking method having very good precision. Though other visual methods could have been used here also, but the reasons for choosing EOG as out visual tracking system is given below:

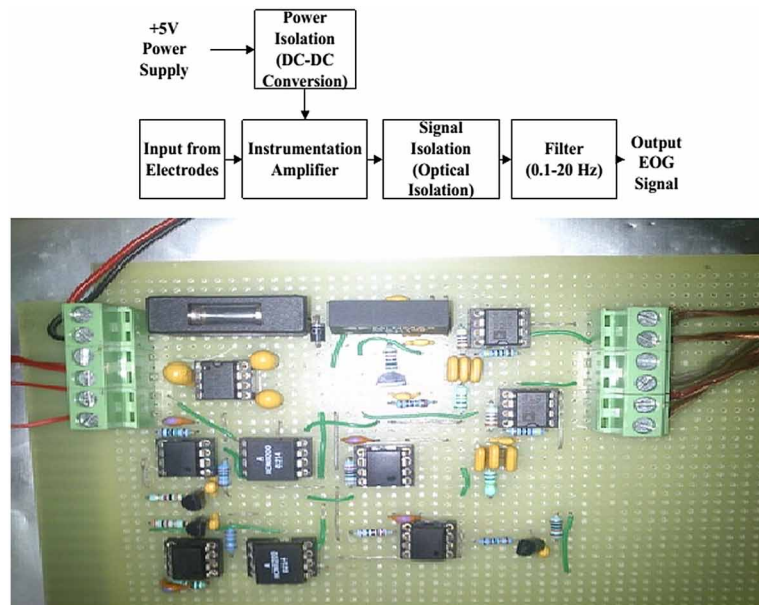
- The first and foremost reason is that the range provided by EOG is quite larger than any other visual methods that tends to provide constrained range owing to large vertical rotations that cause iris as well as the cornea to disappear behind eyelids. Owing to the fact that EOG recording system does not require visualization of the eye hence angular deviation of up to 80 is permissible to be recorded along both the horizontal and vertical plane of rotation using EOG.
- Secondly, the actual eyeball position with respect to head is presented by the EOG signal. So no hindrance of the head movement will come in the way of measuring accurate relative eyeball positions. Thus the necessity of using head movement restrainer can be easily opted out.
- Thirdly, in systems involving cameras, it is always necessary to keep the eyes within the line of sight of the camera and hence often a head rest has to be used to hold the head in position. This can stop the user to be in the front of a computer or users suffering from cerebral palsy. Even if contact lens is used in any visual system it may result in a scratch in the cornea of the user. EOG rules out all these difficulties.
- Fourthly, EOG system is much cheaper than other visual tracking systems. Not only the hardware but also the software of an EOG system comes in low price.
- Lastly, EOG system does not require a subject to keep his eyes wide open as it is in the case of any other visual systems. EOG can thus be used during sleeping conditions even. Also EOG provides instantaneous signal with respect to eyeball positioning and hence eye positions can be very quickly be detected using these signals.

MAIN FOCUS OF THE CHAPTER

Data Acquisition

A potential difference exists between the cornea and the retina of the human eye due to the presence of a large amount of electrically active neurons in the retina compared to the cornea of the eye (Bulling et al., 2011b; Deng et al., 2010). EOG is this standing potential which is detected by the skin electrodes placed around the eye socket. EOG signal magnitudes have a range of 5-20 μV per degree of eye ball

Figure 1. Block diagram (top) and a snapshot (bottom) of the acquisition circuit and ADC used for EOG Acquisition



movement in any direction. The value of EOG amplitude will be positive or negative depending upon the direction in which the eye is moved.

The recording of the EOG signal has been done through a two channel system developed in the laboratory using five Ag/AgCl disposable electrodes at a sampling frequency of 128 Hz. Two electrodes are used for acquiring horizontal EOG and two for vertical EOG, while one electrode acts as the reference (Banerjee et. al., 2015). The frequency range of the acquired EOG signal is below 20 Hz and the amplitude lies between 100-3500 mV. The block diagram of the circuit designed for signal acquisition has been shown in Figure 2. The signal collected from the electrodes is fed to an instrumentation amplifier, implemented by IC AD620, having a high input impedance and a high CMRR. This output is given to a second order low pass filter with a cut off frequency of 20Hz to eliminate undesirable noise. Different stages of filters, implemented using IC OP07s, provide various amounts of gain. Amplifier provides a gain of 200 and a gain of 10 is provided by the filter. Thus an overall gain of 2000 is obtained. For any kind of bio-signal acquisition, isolation is necessary for the subject's as well as the instrument's safety. Power isolation is provided by a dual output hybrid DC-DC converter (MAU 108) and signal isolation is achieved by optically coupling the amplifier output signal with the next stage through HCNR 200. For conversion of the signal in digital format, an Analog to Digital Converter is necessary. The Electrooculogram data has been acquired in the LABVIEW 2012 platform for processing in the computer using National Instruments 12-bit ADC.

To eliminate undesirable noise and obtain EOG in the frequency range of 0.1 to 15 Hz, the range where maximum information is contained as determined experimentally, we implement band pass filtering. An Elliptical band pass filter of order 6 with 1dB passband ripple and 50 dB stopband ripple has been used in the desired frequency band.

Experimental Paradigm

Experiments are conducted on 6 healthy subjects, 3 male and 3 female, in the age group 25 ± 5 years with their consent. The subjects are instructed to comfortably sit on a chair while the stimulus is presented on a screen using a projector. Four types of objects (e.g. human face, abstract, landscape, geometric shape object) were shown to the subjects. The subjects were asked to scan the shown object. The time frame for the presentation of the stimulus follows the pattern shown in Figure 2. For each subject and each day of experiment, initially 30s of relaxation is used to bring EOG to the baseline conditions. This is followed by the presentation of the stimulus for 60s during which EOG is acquired using the acquisition technique mentioned before. Each stimulus is followed by a 30s relaxation period preceding the next stimulus.

This procedure is carried out for 5 days of experimentation on each subject, to include the possible variations in the bio-modalities over different days. The stimulus of experimentation is shown in Figure 2.

Eye Movement Analysis

In order to understand the relation between eye movement and visual perception it is important to know the different kinds of eye movements on the first place. There are three basic types of eye movements that are primarily detected by EOG (Electrooculogram), those are fixation, saccades, and blinks.

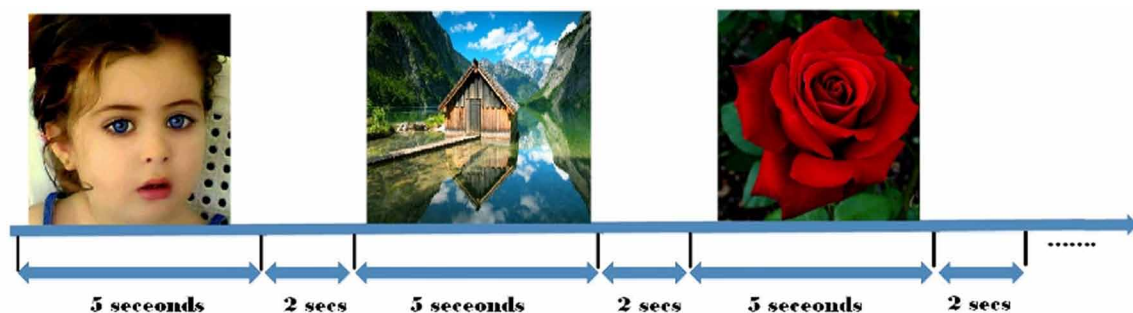
The two basic components of eye movements in the various tasks under consideration here are the movements themselves (called saccades) and the fixations (the period of time when the eyes remain fairly still and new information is acquired from the visual array). Since vision is suppressed during a saccade (Festinger, Sedgwick & Holtzman, 1976), new information is only acquired during fixations.

While viewing something the eyes cannot remain affixed at any point rather it constantly keep on moving to build up a map of those parts which it found out to be interesting. This simultaneous movement of both the eyes together is regarded as saccades and is brought about by the central region of retina known as fovea.

When the eyes are able to fix itself on a certain point in a visual cue then that stationary state of the eye is known to be fixation. Thus in other words it can be alternatively defined to be the duration of time between two successive saccades. It is usually of 100 to 200 ms.

In simple words blinks can be defined to be the opening and closing of eyelids. The main purpose of blinks is to spread the “precornial tear film” all across the surface of cornea. During normal rest stage blink rate is about 12-19 blinks per minute. However the number can vary to a large extent depending

Figure 2. Experimental stimulus



upon the surrounding environmental or physiological conditions like temperature, humidity, excessive work load, fatigue etc.

Eye movements are motor responses that take time to plan and execute. Saccade latency, the time needed to encode the location of a target in the visual field and initiate an eye movement, is of the order of 175 –200 ms (F.C. Volkman, 1962).

However, it varies quite a bit as a function of the exact nature of the situation. Saccade duration, the amount of time that it takes to actually move the eyes, is a function of the distance moved. A 2-deg saccade, typical of reading, takes about 30 ms, while a 5-deg saccade, typical of scene perception, takes around 40 to 50 ms (S. Van der Stigchel, 2010).

Experimental Results

Filtering

To eliminate undesirable noise and obtain EOG in the frequency range of 0.1 to 15Hz, the range where maximum information is contained, we implement band pass filtering. An elliptical band pass filter in the specified frequency range has been used for this purpose.

Feature Extraction

Auto-Regressive (AR) Model: The AR model is used to describe a stochastic stationary time-series. A wide-sense stationary series has a constant mean and the autocorrelation depends only on the time lag (1).

$$\langle x_t \rangle = \text{Constant}; \langle x_t x_{t+k} \rangle = r_k \quad (1)$$

The autoregressive model of order p , AR (p), is given by (2).

$$x_t = \sum_{i=1}^p a_i x_{t-i} + \varepsilon_t \quad (2)$$

where a_i is the AR coefficient, x_t is the series under observation having zero mean and ε_t is the zero-mean Gaussian white noise. In the present work AR coefficients have been calculated by the Yule-Walker Method.

In Yule Walker method (2) is multiplied by x_{t-d} , where d is the delay; then the result is averaged and normalized. Repeating the process for $d=1$ to p , the following set of linear equations called the Yule-Walker equations are obtained (Eshel, 2003). The matrix form of the Yule-Walker Equations is given by (3)

$$\begin{bmatrix} 1 & r_1 & r_2 & \cdots & r_{p-1} \\ r_1 & 1 & r_1 & \cdots & r_{p-2} \\ r_2 & r_1 & 1 & \cdots & r_{p-3} \\ \vdots & \vdots & \vdots & \ddots & \vdots \\ r_{p-1} & r_{p-2} & r_{p-3} & \cdots & 1 \end{bmatrix} \begin{bmatrix} a_1 \\ a_2 \\ a_3 \\ \vdots \\ a_p \end{bmatrix} = \begin{bmatrix} r_1 \\ r_2 \\ r_3 \\ \vdots \\ r_p \end{bmatrix} \quad (3)$$

Here, a_i ($i=1$ to p) are the required AR coefficients for an AR (p) process.

In our work, we have fitted the data using an AR (5) model on segments of EOG signal assumed to be stationary, thereby obtaining 5 coefficients for each data point.

Power Spectral Density: In the present work we have computed the parametric Power Spectral Density (PSD). Parametric power spectral density estimation (Stoica & Moses, 1997) involves fitting the data to an appropriate model and a parametric estimation method to calculate the values of the model parameters. Then the frequency response of the model is evaluated to estimate the PSD of the data.

From (2), we can write

$$x_t - \sum_{i=1}^p a_i x_{t-i} = (1 - \sum_{i=1}^p a_i z^{-i}) x_t = \varepsilon_t \Rightarrow \frac{x_t}{\varepsilon_t} = \frac{1}{1 - \sum_{i=1}^p a_i z^{-i}} = H(z) \Rightarrow H(f) = \frac{1}{1 - \sum_{i=1}^p a_i e^{-ji(2\pi f)T}} \quad (4)$$

Equation (4) states the transfer function of the system where the AR coefficients, a_i , are given by the Yule-Walker Equation (3). The power spectrum, $P_x(f)$, of the time series x_t is given by (5), where $P_x(f)$ is the power spectral density of the white noise, given by its variance σ^2 .

$$P_x(f) = |H(f)|^2 P_\varepsilon(f) = \frac{\sigma^2}{\left| 1 - \sum_{i=1}^p a_i e^{-ji(2\pi f)T} \right|^2} \quad (5)$$

We have used a 129-point discrete approximation of the power spectrum in the present work.

Classification: Support Vector Machine

Support vector machine (SVM) is a well-known supervised machine learning algorithm for classifying data into two different classes (Suykens & Vandewalle, 1999).

Linear SVM (LSVM) works on the principle of separating two classes of data by constructing a hyper plane within the training data points. The hyperplane is defined by the ‘support vectors’. These are the training data points closest to the hyperplane that belong to two different classes. The hyperplane is constructed so as to maximize the distance margin between the support vectors, and thereby maximally separating the two classes. However, use of Linear SVM is limited to situations where the data are linearly separable. This limitation of Linear SVM can be overcome by mapping the data into a larger dimensional space using a kernel function, $K(x,y)$, to make the data points linearly-separable. The

frequently used kernel functions are polynomial and radial basis function (RBF) kernel (Amari & Wu, 1999). The polynomial kernel is defined by (6) where d is the order of the polynomial and c is a constant trading off the influence of higher-order versus lower-order terms in the polynomial.

$$K(x,y) = (x^T y + c)^d \quad (6)$$

The RBF or Gaussian kernel is defined by (7) where σ denotes the width of the Gaussian.

$$K(x,y) = \exp\left(\frac{-\|x-y\|^2}{2\sigma^2}\right) \quad (7)$$

Performance Analysis

A confusion matrix is constructed from each classification result to evaluate the accuracy (8), sensitivity (9) and specificity (10) as performance metrics.

$$Accuracy = \frac{TP + TN}{TP + FN + TN + FP} \times 100\% \quad (8)$$

$$Sensitivity = 1 - \frac{FN}{TP + FN} \quad (9)$$

$$Specificity = 1 - \frac{FP}{TN + FP} \quad (10)$$

In (8-10), TP, TN, FP and FN represent the number of samples classified as true positive, true negative, false positive and false negative respectively. Ideally the accuracy should be close to 100%, while the sensitivity and the specificity should be 1. Sensitivity specifies how much perfectly the classifier can identify a blink as blink. While the precision with which a non-blink movement of the eye is classified as no-blink is indicated by Specificity.

Experimental Results

The EOG data acquired for 30 minutes has alternates of blink and no-blink eye movements. The obtained signal is then filtered using a band-pass elliptical filter. The results of classification in terms of the average value of the performance metrics along with the timing complexity for 5 subjects are noted in Table 1. All the signal processing is done in MATLAB 2014 environment.

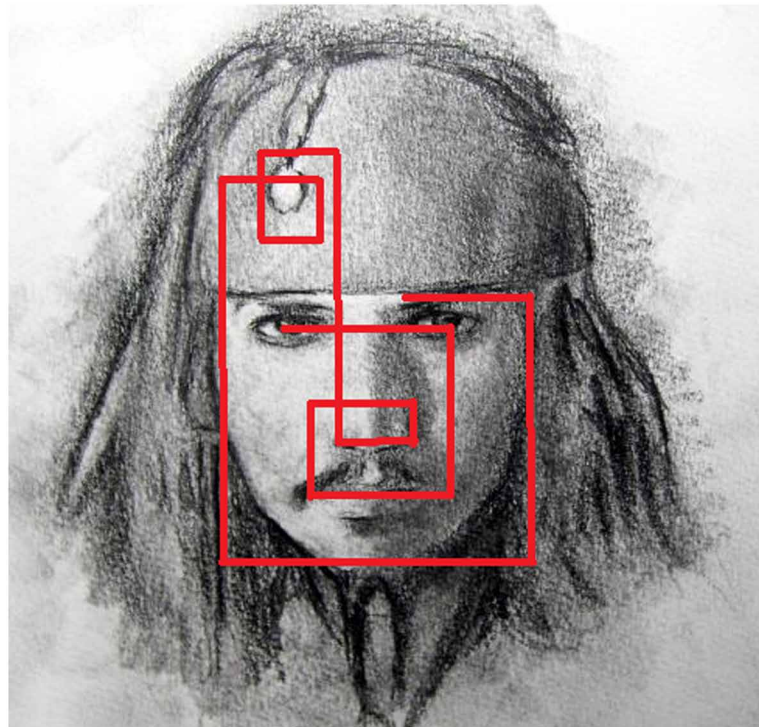
Table 1.

Subject ID	Accuracy (%)	Sensitivity	Specificity	Time (sec)
1	83.33	0.733	0.933	1.1401
2	86.67	0.733	0.8	1.1559
3	83.40	0.91	0.958	1.0907
4	86.67	0.867	0.867	1.1711
5	83	0.667	0.8	1.1438

FUTURE DIRECTIONS

Overall, the results presented in this thesis suggest that eye movements reliably alter peripheral visual processing. Importantly, my studies show that changes in visual perception act to increase or decrease the discriminability of objects in peripheral vision according to the oculomotor demands of a given task. Moreover, my findings show that these changes in perception are independent of changes in the image on the retina, and must therefore result from extra-retinal signals that are generated during the preparation and execution of saccadic and pursuit eye movements. The modification of vision by these extra-retinal signals likely facilitates the subjective impression of visual stability when eye movements continuously alter the image that falls on the retina.

Figure 3. Some eye movements of subject 1 as recorded through EOG (shown picture is a sketch)



CONCLUSION

A key question in visual neuroscience is how our subjective experience of the visual world remains largely uninterrupted by the many eye movements we make, each of which abruptly displaces the retinal image. It has long been hypothesized that extra-retinal signals, generated by voluntary movements of the eye, alter our vision in such a way that facilitates visual perception across eye movements. However, it is unclear how these extra-retinal signals influence the integration of form information, giving rise to our ability to identify visual objects in spite of the fact that eye movements shift those objects on the retina. Thus, I used eye tracking and psychophysics to test the influence of eye movements on object perception in peripheral vision. In this thesis I present studies in which I show for the first time substantial changes in object identification that result from eye movement preparation and execution. The results from these studies show that our visual experience is not just constructed from the different images that hit the retina, but is influenced by eye movement signals that facilitate the perception of objects from one glance to the next.

From Table 1 it is observed that for EEG classification, the values of classification accuracy and F1 score are always above 0.75 for all subjects. The mean values of classification accuracy and F1 score in this case are 0.7917 and 0.7924 respectively. The discriminating capability of EOG signals is somewhat lower in comparison, as from Table 1 it is observed that the mean values of classification accuracy and F1 score for EOG classification are 0.7000 and 0.6886 respectively. However in both the cases the standard deviation of the performance metrics over different subjects is lower than 0.1, indicating that inter subject variation regarding this scheme is not significant, and hence a subject invariant recognition platform can be proposed. The average values show that both feature level fusion and decision level fusion show significantly enhanced performance when compared with individual performances as observed in Table 1. The maximum values of classification accuracy and F1 score reach 0.8253 and 0.8237 respectively for decision level fusion, over all subjects. The standard deviation values of the performance metrics over different subjects is lower than 0.05 for each case of information fusion.

Examination of the eye movement pattern (or the scan path) of a viewer on a scene demonstrates that viewers do not fixate every part of the scene. Most fixations tend to fall on the informative parts of the scene. Thus, viewers tend to not fixate on the sky or the road in front of a house. Furthermore, viewers are able to obtain the gist of the scene in a single glance.

ACKNOWLEDGMENT

This study has been supported by Council of Scientific and Industrial Research (CSIR), India and Jadavpur University.

REFERENCES

Amari, S. I., & Wu, S. (1999). Improving support vector machine classifiers by modifying kernel functions. *Neural Networks*, 12(6), 783–789. doi:10.1016/S0893-6080(99)00032-5 PMID:12662656

- Araujo, C., Kowler, E., & Pavel, M. (2001). Eye movements during visual search: The costs of choosing the optimal path. *Vision Research*, 41(25-26), 3613–3625. doi:10.1016/S0042-6989(01)00196-1 PMID:11718799
- Banerjee, A., Datta, Pal, Tibarewala, & Konar. (2015). Electrooculography Based Reading Speed Analysis As An Assistive Tool. *Biomedical Engineering: Applications, Basis And Communications*, 27(2).
- Banerjee, A., Pal, M., Datta, S., Tibarewala, D. N., & Konar, A. (2014). Eye Movement Sequence Analysis Using Electrooculogram To Assist Autistic Children. *Biomedical Signal Processing and Control*, 14, 134–140. doi:10.1016/j.bspc.2014.07.010
- Banerjee, A., Pal, M., Datta, S., Tibarewala, D. N., & Konar, A. (2015). Voluntary eye movement controlled electrooculogram based multitasking graphical user interface. *Int. J. Biomedical Engineering and Technology*, 18(3), 254–271. doi:10.1504/IJBET.2015.070574
- Banerjee, A., Pal, M., Tibarewala, D. N., & Konar, A. (2015). Electrooculogram Based Blink Detection To Limit The Risk Of Eye Dystonia. In *Advances In Pattern Recognition, IEEE Eighth International Conference On*. doi:10.1109/ICAPR.2015.7050712
- Barea, R., Boquete, L., Mazo, M., López, E., & Bergasa, L. M. (2000). EOG guidance of a wheelchair using neural networks. In *IEEE International Conference on Pattern Recognition*, (vol. 4, pp. 668–671). doi:10.1109/ICPR.2000.903006
- Braun, D. I., Mennie, N., Rasche, C., Schütz, A. C., Hawken, M. J., & Gegenfurtner, K. R. (2008). Smooth pursuit eye movements to isoluminant targets. *Journal of Neurophysiology*, 100(3), 1287–1300. doi:10.1152/jn.00747.2007 PMID:18614758
- Brouwer, A. M., Franz, V. H., & Gegenfurtner, K. R. (2009). Differences in fixations between grasping and viewing objects. *Journal of Vision*, 9(1), 1–24
- Bulling, A., Roggen, D., & Troester, G. (2011). What's in the eyes for context-awareness? *IEEE Pervasive Computing / IEEE Computer Society [and] IEEE Communications Society*, 10(2), 48–57. doi:10.1109/MPRV.2010.49
- Buswell, G. T. (1935). *How people look at pictures*. Chicago: University of Chicago Press.
- Castet, E., & Masson, G. S. (2000). Motion perception during saccadic eye movements. *Nature Neuroscience*, 3(2), 177–183. doi:10.1038/72124 PMID:10649574
- Cerf, M., Frady, E. P., & Koch, C. (2009). Faces and text attract gaze independent of the task: Experimental data and computer model. *Journal of Vision*, 9(12), 1–15.
- Cinar, E., & Sahin, F. (2009). EOG controlled mobile robot using Radial Basis Function Networks. In *IEEE International Conference on Soft Computing, Computing with Words and Perceptions in System Analysis, Decision and Control*. doi:10.1109/ICSCCW.2009.5379485
- Deng, L., Hsu, C., Lin, T., Tuan, J., & Chang, S. (2010). EOG-based Human–Computer Interface system development. *Expert Systems with Applications*, 37(4), 3337–3343. doi:10.1016/j.eswa.2009.10.017

- Eshel, G. (2003). The Yule walker equations for the AR coefficients. In J. Clerk Maxwell (Ed.), *A Treatise on Electricity and Magnetism* (3rd ed.; vol. 2, pp. 68-73). Oxford, UK: Clarendon.
- Festinger, L., Sedgwick, H. A., & Holtzman, J. D. (1976). Visual perception during smooth pursuit eye movements. *Vision Research*, *16*(12), 1377–1386. doi:10.1016/0042-6989(76)90155-3 PMID:1007016
- Gompel, R. V., Fischer, M., Murry, W., & Hill, R. (2007). *Eye movements: A window on mind and brain*. Oxford, UK: Elsevier.
- Henderson, J. M. (2003). Human gaze control during realworld scene perception. *Trends in Cognitive Sciences*, *7*(11), 498–504. doi:10.1016/j.tics.2003.09.006 PMID:14585447
- Kowler, E. (2011). Eye movements: The past 25 years. *Vision Research*, *51*(13), 1457–1483. doi:10.1016/j.visres.2010.12.014 PMID:21237189
- Lanez, E., Ubeda, A., & Azorin, J. M. (2011). Multimodal human-machine interface based on a brain-computer interface and an electrooculography interface. In *Annual International Conference of Engineering in Medicine and Biology Society*, (pp. 4572–4575). Academic Press.
- Leigh, R. J., & Zee, D. S. (1999). *The neurology of eye movements*. New York: Oxford University Press.
- Magosso, E., Ursino, M., Zaniboni, A., Provini, F., & Montagna, P. (2007). Visual and computer-based detection of slow eye movements in overnight and 24-h EOG recordings. *Clinical Neurophysiology*, *118*(5), 1122–1133. doi:10.1016/j.clinph.2007.01.014 PMID:17368090
- Martinez-Conde, S., Macknik, S. L., & Hubel, D. H. (2004). The role of fixational eye movements in visual perception. *Nature Reviews. Neuroscience*, *5*(3), 229–240. doi:10.1038/nrn1348 PMID:14976522
- Najemnik, J., & Geisler, W. S. (2005). Optimal eye movement strategies in visual search. *Nature*, *434*(7031), 387–391. doi:10.1038/nature03390 PMID:15772663
- O'Regan, J. K. (1992). Solving the “real” mysteries of visual perception: The world as an outside memory. *Canadian Journal of Psychology*, *46*(3), 461–488. doi:10.1037/h0084327 PMID:1486554
- Rascol, O., Clanet, M., Montastruc, J. L., Simonetta, M., Soulier-Esteve, M. J., Doyon, B., & Rascol, A. (1989). Abnormal ocular movements in parkinson's disease evidence for involvement of dopaminergic systems. *Brain*, *112*(5), 1193–1214. doi:10.1093/brain/112.5.1193 PMID:2804611
- Rayner, K. (1998). Eye movements in reading and information processing: 20 years of research. *Psychological Bulletin*, *124*(3), 372–422. doi:10.1037/0033-2909.124.3.372 PMID:9849112
- Ringach, D. L., Hawken, M. J., & Shapley, R. (1996). Binocular eye movements caused by the perception of three-dimensional structure from motion. *Vision Research*, *36*(10), 1479–1492. doi:10.1016/0042-6989(95)00285-5 PMID:8762765
- Robinson, D. A. (1963). A method of measuring eye movement using a scleral search coil in a magnetic field. *IEEE Transactions on Bio-Medical Engineering*, *10*, 137–145. PMID:14121113
- Rolfs, M. (2009). Microsaccades: Small steps on a long way. *Vision Research*, *49*(20), 2415–2441. doi:10.1016/j.visres.2009.08.010 PMID:19683016

- Ross, J., Morrone, M. C., Goldberg, M. E., & Burr, D. C. (2001). Changes in visual perception at the time of saccades. *Trends in Neurosciences*, 24(2), 113–121. doi:10.1016/S0166-2236(00)01685-4 PMID:11164942
- Royden, C. S., Banks, M. S., & Crowell, J. A. (1992). The perception of heading during eye movements. *Nature*, 360(6404), 583–587. doi:10.1038/360583a0 PMID:1461280
- Schütz, A. C., Braun, D. I., & Gegenfurtner, K. R. (2011). Eye movements and perception: A selective review. *Journal of Vision (Charlottesville, Va.)*, 11(5), 1–30. doi:10.1167/11.5.9 PMID:21917784
- Spering, M., & Montagnini, A. (2011). Do we track what we see? Common versus independent processing for motion perception and smooth pursuit eye movements: A review. *Vision Research*, 51(8), 836–852. doi:10.1016/j.visres.2010.10.017 PMID:20965208
- Stavrou, P., Good, P. A., Broadhurst, E. J., Bunday, S., Fielder, A. R., & Crews, S. J. (1996). ERG and EOG abnormalities in carriers of X-linked retinitis pigmentosa. *Eye (London, England)*, 10(5), 581–589. doi:10.1038/eye.1996.134 PMID:8977786
- Stoica, P., & Moses, R. L. (1997). *Introduction to spectral analysis*. Upper Saddle River: Prentice hall.
- Stone, L. S., Beutter, B. R., & Lorenceau, J. (2000). Visual motion integration for perception and pursuit. *Perception*, 29(7), 771–787. doi:10.1068/p2979 PMID:11064800
- Suykens, J. A., & Vandewalle, J. (1999). Least squares support vector machine classifiers. *Neural Processing Letters*, 9(3), 293–300. doi:10.1023/A:1018628609742
- Tatler, B. W. (2009). Current understanding of eye guidance. *Visual Cognition*, 17(6-7), 777–789. doi:10.1080/13506280902869213
- Tavassoli, A., & Ringach, D. L. (2009). Dynamics of smooth pursuit maintenance. *Journal of Neurophysiology*, 102(1), 110–118. doi:10.1152/jn.91320.2008 PMID:19369357
- Trommershäuser, J., Glimcher, P. W., & Gegenfurtner, K. R. (2009). Visual processing, learning and feedback in the primate eye movement system. *Trends in Neurosciences*, 32(11), 583–590. doi:10.1016/j.tins.2009.07.004 PMID:19729211
- Ubeda, A., Ianez, E., & Azorin, J. M. (2011). Wireless and portable EOG-based interface for assisting disabled people. *IEEE/ASME Transactions on Mechatronics*, 16(5), 870–873. doi:10.1109/TMECH.2011.2160354
- Valbuena, D., Cyriacks, M., Friman, O., Volosyak, I., & Graser, A. (2007). Brain-Computer Interface for high-level control of rehabilitation robotic systems. In *Proceedings of Tenth International Conference on Rehab. Robotics*, (pp. 619-625). doi:10.1109/ICORR.2007.4428489
- Van der Stigchel, S. (2010). Recent advances in the study of saccade trajectory deviations. *Vision Research*, 50(17), 1619–1627. doi:10.1016/j.visres.2010.05.028 PMID:20553739
- Volkman, F. C. (1962). Vision during voluntary saccadic eye movements. *Journal of the Optical Society of America*, 52(5), 571–578. doi:10.1364/JOSA.52.000571 PMID:13926602

Weleber, R. G. (1989). Fast and slow oscillations of the electro-oculogram in Best's macular dystrophy and retinitis pigmentosa. *Archives of Ophthalmology*, 107(4), 530–537. doi:10.1001/archophth.1989.01070010544028 PMID:2705921

Wissel, T., & Palaniappan, R. (2011). Considerations on Strategies to Improve EOG Signal Analysis. *International Journal of Artificial Life Research*, 2(3), 6–21. doi:10.4018/jalr.2011070102

Yarbus, A. L. (1967). *Eye movements and vision*. New York: Plenum. doi:10.1007/978-1-4899-5379-7

This research was previously published in Biomedical Image Analysis and Mining Techniques for Improved Health Outcomes edited by Wahiba Ben Abdesslem Karâa and Nilanjan Dey, pages 147-163, copyright year 2016 by Medical Information Science Reference (an imprint of IGI Global).

Chapter 8

Case Study:

Resolving Diagnostic Uncertainties in the Clinical Presentation of Ocular Tuberculosis

Swarna Biseria Gupta

L.N. Medical College, Bhopal, India

Divya Verma

L.N. Medical College, Bhopal, India

D. P. Singh

L.N. Medical College, Bhopal, India

ABSTRACT

In the developing countries, incidence of systemic tuberculosis is very high, with over 8 million new cases each year. The incidence of tuberculous uveitis is also rising correspondingly. It is difficult to diagnose ocular tuberculosis because of the lack of specific ocular findings and specific confirmatory laboratory tests. However, in a developing country like India, where the prevalence of latent tuberculosis is high, uveitis of unexplained cause not fitting into known uveitis entities, in presence of Montoux positivity, is more likely to be tubercular in origin. Hence, early diagnosis and prompt treatment with antitubercular treatment may result in dramatic drop in recurrence and improve individual patient outcomes.

INTRODUCTION

The world health organization (WHO) has declared tuberculosis (TB) to be a global emergency (centre for disease control and prevention, 1994 & 2004; Duke-Elders & Perkin, 2004). It has estimated 9 million cases and 2 million deaths from TB for 2005 (Sharma, 2011). Incidence of ocular TB ranges from 1.4 – 5.74% (Sharma A 2011). About 1.4% of people with pulmonary TB (PTB) develop ocular manifestations (Chuka-Okosa, 2006; Gupta, 2005; Biswas, 1996)

DOI: 10.4018/978-1-5225-5195-9.ch008

In 1954, the Wilmer Eye institute ascribed 22% of uveitis were attributable to TB (Woods, 1961). In the 1940's, Guyton and Woods placed TB as the cause of 80% of all granulomatous uveitis.

The diagnosis of ocular TB is important because prompt treatment may improve the individual patient's outcome. Delayed diagnosis can lead to pain, vision loss, and systemic complications of infection. Diagnosis is also important from public health perspective because identification and treatment of coexisting PTB may prevent TB transmission to others. Unfortunately, there is no pathognomonic ophthalmic finding for ocular TB. Hence, ocular TB is difficult to diagnose due to its similarity to other causes of uveitis, the invasiveness of obtaining tissue samples, and limitations of available diagnostic tests. Clinical suspicion is the first step toward the correct diagnosis (Chuka-Okosa,2006; Kurup, 2006; Tabara,2005; Deschenes,2006; Kuruvilla,2003; Demicri, 2004; Varma,2006; Mistr,2006; Devoe, 1964).

CASE NO. 1

A 62-year-old female patient reported to our hospital in January 2012, complaining of blurring of vision and floaters in left eye for 2 months. There were recurrent episodes of the same complaints in the past; the visual acuity in her left eye was 6/9 and that in her right eye was 6/6. Anterior segments were normal. Fundus examination revealed patches of active choroiditis disseminated all over the fundus of left eye. On fundus fluorescein angiography hypofluorescence with late staining was seen. Mantoux was strongly positive (16mm) along with lymphocytosis. Intravenous Methyl prednisolone 1 gm was given for 3 days along with four drugs anti-tubercular treatment (Rifampicin 600mg, INH 300mg, Ethambutol 800mg, Pyrazinamide 1500mg) in addition to maintenance systemic steroids in tapering doses. Lesions healed completely in four weeks. There had been no recurrence even after 2years after completion of treatment.

CASE NO. 2

A 70-year-old male patient presented with complaint of painful diminution of vision with redness in right eye 1 year back. He had a history of recurrent episodes of similar complaints for the last 2 years. Visual acuity in his right eye was found to be 6/60 and in that in his left eye was 6/6. On examination, his right eye showed ciliary flush, along with cells 2+, flare 1+, and old and fresh keratic precipitates along with posterior synechiae at 5 o'clock and 9 o'clock positions. The left eye was quiet. On investigation, Mantoux test was strongly positive (> 10mm induration) and lymphocytosis was present. His chest x-ray showed no signs of pulmonary TB.

The patient was started on four-drug ATT for six months along with systemic and topical steroids with cycloplegic drugs. He was asked to follow up after a month.

Subsequently, the patient was lost to follow-up for a year. He reported back after a year with complaints of pain, redness, blurring of vision in left eye. Vision in his right eye was PL+, PR defective in temporal quadrant and in left eye was 6/60. On examination, the patient had occlusio papillae in right eye and old & fresh KP's with aqueous flare in left eye. The right eye was pseudophakic and media was hazy due to multiple vitreous opacities. On B-Scan-multiple vitreous membranes were seen. On revealing past treatment history, we came to know that he has taken ATT for only one month which was given for his similar complaints in right eye and stopped taking the drugs by himself as he got relieved of his acute symptoms. The patient was restarted on ATT under category 2 as defaulter and his vision improved, and fundus lesions also started to regress.

Case Study

Figure 1. Fundus photograph of left eye, showing active lesion of choroiditis in upper nasal quadrant

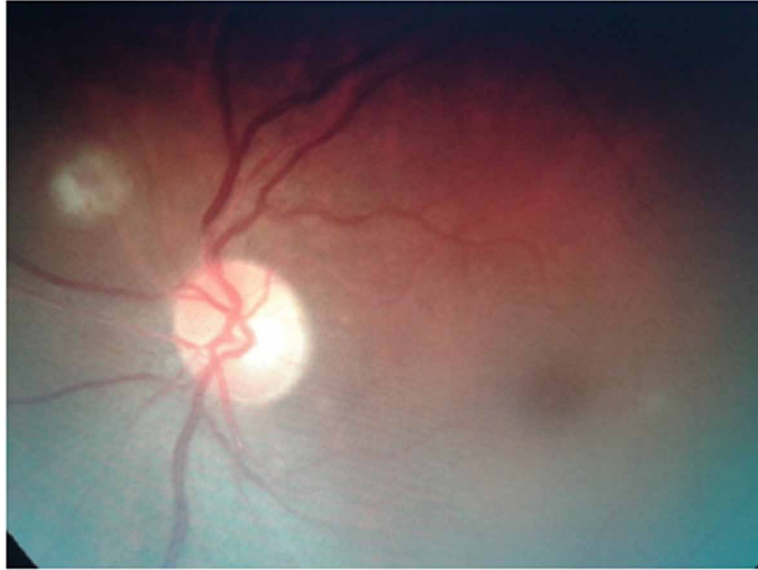


Figure 2. Fundus picture showing active choroiditis with perivasculitis



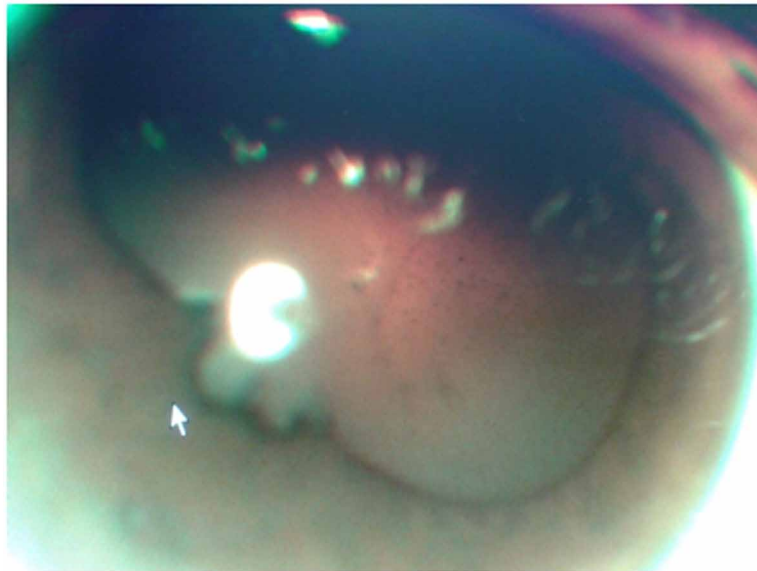
DISCUSSION

The term “ocular tuberculosis” encompasses any infection by *Mycobacterium tuberculosis*, or one of three related mycobacteria species (*M. Bovis*, *M. africanum* and *M. microti*) in, on, or around the eye. (C. Michael Samson M.D). Infection is most often result of hematogenous spread during PTB or extra-pulmonary TB (EPTB). Primary ocular infection is rare and likely to occur in children via direct entry of bacilli

Figure 3. Fundus photograph showing left eye: healed chorioretinal lesions



Figure 4. Picture showing evidence of anterior uveitis, in the form of altered iris pattern, festooned pupil due to posterior synechiae and dust like opacities in the media (aqueous flare)



through conjunctiva (Deschenes, 2006). Infection may also occur via local spread from active sinus or meningeal infections. Additionally, immune mediated ocular TB can occur due to hypersensitivity to *M.tuberculosis* antigens from a distant focus (such as lungs).

Ocular TB is often unilateral and asymmetric (Sahu, 1998; Babu, 2006; Mehta, 2004), the most common sign being choroidal mass, followed by choroiditis (Demicri, 2004; Sarvananthan, 1998; Reddy,

Case Study

2006). There is no specific age of presentation and it may vary from 1–75 years, no gender predilection and the course of the disease is chronic, and although most of the presentations are granulomatous, non-granulomatous uveitis does not exclude TB. Presence of choroidal lesion, with or without inflammation, is strongly correlated with systemic disease, and is an indicator of hematogenous spread of mycobacteria. Tuberculosis can also present as orbital mass, eye lid abscess, TB Scleritis, phlyctenulosis (type IV hypersensitivity reaction), Eale's disease (retinal periphlebitis) and also granulomatous anterior uveitis with positive tuberculin skin testing. (C. Michael Samson M.D).

Purified protein derivative / Montoux skin test is the primary screening and diagnostic tool available since 1912 to aid the decision on whether to institute ATT or not. It has low specificity and sensitivity (Gupta, 2007). Any palpable induration measuring 10mm or more may be considered positive. Nucleic acid amplification techniques have been used to diagnose intraocular TB in uveitis cases. (Kolake S et al; 1994)(Sarvanathan N et al; 1998)(Bowyer JD 1999)(Recillas –Gispert Cetal; 1997). However, PCR is a sensitive and highly specific technique that can amplify mycobacterial DNA several folds and is especially useful for intraocular fluids, as it can be performed with very small sample sizes, either aqueous (Gupta & Gupta, 2005), vitreous humor, sub-retinal fluid or chorio-retinal biopsy, it is extremely useful for early diagnosis of intraocular tuberculosis (Arora et al 1999, Von Gelder, 2001). The combined data of three case control studies comparing patients with TB uveitis versus controls reveals a sensitivity of 22-77% and specificity of 89-97%. (Ortega-Larrocea G, 2003) (Arora SK, 1998), (Gupta V, 1998). In the United States, current recommendation from the CDC, Infectious Disease Society of America suggest to use INH, Rifampicin, PZA and ethambutol as combined therapy for the initial 2 months. Generally, 9 month course of treatment that include INH and rifampicin are effective for extrapulmonary disease such as ocular involvement. (CDC. Treatment of tuberculosis MMWR, 2003).

CONCLUSION

In a country like India, where the prevalence of latent tuberculosis is high, there is greater possibility of presumed ocular tuberculosis and the diagnosis of ocular TB remains a challenge. Thus, a high index of suspicion is required and is the first step towards the correct diagnosis. Prospective studies with strict criteria for the diagnosis of TB and ocular TB are necessary to better define the incidence of ocular TB. Although newer testing methodologies for TB are promising, the utility of there has yet to be established in patients with ocular TB and thus research on their application to ocular TB is also warranted.

It is probably not indicated to treat every uveitic patient with positive PPD with long term anti tuberculous medication in the absence of other evidence of TB, but each case should be treated individually, looking at the risk and benefits of treating or not treating with TB medications.

REFERENCES

Arora, S. K., Gupta, V., Gupta, A., Bambery, P., Kapoor, G. S., & Sehgal, S. (1999). Diagnostic efficacy of polymerase chain reaction in granulomatous uveitis. *Tubercle and Lung Disease*, 79(4), 229–233. doi:10.1054/tuld.1999.0210 PMID:10692991

- Babu, S., Kumarasamy, N., & Therese, L. et al. (2006). Ocular tuberculosis in acquired immunodeficiency syndrome. *American Journal of Ophthalmology*, 142(3), 413–418. doi:10.1016/j.ajo.2006.03.062 PMID:16935585
- Biswas, J., & Badrinath, S. S. (1996). Ocular morbidity in patients with active systemic tuberculosis. *International Ophthalmology*, 19, 293–298. PMID:8864813
- Bowyer, J. D., Gormley, P. D., Seth, R., Downes, R. N., & Lowe, J. (1999). Choroidal tuberculosis diagnosed by polymerase chain reaction. A clinicopathologic case report. *Ophthalmology*, 106(2), 290–294. doi:10.1016/S0161-6420(99)90068-4 PMID:9951479
- CDC, 2003; Treatment of tuberculosis;52(RR11):1-77.
- Chuka-Okosa, C. M. (2006). Tuberculosis and the eye. *Nigerian Journal of Clinical Practice*, 9, 68–70. PMID:16986294
- Demicri, H., Shields, C. L., & Shields, J. L. (2004). Ocular tuberculosis masquerading as ocular tumors. *Survey of Ophthalmology*, 49(1), 78–88. doi:10.1016/j.survophthal.2003.10.009 PMID:14711441
- Deschenes, J., Wade, N. K., & Lalonde, R. (2006). Tuberculosis and atypical Mycobacteria. In W. Tasman & E. Jaeger (Eds.), *Duane's Ophthalmology*. Philadelphia, PA: Lippincott, Williams & Wilkins.
- Devoe, A., & Locatcher-Ichorazo, D. (1964). The external manifestations of ocular tuberculosis. *Tr Am Ophth. Soc.*, 62, 204–211.
- Gupta, A., & Gupta, V. (2005). Tubercular posterior uveitis. *International Ophthalmology Clinics*, 45(2), 71–78. doi:10.1097/01.iio.0000155934.52589.e3 PMID:15791159
- Gupta, V., Arora, S., Gupta, A., Ram, J., Bambery, P., & Sehgal, S. (1998). Management of presumed intraocular tuberculosis: Possible role of the polymerase chain reaction. *Acta Ophthalmologica Scandinavica*, 76(6), 679–682. doi:10.1034/j.1600-0420.1998.760609.x PMID:9881551
- Gupta, V., Gupta, A., & Rao, N. A. (2007). Intraocular tuberculosis-an update. *Survey of Ophthalmology*, 52(60), 561–587. doi:10.1016/j.survophthal.2007.08.015 PMID:18029267
- Kotake, S., Kimura, K., Yoshikawa, K., Sasamoto, Y., Matsuda, A., & Nishikawa, T. et al. (1994). Polymerase chain reaction for the detection of mycobacterium tuberculosis in ocular tuberculosis [letter]. *American Journal of Ophthalmology*, 117(6), 805–806. doi:10.1016/S0002-9394(14)70328-9 PMID:8198167
- Kurup, S. K., Buggage, P. R., Clarke, G., Ursea, R., Lim, W. K., & Nussenblatt, R. B. (2006). Gamma interferon assay as an alternative to PPD skin testing in selected patients with granulomatous intra-ocular inflammatory disease. *Canadian Journal of Ophthalmology*, 41(6), 737–740. doi:10.3129/i06-068 PMID:17224956
- Kurup, S. K., & Chan, C. C. (2006). Mycobacterium related ocular inflammatory disease: Diagnosis and management. *Annals of the Academy of Medicine, Singapore*, 35, 203–209. PMID:16625271
- Kuruvilla, A. (2003). Correspondence: Ocular tuberculosis. *Lancet*, 301(9353), 260–26. doi:10.1016/S0140-6736(03)12295-7 PMID:12547573

Case Study

- Mehta, S. (2004). Ocular lesions in acute disseminated tuberculosis. *Ocul Immunol Inflamm.*, 12, 311-315.
- Ortega-Larrocea, G., Bobadilla-del-Valle, M., Ponce-de-Leon, A., & Sifuentes-Osornio, J. (2003). Nested polymerase chain reaction for mycobacterium tuberculosis DNA detection in aqueous and vitreous of patients with uveitis. *Archives of Medical Research*, 34(2), 116–119. doi:10.1016/S0188-4409(02)00467-8 PMID:12700006
- Recillas-Gispert, C., Ortega-Larrocea, G., Arellanes-Garcia, L., Herrera-Barrios, T., & Sada-Díaz, E. (1997). Chorioretinitis secondary to mycobacterium tuberculosis in acquired immune deficiency syndrome. *Retina (Philadelphia, Pa.)*, 17(5), 437–439. doi:10.1097/00006982-199709000-00013 PMID:9355193
- Reddy, S., Roe, R., & Cunningham, E. T. Jr. (2006). Diagnostic and therapeutic challenges. *Retina (Philadelphia, Pa.)*, 26(8), 954–959. doi:10.1097/01.iae.0000250012.06650.ec PMID:17031299
- Sahu, G. N., Mishra, N., & Bhutia, R. C. 1998, Manifestations in ocular Tuberculosis. Ahmedabad: National Conference on Tuberculosis and chest Diseases. *Ind. J Tub*; 45:153-154. doi:10.1016/S0161-6420(01)00693-5
- Sarvananthan, N., Wiselka, M., & Bibby, K. (1998). Intraocular tuberculosis without detectable Systemic infection. *Archives of Ophthalmology*, 116, 1386–1388. PMID:9790648
- Sharma, A., Thapa, B., & Lavaj, V. P. (2011). Ocular tuberculosis. *Nepal J Ophthalmol*, 3(5), 52–67. PMID:21587325
- Tabara, K. T. (2005). Ocular tuberculosis: Anterior segment. *International Ophthalmology Clinics*, 45(2), 57–69. doi:10.1097/01.iio.0000155935.60213.ac PMID:15791158
- Varma, D., Anand, S., Reddy, A. R., Das, A., Watson, J. P., & Currie, D. C. et al. (2006). Tuberculosis: An under- diagnosed aetiological agent in Uveitis with an effective treatment. *Eye (London, England)*, 20(9), 1068–1073. doi:10.1038/sj.eye.6702093 PMID:16215543
- Woods, A. C. (1961). *Endogenous Inflammations of the Uveal Tract*. Baltimore, Maryland: Williams and Wilkins Company.

This research was previously published in the International Journal of User-Driven Healthcare (IJUDH), 4(3); edited by Ashok Kumar Biswas, pages 38-45, copyright year 2014 by IGI Publishing (an imprint of IGI Global).

Chapter 9

A Comparative Study on Diabetic Retinopathy Detection Using Texture-Based Feature Extraction Techniques

Azam Asilian Bidgoli
University of Kashan, Iran

Hossein Ebrahimpour-Komleh
University of Kashan, Iran

Seyed Jalaeddin Mousavirad
University of Kashan, Iran

ABSTRACT

Diabetic retinopathy is proved to be one of the most important eye disorders in recent decades that late diagnosis of it may cause low vision or even blindness. Specialist are able to detect retinopathy in retinal images using machine learning as a decision support system which helps accelerate and facilitate the diagnosis. The automated diabetic retinopathy is a difficult computer vision problem –with the goal of detecting features of retinopathy. The present chapter is written with the purpose of analyzing and comparing different feature extraction methods to evaluate the best algorithm for detection retinopathy with least error. Extracted features using these methods are used to classify images into normal and altered groups.

INTRODUCTION

In recent years, machine learning and data mining techniques have been considered as good tools for automated medical diagnosis systems (Kononenko, 2001; Kononenko, Bratko, & Kukar, 1997). Bearing in mind that medical diagnosis is a difficult and visual task, it is often carried out by an expert who commonly takes decisions by evaluating the current test results of a patient or comparing the patient

DOI: 10.4018/978-1-5225-5195-9.ch009

with other patients of the same condition by referring to the previous decisions (Polat & Güneş, 2006). Therefore, medical diagnosis is considered as an important but complicated process that requires to be executed accurately and effectively. Machine learning can help experts automate diagnosis and accordingly, reduce the possibility of error in experts dramatically. And, as a result, providing them with more detailed medical data inspected in a shorter time.

Detection of different disease using machine learning methods has been considered in various research works. Such attempts include diagnosis of hepatitis (Bascil & Oztekin, 2012), using neural network, Breast Cancer least square support vector machine (Polat & Güneş, 2007), and heart disease using artificial immune recognition system (Polat, Güneş, & Tosun, 2006).

Nowadays, diabetic retinopathy is the leading cause of blindness in adults all around the world. Most people with diabetes will develop some form of eye disease (retinopathy) causing reduced vision or blindness. Consistently high levels of blood glucose, together with high blood pressure and high cholesterol, are the main causes of retinopathy which can be managed through regular eye checks and keeping glucose and lipid levels at or close to normal ("International federation diabetes," 2014). Therefore, the Importance of early diagnosis of diabetes based on analysis of retinal images is increasing as this disease is affecting more people every day (Klein, Meuer, Moss, & Klein, 1995). As aforementioned, diabetic retinopathy (DR) has a fundamental role in visual impairment, and automated detection of diabetic retinopathy can reduce its lesion.

Regarding the importance of diagnosing the disease, a great deal of attempt has been made to utilize different methods of machine learning to diagnose diabetic retinopathy from retinal images. The process of detection of disease in images using these methods has two steps roughly. First, it should extract some features from images to describe the nature of image. The second step is the classification of these features using a classifier. There are a variety of methods to perform these two steps. Some researchers focus on improving the diagnosis using defining better features, while others outperform different classification methods. (Di Wu, et al, 2006) use Gabor filters to trace and patch the blood vessels together (Wu, Zhang, Liu, & Bauman, 2006). Pinz et al, (Pinz, Bernögger, Datlinger, & Kruger, 1998) use gradient based techniques and hough transforms (Illingworth & Kittler, 1988) to map and localize blood vessels. (Silberman et al, 2010) utilize SIFT feature extractor to describe the images. The second step support machine classifier(SVM) (Conforti & Guido, 2010) is considered to classify the features(Silberman, Ahrlich, Fergus, & Subramanian, 2010). Neovascularization features extracted from retinal images are among other features in this area. (Vatanparast & Harati, 2012) has classified these features using SVM.

Di Wu et al use gabor filters to trace and patch the blood vessels together (Wu et al., 2006). (Pinz et al., 1998) use gradient based techniques and Hough transforms (Illingworth & Kittler, 1988) to map and localize blood vessels. Silberman et al utilize SIFT feature extractor to describe the image. then support machine classifier(SVM)(Conforti & Guido, 2010) is considered to classify the features(Silberman et al., 2010). Neovascularization features extracted from retinal images are other features in this area. (Vatanparast & Harati, 2012) has classified these features using SVM.

In another work, the optic disc is detected by means of morphological filtering techniques and the watershed transformation (Walter, Klein, Massin, & Erginay, 2002). Also (Hoover & Goldbaum, 2003) used fuzzy convergence to determine the origination of the blood vessel network. Some work is performed on vessel segmentation (Niemeijer, Staal, van Ginneken, Loog, & Abramoff, 2004). Retinal vessel segmentation is important for the detection of numerous eye diseases and plays an important role in automatic retinal disease screening systems. (Niemeijer et al., 2004) compared the performance of

retinal vessel segmentation methods. But in all of these researches less attention has paid to use textural features of an image.

As (Tang, 1998) asserts, Texture is the term used to characterize the surface of a given object or region and it is one of the main features utilized in image processing and pattern recognition (Tang, 1998). There are different methods to extract such features from images. These methods are based on statistical features of histogram (Gonzales, Woods, & Eddins, 2004), grey level co-occurrence matrix (GLCM) (Haralick, 1979), grey level run length matrix (GLRLM) (Tang, 1998), wavelet transformation (Vetterli & Herley, 1992), gabor filters (Marčelja, 1980), local binary pattern (LBP) (Ojala, Pietikäinen, & Mäenpää, 2002). Numerous features are extracted from each of these contents. Some of these methods generate features that are not appropriate for classifying images and don't contain useful information; therefore, feature selection methods can be applied to reduce the amount of data in classification phase. Selected features are utilized using a classifier algorithm to classify data into exact group. This chapter compares four mentioned methods to extract texture features, and then the SVM classifier classifies these features based on a class label that is defined in considered dataset. The present experiment which is done on a dataset includes 1200 images. The property of dataset has been explained in experiment section.

TEXTURE BASED FEATURE EXTRACTION

In the present section, several feature extraction methods named, statistical features of histogram, grey-level run lengths, gray-level co-occurrence matrix, local binary pattern, wavelet transform features and gabor are considered. Following that, further details of these algorithms are explained.

Statistical Features of Histogram

Histogram is a graph showing the number of pixels in an image at each different intensity value found in that image. Features based upon statistical information from the histogram of an image can be used as a method to describe its texture. Six statistical features are extracted from histogram. First, the histogram of pixel intensity values is computed and then is normalized to $(p(i))$. After that, based on these vectors $(p(i))$ and the probability of intensity value occurrence, six features are extracted. The definition of features are shown in Table 1. The definition of extracted features based on statistical information of histogram where different variables are as below:

μ_n : The n^{th} moments.

Z_i : Random variable related to intensity values.

$P(z_i)$: The histogram of the pixel intensity values.

L : The maximum value of intensity level.

σ^2 : Variance

In addition to these 6 features, 25 other features based on frequency of pixel intensity value can be computed. Therefore, the range of intensity (0-255) is divided to 25 intervals. Then the number of pixels in the image that are in every interval defined as a feature, meaning that 25 features are extracted from image.

Table 1. The definition of extracted features based on statistical information of histogram

Feature	Computation	Description
Mean	$m = \sum_{i=0}^{L-1} z_i p(z_i)$	The mean of texture intensity. The variance is a measure of the histogram width, that is, a measure of how much the gray levels differ from the mean.
Variance	$\sqrt{\mu_2(2)}$	The variance of texture intensity.
Smoothness	$1 - \frac{1}{(1 + \sigma^2)}$	The value of this feature for smooth area in image is close to zero.
3rd Moment	$\sum_{i=0}^{L-1} (z_i - m)^3 p(z_i)$	This feature shows the skewness of the histogram. Skewness is a measure of the degree of histogram asymmetry around the mean. Symmetric histogram causes zero value.
Uniformity	$\sum_{i=0}^{L-1} P^2(Z_i)$	The maximum value of feature is obtained when the intensity value of pixels are same.
Entropy	$-\sum_{i=0}^{L-1} p(z_i) \log_2 p(z_i)$	Entropy is a measure of histogram uniformity. The closer to the uniform distribution (P(I) constant), the higher the entropy.

Gray-Level Run Lengths

As mentioned earlier, an element in Gray-Level Run Lengths (GLRL) matrix, QRL, presents the number of consecutive pixels having the same gray-level value. In this content, the number of these pixels represents the length of the run. GLRL features include textural information related to the number of times each gray-level appears in different frequencies. For example in the GLRL matrix (2,3) the elements give the number of times gray-level 2 appears in the image with run length of 3.

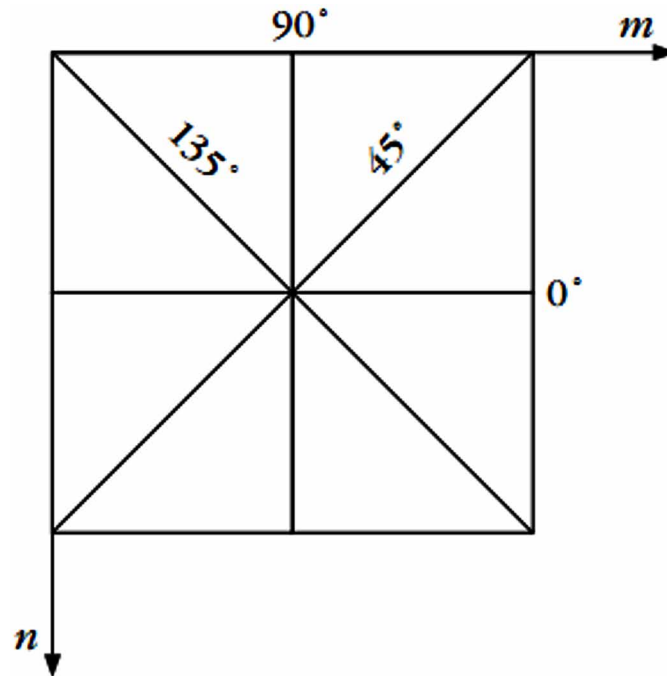
In GLRL matrix, the number of rows indicates possible gray levels in the image (N_g) and the number of columns is equal to the largest possible run length in the image (N_r). A GLRL matrix can be defined in four different directions; horizontal, diagonal, vertical, and anti-diagonal (0°, 45°, 90°, 135°) as shown in Figure 1. For direction 0, each element specifies the number of times a gray level appears in the image by itself, or in pairs, just in direction 0.

For the following image

$$I = \begin{bmatrix} 0 & 0 & 1 & 0 \\ 2 & 1 & 0 & 0 \\ 3 & 2 & 3 & 3 \\ 3 & 2 & 2 & 2 \end{bmatrix}$$

The resulting GLRL matrices for the four principal directions are:

Figure 1. Four different directions for defining GLRL. m and n show the top and left directions of an image respectively.



$$Q_{RL}(0^\circ) = \begin{bmatrix} 1 & 2 & 0 & 0 \\ 2 & 0 & 0 & 0 \\ 2 & 0 & 1 & 0 \\ 2 & 1 & 0 & 0 \end{bmatrix}$$

$$Q_{RL}(45^\circ) = \begin{bmatrix} 3 & 1 & 0 & 0 \\ 0 & 1 & 0 & 0 \\ 5 & 0 & 0 & 0 \\ 4 & 0 & 0 & 0 \end{bmatrix}$$

$$Q_{RL}(90^\circ) = \begin{bmatrix} 3 & 1 & 0 & 0 \\ 2 & 0 & 0 & 0 \\ 3 & 1 & 0 & 0 \\ 2 & 1 & 0 & 0 \end{bmatrix}$$

$$Q_{RL}(135^\circ) = \begin{bmatrix} 5 & 0 & 0 & 0 \\ 2 & 0 & 0 & 0 \\ 2 & 0 & 1 & 0 \\ 4 & 0 & 0 & 0 \end{bmatrix}$$

The first element of the first row of Q_{RL} is the number of times gray-level “0” appears by itself (0 for our example) with direction 45, the second element is the number of times it appears in pairs (2 in the example), and so on. The second row provides the same information for gray-level “1” and so on. Therefore, in matrix (2, 2), for instance, the element indicates the number of times that gray-level “1” appears in pairs.

Based on the preceding definition of the run length matrix, (Tang, 1998) has defined the following features (Tang, 1998). In all equations N_g and N_r indicate possible gray levels in the image and the largest possible run length in the image respectively, while $r(i, j)$ is the element of GLRL matrix.

1. **Short Run Emphasis (SRE):**
$$SRE = \frac{\sum_{i=1}^{N_g} \sum_{j=1}^{N_r} \frac{r(i, j)}{j^2}}{\sum_{i=1}^{N_g} \sum_{j=1}^{N_r} r(i, j)}$$
2. **Long Run Emphasis (LRE):**
$$LRE = \frac{\sum_{i=1}^{N_g} \sum_{j=1}^{N_r} j^2 r(i, j)}{\sum_{i=1}^{N_g} \sum_{j=1}^{N_r} r(i, j)}$$
3. **Gray Level Non Uniformity (GLNU):**
$$GLNU = \frac{\sum_{i=1}^{N_g} \left(\sum_{j=1}^{N_r} r(i, j) \right)^2}{\sum_{i=1}^{N_g} \sum_{j=1}^{N_r} r(i, j)}$$
4. **Run Length Non Uniformity (RLNU):**
$$RLNU = \frac{\sum_{j=1}^{N_r} \left(\sum_{i=1}^{N_g} r(i, j) \right)^2}{\sum_{i=1}^{N_g} \sum_{j=1}^{N_r} r(i, j)}$$
5. **Run Percentage (RP):**
$$RP = \frac{\sum_{i=1}^{N_g} \sum_{j=1}^{N_r} r(i, j)}{n_p}$$
6. **Low Gray Level Run Emphasis (LGRE):**
$$LGRE = \frac{\sum_{i=1}^{N_g} \sum_{j=1}^{N_r} \frac{r(i, j)}{i^2}}{\sum_{i=1}^{N_g} \sum_{j=1}^{N_r} r(i, j)}$$
7. **High Gray Level Run Emphasis (HGRE):**
$$HGRE = \frac{\sum_{i=1}^{N_g} \sum_{j=1}^{N_r} r(i, j) \cdot i^2}{\sum_{i=1}^{N_g} \sum_{j=1}^{N_r} r(i, j)}$$

8. **Short Run Low Gray Level Emphasis (SRLGE):**
$$SRLGE = \frac{\sum_{i=1}^{N_g} \sum_{j=1}^{N_r} \frac{r(i, j)}{i^2 \cdot j^2}}{\sum_{i=1}^{N_g} \sum_{j=1}^{N_r} r(i, j)}$$
9. **Short Run High Gray Level Emphasis (SRHGE):**
$$SRHGE = \frac{\sum_{i=1}^{N_g} \sum_{j=1}^{N_r} \frac{r(i, j) \cdot i^2}{j^2}}{\sum_{i=1}^{N_g} \sum_{j=1}^{N_r} r(i, j)}$$
10. **Long Run Low Gray Level Emphasis (LRLGE):**
$$LRLGE = \frac{\sum_{i=1}^{N_g} \sum_{j=1}^{N_r} r(i, j) \cdot i^2 \cdot j^2}{\sum_{i=1}^{N_g} \sum_{j=1}^{N_r} r(i, j)}$$
11. **Long Run High Gray Level Emphasis (LRHGE):**
$$LRHGE = \frac{\sum_{i=1}^{N_g} \sum_{j=1}^{N_r} \frac{r(i, j) \cdot j^2}{i^2}}{\sum_{i=1}^{N_g} \sum_{j=1}^{N_r} r(i, j)}$$

Each of features gives different information correspondent to the texture of an image. The value obtained using features is different regarding the smoothness or coarseness of texture. For instance, RP takes low values for smooth images or we expect SRE to be large for coarser and LRE to be large for smoother images.

Gray-Level Co-Occurrence Matrix

Grey-level co-occurrence matrix (GLCM) presents the relative positions among pixels. Let d be the relative distance measured in pixel numbers ($d=1$ for neighboring pixels, etc.), and N_g is the possible gray levels in the image as described in the previous section. The Co-occurrence matrix Q is a $N_g \times N_g$ matrix, that elements $Q_{co}(i, j)$ shows the number of pixels at distance d with gray-level values i and j , respectively. This matrix can be constructed in four different directions ($0^\circ, 45^\circ, 90^\circ, 135^\circ$) as defined previously. Therefore, each matrix is defined for a special direction (Φ) and distance (d). For the following image

$$I = \begin{bmatrix} 0 & 0 & 1 & 0 \\ 2 & 1 & 0 & 0 \\ 3 & 2 & 3 & 3 \\ 3 & 2 & 2 & 2 \end{bmatrix}$$

The resulting co-occurrence matrices for the four principal directions are as follows:

$$Q_{co}(0^\circ, d=1) = \begin{bmatrix} 4 & 4 & 0 & 0 \\ 4 & 0 & 2 & 0 \\ 0 & 2 & 4 & 4 \\ 0 & 0 & 4 & 2 \end{bmatrix}$$

$$Q_{co}(90^\circ, d=1) = \begin{bmatrix} 0 & 2 & 0 & 2 \\ 2 & 0 & 0 & 2 \\ 0 & 0 & 4 & 4 \\ 2 & 2 & 4 & 0 \end{bmatrix}$$

$$Q_{co}(135^\circ, d=1) = \begin{bmatrix} 2 & 4 & 2 & 4 \\ 4 & 0 & 2 & 0 \\ 0 & 2 & 2 & 6 \\ 4 & 0 & 6 & 2 \end{bmatrix}$$

The first element of the first row of above $Q_{co}(0^\circ, d=1)$ is the number of times the consecutive pixels ($d=1, \Phi=0$) have the gray value 0. Searching the pixels is performed in the positive and negative directions for each gray level value. So value 4 in the above example, results from searching in the positive and negative directions. From the definition of the co-occurrence matrix, it is apparent that it is a symmetric one that can be used to reduce subsequent computations.

Based on the preceding definition of co-occurrence matrix, some features can be defined (Haralick, Shanmugam, & Dinstein, 1973). These features give information about the texture of image such as coarseness, smoothness, and so on. 10 features extracted from GLCM are presented below. In all equations, N_g indicates possible gray levels in the image. K is the number of rows in the matrix. p_{ij} refers to the probability of occurrence of element i, j that is calculated as below:

$$p_{ij} = \frac{1}{R} q_{ij}, R \text{ is the total number of possible pixel pairs and } q_{ij} \text{ is the element of GLCM matrix.}$$

Extracted features from GLCM matrix.

1. **Max Probability:** $\max(p_{ij})$
2. **Correlation:** $\sum_{i=1}^k \sum_{j=1}^k (i-j)^2 p_{ij}$
3. **Contrast:** $\sum_{i=1}^k \sum_{j=1}^k (i-j)^2 p_{ij}$
4. **Uniformity:** $\sum_{i=1}^k \sum_{j=1}^k p_{ij}^2$
5. **Entropy:** $-\sum_{i=1}^k \sum_{j=1}^k p_{ij} \log_2 p_{ij}$
6. **Homogeneity:** $\sum_{i=1}^k \sum_{j=1}^k \frac{p_{ij}}{1+|i-j|}$

7. **Dissimilarity:** $\sum_{i=0}^k \sum_{j=0}^k p_{ij} |i - j|$
8. **Horizontal Average:** $\mu_i \sum_{i=0}^k \sum_{j=0}^k i(p_{ij})$
9. **Vertical Average:** $\mu_j \sum_{i=0}^k \sum_{j=0}^k j(p_{ij})$
10. **Cluster Shade:** $CS = \sum_{i=0}^k \sum_{j=0}^k ((i - \mu_i) + (j - \mu_j))^3 p_{ij}$
11. **Cluster Prominence:** $CP = \sum_{i=0}^k \sum_{j=0}^k ((i - \mu_i) + (j - \mu_j))^4 p_{ij}$

Local Binary Pattern

Local binary pattern (LBP) is a powerful texture based feature extraction method from images that works in a pixel block of them. This block is considered around each pixel of image to extract a feature for corresponding pixel. The size of block in basic LBP is 3×3 , but the generic formulation of the operator puts no limitations to the size of the neighborhood. The operator performs the process of thresholding, during which the pixels in the block with the center pixel value is considered as the threshold, and every pixel in the neighborhood with gray value greater than center pixel value is labeled by “1” and otherwise “0”. This gives an 8-digit binary number (which is usually converted to decimal for convenience).

The LBP operator performs as in the equation below:

$$LBP_{P,R} = \sum_{i=0}^{P-1} s(g_i - g_c) 2^i S(x) = \begin{cases} 1 & x \geq 0 \\ 0 & x < 0 \end{cases}$$

where P is the number of pixels in the neighborhood. g_i and g_c are the gray value of these pixels and center pixel respectively. These two steps are presented in Figure 2.

A total of $2^8 = 256$ different labels can be obtained depending on the relative gray values of the center and the pixels in the neighborhood. According to the example in figure if the left top corner be the start

Figure 2. The steps of LBP features formation

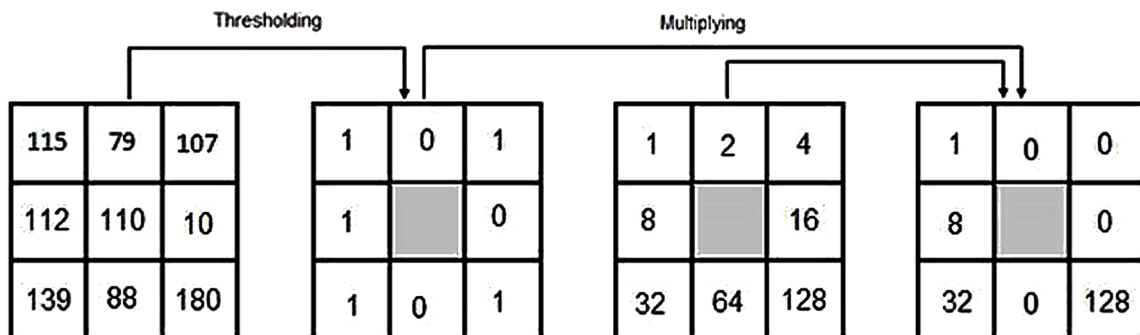
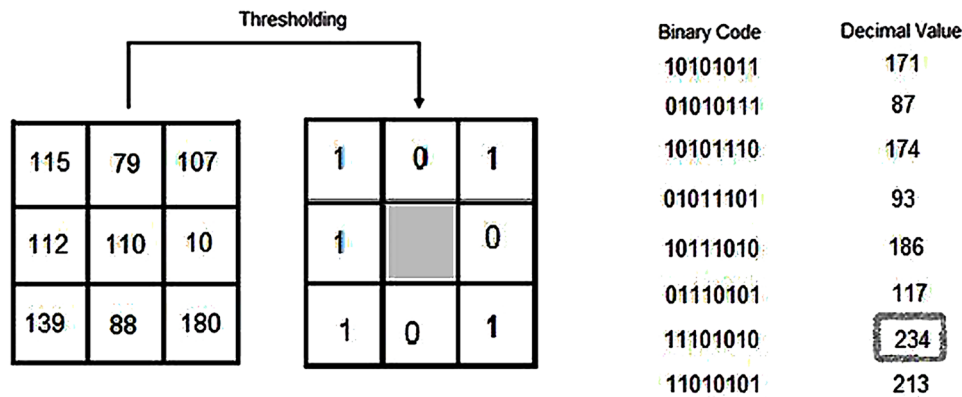


Figure 3. An example of constructing LBP features



place for constructing binary code with clockwise direction, it will ends up with a binary number, like 10101011. This is 10101110 for start point at top-right. To deal with the difference between patterns, a method is considering largest value of 8 different patterns in clockwise direction. This method also generates rotation invariant features. The corresponding decimal value of the generated binary number is then used for labeling the given pixel. The obtained patterns from any of blocks are used as a feature vector for each image and can describe the texture of the images.

The method is shown in Figure 3. In this example the value 234 is the final pattern.

Features Based on Wavelet

Wavelets are based on small waves of varying frequency and limited duration. Conventional Fourier Transforms is a method for analyzing the signal which is based on sinusoids functions. It separates the Sinusoidal and Cosine components. It provides only the notes or frequency information, temporal information is lost in transformation process. Unlike the Fourier transform, wavelet transform represents a compressed transformation based on different resolutions and scales. The result of every scale and resolution is called wavelet coefficient. In other word wavelet transformation separates the signal to wavelet components in different scales and resolutions as it is presented in Figure 4.

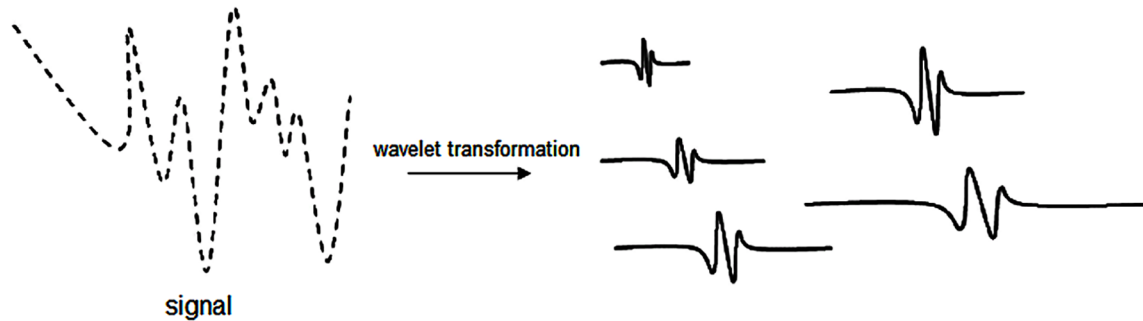
In Continuous wavelet analyzing, the corresponded signal is multiplied to a wavelet function which is Equivalent to window function. The Continuous wavelet is defined as below:

$$CWT_x^\psi(\tau, s) = \Psi_x^\psi(\tau, s) = \frac{1}{\sqrt{|s|}} \int_{-\infty}^{+\infty} x(t) \psi^* \left(\frac{t - \tau}{s} \right) dt$$

τ and s are the transition and scaling parameters respectively. Transition parameter controls the amount of movement of window region. Scaling parameter is reversely related to frequency. ψ is the window function called mother wavelet. The most famous mother wavelets are Haar (Haar, 1910), Daubechies (Daubechies, 1992), Meyer (Meyer, 1995). Each wavelet is defined based on some parameters such as, support width, symmetry and the number of vanishing moments. Support width determines

Figure 4. The concept of wavelet transformation

Source: Misiti, Misiti, Oppenheim, & Poggi, 1997.



the speed of approaching to zero domain in spectral dimension. As a result, large temporal supports for lower frequencies, while maintaining short temporal widths for higher frequencies. The symmetry of wavelet represents the symmetry of signal.

The most digital images don't represent a sinusoidal pattern so it is preferred to analyze the image using a multi resolution wavelet that provides different transformed non sinusoidal pattern (mother wavelet). For calculating wavelet from a discrete signal, it is necessary to apply a low pass filter and high pass filter to signal separately. Through such a pair of filters the signal is decomposed into low- and high-frequency components. In the next step, the obtained low frequency is filtered again using a low pass filter and high pass filter. Through repetition of this procedure, the number of repeating shows the decomposition level of wavelet. This is represented in Figure 5.

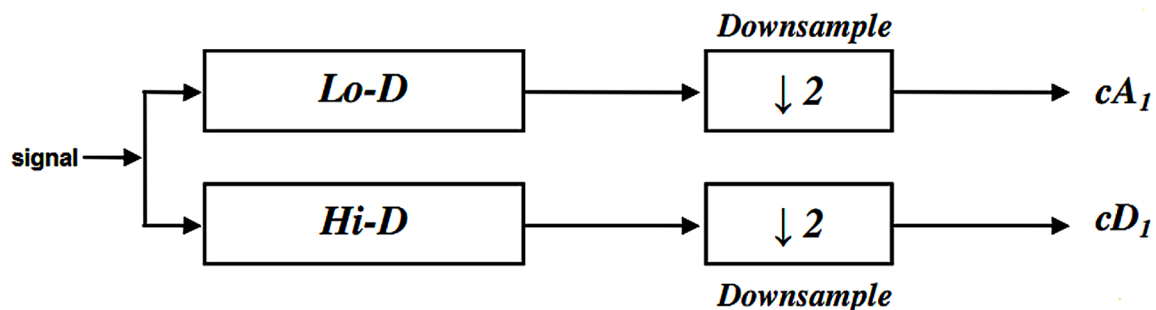
For two dimensional cases the transformation is performed as one dimensional; the horizontal and vertical transformation. The figure shows the diagram of a two dimensional transformation.

In two dimensional wavelet, the image with x and y dimension is divided to 4 components (LL, LH, HL, and HH). Each component has $x/2$ and $y/2$ size. Through the next step, this procedure repeats, and the resulting components are LL^1 , LH^1 , HL^1 , HH^1 with $x/4$ and $y/4$ dimension. The number of repetitions in time is named decomposition level. Finally, the component LL^n is obtained with $x/2^n$, $y/2^n$ dimension.

So in wavelet transformation, image is transformed to a pyramid structure as shown in Figure 6.

Figure 5. One dimensional wavelet transformation

Source: Mallat, 1999.



As it is specified, the first and second letters show the type of filter in horizontal and vertical direction, respectively, while the third one represents the decomposition level of wavelet decomposition.

For wavelet analyzing of an image, the coefficients of wavelet are computed. Decomposition is calculated in 5 levels using Daubechies4 wavelet 4 features are extracted from each level including mean, variance, energy and entropy. Consequently, a total of 80 features can be achieved for an image (20 levels *4 features). The 33 features of better results are as below:

- Entropy of horizontal component from levels number 1,2,3.
- Entropy of vertical component from levels number 1,3.
- Entropy of diagonal component from levels number 1,2,3,4.
- Energy of horizontal component from levels number 1,2,3.
- Energy of vertical component from levels number 1,3.
- Energy of diagonal component from levels number 1,2,3,4.
- Variance of horizontal component from level number 2.
- Variance of vertical component from level number 3.
- Variance of diagonal component from level number 2,3,4,5.

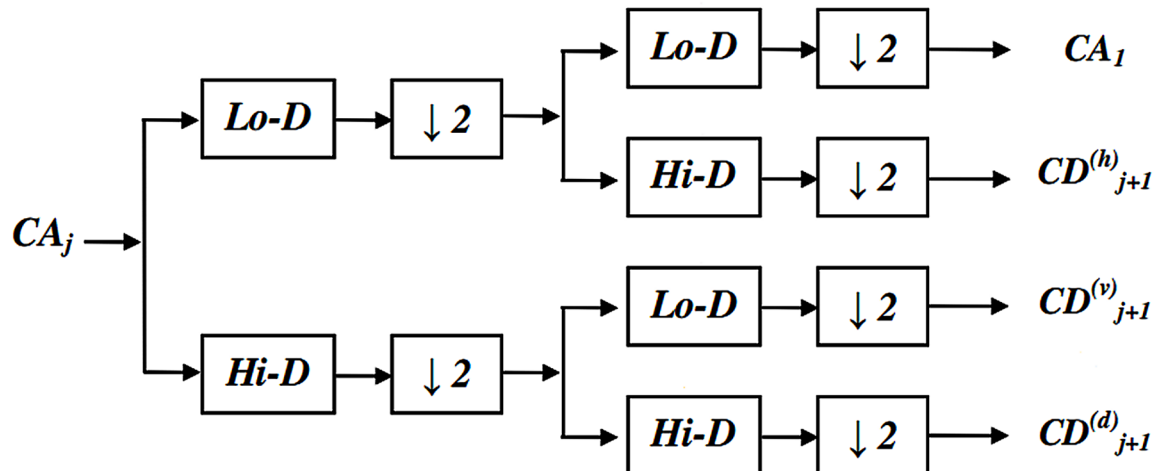
Gabor Filter

Gabor feature is obtained based on convolving an image $I(x,y)$ with a 2-D Gabor function $g(x,y)$. The two-dimensional gabor filter is given as the product of a Gaussian low-pass filter with an exponential that is:

$$\frac{1}{2\pi\sigma_x\sigma_y} \exp\left[-\frac{1}{2}\left(\frac{x^2}{\sigma_x^2} + \frac{y^2}{\sigma_y^2}\right)\right] \exp[2\pi w x]$$

Figure 6. Two dimensional wavelet transformation

Source: Mallat, 1999.



where:

$$\bar{x} = x \cos \theta + y \sin \theta$$

$$\bar{y} = -x \sin \theta + y \cos \theta$$

The parameters σ_x and σ_y are the spatial scaling, which controls the width of the filter, and w defines the frequency bandwidths of the filter. The orientation angle θ is usually chosen to be equal to the direction of the filter.

By varying the free parameters θ, σ , and w arbitrary orientation and bandwidth characteristics are obtained. Gabor filter banks for analyzing the image in a number of bands, in the context of texture classification, have been successfully employed. If one single value is specified, one convolution per orientation will be computed. If a list of values is given (e.g. 0 and 90 as default), multiple convolutions per orientation will be computed, one for each value in the phase offset list. Filters which are centered at different frequencies and have different orientations are used to cover the frequency range of interest, using various frequency and orientation bandwidths. Images are then filtered through this set of filters, and the features are generated from the resulting output samples. New samples include a matrix $f \times d$ (f : the number of different frequencies' and d : the number of different directions of filter). Each element of matrix indicates the response at special direction and frequency.

Four different features are extracted from every direction and frequency. These features include the energy, entropy, mean, variance of filtered image.

EXPERIMENTS

In this section, the results of different feature extraction methods on a standard dataset are evaluated. As it is seen, this chapter focuses on the first step. Evaluation of different feature extraction methods is the main issue in this chapter. The feature reduction step is not important in this scope. The last step is classification that trains a model on training data and then evaluates it by test data. There are different classifiers to build this model. In this chapter, support vector machine (SVM) is utilized. This method is explained in the next section. All methods are implemented in MATLAB R2014a software (Figure 7).

In this chapter, the performance of different feature extraction methods is evaluated based on accuracy, AUC, and confusion matrix criteria.

The definition of accuracy criteria is as below:

Figure 7. A general configuration for medical diagnosis using data mining techniques



$$\text{Accuracy} = \frac{\text{TP} + \text{TN}}{\text{P} + \text{N}}$$

- **True Positives (TP):** These refer to the positive tuples that were correctly labeled by the classifier.
- **True Negatives (TN):** These are the negative tuples that were correctly labeled by the classifier.
- **False Positives (FP):** These are the negative tuples that were incorrectly labeled as positive.
- **False Negatives (FN):** These are the positive tuples that were mislabeled as negative.

Accuracy is the recognition rate of a method. The accuracy measure works better when the data classes are fairly evenly distributed. Therefore, it is not enough for evaluating a method in unbalanced dataset. In this case, other measures, such as AUC, are better suited. AUC means area under the Receiver Operating Characteristic (ROC) curve. ROC curve is created by plotting the true positive rate (precision) against the false positive rate (recall). It presents the tradeoff between the true positive rate and the false positive rate. The maximum value of AUC is 1.

The confusion matrix is another measure. This measure is a table that each element of it indicates one of the above terms (TP, TN, FP and FN).

For a better generalization of classification, the cross validation method is utilized. For this study 10-fold cross validation is applied. In this method, model assessment is done for 10 times using test set. For this goal the whole dataset is divided into 10 subsets randomly. Each time one part of the data is determined as test set and the remaining parts form training data. The errors of each model at every iteration are accumulated to provide the mean absolute test set error.

All of experiments are performed in different states. All methods of feature extraction have been evaluated using different parameters that should be selected in running the algorithm. Thus, effect of parameters on the performances is shown in the next sections.

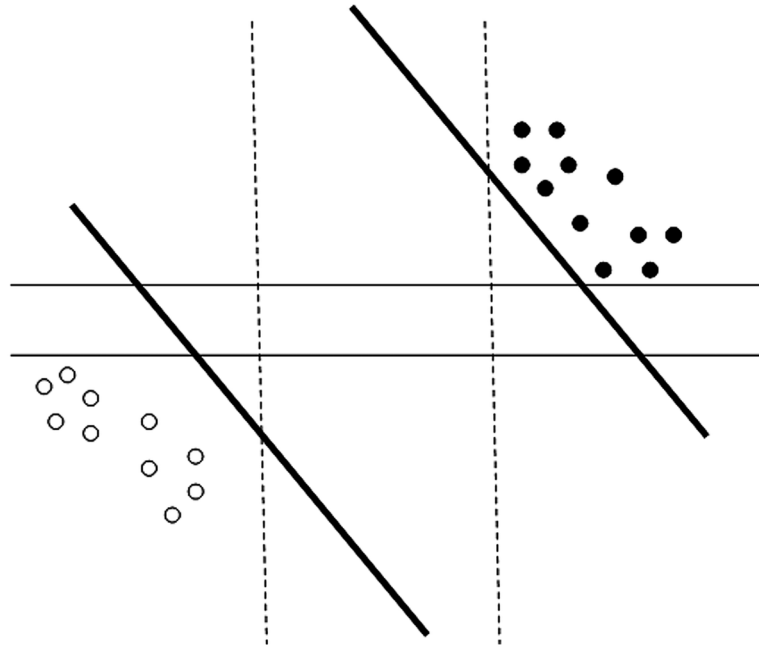
Other experiments are related to the evaluation of methods with different number of images. The number of training samples is 140 images (70 images for normal class and 70 images for abnormal class). The number of test images is selected on 10-fold validation. This experiment is performed on two groups of data: training set and test set. The reports of experiments are based on the mean, max, min and standard deviation of accuracy of performance on test data for 10 folds of cross validation. Besides that, for every method, all of train data is utilized to calculate the efficiency of algorithm. Other experiments are performed on 100 selected images. Since some images have noise and bad quality, such as poor lighting conditions. As a result, removing such images will improve the accuracy of diagnosis.

Support Vector Machine

Support vector machine (SVM) is a method for linear and nonlinear classification (Mousavirad & Ebrahimpour-Komleh, 2014). It transforms the original training data into a higher dimension. Within this new dimension, it searches for the linear optimal hyperplane. Suppose that the data set is a linearly separable two class problem. There are an infinite number of hyperplane for separating of data. Figure 8 illustrates a linearly separable two class problem with three hyperplane.

Figure 9 shows two possible hyperplane and their associated margin. Both hyperplane able to classify the data correctly, but hyperplane with the large margin to be more accurate at classifying new

Figure 8. An example of linearly separable two class problem with three hyperplane

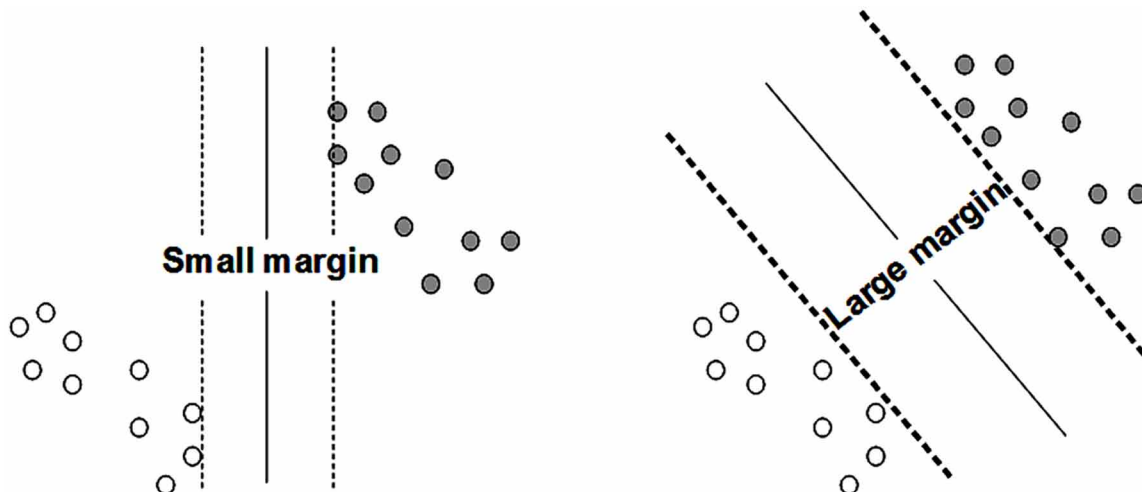


instance than the hyperplane with the small margin. SVM searches maximum marginal hyperplane as best hyperplane.

Let us consider a binary classification problem:

$$\{x_i, y_i\}, \quad i = 1, 2, \dots, L, \quad y_i = \{-1, +1\}$$

Figure 9. Two hyperplane and their associated margin. Hyperplane with large margin has greater generalization than small margin so is appropriate classification hyperplane



A Comparative Study on Diabetic Retinopathy Detection

where x_i are the feature vectors of training set and y_i are the corresponding labels. The goal is to design a hyperplane that classifies correctly all the training vectors. This separating hyperplane can be written as

$$\bar{w} \cdot \bar{x} + b = 0$$

where \bar{w} is a n dimensional weight vector and b is bias. For each training example (x_i, y_i)

$$\begin{aligned} \bar{w} \cdot \bar{x} + b &\leq 0 \quad \text{if } y_i = -1 \\ \bar{w} \cdot \bar{x} + b &\geq 0 \quad \text{if } y_i = +1 \end{aligned}$$

Combining the above two inequality, we get

$$y_i(\bar{w} \cdot \bar{x} + b) \geq 1 \quad \forall i$$

Support vectors are the closet training data to separating hyperplane. For each support vector, the above inequality is an equality. In Figure 10, the support vectors are shown encircled with a thicker border.

The distance between x_s and the hyperplane is $\frac{1}{\|\bar{w}\|}$ where $\|\bar{w}\|$ is the Euclidean norm of \bar{w} , that is $\sqrt{w_1^2 + w_2^2 + \dots + w_n^2}$. Therefore, the maximum margin is $\frac{2}{\|\bar{w}\|}$. The task can be summarized as:

$$\begin{aligned} \text{minimize} \quad & g(w) = \frac{1}{2} \|\bar{w}\|^2 \\ \text{subject to} \quad & y_i(\bar{w} \cdot \bar{x} + b) \geq 1 \end{aligned}$$

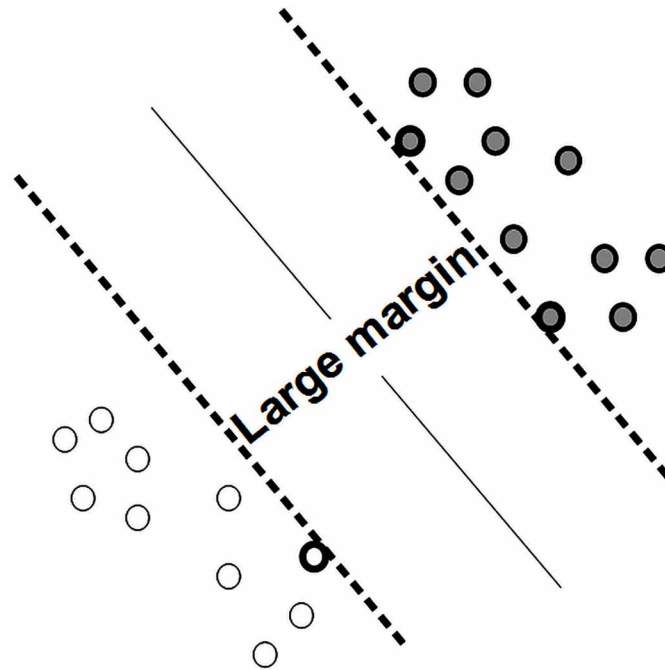
This is a nonlinear optimization task subject to a set of linear inequality constraints. This task can be solve using Karush-Kuhn-Tucker (KKT) conditions. Details can be found in the additional reading list at the end of this chapter.

In order to extend the linear SVMs with nonlinear cases, an extended SVM algorithm is introduced as follows. There are two main steps, first, the original feature vector transforms into a higher dimension space using a non-linear mapping. In the next step, a linear separating hyperplane in the new space is searched.

The computation cost in the training algorithm is very heavy and costly. To overcome this problem, a kernel function, $K(X_i, X_j)$, to the original input vector is applied. That is

$$K(X_i, X_j) = \phi(X_i) \cdot \phi(X_j)$$

Figure 10. Support vectors



In other words, $K(X_i, X_j)$ is replaced with $\phi(X_i) \cdot \phi(X_j)$ in the training algorithm. In this chapter the kernel function of svm is linear kernel, meaning dot product.

Dataset

The Messidor database ("Messidor project," 2004) has been established to facilitate studies on computer-assisted diagnoses of diabetic retinopathy. Messidor is a research program funded by the French Ministry of Research and Defense within a 2004 TECHNO-VISION program. The 1200 eye fundus color numerical images of the posterior pole for the Messidor database were acquired by 3 ophthalmologic departments using a color video 3CCD camera on a Topcon TRC NW6 non-mydratic retinograph with a 45 degree field of view. The images were captured using 8 bits per color plane at 1440*960, 2240*1488 or 2304*1536 pixels.

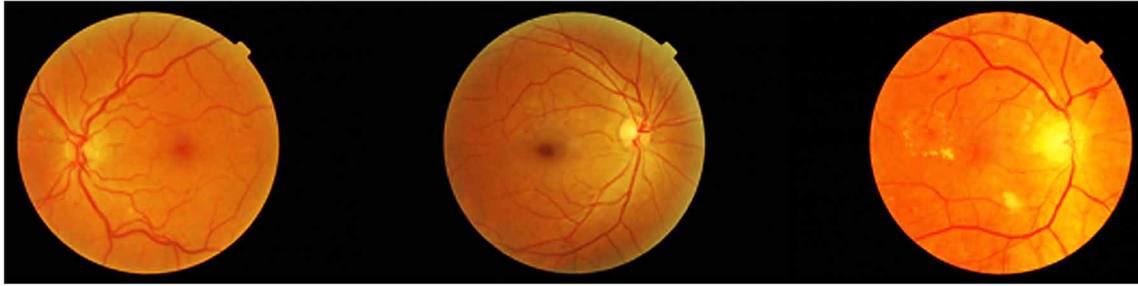
800 images were acquired with pupil dilation (one drop of Tropic amide at 0.5%) and 400 without dilation.

The 1200 images are packaged in 3 sets, one per ophthalmologic department. Each set is divided into 4 zipped sub sets containing each 100 images in TIFF format and an excel file with medical diagnoses for each image. Retinopathy grade has been provided by the medical experts for each image.

- 0 (Normal): ($\mu A = 0$) AND ($H = 0$)
- 1: ($0 < \mu A \leq 5$) AND ($H = 0$)
- 2: ($(5 < \mu A < 15)$ OR ($0 < H < 5$)) AND ($NV = 0$)
- 3: ($\mu A \geq 15$) OR ($H \geq 5$) OR ($NV = 1$)

A Comparative Study on Diabetic Retinopathy Detection

Figure 11. Some samples of normal eyes



That:

μA is the number of micro aneurysms.

H is the number of hemorrhages.

NV = 1 indicates neovascularization.

NV = 0 indicates no neovascularization.

In experiments, all images with grade between 1 and 3 is labeled as abnormal. Some sample images with normal and abnormal states are presented in Figure 11 and Figure 12 respectively. The quality of some images is low. Therefore these images can reduce the performance of extracting features and diagnosis.

Experiments on Statistical Feature of Histogram

Features extracted from histogram are utilized to classify eye images. The size of vector of these features for every image is 31 including 6 statistical feature that are mean, variance, smoothness, 3rd moment, uniformity and entropy, in addition to 25 features from frequency of gray level values. The feature vectors as inputs are learned using SVM. This method doesn't have any parameter to adjust. Table 2 represents the result of classification for eye images using these features. After selecting images without noise, the accuracy of classification is improved. The results are shown in Table 3. Also the ROC curve of classification in two cases (random images and selected images) are presented in Figure 13 and Figure 14 respectively. The AUC criteria can be obtained from these curves. The value of this important criteria is presented in Table 2 and Table 3.

Figure 12. Some samples of altered eyes



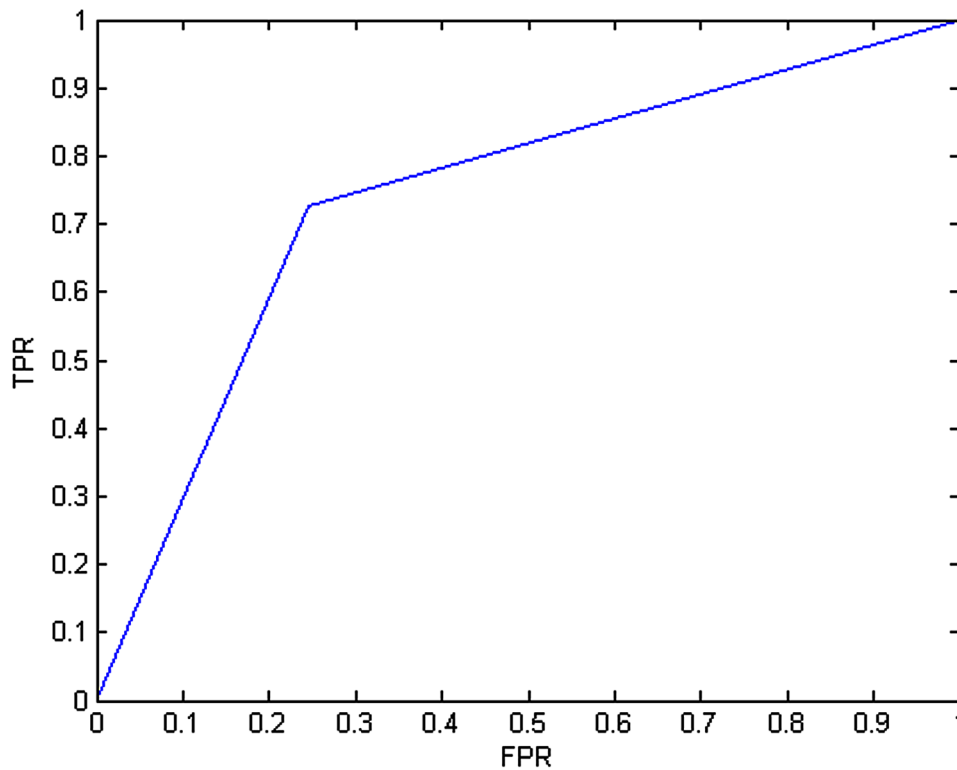
Table 2. The accuracy of method using Statistical Feature of Histogram

Method	Classification Accuracy					
	Training Set	Test Set				
	Accuracy	Mean	Std. Dev.	Max	Min	AUC
Statistical feature of histogram	79.10	60.5	10.14	83.13	53.44	0.72

Table 3. The accuracy of method using Statistical Feature of Histogram on selected images

Method	Classification Accuracy					
	Training Set	Test Set				
	Accuracy	Mean	Std. Dev.	Max	Min	AUC
Statistical feature of histogram with selected images	93.13	77.45	9.23	80.41	59.30	0.82

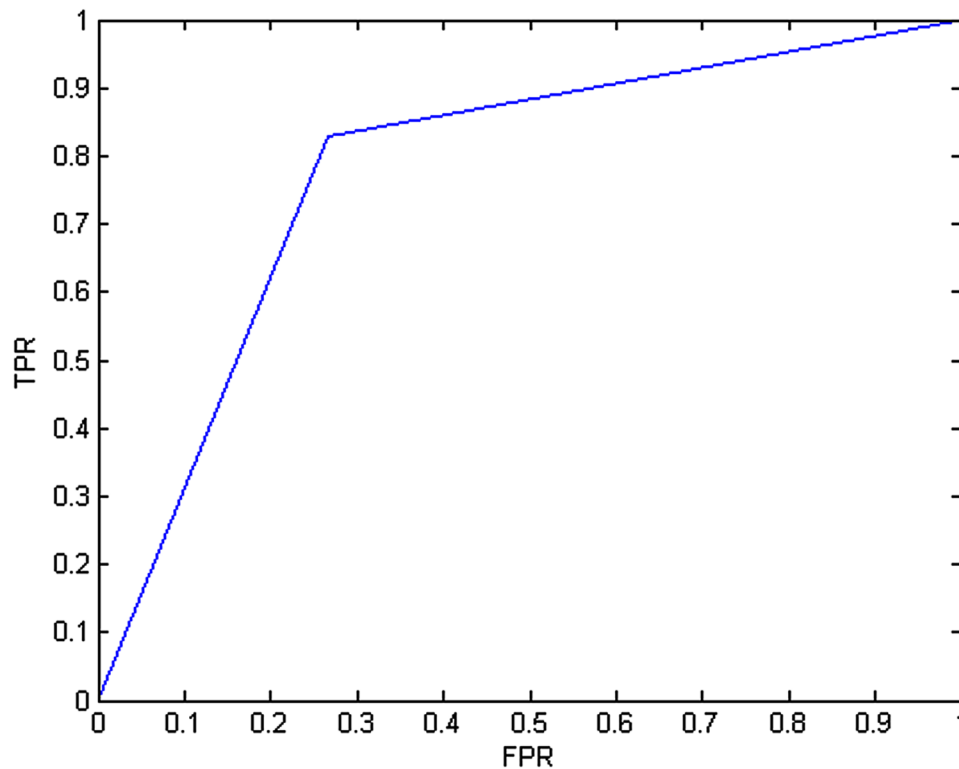
Figure 13. The roc curve for classification using Histogram features



Experiments on Local Binary Pattern

In this Section, the experiment is performed using LBP features extracted from images. The cross validation with $k=10$ is utilized for the experiments. The performance results of classification using local

Figure 14. The roc curve for classification using Statistical Feature of Histogram for selected images



binary pattern are presented in Table 4. The accuracy of method using LBP features The ROC curve for this case is presented in Figure 15. An important parameter in this method is the size of neighborhood. In the sense that the experiments are evaluated with different size of neighborhood. The worst performance is the result of increasing number of pixels used in extracting features. On the other hand, the best result is obtained when the size of neighborhood is 8 (basic LBP). It is obvious that large size of pixels causes high dimensional feature vectors. Thus more computation is required in this situation. For example, in selection of 8 neighbors, the dimension of feature vectors becomes 256, while the choice of 16 pixels results in 65536 features. Table 5 presents the results of LBP on 100 selected images of dataset. According to the table the improvement of results in this case is visible. The ROC curve of performance for 100 selected images are shown in Figure 16.

Experiments on Gray-Level Run Lengths

Table 6 shows the results of diagnosis performance using gray-level run length feature extraction method. The size of feature vectors in this case is 44(Eleven features in every directions (0°,45°,90°, 135°)). The definition of extracted features is presented in previous section. Because of low dimensional feature vectors in this method, the computation is lesser. But the performance of the method decreases. Also, the result of evaluation method on selected images is shown in Table 7. As seen in the table, the performance is improved significantly because of removing some images with bad quality. Figure 17 and Figure 18 show the ROC curve of these classification.

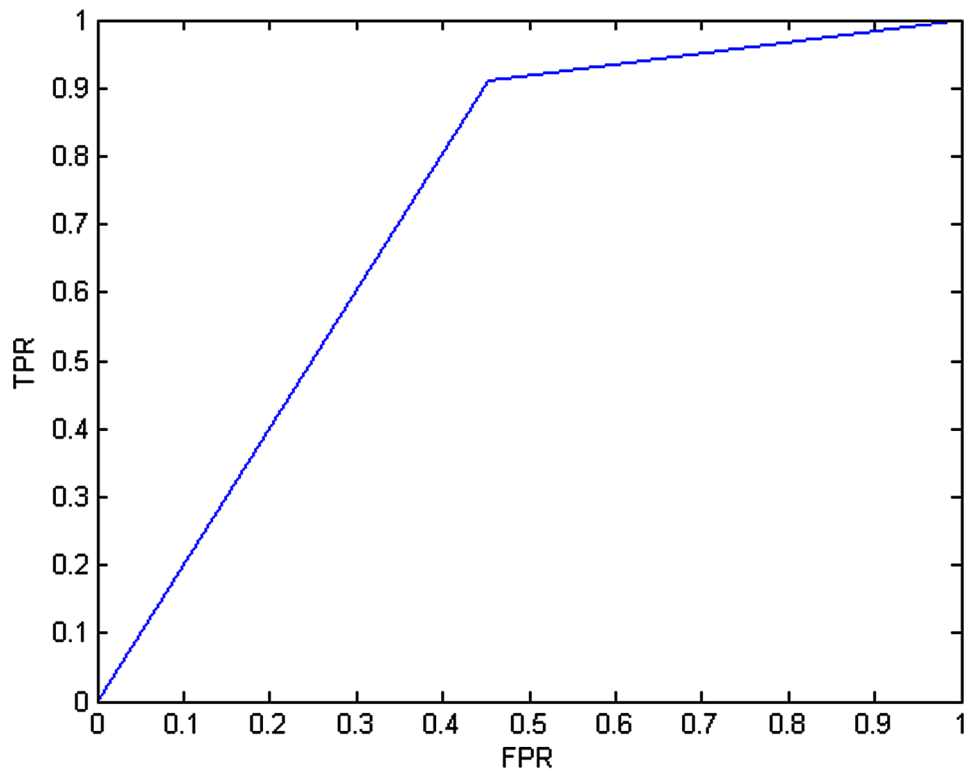
Table 4. The accuracy of method using LBP features

Method	Classification Accuracy					
	Training Set	Test Set				
	Accuracy	Mean	Std. Dev.	Max	Min	AUC
LBP	81.06	72.5	7.5	85.71	65.06	0.90

Table 5. The accuracy of method using LBP features on selected images

Method	Classification Accuracy					
	Training Set	Test Set				
	Accuracy	Mean	Std. Dev.	Max	Min	AUC
LBP with selected images	99.01	95.05	3.23	100	90.00	0.98

Figure 15. The roc curve for classification using LBP features



Experiment on Gray-Level Co-Occurrence Matrix

In this section the result of classification of data using gray-level co-occurrence features have been evaluated. Table 8 shows the accuracy of experiments on 130 images of two classes. The result of these

Figure 16. The roc curve for classification using LBP features for selected images

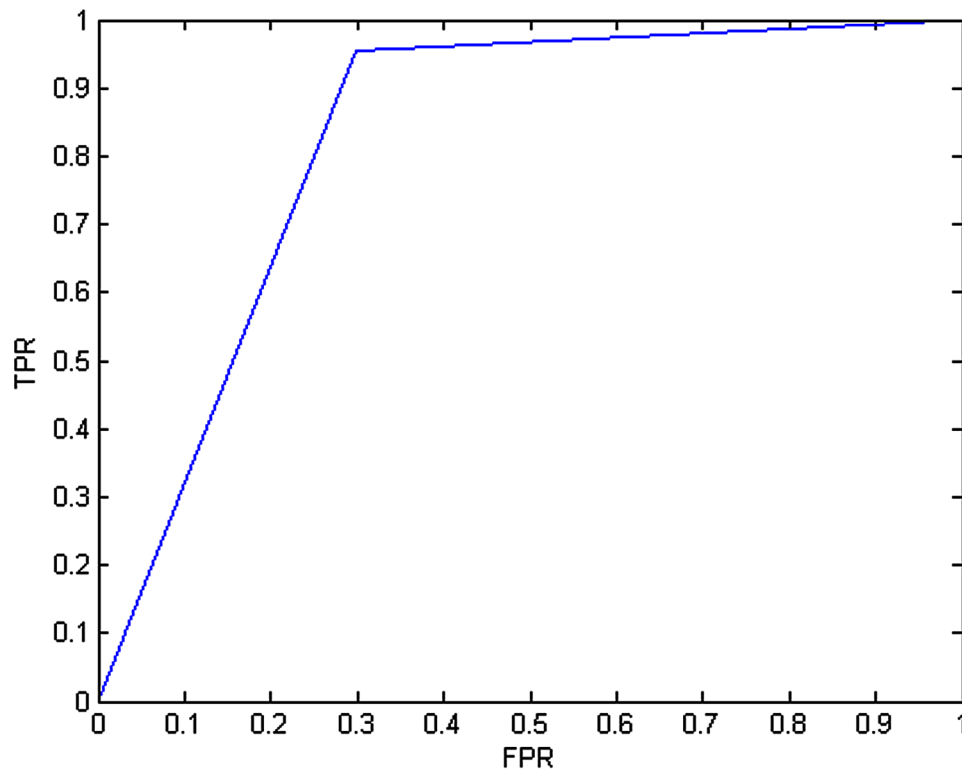


Table 6. The accuracy of method using GLRL features

Method	Classification Accuracy					
	Training Set	Test Set				
	Accuracy	Mean	Std. Dev.	Max	Min	AUC
GLRL	98.45	63.78	8.43	75.65	53.22	0.78

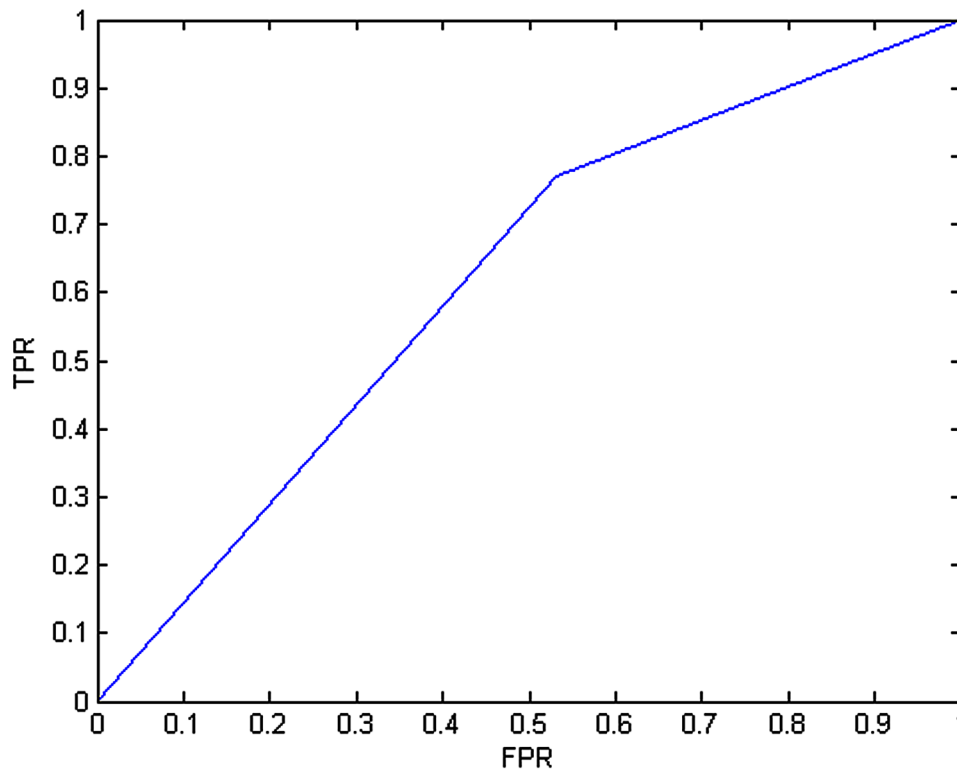
Table 7. The accuracy of method using GLRL features on selected images

Method	Classification Accuracy					
	Training Set	Test Set				
	Accuracy	Mean	Std. Dev.	Max	Min	AUC
GLRL with selected images	99.13	80.45	9.78	88.88	69.10	0.89

features is weaker than two previous methods. The ROC plot of these results is shown in Figure 19.

An important parameter in constructing co-occurrence matrix is the relative distance measured in pixel numbers. At the basic GLCM, the distance is set 1. In these experiments, the change of distance doesn't have effect on the performance. Therefore, considering 1 pixel as neighbor results in the best accuracy. Also, the number of features isn't related to the number of bits in binary number, because

Figure 17. The roc curve for classification using GLRL features



the number of extracted features is 10 despite of the distance considered for constructing matrix. These features have been calculated in 4 different directions (directions (0°,45°,90°, 135°)).

Another experiment for this method is based on 100 selected images. Table 9 exhibits the accuracy of this case. The improving performance is explicit. Some noisy images affect the result of diagnosis. ROC plot of this experiment is also demonstrated in Figure 20.

Experiments on Wavelet Features

As explained in previous section, the 4 types of features (mean, variance, entropy and energy) can be extracted from resulting components of wavelet transformation. From each component resulting from wavelet transformation, 4 features are extracted so the size of feature vector in this method is 80. But all of these features are not adequate for classification. An optimization algorithm like Imperialist Competitive Algorithm (ICA)(Atashpaz-Gargari & Lucas, 2007) can be utilized to select the best feature for classification. Table 10 and Table 11 show the result of classification using these features from random and selected images. The ROC plot of classification based on these experiment also is presented in Figure 21 and Figure 22.

A Comparative Study on Diabetic Retinopathy Detection

Figure 18. The roc curve for classification using GLRL features for selected images

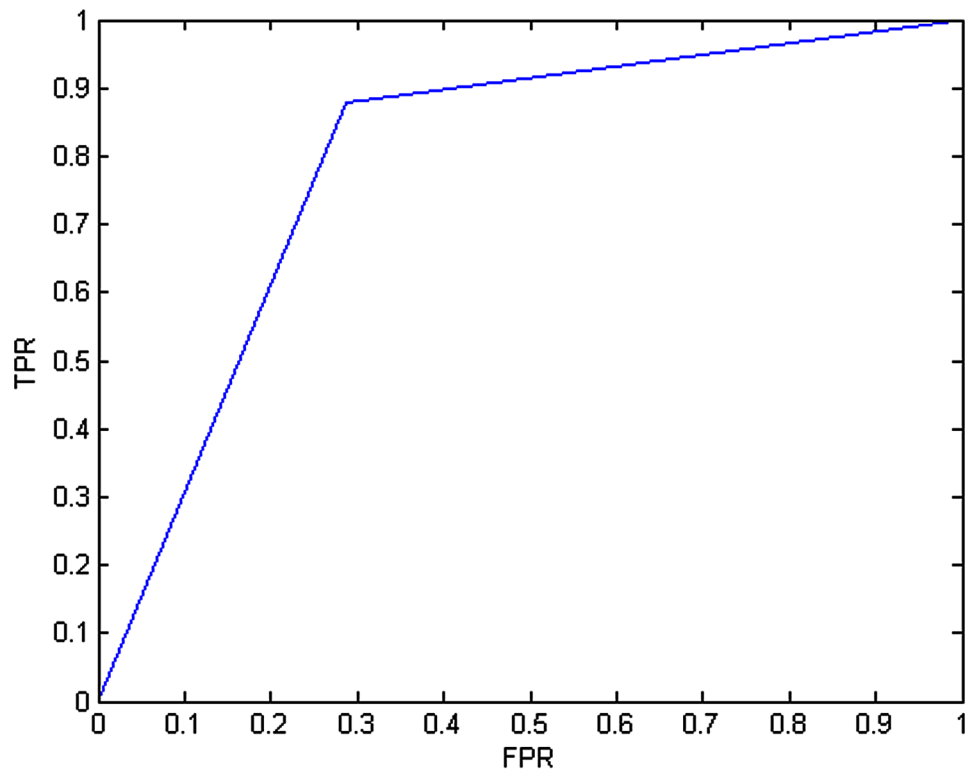


Table 8. The accuracy of method using GLCM features

Method	Classification Accuracy					
	Training Set	Test Set				
	Accuracy	Mean	Std. Dev.	Max	Min	AUC
GLCM	75.45	61.30	12.01	72.12	55.81	0.72

Table 9. The accuracy of method using GLCM features on selected images

Method	Classification Accuracy					
	Training Set	Test Set				
	Accuracy	Mean	Std. Dev.	Max	Min	AUC
GLCM with selected images	90.51	77.54	9.75	90.12	71.40	0.85

Experiments on Gabor Filter

The last method for evaluation is gabor filter. The parameter frequency is 8 and the orientation is along 4 basic directions. The accuracy of this method with 10-fold validation is showed in Table 12. This

Figure 19. The roc curve for classification using GLCM features

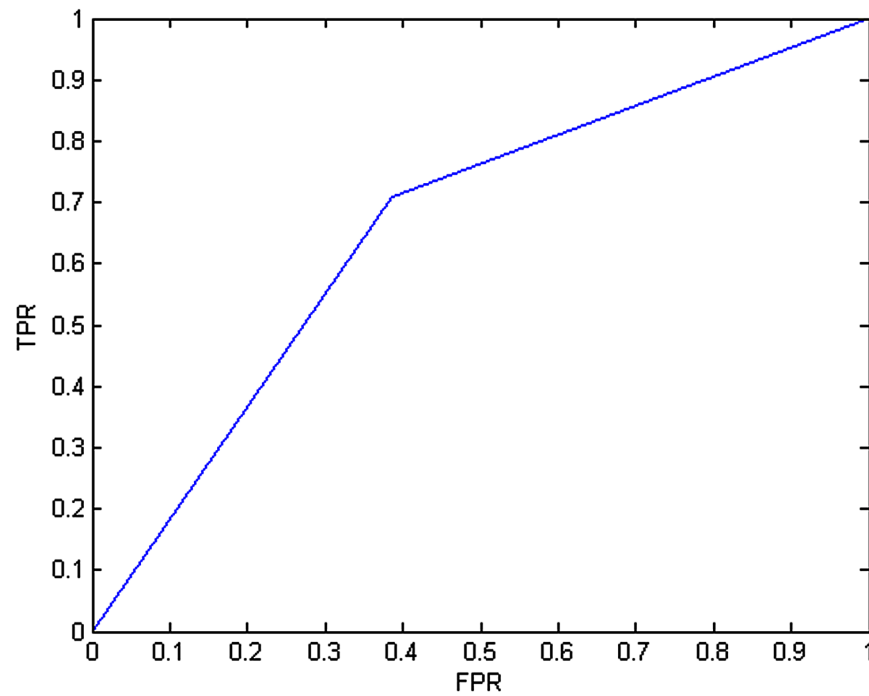
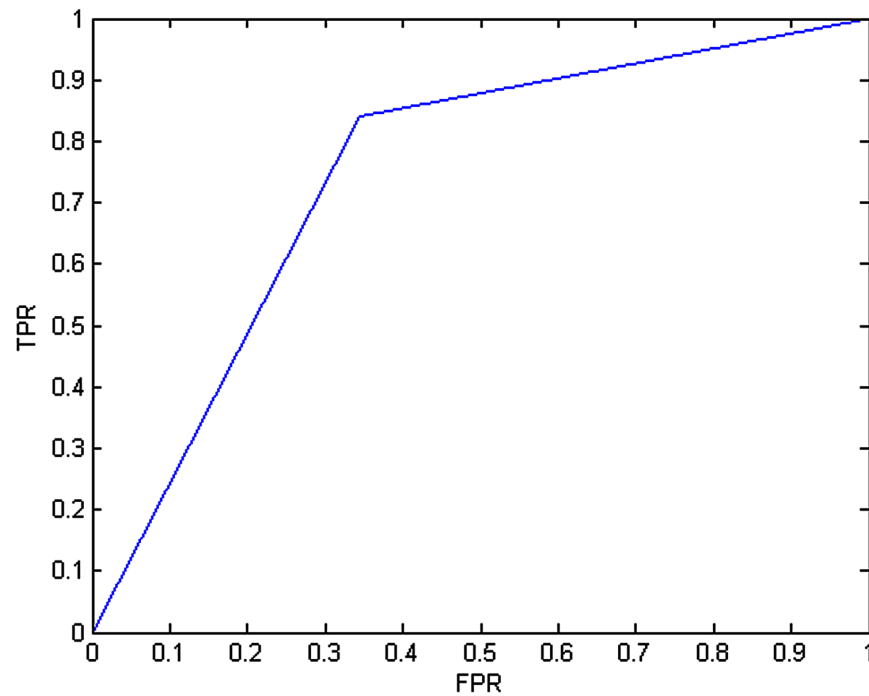


Figure 20. The roc curve for classification using GLCM features for selected images



A Comparative Study on Diabetic Retinopathy Detection

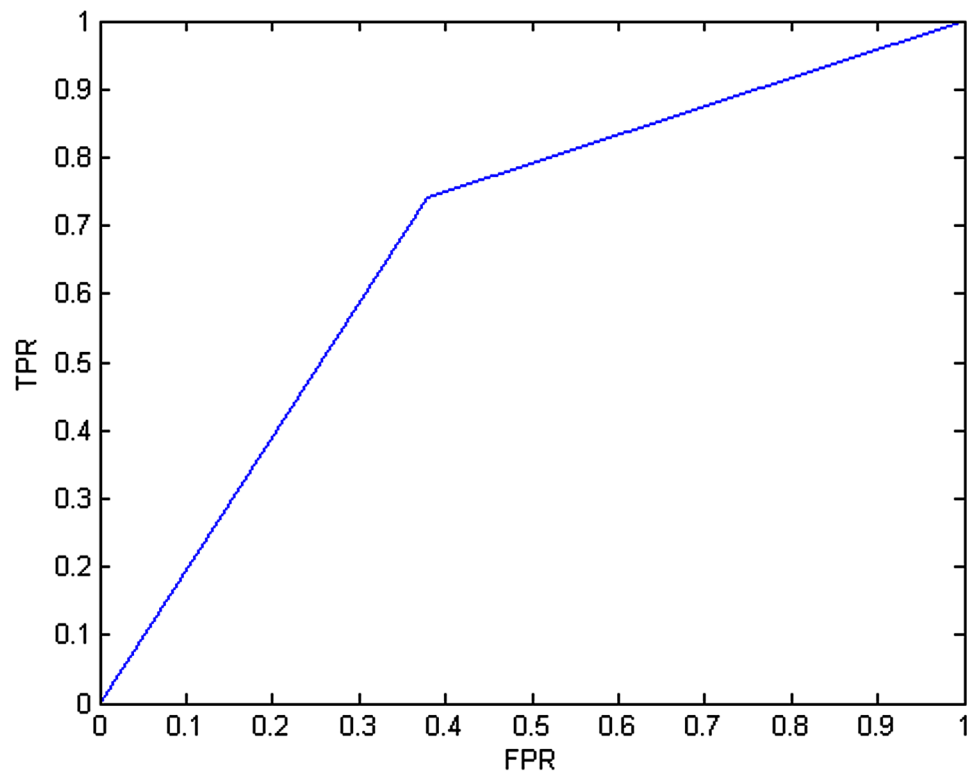
Table 10. The accuracy of method using wavelet features

Method	Classification Accuracy					
	Training Set	Test Set				
	Accuracy	Mean	Std. Dev.	Max	Min	AUC
Wavelet features	91.58	65.12	4.76	69.01	52.20	0.74

Table 11. The accuracy of method using wavelet features on selected images

Method	Classification Accuracy					
	Training Set	Test Set				
	Accuracy	Mean	Std. Dev.	Max	Min	AUC
Wavelet features with selected images	97.5	80.20	3.45	70.30	61.00	0.92

Figure 21. The roc curve for classification using wavelet features



method has weaker results compared to previous feature extraction methods. Using 100 selected images in dataset improves the performance as presented in Table 13. Figure 23 and Figure 24 show the obtained ROC curve of classification results.

Figure 22. The roc curve for classification using wavelet features for selected images

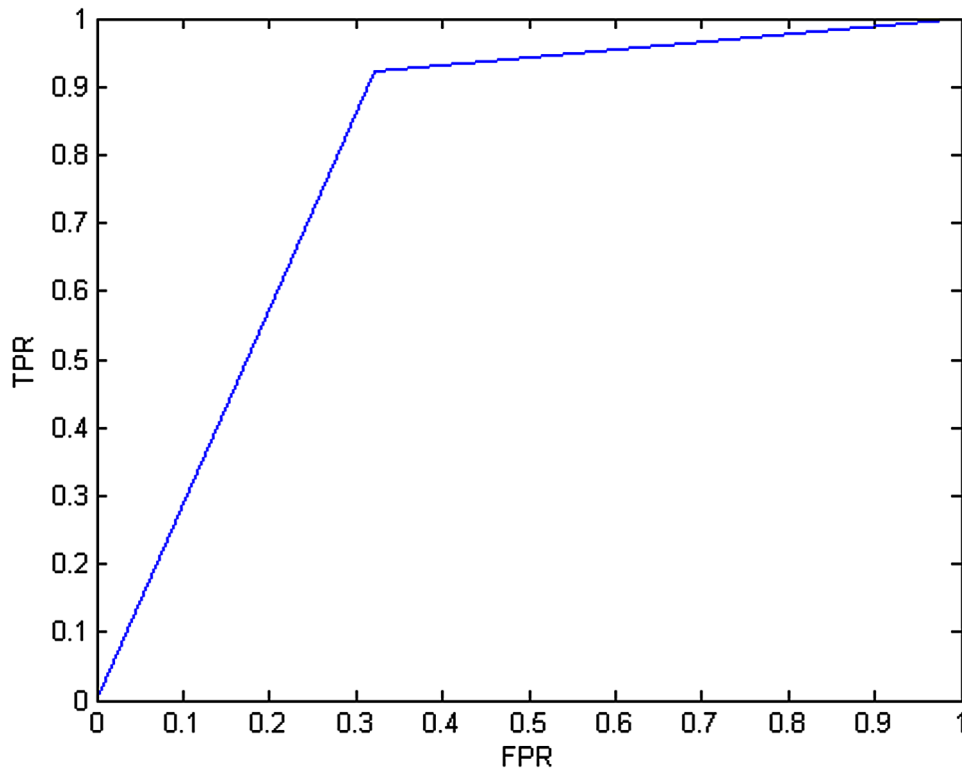


Table 12. The accuracy of method using Gabor filer features

Method	Classification Accuracy					
	Training Set	Test Set				
	Accuracy	Mean	Std. Dev.	Max	Min	AUC
Gabor filer	77.58	54.47	3.28	57.43	50.00	0.55

Table 13. The accuracy of method using Gabor filer features on selected images

Method	Classification Accuracy					
	Training Set	Test Set				
	Accuracy	Mean	Std. Dev.	Max	Min	AUC
Gabor filter with selected images	91.11	65.71	3.15	71.00	63.63	0.62

DISCUSSION

In this section all results from different methods are compared with each other. According to results represented in Table 14 the classification of normal and altered images using features extracted by LBP

A Comparative Study on Diabetic Retinopathy Detection

Figure 23. The roc curve for classification using Gabor Filter features

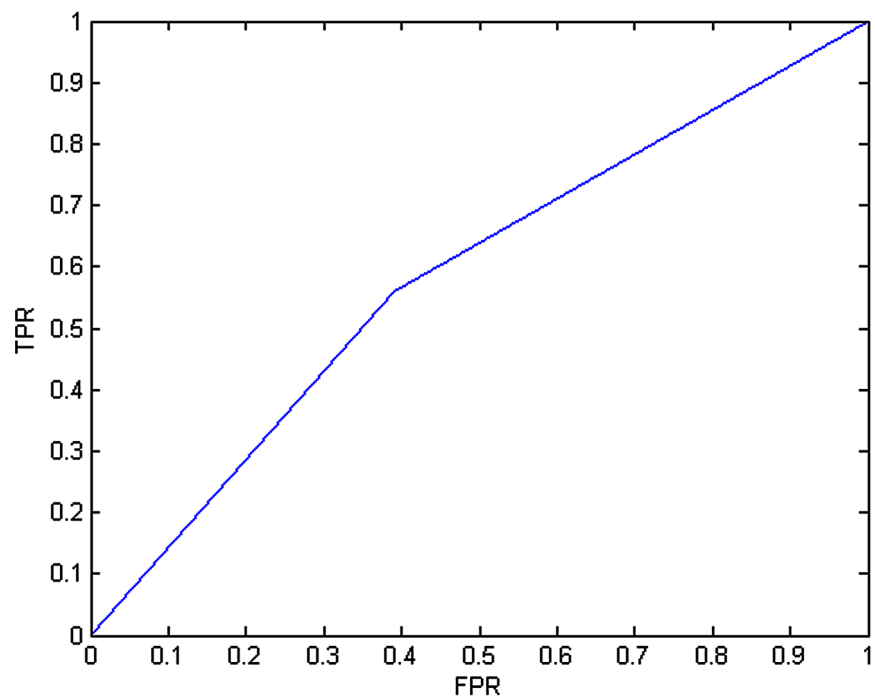


Figure 24. The roc curve for classification using Gabor Filter features for selected images

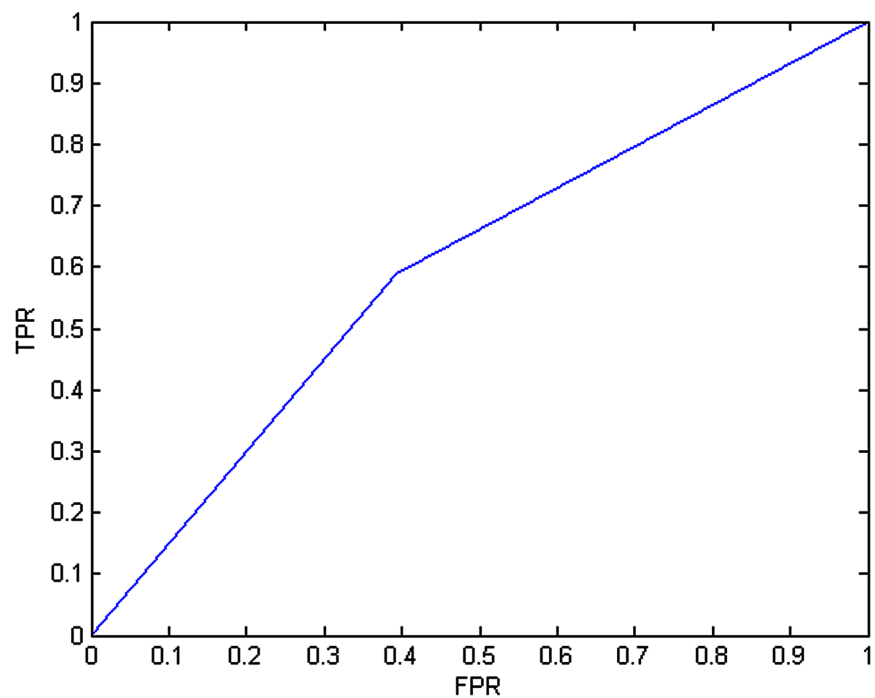


Table 14. The comparison result of different textural feature extraction methods

Method	Accuracy
Statistical feature of histogram	60.5
LBP features	72.5
GLRL features	63.78
GLCM features	61.30
Wavelet features	65.12
Gabor feature	54.47

method has best result. The detection retinopathy can be performed with 72.5 percent accuracy. The other methods outperform LBP method. However some of them such as wavelet features results close to LBP.

CONCLUSION

This chapter presented some predictive techniques for diabetic retinopathy detection. For this purpose, different texture based feature extraction techniques such as statistical features of histogram, grey level co-occurrence matrix, grey level run length matrix, wavelet transform features, gabor filter and local binary pattern has been considered. The results of classification of diabetic retinopathy images is compared. Based on these results, machine learning methods can be utilized to help expert's diagnosis diabetic retinopathy.

REFERENCES

- Atashpaz-Gargari, E., & Lucas, C. (2007). *Imperialist competitive algorithm: an algorithm for optimization inspired by imperialistic competition*. Paper presented at the Evolutionary Computation, 2007. CEC 2007. IEEE Congress on. doi:10.1109/CEC.2007.4425083
- Bascil, M. S., & Oztekin, H. (2012). A study on hepatitis disease diagnosis using probabilistic neural network. *Journal of Medical Systems*, 36(3), 1603–1606. doi:10.1007/s10916-010-9621-x PMID:21057884
- Conforti, D., & Guido, R. (2010). Kernel based support vector machine via semidefinite programming: Application to medical diagnosis. *Computers & Operations Research*, 37(8), 1389–1394. doi:10.1016/j.cor.2009.02.018
- Daubechies, I. (1992). *Ten lectures on wavelets* (Vol. 61). SIAM. doi:10.1137/1.9781611970104
- Gonzales, R. C., Woods, R. E., & Eddins, S. L. (2004). *Digital image processing using MATLAB*. Pearson Prentice Hall.
- Haar, A. (1910). On the theory of orthogonal function systems. *Math. Ann*, 69(3), 331–371. doi:10.1007/BF01456326

A Comparative Study on Diabetic Retinopathy Detection

- Haralick, R. M. (1979). Statistical and structural approaches to texture. *Proceedings of the IEEE*, 67(5), 786–804. doi:10.1109/PROC.1979.11328
- Haralick, R. M., Shanmugam, K., & Dinstein, I. H. (1973). Textural features for image classification. *Systems, Man and Cybernetics, IEEE Transactions on*, (6), 610–621.
- Hoover, A., & Goldbaum, M. (2003). Locating the optic nerve in a retinal image using the fuzzy convergence of the blood vessels. *Medical Imaging. IEEE Transactions on*, 22(8), 951–958.
- Illingworth, J., & Kittler, J. (1988). A survey of the Hough transform. *Computer Vision Graphics and Image Processing*, 44(1), 87–116. doi:10.1016/S0734-189X(88)80033-1
- International Federation Diabetes*. (2014). Retrieved from <http://www.idf.org/complications-diabetes>
- Klein, R., Meuer, S. M., Moss, S. E., & Klein, B. E. (1995). Retinal microaneurysm counts and 10-year progression of diabetic retinopathy. *Archives of Ophthalmology*, 113(11), 1386–1391. doi:10.1001/archophth.1995.01100110046024 PMID:7487599
- Kononenko, I. (2001). Machine learning for medical diagnosis: History, state of the art and perspective. *Artificial Intelligence in Medicine*, 23(1), 89–109. doi:10.1016/S0933-3657(01)00077-X PMID:11470218
- Kononenko, I., Bratko, I., & Kukar, M. (1997). Application of machine learning to medical diagnosis. *Machine Learning and Data Mining: Methods and Applications*, 389, 408.
- Mallat, S. (1999). *A wavelet tour of signal processing*. Academic Press.
- Marčelja, S. (1980). Mathematical description of the responses of simple cortical cells*. *JOSA*, 70(11), 1297–1300. doi:10.1364/JOSA.70.001297 PMID:7463179
- Messidor Project. (2004). Retrieved from <http://messidor.crihan.fr/download-en.php>
- Meyer, Y. (1995). *Wavelets and operators* (Vol. 1). Cambridge university press.
- Misiti, M., Misiti, Y., Oppenheim, G., & Poggi, J.-M. (1997). Wavelet toolbox. *Matlab User's Guide*, 64.
- Mousavirad, S. J., & Ebrahimpour-Komleh, H. (2014). A Comparative Study on Medical Diagnosis Using Predictive Data Mining: A Case Study. *Data Mining and Analysis in the Engineering Field*, 327.
- Niemeijer, M., Staal, J., van Ginneken, B., Loog, M., & Abramoff, M. D. (2004). *Comparative study of retinal vessel segmentation methods on a new publicly available database*. Paper presented at the Medical Imaging 2004. doi:10.1117/12.535349
- Ojala, T., Pietikäinen, M., & Mäenpää, T. (2002). Multiresolution gray-scale and rotation invariant texture classification with local binary patterns. *Pattern Analysis and Machine Intelligence. IEEE Transactions on*, 24(7), 971–987.
- Pinz, A., Bernögger, S., Datlinger, P., & Kruger, A. (1998). Mapping the human retina. *Medical Imaging. IEEE Transactions on*, 17(4), 606–619.
- Polat, K., & Güneş, S. (2006). Hepatitis disease diagnosis using a new hybrid system based on feature selection (FS) and artificial immune recognition system with fuzzy resource allocation. *Digital Signal Processing*, 16(6), 889–901. doi:10.1016/j.dsp.2006.07.005

- Polat, K., & Güneş, S. (2007). Breast cancer diagnosis using least square support vector machine. *Digital Signal Processing*, 17(4), 694–701. doi:10.1016/j.dsp.2006.10.008
- Polat, K., Güneş, S., & Tosun, S. (2006). Diagnosis of heart disease using artificial immune recognition system and fuzzy weighted pre-processing. *Pattern Recognition*, 39(11), 2186–2193. doi:10.1016/j.patcog.2006.05.028
- Silberman, N., Ahrlich, K., Fergus, R., & Subramanian, L. (2010). *Case for Automated Detection of Diabetic Retinopathy*. Paper presented at the AAAI Spring Symposium: Artificial Intelligence for Development.
- Tang, X. (1998). Texture information in run-length matrices. *Image Processing. IEEE Transactions on*, 7(11), 1602–1609.
- Vatanparast, M., & Harati, A. (2012). *A feasibility study on detection of Neovascularization in retinal color images using texture*. Paper presented at the Computer and Knowledge Engineering (ICCKE), 2012 2nd International eConference on. doi:10.1109/ICCKE.2012.6395382
- Vetterli, M., & Herley, C. (1992). Wavelets and filter banks: Theory and design. *Signal Processing. IEEE Transactions on*, 40(9), 2207–2232. doi:10.1109/78.157221
- Walter, T., Klein, J.-C., Massin, P., & Erginay, A. (2002). A contribution of image processing to the diagnosis of diabetic retinopathy-detection of exudates in color fundus images of the human retina. *Medical Imaging. IEEE Transactions on*, 21(10), 1236–1243.
- Wu, D., Zhang, M., Liu, J.-C., & Bauman, W. (2006). On the adaptive detection of blood vessels in retinal images. *Biomedical Engineering. IEEE Transactions on*, 53(2), 341–343.

This research was previously published in Computational Tools and Techniques for Biomedical Signal Processing edited by Butta Singh, pages 242-271, copyright year 2017 by Medical Information Science Reference (an imprint of IGI Global).

Chapter 10

A New EYENET Model for Diagnosis of Age-Related Macular Degeneration: Diagnosis of Age-Related Macular Degeneration

Priya Kandan

Annamalai University, India

P. Aruna

Annamalai University, India

ABSTRACT

Age-related macular degeneration is an eye disease, that gradually degrades the macula, a part of the retina, which is responsible for central vision. It occurs in one of the two types, DRY and WET age-related macular degeneration. In this chapter, to diagnose Age-related macular degeneration, the authors have proposed a new EYENET model which was obtained by combining the modified PNN and modified RBFNN and hence it poses the advantages of both the models. The amount of the disease spread in the retina can be identified by extracting the features of the retina. A total of 250 fundus images were used, out of which 150 were used for training and 100 images were used for testing. Experimental results show that PNN has an accuracy of 87%, modified PNN has an accuracy of 90% RBFNN has an accuracy of 80%, modified RBFNN has an accuracy of 85% and the proposed EYENET Model has an accuracy of 94%. This infers that the proposed EYENET model outperforms all other models.

INTRODUCTION

Age-related macular degeneration [ARMD] is defined as an ocular disease leading to loss of central vision in the elderly stage. Therefore, regular Screening of ARMD affected patients retina is very important. With the advent of computing techniques, the automated segmentation and analysis is expected to support

DOI: 10.4018/978-1-5225-5195-9.ch010

the ophthalmologist in the clinical decision making process. Automated or computer-assisted analysis of ARMD affected patients retina can help eye care specialist to screen larger populations of patients. Dry ARMD is characterized by thinning of the retina and drusen, small yellowish-white deposits that form with-in the retina. It results in slow, gradual progressive “dimming” of the central vision. Wet ARMD is characterized by abnormal growth of new blood vessel under the retina called “Neovascularization”. Blood vessels are unusually weak in their structure and prone to leaky and be easily break and bleed. During the recent years, there have been many studies on automatic diagnosis of ARMD using several features and techniques.

Hoover, A., et al. (2000) described an automated method to locate the optic nerve in images of the ocular fundus. Zakaria Ben Sbeh et al. (2001) proposed a new segmentation method based on new transformations, they introduced in mathematical morphology. It is based on the search for a new class of regional maxima components of the image. These maxima correspond to the regions inside the drusen. Rapantzikos.K et al. 2003 developed a novel segmentation technique for the detection of drusen in retina images. They introduced and tested a histogram-based enhancement technique, which uses histogram equalization as its core operator and a histogram-based segmentation technique (HALT) to segment areas that differ slightly from their background regions. Zhu Hong Qing, (2004) presented a novel automated method for the segmentation of blood vessels in retinal images based upon the enhancement and maximum entropy thresholding. Ingrid E. Zimmer-Galler and Ran Zeimer, (2005) detected the presence of age-related macular degeneration(AMD) at a level requiring referral to an ophthalmologist for further evaluation and possible treatment. Nageswara Rao Pv et al. (2005-2009), proposed a new approach for protein classification based on a PNN and feature selection. Ana Maria Mendonca and Aurelio Campilho, (2006) presented an automated method for the segmentation of the vascular network in retinal images. The outputs of four directional differential operators are processed in order to select connected sets of candidate points to be further classified as centerline pixels using vessel derived features. Niall Patton et al. 2006 described current techniques used to automatically detect landmark features of the fundus, such as the optic disc, fovea and blood vessels.

W.Kenneth et al. 2007 proposed optic nerve and localization of the macula using digital red-free fundus photography. Maria Garcia et al, 2007 extracted a set of features from image regions and selected the subset which best discriminates between Hard Exudates and the retinal background. The selected features were then used as inputs to a multilayer perceptron classifier to obtain a final segmentation of Hard Exudates in the image. Saurabh Garg et al. 2008 explained two methods namely texture- based detection and model based approach that they have developed to reliably detect and count drusens. O Sheba et al. 2008 developed an automated method using the principle of mathematical morphology for finding the drusen exudates using retinal image analysis. JieTian et al. 2009 used PNN as a classifier for the automated classification of underwater objects. LiliXu and Shuqian Luo, 2009 presented a novel method to identify hard exudates from digital retinal images. A feature combination based on stationary wavelet transform and gray level co-occurrence matrix was used to characterize hard exudates candidates. Maria Garcia et al. 2009 automatically detected one of these lesions, hard exudates, in order to help ophthalmologists in the diagnosis and follow-up of the disease. Three NN classifiers were investigated: multilayer perceptron, RBFNN and support vector machine (SVM). Alireza Osareh & Bitashadgar, 2010 proposed an automated method for identification of blood vessels in color images of the retina. For every image pixel, a feature vector is computed that utilizes properties of scale and orientation selective Gabor filters. The extracted features are then classified using generative Gaussian mixture model and discriminative support vector machine classifiers. D. Jayanthi et al. 2010 gave only the frame work

for diagnosing human retinal diseases. UsmanAkram M and Aasia Khanum, 2010 proposed a wavelet based method for vessel enhancement, piecewise threshold probing and adaptive thresholding for vessel localization and segmentation respectively.

Retinal imaging has rapidly grown within ophthalmology in the past twenty years. The availability of cameras to take direct images of the retina, fundus photography, makes it possible to examine the eye for the presence of many different eye diseases with a simple, non-invasive method. Research has focused on automatic early detection of ARMD from fundus photographs. We are currently also applying the computer-aided detection and quantification techniques, we have developed to diagnosis and quantification of ARMD. A mass screening facility with teleophthalmology or telemedicine in combination with computer-aided analysis for large rural-based communities may identify more individuals suitable for early stage ARMD prevention. Digital imaging of the retina is useful for detection and classification of ARMD. Also, so far in the literature only drusen detection has been done, but ARMD classification of Dry and Wet images using pattern classification models have not been proposed. So this work differs from previous methods in that we have used five classifiers and found a more suitable classifier for classification of ARMD.

MAIN FOCUS OF THE CHAPTER

In this chapter, an automated approach for classification of the disease ARMD using fundus images is presented. In order to diagnose the disease ARMD, number of features such as area, mean, standard deviation etc of the pre-processed images are extracted to study the image content. Then Modeling Techniques like Probabilistic Neural Network [PNN] which is a probabilistic model, Radial Basis Function Neural Network [RBFNN] which is a neural network model and our proposed EYENET models are used and their performances are compared. The classifiers are applied to analyze the training data to find an optimal way to classify images into their respective classes namely Dry ARMD, Wet ARMD or Normal. The main goal is to detect automatically and segment the disease ARMD in retina without any human supervision and interaction. *Figure 1.* illustrates the block diagram for comparison between five classifiers for diagnosis of ARMD.

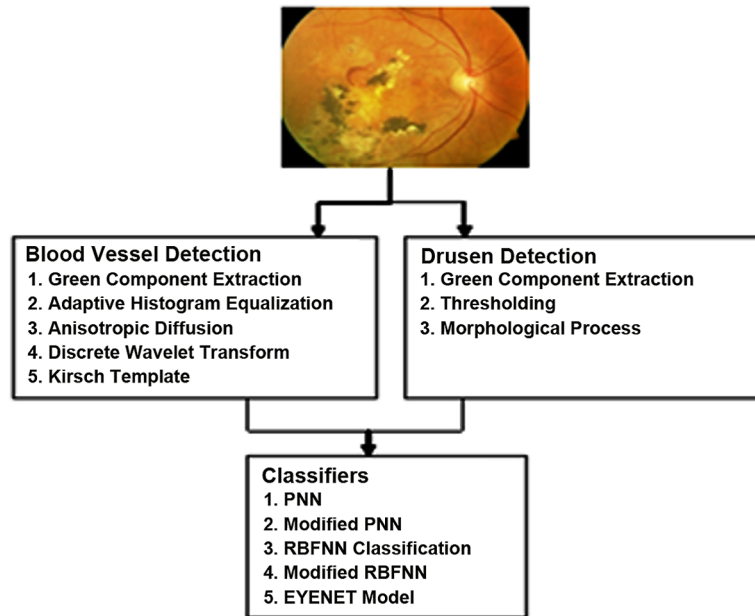
Blood Vessel Detection

A combination of normal and ARMD affected images are taken for processing. The size of the input retinal images is 1280×1024 pixels.

1. Green Component

First, the green component is extracted from the color retinal image. The green channel is considered in several works as the basis for vessel segmentation because it normally presents a higher contrast between vessels and retinal background.

Figure 1.



2. Histogram Equalization

After green component extraction, histogram equalization is used to enhance the contrast and improve the quality of the retinal image. It enhances the contrast of images by transforming the values in the intensity image. It operates on small data regions (tiles), rather than the entire image. Each tile's contrast is enhanced, so that the histogram of the output region approximately matches the specified histogram.

3. Anisotropic Diffusion

Anisotropic diffusion is a non-linear and space-variant transformation of the original image. The filter iteratively uses diffusion equation in combination with information about the edges. As a consequence, the homogenic (but noisy) areas are blurred and the edges are preserved. The anisotropic diffusion equation is defined as,

$$I \operatorname{div}(c(x, y, t) \nabla I) = c(x, y, t) \Delta I + \nabla c \nabla I \quad (1)$$

where div is the divergence operator, ∇ is a gradient and Δ is a Laplacian operator, c represented the conduction coefficient function. Index 't' denotes the time (iterations). The filtering or non-linear smoothing approach using anisotropic diffusion is applied on green band of fundus image after histogram equalization to smooth unwanted data, such as small and tiny capillaries. Finally an-isotropic diffusion is applied to enhance the blood vessel structure.

4. Discrete Wavelet Transform

The transform of a signal is just another form of representing the signal. The Discrete Wavelet Transform (DWT), which is based on sub-band coding, is found to yield a fast computation of Wavelet Transform. Wavelet transform decomposes a signal into a set of basis functions. These basis functions are called wavelets. Wavelets are obtained from a single prototype wavelet $\psi(t)$ called mother wavelet by dilations and shifting:

$$\psi_{a,b}(t) = \frac{1}{\sqrt{a}} \psi\left(\frac{t-b}{a}\right) \quad (2)$$

where 'a' is the scaling parameter and 'b' is the shifting parameter. The mother wavelet used to generate all the basis functions is designed based on some desired characteristics associated with that function. Discrete wavelet Transform is applied to the an-isotropic diffused image. As a result of applying this DWT, four types of filters like 2-D lowpass filter to the top left of the image, horizontal highpass and vertical lowpass filter to the top right of the image, horizontal lowpass and vertical highpass filter to the lower left of the image and a 2-D highpass filter to the lower right of the image are applied. Also the size of the images are reduced to half.

5. The Kirsch Operator

The Kirsch operator is made up of a number of templates. Each template focuses on the edge strength in one direction. This edge detector performs convolution with 8 masks calculating gradients. The Kirsch edge detection algorithm uses a 3×3 table of pixels to store a pixel and its neighbors while calculating the derivatives. The 3×3 table of pixels is called a convolution table, because it moves across the image in a convolution-style algorithm. The Kirsch edge detection algorithm identifies both the presence of an edge and the direction of the edge and finally detects the blood vessels. For a convolution table, calculating the presence and direction of an edge is done in three major steps:

1. Calculate the derivative for each of the eight directions.
2. Find the value and direction of the maximum derivative.

$$EdgeMax = Maximumofeightderivatives \quad (3)$$

$$DirMax = DirectionofEdgeMax \quad (4)$$

3. Check if the maximum derivative is above the threshold.

The templates of the Kirsch operator are shown in *Figure 2*. The threshold value used here is 30 which is obtained by trial and error method. The kirsch operator is applied to the discrete wavelet transformed image to segment the blood vessels. *Figure 3*. (a),(b) and (c) shows the original eye images which is a

combination of Normal, Dry ARMD and Wet ARMD. (d),(e) and (f) shows their corresponding blood vessel detected images.

Drusen Detection

Drusens are accumulation of lipid and other waste material from different layers of the retina. These are markers of ARMD as their increasing number generally indicates risk for ARMD. So the criterion for finding the abnormal images are drusen present in the Dry and Wet images.

1. Green Component

The retinal image is taken in the RGB form by fundus camera. The green channel of the RGB space is extracted and chosen for detection of exudates because exudates appear most contrasted in this channel.

2. Thresholding

Thresholding is a simple shape extraction technique, where the images could be viewed as the result of trying to separate the eye from the background. Thresholding is a method of producing regions of uniformity within an image based on some threshold criterion, T. T can be defined as

Figure 2.

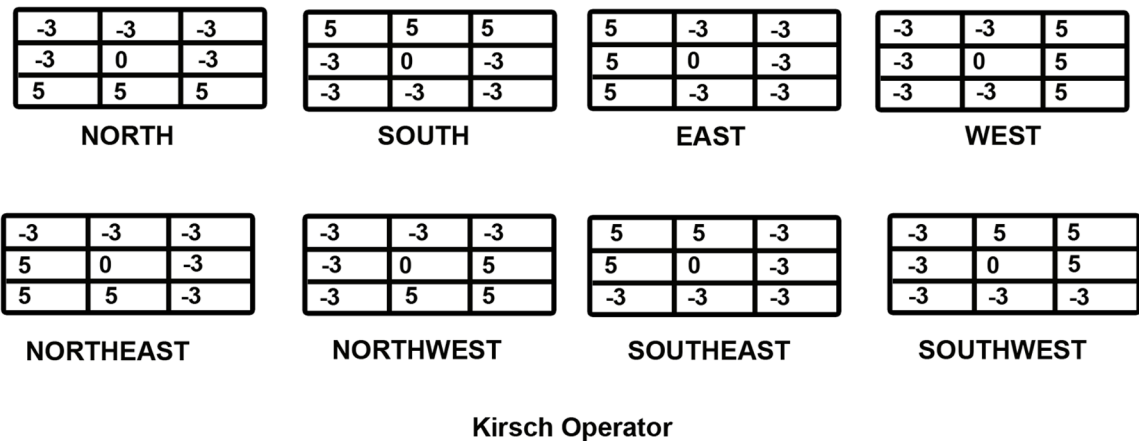
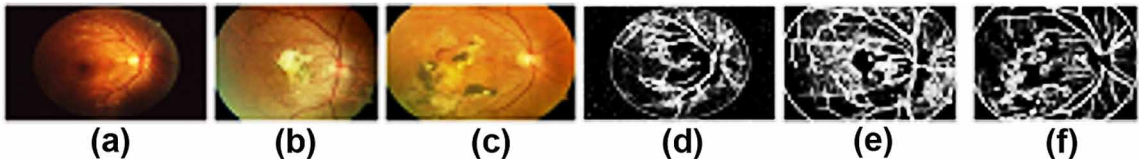


Figure 3.



$$T = T\{x, y, A(x, y), f(x, y)\} \quad (5)$$

where $f(x, y)$ is the gray level of the pixel at (x, y) and $A(x, y)$ denotes some local property such as mean, standard deviation etc in the neighbourhood of this pixel. Here we have considered the mean value. A thresholded image

$$g(x, y) = 1 \text{ if } f(x, y) \geq T \quad (6)$$

$$g(x, y) = 0 \text{ if } f(x, y) < T \quad (7)$$

A Local thresholding technique is one that partitions the given image into sub-images and determines the threshold for each of these sub-images.

$$T = T\{A(x, y), f(x, y)\} \quad (8)$$

where T is dependent upon a neighbourhood property of the pixel as well as its grey-level value. The main task of thresholding is to highlight high values of wavelet coefficients which almost correspond to the drusen areas and suppress small values which correspond to noise or unimportant structures in the image. To the green component extracted image, local thresholding is applied. Here the threshold value is chosen to be in the range 50-60 by trial and error method.

3. Morphological Processing

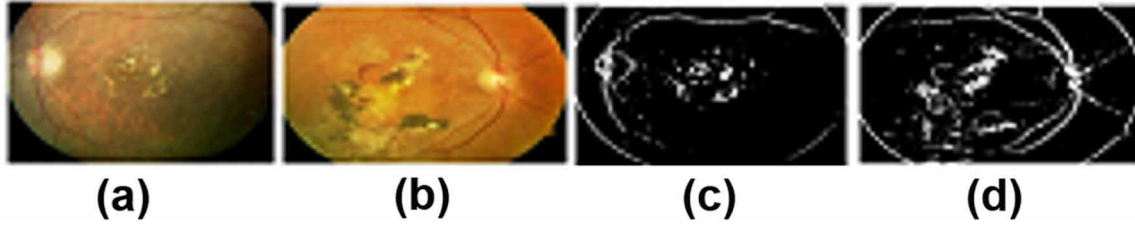
Erosion involves the removal (alteration) of pixels at the edges of regions, for example changing binary 1 values to 0, while dilation is the reverse process with regions growing out from their boundaries. These two processes are often carried out using a form of kernel known as a structural element. A structural element is an $N \times N$ kernel with entries classified according to a binary scheme, typically as 0 or 1. If all entries are coded 1 then the structural element is a solid square block, the center of which is laid over each pixel in the source image in turn. The shape of the structural element may vary, for example as a vertical bar, horizontal bar, cross shape or a user-defined pattern. If dilation is followed by erosion the process is described as a closing operation, while erosion followed by dilation is known as opening. Here dilation is used after thresholding and the Drusen is detected. Disk shaped structuring element is used here. *Figure 4.* (a) and (b) gives the Dry and Wet ARMD affected images and (c), (d) their corresponding Drusen detected images.

Feature Extraction

1. Features Detecting the Optic Nerve

After applying the pre-processing techniques, we obtain a better contrast image.

Figure 4.



Vessel Density, $A(x,y)$

Vessel density is defined as the number of vessels existing in a unit area of the retina. Since the vasculature that feeds the retina enters the eye, the vessels tend to be most dense in this region.

$$\rho(x, y) = b_t(x, y) \bullet w_v(x, y) \quad (9)$$

where, $b_t(x, y)$ is the skeletonized image. we have used the morphological method to get the skeletonized image. $w_v(x, y)$ is the convolution window also known as morphologically skeletonized window. This window can be considered as a structuring element that searches for long, narrow, and vertical vessels entering the optic nerve. The value of $w_v(x, y)$ is 0.6×3.0 .

Average Vessel Thickness, $t(x,y)$

Vessels are also observed to be thickest near the optic nerve since most branching of both the arterial and venous structure does not take place until the tree is more distal from the optic nerve

$$t(x, y) = \frac{b(x, y) \bullet w_v(x, y)}{b_t(x, y) \bullet w_v(x, y)} \quad (10)$$

where $b(x,y)$ is the binary representation of the vascular tree image.

2. Features Detecting Diseases

Some of the features that are extracted for detecting diseases are Area, Radius, Diameter, Perimeter, Centre angle, Arc length, Radian, Chord length, Half range area. Binary radian, Navigation, Hour angle and Minutes of arc.

Area

Area is determined by the formula.

$$Area = \pi r^2 \quad (11)$$

Radius

The radius of the circle is determined by the formula

$$\text{Radius}, r = \frac{\sqrt{\text{Area}}}{\pi} \quad (12)$$

Diameter

The diameter of the circle is determined by the formula

$$\text{Diameter}, d = 2r \quad (13)$$

Perimeter

The formula to find the perimeter is given by

$$\text{perimeter}, p = 2\pi r (\text{or}) p = \pi d \quad \text{Perimeter, } p = 2\pi r (\text{or}) p = \pi d \quad (14)$$

Centre Angle

The formula to find the center angle is given by

$$CA = \left(\text{perimeter} / 360 \right) * \left(2 * \pi * \text{radius} \right) \quad (15)$$

Arc Length

The formula to find the arc length is given by

$$AL = \left(\text{radius} \right) * \left(\left(2 * \pi * \text{center angle} \right) / 360 \right) \quad (16)$$

Radian

The formula to find the radian is given by

$$\text{Rad} = \text{radius} * \text{center angle} \quad (17)$$

Chord Length

The formula to find the chord length is given by

$$CL = \left(area * 360 \right) / \left(center \ angle * \pi * radius \right) \quad (18)$$

Half Range Area

The formula to find the half range area is given by

$$HA = 1 / 2 * Area \quad (19)$$

Binary Radian

$$BR = Area / 256 \quad (20)$$

Navigation

$$N = Area / 32 \quad (21)$$

Hour Angle

$$HR = Area / 24 \quad (22)$$

Minutes of Arc

$$MA = hour \ angle * 15 \quad (23)$$

Classifiers

In our experiments we apply five different classifiers namely PNN, RBFNN, modified PNN, modified RBFNN and our proposed EYENET model.

1. PNN

There were thirteen input features, which created a thirteen dimensional input vector $(x_1, x_2, x_3, \dots, x_{13})$. Each image had a combination of specific values of the input vector—called an input pattern—that described the operating features of the image. The PNN model classifies that image from its input pattern into one of three categories (Normal, Dry ARMD, Wet ARMD) as follows: In the input layer, the number of neurons is equal to the number of input features. In the pattern layer, the total number of neurons is the sum of the numbers of neurons used to represent the patterns for each category. Each category may contain many training patterns (training vectors) whose dimension is equal to the number of input factors, and taking a set of specific values of input factors. The training vectors are imported from sample data and hence they are not always necessarily representative of all existing patterns for that class. The activation function used in the pattern layer, is the Gaussian kernel. In the summation layer, the number of neurons is equal to the number of categories. The activation is simply a weighted sum function. In the output layer, there is one neuron to represent the classification result. The activation function is an arg max function, which outputs the category associated with the largest value between incoming signals. Suppose, h_{dn} is the input to the pattern layer for ‘d’ varies from 1, 2, ... 100, corresponding to 100 tested images and ‘n’ varies from 1, 2,, 13 corresponding to the feature vector. The pattern layer can be processed and the output layer has a node for each pattern classification. The sum for each hidden node is sent to the output layer and the highest values wins. This method has been done for three classes namely normal, Dry ARMD and Wet ARMD.

2. Modified PNN

PNN are slower than multilayer perceptron networks at classifying new cases. PNN requires more memory space to store the model. In modified PNN the manhattan distance is used instead of Euclidean distance and netinverse transfer function is used instead of radial basis transfer function. Since the manhattan distance follows a grid like path, the accuracy obtained is more. Transfer functions calculate a layer’s output from its net input. Inverse function handles both continuous and discrete data. So the netinverse transfer function gives better results than Radial basis Functions.

We have applied the preprocessing techniques to all the 200 images and obtained the feature values. These feature values are used as input to the classifiers. we have used the 400 images data set values and trained the classifier. For PNN, we obtain a set of results after training and testing. The values obtained are given as inputs for training. Then we fed the testing values and evaluated the classifier performance from the results obtained during testing. In Cartesian coordinates, if $p = (p_1, p_2, \dots, p_n)$ and $q = (q_1, q_2, \dots, q_n)$ are two points in Euclidean n -space, then the distance from p to q , or from q to p is given by:

$$d(p, q) = d(q, p) = \sqrt{(q_1 - p_1)^2 + (q_2 - p_2)^2 + \dots + (q_n - p_n)^2} = \sqrt{\sum_{i=1}^n (q_i - p_i)^2} \quad (24)$$

The formula for manhattan distance between a point $X=(X1, X2, \text{etc.})$ and a point $Y=(Y1, Y2, \text{etc.})$ is:

$$d = \sum_{i=1}^n |X_i - Y_i| \quad (25)$$

The results of the PNN and modified PNN classification Procedures are shown in *Table 1*. *Table 2* shows the result of Sensitivity, Specificity and Percentage of accuracy for the three classes of eye images. Sensitivity and specificity are statistical measures of the performance of a binary classification test, also known in statistics as classification function. Sensitivity measures the proportion of actual positives which are correctly identified. Specificity measures the proportion of negatives which are correctly identified.

1. **True Positive:** ARMD affected images are correctly identified as ARMD.
2. **False Positive:** Normal image incorrectly identified as ARMD.
3. **True Negative:** Normal image correctly identified as normal.
4. **False Negative:** ARMD image incorrectly identified as normal.

Sensitivity: Sensitivity of the test is the proportion of the images that have the disease test positive for it.

$$sensitivity = \frac{NumberofTruePositive}{NumberofTruePositive + NumberofFalseNegative} \quad (26)$$

Specificity: Specificity of the test is the proportion of the images that do not have the disease test negative for it.

$$specificity = \frac{NumberofTrueNegative}{NumberofTrueNegative + NumberofFalsePositive} \quad (27)$$

Accuracy: Accuracy of the measurement system is the degree of closeness of measurements of the quantity to the quantity's actual (true) value. Accuracy is also used as a statistical measure of how well a binary classification test correctly identifies or excludes a condition. Accuracy is the proportion of true results in the population.

$$Accuracy = \frac{NumberofTP + NumberofTN}{NumberofTP + NumberofFP + NumberofFN + NumberofTN} \quad (28)$$

3. RBFNN

The RBFNN consists of three layers with extremely different roles. The input to an RBFNN is non-linear while the output of the network is linear combination of outputs from the radial basis functions. The input layer is made up of source nodes that connect the network to its environment. The second layer has only one hidden layer h_{r1} in the network, which applies a nonlinear transformation from the input layer to hidden layer. The output layer is linear, supplying the response of the network to the activation pattern applied to the input layer. RBFNN is an artificial neural network that uses radial basis function

Table 1. Results of PNN and modified PNN classification

Models	Methods Used	True Positive	True Negative	False Positive	False Negative
PNN	Euclidean distance radial basis transfer function	62	25	8	5
Modified PNN	Manhattan distance Radial basis for PNN	67	23	6	4

as an activation function. It is a linear combination of radial basis functions. The most common one is the Gaussian function defined by,

$$g_i(x_j) = \exp\left(\frac{-\|x_j - \mu_i\|^2}{2\sigma_i^2}\right) \quad (29)$$

where σ is the width parameter, μ is the vector determining the center of basis function f and x is the d -dimensional input vector. The input layer of this network has x_i units which is a x_{13} dimensional input vector corresponding to thirteen features. The input units are fully connected to the h_n hidden layer units, which are in turn fully connected to the y_c output layer units, where y_c is the number of output classes for three classes namely normal, Dry ARMD and Wet ARMD.

4. Modified RBFNN

RBFNN, possess slower execution of the network and requires a representative training set. In the case of modified RBFNN, Manhattan distance is used instead of Euclidean distance and triangular basis transfer function is used instead of linear transfer function. The triangular function can be seen as the convolution of two half-size rectangular windows giving it twice the width of the rectangular windows. Since the convolution operator is used in triangular basis function, the system gives the better results than the linear model.

The results of the RBFNN and modified RBFNN classification Procedures are shown in *Table 3*. *Table 4* shows the result of Sensitivity, Specificity and Percentage of accuracy for the three classes of eye images.

Table 2. Results of sensitivity, specificity, % of accuracy

Models	Sensitivity	Specificity	Accuracy
PNN	92.54	75.76	87
Modified PNN	94.37	79.31	90

Table 3. Results of RBFNN and modified RBFNN classification

Models	Methods Used	True Positive	True Negative	False Positive	False Negative
RBFNN	Linear transfer for RBFNN	60	20	12	8
Modified RBFNN	Triangular basis for RBFNN	68	17	11	6

5. EYENET Model

EYENET model was obtained by combining modified PNN and modified RBFNN and hence it poses the advantages of both the methods. The EYENET model took both modified PNN and modified RBFNN models as inputs and the perceptron training algorithm was used for combining both the models. The main reasons for combining the models are to increase the efficiency and accuracy for which multistage combination rules can be adopted. Figure 5 gives the Architecture of EYENET Model. The perceptron is the simplest form of a neural network. Basically it consists of a single neuron with a number of adjustable weights. The neuron is the fundamental processor of a neural network. It has three basic elements: A set of connecting links, each link carries a weight w_0 to w_n . A summation unit that sums the input signals after they are multiplied by their respective weights. An activation function $f(x)$, limits the output of the neuron. Typically the output is limited to the interval 0 to 1 or alternatively -1 to 1. The basic building block of a perceptron is an element that accepts a number of inputs x_i , $i=1$ to n and computes a weighted sum of these inputs where, for each input, its fixed weight β can be only 1 or +1. Here the input to the perceptron is the output of radial basis function neural network and probabilistic neural network. The output layer corresponds to one of three classes namely normal, DRY ARMD and WET ARMD. Moreover the inputs and outputs to the perceptron classifier correspond to the binary inputs and outputs respectively. Mathematically the input to the neuron is represented by a vector $x=x_1$ to x_n , and the output is a scalar $y=f(x)$. The weights of the connections are represented by the vector $w=w_0$ to w_n , where w_0 is the offset. The output is calculated as,

$$y = \begin{cases} 1 & \text{if } [\sum_{i=1}^n \beta_i x_n] \geq 0 \\ 0 & \text{if } [\sum_{i=1}^n \beta_i x_n] < 0 \end{cases} \quad (30)$$

To test the model, the test data were applied to modified PNN and modified RBFNN. The tested outputs of both the models were applied to the perceptron network of the EYENET model. Then the classifier performance was evaluated from the results obtained during testing. The results of the EYENET classification Procedure are shown in Table 5. Table 6 shows the result of Sensitivity, Specificity and Percentage of accuracy for the three classes of eye images using the EYENET classifier. Clearly, the

Table 4. Results of sensitivity, specificity, % of accuracy

Models	Sensitivity	Specificity	Accuracy
RBFNN	88.24	62.5	80
Modified RBFNN	93.15	62.96	85

Figure 5.

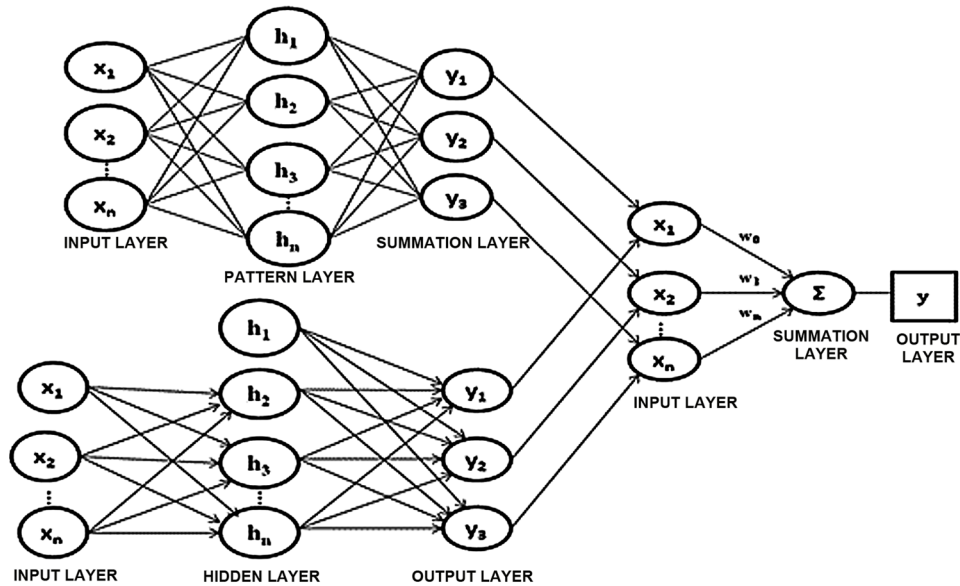


Table 5. Results of EYENET classification

Model	True Positive	True Negative	False Positive	False Negative
EYENET Model	76	18	4	2

Table 6. Results of sensitivity, specificity, % of accuracy

Model	Sensitivity	Specificity	Accuracy
EYENET Model	97.44	81.82	94

proposed EYENET model produces encouraging results. Our system is far better as compared to the other works discussed so far.

SOLUTIONS AND RECOMMENDATIONS

The Proposed method was implemented in Matlab and Microsoft visual basic 6.0. We have used a set of 250 images for processing out of which 150 images were used for training and 100 images were used for testing. Experimental results show that PNN has an accuracy of 87%, modified PNN has an accuracy of 90%, RBFNN Classifier has an accuracy of 80%, modified RBFNN has an accuracy of 85% and the proposed EYENET model has an accuracy of 94%.

ROC Curve

The ROC curve is a graphical representation of the sensitivity and specificity for a model with continuous predictions, obtained by plotting the observed sensitivity versus 1- specificity. Each point on the curve represents the sensitivity and specificity for a prediction based on classifying a patient with disease and without diseases using a threshold. Receiver operating characteristic (ROC) curve analysis can provide an objective measure of a model's sensitivity and specificity over a range of output cutoffs. The overall performance can be expressed as the area under the receiver operating characteristic curve. The ROC graphs are a useful technique for organizing classifiers and visualizing their performance. Figure.6 gives the comparison of ROC curve for all the models. These results infer that the proposed EYENET model outperforms other existing models PNN and RBFNN.

Equal Error Rate

Equal error rate (EER) is the result obtained by adjusting the system threshold such that false acceptance rate (FAR) and false rejection rate (FRR) are equal. Generally, FAR and FRR depend on the system threshold t . The FAR(t) and FRR(t) are increasing and decreasing functions, respectively, as shown in Figure 7. The error at which the two curves in Figure 7 intersect represent the EER. If the value of EER is the least, then the performance of the model is the best. In the plot, ZeroFAR denotes FRR when FAR = 0, and ZeroFRR denotes FAR when FRR = 0.

The EER value of the EYENET model for diagnosing ARMD is 0.06 as shown in Figure 8. In this work, normal, Dry ARMD and Wet ARMD cases of the ARMD are correctly identified with an accuracy of more than 79% and a sensitivity of more than 88% in all the five models.

Figure 6.

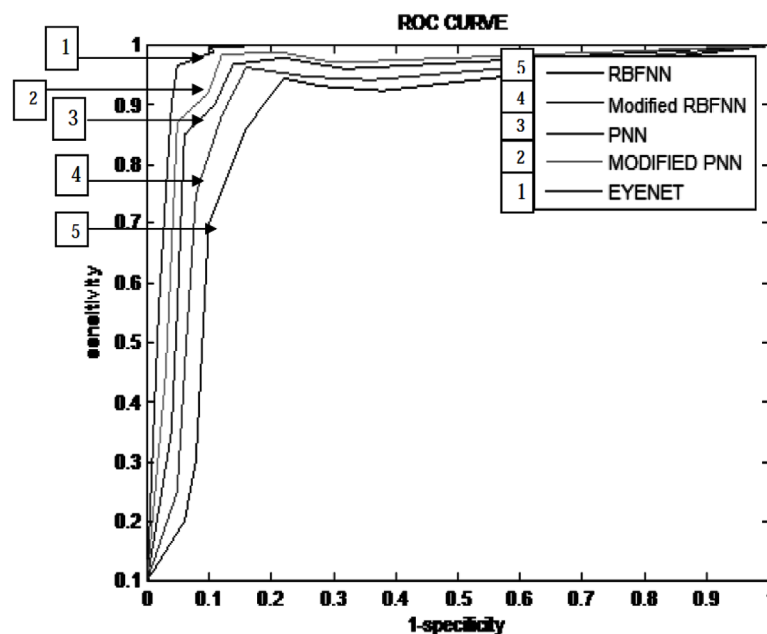


Figure 7.

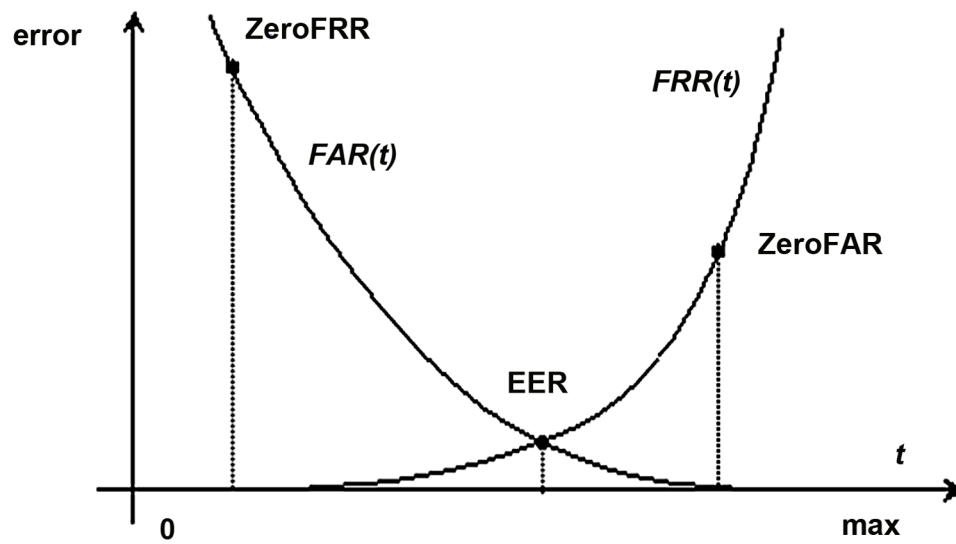
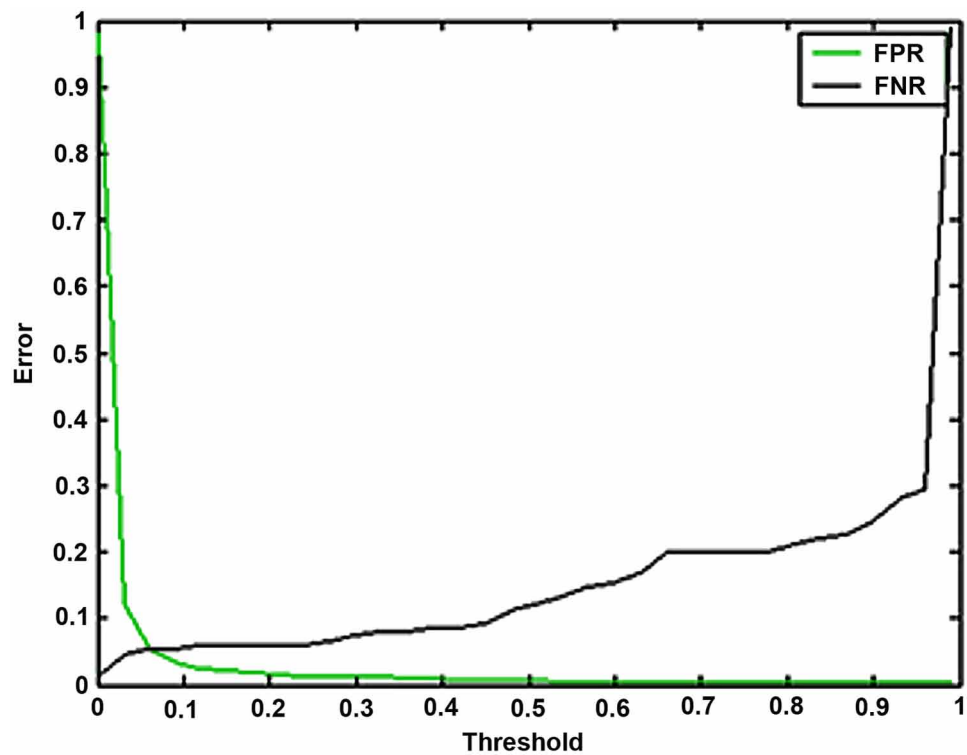


Figure 8.



FUTURE RESEARCH DIRECTIONS

The system can be further used for diagnosis of other retinal diseases such as eye cancer, cataract diseases, etc. The database and our system can be hosted in the medical websites for online diagnosis of the diseases. Due to the limitation of medical facilities and the number of ophthalmologists, the data regarding the screening can be transmitted via satellite links to the ophthalmologists at the hospitals and the result can be communicated via these links. This can be further enhanced by the use of wifi long distance networks which provide video conferencing facility between the patients at the rural camp and the doctors at the hospital. These systems can be interfaced with an ophthalmoscope from which the retinal image is given as input and a separate display device can be used to display the result regarding the presence or absence of the disease. Further the algorithms can be enhanced to produce results regarding the grade and the severity of the disease.

CONCLUSION

Advanced techniques in image processing and analysis are being extensively used to assist clinical diagnosis. Digital color retinal fundus images are widely utilized to investigate various eye diseases. Performance analysis of various classifiers is done in terms of sensitivity, specificity, true positive, true negative, false positive and false negative. Mass screening of retinal images of patients for the presence of retinal diseases can effectively reduce the possibility of blindness in affected patients. Such screening systems mainly benefit patients from rural areas who are actually unaware of the presence of the disease. The performance of the models are evaluated using area under curve of roc which is one of the best performance measuring techniques. The five classifiers are developed for diagnosis of ARMD. A user friendly model was developed for diagnosing ARMD and its performance is analyzed. Thus this work has given a successful age-related macular degeneration diagnosing method which helps to diagnose the disease in early stage which mutually reduces the manual work.

REFERENCES

- Akram, & Khanum. (2010). Retinal Images: Blood Vessel Segmentation by Threshold Probing. *IEEE Symposium On Industrial Electronics And Applications(ISIEA)*.
- Ben Sbeh, Z., Cohen, L. D., Mimoun, G., & Coscas, G. (2001). A New Approach of Geodesic Reconstruction for Drusen Segmentation in Eye Fundus Images. *IEEE Transactions on Medical Imaging*, 20(12), 1321–1333. doi:10.1109/42.974927 PMID:11811832
- Zimmer-Galler, & Zeimer. (2005). Feasibility of Screening for High-Risk Age- Related Macular Degeneration With an Internet-Based Automated Fundus Camera. *Ophthalmic Surgery, Lasers & Imaging*, 36(3), 228–236. PMID:15957480
- García, Hornero, Sanchez, Lopez, & Díez. (2007). Feature Extraction and Selection for the Automatic Detection of Hard Exudates in Retinal Images. *Proceedings of the 29th Annual International Conference of the IEEE EMBS*.

- Garcia, Sanchez, Lopez, Abasolo, & Hornero. (2009). Neural network based detection of hard exudates in retinal images. *Computer Methods and Programs in Biomedicine*, 93, 9-19.
- Garg, Sivaswamy, & Joshi. (2008). Automatic Drusen Detection from Color Retinal Images. Center for Visual Information Technology, IIT Hyderabad.
- Hoover, A., Kouznetsova, V., & Goldbaum, M. (2000). Locating blood vessels in retinal images by piecewise threshold probing of matched filter response. *IEEE Transactions on Medical Imaging*, 19(3), 203–209. doi:10.1109/42.845178 PMID:10875704
- Jayanthi, Devi, & Parvathi. (2010). Automatic Diagnosis of Retinal Diseases from Color Retinal Images. *International Journal of Computer Science and Information Security*, 7(1), 234-238.
- Mendonca, A. M., & Campilho, A. (2006). Segmentation of Retinal Blood Vessels By Combining the Detection of Centerlines and Morphological Reconstruction. *IEEE Transactions on Medical Imaging*, 25(9), 1200–1213. doi:10.1109/TMI.2006.879955 PMID:16967805
- Nageswara, Uma, Dsvvk, Sridhar, & Rao. (n.d.). A Probabilistic Neural Network Approach For protein Super family Classification. *Journal of Theoretical and Applied Information Technology*, 6(1), 101 – 105.
- Osareh & Shadgar. (2010). An Automated tracking approach for extraction of retinal vasculature in fundus images. *Journal of Ophthalmic And Vision Research*, 5(1), 20–26. PMID:22737322
- Patton, N., Aslam, T. M., MacGillivray, T., Deary, I. J., Dhillon, B., Eikelboom, R. H., & Constable, I. J. et al. (2006). Retinal image analysis: Concepts, applications and potential. *Progress in Retinal and Eye Research*, 25(1), 99–127. doi:10.1016/j.preteyeres.2005.07.001 PMID:16154379
- Qing. (2004). Segmentation Of Blood Vessels In Retinal Images Using 2-D Entropies Of Gray Level-Gradient Co-Occurrence Matrix. *ICASSP*, III-509 – III-512.
- Rapantzikos, K., Zervakis, M., & Balas, K. (2003). Detection and Segmentation of Drusen Deposits on Human Retina: Potential in the diagnosis of age-related macular degeneration. *Medical Image Analysis*, 7(1), 95–108. doi:10.1016/S1361-8415(02)00093-2 PMID:12467724
- Sheba, O., & Suresh Kumar, A. (2008). Automated Diagnosis of Macular Degeneration through Image Processing. *IE(I) Journal-CP*, 3-6, 89.
- Tian, Xue, & Huang. (2009). Classification of Underwater Objects Based on Probabilistic Neural Network. *Fifth International Conference on Natural Computation*, (pp. 38-42).
- Xu & Luo. (2009). Support Vector Machine Based Method For Identifying Hard Exudates In Retinal Images. Academic Press.

This research was previously published in Emerging Technologies in Intelligent Applications for Image and Video Processing edited by V. Santhi, D. P. Acharjya, and M. Ezhilarasan, pages 422-440, copyright year 2016 by Information Science Reference (an imprint of IGI Global).

Chapter 11

A Reversible Data Hiding Scheme for Efficient Management of Tele-Ophthalmological Data

Abhilasha Singh

Amity University, Noida, India

Malay Kishore Dutta

Amity University, Noida, India

ABSTRACT

Advancements in medical sciences and induction of advanced technologies have led to increased role of medical images in tele-diagnosis. This paper proposes a technique for easy, efficient and accurate management of distributed medical databases and alleviates the risk of any distortion in images during transmission. It also provides remedy of issues like tampering, accidentally or intentionally, authentication and reliability without affecting the perceptual properties of the image. The technique is blind and completely reversible. Values of PSNR and BER imply that the changes made to original images are imperceptible to the Human Visual System. Performance of the technique has been evaluated for fundus images and the results are extremely encouraging. The technique is lossless and conforms to the firm necessities of medical data management by maintaining perceptual quality and diagnostic significance of the images, therefore is very practical to be used in health care centers.

INTRODUCTION

Advancements in medical domain have led to the growth of a range of electronic medical appliances for the purpose of diagnosis and cure of diseases. Improvements in communication techniques through internet allow for remote access of this medical diagnostic information for manifold purposes like tele-diagnosis and tele-consultation.

DOI: 10.4018/978-1-5225-5195-9.ch011

In majority of hospitals and health care centers, the patient related information and associated medical images are stored independently in large databases as different files. Storage and distribution of these images require a key, patient's name or unique ID, for identification of images. The images, if detached from records, can lose their identity (Goldbaum et al., 1990, Singh et al., 2016). Therefore, patient details and medical images should be properly structured, so as to avoid mistreatment and loss of data. Also, this data is not protected from any illegal access and may be manipulated easily. So, there is an urgent necessity to protect and handle this data unflinching. For authentication purposes, it is essential that some watermark with identity of patient must be embedded in the original image itself (Meher et al., 2006). This can be achieved by watermarking or data hiding. However, the embedding procedure will deform the images. These changes due to the insertion process are not acceptable to medical practitioners because deformation may make the modified medical images unfit for advance diagnosis. Therefore, it is important to strike the best possible balance between embedding capacity and the image quality as the requirements in medical images are different from those of general functions of data hiding.

The reversible data hiding schemes may be the solution for this difficulty. Reversible data hiding gives the capability to recover the exact cover image after the extraction of watermark. The lossless insertion may increase the size of the original image but after extraction of data, original image is recovered in its original size (Rocek et al., 2016; Celik et al., 2006). Lossy insertion process cannot be applied in medical applications. Reversibility can be assured if adequate free space can be found or formed to hide the data within the host image while maintaining the features of the cover uncontaminated. In medical applications, the deformations after removing the watermark should be zero (Fridrich et al., 2002).

Studies on medical image watermarking have identified three possible classes of algorithms (Coatrieux et al., 2006). The first-class techniques are those which embed the data in Region of Non-Interest (RONI) while leaving the Region of Interest (ROI) to medical practitioner (Anisha Joseph et al., 2015; Coatrieux et al., 2013; Eswaraiah et al., 2015). The second-class methods are based on reversible watermarking (Irany et al., 2011; Gouenou Coatrieux et al., 2013, Singh et al., 2016). As soon as hidden information is extracted, original image can be retrieved. Third category is based on non-reversible traditional watermarking techniques which bring in minimal alteration up to acceptable limits (Dutta et al, 2014, Dutta et al., 2015).

Watermarking process can be carried out in two major domains namely, spatial and frequency. The spatial domain based techniques started with LSB (Least Significant Bit) substitution (Shanmugam et al., 2008; Eswaraiah et al., 2012; Velumanil et al., 2010, Sharma et al., 2015). In frequency domain, watermark is hidden in transform domain coefficients. For the reason that the watermark is spread across the image, this practice is not vulnerable to numerous attacks (Chen et al., 2012; Karasad et al., 2016; Dey et al., 2012; Kumar et. al., 2013, Poonkuntran et. al. 2014). Literature review reveals that the techniques mentioned have several disadvantages like some of them are irreversible, some have tedious task of deciding and separating ROI from RONI and many are not perfectly reversible. Therefore, a need was felt to develop a technique which would have zero distortion effect on the image after extraction of hidden data.

The main contribution of this paper is a data hiding scheme for fundus images which may assist tele-ophthalmological applications. The proposed scheme is fragile which means that if the image is manipulated by any means, either legal or ethical, the image will be declared unfit for advance diagnosis. Watermark contains patient information as name, id, and date of image acquisition, thus making the image self-identifiable. This proposed scheme completely satisfies the primary requirement of watermarking in

medical images that the distortion in recovered image at receiver's side should be zero so that accurate diagnosis of image can be done.

Other challenge in this context is to devise a lossless as well as blind data hiding scheme. This approach satisfies both the design requirements. At the receiver side, only modified image is required for extraction of hidden data, thus categorizing this scheme as blind. The proposed method is lossless which declares it to be appropriate for medical images as no information is tampered in the recovered image at receiver's side. This scheme has been validated on publicly available DRIVE database which indicates that it has potential applications in the areas where images contain very sensitive data and conforms to the firm necessities of medical data management by maintaining their perceptual quality and diagnostic significance.

Rest of the paper is organized as follows. The need for watermarking of medical data is given in Section 2; the choice of data hiding technique is presented in Section 3. Section 4 presents the proposed data hiding algorithm. Section 5 shows the experimental results and comparison with existing research work. In Section 6, discussion and final remarks on experimental results are made and finally in section 7, the conclusions are drawn.

Need for Reversible Data Hiding in Medical Images

Tele-diagnosis is a regular practice these days and requires remote access of medical data for the purpose of identification and cure of diseases. Medical images are stored in large centralized databases at hospitals. Individual image is accessible by some key like unique id or patient name. If this key is lost, then identification of image can become nearly impossible (Goldbaum et al., 1990). Thousands of images stored in large centralized databases are transmitted in bulk through transmission channels. If text information corresponding to images is received out of sequence at receiving end, rearranging the same can be a very tedious task. Therefore, this data needs to be properly structured, so as to avoid mistreatment and loss of data. Also, this data is not protected from any illegal access. So, there is a vital necessity to protect and handle this data unflinching.

Possible solution to this problem is to embed some watermark or hide identity of patient in the image itself which can be achieved by data hiding. But requirements in medical images are different from those of general functions of data hiding. Deformations due to insertion process are unacceptable in medical images and therefore all the changes should get reversed after extraction of hidden data. The firm necessities concerning the perceptual properties of the medical images could be met by lossless and reversible data hiding, which has the potential to revive the exact original image from a modified image

Reversible data hiding is done in order to achieve following objectives (Poonkuntran et al. 2014):

- **Fidelity:** It is a measurement of dissimilarity between the original host image and the extracted host image.
- **Computational Cost:** It is computed by the time required and the speed with which the data hiding system should work in application.
- **Efficiency:** It is the quantity of data that can be inserted into the host image without influencing the perceptual quality of the cover image.
- **Reliability:** It can be assured by two features:
 - **Integrity:** Making sure that the images have not been customized by unauthorized and illegitimate person.

A Reversible Data Hiding Scheme

- **Authentication:** Making sure that the image characterizes the right patient and source (Das et al., 2013, Singh et al., 2016).

Fundus imaging has come out to be a usual component of the ophthalmologic assessments. Data hiding and watermarking has been applied on other modalities of medical images like Ultrasounds, X-rays, MRI images, CT scans and Mammograms but comparatively less on fundus images in existing literature. This explains the reason behind the selection of fundus images.

Choice of Data Hiding Method for Medical Images

Fundus images stored in large databases are transmitted through the unsecured open networks for the purpose of tele-ophthalmology. These images can be manipulated during transmission or storage for legal and ethical purposes. Therefore, data hidden in the image should be fragile so that it gets disrupted as soon as it is attacked thus ensuring the reliability of the image and the method. This is the reason for the selection of spatial domain for data hiding. Data hiding methods in spatial domain are generally fragile (Panyindee et al., 2012; Dutta et al, 2015; Eswaraiah et al., 2012). This paper uses ‘Generic Insertion’ in spatial domain for the above-mentioned purpose.

Due to different requirements of data hiding in medical images, data has been inserted into the image rather than modification. One possible way for watermarking medical images is to leave Region of Interest (ROI) unperturbed and hiding details in Region of Non-Interest (RONI). But this task is not feasible sometimes without the consultation of the medical practitioner. Proposed scheme overcomes the tedious task of deciding and separating ROI from RONI (Al-Qershi et al., 2010; Eswaraiah et al., 2012).

Proposed Data Hiding Algorithm

In this section, the watermark insertion and extraction processes for fundus images are discussed in detail.

Insertion Procedure

This includes pre-processing of the data to be hidden followed by hiding it into the host image. Colour fundus images have been used as host images in this work. Data to be hidden includes patient name, ID and date of the image acquisition. Here, host image is taken in BMP format and watermark is a binary image. Modified output can be either transmitted over the communication channels for tele-ophthalmological applications or stored in the distributed medical databases for future references. Detailed algorithm is described as follows:

Algorithm 1: Insertion Process

- Step 1: Read cover image C_{img} .
- Step 2: Divide it into its RGB (Red, Green, Blue) components.
- Step 3: Read watermark image W and reshape watermark as column vector.
- Step 4: Choose the positions (columns) in any plane (here r-plane) of cover image where watermark is to be hidden. First position will act as a key to be sent to the receiver for extraction purpose.

Positions are to be chosen on the basis of the size of watermark, such that the watermark gets evenly spread throughout the selected plane.

Step 5: Pre-process the watermark by modifying it according to the pixels in the immediate neighbourhood of the embedding position in cover image so that it becomes imperceptible after hiding according to following process:

for all bits of watermark

if $W_{bit} == 0$

if $(C_{img}(x,y) \% 2) == 0$

then

$W_{bit} = C_{img}(x,y);$

else

$W_{bit} = C_{img}(x,y) + 1;$

else if $W_{bit} == 1$

if $(C_{img}(x,y) \% 2) == 0$

then

$W_{bit} = C_{img}(x,y) + 1;$

else

$W_{bit} = C_{img}(x,y);$

where W_{bit} is the watermark bit, C_{img} is cover image and (x,y) are the coordinates of left neighbor pixel of the embedding position in cover image.

Step 6: Declare a matrix 'temp'.

Step 7: Store all pixels of cover image prior to first embedding position (column) in 'temp'.

Step 8: Put watermark values at the first decided position.

Step 9: Store other slot of pixels of cover image between the current position of hidden watermark and the next position at which next slot of watermark values are to be hidden.

Step 10: Repeat steps 7-9 till the end of the watermark and then store the remaining pixels of cover image in temp.

Step 11: Combine RGB to obtain final modified image.

for cover image

for watermark

for columns prior to first embedding position

$W_{img}(x,y) = C_{img}(x,y);$

for first embedding position(column)

$W_{img}(x,y) = W_{bit}(m,1);$

for columns between first and second embedding position

$W_{img}(x,y) = C_{img}(x,y);$

for second embedding position(column)

$W_{img}(x,y) = W_{bit}(m,1);$

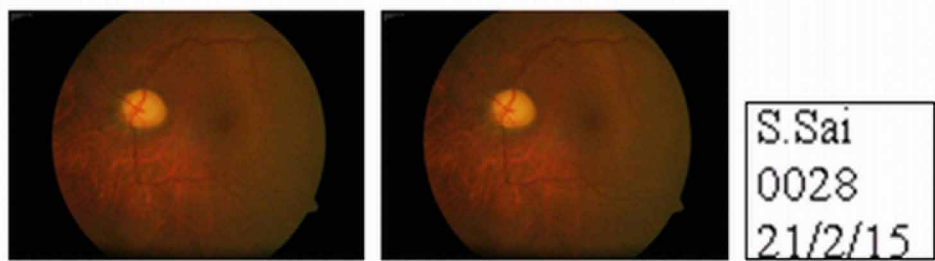
...upto nth column.

where W_{img} is watermarked image, W_{bit} is the watermark bit, C_{img} is cover image pixel and (x,y) and $(m,1)$ are the coordinates of the pixel values of watermarked image and watermark.

Figure 1 shows a sample original image with corresponding modified or watermarked image and a sample watermark.

A Reversible Data Hiding Scheme

Figure 1. Original cover Image (left), modified Image (middle) and Watermark (right)



Extraction Procedure

This procedure extracts the hidden data from the received image and recovers the original image back after extraction of watermark. In proposed algorithm, the data can be extracted without the requirement of original watermark or original host image, thus making this scheme blind. After successful extraction of watermark, original image can also be extracted exactly with correlation equal to 1 and PSNR equal to infinity. First embedding position is received as a key from sender's side and difference between the first column and first position (column) will let the receiver know about the next embedding position. Detailed process is described as follows:

Algorithm 2: Extraction Process

- Step 1: Read modified Image W_{img} .
- Step 2: Divide it into its RGB components.
- Step 3: Restore the pixel value of the Watermarked Image (r-plane) prior to first hidden position of watermark in a matrix "r_orig"
- Step 4: Now read the hidden watermark value from the first embedding position and store them in matrix "extracted watermark".
- Step 5: Again read the pixel value of watermarked image between two consecutive positions of watermark values hidden and store them in "r_orig" at contiguous position.
- Step 6: Repeat steps 3-5 until all pixel of watermarked image are read and restored as "r_orig" and "extracted watermark".
 - for watermarked image
 - for columns prior to first embedding position
 - $Rec_{orig}(x,y)=W_{img}(x,y);$
 - for first embedding position(column)
 - $Ext_wat(m,n)=W_{img}(m,n);$
 - for columns between first and second embedding position
 - $Rec_{orig}(x,y)=W_{img}(x,y);$
 - for second embedding position(column)
 - $Ext_wat(m,n)=W_{img}(m,n);$
- Step 7: 'Extracted watermark' is modified so as to get final watermark as follows:
 - if $(Ext_wat(m,n)\%2)==0$

```

then
Finwat(x,y)=0 ;
else if (Ext_wat(m,n)%2)!=0
then
Finwat(x,y)=1 ;

```

where W_{img} is watermarked image, Ext_wat is extracted and modified watermark, Fin_{wat} is the actual and final watermark and Rec_{orig} is recovered r-plane,(x,y) and (m,n) are coordinates of pixel values.

Step 8: Combine RGB to get recovered original image.

Figure 2 shows the extracted data from received image and the recovered original image after extraction process.

Figure 3 shows the block diagram of watermark insertion and extraction process. Insertion process basically consists of three steps: pre-processing of watermark, insertion process and finally getting modified image. Extraction process has three steps too: finding insertion positions, extraction of hidden data and recovering original image.

Overflow/Underflow Problem

The problem of overflow/underflow is also considered in this work. It has been foreseeable that the modified signal has pixel values outside the standard range. Concept can be better understood by considering an 8-bit image. In this context, if modified image has pixel values lesser than 0 and higher than 255, situations are defined as underflow and overflow respectively. It is necessary that dynamic range should not change after embedding. Many techniques do not consider this condition and some have used location map to overcome the situation. Here, this problem has been dealt by adjusting the pixel values in the range of [0, 255] without using any location map.

Figure 2. Recovered original Image (left) and Extracted watermark (right)

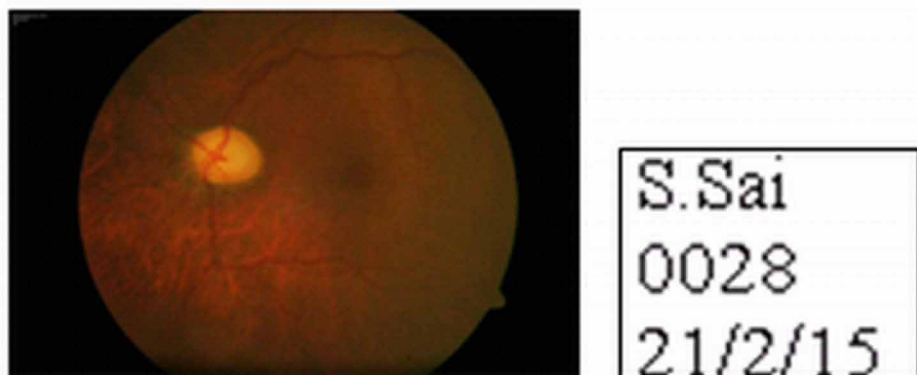
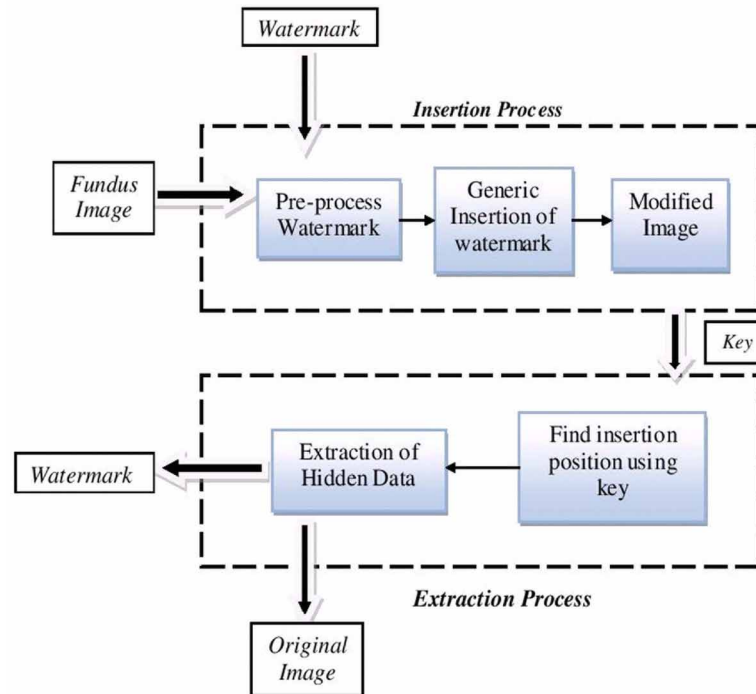


Figure 3. Block Diagram of Insertion and Extraction Process of watermark in proposed method



Experimental Results

This segment demonstrates the investigational results of projected method. The procedure has been tested exclusively on fundus images and outcomes on fifteen images are presented in this section. Embedding is carried out in r-plane.

Figure 4 displays some sample images used in the experiments along with the respective modified images. Experiments were performed on publicly available DRIVE database. All the experiments were performed on BMP images.

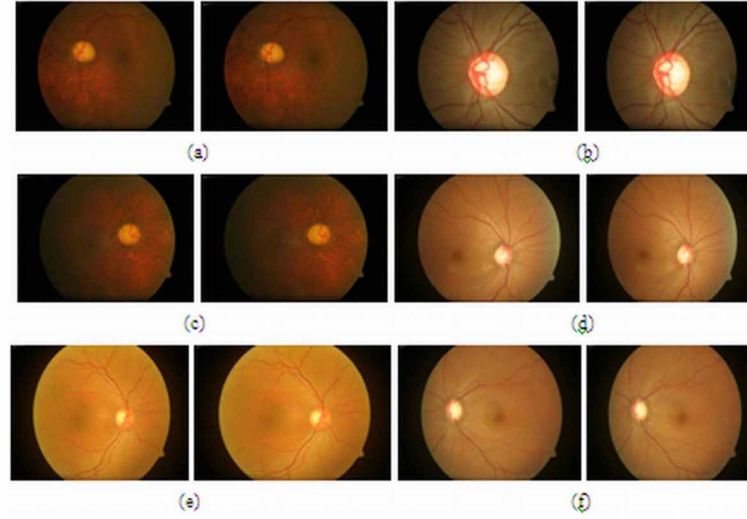
Peak Signal to Noise Ratio (PSNR) Analysis

In order to measure the efficiency of the scheme, quantitative analysis was accomplished. Peak Signal to Noise Ratio (PSNR) provides quantitative assessment of peak error between original cover image and modified image considering original image as a signal and modified image as a noise. It is generally used to measure the excellence of output image. PSNR can be mathematically represented as:

$$PSNR = 20 \log_{10} \left(\frac{MAX_f}{\sqrt{MSE}} \right) \quad (1)$$

where MSE stands for Mean Square Error and is calculated as:

Figure 4. Few Sample Images (left) used in experiments with resultant modified images (right) in every couple of images



$$MSE = \frac{1}{mn} \sum_{i=0}^{m-1} \sum_{j=0}^{n-1} \|f(i, j) - g(i, j)\|^2 \quad (2)$$

where f and g are original image and modified image respectively, m and n represents numbers of rows and columns of pixels of the images and i, j are the indexes of rows and columns. MAX_f is the maximum signal strength of original cover image.

Value of MSE is zero for two indistinguishable images, and PSNR is infinity which signifies the greater the PSNR, the similar the modified image is to the original.

Bit Error Rate (BER) Analysis

BER is defined as the ratio of number of bit errors and total number of bits original image. This can be calculated by following formula:

$$BER = \frac{\sum_i^N \sum_j^N P_0(i, j) + P_r(i, j)}{N \times N} \quad (3)$$

where “+” symbolizes logical XOR function.

Table 1 displays high values of PSNR and low values of BER between original and modified images which clearly imply that the algorithm does not negotiate with the perceptual properties of the images.

Correlation Analysis

Normalized Correlation (NC) denotes the similarity factor between embedded and extracted data and original host image and recovered host image after data extraction.

A Reversible Data Hiding Scheme

Table 1. PSNR and BER between original and modified images

Images	PSNR	BER
Sample Image 1	55.43	0.0900
Sample Image 2	54.37	0.1553
Sample Image 3	54.61	0.1324
Sample Image 4	51.49	0.1840
Sample Image 5	50.16	0.1777
Sample Image 6	52.13	0.1082
Sample Image 7	47.23	0.1526
Sample Image 8	47.54	0.1144
Sample Image 9	56.07	0.1509
Sample Image 10	54.95	0.1070
Sample Image 11	50.40	0.1935
Sample Image 12	51.95	0.1271
Sample Image 13	52.06	0.1655
Sample Image 14	52.61	0.1160
Sample Image 15	51.71	0.1128

The Normalized Correlation is can be mathematically calculated as:

$$NC(W, W') = \frac{\sum_{i=1}^m \sum_{j=1}^n [w(i, j) \cdot W'(i, j)]}{\sum_{i=1}^m \sum_{j=1}^n [w(i, j)]^2} \quad (4)$$

where W and W' represents embedded and extracted watermark respectively and m, n are the dimensions of watermark. The highest possible value of Normalized Correlation is 1 which shows that original and extracted watermark are entirely indistinguishable and the lowest value of NC is 0 which shows that original and extracted watermark are entirely different.

Table 2 shows that at receiver side, after extraction of watermark with correlation equal to 1, original image is also recovered with correlation equal to 1, thus showing that our scheme is fully reversible and therefore fulfils medical image requirements.

PSNR between the original and recovered image after extraction of watermark was also evaluated, results of which are shown below.

Table 3 reveals that every time the original image is recovered from the watermarked image, PSNR between original and recovered image comes out to be infinity and Normalized Correlation gives value equal to 1. This shows the fact that recovered image is exactly equal to the original image and thus the scheme is completely lossless.

Computational cost (time of execution) of the algorithm is also calculated and results are shown quantitatively in following table to validate the outcome.

Table 4 shows that the execution time of the algorithm is significantly short.

Table 2. Normalized correlation of recovered original image and extracted watermark

Images	Normalized Correlation	
Sample Image 1	Recovered Original Image	1
	Extracted Watermark	1
Sample Image 2	Recovered Original Image	1
	Extracted Watermark	1
Sample Image 3	Recovered Original Image	1
	Extracted Watermark	1
Sample Image 4	Recovered Original Image	1
	Extracted Watermark	1
Sample Image 5	Recovered Original Image	1
	Extracted Watermark	1
Sample Image 6	Recovered Original Image	1
	Extracted Watermark	1
Sample Image 7	Recovered Original Image	1
	Extracted Watermark	1
Sample Image 8	Recovered Original Image	1
	Extracted Watermark	1
Sample Image 9	Recovered Original Image	1
	Extracted Watermark	1
Sample Image 10	Recovered Original Image	1
	Extracted Watermark	1
Sample Image 11	Recovered Original Image	1
	Extracted Watermark	1
Sample Image 12	Recovered Original Image	1
	Extracted Watermark	1
Sample Image 13	Recovered Original Image	1
	Extracted Watermark	1
Sample Image 14	Recovered Original Image	1
	Extracted Watermark	1
Sample Image 15	Recovered Original Image	1
	Extracted Watermark	1

Attack Analysis

The method has been tested for a range of image processing attacks. Investigational results demonstrate that the proposed method is highly sensitive to all attacks. Table 5 shows the disrupted data on application of different attacks.

Table 5 shows extracted watermarks after application of different attacks on watermarked image. It is evident from the results that the watermark is extracted exactly as original in absence of any attack

A Reversible Data Hiding Scheme

Table 3. PSNR and NC between Original and Recovered image after extraction of watermark

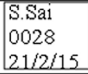





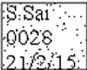


Images	PSNR between original and recovered image	NC
Sample Image 1	Inf	1
Sample Image 2	Inf	1
Sample Image 3	Inf	1
Sample Image 4	Inf	1
Sample Image 5	Inf	1
Sample Image 6	Inf	1
Sample Image 7	Inf	1
Sample Image 8	Inf	1
Sample Image 9	Inf	1
Sample Image 10	Inf	1
Sample Image 11	Inf	1
Sample Image 12	Inf	1
Sample Image 13	Inf	1
Sample Image 14	Inf	1
Sample Image 15	Inf	1

Table 4. Computational Cost (Execution time in seconds) for Insertion and Extraction process

Sample Image	Insertion Time (in Seconds)	Extraction Time (in Seconds)
1	1.504929	1.545382
2	1.443840	1.500548
3	1.444153	1.42098
4	1.408029	1.433765
5	1.501452	1.416977
6	1.452265	1.345281
7	1.579943	1.402725
8	1.597088	1.427443
9	1.492429	1.415480
10	1.507087	1.386537
11	1.506837	1.448051
12	1.520487	1.584703
13	1.554153	1.443692
14	1.434591	1.409358
15	1.482131	1.362506

but as soon as the image is attacked, the watermark gets disrupted thus directing the medical expert to discard the image and declaring it unfit for further diagnosis.

Table 5. Results on application of different attacks

S.No.	Type of Attack	Recovered Watermark
1	No Attack	
2	Median Filtering	
3	Contrast Enhancement	
4	Image Blurring	
5	JPEG Compression	
6	Histogram Equalization	
7	Salt & Pepper Noise	
8	Speckle Noise	
9	Gaussian Filter	

State of Art Comparison With Other Similar Existing Methods

Various comparable works has been accounted that uses different modalities of medical images like ultrasounds, CT Scan, MRI images and mammograms. A comparative table is presented in Table 6.

Table 6 points out that the proposed technique has relatively higher performance in terms of PSNR. Normalized Correlation coefficient of extracted watermark is 1 which is not the case in any of the work reported in above table. Also, either the scheme is lossy or not reported in above mentioned techniques whereas proposed scheme is lossless. Therefore, the state of art comparison with similar works clearly shows that the proposed technique can be a better solution than the mentioned existing schemes in Table 6.

Table 6. Comparison table

	Type of Image	Type of Medical Data Used as Host Image	Data Hiding Method Used	PSNR of Modified/Watermarked Image	Correlation of Extracted Watermark	Reversible/ Non-Reversible	Correlation of Recovered Original Image	Blind/ Semi-Blind/ Non-Blind	Lossy/ Lossless
C. Panyindee et al.	Gray Scale Image	Medical Images(CT, MRI, US, PET)	Prediction Error Expansion+ Histogram Shifting	36.04-84.65	Not Reported	Reversible	Not Reported	Blind	Loss-less
Poonkuntran Shanmugam et al.	Colored Depth Image	Fundus Image	Generic Insertion	76.8838-84.939	Not Reported	Reversible	Not Reported	Blind	Lossy
Nilanjan Dey et al.	Gray Scale Image	Electrooculogram signals	DWT-DCT-SVD	31.5572	0.9965	Non-Reversible	-	Blind	Not Reported
Praveen Kumar E et al.	Gray Scale Image	MRI, CT Scan	DWT-SVD	30-40	0.9821-0.9996	Non-Reversible	-	Not Reported	Not Reported
Proposed Method	Colored Depth Image	Fundus Image	Generic Insertion	48.80-56.96	1	Reversible	1	Blind	Loss-less

DISCUSSION AND FINAL REMARKS ON EXPERIMENTAL RESULTS

- The projected method has been assessed for perceptual properties of the cover image. The investigational results have been examined by inspecting the Peak Signal to Noise Ratio (PSNR) and Bit Error Rate (BER) which is shown in Table 1. The results are quite encouraging as the PSNR values obtained are more than 50 db and BER is quite low which means that perceptual properties of the host image are not compromised in the proposed technique.
- The proposed method has been assessed for reversibility. This attribute has been analysed by the checking the PSNR and Normalized correlation coefficients (Table 2 and Table 3). NC and PSNR are found to be 1 and infinity respectively in case of every sample image, whether it be extracted data or recovered original image, which confirms that the system is fully reversible and fully satisfies the key requisite of data hiding in medical images.
- The scheme has been also assessed for its computational cost in terms of execution time (in seconds) for insertion and extraction processes (Table 4).
- The method has been analysed for a range of image processing attacks, like filtering and various noises, either for legal or for ethical purposes. Investigational results show that the proposed scheme is highly sensitive to all attacks. Table 5 shows the disrupted data on application of different attacks. This implies that proposed algorithm is fragile in nature.
- The proposed scheme is lossless which is very clear by the results shown in Table 2 and Table 3. Original image can be entirely recovered each time after the extraction of hidden data from the modified image, implying no loss of data.
- The proposed technique can be categorized as blind because it does not necessitate the original image as well as the original watermark for the extraction process.

CONCLUSION

This paper puts forward a spatial domain based blind, fragile and fully reversible data hiding scheme which is highly suitable for the images which contain very sensitive information and cannot afford any deformation even if data hiding is required. The main purpose of this method is to preserve the integrity and authenticity of highly sensitive data. Investigational results show that the method is relatively simple and can be put functional to the medical images before storing them in database or transmitting over a network. The scheme is highly fragile to almost all types of attacks. High PSNR and low BER show that the changes made to original images are imperceptible to the Human Visual System and those actually made will be reversed after extraction of watermark. This method is applicable to all modalities of medical images and can have potential applications in the area. Future work includes hiding relevant data in other two planes of RGB image.

REFERENCES

- Al-Qershi, O. M., & Khoo, B. E. (2010). ROI-based Tamper Detection and Recovery for Medical Images Using Reversible Watermarking Technique. *Proceedings of the IEEE International Conference on Information Theory and Information Security (ICITIS)* (pp. 151-155). doi:10.1109/ICITIS.2010.5688743
- Celik, M. U., Sharma, G., & Tekalp, A. M. (2006). Lossless Watermarking for Image Authentication: A New Framework and an Implementation. *IEEE Transactions on Image Processing*, 15(4), 1042-1049.
- Coatrieux, G., Huang, H., Shu, H., Luo, L., & Roux, C. (2013). A Watermarking-Based Medical Image Integrity Control System and an Image Moment Signature for Tampering Characterization. *IEEE Journal Of Biomedical And Health Informatics*, 17(6), 2057–1067. doi:10.1109/JBHI.2013.2263533 PMID:24240724
- Coatrieux, G., & Lecornu, L. (2006). A Review of Image Watermarking Applications in Healthcare. *Proceedings of the 28th Annual International Conference of the IEEE: Engineering in Medicine and Biology Society* (pp. 4691 – 4694). doi:10.1109/IEMBS.2006.259305
- Coatrieux, G., Wei Pan, , Cuppens-Boulahia, N., Cuppens, F., & Roux, C. (2013). Reversible Watermarking Based on Invariant Image Classification and Dynamic Histogram Shifting. *IEEE Transactions on Information Forensics and Security*, 8(1), 111–120. doi:10.1109/TIFS.2012.2224108
- Das, S., & Kundu, M. K. (2013). Effective management of medical information through ROI-lossless fragile image watermarking technique. *Journal of Computer Methods and Programs in Biomedicine*, 3(3), 662–675. doi:10.1016/j.cmpb.2013.05.027 PMID:23816251
- Dey, N., Biswas, D., & Bardhan, A., Das, R.A., & Chaudhuri, S.S. (2012). DWT DCT SVD Based Blind Watermarking Technique of Gray Image in Electrooculogram Signal. *Proceedings of the IEEE International Conference on Intelligent Systems Design and Applications (ISDA)* (pp. 680-685). doi:10.1109/ISDA.2012.6416619

A Reversible Data Hiding Scheme

- Dutta, M.K., Singh, A., Parthasarathi, M., & Travieso, C.M. (2014). Imperceptible Digital Watermarking in Medical Retinal Images for Tele-Medicine Applications. *Proceedings of the IEEE International Conference on Contemporary Computing and Informatics* (pp. 517-521).
- Dutta, M. K., Singh, A., Singh, A., Burget, R., & Prinosil, J. (2015). Digital Identification Tags for Medical Fundus Images for Tele-Ophthalmology Applications. *Proceedings of the 37th IEEE International Conference on Telecommunications and Signal Processing*, Berlin, Germany (pp. 678-681). doi:10.1109/TSP.2015.7296372
- Eswaraiah, R., & Reddy, E. S. (2015). Robust medical image watermarking technique for accurate detection of tamperers inside region of interest and recovering original region of interest. *IET Image Process.*, 9(8), 615–625. doi:10.1049/iet-ipr.2014.0986
- Eswaraiah, R., & Sreenivasa Reddy, E. (2012). A Fragile ROI-Based Medical Image Watermarking Technique with Tamper Detection and Recovery. *Proceedings of the Fourth International Conference on Communication Systems and Network Technologies* (pp. 896-899).
- Fridrich, J., Goljan, M., & Du, R. (2002). Lossless Data Embedding—New Paradigm in Digital Watermarking. *EURASIP Journal on Applied Signal Processing*, 2002(2), 185–196. doi:10.1155/S110865702000537
- Goldbaum, M. H., Chatterjee, S., Chaudhuri, S., & Katz, N. (1990). *Digital Image Processing for Ophthalmology. In Noninvasive Diagnostic Techniques in Ophthalmology* (pp. 548–568). Springer. doi:10.1007/978-1-4613-8896-8_29
- Irany, B.M., Guo, X.C., & Hatzinakos, D. (2011) 'A high capacity reversible multiple watermarking scheme for medical images. *Proceedings of the 17th IEEE International Conference on Digital Signal Processing (DSP)* (pp. 1-6). doi:10.1109/ICDSP.2011.6004968
- Joseph, A., & Deepa, S.S. (2015). An Efficient Watermarking Based Integrity Control System for Medical Images. *Proceedings of the IEEE International Conference on Control, Communication & Computing India (ICCC)* (pp. 357-361). doi:10.1109/ICCC.2015.7432920
- Karasad, M., Bouslimi, D., Cozic, M., & Coatrieux, G. (2016). Watermarking of radiographic images based on quantum noise modulation. *Proceedings of the IEEE-EMBS International Conference on Biomedical and Health Informatics (BHI)* (pp. 9-12). doi:10.1109/BHI.2016.7455822
- Ko, L.T., Chen, J.E., Shieh, Y.S., & Sung, T.Y. (2012). A Novel Fractional Discrete Cosine Transform Based Reversible Watermarking for Biomedical Image Applications. *Proceedings of the International Symposium on Computer, Consumer and Control* (pp. 36-39).
- Kumar, E.P., Philip, R.E., Kumar, P.S., & Sumithra, M.G. (2013). DWT-SVD Based Reversible Watermarking Algorithm for Embedding the Secret Data in Medical Images. *Proceedings of the Fourth IEEE International Conference on Computing, Communications and Networking Technologies (ICCCNT)* (pp. 1-7).
- Meher, P.K., Patra, J.C., & Meher, M.R. (2006). Low-Complexity Technique for Secure Storage and Sharing of Biomedical Images. *Proceedings of the IEEE International Symposium on Circuits and Systems (ISCAS)* (pp. 4803-4806).

Panyindee, C., & Pintavirooj, C. (2012). Reversible Watermarking Algorithm in Application for Medical Images. *Proceedings of the Biomedical Engineering International Conference (BMEiCON)* (pp. 1-5). doi:10.1109/BMEiCon.2012.6465467

Poonkuntran, S., & Rajesh, R. S. (2014). Chaotic model based semi fragile watermarking using integer transforms for digital fundus image authentication. *Multimedia Tools and Applications, Springer*, 68(1), 79–93. doi:10.1007/s11042-012-1227-5

Rocek, A., Slavíček, K., Dostál, O., & Javorník, M. (2016). A new approach to fully-reversible watermarking in medical imaging with breakthrough visibility parameters. *Signal Processing and Control*, 29, 44–52. doi:10.1016/j.bspc.2016.05.005

Shanmugam, P., Rajesh. R.S, Eswaran Perumal (2008). A Reversible Watermarking with Low Warping: An Application to Digital Fundus Image. *Proceedings of the IEEE International Conference on Computer and Communication Engineering* (pp. 472 – 477). doi:10.1109/ICCCE.2008.4580649

Sharma, S., & Ghanekar, U. (2015). A rotationally invariant texture descriptor to detect copy move forgery in medical images. *Proceedings of the IEEE International Conference on Computational Intelligence & Communication Technology* (pp. 795-798). doi:10.1109/CICT.2015.88

Singh, A., & Dutta, M. K. (2016). Wavelet-based reversible watermarking system for integrity control and authentication in tele-ophthalmological applications. *Int. J. Electronic Security and Digital Forensics*, 8(4), 392–411. doi:10.1504/IJESDF.2016.079452

Singh, A., Dutta, M. K., Raghuvanshi, N., Burget, R., & Masek, J. (2016). An SVD Based Zero Watermarking Scheme for Authentication of Medical Images for Tele-medicine Applications. *Proceedings of the 39th IEEE International Conference on Telecommunications and Signal Processing*, Vienna, Austria, (pp. 511-514). doi:10.1109/TSP.2016.7760932

Singh, A., Dutta, M. K., & Sharma, D. K. (2016). Unique Identification Code for Medical Fundus Images Using Blood Vessel Pattern for Tele-ophthalmology Applications. *Computer Methods and Programs in Biomedicine*, 135, 61–75. doi:10.1016/j.cmpb.2016.07.011 PMID:27586480

Velumani, R., & Seenivasagam, V. (2010). A Reversible Blind Medical Image Watermarking Scheme for Patient Identification, Improved Telediagnosis and Tamper Detection with a Facial Image Watermark. *Proceedings of the IEEE International Conference on Computational Intelligence and Computing Research (ICCIC)* (pp. 1-8).

This research was previously published in the International Journal of E-Health and Medical Communications (IJEHMC), 8(3); edited by Joel J.P.C. Rodrigues, pages 38-54, copyright year 2017 by IGI Publishing (an imprint of IGI Global).

Chapter 12

An Efficient and Lossless Cryptosystem for Security in Tele-Ophthalmology Applications Using Chaotic Theory

Garima Mehta

Amity University, Noida, India

Malay Kishore Dutta

Amity University, Noida, India

Pyung Soo Kim

Korea Polytechnic University, South Korea

ABSTRACT

Tele-ophthalmology has gained a lot of popularity as it involves retinal fundus images which can be analyzed for identification of severe diseases like diabetic retinopathy and glaucoma. With this increasing popularity, requirement for medical data confidentiality and privacy has also increased during transmission or storage. To meet this challenge, this paper propose an efficient and lossless cryptosystem based upon chaotic theory for encryption of medical fundus images. In the proposed encryption scheme a strategic combination of scrambling and substitution architecture is proposed which complements each other. The proposed scheme of encryption for fundus images is challenging as these images are 3-D color image and cannot be compressed as compression may not be able to retain all relevant medical information. For performance analysis, the proposed algorithm has been evaluated for perceptual and cryptographic security. The experimental results indicate that the proposed method is lossless and resistant against attacks making the proposed scheme suitable for real time applications.

DOI: 10.4018/978-1-5225-5195-9.ch012

1. INTRODUCTION

In today's growing health care sector, telemedicine, the art of transfer of medical data over telecommunication channels (Montagnat, 2004; Nayak, 2009; Nayak, 2004) for specialized medical expertise and improved patient care is gaining a lot of popularity. Telemedicine offer either offline/ online consultation with medical professionals for routine or specialized consultation on current medical health of the patient. Telemedicine may be applied to various types of medical data like MRI, Eco graphic images, X-Ray images, CT scan or retinal images etc. stored in electronic format in the medical databases (Norcen, 2003). These medical databases are specially designed for acquisition and storage of medical image data acquired from the patients worldwide to reduce the wastage of resources or duplicate examinations, analysis and medical health checkups.

One of the budding branches of telemedicine is tele-ophthalmology (Ng, 2009) which enables ophthalmologists to take ocular images to quantify microcirculation for diagnosing diseases like Diabetic Retinopathy and Glaucoma (Helen, 1999). The benefit of using tele-ophthalmology is to diagnose and monitor ophthalmic diseases for the patients living in distant areas. For security and data confidentiality in tele-ophthalmology applications there is a need to create a secure communication channel through which retinal images can be transferred. Hence to reduce the security risks, encryption may be introduced in area of tele-ophthalmology. Another reason for encryption of medical data is to provide the medical data confidentiality and accessible to authorized users only (Formazin, 2008) The choice of encryption method employed is very important since conventional cryptography mechanisms like RSA and AES are not suitable for encryption of medical data (Fu, 2013) due to its relatively large size and highly complexity. Further this method doesn't support real time applications because of computational complexities. To solve these issues different encryption algorithms were developed.

As telemedicine is emerging as powerful technology advancement in the field of health care, the transmission of bulky medical images over the networks has also increased. As transmission networks are vulnerable to security breaches, the need of securing digital medical images is becoming an important concern. Encryption seems to provide an effective way around to prevent the loss of identity of medical images as it maintains confidentiality and integrity of the medical images. Existing work related to encryption of medical data has been done over CT images, X-Ray images, echo-graphic images, mammographic images in chaotic domain (Ashtiyani, 2008; Abokhdair, 2010; Fu, 2013). All these kind of medical images are usually 2-dimensional images whereas retinal images considered in this work are three dimensional color depth images. Moreover, for these retinal images dimensional reduction or compression may not be possible as well as loss of information during encryption and decryption process is undesirable since any loss of information may lead to false diagnosis. Thereby there is a need to develop a lossless and efficient encryption scheme to secure these colored retinal images.

The major contribution is to propose a chaotic based block wise, lossless and efficient cryptosystem that provides a potential solution for securing colored fundus images for transmission via telecommunication channels or storage in the distributed medical infrastructure networks. In the proposed cryptosystem coalition of rearrangement and replacement is done using arnold cat map and piece wise linear chaotic map respectively to achieve the desired level of confidentiality. Arnold cat map is used to scramble the original image into unintelligible format to increase the security, while piecewise linear chaotic map is used for substitution as it has good dynamical and statistical properties which are required for an efficient encryption scheme. This combination which complements each other also increases the key space to enhance the ability to withstand brute force attacks.

Another challenge in this work is unlike existing work of encrypting medical images like CT scan, MRI images, Eco-graphic images, X-Ray which are gray scale 2-D images, this work is an attempt to encrypt 3 dimensional color fundus images. These images are depth images and have voluminous data this paper propose a strategic efficient and lossless encryption algorithm to encrypt these 3 dimensional fundus images in a block wise manner as compared to full medical image encryption because of its large size which makes it suitable for real time applications in tele-ophthalmology.

The paper is organized as follows. The need for encryption of medical data security and choice of encryption method is described in section 2 whereas section 3 shows the proposed encryption algorithm. Experimental results and security analysis of proposed algorithm are shown in section 4. Finally, the paper is compared with existing research work and hence conclusion is presented.

2. NEED FOR ENCRYPTION OF MEDICAL DATA

In most of the existing work (Ashtiyani, 2008; Abokhdair, 2010; Lavanya, 2012) encryption has been done on medical images like MRI, CT Scan, X-Ray, echo-graphic, mammographic for data confidentiality and patient credentials security and to prevent data modifications. In this paper, encryption of ophthalmological images has been reported. Fundus photography is becoming popular among ophthalmologist for the early detection of diabetic retinopathy and glaucoma among diabetic patients to prevent incurable blindness and hence to reduce the risks of false diagnosis and hence there is need to secure this ophthalmological data.

Medical Data encryption is required since there is a fast exchange of data between patients, doctors and specialists which should be complete and right for accurate diagnosis of the disease. Thus, there is a need to protect this data and restrict unauthorized access. Another reason for securing the medical data is that, the third party data centers are used due to lack of storage space at the origin which raises concerns about the privacy of sensitive information. In particular, in the health care sector, sensitive personal patient records need to be kept confidential by hospitals or large companies however it also introduces new threats such as breach of privacy and tampering of results.

Medical data encryption is done in order to achieve following goals (Dong, 2012):

- **Confidentiality:** Confidentiality refers that only authorized users have access to data.
- **Data Consistency:** Consistency refers that the data stored in database has not been modified by unwanted user.
- **Authentication:** Authentication refers that the credentials of the person being verified are matched with the data of authorized user stored in the database.
- **Non-Repudiation:** Non-repudiation means that the sender cannot deny the authenticity of their signature.

Fundus images may not be secure from malicious attacks over insecure network channels during the transmission to distant places for specialized treatment as an eavesdropper may modify the information and also fundus images need protection while storage in centralized database infrastructure (Norcen, 2003) (Chiu, 2007) where every doctor can access to patients existing medical data electronically. This signifies that there is an urgent need to protect the confidential medical records of patients stored in databases and transmitted over unsecured networks that can be accessed by all. Therefore, for legal and

ethical reasons (Zhou, 2009) healthcare institutions are obliged to take proper measures to protect the confidentiality of patient's records (Formazin, 2008) stored as well as of those any kind transmitted. Thus, to protect the confidentiality encryption is best suited which ciphers the medical data by exploiting the correlation among adjacent pixels in such a way that only authorized user can access it.

For encryption of medical images conventional encryption algorithms like Rivest-Shimer-Adleman (RSA), Data Encryption Standard (DES) (Fu, 2013) are not reliable due to large size, complicated structure and mathematical features of digital medical images increase the computational overhead and procedural time which introduces a delay in real time tele-ophthalmology applications. To overcome the drawbacks of existing standard encryption algorithms the concept of chaotic theory (Ashtiyani, 2008) has been used for encrypting the medical images for safe transmission. Requirement of high security for medical image transmission leads to the choice of chaotic encryption. Intrinsic properties of chaotic systems i.e. high sensitivity towards initial conditions, pseudorandom behavior, ergodicity, low computational complexity, and non-periodicity fulfills the desired characteristics i.e. avalanche, confusion and diffusion of chaotic cryptosystem (Ashtiyani, 2008; Mehta, 2014). In the present work, the rearrangement and replacement methodology is used where Arnold map is used for rearrangement and piecewise linear chaotic map is used for replacing pixel values by the pseudorandom numbers generated using PWLCM. Encryption algorithms are generally evaluated on performance measures such as high perceptual security, low PSNR (Peak Signal to Noise Ratio), low correlation coefficients among neighboring pixels of original and encoded image and low computational complexity.

3. PROPOSED ENCRYPTION ALGORITHM

This section proposed the encryption method for fundus images. To encrypt the fundus image a strategic combination of arnold chaotic transformation and piecewise linear chaotic map is used. Arnold chaotic transformation is used for the rearrangement operation while PWLCM is used for generation of pseudorandom numbers to be used for the replacement procedure. Multiple rounds of permutation alone may not be able to encrypt the image efficiently since after a few iterations original image is retrieved back. Therefore, in replacement stage pseudorandom sequence generated by PWLCM is used to encrypt the image to attain satisfactory security level. The advantage of using PWLCM over logistic map is that it is highly sensitive to initial conditions and has better dynamical and analytical properties than 1-D chaotic map (Zhou, 1996). Also, the chaotic encryption provides a large key space making the cryptosystem more resistive to brute force attacks. Even a very minor change in the initial values propagates a significant difference in encoded output to make present cryptosystem more efficient and sturdy one.

3.1. Use of Arnold Cat Map in Medical Data Encryption

Arnold cat map (Peterson, 1997) (Mehta, 2014) (Mehta, 2016) is a two dimensional transformational map used for rearrangement of pixel positions and expressed mathematically as:

$$\begin{bmatrix} x_{n+1} \\ y_{n+1} \end{bmatrix} = \begin{bmatrix} e & f \\ g & h \end{bmatrix} \begin{bmatrix} x_n \\ y_n \end{bmatrix} \text{ mod } N \quad (1)$$

where e, f, g and h are positive integers, $eh - fg = \pm 1$

x_n, y_n, x_{n+1} and y_{n+1} are integers in $\{0, 1, 2, \dots, N-1\}$

The Arnold cat map rearranges the pixel positions in the medical image thereby making a recognizable content into a scrambled non recognizable content. Periodicity T of an image of size $N \times N$ is defined as the number of iterations after which original image will reappear.

3.2. Use of Piece Wise Linear Chaotic Map in Medical Data Encryption

Piece wise Linear Chaotic Map (Zhou, 1996) is a chaotic map consisting of multiple line segments. This map has uniform invariant distribution, good correlation coefficients and better dynamical and analytical properties. It also provides a good combination of confusion and determinacy which generates a random sequence required for an efficient encryption scheme. Mathematically, PWLCM can be expressed as

$$x(k+1) = C[x(k); \mu] = \begin{cases} \frac{x(k)}{\mu}, & \text{if } x(k) \in [0, \mu) \\ \frac{x(k) - \mu}{0.5 - \mu}, & \text{if } x(k) \in [\mu, 0.5) \\ C[1 - x(k); \mu], & \text{if } x(k) \in [0.5, 1) \end{cases} \quad (2)$$

where μ can take the value between 0 & 0.5 and control parameter x is between 0 & 1. Upon comparison with the logistic map, PWLCM shows good balance property i.e. map is uniform in nature and there is no blank window in chaotic region which also enhances the security of the present encryption algorithm.

In the present work, set of random numbers are generated using piece wise linear chaotic map which are further arranged into a matrix R1 of size $m \times m$ used for substituting the values of each divided block. The rate at which nearby orbits converge or diverge is given by Lyapunov exponents. Till the values of Lyapunov constant are positive the sequence is chaotic in nature. The Lyapunov exponent for a map is defined as follows:

$$\lambda = \frac{1}{n} \sum_{i=0}^{n-1} \log_e |C'[x_i; \mu]| \quad (3)$$

Table 1. Arnold chaotic map periodic table

Size	50	74	100	150	256
Period	150	114	150	300	192

Lyapunov constant curve for logistic map is non uniform as the output value varies between negative and zero for many values of μ . While on the other hand for PWLCM the curve is uniform and the output values are always positive for any value of μ . Figure 1 shows the comparison between 1-D logistic map and piecewise linear chaotic map on the basis of bifurcation diagram. Figure 1(a, b) depicts the bifurcation diagram for logistic and PWLCM respectively. This is a way of comparison between two maps. As seen in figure 1(a) in a chaotic region for logistic map, there are blank windows and these blank windows increase the security risks which should be minimum upon encryption. However, in PWLCM no such risks factors are involved due to non-existence of blank windows. Thus after this comparison PWLCM becomes first choice for generation of multiple linear segments used for encryption process.

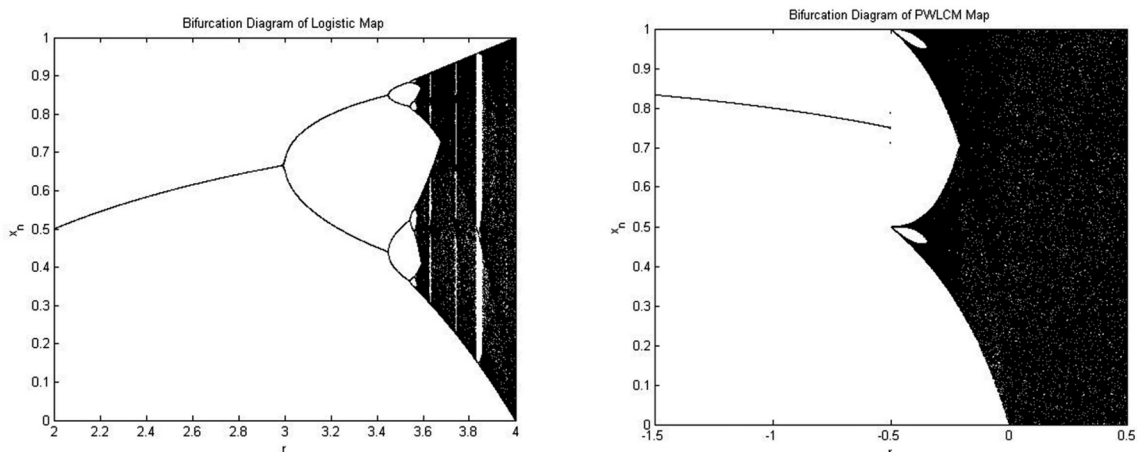
3.3. Proposed Encryption Algorithm

The proposed algorithm uses the scrambling and substitution architecture based upon arnold chaotic map and piecewise linear chaotic theory. Colored fundus image is used as an input and the block wise encryption is done due to large size of the fundus image. Block wise encryption reduces the computational complexity of the proposed algorithm because number of iterations for arnold cat map for a small block is less as compared to complete image for encryption and decryption. As well as the computational time to generate a small pseudorandom sequence from piece wise linear chaotic map is less if compared with generation of sequence for complete image.

The encryption technique described in present work is expressed as follows:

Figure 2 shows the block diagram of the present security solution for teleophthalmologic images. Encryption process of colored fundus images in which image is divided into corresponding RGB components and then each component is divided into blocks of size $m \times m$ strategically. Arnold iterations are done to scramble these blocks and thereafter a linear segment of random numbers are generated using piece wise linear chaotic map which are resized into square sized matrix and bit xored with scrambled blocks. Combine each component of image to obtain encoded medical image i.e. fundus image which is unintelligible to invader. Reverse process is performed at decryption end to decrypt the original fundus image.

Figure 1. (a) & (b) Bifurcation diagram of 1-D Logistic and Multiple Segment Piece Wise Linear Chaotic Map

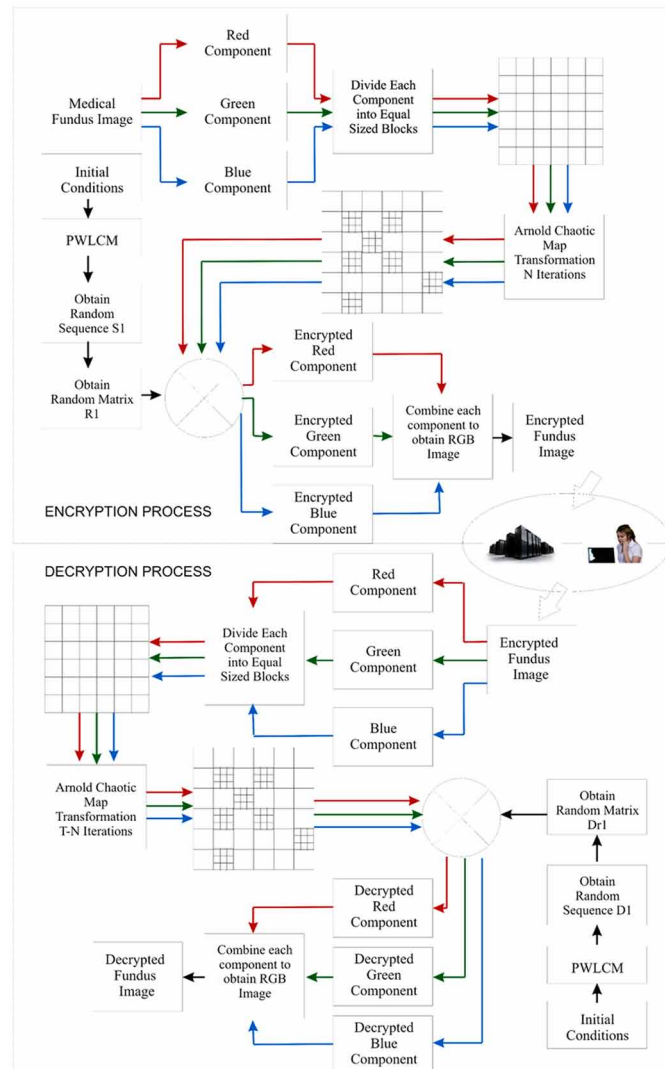


Algorithm 1. Encryption scheme

```
1 SET Input Image to RGB Fundus Image
2 DIVIDE Input Image into RGB Components
3 FOR each component DO
4 DIVIDE each component into blocks of size m*m
  // m = 64, size of each block
5 ENDFOR
  // GENERATE RANDOM SEQUENCE
6 rs=linspace(a,b,N)% vector of r values
7 INIT M=4096% number of iterations of pwlcmm
8 FOR j = 1: length // Random Sequence
9 r = rs(j) % get current "r"
10 X=zeros (M, 1); % allocate memory
11 INIT X (1) = 0.9; % initial condition
12 i=2;
13 WHILE i <= M
14 X1 = CALL palgo(X(i-1), R)
15 X(i) = X1
16 INCREMENT i
17 ENDWHILE
18 ENDFOR
  // GENERATE RANDOM MATRIX EM
19 INIT A = 1
20 FOR j = 1: m // Random Matrix
21 FOR i = 1: m // Random Matrix
22 EM(i, j) = X(A)// EM Encryption Matrix
23 INCREMENT A
24 ENDFOR
25 ENDFOR
  // ENCRYPTION PROCEDURE
26 FOR each component DO
27 FOR i = 1: N // N = 8
28 FOR j = 1: N
29 A{i,j} = CALL arnold(R1{i,j}, n1)// n1 is number of arnold iterations
30 B{i,j} = CALL bitxor(A{i,j},EM)
31 ENDFOR
32 ENDFOR
33 ENDFOR
34 COMBINE R,G,B Components to obtain Encoded Image
35 palgo(innum, p) ROUTINE
36 outnum = CALL palgo(innum, p)
37 IF innum >= 0 AND innum < p
38 outnum = innum / p
39 ELSEIF innum >= p AND innum < 0.5
40 outnum = (innum - p) / (0.5 - p)
41 ELSEIF innum >= 0.5 AND innum < 1
42 temp = 1 - innum
43 ENDIF
44 IF temp >= 0 AND temp < p
45 outnum = temp / p
46 ELSEIF temp >= p AND temp <= 0.5
47 outnum = (temp - p) / (0.5 - p)
48 ENDIF
49 ENDIF
```

Figure 3 shows how the encryption has been performed. Fig.3 (a) shows the original fundus image to be encoded while Figure 3(b), (c) & (d) shows the Red, Green and Blue Components of the original image. Figure 3(e) shows the chaotic sequence matrix generated for substitution process and finally Fig.3 (f), (g), (h) shows the encoded R G B components respectively. Figure 3(i) shows the encoded colored fundus image.

Figure 2. Block diagram of the present work

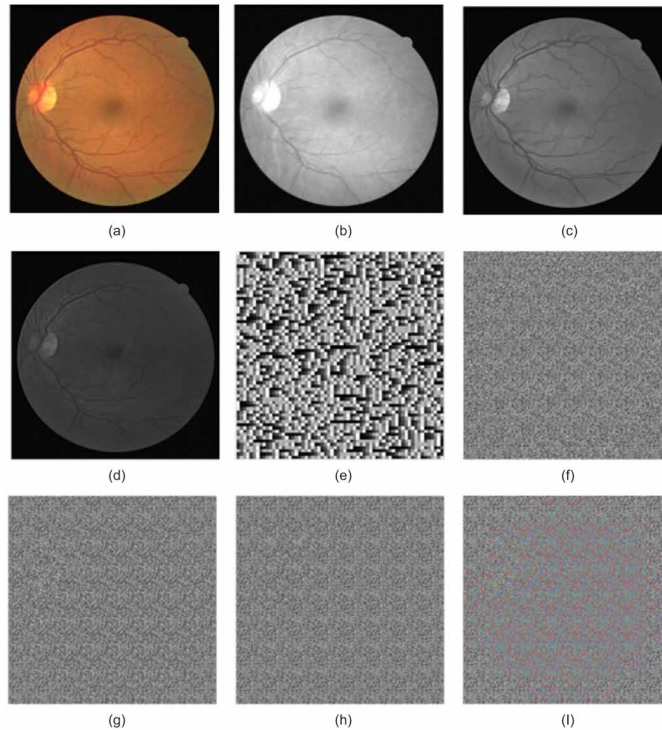


Decryption Process

During decryption either at the other end of communication channel or being referred the medical database the intruder needs to have the complete and accurate knowledge about encryption key. The decryption process is as follows:

Figure 4 shows the decryption procedure. Figure 4(a) shows the encoded fundus image while Figure 4(b), (c) & (d) shows the Red, Green and Blue Components of the same. Figure 4(e) shows the chaotic sequence matrix generated for substitution process and finally Figure 4 (f), (g), (h) shows the decrypted R G B components respectively and Figure 4(i) shows the decrypted fundus image.

Figure 3. Results of encryption process in a sample fundus image



4. EXPERIMENTAL RESULTS AND SECURITY ANALYSIS OF PROPOSED ALGORITHM

This section shows the experimental results of encryption and decryption scheme employed over fundus images. Next the proposed algorithm is evaluated for the security aspects it is being employed for. The security analysis includes perceptual attack analysis by calculating peak signal to noise ratio and visual inspection. Further cryptographic security is discussed to verify the ability of proposed algorithm to withstand cryptanalysis attacks like key related attacks, statistical attacks and differential attacks. Sample fundus images used in experiments are colored depth images having size 512*512.

4.1. Perceptual Attack Analysis

Perceptual Security signifies the degree of encryption which signifies that an intruder can gain how much information from encoded data. Perceptual security of an algorithm can be evaluated using Peak Signal to Noise Ratio (PSNR) or can be analyzed visually.

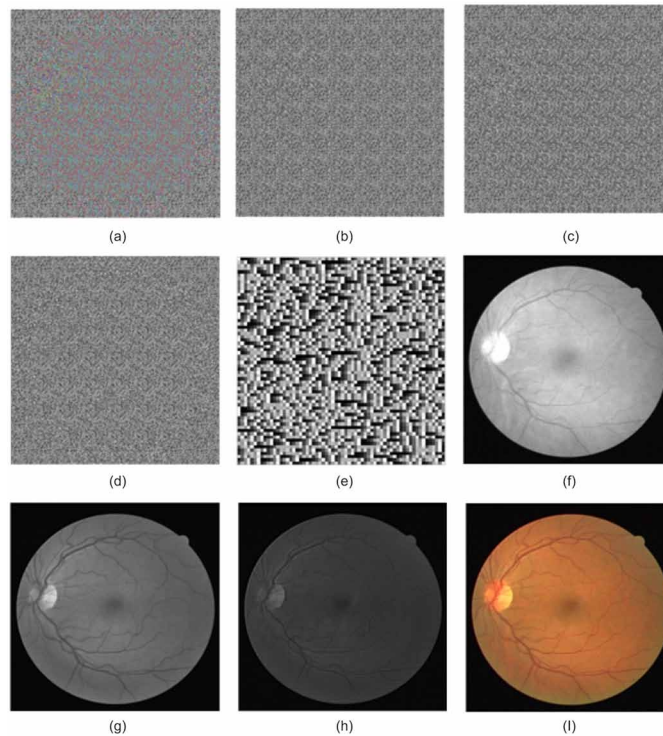
4.1.1. Peak Signal to Noise Ratio (PSNR)

Peak Signal to Noise Ratio gives the quantitative approximation of peak error between original and encoded image taking original image as a signal and encoded image as a noise. It is usually used to

Algorithm 2. Decryption scheme

```
1 SET Input Image to Encrypted Fundus Image
2 DIVIDE Input Image into RGB Components
3 FOR each component DO
4   DIVIDE each component into blocks of size m*m
   // m = 64, size of each block
5 ENDFOR
   // GENERATE RANDOM SEQUENCE
6 rs=linspace(a,b,N)% vector of r values
7 INIT M=4096% number of iterations of pwlcmm
8 FOR j = 1: length // Random Sequence
9   r = rs(j) % get current "r"
10  X=zeros (M, 1); % allocate memory
11  INIT X (1) = 0.9; % initial condition
12  i=2;
13  WHILE i <= M
14    X1 = CALL palgo(X(i-1), R)
15    X(i) = X1
16    INCREMENT i
17  ENDWHILE
18 ENDFOR
   // GENERATE RANDOM MATRIX DM
19 INIT A = 1
20 FOR j = 1: m // Random Matrix
21   FOR i = 1: m // Random Matrix
22     DM(i, j) = X(A)// DM Decryption Matrix
23   INCREMENT A
24 ENDFOR
25 ENDFOR
   // DECRYPTION PROCEDURE
26 FOR each component DO
27   FOR i = 1: N // N = 8
28     FOR j = 1: N
29       A{i,j} = CALL bitxor(R1{i,j},DM)
30       B{i,j} = CALL arnold(A{i,j}, t-n1) // n1 is number of arnold iterations and
       t is periodicity
31     ENDFOR
32   ENDFOR
33 ENDFOR
34 COMBINE R, G, B Components to obtain Decoded Image
```

Figure 4. Results of decryption process in a sample fundus image



access the quality of output image after any mathematical operation like encryption, compression and watermarking. Computed PSNR values for fundus images are shown in Table 2.

Table 2 depicts the PSNR value between the original and encoded image. The values obtained are far less than 28 db which is considered to be the threshold value for perceptual similarity thus validating that the encryption technique is highly resistant to perceptual attacks.

Perceptual security of an algorithm can also be analyzed visually. The results of original and encoded fundus image are shown as below:

Figure 5 (a) shows the original fundus image and Figure 5 (b) shows that encoded images are completely unintelligible to the invader and does not leak any kind of information.

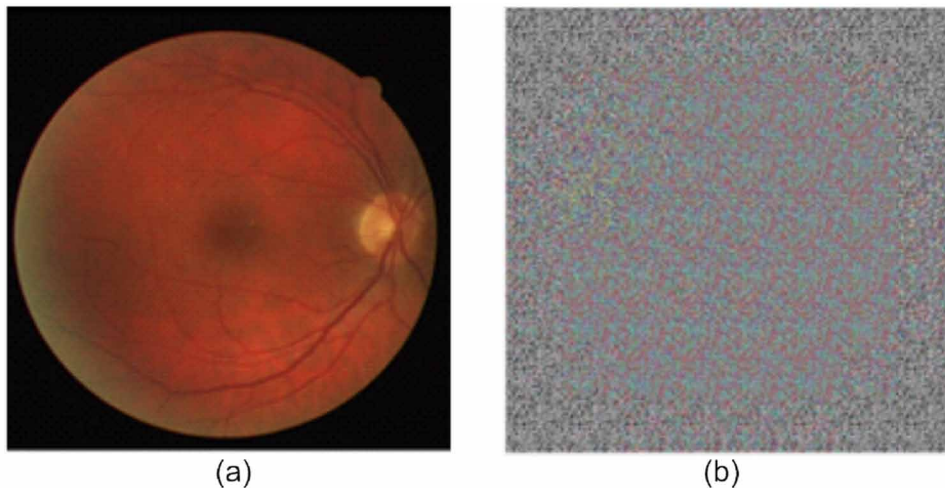
4.2. Cryptographic Security Analysis

Resistance of the proposed encryption algorithm towards cryptanalysis is studied under cryptographic security. Intrusion into a cryptographic security system and to gain access to encoded data even though security keys are not known is called cryptanalysis. These attacks can be key related attacks, statistical attacks or differential attacks.

Table 2. PSNR Analysis

Fundus Image Sample	PSNR (dB)
Sample 1	7.3147
Sample 2	6.8988
Sample 3	6.4968
Sample 4	6.7993
Sample 5	7.1711
Sample 6	6.9443
Sample 7	6.9830
Sample 8	7.4747
Sample 9	7.0110
Sample 10	6.8948
Sample 11	6.9391
Sample 12	7.1637
Sample 13	7.1964
Sample 14	6.7733
Sample 15	7.0417
Sample 16	7.4212
Sample 17	7.4692
Sample 18	7.6725
Sample 19	7.2211
Sample 20	7.0891

Figure 5. (a) Original Fundus Image; (b) Encoded Output for Fundus images



4.2.1. Key Space and Key Sensitivity

Analysis of Key Space: Kirchhoff's principle is used to perform key space analysis, in which the attacker has the knowledge related to the encryption process and the communication path but the information related to encryption key and decryption are unknown. Now if these keys are not selected wisely or due to small key space even the most secured and well implement algorithm will crumble leading to a security breach.

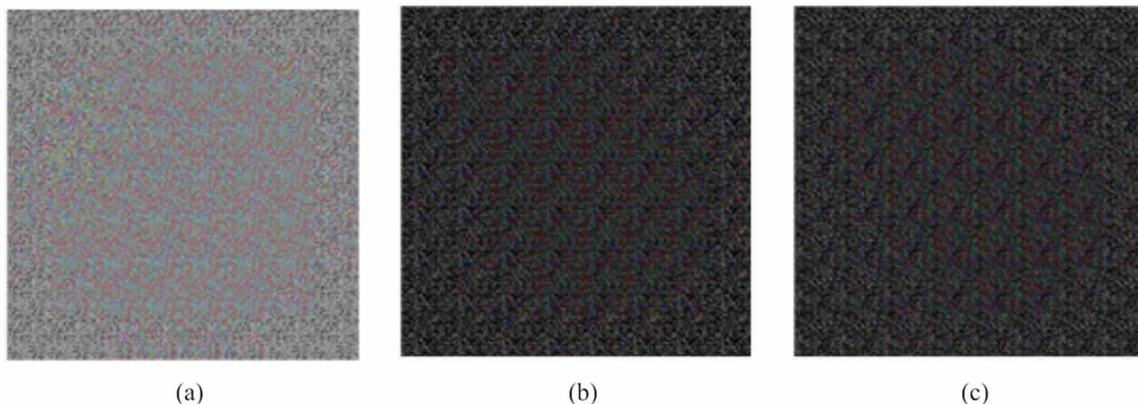
In the proposed encryption process, the key structure is $(a_1, b_1, x_1, n_1, n_2, n_3)$ where n_1, n_2, n_3 are the arnold iterations for rearranging the pixel positions of fundus image and the initial conditions of PWLCM i.e. a_1, b_1, x_1 are used for generation of pseudorandom matrix. For the decryption algorithm $(a_1, b_1, x_1, t-n_1, t-n_2, t-n_3)$ key structure is used in which t describes the periodicity of arnold chaotic map.

To verify the first parameter of key sensitivity, the original encryption key EK: $(-1.5, 4.999, 0.9, 10, 10, 10)$ is slightly modified as $EK_1: (-1.5, 4.999, 0.9000000001, 10, 10, 10)$, $EK_2: (-1.5000000001, 4.999000001, 0.9000000001, 10, 10, 10)$. In the slightly changed keys, integer part is kept same and fractional parts are given variation of approximately 10^{-14} to 10^{-15} for a & b whereas for x there is a key sensitivity of 10^{-16} . Thus resulting key space of the proposed algorithm is 10^{45} i.e. 150 bits which does not include the bits used in three rounds of arnold chaotic map. Thus the proposed algorithm yields a final key space is of 168 bits $(150+18)$, which is sufficiently large to resist brute force attacks.

Key Sensitivity: Key sensitivity analysis, as the name suggests is used to differentiate between two encoded outputs, when there is a minor change done in the encryption key and the original data is encoded using both.

Figure 6(a) shows the encoded output with original set of key (EK). Fig 6(b) presents the encoded output with slightly modified set of encryption key (EK_1) and Figure 6(c) shows encoded output with slightly further modified set of encryption key (EK_2). Correlation coefficients are calculated between original and encoded images with small change in fractional part of the keys. C1 shows the correlation of encoded image with correct set of keys EK while C2, C3 shows the correlation of encoded image with slightly modified set of keys i.e. EK_1, EK_2 . Difference between C1 and C2 (-0.3847) and C1 and C3

Figure 6. (a) Encoded Output for one sample fundus image with original set of encryption key (EK); (b) Encoded Output with slightly modified set of encryption key (EK_1); (c) Encoded Output with slightly modified set of encryption key (EK_2)



(-0.4961) is calculated and a very small difference shows that encoded images with slightly difference in fractional part of the keys looks similar but they are significantly different from each other which depicts the high key sensitivity at encryption end.

Key sensitivity can also be employed at the decryption end to differentiate the decrypted output with modified key structure.

Figure 7(a) depicts the wrong decrypted output with incorrect initial condition of PWLCM. Fig 7(b) shows the incorrect decrypted output with wrong Arnold iterations. Figure 7(c) shows the correct decrypted output with original keys. Hence it shows that presented encryption/decryption system is highly key sensitive at decryption part also.

4.2.2. Statistical Attacks

The proposed fundus image encryption algorithm has the ability to withstand the statistical attacks which can be determined by determining the relationship between original fundus image and the encoded fundus image. Correlation coefficient analysis and histogram evaluation also has been done between original and encoded fundus image pair to predict the similarity among both images. To find the relationship between the original and encoded fundus image, correlation coefficient is calculated among neighborhood pixels in both directions i.e. horizontal and vertical. High value of correlation coefficient is obtained for original fundus images in comparison to low value of encrypted images.

Correlation coefficient values obtained for original and encoded fundus image amongst adjacent pixels are shown in Table 3. Low correlation coefficient for encoded format shows that encoded format is completely unintelligible whereas high correlation coefficient amongst pixels of original image shows that image is completely intelligible as there is strong correlation amongst neighboring pixels.

Correlation among neighboring pixels is also analyzed using a correlation plot to show how the neighboring pixel correlation is disturbed on encryption and make the encoded output resistant to statistical attacks.

Figure 8(a) (b) shows correlation plot for original fundus image in horizontal and vertical direction while fig.8(c), (d) shows the correlation plot for encoded fundus image in horizontal and vertical direc-

Figure 7. (a) Decrypted Output for one sample fundus image with incorrect initial condition of PWLCM; (b) Decrypted Output with incorrect Arnold iterations; (c) Decrypted output with correct keys

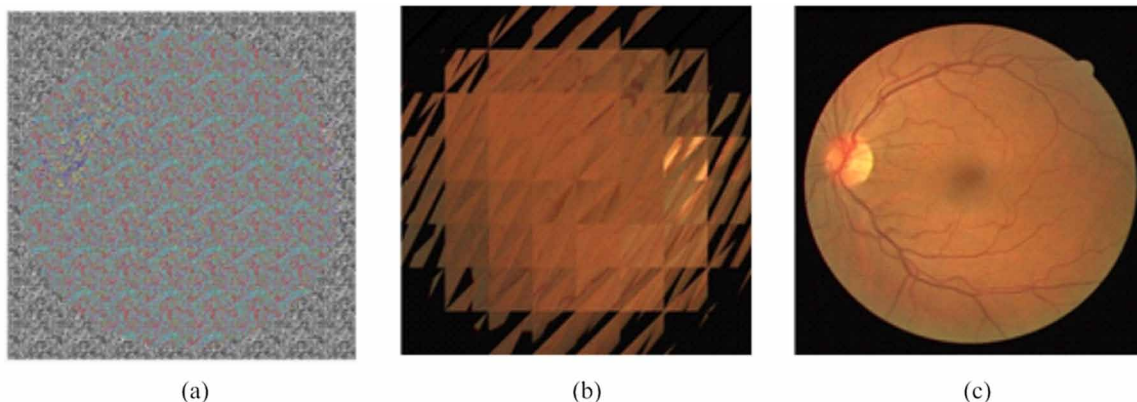


Table 3. Correlation coefficient analysis of original and encoded fundus image in horizontal and vertical direction

Fundus Image Sample	Horizontal Pixel Correlation		Vertical Pixel Correlation	
	Original Fundus Image	Encoded Fundus Image	Original Fundus Image	Encoded Fundus Image
Sample 1	0.9958	-0.0106	0.9985	-0.0126
Sample 2	0.9940	-0.0108	0.9981	-0.0111
Sample 3	0.9962	-0.0080	0.9987	-0.0137
Sample 4	0.9946	-0.0151	0.9981	-0.0091
Sample 5	0.9961	-0.0145	0.9982	-0.0077
Sample 6	0.9955	-0.0155	0.9978	-0.0075
Sample 7	0.9945	-0.0160	0.9980	-0.0109
Sample 8	0.9952	-0.0177	0.9982	-0.0082
Sample 9	0.9956	-0.0159	0.9979	-0.0044
Sample 10	0.9946	-0.0181	0.9979	-0.0076
Sample 11	0.9939	-0.0188	0.9980	-0.0079
Sample 12	0.9940	-0.0139	0.9979	-0.0052
Sample 13	0.9947	-0.0150	0.9981	-0.0090
Sample 14	0.9963	-0.0124	0.9981	-0.0056
Sample 15	0.9966	-0.0170	0.9983	-0.0046
Sample 16	0.9963	-0.0155	0.9986	-0.0093
Sample 17	0.9960	-0.0071	0.9979	0.0049
Sample 18	0.9968	0.0004	0.9982	0.0075
Sample 19	0.9968	-0.0012	0.9982	0.0071
Sample 20	0.9936	-0.0121	0.9974	0.0098

tion respectively. Correlation plot for original image is concentrated while a distributed correlation plot is obtained from encoded fundus image. This shows that high correlation between neighboring pixels in the original image is completely disturbed in encoded fundus image by defined encryption scheme.

4.2.2.1. Histogram Analysis

Another parameter to analyze the efficiency of proposed cryptosystem against statistical attacks is histogram analysis. Histogram analysis is a subjective check for data distribution. Histogram of an image refers to the distribution of intensity values on each pixel position. Histogram of colored fundus image is shown by taking the histogram of individual red, green and blue channel.

Figure 9(a) (b) (c) shows the non-uniform histogram of R G B components of original colored fundus image as compared to uniform histogram of R G B components of encoded fundus image in figure 9(d) (e) (f) which makes difficult for an invader to find any similarity between original and encoded fundus image pair.

Figure 8. (a), (b) Horizontal and vertical correlation plot for original fundus image; (c), (d) Horizontal and vertical correlation plot for encoded image

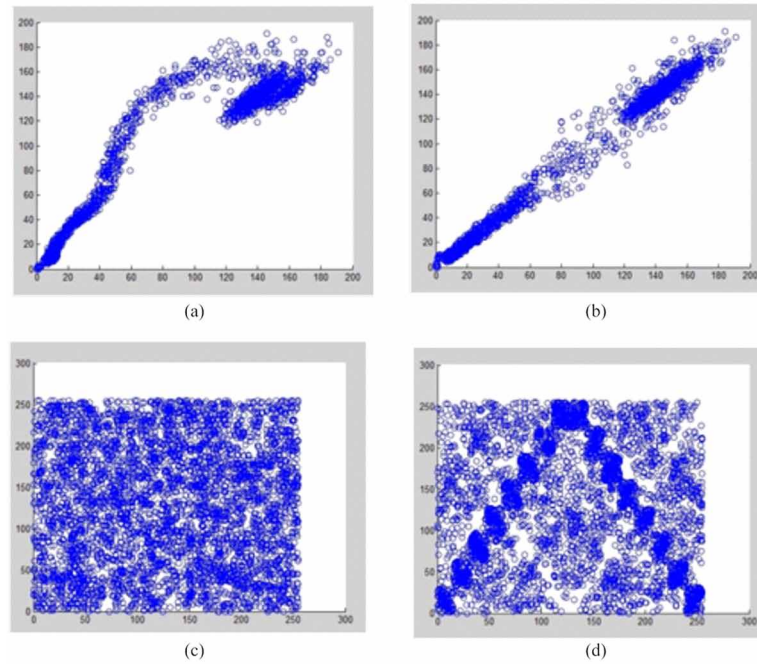
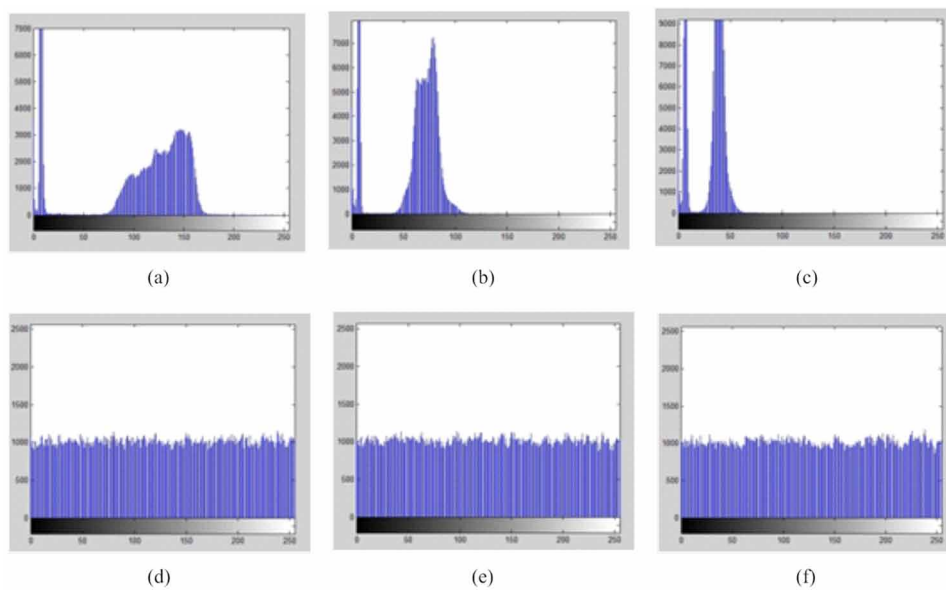


Figure 9. (a), (b), (c) Histogram for individual components of original colored fundus image; (d), (e), (f) Histogram for individual components of encoded colored fundus image



4.2.3. Differential Attacks

Net Pixel Change Rate (NPCR) and Unified Average Change Intensity (UACI) are calculated to check the resistance of proposed algorithm against differential attacks. Now, the mathematical formula to calculate NPCR & UACI is expressed below:

C^1 denotes the original data & C^2 denotes the modified data (Lokesh, 2015):

$$D(i, j) = \begin{cases} 0 & \text{if } C^1(i, j) = C^2(i, j) \\ 1 & \text{if } C^1(i, j) \neq C^2(i, j) \end{cases}$$

$$NPCR = \sum_{i,j} \frac{D(i, j)}{M * M} * 100\% \quad (4)$$

$$UACI = \sum_{i,j} \frac{|C^1(i, j) - C^2(i, j)|}{M * M} * 100\% \quad (5)$$

where i, j denotes the pixel position, $M*M$ denotes the size of C^1 and C^2 .

For calculating these parameters, in the original data only one pixel value is changed to obtain a modified data. Now both of them are encoded using the same encryption method in order to calculate the difference between the two encoded outputs.

Table 4 above shows NPCR and UACI values derived from proposed algorithm. For the encryption scheme to be efficient the desirable value for NPCR should be high and that of UACI should be low so that there is no similarity amongst the original encoded data and in modified encoded data. As seen from the tabulated data, NPCR calculated is high while UACI calculated is low which is desirable and proves the proposed method to be resistant to differential attacks.

5. COMPARATIVE ANALYSIS WITH PAST WORK

Some papers have reported medical image encryption for medical images like CT scan, MRI, X-Ray and Eco graphic images. Table 5 shows the comparison amongst existing work and proposed work. A very less work has been reported on encryption of ophthalmologic images. The proposed method has competitive high performance for these parameters such as Peak Signal to Noise Ratio, Correlation Coefficient, key sensitivity and key space. Large size of ophthalmologic images doesn't increase the overall computational time of the proposed algorithm.

Table 4. Analysis of NPCR and UACI parameters for colored fundus images

Fundus Sample	NPCR	UACI
Sample 1	0.9980	0.1068
Sample 2	0.9980	0.1024
Sample 3	0.9980	0.1024
Sample 4	0.9980	0.1070
Sample 5	0.9980	0.1074
Sample 6	0.9980	0.1064
Sample 7	0.9980	0.1065
Sample 8	0.9980	0.1072
Sample 9	0.9980	0.1066
Sample 10	0.9980	0.1069
Sample 11	0.9980	0.1073
Sample 12	0.9980	0.1072
Sample 13	0.9980	0.1065
Sample 14	0.9980	0.1068
Sample 15	0.9980	0.1074
Sample 16	0.9980	0.1069
Sample 17	0.9980	0.1071
Sample 18	0.9980	0.1072
Sample 19	0.9659	0.1073
Sample 20	0.9662	0.1074

5.1. Final Briefing on Experimental Results

1. The experimental results for perceptual security are analysed by calculating peak signal to noise ratio tabulated in Table 2. The results are convincing as the values obtained are far less than 28 db which is considered as threshold value for perceptual similarity thus verifying that the encryption technique is highly resistant to perceptual attacks. Also when visually analyzed the encoded fundus images are unintelligible and doesn't give any clue about original medical data. Thus the proposed algorithm has good perceptual security which is essential requirement of an encryption scheme.
2. The experimental results for key sensitivity analysis shows high key sensitivity. Table 3 indicates experimental results for correlation coefficient for proposed algorithm in both vertical and horizontal domain. Low values of correlation coefficients obtained and distributed correlation plot for Encodedfundus image shows high resistance towards statistical attacks Further, the non uniform histogram of R G B components of original colored fundus image as compared to uniform histogram of R G B components of Encodedfundus image shows that it is difficult for an invader to find the similarity between original and encoded fundus image pair. Table 4 shows the resistance to dif-

Table 5. Comparison table for encryption

	Image Format	Medical Data used for encryption / Size	Encryption method used	Encryption Type	PSNR	Robustness Against	Key Space	Lossy/ Lossless
Norcen et al., 2003	Gray Scale Image 512*512	Angiograms	Selective Bit Plane Encryption	Selective Encryption	10.51	NR	NR	NR
Fu et al., 2013	Gray Scale Image 558*558	CT Scan	Chaos Based Image Encryption	Full Encryption	NR	Statistical Attacks as well as differential attacks	2^{146}	NR
Ashtiyani et al., 2008	Gray Scale Image 256*256	Mammography	Chaotic theory	Full Encryption	NR	Statistical Attacks & Histogram Analysis done	NR	NR
Zhang et al., 2014	Gray Scale Image 512*512	CT Scan Image of Abdomen	Chaotic Map	Full Encryption	NR	Statistical Attacks Correlation Coefficient, Histogram Analysis Done	2^{114}	NR
Zhou et al., 2009	Gray Scale Image	MRI, CT Scan, X-Ray	Edge Based Encryption	Full Encryption	NR	Plaintext Attacks	Unlimited	Lossless
Proposed Method	Colored Depth Image 512*512	Fundus Image	Chaotic Encryption	Block Wise Encryption	7.7140	Statistical Attacks, Perceptual Attacks. Differential Attacks	2^{168}	Lossless

ferential attacks. NPCR higher values and UACI lower vlaues signifies that there is no similarity between encoded images makes the proposed encryption scheme efficient.

6. CONCLUSION

This paper proposes an efficient and lossless cryptosystem based upon chaotic theory for encryption of fundus images for real time transmission for tele-ophthalmology applications and for secured storage in distributed medical database infrastructure. Fundus images are large in size in comparison to other medical images and the proposed algorithm presents a method based on 2-D arnold cat map and 1-D piece wise linear chaotic map which complements each other for securing the fundus images efficiently so that the computational complexity is low making and the proposed scheme suits the real time applications.

Also, the proposed scheme gives encouraging results against attacks related to keys. Key space provided by the proposed method is high enough to resist against brute force attacks and key sensitivity is also high at encryption/decryption end. Proposed algorithm also shows good results for differential

attacks analysis. Future work can be extended by exploring the possibility of encoding of fundus images in frequency domain and concept of joint watermarking and encoding can also be done to secure fundus images.

REFERENCES

- Abokhdair, N. O., Azizah, B. A. M., & Zamani, M. (2010). Integration of Chaotic Map and Confusion Technique for Color Medical Image Encryption. *Proceedings of the International Conference on Multimedia Technology and its applications* (pp. 20-23).
- Ashtiyani, M., Birgani, P. M., & Hosseini, H. M. (2008). Chaos-based medical image encryption using symmetric cryptography. *Proceedings of the 3rd international conference on information and communication technologies* (pp. 1–5). doi:10.1109/ICTTA.2008.4530291
- Ashtiyani, M., Birgani, P. M., & Hosseini, H. M. “Chaos- Based Medical Image Encryption Using Symmetric Cryptography,” information and communication technologies: from theory to applications in proceedings of the 3rd international conference on information and communication technologies, pp. 1-5, 2008. doi:10.1109/ICTTA.2008.4530291
- Chiu, D.K.W., Hung, P.C.K., Cheng, V.S.Y., & Kafeza, E. (2007). Protecting the exchange of medical images in healthcare process integration with web services. *Proceedings of the 40th Annual Hawaii international conference on system sciences*. Retrieved from <http://medical.nema.org/>
- Dong, C., Li, J., Huang, M., & Bai, Y. (2012). The medical image watermarking algorithm with encryption by DCT and logistic. *Proceedings of the Ninth Web Information Systems and Applications Conference* (pp.199- 124).
- Formazin, M., Netto, D.B.S., Jr., Cavenaghi, M.A., & Marana, A.N. (2008). Protecting medical images with biometric information (pp. 284–289). In *Advances in Computer and Information Sciences and Engineering*. Springer.
- Fu, C., Wei-hong, M., Yong-feng, Z., Zhi-liang, Z., Lau, F. C. M., Tse, C. K., & Hong-feng, M. (2013). An efficient and secure medical image protection scheme based on chaotic maps. *Computers in Biology and Medicine*, 43(8), 1000–1010. doi:10.1016/j.compbiomed.2013.05.005 PMID:23816172
- Hu, J., & Han, F. (2009). A pixel-based scrambling scheme for digital medical images protection. *Journal of Network and Computer Applications*, 32(4), 788–794. doi:10.1016/j.jnca.2009.02.009
- Lavanya, A., & Natarajan, V. (2012). Watermarking patient data in Encoded medical images. *Indian Academy of Sciences*, 37, 723–729.
- Li-bo, Z., Zhi-liang, Z., Ben-qiang, Y., Wen-yuan, L., Hong-feng, Z., & Ming-yu, Z. (2014). Crypt-analysis and improvement of an efficient and secure medical image protection scheme. *Mathematical Problems in Engineering*.

- Li Helen, K. (1999). Telemedicine and Ophthalmology. *Survey of Ophthalmology*, 44(1), 61–72. doi:10.1016/S0039-6257(99)00059-4 PMID:10466589
- Lokesh, B.S., Manjunatha, M.B., & Panduranga, H.T. (2015). Novel Method for thermal image encryption. *Proceedings of the International Conference on Innovations in Information Embedded and Communication Systems*.
- ManCho, N., Nathoo, N., Rudnisky, C. J., & Tennant, M. T. S. (2009). Improving access to eye care: Teleophthalmology in Alberta, Canada. *Journal of Diabetes Science and Technology*, 3(2), 289–296. doi:10.1177/193229680900300209 PMID:20144360
- Mehta, G., Dutta, M.K., Travieso-Gonzalez, C.M., & Kim, P.S. (2014). Edge Based Selective Encryption scheme for Biometric Data Using Chaotic Theory. *Proceedings of the International conference on contemporary computing and informatics (IC3I)* (pp. 383-386).
- Mehta, G., Dutta, M. K., & Kim, P. S. (2016). A Secure Encryption method for Biometric Templates based on Chaotic Theory. In *Transactions on Computational Sciences* (pp. 120-140). Springer Verlag Publishers. doi:10.1007/978-3-662-50412-3_8
- Mehta, G., & Dutta, M.K., Karasek, J., & Kim, P.S. (2013). An Efficient and Lossless Fingerprint Encryption Algorithm Using Henon Map & Arnold Transformation. *Proceedings of ICCV '13* (pp. 485–489).
- Mehta, G., Dutta, M.K., & Kim, P.S. (2014). An Efficient & Secure Encryption Scheme for Biometric Data Using Holmes Map & Singular Value Decomposition. *Proceedings of the 2014 International Conference on Medical Imaging, m-Health and Emerging Communication Systems (MedCom)* (pp. 211–215). Springer.
- Montagnat, J., Bellet, F., & Benoit-Cattin, H. (2004). Medical images simulation, storage, and processing” on the European Data Grid testbed. *Journal of Grid Computing*, 2, 387–400. doi:10.1007/s10723-004-5744-y
- Nayak, J., Subbanna Bhat, P., Rajendra Acharya, U., & Sathish Kumar, M. (2009). *Efficient Storage and Transmission of Digital Fundus Images with Patient Information Using Reversible Watermarking Technique and Error Control Codes*. *J. Med. Syst.*, 33(3), 163-171.
- Nayak, J., Bhat, P. S., Kumar, M. S., & Acharya, U. R. (2004). Reliable and robust transmission and storage of medical images with patient information. *Proceedings of the International Conference on Signal Processing and Communications (SPCOM)* (pp. 11-14).
- Norcen, R., Podesser, M., Pommer, A., Schmidt, H. P., & Uhl, A. (2003). Confidential storage and transmission of medical image data. *Computers in Biology and Medicine*, 33(3), 277–292. doi:10.1016/S0010-4825(02)00094-X PMID:12726806
- Peterson, G. (1997). Arnold’s cat map. Retrieved from <http://online.redwoods.cc.ca.us/instruct/darnold/maw/catmap3.htm>, 1997

Zhou, H. (1996). A design methodology of chaotic stream ciphers and the realization problems in finite precision [Ph.D. dissertation]. Fudan Univ., Shanghai, China.

Zhou, Y., & Agaian, S. (2009). A Lossless Encryption Method for Medical Images Using Edge Maps. *Proceedings of the International Conference of IEEE EMBS* (pp. 3707-3710). doi:10.1109/IEMBS.2009.5334799

This research was previously published in the International Journal of E-Health and Medical Communications (IJEHMC), 7(4); edited by Joel J.P.C. Rodrigues, pages 28-47, copyright year 2016 by IGI Publishing (an imprint of IGI Global).

Chapter 13

Case Study:

Glaucoma and Epidemic Dropsy – A Past Possible Association Revisited

Swarna Biseria Gupta

L.N. Medical College, Bhopal, India

Divya Verma

L.N. Medical College, Bhopal, India

D. P. Singh

L.N. Medical College, Bhopal, India

ABSTRACT

*Epidemic dropsy is a multi-system disease involving the cardiovascular, hepatic, renal, ocular and other systems. Onset is usually subacute or insidious with watery diarrhea and vomiting. This lasts from a few days to more than a week. Bilaterally symmetrical pitting edema of the lower limbs extending from the ankles up to the scrotum and abdominal wall is a constant feature. It is a toxic disease caused by the unintentional ingestion of *Argemone mexicana* (prickly yellow poppy) seeds as an adulterant of wheat flour, or more commonly, of cooking oil such as mustard oil. Sanguinarine and dehydrosanguinarine are two major toxic alkaloids of *Argemone* oil. It is a rare phenomenon for practicing ophthalmologists to observe cases of epidemic dropsy, and the possibility of glaucoma should be kept in mind in cases of epidemic dropsy, when members of same family or village report with raised IOP, pedal edema and history of use of mustard oil for cooking or massage. Glaucoma is hypersecretory in nature; prostaglandin and histamine release may have significant roles in its pathogenesis. The disease has self limiting course but needs good control of intraocular pressure (IOP) medically till it returns to normal and visual field changes have stabilized. Its early diagnosis is very important to prevent grievous complications; hence, all cases should be followed up regularly for IOP measurement and visual field analysis up to 8-12 weeks, because, if ignored, optic atrophy may develop.*

DOI: 10.4018/978-1-5225-5195-9.ch013

INTRODUCTION

Epidemic Dropsy is an acute toxic disease, which was recognized in 1877, when it appeared as an epidemic outbreak in Calcutta. However this drew the attention of ophthalmologists only in 1909 when Maynard reported occurrence of glaucoma in cases of epidemic dropsy. (Rathore, 1982). It occurs due to contamination of edible oil with seeds of *Argemone mexicana* and may also occur following massage with contaminated sanguinarine hydrochloride – an alkaloid of benzphenanthrine subgroup of isoquinoline group isolated from oil of *Argemone mexicana*.

Pathologically, sanguinarine hydrochloride gives rise to dilatation and engorgement of capillaries in various tissues of the body. All ages are affected and both sexes have equal predilection.

Clinical presentation include bilateral symmetrical pitting edema of lower limbs; edema extending from ankles up to the scrotum and abdominal wall is a constant feature (Sharma et al, 1999). Additionally, there maybe anemia, low grade fever, gastrointestinal disturbances, dyspnea, and cardiac failure.

Among ocular findings, glaucoma has been reported in various epidemics in 0 – 12% of cases (Mohan et al, 1984; Rathore, 1982). Glaucoma usually manifests after about 4 weeks and is always bilateral. During the early stages, field defects may be present (Sachdev et al, 1988), which, if undetected, may lead to severe visual impairment. Since the severity of glaucoma is independent of the severity of systemic features, there are no signs of anterior segment inflammation and chamber depth is usually normal. Therefore all cases suspected of epidemic dropsy should be subjected to regular eye examination. Fundus shows venous dilatation and tortuosity, hemorrhages and disc edema.

The diagnosis of epidemic dropsy must be considered during an outbreak of bilaterally symmetric edema in more than one member of a family or community, consuming mustard oil, especially when tendon jerk reflexes are well preserved; otherwise there is no laboratory parameter considered specific for epidemic dropsy.

Withdrawal of contaminated cooking oil is the most important initial therapeutic step. Bed rest with leg elevation and protein rich diet is useful. Medical treatment is advised for glaucoma till IOP returns to normal, visual fields should be monitored, otherwise filtering surgery is indicated to decrease the IOP.

CASE REPORT 1

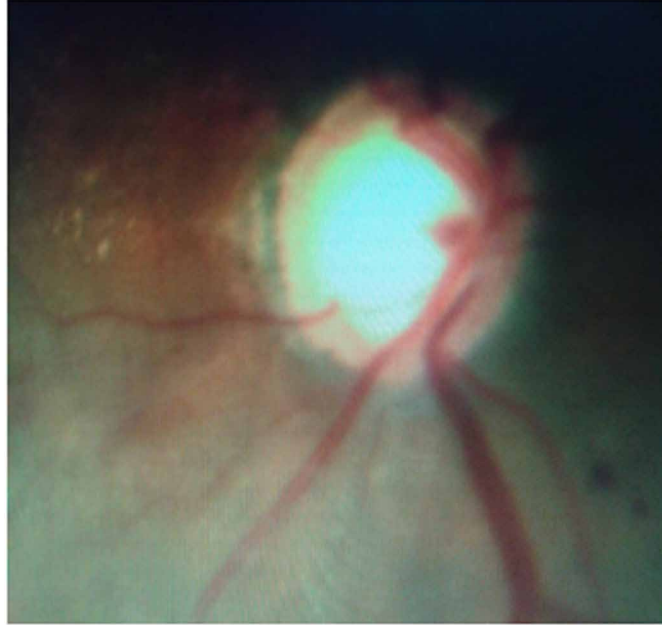
A 25-year-old female patient came to the Ophthalmology OPD for routine checkup of IOP as she was a known patient of glaucoma who had received the diagnosis prior to presenting at our facilities. She was asymptomatic.

On examination, she had visual acuity 6/6 in both eyes, clear conjunctiva, clear cornea, deep anterior chambers, normal pupils, intra-ocular pressure was 20mm Hg in both eyes on applanation tonometry, gonioscopy revealed both eyes had open angles, OD evaluation showed a vertical C:D ratio of 0.8 with superior and inferior NRR thinning in the right eye. The results from her carotid colour doppler studies were within normal limits.

She also had a history of difficulty in breathing, gastrointestinal distress, and a mild, but constant, heaviness in both eyes. On further probing, she provided a history of use of mustard oil for many years. There was a corroborative history of mass disease of swelling of feet in her village community, hence the patient was also investigated for epidemic dropsy. After initiating treatment to control IOP, the patient was referred to the Department of Medicine for further assessment and management of *Argemone* intoxication.

Case Study

Figure 1. Fundus photograph of right eye showing, VCD:0.7-0.8, nasal shifting of blood vessels along with, inferior thinning of NRR



CASE REPORTS 2, 3, AND 4

A female aged, 38 years and her two children, one boy of 12 years and a girl of 14 years, came with a history of blurring of vision in both eyes, with mild pain.

On examination, the mother had a visual acuity of 6/12, intraocular tension of 29 mm Hg in both eyes and had corneal edema; both her children had vision 6/9, intraocular tension of 22.4 mm Hg with clear cornea and normal anterior chamber both eye. OD evaluation and visual field examination was normal in mother and both the children.

The mother provided a history of similar complaints in other people of village also. On further probing, she also gave a history of chronic use of mustard oil for cooking. She was given topical antiglaucoma drugs to lower the IOP and was followed up for six months for regular measurement of IOP, OD evaluation and visual field examination.

Intraocular tension remained low even after four months of stopping antiglaucoma drugs without any disc and field changes.

DISCUSSION

Epidemic dropsy is a multi-system disease involving the cardiovascular, hepatic, renal, ocular and other systems. It is a toxic disease caused by the unintentional ingestion of *Argemone mexicana* (prickly yellow poppy) seeds as an adulterant of wheat flour, or more commonly, of cooking oil such as mustard oil.

The condition was first reported by Lyon in 1877 from Calcutta and has since occurred in other countries including the Fiji Islands, Mauritius, Madagascar, South Africa and Burma (Myanmar) (Manson-Bahr, 1982). In India, it has been reported from time to time from the States of West Bengal, Bihar, Orissa, Madhya Pradesh, Uttar Pradesh, Gujarat, Maharashtra and Delhi, (Chopra *et al*, 1935; Chopra *et al*, 1940; Lal, 1951; Shanbagh *et al*, 1968; Krishnamachari *et al*, 1972; Deodhar, 1970; Sainani *et al*, 1972; Mohan *et al*, 1984; Gomber *et al*, 1997; Gomber *et al*, 1994; Tandon *et al*, 1975) generally sparing South Indian States where the predominant cooking fat is coconut oil.

It occurs due to the use of contaminated mustard oil (with which *Argemone* oil is completely miscible) for cooking and massage (Sood *et al*, 1985). Adulteration of other types of oils (linseed, rapeseed, groundnut, and other vegetable oils) has also been reported (Gupta, 1987; Singh *et al*, 1975; Khanna *et al*, 1986).

The active toxic principle of *Argemone* oil, the alkaloid sanguinarine, is able to withstand normal cooking temperatures and hence appears to be heat stable. Sanguinarine can be retained in the gastrointestinal tract, liver, lung, kidney, heart and serum, for up to 96 hours after ingestion, due to binding to plasma proteins (Upreti *et al*, 1989; Tandon *et al*, 1993). This may lead to cumulative toxicity even with low-dose exposure over prolonged period (Chakravarty *et al*, 1951).

The incidence of glaucoma in cases of Epidemic Dropsy has been variable. In some of the epidemics, glaucoma has been dominating feature. (10 to 12% as reported by Chopra *et al*, 1940) While in other epidemics clinical findings other than glaucoma were also found (Sainani, 1976; Shanbhag, 1968; Shah, 1969).

The pathophysiology underlying the occurrence of glaucoma is still not clearly understood. Hakim (1954), in his experimental studies, found ocular changes similar to those found in chronic simple glaucoma. Sachdev MS *et al* (1988), in their study of the pathogenesis of epidemic dropsy associated glaucoma concluded that dropsy glaucoma is hypersecretory in nature; they also postulated that prostaglandin and histamine release may have significant roles in its pathogenesis.

Malik KP *et al* (2004), in their study, found that the rise of IOP in cases of epidemic dropsy appeared to be a transient phenomenon, and drugs needed to be titrated on a weekly basis. (Malik KP *et al*, 2004). Some other investigators have found that in cases of epidemic dropsy, acute visual field defects occur independent of rise of intraocular pressure and more frequently in the early stage of the disease. (Singh K *et al*, 2006)

It was also observed that the severity of Epidemic Dropsy (generalized symptoms and signs) was fairly closely related to retinal venous engorgement. Cases with mild or low grade symptoms had no venous engorgement while acute and severe type of cases showed engorgement of the retinal veins, and even hemorrhages (Rathore, 1982). Shah (1969) observed early venous congestion in 10 cases out of 67 (14.99%), probably as a part of generalized telangiectatic dilatation of capillaries without inflammatory reaction, which may be due to histamine-like action of sanguinarine hydrochloride. Papilledema has been reported in two out of 119 (1.7%) cases in a study by Sainanis *et al* (1976).

CONCLUSION

The possibility of glaucoma should be kept in mind in cases of epidemic dropsy, when members of same family, or village report with raised IOP, pedal edema, and a history of use of mustard oil for cooking or massage. Disease has self-limiting course but needs control of IOP medically till it returns to normal and visual field changes have stabilized. All cases should be followed up regularly for IOP measurement

Case Study

and visual field analysis up to 8-12 weeks because visual field defects occur independent of rise in IOP and the severity of glaucoma is independent of severity of systemic features. Hence, strict vigilance must be kept for such patient because if ignored optic atrophy may develop.

REFERENCES

- Chakravarty, N. K., & Chaudhuri, R. N. (1951). Production of epidemic dropsy in monkeys. *Indian Medical Gazette*, 86, 392–397. PMID:14897423
- Chopra, R. N., & Chaudhuri, R. N. (1935). A preliminary report on an Epidemic Dropsy outbreak in Purulia. *Indian Medical Gazette*, 70, 481–487.
- Chopra, RN, & Pasricha, CL & Banerjee. (1940). Outbreak of epidemic dropsy. *Indian Medical Gazette*, 75, 261–266.
- Deodhar, N. S. (1970). Epidemic dropsy in Poona 1959. *Maharashtra Medical Journal*, 17, 131–13.
- Gomber, S., Daral, T. S., Sharma, P. P., & Faridi, M. (1997). Resurgence of Epidemic Dropsy. *Indian Pediatrics*, 34(10), 953–957. PMID:9567567
- Gomber, S., Daral, T. S., Sharma, T. S., & Faridi, M. M. (1994). Epidemic dropsy in Trans Yamuna areas of Delhi and UP. *Indian Pediatrics*, 31, 671–67. PMID:7896391
- Gupta, Y. P. (1987). Are edible oils safe? *Scientific Reports*, 24, 501–504.
- Hakim, S. A. E. (1954). Argemone Oil, Sanguinarine, and Epidemic-Dropsy Glaucoma. *The British Journal of Ophthalmology*, 38(4), 193–216. doi:10.1136/bjo.38.4.193 PMID:13149763
- Khanna, S. K., Upreti, K. K., & Singh, G. B. (1986). Trend of adulteration of mustard oil in rural markets of Uttar Pradesh. *Sci Cult*, 52, 149–156.
- Krishnamachari, K. A. V. R., & Satyanarayan, K. (1972). Epidemic dropsy in Andhra Pradesh. *The Indian Journal of Medical Research*, 60, 741–746. PMID:4663243
- Lal, S. B. (1951). Epidemic dropsy in Bihar. *Indian Medical Gazette*, 86, 6. PMID:14850133
- Malik KP, Dadeya S, Gupta VS, Sharan P, Guliani & Dhawan M. (2004, Jul 34), Pattern of intraocular pressure in epidemic dropsy in India; *Trop Doct*. 3:161-2.
- Manson-Bahr. (1982) Plant poisons. *Manson's Tropical diseases* (Bailliere, Tindall and Cassell Ltd, London), 16th edn. pp 571–572
- Mohan, M., Sachdev, H. P., Daral, T. S., Sachdev, M. S., & Bhargava, S. K. (1984). Epidemic dropsy in Delhi. *Indian Pediatrics*, 21, 241–247. PMID:6490146
- Mohan, M., Sood, N. N., Dayal, N., Sachdeva, M. S., Chandrashekhar, G., & Gupta, M. S. (1984). Ocular and clinic epidemiological study of epidemic dropsy. *The Indian Journal of Medical Research*, 80, 449–456. PMID:6532956

Rathore, M. K. (1982). Ophthalmological study of epidemic dropsy. *The British Journal of Ophthalmology*, 66(9), 573–575. doi:10.1136/bjo.66.9.573 PMID:7104277

Rathore, M. K. (1982). Ocular manifestations of epidemic dropsy. *Indian J Ophthalmol*, 307-309.

Sachdev, M. S., Sood, N. N., Verma, L. K., Gupta, S. K., & Jaffery, N. F. (1988). Pathogenesis of epidemic dropsy glaucoma. *Archives of Ophthalmology*, 106(9), 1221–1223. doi:10.1001/archophth.1988.01060140381037 PMID:3415547

Sainani, G. S. (1976), Epidemic Dropsy. Progress in Clinical Medicine in India, Edited by M.M.S. Ahuja, Arnold Heinemann, Publishers, India) P.P. 92-98.

Sainani, G. S., Rajkondawar, V. L., Wechalekar, M. D., & Wechalekar, D. L. (1972). Epidemic dropsy in Chandanpur (Maharashtra). *The Journal of the Association of Physicians of India*, 20, 301–307. PMID:5026518

Shah, M. J. (1969).. *The Indian Journal of Medical Research*, 57, 1878. PMID:5372173

Shanbagh, V. V., Jha, S., Kekre, M. S., & Rindani, G. J. (1968). Epidemic dropsy in Bombay city suburbs. *The Indian Journal of Medical Research*, 22, 226–236. PMID:5668633

Sharma, B. D., Malhotra, S., & Rathee, M. (1999). Epidemic dropsy in India. *Postgraduate Medical Journal*, 75, 657–661.

Singh, G. B., Khanna, S. K., & Singh, S. B. (1975). Extent of adulteration in Vanaspati oils, ghee and butter. *Oil & Oilseeds J*, 27, 13–20.

Singh K, Singh MJ & Das JC. (2006), Visual field defects in epidemic dropsy, *Clin Toxicol (Phila)*, 44(2):159- 63.

Sood, N. N., Sachdev, M. S., Mohan, M., Gupta, S. K., & Sachdev, H. P. S. (1985). Epidemic dropsy following transcutaneous absorption of Argemone mexicana oil. *Transactions of the Royal Society of Tropical Medicine and Hygiene*, 79(4), 510–512. doi:10.1016/0035-9203(85)90079-3 PMID:4082260

Tandon, R. K., Singh, D. S., Arora, R. R., Lal, P., & Tandon, B. N. (1975). Epidemic dropsy in New Delhi. *The American Journal of Clinical Nutrition*, 28, 883–888. PMID:1146749

Tandon, S., Das, M., & Khanna, S. K. (1993). Biometabolic elimination and organ retention profile of Argemone alkaloid, sanguinarine, in rats and guinea pigs. *Drug Metabolism and Disposition: the Biological Fate of Chemicals*, 21, 194–197. PMID:8095219

Upreti, K. K., Das, M., Kumar, A., Singh, G. B., & Khanna, S. K. (1989). Biochemical toxicology of Argemone oil: Short term oral feeding response in rats. *Toxicology*, 58(3), 285–298. doi:10.1016/0300-483X(89)90142-X PMID:2799830

This research was previously published in the International Journal of User-Driven Healthcare (IJUDH), 4(3); edited by Ashok Kumar Biswas, pages 31-37, copyright year 2014 by IGI Publishing (an imprint of IGI Global).

Chapter 14

Human Health Diagnosis System Based on Iris Features

Poonguzhali N

Pondicherry Engineering College, India

M. Ezhilarasan

Pondicherry Engineering College, India

R. Hariharan

Pondicherry Engineering College, India

N. Praveen Devaraajan

Pondicherry Engineering College, India

ABSTRACT

Iris feature has been used in authentication systems in many real time applications and is proved to provide high accuracy. Apart from authentication iris features can also be used for detecting pathological changes in human body and diagnose human health. The present study analyses the relationship between human iris anatomy and their health, as it is proved that changes in human health condition reflects the iris. Basically, in authentication system iris texture features are used for identification, in the proposed work iris texture and geometric features can also be deployed in diagnosing human health. The texture features present in the human iris are extracted using the mathematical statistical measure which is used to specify the characteristics of the texture of an image using gray-level co-occurrence matrix. The iris and pupil are extracted and correlated to the compactness features of the circle. Based on the comparison the system enables in prediction of abnormalities in the iris texture and identifies the affected person.

INTRODUCTION

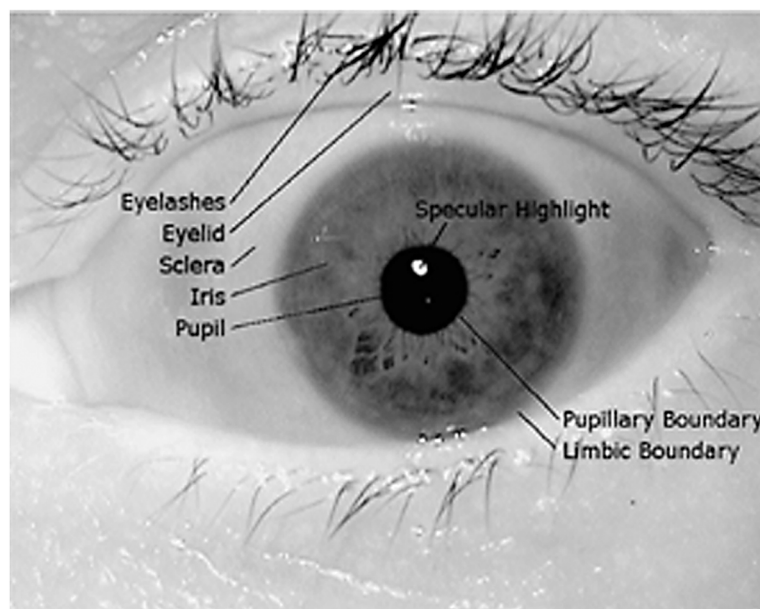
A biometric system inculcates automatic recognition of a person on the basis of some characteristic or unique feature possessed by the individual, on whom some identification processes are carried out (Wildes 1997). There are various types of biometric system, which are based on hand geometry, handwriting, facial features, fingerprints, voice, retina, iris (Sanderson & Erbetta 2000). Iris biometric is said to be

DOI: 10.4018/978-1-5225-5195-9.ch014

the feature that is highly unique and accurate, so the chances of any two individuals having the similar characteristic will be minimal and it will never change during one's life time. The current state-of-art of iris technologies in biometric are used for recognition system. This study is an attempt on iris biometric trait for the prediction of diseases or pathological organs in human body. In early days, iridology was a branch of science for iris diagnosis of human anatomy and used to diagnose disease based on manual investigation of iris texture pattern. Hence the system is automated using image processing techniques. The iris biometrics was generally used for authentication purpose, but in this paper, the approach is towards using the iris biometrics as a means for iris diagnosis. The iris is an annular part between the pupil and sclera, which is externally visible in an eye as shown in Figure 1.

Iris consists of two parts, the inner part is the pupillary zone and the outer part is the ciliary zone, which are divided by a zigzag pattern region called collarette (Adler, 1965). These characteristic features make it very useful for identifying the individuals (Daugman, 1994), (Boles & Boashash 1998). Image processing techniques can be implemented to bring out the discreet iris pattern and to encode them into a biometric template. The biometric template is later stored in a database. This template of the biometric consists of quiet a few mathematical representation of the uniqueness of the iris, and allows comparisons to be done between templates. When an individual is to be identified by an iris biometric recognition system, the input human eye image is captured using sensors and a template is created for the iris region of the eye. This template is subjected to comparison with other templates, which are previously stored and either a matching is found, on identifying a person or a matching is note found. Iris recognitions is generally considered as the most unique, reliable and high accuracy form of biometric technology, compared to finger prints, voice, face and other form of recognitions. The iris biometric system is said to undergo various processing techniques of image processing such as segmentation, normalisation, encoding and matching.

Figure 1. Iris regional boundaries



In the embryonic stage of development, the first cells to form are the neurons (Wolff, 1976), (the basic cell of the brain and all the nervous system). The eye which starts as part of the brain, then get detached from the brain and is connected to the brain by the optic nerve, (bundle of millions of neurons), blood vessels and other tissues. Any changes that occur in the body will be reflected in the iris. The iris is made of muscles, nerve endings and other tissues. The nerve fibers in the iris as well as other tissues respond to changes in the body tissues by manifesting a reflex physiology that corresponds to the specific tissue changes and locations. This will manifest itself in changes in colour in certain parts of the iris. The weave of the muscular structure of the iris, can get retracted or atrophied (loss of thickness due to lack of blood & nerve supply) in certain areas, which will correspond or reflect the condition of certain organs in the body, as shown in Figure 2.

The proposed work is based on the texture pattern of the iris region in the eye, where the Bernard Jensen's iridology chart is being used to check for the possible pathological changes in the organ. The Bernard Jensen's chart (Jensen, 1980) is shown in Figure 3. Iridology is a branch of science, particularly health science which can describe about the disturbances in the organs inside a human body, it can identify which organ is affected and it can also reveal about the progress of such disturbances. In this science, it's about analysing the signs and fibre colours in the eye, which leads to the pathological changes in the organ. When the eye is observed under the magnifying instrument, one can clearly see that it is a splash of non-uniform colours, having various shapes and flaws, patterns, markings, etc., which gives a message about the organs and its functions. Similar to how computer stores information about various things, the iris also receives and stores the information about the whole human body. It is a receptor of all the signals from the body and imprints it in itself. The iris, which is also said to be a constituent of the nervous system, has thousands of nerve endings and impulses on it, which receive them from the rest of the body.

The paper is structured as follows. In Section 2, the related work is presented. The Section 3 reveals the image processing technique used for feature extraction. Section 4 deals with the inference obtained from the Bernard Jensen's Chart with regards to texture features. Section 5 depicts the experiment results on processing the real time database. Finally in Section 6, the conclusion for the proposed work in presented.

Figure 2. Anatomy of iris: top view (left); cross-section view (right)

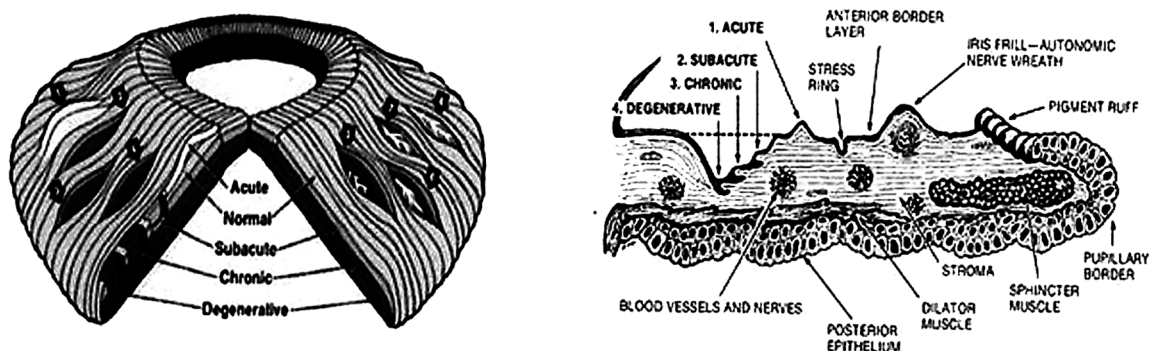
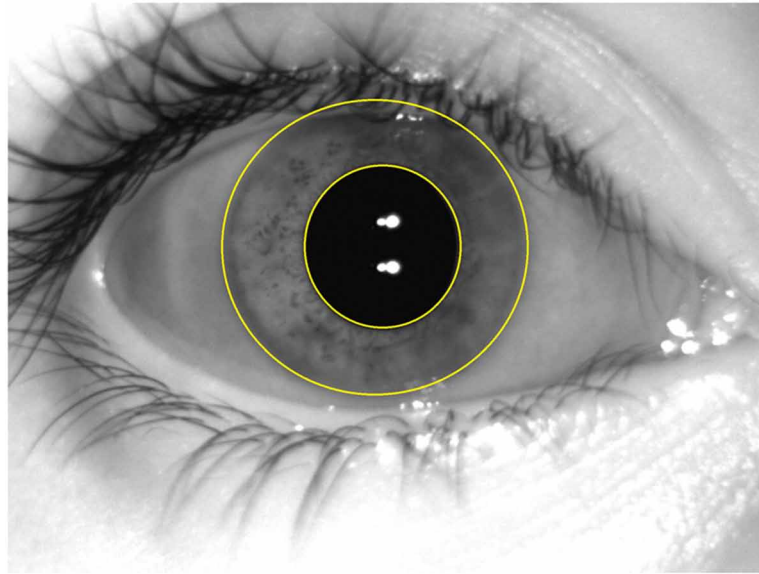


Figure 3. Iridology chart



RELATED WORK

The patterns in iris are generally used for identification of individuals. There exist several methods for the analysis of iris patterns; the proposed system is concerned towards texture based analysis methods (Li Ma, Tieniu Tan, Yunhong Wang & Dexin Zhang, 2003). In history, the iridology was first formulated by Dr. Ignatz Von Peczely. Iridology is a comfortable and convenient approach for patients towards medical diagnosis as it involves no pain and its precision is quiet high. In another work, the iris detection system has been built to facilitate the users, who are not familiar to the software. In this, (Lodin, 2009) has proposed to improvise the previously mentioned work to create a semi automated system. In (Ramlee & Ranjit, 2009), a system was developed to detect the cholesterol level present in the human body. Their work was based on recognize alimentary canal disease and nerve system. To detect chronic diseases such as bronchitis, erectile dysfunctions and brain dysfunction has been developed, in which the iris image in normalized using pseudo-polar coordinate system and the filter used here is Gaussian in vertical direction with which thinning algorithm is used to eliminate useless profiles by thinning the obtained binary image from the converted original image.

Diagnosis of diabetes mellitus has been proposed in (Wibawa & Purnomo, 2006), where procedures for finding the pancreas region in iris have been developed. The input iris image was transformed to gray level and filters were applied. Detection of iris was done using a novel case-based object recognition and case mining method. To obtain accurate iris image, a new method called water flow method have been incorporated in (Othman & Prabuwno, 2010). In this method new technique of segmentation in iris recognition was used to overcome the problem of noting down or considering the density of iris, its colour, the location of body organ in iris image and sign on iris image.

An eye detection system was proposed to provide the an reliable diagnosis clues about the patient based on the pupil. The algorithm detects the pupil and based on the change in the pupil size and pupillary response to light the system was deployed (Yan & Zhang, 2011). The gabor features extracted from

iris code is used to diagnosis diabetic in an individual (Durga devi & Preethi, 2014) and was able to detect ophthalmic disease like corneal oedema, iridotomies and conjunctivitis. SVM technique had been proposed to detect diabetics in human from the iris image. The experimental results has been compared with the traditional iridology system and proved that existing iris recognition algorithm can be used to detect the disease (More & pergad 2015). An accurate diabetes detection method based on the broken tissues in the iris was primarily analysed. As a next step with the reference of iridology chart the change of color in the pancreases region has been detected and classification was performed using artificial neural network. (Jamal Firmat Banzi & Zhaojun Xue, 2015). A computer aided design is proposed to enable as an screening level for medical practinoer based on the ocular region of the human eye (Ramlee et al., 2015).

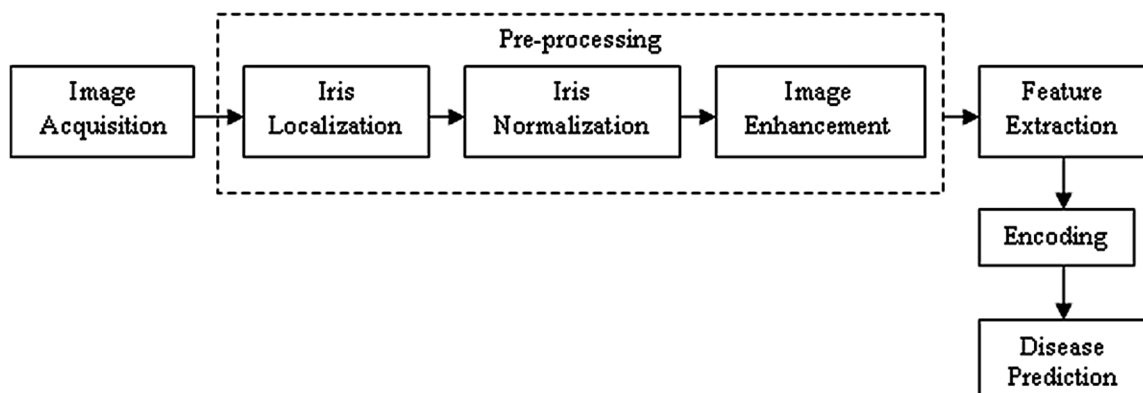
In (Haralick, 1973) has defined various textural features, based on his work. Specify an array of offsets to the gray co-matrix function to create multiple GLCMs, whose offsets can define pixel relationships of varying distance and direction. The statistics are manipulated from these GLCMs for the input images. A threshold value is fixed by taking the difference of the images in the database with input images.

TEXTURE FEATURE EXTRACTION

The proposed system is developed to ease the work of medical practitioners to automatically diagnose the patient, as medical images are quiet difficult to be analysed manually. The efforts of iris detection algorithms have been a great help to iridology practitioners to obtain accuracy in detecting changes in a person's iris. The modules in the proposed system are image acquisition, image pre-processing, feature extraction, feature encoding and disease prediction as shown in Figure 4.

The block diagram describes how the given input image is processed at each stage and how it is used for the next computational event. The first process is image acquisition where obtaining of eye images are discussed. The second part is the process of extraction of required region i.e. the iris from the whole obtained eye image. The third part is the conversion of the region of iris to required specifications for computational texture analysis. The final module is the process of analysing the texture features and the inference is obtained from the results of the analysis. In the data flow of this model, where the initial

Figure 4. Block diagram of the proposed work



input is raw image and conversion of the raw image into various forms in the intermediate modules and the final arrival of inference of disease prediction as shown in Figure 5.

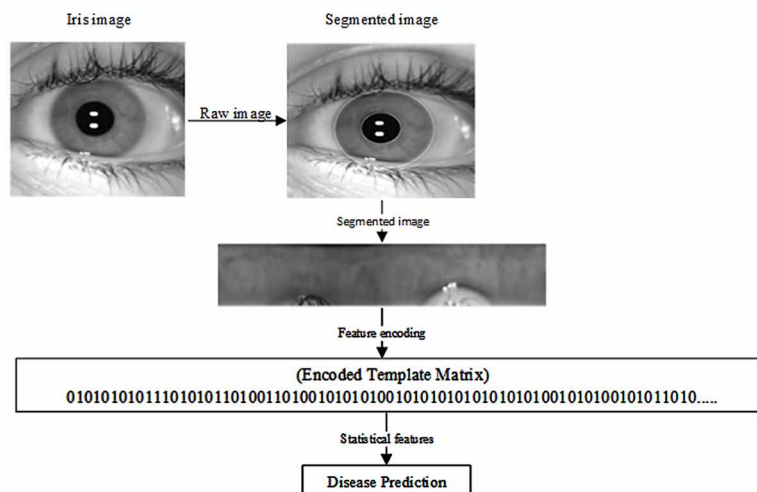
Image Acquisition

The image acquisition is the process to capture a pair of iris images from the subject using a specifically designed sensor. One of the major hurdles for practical applications is getting iris images, of extremely fair quality. As the iris is very small (diameter is about 1 cm), it shows numerous and variable texture features under near infrared lighting. The lighting, the positioning, and the physical capture of the system are the three main aspects one should consider when designing an image acquisition environment. Usually sequence of images is obtained rather than a single image, while capturing the eye images. Unfortunately, not all images captured are clear and sharp enough for further processing. The image may be out of focus or may contain many noticeable disturbing or overlapping lines, especially in regions close to the boundary, caused by eye motion, or severe occlusions by eyelids and eyelashes. Therefore, it is necessary to acquire a suitable image of high quality from an input sequence before it is used for processing in the forthcoming steps. Assessment of the image quality is a necessary factor as it affects the recognition accuracy of the obtained image. The subject has to be positioned in an appropriate place in the focal plane, if the subject moves during acquisition; a motion blurred image will result. When the subject opens his eye partially, the resulting image contains little useful information.

Image Pre-Processing

An iris image contains not only the region of interest (iris) but also some “unuseful” parts (e.g., eyelid, eyelashes and pupil). A change in the camera-to-eye distance may also result in variations in the size of the same iris. Furthermore, the brightness is not uniformly distributed because of non-uniform illumination. Therefore, before feature extraction, the original image needs to be pre-processed to localize iris, normalize iris, and reduce the influence of the factors mentioned above. Such pre-processing is detailed

Figure 5. Architecture of the proposed system



in the following subsections. The iris is an intermediate part between the ‘sclera’, which is said to be the outer boundary and the ‘pupil’, said to be the inner boundary. Both the outer and the inner boundary of an iris can be approximately taken as circle.

Iris Localization

The main aim of the process of localization is to segment the iris region from the rest of the image of eyes. There are different approaches in iris image pre-processing such as Daugman Integro-Differential Operator (Libor, 2003), (Widles & Asmuth, 1994) and Active Contours Model (Kass, Witkin & Terzopoulos, 1987). The localization process begins with the process of edge detection.

Canny Edge Detection

Edge detection of an image is defined as identifying points in a digital image at which the image brightness changes sharply or more formally, has discontinuities. The points at which image brightness changes sharply are typically organized into a set of curved line segments termed edges. These edges in this context refer to the edges of iris and pupil region. There are several methods in edge detections, one of the most suitable and efficient one, used in this work is the Canny’s Edge Detection algorithm, has the following Steps:

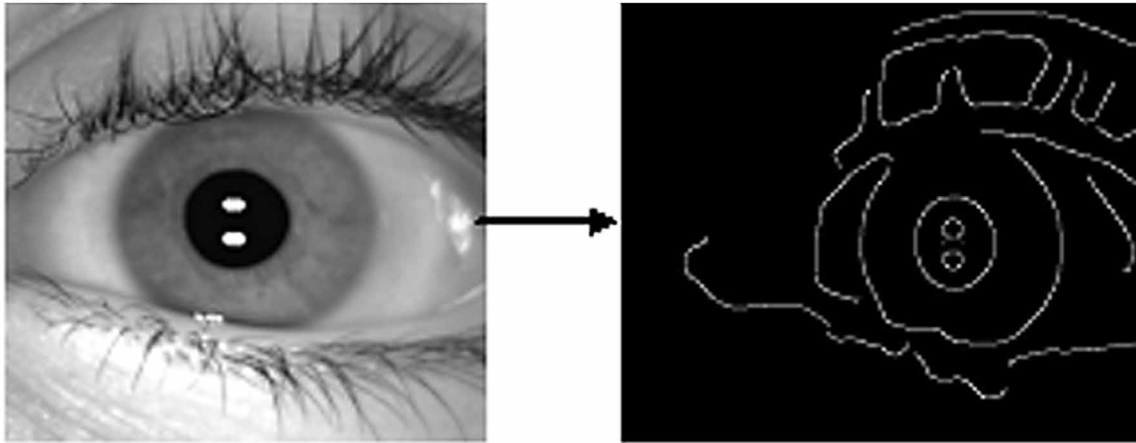
1. **Smoothing:** Smooth the image with a Gaussian filter
2. **Finding Gradients:** Compute the gradient magnitude and orientation using finite-difference approximations for the partial derivatives.
3. **Non-Maximum Suppression:** It is to convert the blurred edges in the image of the gradient magnitudes to make sharp edges.
4. **Double Thresholding:** The edge-pixels remaining after the non-maximum suppression step are marked with their strength pixel-by-pixel.
5. **Edge Tracking by Hysteresis:** Strong edges are interpreted as “certain edges”, and can directly be included in the final edge image. Weak edges are included if and only if they are connected to strong edges.

The maximum value of first derivative also corresponds to the minimum of the first derivative. In other words, both points with dramatic change of gray-scale (strong edge) and points with slight change of grayscale correspond to the second derivative zero-crossing point. Thus these two thresholds are used to detect strong edges and weak edges. Canny algorithm is not susceptible to noise interference enables its ability to detect true weak edges. It’s an optimal edge detection algorithm. Figure 6 illustrates how Canny edge detection algorithm gives a binary threshold of image as output after edge detection.

Hough Transform

Parameters pertaining to simple geometric objects, present in an image such as circles, lines, etc., can be found out using a standard image processing algorithm called Hough Transform. The centre and radius of the pupil can be deduced from an iris region using circular Hough Transform. In doing this edge detection stage, Wildes et al. (1994) bias the obtained derivatives in the vertical orientation for finding the

Figure 6. Canny edge of iris image



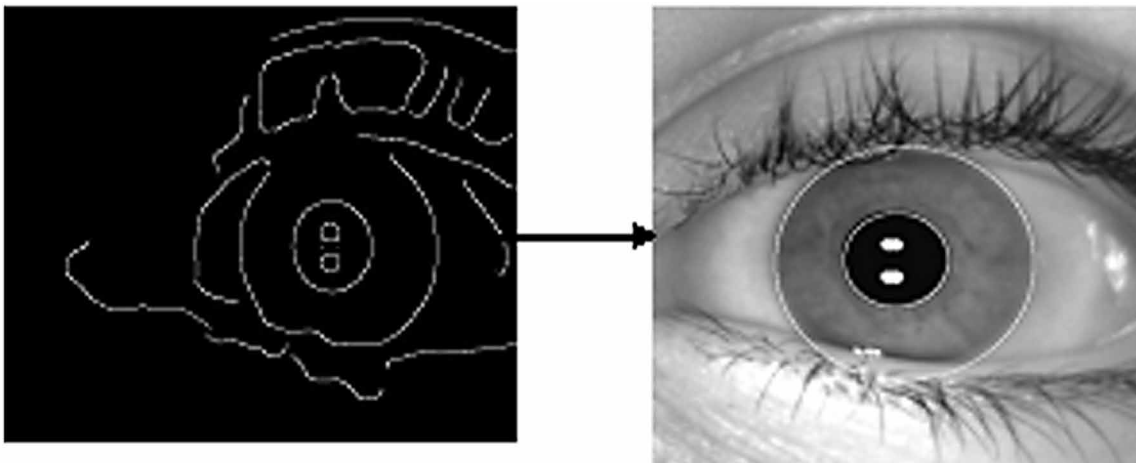
outer circular boundary of the iris and in the horizontal orientation for detecting the eyelids. The reason for this is that the eyelids are normally aligned in the horizontal orientation and also the eyelid map will affect the circular boundary in the iris edge map, if one uses all the gradient data.

On considering only the vertical gradients for locating the iris boundary will minimise the influence of the eyelids when carrying out the circular Hough transform and not all the edge pixels are required. This makes it more efficient as well as accurate as only less edge points are used. The processes of Hough transform are illustrated, as shown below, in the Figure 7.

Iris Normalization

Various factors affect the size of the iris during acquisition. So compensating for iris deformation is a necessary factor for which Daugman found out a solution by projecting the iris image into a doubly

Figure 7. Circular Hough transform



dimensionless pseudo polar coordinate system other than in a Cartesian coordinate system. This normalises iris of different size, to be the same as it represents the parameters in a fixed interval. And in a similar manner the image can be unwrapped in counter clockwise direction, from a circular ring into rectangular block of fixed size m , which is denoted as,

$$I_n(X, Y) = I_o(x, y) \quad (1)$$

$$x = x_p(\theta) + (x_i(\theta) - x_p(\theta)) \frac{Y}{M} \quad (2)$$

$$y = y_p(\theta) + (y_i(\theta) - y_p(\theta)) \frac{Y}{M} \quad (3)$$

$$\theta = 2\pi \frac{X}{N} \quad (4)$$

where I_n is an $M \times N$ (64 x 512 in our experiments) normalized image, and $(x_p(\theta), y_p(\theta))$ are the coordinates of the inner and outer boundary points in the direction θ in the original image I_o .

This simplifies the subsequent processing of the iris image, which reduces the iris distortion to a great extent. In spatial domain, some particular filters such as Gabor filters are used to extract information of an image of certain geometric orientation and can be scaled.

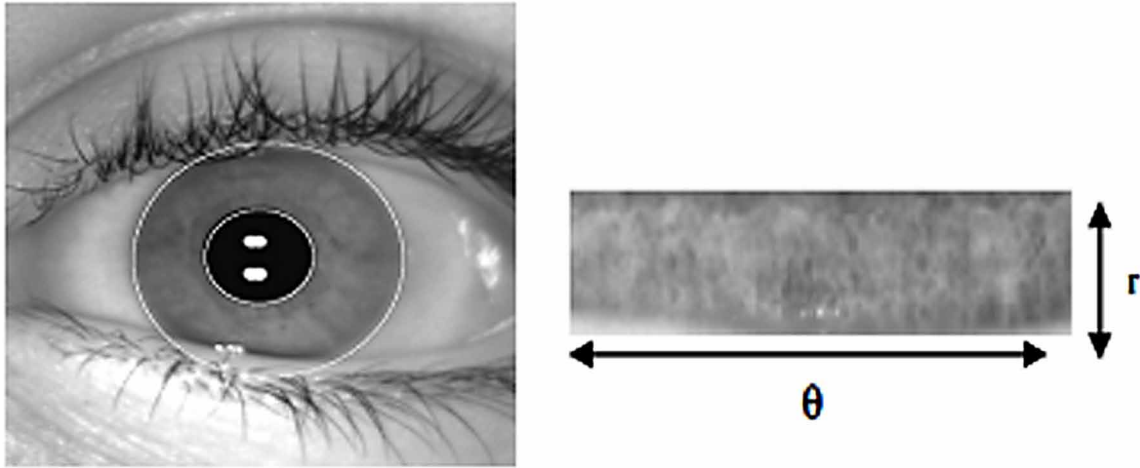
The process of Daugman Rubber-sheet model is illustrated in Figure 8, where we transform the iris which appears like a circular ring, into rectangular block.

Image Enhancement

For texture analysis methods, Gabor filters are widely used and its elementary functions are oriented from complex sinusoidal functions of Gaussian modulations. New spatial filters can be defined according to the characteristics of iris texture. The difference between a defined filter and Gabor filter lies in the modulating sinusoidal function and their kernels as given below (even symmetric Gabor filters are used here),

$$G(x, y, f) = \frac{1}{2\pi\delta_x\delta_y} \exp\left[-\frac{1}{2}\left(\frac{x^2}{\delta_x^2} + \frac{y^2}{\delta_y^2}\right)\right] M_i(x, y, f); i=1, 2. \quad (5)$$

Figure 8. Daugman rubber-sheet model



$$M_1(x, y, f) = \cos \left[2\pi f \left(\sqrt{x^2 + y^2} \right) \right], \quad (6)$$

$$M_2(x, y, f) = \cos \left[2\pi f (x \cos \theta + y \sin \theta) \right]. \quad (7)$$

Due to positioning of light source, the normalized image has a low contrast and non-uniform brightness, and all these may have a negative impact on further processing in matching and feature extraction. It is first started by approximating the intensity of variations in the image so that a more well spread texture image can be obtained.

The mathematical mean of every 8 x 8 small blocks gives a rough estimate of the illumination in the background, which can be further expanded by bicubic interpolation of the normalized image. By subtracting the normalized image to compensate for various lighting conditions after which the enhancement could be done. After the above process the corrected image undergoes histogram equalization in every 16 x 16 regional blocks. This contributes for improving the contrast of the image.

Figure 9 shows the histogram equalization before enhancement and Figure 10 shows the histogram equalization after enhancement.

Iris Texture Feature Extraction

The iris has a particularly interesting structure and provides abundant texture information. So, it is desirable to explore representation methods which can capture local underlying information in an iris. From the viewpoint of texture analysis, local spatial patterns in an iris mainly involve frequency and orientation information. Generally, the iris details are spread along the radial direction in the original image corresponding to the vertical direction in the normalized image. As a result, the differences of orientation information among iris not seem to be significant. That is, frequency information should account for the major differences of iris from different people. We thus propose a scheme to capture

Figure 9. Iris enhanced rubber-sheet image and its histogram

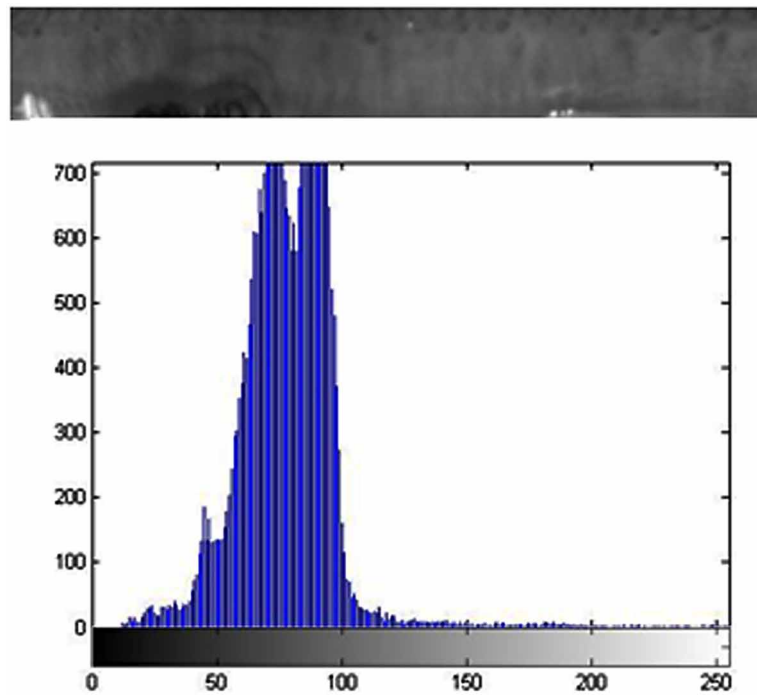
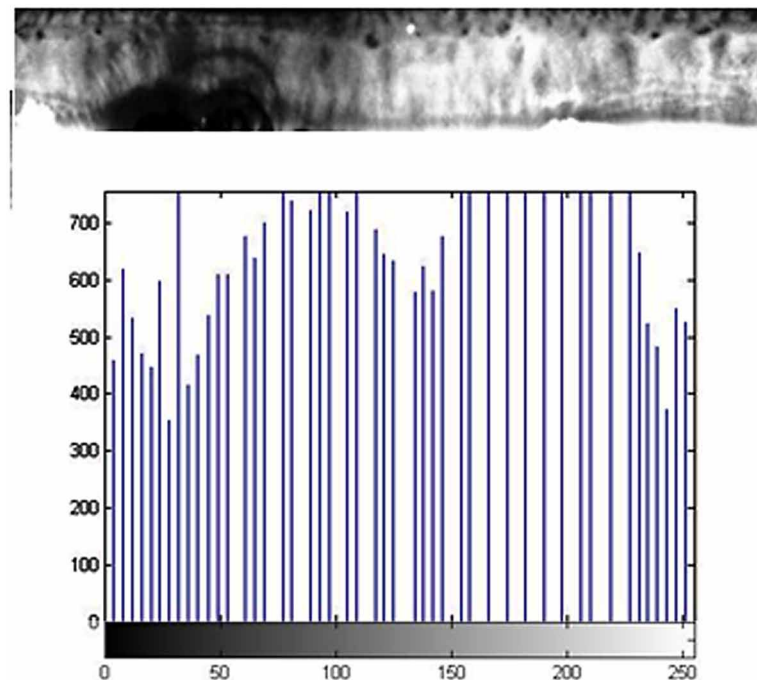


Figure 10. Image enhancement process



such discriminating frequency information which reflects the local structure of the iris. In general, the majority of useful information of the iris is in a frequency band of about three octaves. Therefore, a bank of filters is constructed to reliably acquire such information in the spatial domain. As we know, coefficients of the filtered image effectively indicate the frequency distribution of an image.

This is implemented by refining the normalised iris pattern with 1D Log-Gabor wavelets. The 2D normalised patterns are spliced into a number of 1D signals and then these 1D are mixed with 1D Gabor wavelets. The rows in the 2D normalised pattern are considered as 1D signal. Each row corresponding to a circular ring on the iris region and instead of considering the radial direction the angular one is considered, which depicts to the columns of the normalised pattern because the maximum independence happens in the angular direction only. The average intensity of surrounding pixels is used instead of the intensity values at known noise areas in the normalised pattern in order to prevent the contribution of noise in the filtering output. After this, the output of filtering is phase quantised to four levels by the use of the filter, giving two bits of data for each phase. The output obtained here is a gray code, so that only one bit changes when going from one quadrant to another, which will in turn minimise the number of bits, not coming into the picture.

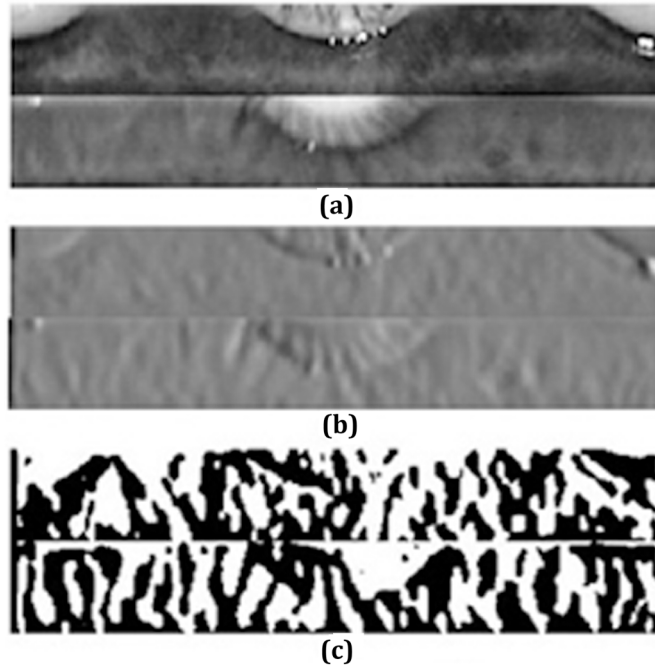
The process of encoding gives a bitwise template having information of number of bits, and an equivalent noise mask which implies to corrupt regions inside the iris pattern, and marks the bits in the template as corrupt. These regions where amplitude is zero are also marked in the noise mask, since the phase information will be meaningless. The total number of bits in the template will be the angular resolution times the radial resolution, times 2, times the number of filters used. Two statistic values are thus extracted from each small region in the filtered image to represent local texture information of the iris. A feature vector is an ordered collection of all features from the local regions.

Gray Level Co-Occurrence Matrix (GLCM)

In the proposed method the mathematical statistical measure, is used to specify the characteristics of the texture of an image using GLCM (gray-level co-occurrence matrix), also known as the gray-level spatial dependence matrix (Sarvesh, 2005). This method calculates the frequency of the occurrence of pairs of pixel, with specific values and in a specified spatial relationship and then by extracting the statistical measures from this matrix. Spatial relationship is known as the pixel of interest and the pixel to its horizontally adjacent (immediate) right, but one can specify the other relationships between the two pixels. Each and every element (i, j) in the resultant GLCM is the ratio of sum of the number of times the pixel with ' i ' value occurred in the spatial relationship to the pixel value ' j ' in the input image.

At first, the dynamic scale range of the given image is brought down to reduce the number of intensity values. The size of the GLCM determines the number of gray levels. The certain properties about the spatial distribution of the gray levels in the texture image can be determined from the gray-level co-occurrence matrix. For instance, if many entries in the GLCM are intensified along the diagonal, then the texture is coarse in the specified offset. But, a single GLCM may not be enough to depict the textural features of the input image. For instance, gray co-matrix can create multiple GLCMs for a single input image, if a single horizontal offset might not be sensitive to texture with a vertical orientation. After the process of feature encoding, the process of computation and analysis of the obtained gray-scale co-occurrence matrix is done. As a process of encoding, using the Gabor filter, the image matrix has been converted as a grayscale co-occurrence matrix with which further computations are to be done.

Figure 11. a) Normal iris image b) Iris image with filter applied c) Iris image after threshold



In our approach the original masked image is resized to [256, 256] shown in Figure 11 below and then obtaining features by using GLCM.

The original encoded iris image is 64 x 512 pixels. In iris based disease prediction system the whole part of iris has its importance as each part points to a particular region of human body. In such a case, occlusions affect at a higher rate of efficiency in disease prediction. These images often occur in a captured sequence since the eye is in the state of continual motion and non-invasive image acquisition also requires users to adjust their position (hence, body motion). In the proposed study an analysis is made on the pupillary region of iris. This region of iris is related to gastro intestinal tract. Hence the first 8 rows of the grayscale co-occurrence matrix are taken as this particular part represents the pupillary region. The first process of computation is to extract the 8 x 512 matrix from the 64 x 512 co-occurrence matrix.

After the separation of this part, the texture feature analysis is made with the gray level co-occurrence matrix. The first order gray level histogram represents the probability of occurrence of gray levels in an image (Kramer & Aghdasi, 1999). A gray level co-occurrence matrix is considered to measure the second order histogram as it considers gray level distributions of pairs of pixels in each direction (Tuceryan and Jain, 1993). The gray level co-occurrence matrix is defined as $H(x, y, d)$, where H represents the matrix computing the frequency of occurrence of all pairs of gray level values (i, j) , with i and j in $[0, 255]$, separated by a distance ' d ' (dx, dy) in direction ' θ '. That is, in a co-occurrence matrix the element (i, j) represents the number of pixel pairs in the image separated by a distance ' d ' in a direction such that the intensity of the first pixel is i and that of the second pixel is j . There is no criteria to select the distance ' d '. This results in a number of sparse co-occurrence matrices for different combinations of the distance value. These matrices do provide some amount of information on the spatial dis-

tribution of gray levels with respect to the displacement ‘ d ’ and direction ‘ θ ’. For example if the diagonal of a co-occurrence matrix with displacement ‘ d ’ is concentrated then the texture is coarse in direction. But these matrices are not used directly to analyze texture. Many textural features can be computed from these matrices.

The statistical parameters of texture features that can be derived for GLCM are energy, entropy, contrast, homogeneity and correlation. These features can be used in isolation, or combinations classification.

In the proposed work, the following are statistical features used. The following are the formulas used to compute certain textural features from the co-occurrence matrix $M(i, j)$ where μ_x, μ_y, σ_x and σ_y are the means and standard deviations of $M(x)$ and $M(y)$ where,

$$M(x) = \sum_i (x, j) \quad (8)$$

$$M(y) = \sum_i (y, i) \quad (9)$$

1. **Energy:** Energy provides the sum of squared elements in the GLCM.

$$Energy = \sum_i \sum_j M^2(i, j) \quad (10)$$

2. **Entropy:** Entropy is high when the elements of GLCM have relatively equal values. Low when the elements are closer to either 0 or 1.

$$Entropy = \sum_i \sum_j M(i, j) \log M(i, j) \quad (11)$$

3. **Contrast:** Contrast measures the local variations in the gray-level co-occurrence matrix.

$$Contrast = \sum_i \sum_j M(i, j)^2 M(i, j) \quad (12)$$

4. **Homogeneity:** Homogeneity measures the closeness of the distribution of elements in the GLCM to the GLCM diagonal.

$$Homogeneity = \sum_i \sum_j \frac{M(i, j)}{1 + |i - j|} \quad (13)$$

5. **Correlation:** Correlation metrics use the intensity-based methods to compare intensity patterns in images.

$$Correlation = \frac{\sum_i \sum_j (i - \mu_x)(j - \mu_y)M(i, j)}{\sigma_x \sigma_y} \quad (14)$$

INFERENCES OF TEXTURE FEATURE ANALYSIS BASED ON BERNARD JENSEN'S CHART

By analysing the texture features of the iris templates of the images, the first process of computation was made with the whole dataset available. There were several factors which were influencing the process of computation. As this process is a diagnosis based approach, real datasets are needed to check the efficiency of the system.

The first process was to obtain the data values of the texture features of the iris pairs, followed my special examination of the abnormal iris which were marked during the process of data collection. Before the application of texture features, the exhaustive study over Bernard Jensen's chart was done for computation of the texture features. The first eight rows of the iris encoded image denote the pupillary region of iris which has been inferred from proper examination of Bernard Jensen's Chart.

According to the chart the pupillary are is correlated with some of the gastro intestinal diseases. The following abnormalities are based on the chart:

- **Central Toxemia:** Orange/brown around the pupil. This condition prohibits efficient digestion and ability to absorb nutrients as toxic environment leads to lethargy. This is caused by junk food, medications especially antibiotics killing of friendly bacteria, negative emotions, anger, and depression. The liver, which filters the accumulated toxins, will be under stress. Flatulence and lethargy are the common symptoms.
- **Hyperacidity:** Silverfish/white ring immediately around the pupil that comes from consumption of acid-forming food/stress. Often leads to hypo acidity and the symptoms may include indigestion, heartburn and ulcers.
- **Hypo-Acidity:** Brown/black ring, in this case there is a difficulty in absorbing acid-forming food and a simple diet is required to put as little stresses possible on the digestive process in the stomach. The most common symptom includes indigestion.
- **Spastic Colon:** Happens when the colon has lost its tone and miss-shapen causing erratic bowel movements. It builds over the years caused by stress, diet of refined white flour and symptoms may include inability to maintain the peristaltic movement.
- **Tight Colon:** Tension in the walls, the colon squeezes and narrows the area through which the feces moves leading to constipation. Causes may include refined/spiced food. Constipation is the most common symptom.

- **Ballooned Colon:** Loss of tone and strength leading to sluggish bowel movement. The hormonal glands which lie directly outside the ANW (Autonomic Nervous Wryth) are also affected. Symptoms include constipation, flatulence and bloatedness.
- **Pancreas:** In case of under-functioning sugars and protein-rich foods will add strain.

Bowel pockets/Diverticulae may be caused by old fecal matter stuck in the inner wall of the intestines because of sluggish bowel movements. Signs include black/dark brown holes or pockets inside the ANW. Impactions in the ascending colon may create a reaction in the liver, breast or lungs. The most common symptom includes irritable bowels. The main digestive organs are Liver/Gall bladder/Pancreas. Toxicity is caused by high fat diet sugars, alcohol, drugs, medicines, anger frustration and other toxicity in the body leading to under-functioning liver (incapable to filtrate the toxins). Gall bladder is affected by high saturated fats, chocolates, cheeses, meat creams etc.

EXPERIMENTAL RESULTS AND ANALYSIS

The proposed work is experimented with real time database. In real time dataset, iris scanners were used where around eyes of 150 subjects of age group 19-25 years were scanned (300 iris). The subjects were engineering under graduate students. During image acquisition the student were orally enquired about their health condition and was noted. Iris of subjects who reported about their problems in health was set as the test cases and the rest of the data were the training set. The data base consists of 150 subjects of which 110 was test set and 40 was training set. The iris image is acquired using a Moblie-Eyes™ sensor which is a product of L-1 Identify Solution. The images are captured under near infra-red (NIR) illumination. It captures 752 x 480 wide SVGA images. The image capture rate is 30 frames per second. The device is a dual-iris enrolment i.e., both the left and right eyes are auto captured simultaneously. It operates in bright sunlight as well as in dark operating environment. The scanned image is stored in .PNG file format and the resolution of the image is set as 640 x 480. The sensors operate on Iris Analysis Software SDK which has image segmentation module, encoding module, image assessment scoring module and focus measure module. The scanners are kept at about 5 cm distance from the subject and were taken under normal room lightning. The subjects were instructed to wide open their eyes in order to avoid occlusions. This is also taken care by the image assessment scoring module present in the SDK which stores or captures image only if it is above certain assessment score. The experiment was done in two ways, first the individual iris (300 iris) were considered and next it was experimented on both the iris (left and right iris) for 150 image pairs.

Experiment 1: Analysis with Individual Iris Images

By analysis, the values from the abnormal iris were used to fix the threshold values based on the statistical values of mean, standard deviation, energy, entropy, contrast, correlation. Among these five values of the abnormal iris, the values deviate drastically than that of a normal iris. These values were analysed and then the obtained threshold limits were applied over the real time data set. The mean and standard deviation distribution of the each individual value of the features are shown in Figure 12 and Figure 13 respectively.

Figure 12. Distribution of mean values

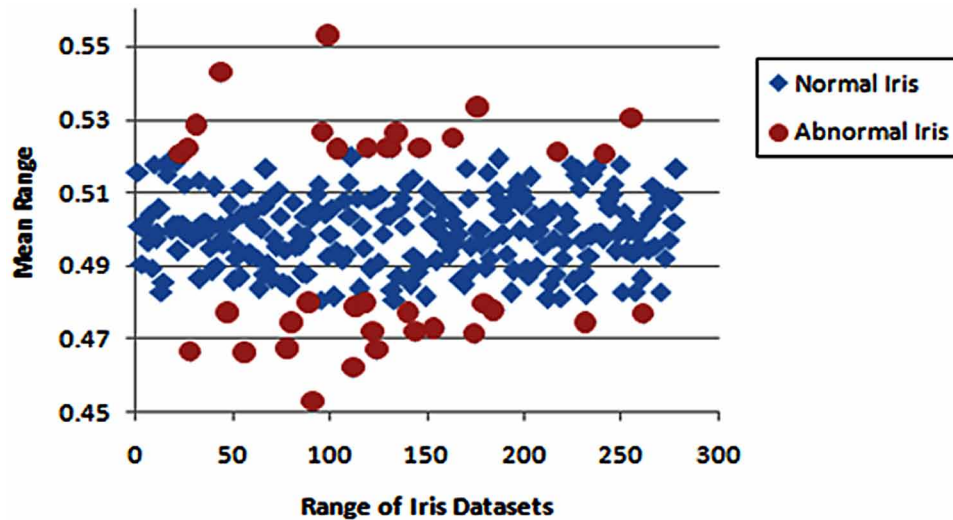
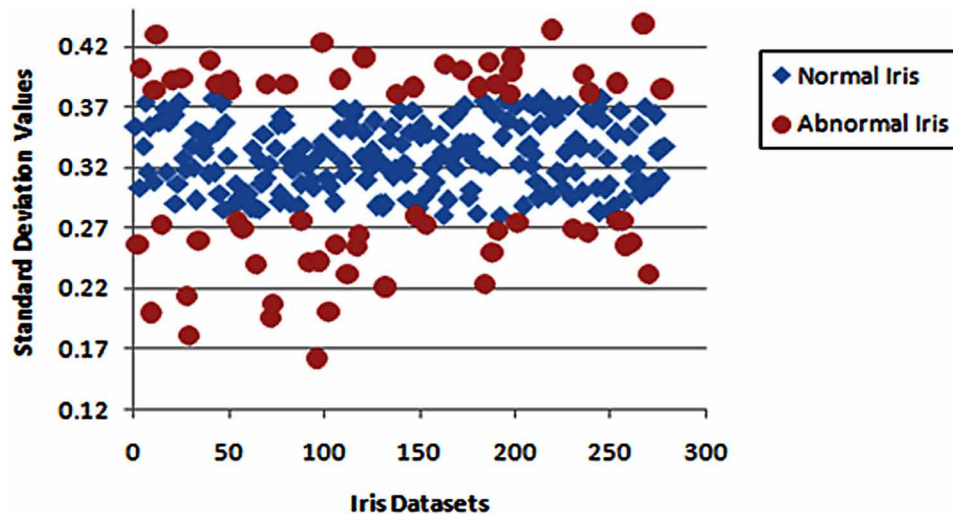


Figure 13. Distribution of standard deviation values



The energy and entropy distribution of the each individual value of the statistical features are shown in Figure 14 and Figure 15 respectively.

The contrast distribution of the each individual iris is shown in Figure 16. The sample data sets for all the statistical values of texture features in experiment 1 is shown in Table 1.

Experiment 2: Consistency between the Pair of Iris

Another property of iris is that the consistency in the texture pattern between the left and the right iris. The Bernard Jensen's Chart of left iris and the right iris is reflex to each other. But the pupillary region in

Figure 14. Distribution of energy values

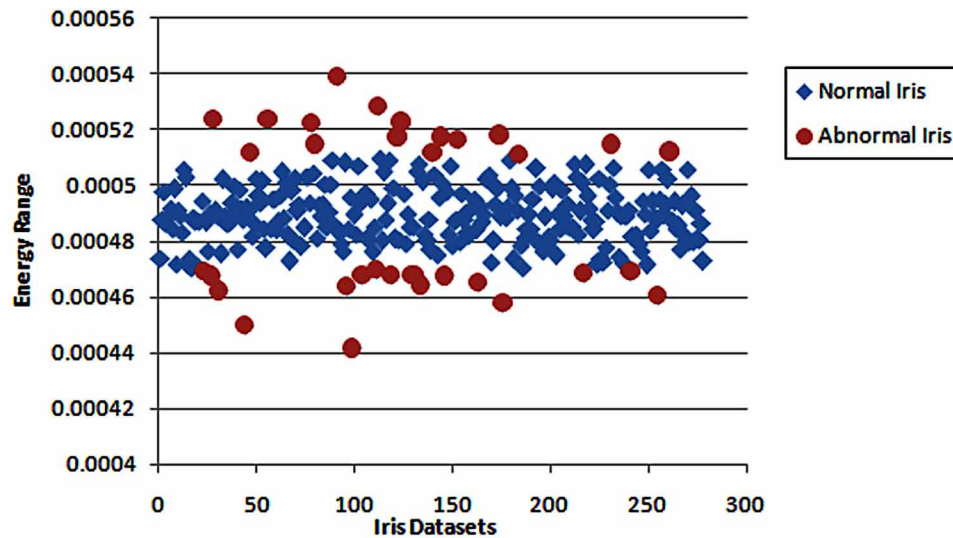
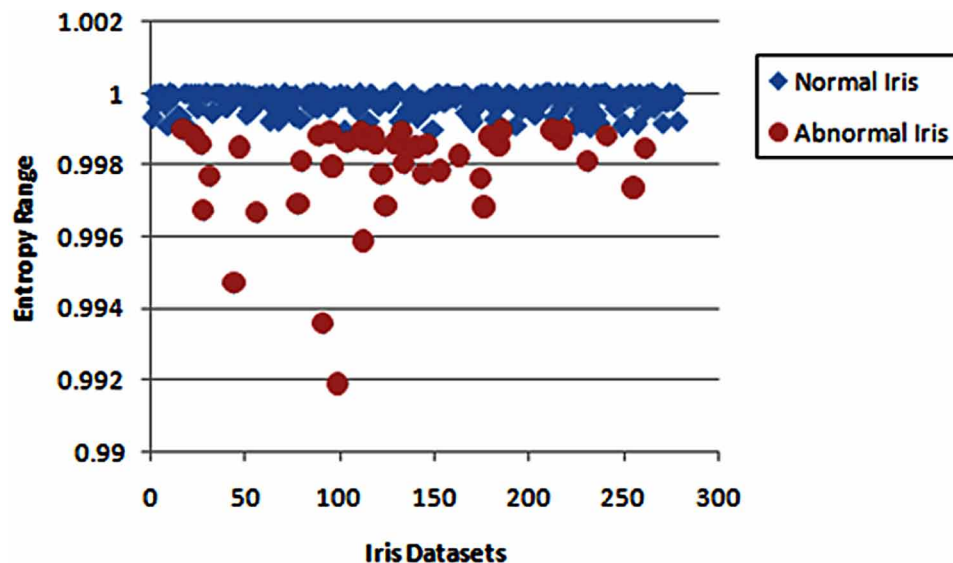


Figure 15. Distribution of entropy values



both the charts represents the gastrointestinal organs. Hence an easy comparison can be made between a person's left and right iris. The consistency here refers to the consistent pattern between the pair of iris but not similarities in the iris. By comparing the values of the pair of iris, the values does not change much among the pair of iris i.e., even though they are not the same, their intensity and texture pattern are nearly constant to one another for a normal pair of iris.

By comparing the mean values of the left as well as the right iris, their difference in mean was computed and the difference was in a range of 0 to .0025, which is very meagre. This once again gives us the

Figure 16. Distribution of contrast values

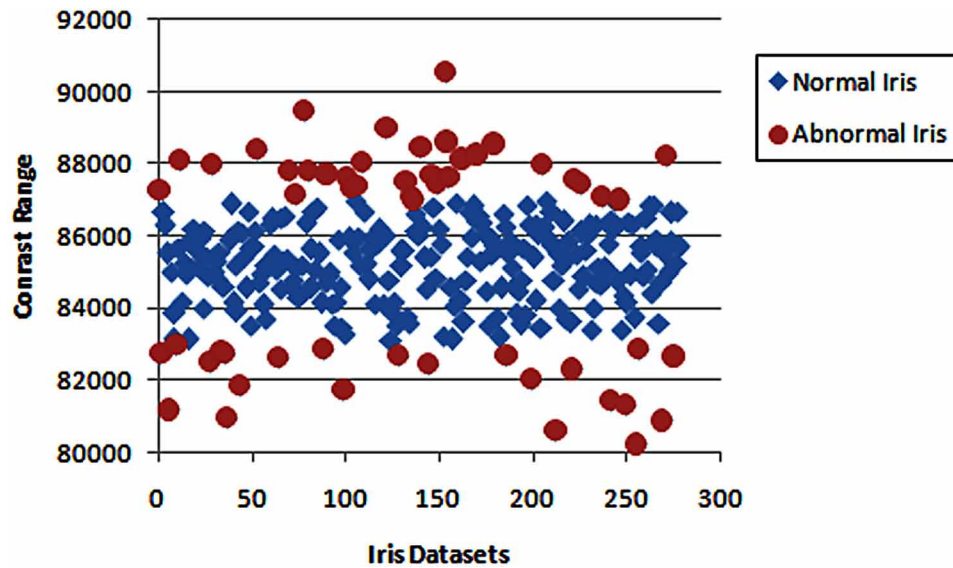


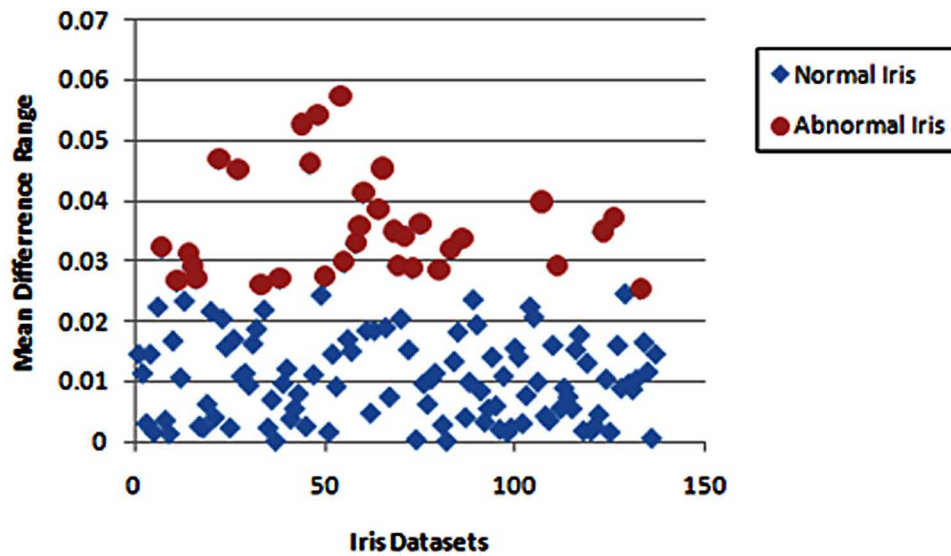
Table 1. Sample statistical values of texture features for Experiment 1

Sl. No.	Mean	Standard Deviation	Energy	Entropy	Contrast
1	0.499268	0.389489	0.000489	0.999998	86330.25
2	0.500977	0.275758	0.000487	0.999997	83716.92
3	0.530273	0.367724	0.00046	0.997354	80215.47
4	0.493164	0.275936	0.000495	0.999865	82851.42
5	0.482666	0.292676	0.000506	0.999133	85545.44
6	0.498779	0.25492	0.000489	0.999996	85689.54
7	0.495361	0.346297	0.000493	0.999938	84876.24
8	0.486328	0.323467	0.000502	0.999461	86489.3
9	0.476807	0.257302	0.000512	0.998447	85068.43
10	0.501465	0.307336	0.000487	0.999994	86850.27
11	0.494141	0.322882	0.000494	0.999901	84391.61
12	0.503906	0.355359	0.000484	0.999956	86838.16
13	0.50293	0.310352	0.000485	0.999975	85734.85
14	0.511719	0.297915	0.000477	0.999604	85879.35
15	0.495361	0.43832	0.000493	0.999938	83578.53

conclusion of a strong evidence of concurrency between the pair of iris. Figure 17 gives the graphical representation of the means difference in the iris.

By analysing the standard deviation in the similar way, the value range is around 0 to 0.0007 which is a very less change in deviation of the values between the iris pair, as shown in Figure 18. Whenever

Figure 17. Distribution of difference of means between left and right iris



an abnormality is seen, there is a change in intensity at either of the iris which also results in the easy detection via the comparison among the pair of iris.

The values of energy also change in the similar way like mean and standard deviation with the range of 0 to 0.00003, as given in Figure 19. The only limitation which we can pose here is that this way of comparison of values between the pair of iris can only be made to Gastro-Intestinal organs where the chart is same representing the same region for both the iris. Some sample data sets for statistical values of texture features of left iris for experiment 2 is shown in Table 2.

Figure 18. Distribution of difference in standard deviation of left and right iris

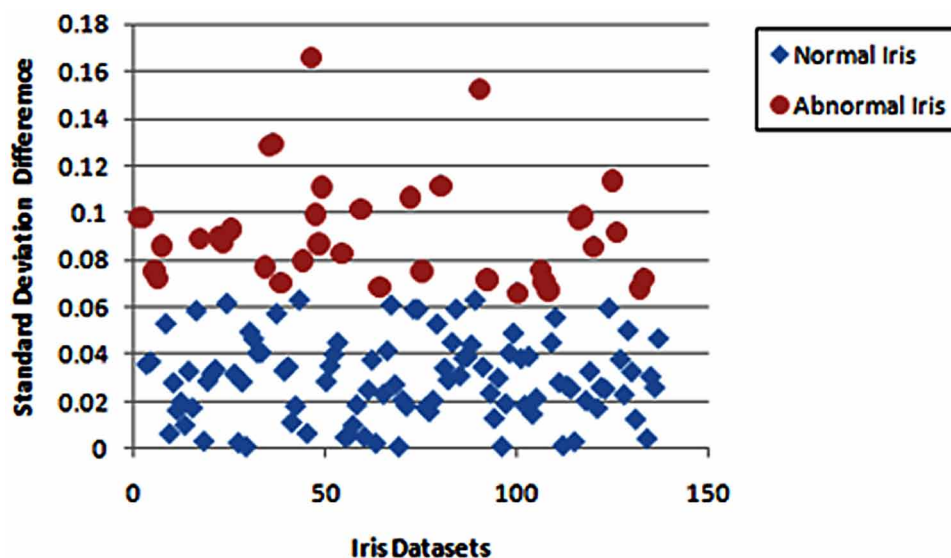
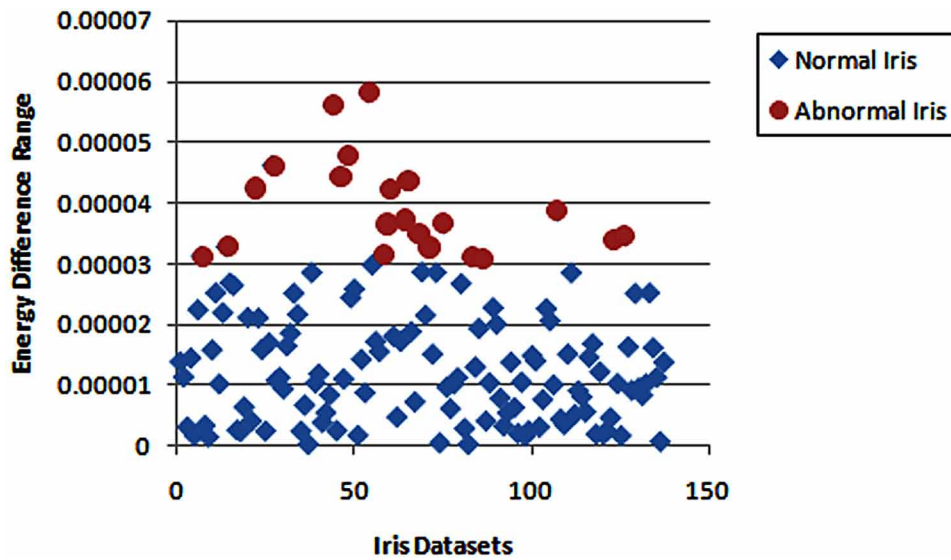


Figure 19. Distribution of difference in energy of left and right iris



The sample data set for statistical values of texture features of right iris for experiment 2 is shown in Table 3.

From the above analysis the changes in human health causes abnormality in the iris. A E factor is initially analyzed for abnormal iris with which the normality range is being fixed. The E factor is defined as:

Table 2. Sample statistical values of texture features of left iris

Left Iris					
Sl. No.	Mean	Standard Deviation	Energy	Entropy	Contrast
1	0.515381	0.354158	0.000474	0.999317	87277.42
2	0.490479	0.303509	0.000498	0.999738	86644.06
3	0.499512	0.33807	0.000489	0.999999	85508.62
4	0.50415	0.316832	0.000484	0.99995	85016.66
6	0.497314	0.308315	0.000491	0.999979	82998.73
7	0.505371	0.429532	0.000483	0.999917	88093.11
8	0.485596	0.358636	0.000503	0.999401	85203.66
9	0.515137	0.369298	0.000474	0.999339	83123.07
11	0.499756	0.357831	0.000489	1.000000	85108.66
12	0.518066	0.392354	0.000471	0.999058	85800.86
14	0.493896	0.290697	0.000494	0.999893	85124.67
15	0.501465	0.373285	0.000487	0.999994	84002.29

Table 3. Sample statistical values of texture features of right iris

Right Iris					
Sl. No.	Mean	Standard Deviation	Energy	Entropy	Contrast
1	0.500732	0.256266	0.000488	0.999989	86281.49
2	0.501953	0.40152	0.000486	0.999961	81157.85
3	0.496338	0.373777	0.000492	0.999682	83120.64
4	0.489502	0.353588	0.000499	0.999997	85655.74
6	0.499023	0.383762	0.000489	0.999157	84178.14
7	0.48291	0.357372	0.000506	0.999083	84934.19
8	0.517822	0.272521	0.000471	0.99898	85841.68
9	0.518799	0.316382	0.000471	0.999996	86190.77
11	0.501221	0.364176	0.000487	0.999996	85564.09
12	0.501221	0.364483	0.000487	0.998786	85974.02
14	0.520508	0.306824	0.000469	0.99957	86150.83
15	0.512207	0.392953	0.000477	0.998575	84884.54

$$E \text{ factor} = \frac{m}{m_m} + \frac{sd}{sd_m} + \frac{enr}{enr_m} + \frac{ent}{ent_m} + \frac{cont}{cont_m} \quad (15)$$

The $E \text{ factor}$ is a value which gives a range, within which the normal and abnormal iris are classified for prediction and the value of E plays a predominant role in prediction of abnormal iris.

$$m_m = \sum_{i=1}^n m_i \quad (16)$$

$$sd_m = \sum_{i=1}^n sd_i \quad (17)$$

$$enr_m = \sum_{i=1}^n enr_i \quad (18)$$

$$ent_m = \sum_{i=1}^n ent_i \quad (19)$$

$$cont_m = \sum_{i=1}^n cont_i \quad (20)$$

Thus, the texture feature is a set of patterns rather than a set of values and these values were normalized into a single value of texture pattern, with which the disease prediction was done. In the data set about 40 were identified to have health issues related to Gastro-intestinal. In the 40 abnormal iris, 32 iris were abnormal when experimented with the proposed system. Hence, the proposed system gives a better result in predicting the human health with iris texture features.

CONCLUSION

The proposed work is designed as an assisting tool for medical practitioners. The system takes human iris as input. The image processing techniques such as iris localization, normalization, enhancement, feature extraction and encoding were applied for the input. Later the texture patterns nearer to the pupil region were extracted. The texture patterns in the iris region were experimented with real time database which reveals the human health condition. The statistical features for the texture pattern are computed and used for predicting the abnormalities. The results based on the prediction of the proposed system were also approved by medical practitioner.

REFERENCES

- Adler, F. (1965), *Physiology of the Eye: Clinical Application* (4th ed.). London: The C.V. Mosby Company.
- Banzi & Xue. (2015). An Automated Tool for Non-contact, Real Time Early Detection of Diabetes by Computer Vision. *International Journal of Machine Learning and Computing*, 5(3), 225–229. doi:10.7763/IJMLC.2015.V5.511
- Boles, W., & Boashash, B. (1998). A Human Identification Technique Using Images of the Iris and Wavelet Transform. *IEEE Transactions on Signal Processing*, 46(4), 1185–1188. doi:10.1109/78.668573
- Daugman, J. (1994). *Biometric Personal Identification System Based on Iris Analysis*. United States Patent no. 5291560.
- Devi & Preethi. (2014). Disease Identification in Iris Using Gabor Filter. *International Journal of Engineering And Computer Science*, 3(4), 5396–5399.
- Haralick, , & Shanmugam, & Dinstein. (1973). Textural features for image classification. *IEEE Transactions on Systems, Man and Cybernetics*, 3 (6), 610–621. doi:10.1109/TSMC.1973.4309314
- Jensen, B. (1980). *Iridology Simplified* (2nd ed.). Escondido.
- Kass, M., Witkin, A., & Terzopoulos, D. (1987). Snakes: Active Contour Models. *International Journal of Computer Vision*, 321–331.

- Kramer, D., & Aghdasi, F. (1999). Texture analysis techniques for the classification of micro calcifications in digitised mammograms. *IEEE AFRICON*, 1, 395–400.
- Lodin & Demea. (2009). Design of an iris-based medical diagnosis system. *International Symposium on Signals, Circuits and Systems*, 1(4), 9–10.
- Ma, L., Tan, T., Wang, Y., & Zhang, D. (2003). Personal identification based on iris texture analysis. *IEEE Transactions on Pattern Analysis and Machine Intelligence*, 25(12), 1519–1533. doi:10.1109/TPAMI.2003.1251145
- Masek, L. (2003). *Recognition of Human Iris Patterns for Biometric Identification*. The University of Western Australia.
- More & Pergad. (2015). On A Methodology For Detecting Diabetic Presence From Iris Image Analysis. *International Journal of Engineering Sciences & Research Technology*, 4(7), 2277–9655.
- Othman, Z., & Prabuwnono, A. S. (2010). Preliminary study on iris recognition system: Tissues of body organs in iridology. *IEEE Conference on Biomedical Engineering and Sciences*, 115–119.
- Ramlee, R. A., Ramli, A. R., & Sulaiman, H. A. (2015). A Review on Diseases Manifestation by Ocular Diseases using Computer Aided Diagnosis (CAD). *IACSIT International Journal of Engineering and Technology*, 7(4), 1343–1348.
- Ramlee, R. A., & Ranjit, S. (2009). Using Iris Recognition Algorithm, Detecting Cholesterol Presence. *International Conference on Information Management and Engineering*, 714(717), 3–5. doi:10.1109/ICIME.2009.61
- Sanderson, S., & Erbetta, J. (2000). Authentication for secure environments based on iris scanning technology. *IEEE Colloquium on Visual Biometrics*, 1–7. doi:10.1049/ic:20000468
- Sarvesh, M. (2005). *Analyses and synthesis of iris images* (M.S. thesis). West Virginia University, Morgantown, WV.
- Wibawa & Purnomo. (2006). Early Detection on the Condition of Pancreas Organ as the Cause of Diabetes Mellitus by Real Time Iris Image Processing. *IEEE Asia Pacific Conference on Circuits and Systems*, 1008(1010), 4–7.
- Wildes, R. P. (1997). Iris Recognition: An Emerging Biometric Technology. *Proceedings of the IEEE*, 85(9), 1348–1363. doi:10.1109/5.628669
- Wildes, R. P., & Asmuth, J. C. (1994). A System for Automated Iris Recognition. *Second IEEE Workshop on Applications of Computer Vision*, 121–128.
- Wolff, E. (1976). *Anatomy of the Eye and Orbit* (7th ed.). H. K. Lewis & Co. LTD.
- Yan, H., & Zhang, Y. (2011). Medical Eye Image Detection System. *ICAIC, Part V, CCIS*, 228, 619–627.

This research was previously published in Recent Advances in Applied Thermal Imaging for Industrial Applications edited by V. Santhi, pages 118–145, copyright year 2017 by Engineering Science Reference (an imprint of IGI Global).

Chapter 15

An Approach for Automatic Detection and Grading of Macular Edema

Jyoti Prakash Medhi
Gauhati University, India

ABSTRACT

Prolonged Diabetes causes massive destruction to the retina, known as Diabetic Retinopathy (DR) leading to blindness. The blindness due to DR may consequence from several factors such as Blood vessel (BV) leakage, new BV formation on retina. The effects become more threatening when abnormalities involves the macular region. Here automatic analysis of fundus images becomes important. This system checks for any abnormality and help ophthalmologists in decision making and to analyze more number of cases. The main objective of this chapter is to explore image processing tools for automatic detection and grading macular edema in fundus images.

INTRODUCTION

The retina is a light sensitive tissue found at the back of the eye. It perceives light signal passed through the lens and accumulates at the center of retina called macula. The perceived signal is then send to the brain through optic nerve, where it is translated to the picture we see. The legitimate functioning of retina depends on constant supply of oxygen carried through blood vessel (BV)s (Diabetes Care, 2004; Diabetes Care, 2003; NHS Choices, 2014). Inadequate supply of oxygen gradually ceases the functionality of retina leading to vision complexities. There are various aspects causing impairment of the retina such as, hypertension, diabetes, old age, heart diseases etc. Various complexities of the retina is commonly known as ‘Retinopathy’. Retinopathy begins with blockage of BV leading to blood leak over the retina. With gradual progression of the disease blood constituents like lipids and fatty materials also get deposited over retina. With deposition of such materials, the vision becomes blur. We may visualize it as being looking into an object through these depositions as shown Figure 1. As shown in second image

DOI: 10.4018/978-1-5225-5195-9.ch015

of Figure 1 we observe the image as blur, because blood is not clear as water and the black region in the image represents the fatty material depositions over retina.

The macula (Cataract and Laser Institute, 2012) of the retina consists of large number of cone cells located at the posterior pole of the eye, between the superior and inferior temporal arteries and is responsible for the central and sharp vision, for example, reading, watching television, writing, recognizing objects, colors etc. During progression of retinopathy, if depositions include macula or neighborhood of macula it is known as maculopathy. During maculopathy the vision severely gets effected and if not taken care at early stage, it may lead to vision loss. Various symptoms of maculopathy (Patient, 2014) includes, gradual loss of central vision causing obstruction or blurred patch as shown in Figure 2, distortion of image size and shape etc. As shown in the figure, the patient is able to see the clock but not the time.

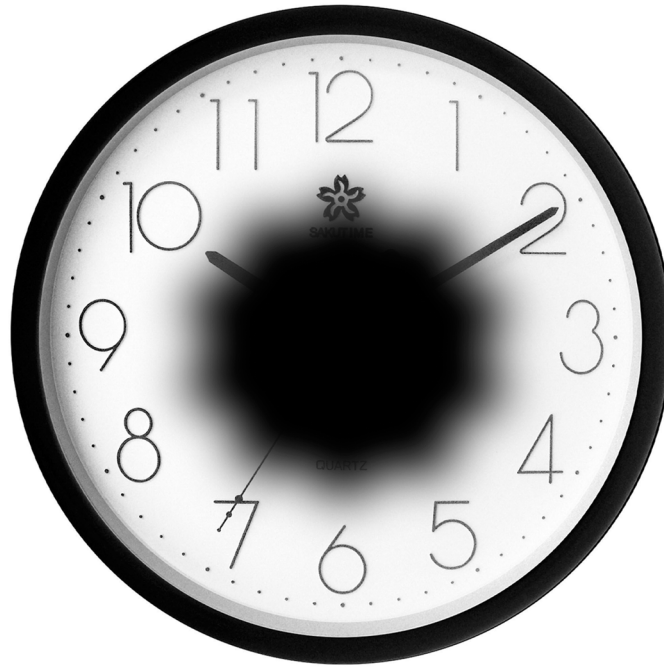
Generally maculopathy occurs with age, (EyeSmart, 2013; ILMO, 2012) commonly known as Age related Macular Degeneration (AMD). Generally AMD starts after the age of 50. During AMD lipid structures leak from epithelial layer of eye and fall in neighborhood and/or over the macula. Maculopathy is also observed in younger age with patients having diabetes, known as Diabetic Macular Edema (DME). At initial stages of diabetes it is not much effective, but gradually with progression of disease the depositions will severely affect the vision and lead to blindness. Therefore one must go for regular eye examinations, at least once a year to avoid such complications. Ophthalmologists widely use fundus images for analysis of retinopathy. To investigate more features Optical Coherence Tomography (OCT) (EyeSmart, 2015) and Fluorescein angiography (MedlinePlus, 2015) are performed. The number of ophthalmologists compared to the retinopathy patients is very less with a ratio of 1:70,000. Thus, analysis of retinopathy with such huge extent is not easy. Many national screening programs have already started but will need time to meet the requirement. Automatic screening programs for analysis of retinopathy provides a helping hand in this regard. The automatic screening algorithms uses fundus images for analysis.

The chapter contains a direction towards automatic detection of maculopathy using fundus images. Few fundus image analysis methods for detection and grading of maculopathy have been presented along with the results and comparison statistics with existing methods. The organization of the chapter contains brief introduction of the fundus image and its imaging technique, discussion on various patho-

Figure 1. Normal vision vs. Vision with Retinopathy



Figure 2. Effect of maculopathy in vision



gens existence during maculopathy, literature review for the automatic detection approach, proposed methods and finally results.

FUNDUS PHOTOGRAPHY

Fundus means hollow, the eye is also a hollow organ and imaging of eye therefore called as Fundus Image / Photograph. Fundus imaging is the process whereby a 2D representation of the 3D semitransparent tissues projected onto imaging plane. The image intensities of the 2D image represent the amount of reflected light. Fundus camera as shown in Figure 3 is a low power microscope with an attached camera for fundus imaging or fundus photography, for imaging retina shown in Figure 4.

The fundus image shown in Figure 4 is authors own retinal image being taken at Biomedical Laboratory of Indian Institute of Technology, Guwahati. The fundus image shows the labelled retinal landmarks.

RETINOPATHY

Retinopathy is a sight threatening disease of the retina. Damage to the retina causes vision deficits and even blindness. The retina contains many blood vessels. Abnormalities in these vessels are a major cause of retinopathy. There are several types of retinopathy,

Figure 3. Fundus Camera
(Wikipedia, 2007).

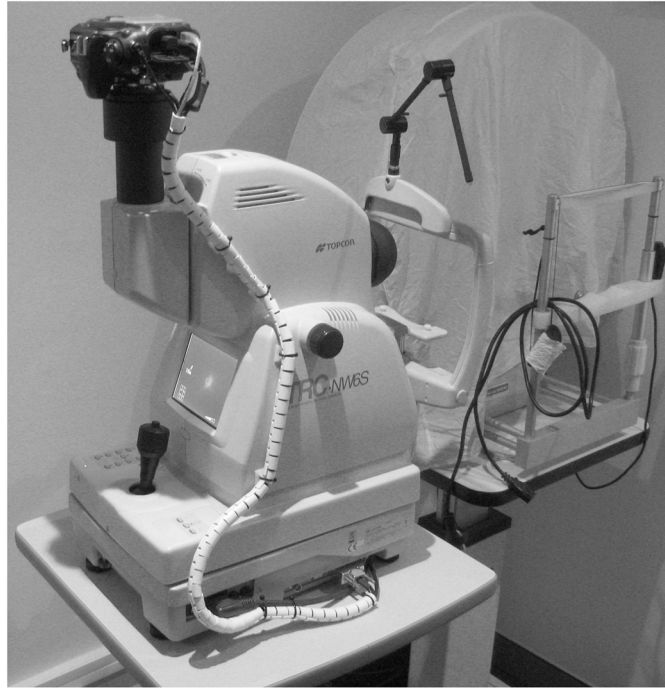
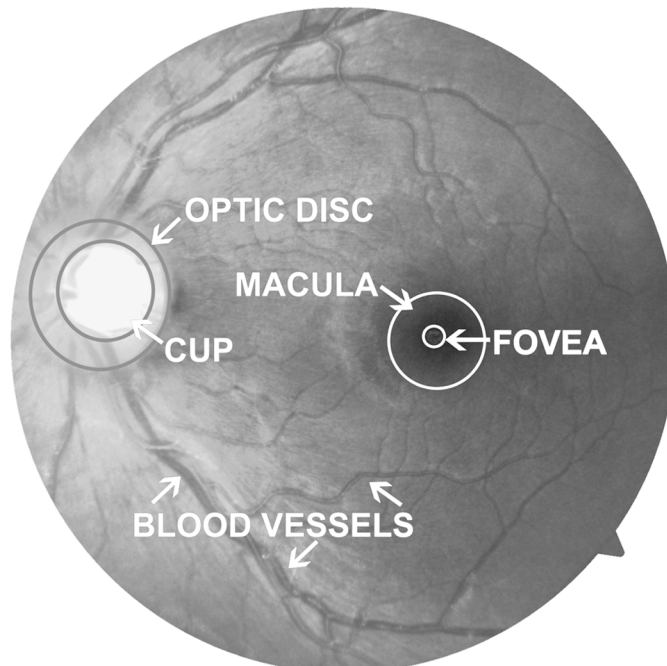


Figure 4. Fundus Image



- **Retinopathy of Prematurity (ROP):** A child born too early doesn't have full grown retinal BVs. It will cause retinal disorders and may lead to retinal detachment.
- **Diabetic Retinopathy (DR):** During diabetes the retinal BVs were inadequate to provide proper oxygen supply to the retina causing DR.
- **Hypertensive Retinopathy:** High blood pressure causes alteration of the BVs leading to retinal dysfunctions.
- **Central Serous Retinopathy:** Accumulation of fluid behind the retinal layer causes blurred and poor night vision.

DIABETIC RETINOPATHY (DR)

DR (VRMNY, 2013; AOA, 2014; EyeSmart, 2013; RNIB, 2014) is one of the commonest causes of blindness in adults between 30 and 65 years of age in developed countries which happens because of diabetes mellitus. Retinal photocoagulation is an effective treatment, particularly if it is given at a relatively early stage when the patient is usually symptomless. Two types of changes are described in DR- background (Non-proliferative NPDR) and proliferative retinopathy. Background (NPDR) is the initial retinal capillary microangiopathy. The following changes are seen – basement membrane thickness, degeneration of pericytes and some loss of endothelial cells are found, capillary microaneurysms are found, waxy exudates accumulate in the vicinity of microaneurysms and lot hemorrhages in the deeper layer of retina are produced and soft cotton wool spots appear on the retina which are micro infarcts of nerve fiber layers of retina. After many years, retinopathy becomes proliferative. The following changes are seen in this case- Neovascularization at the OD, friability of newly formed blood vessels causes them to bleed easily and result in vitreous hemorrhages, proliferation of astrocytes and fibrous tissues around new blood vessels, fibro vascular and gliotic tissue contracts to cause retinal detachment and blindness.

Anomalies Due to DR

The clinical features of DR include- Microaneurysms, Hemorrhages, Exudates, Cotton wool spools, Intra-retinal micro vascular abnormalities and Neovascularization as shown in Figure 5.

- **Microaneurysms:** In most cases these are the earliest clinical abnormality detected. They appear as tiny, discrete, circular, dark red dots near to, but apparently different from, the retinal vessels. They look like tiny hemorrhages but they are in fact minute aneurysms arising mainly from the venous end of capillaries. They may give rise to retinal leakage of plasma constituents.
- **Hemorrhages:** These most characteristically occur in the deeper layers of the retina and hence are round and regular in shape and described as 'blot' hemorrhages. The smaller ones may be difficult to differentiate from microaneurysms and the two are often grouped together as 'dots and blots'. Superficial flame-shaped hemorrhages in the nerve fiber layer may also appear, especially if the patient is hypertensive.
- **Exudates:** These are characteristic of diabetic retinopathy. They vary in size from tiny specks to large confluent patches and tend to occur particularly in the peri macular area. They result from leakage of plasma from abnormal retinal capillaries and overlie areas of neuronal degeneration.

- **Cotton Wool Spots:** These are similar to retinal changes that occur in hypertension, and also occur particularly within five disc diameters of the OD. They represent arteriolar occlusions causing retinal ischaemia and, if it is numerous, may represent pre-proliferative diabetic retinopathy; they are most often seen in rapidly advancing retinopathy or in association with uncontrolled hypertension
- **Intra-Retinal Micro Vascular Abnormalities:** Intra-retinal micro vascular abnormalities (IRMA) are dilated, tortuous capillaries which develop in severe pre-proliferative retinopathy. They represent the remaining patent capillaries in an area of ischemic retina where most have been occluded.
- **Neovascularization:** New vessel formation may arise from the venous circulation either on the OD (NVD) or elsewhere in the retina (NVE), in response to widespread retinal ischemia. The earliest appearance is that of fine tufts of delicate vessels forming arcades on the surface of the retina. As they grow, they may extend forwards on to the posterior surface of the vitreous. They are fragile and leaky, and are liable to rupture during vitreous movement, causing a pre-retinal ('subhyaloid') or a vitreous hemorrhage. New vessels may be symptomless until hemorrhage appear, when there may be acute visual loss. Serous products leaking from these new vessels stimulate a connective tissue reaction, called gliosis and fibrosis. This first appears as a white, cloudy structure among the new vessels. As it extends, the new vessels may be obliterated and the surrounding retina is covered by a dense white sheet. By this stage, hemorrhage is less common but retinal detachment can occur through traction on adhesions formed between the vitreous and the retina, causing serious visual impairment.

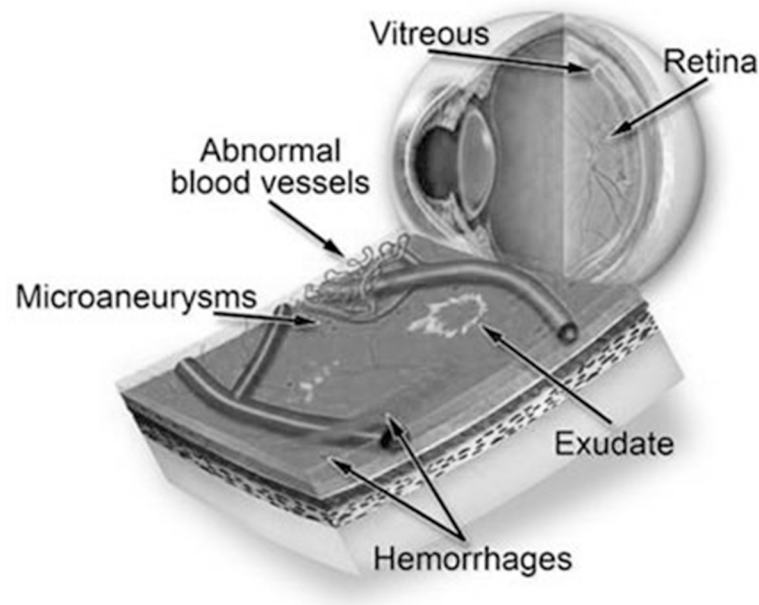
MACULAR EDEMA

Although proliferative retinopathy is the most dramatic series of retinal lesions in diabetes, and may produce the most profound visual loss even to total blindness. The most common reason for visual impairment in diabetic individuals is macular edema. By definition macular edema is the result of an inflation of fluid in the retinal slab around the macula (Creteil, 2010). It causes vision loss by altering the functional cell relationship in the retina and promoting an inflammatory reparative response. Macular edema is a nonspecific sign of ocular disease. It may be viewed as a clinically relevant type of macular response to a retinal environment being altered. In most cases, it is associated with an alteration of the blood-retinal barrier (BRB). Macular edema may occur in a wide variety of ocular situations including uveitis, trauma, intraocular surgery, vascular retinopathies, vitreoretinal adhesions, hereditary dystrophies, diabetes, and age-related macular degeneration. The histopathological picture of this condition is an accumulation of fluid in the outer plexiform and inner nuclear and plexiform layers of the retina. The increase in water content of the retinal tissue characterizing macular edema.

Diabetic Macular Edema (DME)

Macular edema is the most important complication of diabetes mellitus leading to an impairment of visual sensitivity (Creteil, 2010). A diabetic macular edema is defined as a retinal thickening caused by the accumulation of intraretinal fluid and/or hard exudates within 2 disk diameters of the center of

Figure 5. Anomalies due to DR
(Retinal Eye Care Associates, 2014)



the macula, the fovea. The incidence of diabetic macular edema is closely associated with the degree of diabetic retinopathy and the duration and type of the disorder. The 25-year collective incidence in persons with type 1 diabetes mellitus is subjected to 29% for macular edema and 17% for clinically significant macular edema. There are two subtypes of diabetic macular edema, a focal and a diffuse form. Focal macular edema refers to localized areas of retinal thickening, caused by locus of vascular dysfunction, mainly microaneurysms, and less caused by intraretinal micro vascular abnormalities. Here fluid leakage occurs at a great extent, which is usually followed by hard exudates. The hard exudate pattern may be either focal or ring structured. Diffuse macular edema is caused by a general diffuse leakage from dilated retinal capillaries (and from microaneurysms and arterioles) throughout the posterior pole of the retina. It is usually observed in both eyes with the similar or extensively different degree of leakage. There are also classifications for ischemic and exudative macular edema. In most situations, a hybrid type can be observed.

A clinically significant macular edema (CSME) is the early DR study which includes features like thickening of the retina at or within 500 mm from fovea and presence of hard exudates obtained in the same region, if linked with thickening of the adjacent retina.

Age-Related Macular Degeneration (AMD)

Age-related macular degeneration (AMD) is the term applied to ageing changes without any obvious cause that occur in the macula in people with age 50 years and above. It begins with accumulation of lipid material as deposits beneath the retinal pigment epithelium (RPE). When focal collections of lipid material are present these are referred to as drusen and can be seen as pale yellow spots on fundus

image. Generally drusen and RPE irregularities are not associated with disturbances of central vision. A proportion of people having these early alterations will progress to severe central vision loss when development of geographic atrophy and/or exudative disease occurs. AMD can be sub-classified into two major forms: the atrophic or dry form and the exudative or wet form. Atrophic macular degeneration without exudative changes does not generally lead to macular edema. The exudative form with choroidal neovascularization may cause a serous detachment of the overlying retina, resulting in CME. The presence of CME is more likely if the serous detachment of the macula has been present for 3-6 months or if the choroidal neovascular membrane has involved the sub foveal region.

LITERATURE SURVEY

A large numbers of articles have been published in the literature on retinal image analysis and segmentation of retinal features. For proper understanding they are classified as follows:

- Localization of Macula.
- Localization of Abnormalities.
- Analysis of maculopathy.

Localization of Macula

The macula is an oval-shaped highly pigmented yellow spot near the center of the retina (Siegel & Sapru, 2006). It is of diameter around 6 mm and is often defined as having two or more ganglion cells layers. Its center is called fovea, a small region that contains high concentration of cone cells in the eye. Fovea is responsible for central, high resolution vision.

The contrast of the macular region is often quite low and it may be wrapped by exudates or hemorrhages. As a result to obtain a global correlation often fails. The fovea is located approximately 2–2.5 disk diameters temporal to the optic disk (OD) and between superior and inferior temporal arteries. These positional constraints have been used by several authors to identify a small search area for the macula.

Siddalingaswamy, P. C. & Prabhu, (2010) have used the OD as the reference point and have used the positional constraint with respect to OD. The Macula is said to be situated 2 disc diameter (DD) temporal to OD and the mean angle between macula and the center of OD against the horizon is -2.3° to -8.9° . In that area a rectangular search window has been created and the center of window having the lowest average intensity is taken as center of the macular region.

Mubbashar, M., Usman & Akram, (2011) also used OD the reference point and the maximum value is calculated in front of the OD. The mean of these maximum value is calculated and plotted on a thresholded image which gives the macula.

Sekher, Al-Nuaimy & Nandi, (2008) have searched for the vicinity of the OD. The candidate macula ROI is defined as the portion of a sector subtended at the center of the OD by 30° above and below the center of the OD and the image. The macula is identified by iteratively applying a threshold and then applying a morphological opening on the resulting blob.

Niemeijer, M., Abramoff & Bram, (2007) have used a different approach to locate macula. A cost function has been used combining local as well as global cues to detect anatomical structures in fundus images. The parametric model that has been used in this work can be given as $S_{\text{result}} = G(b, F, I, O)$, where

G is the model ; b is a set of parameter, F is a cost function, I is the image and O the optimizing algorithm. So given a set of model parameters b, a certain configuration of the 16 points should be generated. Then, taking I and s as input the cost function F will generate a value for the current configuration indicating how well S fits to I. Optimization algorithm O will then attempt to find the b where F has the lowest value. When O has found the set of parameters where F is minimal, the corresponding point configuration is S_{result} *

Poshtyar,A., Ghassabi & Shanbehzadeh, (2011) used the spatial information of the optic cup to detect OD and macula. The fovea is assumed to have the row coordinate same as the row coordinate of middle pixel of the image (i.e. row/2) in ideal situation. But that isn't the usual case hence the row coordinate of fovea is assumed to be smaller or larger than the row coordinate of middle pixel of image, therefore is computed accordingly. The column coordinate of fovea is computed in each 1/8 of image which the OD is appeared. Macular area is an approximate ellipse with fovea coordinates in the center.

Singh, Joshi & Sivaswamy, (2008) have used the appearance of macula as a property to determine its location. Signal to Noise Ratio (SNR) boosting is performed to enhance the darker profile of macula. Green channel image is subtracted from complemented red channel image to retain the dark intensity information. The resultant image is later binarized to detect macula.

LOCALIZATION OF ABNORMALITIES

Microaneurysms, small outpunching of the capillary walls, are the first micro-vascular changes to appear and are sentinel markers for early diabetic retinopathy. With disease progression small intraretinal dot haemorrhages, often indistinguishable from Microaneurysms appear and later larger blot haemorrhages. Excessive capillary permeability is manifest as retinal edema usually accompanied by lipid exudation. If the exudates are on the macula, it can be sight threatening (diabetic maculopathy). Figure 6 shows a fundus with abnormalities.

Detection of Microaneurysms

Quelleg *et al.*, (Quelleg et al., 2008) modelled the microaneurysms with 2-D rotation-symmetric generalized Gaussian function given by

$$f(r; \alpha; \gamma; \delta) = \gamma + \delta_{\text{exp}} \left(\left(\frac{|r|}{\alpha} \right)^{\beta} \right)$$

where, $r = \sqrt{x^2 + y^2}$ and α are the parameters for modelling the lesion size, β is for modelling lesion sharpness, γ is for background intensity and δ is for modelling lesion height. Gaussian shape was found to be convenient for modelling wide range of shapes of MAs.

Hatanaka et al. 2008, (Hatanaka, Nakagawa, Hayashi, Hara & Fujita, 2008) proposes a new method for detection of haemorrhages. The author first performs brightness correction using hue-saturation-value (HSV) space. The brightness corrected value is given by:

$$B_c(i, j) = \sqrt{1 - (V(i, j) - 1)^2}$$

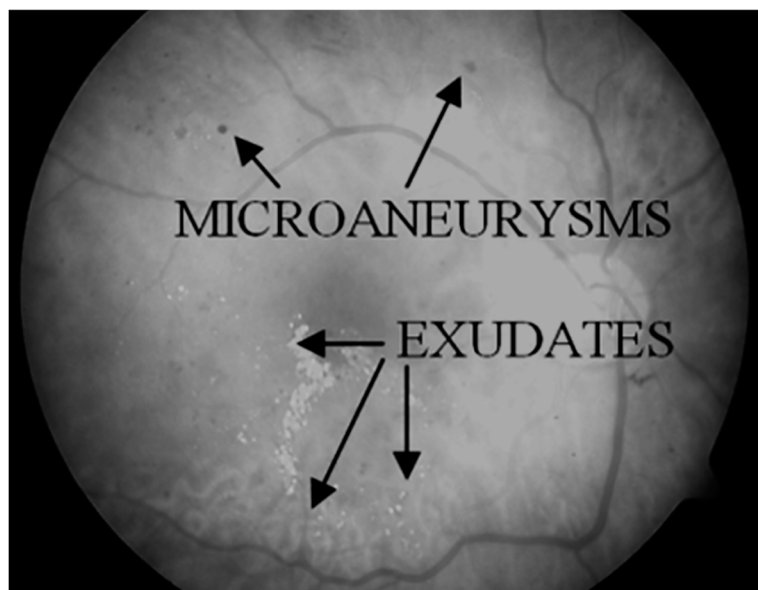
where, $V(i, j)$ = brightness value of HSV space. Then the $B_c(i, j)$ are processed by gamma correction. Gamma value was experimentally set at 1.5. First optic nerve head was extracted by thresholding method from green component of fundus image. Then haemorrhages were detected by density analysis. Two smooth images were made by using masks of 3×3 and 9×9 . Then the difference of the pixel values of the two smoothed images was calculated and haemorrhages were detected. This method was not able to detect the haemorrhages connected to blood vessels.

Detection of Exudates

Drusens appear as yellowish, cloudy blobs in a retinal image. They exhibit no specific size or shape. The modification of size in individual drusens and their confluence seem to be an essential risk factor in developing macular degeneration. Exudates are characteristic of diabetic retinopathy. They vary in size from tiny specks to large confluent patches and tend to occur particularly in the perimacular area. They result as leakage of plasma from abnormal retinal capillaries and overlie areas of neuronal degeneration.

Walter et al. (2007) identified exudates from green channel using the gray-level variations. They have used the mathematical morphology for determining the contour of exudates after initial localization. This method has three parameters: local window (used for calculation of local pixel variation) and two threshold values. First threshold determines the minimum variation value within each local window. Exudates regions are found by first threshold value. Second threshold value represents the minimum value, by which candidate differs from its surrounding background pixels.

Figure 6. Fundus image with abnormalities
(IMAGERET, 2007)



Harangi, B. & Hajdu, (2013) have extracted possible candidate exudate regions by applying morphological operations. These extracted regions are treated as initial mask for an active contour method. At the preprocessing level nine separate methods has been. Nine different boundaries are extracted for each of the exudates one by one and combined to fit best to manually segmented exudates in the training database.

Siddalingaswamy, P. C & Prabhu, (2010) have extracted candidate exudate by clustering technique, then the OD is removed from the clustered image to get rid of false positive. Later candidate region is segmented using morphological operations. The finely segmented candidate exudate region is overlaid on the green channel to get the marker image and the original green channel is used as the mask. Finally the exudate region are obtained by thresholding the difference between the original image and the reconstructed image.

Tariq, Akram, Shaukat & Khan, (2012) has initially extracted the candidate exudate. It is done in the following way- (1) blood vessels & dark lesions are removed by morphological closing (2) contrast of the exudates are improved by adaptive contrast enhancement (3) to further enhance the bright lesions Gabor kernel is convolved with the contrast enhanced image. The feature of this candidate regions is fed to a support vector machine (SVM) which determines whether it is an exudate or not.

Haniza, Hamzah & Hazlita, (2012) have used the strategy that involves the applications of fuzzy c-means (FCM) clustering, edge detection and OTSU thresholding to separate edge pixels of the exudates from the background. Then inverse surface thresholding is employed to extract the exudates. The FCM will segment the fundus images into the above five categories- the area outside of the eyeball, the blood vessel, the healthy background retina, the low intensity exudates (cotton wools) and the high intensity exudates (hard exudates). Since only the area containing exudates the ROI, only the last two groups is to be processed further. Once the region containing the soft and hard exudate is identified the rest of the area will be disregarded, then Prewitt operator is applied to identify the boundaries of the exudates. To avoid manually selecting a threshold value which can be effected by uneven illumination and contrast OTSU method is applied. The threshold splits the resulting image of the previous phase into the edge and non-edge pixels. Now OD is detected by applying variance intensity of the adjacent pixels. Now inverse surface is used to locate the OD and exudates. The intensity of the inverse surface is derived from the gradients of the original image and the negative image in four passes. The final inverse surface is the average of the four primary surfaces. The final step is to do surface thresholding so as to adjust the position of the inverse surface so that only the areas containing defects will intersect with the original image.

Welfer, D., Scharcanski & Marinho, (2010) have converted the RGB image to LUV color model then on L channel contrast enhancement has been done by applying Top Hat morphological operation on L channel followed by Bottom hat morphological operation on L channel. The top hat image is then added to, and bottom hat image is subtracted from the L channel which makes the bright area brighter and dark area darker. At this stage regional minima is obtained and a morphological reconstruction is done from the regional minima. The difference between the reconstructed image and the contrast enhanced image is obtained. The H- maxima transform is computed from the difference image. This image is further thresholded to give a coarsely segmented image which serves as the marker image for finer exudate detection. A morphological reconstruction of the marker is done. Again a difference image is obtained from the green channel and the reconstructed image. Again the image is thresholded which gives the final exudate lesion.

Analysis of Maculopathy

Maculopathy analysis depicts the accumulation of anomalies over and around neighborhood of macula. Depending on the region of presence of these anomalies maculopathy is classified into three stages namely mild, moderate and severe. The anomalies are classified as significant if they are within the range of macula neighborhood. Otherwise they are classified as non-significant macular edema. Automatic grading of maculopathy is performed by estimating the density and location of anomalies from the center of macula. The stages are classified as follows,

- **Mild:** If the anomalies lie far away from the macula neighborhood. At 2 OD diameter away from macula center.
- **Moderate:** If the anomalies lie in macula neighborhood. At 1 OD diameter away from macula center.
- **Severe:** If anomalies fall over the macula. The condition turns sight threatening when anomalies involves fovea. At 1/3rd OD diameter from fovea center.

Very few papers have been published in the literature for maculopathy analysis, Deepak, K.S, & Sivaswamy, (2012) have performed global image analysis for determining exudates by analyzing motion pattern. Motion pattern formed on healthy fundus images were considered for generating test images. The test images were then compared with the motion pattern images containing exudates. The variation determines the amount of exudates present in the image. Same patterns were then generated for macular region to find out severity of maculopathy.

Siddalingaswamy, P.C, & Prabhu, (2010) have generated macular regions to identify maculopathy stages by determining the amount of exudates present over them. Here the author classifies the stages of maculopathy and performs the severity measurement.

Medhi, Nath & Dandapat, (2012) have detected macula using intensity property. BV removed green channel image and red channel image are processed to obtain the dark intensity region of fundus image and using an adaptive threshold macula region is identified. On the macular a mask is created to analyze severity of maculopathy. The exudates and microaneurysms are later detected using mathematical morphology. The amount of anomalies presence over macular mask determine the severity of the disease.

OPEN ISSUES AND MOTIVATION

Automatic detection and classification of maculopathy involves detection of anomalies presence over macular regions. In this direction we have to follow mainly three step analysis. The first stage involves identification of anomalies present in the image. Secondly gathering information of fovea location and lastly, to generate macular regions from fovea and to identify amount of anomalies present over them.

All the stages have various challenges and limitations of analysis. Various issues are mentioned as follows for each analysis step.

- *Detection of anomalies is a challenging task.* If the image is not illuminated properly, the intensity values of anomalies are near to those of the background. Classification applied on such images may lead to background classification along with abnormalities. Irregular shapes, varying struc-

ture and intensity of the unhealthy area also makes it difficult to classify them. The intensity of OD and exudates both appear bright in intensity. Therefore OD masking is essential before segmenting exudates. Improper masking of OD may result as misclassified unhealthy areas. The exudates may also be so near to OD that it might seem part of the OD. Microaneurysms are very close to the BV intensities. Thus classifying microaneurysms is also challenging.

- *The fovea is located at 2 OD diameter temporal to OD center.* Using this property the fovea location may be determined. The primary requirement of this method is to identify OD location. OD center is then to obtain from the detected OD. From the center using spatial relationship the region containing fovea is to be located. The main challenge in this analysis is to locate the exact position of OD center. If any exudate be misclassified as OD the whole process will fail. Another way of determining fovea is to locate the dark intensity region, as macula has dark profile. BV removal may be needed in this process as BVs also share the same intensity. The main limitation in this method is, if the macula region is not dark or not visible properly the algorithm fails. Also if hemorrhages lie with similar intensity they might get misclassified as fovea. Thus identifying fovea demands efficient algorithms.
- *Classification of maculopathy stages requires proper identification of fovea and OD diameter.* Using these properties different regions can be obtained and later presence of anomalies over them is identified and graded.

Considering all the pros and cons of automatic detection we present few methods to analyze macular edema.

METHODS FOR AUTOMATED ANALYSIS OF MACULAR EDEMA

The automatic detection of retinal landmarks is based combination of *inpainting, morphology and thresholding technique* applied to different color planes of fundus image. It is an approach for modification of RGB model by processing HSI and yCbCr color model. Before segmentation, the original fundus image has to undergo preprocessing for enhancement of the image quality. After segmentation of the anomalies grading is also performed to detect the severity of the disease (e.g. DR). The proposed algorithm is represented by the block diagram shown in Figure 7

PREPROCESSING

The diagnostic process of DR have been affected if the illumination of fundus image is not proper. Improper reflection of camera flash, retinal pigmentation etc. causes variation in illumination. Thus for reducing the image variability preprocessing step is very much significant for success of the algorithm.

The databases of fundus images which we worked have resolution and illumination variations. Thus we have to go through various illumination correction methods and generalize the images to a single resolution. Thus we have fixed all the images size to be 576×720. Depending on the properties of the images color normalization and contrast enhancement of the fundus photographs are needed. Various preprocessing tools were applied to the images depending on their intensity variations. Median filtering is performed in all the RGB planes to remove noise present in fundus. Contrast enhancement is applied on

Hue plane and the enhanced image is converted back to RGB. For illumination equalization we consider all the RGB image planes and apply the algorithm. To apply CLAHE, RGB image is first converted to HSI color plane and enhancement is applied to intensity (I) plane. Then the HSI_{modified} image is converted back to RGB color image which is contrast enhanced image. The Homomorphic filtering and White top transformations are applied on gray scale image. All these preprocessing techniques were described in (Harangi & Hajdu, 2013).

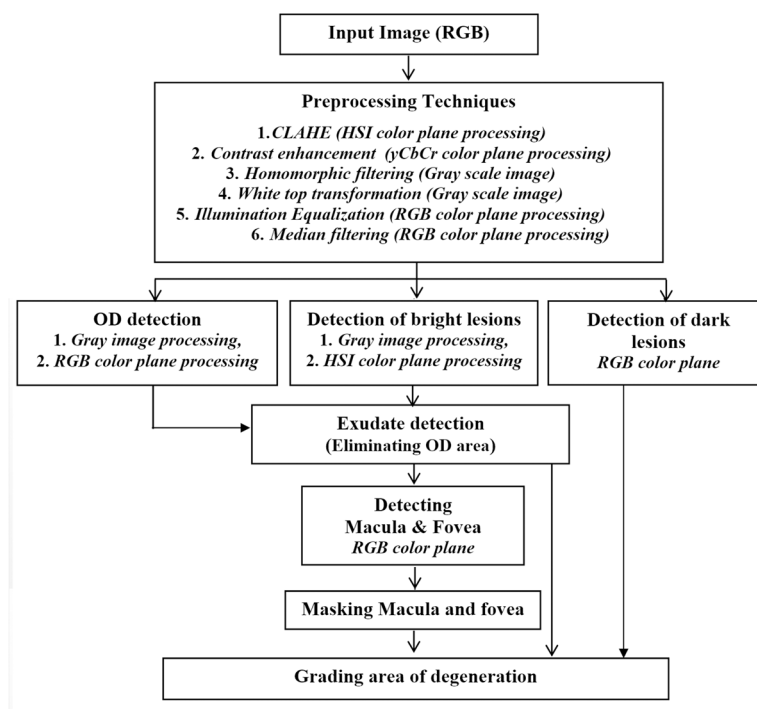
BLOOD VESSEL REMOVAL

The fundus image consists of numerous blood vessels (BV) having its boarders along different retinal land marks such as OD, macula causing difficulty for proper segmentation. Thus, BV network is removed using image inpainting method (Bertalmio, Sapiro, Caselles & Ballester, 2000). For BV to be inpainted the binary mask of BV is to be segmented. For segmentation of BV mathematical morphology is used.

OD DETECTION AND MASKING

OD has maximum intensity pixels then other retinal landmarks. On the other hand exudates are also bright in nature having similar range of intensity values. Thus detection of exudates also finds OD. Therefore OD is to be located and masked before detecting exudates.

Figure 7. Block diagram of proposed algorithm



For detection of OD we have selected the intensity property and applied a threshold to detect the maximum intensity pixels. After correcting illumination on gray scale image we set a threshold of maximum 40 gray levels and detect the pixels having intensity within that range. After the pixels being detected we apply a mask of radius 70 from the center of detected region. This mask is then used to remove the OD in hue color plane as it will be used for detection of exudates.

Exudate Detection

For exudate detection we have performed three methods using different properties of image processing. To enhance exudate detection in all the cases we detect the outer boundary of the fundus image using morphological boundary tracing operations as preprocessing requirement. After the boundary being detected it is masked such that the boundary pixels don't interfere in exudate segmentation.

Method 1: The hue color plane of HSI color model contains the color information of all the pixels. The high valued pixel of hue plane corresponds to exudates. Using this property we have extracted out the exudates from color fundus image. First RGB image is converted to HSI color model and hue plane is extracted. In the hue plane a threshold of maximum 70 is applied and pixels above which are marked as exudates.

Method 2: Another method for exudate detection is applied on gray scale image. In this connection we have considered the BV and OD removed gray scale image and applied morphological closing to enhance the exudate area removing all the unwanted noisy pixels. Then a threshold is applied and pixels above which are marked as exudates.

Method 3: For feature extraction and pattern recognition, contour tracing is a handy preprocessing techniques performed on digital images. This is because of the contour pixels are small subset of the total number of pixels representing a pattern. As the contour of a given pattern is obtained, its different properties can be examined and used as features for pattern classification. The boundary tracing algorithm used in this connection is Moore-Neighbor tracing (Contour Tracing, 2000).

The BV removed image is used for this purpose. The boundary tracing algorithm is applied to all enhanced preprocessed image. The result of boundary extraction is then used to determine the area covered by the exudates. The image containing maximum area is considered to be the best result and it is chosen for further processing.

To display the exudates in the color image we have collected the coordinates of detected pixels and highlight those locations in original image by using a single color. This method have been taken from our previous work (Majumder & Medhi, 2014).

Microaneurysms (MA) Detection

The MAs are detected from the preprocessed images. Green channel of RGB color plane is used for the analysis. The mathematical morphology is used for MA detection. The outlines of the image is detected by canny edge detection method applied to the histogram equalized image. The circular boarder detected in preprocessing is removed. Subtracting the edge image gives the MAs. This image also contains the noisy pixels, like BVs and exudates. The image is then subtracted from the previous processed images

containing exudates and BVs. Finally the MAs image is obtained. It is an enhancement of our previous method (Medhi, Nath & Dandapat, 2012).

Macula and Fovea Detection

For macular region detection we have performed two methods using different properties of image processing. The macula appears dark in intensity and the information is intact in RGB plane.

Method 1: It is the extension of the processed output obtained from the first exudate detection method.

After the exudates are detected in hue plane the resultant HSI image is converted back to RGB image. In the RGB image green color plane contains the information of macula more than the other color planes. Thus a threshold is applied to obtain pixels with intensity value less than. The pixels detected are the macular region. On decreasing the threshold value the detected pixels represent fovea.

Method 2: This method have been taken from our previous work (Medhi, Nath & Dandapat, 2012).

Blood vessel removed red channel and the green channel images of the preprocessed image are used for detection of macula. The green channel image is subtracted from complemented red channel image. A fixed global threshold is used and the macula is separated. On increasing the threshold value fovea is separated.

Grading Macular Edema

Maculopathy grading requires information of exudates detected in macular region (Severe stage), in neighborhood of macula (Moderate stage) and far away from macula (Mild stage). Thus for grading, regions of macula are to be determined earlier. The segmented pathogenic image is overlapped with all the macular masks. The area of overlapped region of abnormality and different macular masks are determined. The result shows the severity level of maculopathy, i.e. whether the patient is suffering from mild, moderate or severe case. After classification of the stages the amount of severity is determined by obtaining the ratio of overlapping pixels to the masks pixels.

MATERIALS/ DATABASE USED

For analysis three databases of fundus images were used which are available on the web, DRIVE (Digital Retinal Images for Vessel Extraction), DIRETDB1 and HRF (High-Resolution Fundus Image).

The DRIVE database (Image Sciences Institute, 2004) consists of 40 color image varying in quality with 584×565 pixels in TIFF format captured by Canon CR5 non-mydratic 3CCD camera with a 45 degree field of view (FOV). It contains training set and test set having equal number of images out of which 7 images (15% of images) have signs of mild DR. The DIARETDB1 (IMAGERET, 2007) database consists of 89 color fundus images with 1500×1152 pixels and captured using 50 degree FOV digital fundus camera with varying imaging settings. Out of 89 images 5 images are normal and 84 images contain mild NPDR signs (94.39% of images). Among the mild NPDR sign images 47 retinal images (55.95% of images) contain hard exudates. HRF database (TECHNISCHE FAKULTAT, 2013) consists of 45 images with 3504×2336 pixels in JPG format captured by Canon CR-1 fundus camera with a 45°

FOV. Out of 45 images 15 images (33.33% of images) have signs of DR and 15 images (33.33% of images) have signs of glaucoma.

RESULTS

The results obtained are divided into three methods. But image enhancement is the basic requirement of any one of the algorithm. Therefore we have performed six different image enhancement techniques to meet our requirements.

Preprocessing

Preprocessing of the input RGB image is performed initially before segmentation. After preprocessing the BV are removed using inpainting. Figure 8(a) shows original image and Figure 8(b)-(i) show the entire enhanced image obtained using the methods discussed in section 4.1. Figure 9(a)-(d) shows the blood vessel removed RGB, green plane, red plane and gray image.

Method 1

This method describes the automatic detection of maculopathy using different color plane processing. In this process we first enhanced image by median filtering and then contrast enhancement for RGB image. Whereas for gray scale image we performed Homomorphic filtering. After enhancing, the OD is detected and masked using gray scale image and the co-ordinates of the mask are stored and applied to the color planes. In this method we don't require BV removal. After OD is masked the RGB_{modified} is converted to HSI and the Hue plane is considered for determining the exudates, as described in method 1 of section 4.3. After exudates being determined the macula is detected, as mentioned in method 1 of section 4.5. After detecting all the landmarks grading is performed on the results obtained using the method described in section 4.6. Figure 10(a)-(h) shows all the steps of implementation for Method 1.

Here, image (a) is the original input image. Upon application of preprocessing the enhanced image is shown in image (b). Figure (c) represents the OD masked. Exudate detection is shown in image (d), and zoomed version in (f). Detected macula is depicted in image (g) and image (h) shows the combination of the detected sections together where fundus boundary is shown in red, exudates detected in black inside fundus and macula detected in light brown color.

Method 2

This method describes the automatic detection of maculopathy using intensity property of fundus as the macula appears dark in color and OD has maximum brightness. In this process we have used the BV removed green plane, red plane and gray scale image. The images are then enhanced using median filtering and CLAHE. As described in method 2 of section 4.5 we detect the macula and fovea. If we invert the original image OD appears as dark in intensity. Thus same method is implemented to detect the OD and removed for proper exudate detection. The microaneurysms and exudates are detected using gray scale image as shown in section 4.4 and 4.3 respectively. After detection of the land marks, grading is done as described in section 4.6. Figure 11 and 12 shows all the steps of implementation for Method 2.

Figure 8. (a) Original image RGB, (b) Median filtered image RGB, (c) Contrast enhanced image RGB, (d) CLAHE image RGB, (e) Illumination equalized image RGB, (f) Illumination equalized image Green Plane of RGB, (g) Original image Gray scale, (h) Homomorphic filtered image Gray scale and (i) White Top transformed image Gray scale.

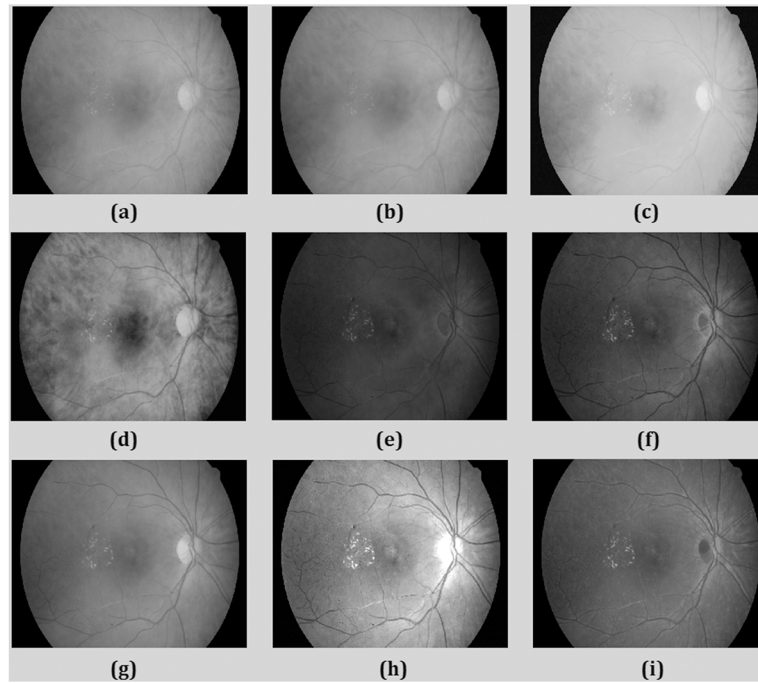
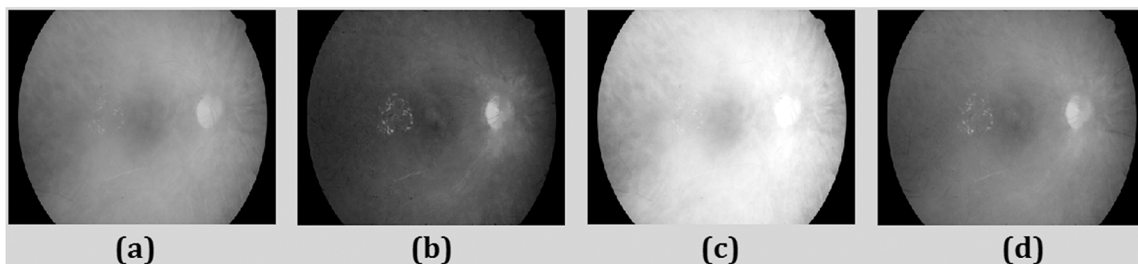


Figure 9. (a) BV removed image RGB, (b) BV removed image Green plane, (c) BV removed image Red plane and (d) BV removed image Gray scale.



Discussion: The proposed method detects macula and fovea on both normal and pathological images with 97.53% efficiency (158 out of 162). Out of 172 images of the databases 9 images have been eliminated from the analysis as the illumination of the images is very poor and/or macula regions doesn't have dark intensity profile. The method is also applied on images with anomalies. The selected images show severe level in 27 images with amount of overlapping region more than 25%. Moderate level is found in 22 images and 39 images show mild DR. The method is compared with the existing methods in the literature. The comparisons are given in Table I. The proposed method performs better.

Figure 10. (a) Original image, (b) Enhanced image, (c) OD masked, (d) Exudates detected (green pixels), (e) Zoomed input image, (f) Exudates detected in zoomed image, (g) Macula detected and boundary of image formed, (h) Combined result showing all segmented image in different color. (Red=boundary, Green=fundus image, Black=exudates, Light brown=macula)

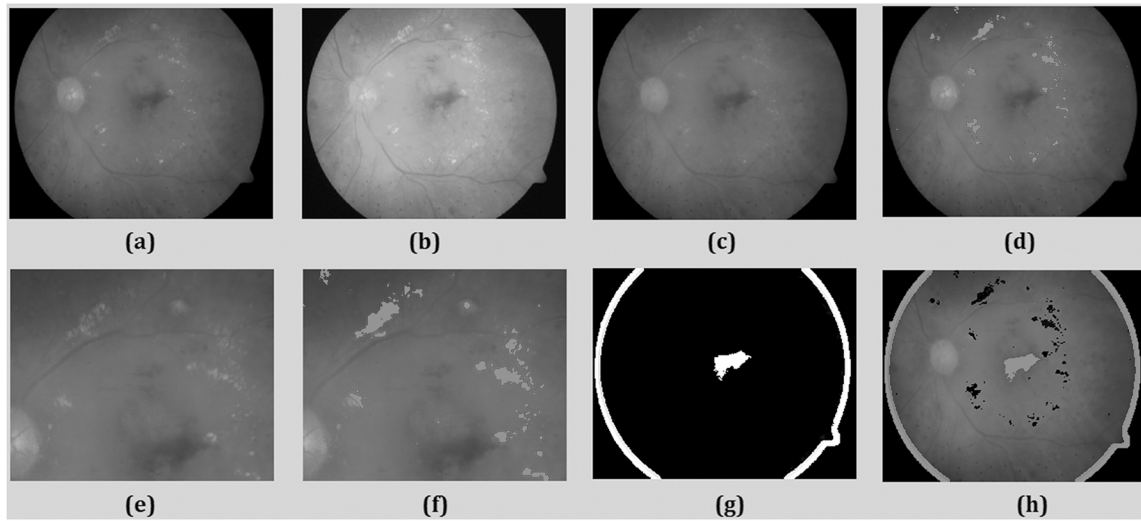


Figure 11. (a) Original image RGB, (b) BV removed RGB and (c) Enhanced BV removed RGB (d) BV removed Red channel image of RGB, (e) BV removed Green channel image of RGB, (f) BV removed Gray scale image, (g) Enhanced BV removed Red channel image of RGB, (h) Enhanced BV removed Green channel image of RGB and (i) Enhanced BV removed Gray scale image

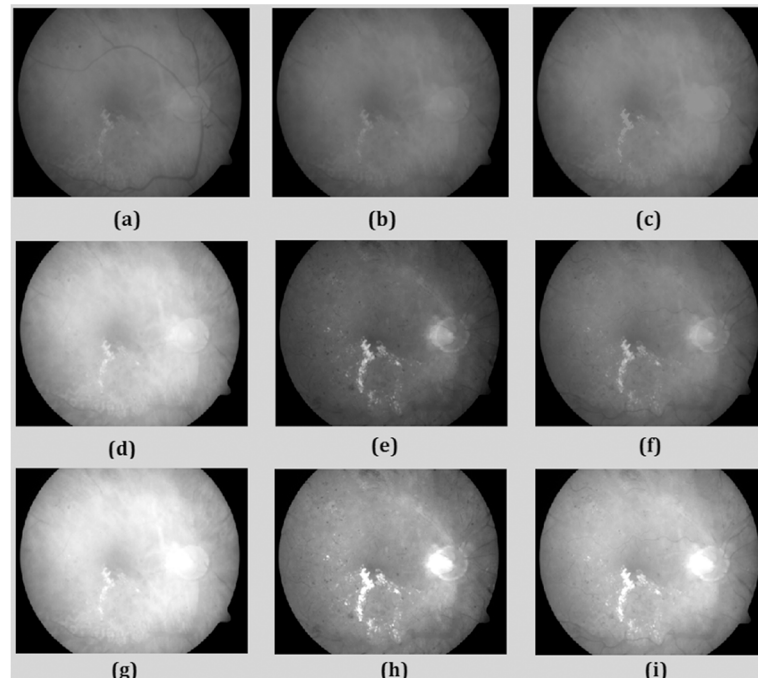
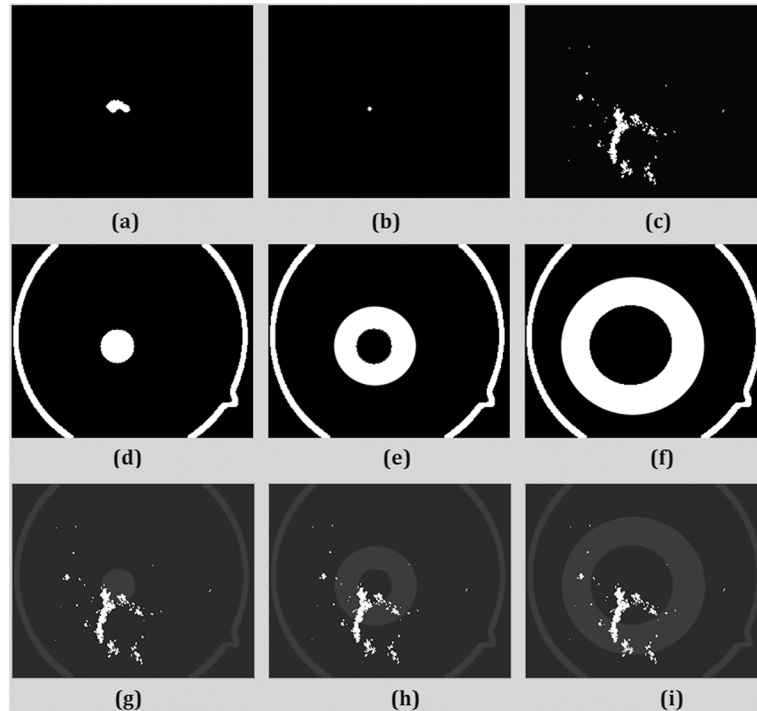


Figure 12. (a) Macula detected, (b) Fovea detected, (c) Anomalies detected, (d-f) Macula mask 1,2,3 (g-i) Overlapping of macular mask and anomalies for grading severe, moderate and mild stage respectively.



Method 3

In this method we propose a novel approach to detect exudates from multiple contours. Here we have considered the images enhanced by different methods as mentioned in section 4.1. And then determined the contours (method 3, section 4.3) of the anomalies. OD is priory removed from the images to avoid false detection. The areas of these boundaries are calculated and this descriptor is used to find the exu-

Table 1. Performance comparison of Macula detection method

Method	Technique	Dataset	Accuracy
Li and Chutatape (Li & Chutatape, 2004)	ROI selection, Mathematical Morphology	Not Specified	100%
Niemeijer et al. (Niemeijer, Abramoff & Bram, 2007)	Point distribution and Cost Function	Local	94.40%
Sagar et al. (Sagar, Balasubramanian & Chandrasekaran, 2007)	ROI selection & morphology	DRIVE, STARE	96%
Singh et al. (Singh, Joshi & Sivaswamy, 2008)	Appearance Based	DRIVE, STARE	96.61%
Proposed Method	Morphology and thresholding Based	DRIVE, HRF,DIARETDB1	97.53%

date present in the image if any. The boundary with the maximum area is declared to be the one with exudates as can be seen in results in Figure 13.

Discussion: The best method comprising maximum area is contrast enhancement output as obtained in the above implementation. Among the result obtained 10 images of DIARETDB1 results is shown in Table 2. Comparison of our work has been done based on Sensitivity analysis with manually segmented images shown in Table 3. The methodology is 100% sensitive to hard exudate. From the analysis we have found that contrast enhancement in our case has better result when compared with manual segmentation. Thus we can say that the preprocessing image of contrast enhancement has been more successful than the rest. The primary limitation of this method is for the images where the size of intensity of the exudates having nearby values as that of the background then the methodology did not produce promising result.

CONCLUSION

Automation for mass screening procedure has not been perfected. It has been found that the anatomy of each eye may vary from person to person. Hence automation is a challenging task. Here in this study we have aimed to determine an automated method for retinal image scanning and detection of macular degeneration. In this regard we have determined three methods for automatic analysis. It includes image properties such as intensity, chromaticity and appearance etc. Along with abnormality detection classification of severity is also determined. During the analysis it has been observed that due to improper illumination and reflections, images of the databases are not uniform in intensity. Thus these issues give rise to difference in anomalies intensity and if not properly equalized the exact amount of anomalies present could not be determined. Therefore in the third algorithm we have tried to identify the best preprocessing method. The advantage of our proposed algorithm for macular degeneration is that, it is independent of relative positions of macula from OD or BV. Although the algorithm detects macula but

Figure 13. Preprocessed image after applying (a) Contrast Enhancement (b) CLAHE (c) Illumination equalization (d) White top transformation (e) Chromaticity normalization. (f)-(j) Boundary of the exudates detected respectively.

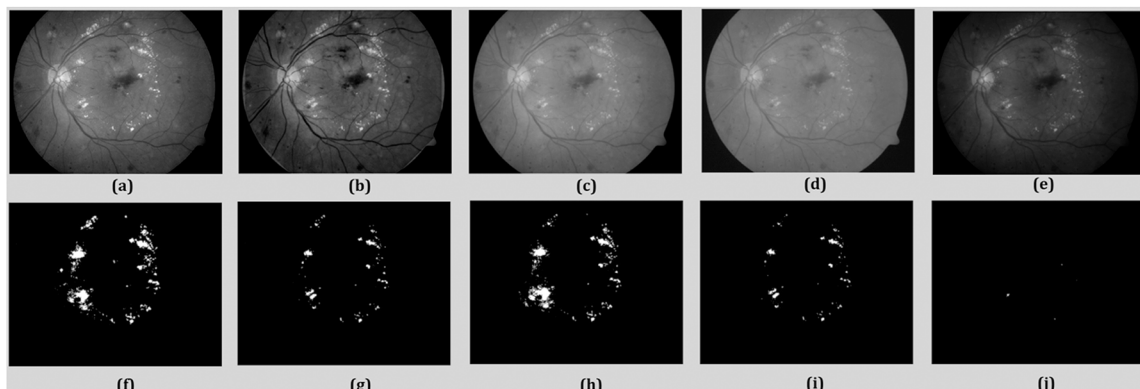


Table 2. Performance of proposed method for DIARETDB1

Images	Area using Method 1	Area using Method 2	Area using Method 3	Area using Method 4	Area using Method 5	Manual Segmentation	Sensitivity (%)	Best Method
Image 1	8856	5436	6578	3981	1100	9025	70	Method 1
Image 2	6753	1236	9876	4532	5686	7036	78	Method 1
Image 3	7854	3459	6375	2987	3475	8027	89	Method 1
Image 4	2865	3987	1065	1024	963	6692	85	Method 1
Image 5	9866	2562	1245	1136	784	11566	70	Method 1
Image 6	8963	6354	9012	2587	1245	9876	70	Method 3
Image 7	2834	7821	5632	4529	3254	5529	76	Method 1
Image 8	8919	3689	2371	6421	2351	9452	70	Method 1
Image 9	6789	1893	2346	5432	1853	7746	75	Method 1
Image 10	2965	2136	1978	3296	1241	3065	72	Method 1
Average	6666.4	3857.3	4647.8	3592.5	2195.2	7801.4	75.5	

Table 3. Performance comparison of Exudate detection methods

Methods	Sensitivity (%)
Proposed Method	77.6
Harangi (Harangi & Hajdu, 2013)	76
T. Walter (Walter, 2007)	76
D. Welfer (Welfer, Scharcanski & Marinho, 2010)	19

it will be more efficient if the preprocessing algorithms can be improved to have uniform intensities therefore it could be considered as future aspect.

REFERENCES

- Bertalmio, M., Sapiro, G., Caselles, V., & Ballester, C. (2000). Image Inpainting. *Proceedings of the 27th Annual Conference on Computer Graphics and Interactive Techniques* (pp. 417–424), New York: ACM Press/Addison-Wesley.
- Creteil, G. C. (2010). *Macular edema- a practical approach*. Paris: Karger.
- Deepak, K. S., & Sivaswamy, J. (2012). Automatic assessment of macular edema from color retinal images. *IEEE Transactions on Medical Imaging*, 31(3), 766–776. doi:10.1109/TMI.2011.2178856 PMID:22167598
- Diabetic Retinopathy. (2012). *St. Luke's Cataract and Laser Institute*. Retrieved from <http://www.st-lukeseye.com/conditions/DiabeticRetinopathy.html>

Diabetic retinopathy. (2013). *NHS Choices*. Retrieved from <http://www.nhs.uk/conditions/diabetic-retinopathy/Pages/Introduction.aspx>

Diabetic Retinopathy [Image]. (2013). *Vitreous-Retina-Macula Consultants of New York*. Retrieved from <http://www.vrmny.com/education-center/educational-topics/diabetic-retinopathy.html>

Diabetic Retinopathy. (2014). American Optometric Association. Retrieved from <http://www.aoa.org/patients-and-public/eye-and-vision-problems/glossary-of-eye-and-vision-conditions/diabetic-retinopathy?sso=y>

Diabetic Retinopathy [image]. (2014). Retinal Eye Care Associates. Retrieved from <http://www.retinaleyecare.com/common/images/diabetic-retinopathy.jpg>

DRIVE: Digital Retinal Images for Vessel Extraction. (2004). *Image Sciences Institute*. Retrieved from <http://www.isi.uu.nl/Research/Databases/DRIVE>

Flourescein angiography. (2012, September 17). *MedlinePlus*. Retrieved from <http://www.nlm.nih.gov/medlineplus/ency/article/003846.htm>

Fong, D., Aiello, L., Gardner, T.W., King, G.L., Blankenship, G., Cavallerano, J.D., Ferris III, F.L., & Klein, R. (2003). Retinopathy in Diabetes. *Diabetes Care*, 26(1), 226-229. Retrieved from <http://care.diabetesjournals.org/content/26/1/226.full?sid=2012dd7a-64a7-4816-929d-46b3d4591a49>

Fong, D., Aiello, L., Gardner, T.W., King, G.L., Blankenship, G., Cavallerano, J.D., Ferris III, F.L., & Klein, R. (2004). Retinopathy in Diabetes. *Diabetes Care*, 27(Supplement 1), s84-s87. Retrieved from http://care.diabetesjournals.org/content/27/suppl_1/s84.long

Ghuneim, A.G. (2000). *Moore-Neighbor tracing*. Retrieve from http://www.imageprocessingplace.com/downloads_V3/root_downloads/tutorials/contour_tracing_Abeer_George_Ghuneim/moore.html

Haniza, Y., Hamzah, A., & Hazlita, M. I. (2012). Exudates segmentation using inverse surface adaptive thresholding. *Journal of Measurement, Elsevier*, 45(6), 1599–1608. doi:10.1016/j.measurement.2012.02.016

Harangi, B. & Hajdu. (2013). Improving automatic exudate detection based on the fusion of the results of multiple active contours. *Proceedings of IEEE 10th International Symposium on Biomedical Imaging* (pp. 45-48). San Francisco, CA, USA. IEEE. doi:10.1109/ISBI.2013.6556408

Hatanaka, Y., Nakagawa, T., Hayashi, Y., Hara, T., & Fujita, H. (2008). Improvement of automated detection method of hemorrhages in fundus images. *Proceedings of IEEE 30th Annual International Conference on Engineering in Medicine and Biology Society* (pp.5429-5432). Vancouver, British Columbia, Canada. IEEE. doi:10.1109/IEMBS.2008.4650442

High-Resolution Fundus Image Database. (2007). *Department Informatik, Technische Fakultat*. Retrieved from <http://www5.cs.fau.de/research/data/fundus-images/>

Kauppi, T., Kalesnykiene, V., Kamarainen, J. K., et al. (2006). *DIARETDB1 database*. <http://www2.it.lut.fi/project/imageret/diaretdb1/>

- Li, H., & Chutatape, O. (2004). Automated feature extraction in color retinal images by a model based approach. *IEEE Transactions on Bio-Medical Engineering*, 51(2), 246–254. doi:10.1109/TBME.2003.820400 PMID:14765697
- Lowth, M. (2014). Macular disorders. *Patient*. Retrieved from <http://www.patient.co.uk/doctor/macular-disorders>
- Maculopathy and macular degeneration. (2014). *ILMO.it*. Retrieved from <http://www.ilmo.it/en/solutions/surgery-at-ilmo/vision-problems-and-eye-diseases/maculopathy-and-macular-degeneration/>
- Majumder, P., & Medhi, J. P. (2014). Automatic exudate detection based on amalgamation of results of multiple contours. *Proceedings of International Conference on Green Materials through Science, Technology and Management*. Assam, India.
- Medhi, J. P., Nath, M. K., & Dandapat, S. (2012). Automatic grading of macular degeneration from color fundus images. *Proceedings of World Congress on Information and Communication Technologies* (pp. 511-514). IEEE. doi:10.1109/WICT.2012.6409131
- Mubbashar, M., Usman, A., & Akram, M. U. (2011). Automated system for macula detection in digital retinal images. *Proceedings of Conference on Information and Communication Technologies* (pp. 1-5). Karachi. IEEE.
- Niemeijer, M., Abramoff, M. D., & Bram, V. G. (2007). Segmentation of the Optic Disc, Macula and Vascular Arch in Fundus Photographs. *IEEE Transactions on Medical Imaging*, 26(1), 116–127. doi:10.1109/TMI.2006.885336 PMID:17243590
- Poshtyar, A., Ghassabi, Z., & Shanbehzadeh, J. (2011) Detection of Optic Disc Center and Macula using Spatial Information of Optic Cup. In *Proceedings of 4th International Conference on Biomedical Engineering and Informatics* (pp.255-258). Shanghai: IEEE. doi:10.1109/BMEI.2011.6098351
- Quelleg, G., Lamard, M., Josselin, P. M., Cazuguel, G., Cochener, B., & Roux, C. (2008). Optimal wavelet transform for the detection of microaneurysms in retinal photographs. *IEEE Transactions on Medical Imaging*, 27(9), 1230–1241. doi:10.1109/TMI.2008.920619 PMID:18779064
- Sagar, A. V., Balasubramanian, S., & Chandrasekaran, V. (2007). Automatic detection of anatomical structures in digital fundus retinal images. In *Proceedings of IAPR Conference on Machine Vision Applications* (pp. 483–486). Tokyo, Japan.
- Sekher, S., Al-Nuaimy, W., & Nandi, A. K. (2008). Automated localisation of optic disc, and fovea in retinal fundus image. *Proceedings of 16th European Signal Processing Conference*. Lausanne, Switzerland. IEEE.
- Siddalingaswamy, P. C., & Prabhu, K. G. (2010). Automatic grading of diabetic maculopathy severity levels. *Proceedings of International Conference on Systems in Medicine and Biology*. Kharagpur, India. doi:10.1109/ICSMB.2010.5735398
- Siegel, A., & Sapru, H. N. (2006). B. Sun, (Ed.) *Essential Neuroscience*. Baltimore, Maryland: Lippincott Williams & Wilkins.

Singh, J., Joshi, G., & Sivaswamy, J. (2008). Appearance-based object detection in colour retinal images. *Proceedings of IEEE International Conference on Image Processing* (pp.1432-1435). IEEE. doi:10.1109/ICIP.2008.4712034

Tariq, A., Akram, M. U., Shaukat, A., & Khan, S. A. (2012). A computer aided system for grading of maculopathy. *Proceedings of Cairo International Biomedical Engineering Conference*. Cairo, Egypt. IEEE. doi:10.1109/CIBEC.2012.6473318

Understanding eye conditions related to diabetes. (2014). *RNIB*. Retrieved from <http://www.rnib.org.uk/eye-health-eye-conditions-z-eye-conditions/understanding-eye-conditions-related-diabetes>

Walter, T., Massin, P., Erginay, A., Ordonez, R., Jeulin, C., & Klein, J. C. (2007). Automatic detection of microaneurysms in colour fundus images. *Journal of Medical Image Analysis*, 11(6), 555–566. doi:10.1016/j.media.2007.05.001 PMID:17950655

Welfer, D., Scharcanski, J., & Marinho, D. R. (2010). A coarse-to-fine strategy for automatically detecting exudates in color eye fundus images. *Journal of Computerized Medical Imaging and Graphics*, 34(3), 228–235. doi:10.1016/j.compmedimag.2009.10.001 PMID:19954928

What is age-related Macular Degeneration? (2013). *Geteyesmart.org*. Retrieved from <http://www.geteyesmart.org/eyesmart/diseases/age-related-macular-degeneration/>

What is Diabetic Retinopathy? (2013). *Geteyesmart.org*. Retrieved from <http://www.geteyesmart.org/eyesmart/diseases/diabetic-retinopathy/>

What is Optical Coherence Tomography? (2015). *Geteyesmart.org*. Retrieved from <http://www.geteyesmart.org/eyesmart/diseases/optical-coherence-tomography.cfm>

Fundus camera picture. (2007). *Wikipedia*. Retrieved from http://en.wikipedia.org/wiki/File:Retinal_camera.jpg

ADDITIONAL READING

Baumann, W. B. (2007). *Developments in ophthalmology*. Karger.

Browning, D. J. (2010). *Diabetic retinopathy – evidence based management*. Springer. doi:10.1007/978-0-387-85900-2

Cheung, W., & Hamarneh, G. (2007). N-SIFT: N-dimensional scale invariant feature transform for matching medical images. *Proceedings of 4th IEEE International Symposium Biomedical Imaging: From Nano to Macro*. doi:10.1109/ISBI.2007.356953

Duh, E. (2008). *Diabetic retinopathy*. Humana Press. doi:10.1007/978-1-59745-563-3

Hammes, Porta (2010). *Experimental approaches to Diabetic Retinopathy*.

- Kim, J. S., Ishikawa, H., Gabriele, M. L., Wollstein, G., Bilonick, R. A., & Kagemann, L. et al. (2010). Retinal nerve fiber layer thickness measurement comparability between time domain optical coherence tomography (OCT) and spectral domain OCT. *Investigative Ophthalmology & Visual Science*, 51(2), 896–902. doi:10.1167/iovs.09-4110 PMID:19737886
- Medhi, J. P., & Deka, D. (2014). Morphology based automatic classification of colour fundus image. In *Proceedings of International Conference on Green Materials Through Science, Technology and Management*. Assam, India.
- Olk, R. J & Lee, C. M. (1993). Diabetic Retinopathy – Practical Management.
- Saxena, S. (2012). *Diabetic retinopathy*. Jaypee.
- Scanlon, Wilkinson, Aldington, & Matthews. (2009) *A Practical Manual of Diabetic Retinopathy Management*.
- Strouthidis, N. G., Yang, H., Reynaud, J. F., Grimm, J. L., Gardiner, S. K., Fortune, B., & Burgoyne, C. F. (2009). Comparison of clinical and spectral domain optical coherence tomography optic disc margin anatomy. *Investigative Ophthalmology & Visual Science*, 50(10), 4709–4718. doi:10.1167/iovs.09-3586 PMID:19443718
- Wu, G. (2010). Diabetic retinopathy – the essentials.

KEY TERMS AND DEFINITIONS

Contrast Limited Adaptive Histogram Equalization (CLAHE): This is a type of adaptive histogram equalisation method used to enhance the contrast of an image. This method differs from ordinary adaptive histogram equalization in its contrast limiting. Unlike ordinary adaptive histogram equalization this method prevents the over amplification noise.

Cotton Wool Spots: These are fluffy white patches of the abnormal retinal image that occurs due to damage of nerve fibers.

Diabetic Macular Edema (DME): A retinal disease caused by complication of diabetes mellitus. DME affect the central vision the patient.

Diabetic Retinopathy (DR): A sight threatening retinal disease caused by complications of diabetes.

Exudates: Exudates are the lipid deposits in the retina which appear as bright yellow lesions.

Neovascularization: Growth of new blood vessels at the advance stage of diabetic retinopathy called as proliferative diabetic retinopathy.

This research was previously published in Intelligent Applications for Heterogeneous System Modeling and Design edited by Kandarpa Kumar Sarma, Manash Pratim Sarma, and Mousmita Sarma, pages 204-231, copyright year 2015 by Information Science Reference (an imprint of IGI Global).

Section 2

Drug Delivery and Design

Chapter 16

Bioactive Compound Analysis of *Coriandrum Sativum* L against Microbial Keratitis

V. Nithya

Alagappa University, India

ABSTRACT

In recent years, multiple drug resistance has been developed due to indiscriminate use of existing drugs in the treatment of infectious diseases. One such herbal drug is Coriandrum Sativum L that possesses potential pharmaceutical activities and used in several ayurvedic formulations. Keratitis caused by bacteria, viruses, fungi and parasites. The main goal of this study is to evaluate the antibacterial, anti-fungal activity, anti-oxidant activity and anti-inflammatory activity of Coriandrum Sativum L leaves and seeds using various organic solvent of plant extract against keratitis disease. The present study carried out the effect on various organic solvents extract of leaves and seeds of Corindrum sativum not only on the bacterial and fungal populations isolated from the conjunctivitis infected eyes but also to screen the phytochemical, anti-inflammatory and in vitro antioxidant potential of the leaf and seed extracts.

INTRODUCTION

Microbial keratitis is a major cause of monocular blindness in developing countries. Corneal scarring listed second only to cataracts as an important cause of blindness and visual impairment in many developing countries in Asia, Africa and the Middle East. India too suffers a major setback in public health due to blindness caused by microbial keratitis (Alexandrakis, Alfonso, & Miller, 2000). Corneal lesions were found to be responsible for 9% of all blindness in India in a recent national survey. The factors that can predispose to infectious keratitis include age, occupation, environmental factors, trauma into the eye, foreign bodies, extended wear of conventional contact lenses (Alfonso, Mandelbaum, Fox, et al., 1986). chronic ocular surface disease, prior ocular surgery, diabetes mellitus, leprosy, rheumatoid arthritis, use of topical corticosteroids. Rapid initiation of treatment is required to halt the progression of disease so

DOI: 10.4018/978-1-5225-5195-9.ch016

that the extent of corneal scarring can be limited and thereby loss of vision (Ahmadi & McKenna 2003; Baker, Smith, & Cowan, 2003).

The antibiotics and steroid-based eye drops for the management of ophthalmic disorder has been found clinically unsafe in recent times and a current demand is to investigate alternative drug. A serious adverse drug reactions (ADRs) occurring due to use of herbal drugs is very rare event. A common argument that favours the use of herbal medicines is that they have a longstanding history of traditional use. Even after being used from ancient times, plant-derived medicines can result in some adverse reaction so needs have been raised for safety evaluation. Microorganisms develop resistance to present day antibiotics that has created immense clinical problem in the treatment of infectious diseases. However, today it is necessary to provide scientific proof as to whether or not it is justified to use a plant or its active principles. It is still a problem to use these medicinal plants for ophthalmic problems.

Coriandrum is the dried fruit of the tall perennial herbaceous plant, *Coriandrum Sativum*, and belonging to the family Apiaceae. This herb is cultivated commercially in Europa, Asia and Africa. The leaves are lanceolate, green or dark green, glabrous on both surfaces with acuminate apex. The fruit are, ovoid. The *Coriandrum* seeds have a warm, slightly pungent and highly aromatic flavour. Therefore, it is used as a spice in meat products such as Bologna and Frankfurter. *Coriandrum* oil is used in food, perfumery, and liquor in pharmaceutical industries as a flavour and a carminative. In medicine, it is used as a powerful aromatic, antiseptic, stimulant, carminative, stomachic, expectorant, anti-spasmodic and diuretic. In some parts of the world, especially the Near East and Saudi Arabia, *Coriandrum* is used mostly in the preparation of “Gahwa” a strong *Coriandrum* coffee concoction.

The World Health Organization (WHO) noted that the majority of the world’s population depends on traditional medicine for primary healthcare. Medicinal and aromatic plants are widely used as medicine and constitute a major source of natural organic compounds. Some medicinal plants have been used for a wide variety of purposes such as food preservation, pharmaceutical, alternative medicine, and natural therapies for many thousands of years (Chopra, Nayar, & Chopra, 1965). It is generally considered that compounds produced naturally, rather than synthetically, will be biodegraded more easily and therefore be more environmentally acceptable.

In the present study, the *Coriandrum Sativum* L was extracted by using various solvents of increasing polarity like petroleum ether, benzene, ethyl acetate, acetone, methanol and water. These extracts were characterized to demonstrate photochemical screening of secondary metabolites, antimicrobial property against microbes causing eye infections such as bacteria and fungi. The active antioxidants property and scavenging free radical activity was evaluated using FRAP assay. The anti-inflammatory activity of plant extracts using UV-VIS.

BACKGROUND

Plants have a vast potential for their use as curative medicine. In India, medicinal plants are widely used by all sections of people both directly as folk medicines in different indigenous systems of medicine like Siddha, Ayurveda and Unani and indirectly in the pharmaceutical preparations. India has about 4.5 million plant species and among them, several thousands have been claimed to possess medicinal properties against human diseases (Nadakarni, 1973). Although traditional medicinal healers have used medicinal plants for treatment of ailments for hundreds of years, there has always been a lingering question in scientific circles about their therapeutic efficacy. As a consequence, the pharmacological activity

of many medicinal plants has been studied, even though the vast majority of medicinal plants remain to be studied for their phytochemical components and pharmacological effects (Tripathi, 1994).

C. sativum extract protects liver from oxidative stress induced by carbon-tetrachloride (CCl₄) and thus helps in evaluation of traditional claim on this plant. Pretreatment of rats with different doses of plant extract (100 and 200 mg/kg) significantly lowered serum glutamate oxaloacetate transaminase (SGOT), serum glutamate pyruvate transaminase (SGPT), and TBARS levels against CCl₄ treated rats. Hepatic enzymes like superoxide dismutase (SOD), catalase (CAT), and glutathione peroxidase (GPx) were significantly increased by treatment with plant extract, against CCl₄ treated rats. Oral administration of the leaf extract at a dose of 200 mg/kg significantly reduced the toxic effects of CCl₄. The activity of leaf extract at this dose was comparable to the standard drug, silymarin (Ohkawa, Ohishi, & Yagi, 1979).

Coriandrum essential oil is obtained by steam distillation of the dried fully ripe fruits (seeds). Based on the results of a 28-day oral gavage study in rats, a no-observed effect level (NOEL) for Coriandrum oil is approximately 160 mg/kg/day. In a developmental toxicity study, the maternal no-observed adverse effect level (NOAEL) of Coriandrum oil was 250 mg/kg/day and the developmental NOAEL was 500 mg/kg/day. Coriandrum oil is not clastogenic, but results of mutagenicity studies for the spice and some extracts are mixed. The major component of the essential oil, linalool, is non-mutagenic. Coriandrum oil has broad-spectrum, antimicrobial activity. Coriandrum oil is irritating to rabbits, but not to humans; it is not a sensitizer, although, the whole spice may be. Based on the history of consumption of Coriandrum oil without reported adverse effects, lack of its toxicity in limited studies and lack of toxicity of its major constituent, linalool, the use of Coriandrum oil as an added food ingredient is considered safe at present levels of use. The median lethal dose (LD₅₀) of *C. sativum* essential oil was determined as 2.257 ml/kg. *C. sativum* as an oilseed crop grown in Italy was investigated regarding anti-nutritive compounds such as glucosinolates, sinapine, inositol phosphates, and condensed tannins, which can adversely affect the nutritional value of residues from the oilseed processing. All these compounds were found in *C. sativum* fruits in different amounts.

MAIN FOCUS OF THE CHAPTER

Preparation of *Coriandrum Sativum* L Extract of Leaves and Seeds

The *Coriandrum Sativum* L leaves and seeds will be collected and identified. The leaves were shade dried at room temperature and powdered the dried leaves and seeds. 500gm of *Coriandrum Sativum* L. leaves and seeds powder was taken in a beaker. Extracts will be prepared in the series of 500ml of different solvents based on increasing polarity (Ethyl acetate, Acetone, Methanol, and Water) using Soxhlet extraction method.

Macroscopic and Microscopic Studies

Macroscopic studies were carried out by simple determination, technique like the shape, size, colour, odour, margin and apex. The stem and leaf specimens were fixed in FAA and microtome slides were prepared and stained. Photomicrographs of with different magnifications were taken with microscopic unit.

Determination of Physicochemical Parameters

Total ash value, water and acid, soluble and insoluble ash value, and moisture content will be determined as per Indian pharmacopoeia.

Preliminary Phytochemical Analysis

The preliminary phytochemical analysis of the various organic solvent extract will be carried out using standard methods. The presence and absence of the secondary phytoconstituents such as alkaloids, steroid and /or triterpenoids and their glycosides, tannins, flavonoids and their glycosides, carbohydrates and cardiac glycosides using different phytochemical tests will be noted.

Sample Collection

All patients were examined under a slit-lamp biomicroscope by an ophthalmologist. Corneal scrapings were collected after instillation of 4% lignocaine without preservative under aseptic conditions from each ulcer by an ophthalmologist using a sterile Bard Parker blade. Scrapings were directly inoculated onto the surface of solid media such as sheep blood agar, chocolate agar and Sabouraud Dextrose Agar (SDA) in a row of C- shaped streaks and also deep inoculation in the liquid media such as Brain Heart Infusion (BHI) broth without gentamicin sulphate and thioglycollate medium.

Isolation of Bacteria from Sample

As per the standard protocol, microbial cultures were considered positive only if growth of the same organism was demonstrated on 2 or more solid media or there was confluent growth at the site of inoculation on 1 solid medium and which was subsequently sub-cultured and Gram stained for identification.

Identification of Bacteria

Both morphological and biochemical test for microorganism identifications were carried out. The biochemical tests were performed in order to identify the unknown bacteria. Some of the tests provided immediate results while others had to be incubated for a period of time.

Isolation of Fungi from Sample

Fungi were identified by their colony characteristics on PDA by their microscopic appearance in Lactophenol cotton blue. Fungal cultures from cases with smears negative for fungi were discarded as possible contaminants, although Chin et al., pointed out that negative smears and cultures do not necessarily rule out fungal infection Garg, Gopinathan, Choudhary, & Rao, 2000).

Determination of Antibacterial and Antifungal Activity of Plant Leaves and Seed Extract Using Agar Well Diffusion Method

Antibacterial activities of all the solvent extracts of plant leaves and seed will be determined by agar well diffusion method (Alastruey-Izquierdo et al., 2008). The extracts were dissolved in DMSO (dimethylsulphoxide). The microbial cultures were revived at 37°C for 18h in a broth medium. The 20µl of the culture was spread on Muller Hinton agar plates and wells of 9mm diameter were punched into the agar plates. 100µl of the solvent-free extracts of concentration 0.5mg/100µl and 1mg/100µl were used for determination of ZOI (Zone of Inhibition). After holding the plates at room temperature for 2 hours to allow diffusion of the extract into the media, the plates were incubated at 37°C for 24h. DMSO and Gentamicin was used as a negative control and as reference antibiotic (positive control) respectively. The test was performed in triplicates and the final results were presented as the mean zone of inhibition (Barik, Yegneswaran, Tayung, & Sahu, 2011).

Determination of Ferric Reducing Antioxidant Potential (FRAP)

The ferric reducing power of the plant extracts was determined by using potassium ferricyanide-ferric chloride method (Oyaizu, 1986). Different dilutions of extracts amounting to 1 ml were added to 2.5ml 0.2M phosphate buffer (pH6.6) and 2.5ml potassium ferriocyanide (1%). The mixtures were incubated at 50°C for 20 minutes, after which 2.5ml trichloroacetic acid (10%) was added. 2.5 ml of the mixture was taken and mixed with 2.5ml water and 0.5ml 1% FeCl₃. The absorbance at 700 nm was measured after allowing the solution to stand for 30 minutes. A graph of absorbance vs. plant extract concentration was plotted to observe the reducing power.

Antioxidant Activity of Fruit Juices by DPPH Free Radical Scavenging Assay

The scavenging activity of the extract was determined based on 2,2-diphenyl-1-picryl hydrazyl free radical (DPPH) scavenging assay described by Lai et al. (2001). The pepper extract (200 µl) was mixed with 800 µl of 100mM TrisHCl buffer, pH 7.4. The mixture was then added to 1.0ml of 500 µM DPPH (previously prepared in methanol). This was made up to the DPPH final concentration of 250 µM. The control was performed by mixing 200 µl of methanol with 1.0 ml DPPH. The mixture was then shaken vigorously and left to stand for 20 min at room temperature in a dark room. The absorbance was read using a UV-vis spectrophotometer at 517 nm with methanol as the blank. Triplicate measurements were carried out and their activity was calculated based on the percentage of scavenged DPPH.

Anti-Inflammatory Activity of Plant Extract Using UV-VIS Effect on Protein Denaturation

Protein denaturation was performed as described with slight modifications (Park, 2006). Test solution consisting of 1ml of different concentrations of Herbal Preparation (HP-4) ranging from 100-500 µg/ml or standard acetylsalicylic acid 100 and 200 µg/ml was mixed with 1ml of egg albumin solution (1mM) and incubated at 27 ± 1°C for 15 minutes. Denaturation was induced by keeping the reaction mixture at 70°C in a water bath for 10 minutes. After cooling the turbidity was measured spectrophotometrically at 660 nm. Percentage inhibition of denaturation was calculated from control where no drug was added. Each experiment was done in triplicate and the average was taken.

SOLUTIONS AND RECOMMENDATIONS

Anatomical Studies

Fresh *Coriandrum* leaf, stem, and root were collected and used to take hand section to study the internal features. The materials were trimmed and placed in thermocol and hand section were taken with safety blade. The thin section were selected, stained with Toluidine blue, observed and the microscope, the photographs were taken, with help of Olympus microscope. The images were saved and printed shown in Figures 1, 2, and 3. The photographs were taken in 10x and 45x magnification.

The leaf has upper and lower epidermis. The epidermis is single layered with barrel shaped cells. The radial cells of thick in between the dermises. Mesophyll tissue is present palisade parenchyma and sponge parenchyma. The cells of the palisade parenchyma is having chloroplast. The median central vein has both xylem and phloem as the connecting tissue. The stem is more are less circulating outline having single layered epidermis without any intracellular spaces, it is followed by hypodermis having small isodiametric cell it is four to five layer. The hypodermal layer is followed by large thin walled cortical cells having large intracellular spaces. The vascular bundle are arranged, peripherally. The vascular bundle are central arranged form of a ring plate. The root is circular outline the root epidermis layer followed by five to six hypodermis. The root cortex of made up of parenchyma, which is 20 to 25 layered. The next to root cortex, single layer endodermis is present. The central region root is having exact vascular bundle without any pitch.

Figure 1.

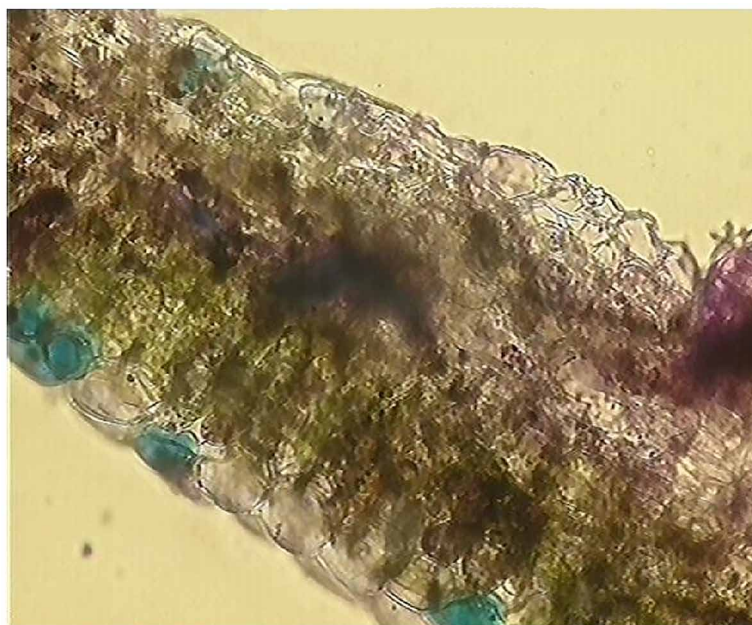


Figure 2. Cross section of Coriandrum stem

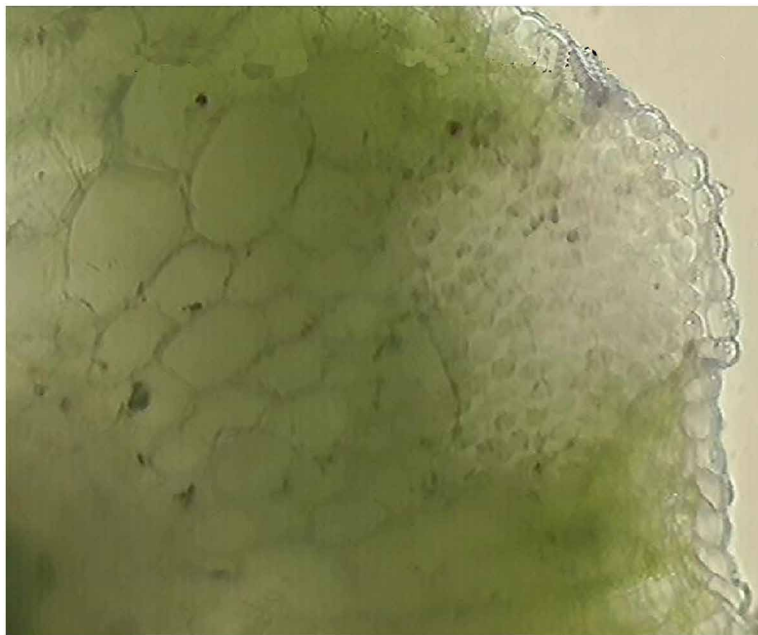


Figure 3. Cross section of Coriandrum root



Total Ash Value Content

The qualitative analysis of Coriandrum sativum L. powder of moisture content, total ash value, water soluble ash, acid soluble ash, content are shown in Table 1.

The results of physical constance of raw material lie within the limit, which is mentioned in Table 2. This signifies that the quality and purity of raw material was good enough. It is absorbed the moisture content of the material was found to be (2.3 gm). Which signify that the drug is properly dried and stored. The total ash (1.7 gm) particularly important in the evaluation of purity of material. The water soluble ash was found to be (1.2 gm) whereas the acid insoluble ash was found to be (0.23 gm) which is within fairly wide limit. As the ash value of the plant material with in the fair limit which signify is quality, purity and give an idea about the total inorganic compounds.

In the aqueous extract, alkaloids, flavanoids, carbohydrate, tannins, saponins, terpenoids, phenolic compounds are present and quinones and anthocyanin are absent. The carbohydrate saponins, terpenoids are absent in the acetone extract of Coriandrum sativum L and other also present.

In the methanolic extract of Coriandrum sativum L. contains the phytochemical constituent are alkaloids, carbohydrate, flavanoids, tannins, saponin, terpenoids, phenol, and anthocyaanin are present except quinones. The chloroform extract having alkaloids, tannins, terpenoids, and anthocyanin are

Table 1. Coriandrum sativum L. powder of moisture content, total ash value, water soluble ash, acid soluble ash, content

Ash Type and Content	Total gm per Sample
Total ash	1.7
Insoluble ash in hcl	0.23
Soluble ash in distilled water	1.2

Table 2. Phytochemical studies on Coriandrum sativum L. with various extract

Phytochemical Constituents	Phytochemical Test	Aqueous	Acetone	Methanol	Chloroform
Alkaloids Test	Wagners	+	+	+	+
Carbohydrate Test	Molischs Test	+	–	+	–
Carbohydrate Test	Fehlings Test	+	–	+	–
NaOH Test	Flavonoids	+	–	+	–
Ferric Chloride Test	Tannins	+	+	+	+
Foam Test	Saponins	+	–	+	–
Quinones Test	Quinones	–	+	–	–
Liebermann-Burchard Test	Terpenoids	+	-	+	+
Liebermann-Burchard Test	Sterols	+	+	–	–
Liebermann-Test	Phenols	+	+	+	–
Naoh Test	Anthocyanin	+	+	+	+

+ Present; - Absent

present (Table 3) from the result the aqueous and methanolic plant extract showed. More phytochemical constituents when compare with other extract.

The results of quantitative estimation of protein, phenol, and flavanoids are tabulated in Tables 3 and 4. The total phenol content was significantly high in aqueous extract *Coriandrum sativum L*. When compared with methanolic extract likewise the total flavanoid content was significantly high in methanolic extract *Coriandrum sativum L*. followed by aqueous extract.

Antibacterial Activity

The antibacterial activity of selected reference drugs against microorganisms was determined using three different concentrations. The development of drug resistance in human pathogens against commonly used antibiotics has necessitated a search for new antimicrobial substances from other sources including plants and microbes. The results on antimicrobial screening of the crude extracts of the *Coriandrum Sativum L*. plants are shown in Table 5. The antibacterial activity of the crude extract of plant extracts resulted in clear inhibition zones of at least 10mm for all the strains tested. showed high degree of antibacterial activity tested against bacterial species. Different extracts of activity against *Coriandrum Sativum L*. plants showed antibacterial activity against *Proteus* and *Bacillus*, *salmonella*, *shigella flexneri*, *pseudomonas*, *E.coli*, *streptococcus pyogens*, *staphylococcus aureus*, *klebsiella*, *vibrio*,. reported that *Coriandrum Sativum L*. contains large amount of phytoconstituents and the antibacterial activity may be indicating the presence of some secondary metabolites.

Antifungal Activity

Antifungal activity of the methanol, acetone and aqueous extracts of *Coriandrum sativum L*. were determined against *Candida albicans* and *Aspergillus* were shown in Table 6. Maximum inhibition zones of *Coriandrum* plant extracts against *C. albicans* were obtained in 20, 40, 60, µl concentraion respectively. It should be noted that, the *Coriandrum* plant extracts had antifungal activity in 20,40,60 µl concentration. It is shown that there is direct relationship between concentration and inhibition zone against standard antibiotic components of the clotrimazole and amphotericin B. The results are shown in Table 6.

Table 3. Total phenolic content

Plant Constituents	Aqueous Extract	Methanol Extract
phenols	1.24mg	1.1g

Table 4. Total flavonoid content

Plant Constituents	Aqueous Extract	Methanol Extract
Flavonoides	0.92mg	0.88g

Table 5. The antibacterial activity of Coriandrum Sativum L

Microorganisms	Zone of Inhibition (mm)			
	Antibiotic Disc	AQE	ME	AE
<i>E. coli</i>	Amp -	22	24	15
<i>Shigella. flexneri</i>	Str 7	15	14	12
<i>Salmonella</i>	Str 5	12	22	17
<i>Vibrio</i>	Str 8	20	22	17
<i>Pseudomonas aeruginosa</i>	Amp -	12	18	16
<i>Proteus</i>	Pen -	15	20	11
<i>Streptococcus pyogenes</i>	Pen -	7	16	12
<i>Staphylococcus</i>	Amp -	12	15	13
<i>Klebsiella</i>	Pen -	19	25	20
<i>Bacillus</i>	Amp-	10	16	15

Amp=Ampicillin, Str=Streptomycin, Pen=Penicillin, - =No zone, Aqe=Water Extract, Me=Methonal Extract, Ae =Acetone Extract.

Antioxidant Result

The data for the antioxidant capacity by phosphomolybdenum method and the antioxidant capacity of fraction was measured spectro photometrically through phosphomolybdenum method, which was based in the reduction of Mo (VI) to Mo (V) by the sample analytic and the supssequent formation of green phosphate Mo (V) compounds with a maximum absorbtion at 695 nm. The antioxidant capacity of the extract Coriandrum sativum L. was found to increase in methanolic extract and comparing in aqueous extract (Table 7).

REDUCING POWER ASSAY

Table 8 shows the reducing power of the Coriandrum sativum L extract by both the method. In this assay the yellow colour of the test solution changes to various shades of green and blue, depending on the reducing power of each compound. The presence of reducers causes the reduction of the Fe³⁺/ ferri-cyanide complex to the ferrous form. Therefore by measuring the formation of perl,s prussion blue at 700 nm, we can monitor the Fe²⁺ concentration. The reducing properties as generally of reductones, which have been showed to extract antioxidant action by breaking the free radical chain by donating a

Table 6. The antifungal activity of Coriandrum Sativum L

Microorganisms	Zone of Inhibition (mm)			
	Antibiotic Disc	AQE	ME	AE
<i>Aspergillus</i>	Amphotericin. B 7	10	18	14
<i>Candida albicans</i>	Clotrimazole10	12	16	13

Aqe=Aqueous Extract, Me=Methonal Extract=, Ae=Acetone Extract.

Table 7. Antioxidant activity of Coriandrum sativum L, leaves in methonal extract using phospho molybdate assay

Tests	Ascorbic Acid	Methanol Extract
B	0,00	0.00
S1	0.136	0.99
S2	0.137	0.162
S3	0.150	0.179
S4	0.158	0.280
S5	1.161	1.179

hydrogen atom. However as anticipated the reduction power of ascorbic acid was relatively more pronounced than that of *Coriandrum sativum* L. *sativum* L. was found to increase in methanolic extract and comparing in aqueous extract.

The major thrust is to establish alternative antimicrobial agent in order to treat microbial infections with less or no toxicity and less or negligible side effects. The herbal medicines have shown potential to overcome the limitation associated with conventional drugs. The herbal drug is *Coriandrum Sativum* L that possesses potential pharmaceutical activities and used in several ayurvedic formulations. *Coriandrum* is a very good disinfectant and has antimicrobial properties which protect the eyes from contagious diseases like conjunctivitis.

The electron donating ability of fruits and vegetables is a suitable parameter to establish the possession of oxidative stress quenching ability and their health studies have shown that are good sources of antioxidants. Though, high correlations have often been observed between phenolics and antioxidant capacity, our results indicate that flavonoids which are a group in phenolic compounds had highest correlation coefficient with antioxidants capacity.

Phenolics are most abundant in plants and are very common in fruits, vegetables, seeds, stems, and flowers and in tea. In plants, accumulation of phenolics varied from one part to another part and also depended on the age and developmental stage of the concerned plant parts; hence the differences observed in phenolics content in *Coriandrum Sativum* L.leaves and rhizomes extracts. In the present study, we employed DPPH assay to determine the antioxidant potential of *Coriandrum Sativum* L. leaves. The antioxidant capability of the medicinal plants is also often measured by their reducing power.

Table 8. Antioxidant activity of Coriandrum sativum L, leaves in aqueous extract using determination of reducing power assay

Tests	Ascorbic Acid	Aqueous Extract
B	0.00	0.00
S1	0.136	0.19
S2	0.137	0.21
S3	0.150	0.33
S 4	0.158	0.47
S 5	1.161	0.77

In our present study, the antioxidant property, of 50% ethanolic extract of *Coriandrum Sativum* L. was found to be changed in SOD, CAT, and LPO levels in rat gastric mucosa. During the ulcer condition there is an increase in gastric mucosal SOD and LPO activities. This indicated that the generation of reactive oxygen species during stress might be the causative factor for the inactivation of gastric peroxidase. *Moringa oleifera* Lam. exerts its antioxidant defense mechanism probably by metabolising lipid peroxides and scavenging endogenous H₂O₂. The superoxide anion (O₂⁻), H₂O₂ and hydroxyl radical (OH⁻) are the major reactive oxygen species (ROS) which induce cell degeneration by increasing LPO of cell membrane lipids. The toxic end products of peroxidation induce damage of the structural and functional integrity of cell membrane, break DNA strands and denature cellular proteins. The natural cellular antioxidant enzyme includes SOD, which scavenges superoxide radicals by speeding up their dismutation, CAT, a heme enzyme which removes H₂O₂. Detoxification of the superoxide anion is not a terminating step in free radical scavenging, since the enzyme catalysed dismutation results in the production of H₂O₂ which ultimately accumulates in the mitochondria and cytosol.

Phenolic compounds are secondary metabolites in fruits and vegetables. They have been re-ported to exhibit antioxidant activity which allows them to scavenge both active oxygen species and electrophiles, to inhibit nitrosation and to chelate metal ions, to have the potential for autoxidation and the capability to modulate certain cellular enzyme activities. Flavonoids, a class of phenolic compounds has been shown to possess anti-inflammatory, antiviral, anticarcinogenic, antithrom-botic, antiallergic and hepatoprotective. Carotenes have been proved to possess antioxidant activity due to their ability to quench singlet oxygen and inhibit lipid per oxidation. Thus, diets rich in fruits and vegetables are believed to play an important role in preventing diseases but human choices of diet are driven by necessity and economy. Lack of knowledge on the importance of good diet and prevalence of poverty has influenced the composition of diets taken by Nigerians. Coupled with this, the exposure to different kinds of toxic substances such as smoke from generators, sec-ond-hand vehicles and pesticide which are capable of in-ducing oxidative stress through production of free radicals.

FUTURE RESEARCH DIRECTION

Furthermore, the molecular docking studies carry out by using in silico studies used to initiate appropriate anti microbial therapy. The present study is used to create an efficient public health programme for rapid referral and treatment of microbial keratitis in the population at risk.

Molecular Docking Process Based on *In Silico* Approach

Microbial infections are a growing problem in contemporary medicine in keratitis, yet only a few antimicrobial agents are used in clinical practice. Most drug molecules inhibit the specific activity of a specific protein by blocking its active site. Docking methods are used to predict the manner in which a ligand binds to a protein receptor. The protein structure from the causative organism that contains the bound ligands most similar to the docked ligand increases docking accuracy for all methods (“similarity selection”). Identifying the most successful protein conformer (“best selection”) and similarity selection substantially reduce the difference between self-docking and average cross-docking accuracy.

CONCLUSION

The research work was carried out on the ten selected medicinal plants which shows that phytochemical constituents i.e., terpenoids, flavonoids, alkaloids, reducing sugars and tannins are either present or absent in these plants and the results were summarized. In our studies it was investigated that alkaloids and flavonoids are present in *Coriandrum Sativum* L and tannins, whereas reducing sugars and terpenoids were found to be absent. In previous studies it was reported that flavonoids and terpenoids were present in aqueous extract of the while alkaloids and phlobatannins were found to be absent in it. The recent research studies and previous research studies results were different so it might be due to the change in location and genetic variation due to cross pollination, so their genetic makeup were changed and that is why shows the different results.

It was observed that *Coriandrum Sativum* L showed highest concentration of phytochemicals by qualitative and quantitative. So it can be used as a good source of secondary metabolites. Herbs are enormously important in both traditional and western medicine. Hence it is essential to analyze the phytochemicals present in the plant through a potential technique. Based upon the qualitative and quantitative it can be concluded that this analytical technique is a convenient method to identify the presence of numerous constituents present in the methanolic, aqueous acetone and chloroform extract. The qualitative concentration of flavonoids and phenols in herbs have high amount of constituents.

The plant extract studied could be an answer to the people seeking for better therapeutic agents from natural sources which is believed to be more efficient with little or no side effects when compared to the commonly used synthetic chemotherapeutic agents. The present study verified the traditional use of *Coriandrum Sativum* L plants for various human ailments especially for various infectious diseases. Thus this plant could be utilized as an alternative source of useful antimicrobial drugs. Further studies are needed to isolate, characterize and elucidate the structure of the bioactive compounds of this plant for antimicrobial drug formulation.

This research was previously published in Examining the Development, Regulation, and Consumption of Functional Foods edited by Sailas Benjamin, pages 109-125, copyright year 2017 by Medical Information Science Reference (an imprint of IGI Global).

REFERENCES

- Ahmadi, S., & McKenna, K. (2003). Keratitis-ichthyosis-deafness syndrome and carotenaemia. *Clinical and Experimental Dermatology*, 28(4), 394–396. doi:10.1046/j.1365-2230.2003.01316.x PMID:12823302
- Alastruey-Izquierdo, A., Cuenca-Estrella, M., Monzon, A., Mellado, E., & Rodriguez-Tudela, J. L. (2008). Antifungal susceptibility profile of clinical *Fusarium* spp. isolates identified by molecular methods. *The Journal of Antimicrobial Chemotherapy*, 61(4), 805–809. doi:10.1093/jac/dkn022 PMID:18263569

Alexandrakis, G., Alfonso, E. C., & Miller, D. (2000). Shifting trends in bacterial keratitis in south Florida and emerging resistance to fluoroquinolones. *Ophthalmology*, 107(8), 1497–1502. doi:10.1016/S0161-6420(00)00179-2 PMID:10919897

Alfonso, E. C., Mandelbaum, S., Fox, M. J., & Forster, R. K. (1986). Ulcerative keratitis associated with contact lens wear. *American Journal of Ophthalmology*, 101(4), 429–433. doi:10.1016/0002-9394(86)90641-0 PMID:3963102

Baker, G. C., Smith, J. J., & Cowan, D. A. (2003). Review and re-analysis of domain specific 16s primers. *Journal of Microbiological Methods*, 55(3), 541–555. doi:10.1016/j.mimet.2003.08.009 PMID:14607398

Barik, B. P., Yegneswaran, P. P., Tayung, K., & Sahu, H. K. (2011). Molecular Identification and in-vitro Antifungal Susceptibility of Fusarium sp. isolated from Corneal Scrape. *Journal of Life Science*, 3(2), 127–130.

Chopra, R. N., Nayar, S. L., & Chopra, I. C. (1965). Glossary of Indian Medicinal Plants with active principles Part-I (a-k). National Institute of Science Communication.

Garg, P., Gopinathan, U., Choudhary, K., & Rao, G. N. (2000). Keratomycosis: Clinical and microbiologic experience with dematiaceous fungi. *Ophthalmology*, 107(3), 574–580. doi:10.1016/S0161-6420(99)00079-2 PMID:10711898

Lai, L. S., Chou, S. T., & Chao, W. W. (2001). Studies on the antioxidative activities of hsian-tsao (*Mesona procumbens* Hemsl) leaf gum. *Journal of Agricultural and Food Chemistry*, 49(2), 963–968. doi:10.1021/jf001146k PMID:11262057

Nadakarni, A. K. (1973). *Indian Meteria Medica*. Mumbai. *Popular Prakashan*, 1(1), 72.

Ohkawa, H., Ohishi, N., & Yagi, K. (1979). Assay for lipid peroxidase in animal tissues by thiobarbituric acid reaction. *Analytical Biochemistry*, 95(2), 351–358. doi:10.1016/0003-2697(79)90738-3 PMID:36810

Oyaizu, M. (1986). Studies on products of browning reactions: Antioxidative activities of products of browning reaction prepared from glucosamine. *Japanese Journal of Nutrition*, 44(6), 307–315. doi:10.5264/eiyogakuzashi.44.307

Park, E. K., Ryu, M. H., Kim, Y. H., Lee, Y. A., Lee, S. H., Woo, D. H., & Kim, K. S. et al. (2006). Anti-inflammatory effect of an ethanolic extract from *Clematis mandshurica* Rupr. *Journal of Ethnopharmacology*, 108(1), 142–147. doi:10.1016/j.jep.2006.04.025 PMID:16787723

Tripathi, K. D. (1994). *Essentials of Medical Pharmacology*. Jaypee Brothers Medical Publishers.

KEY TERMS AND DEFINITIONS

Antibacterial: Anything that destroys bacteria or suppresses their growth or their ability to reproduce.

Antifungal: A medication that limits or prevents the growth of yeasts and other fungal organisms.

Anti-Inflammatory: Acting to reduce certain signs of inflammation, as swelling, tenderness, fever, and pain.

Antioxidant: A substance that reduces damage due to oxygen, such as that caused by free radicals.

Free Radicals: An especially reactive atom or group of atoms that has one or more unpaired electrons.

Keratitis: An inflammation of the cornea, the transparent membrane that covers the colored part of the eye (iris) and pupil of the eye.

Phytochemicals: Chemical compounds that occur naturally in plants.

Chapter 17

Nanotechnology for Omics–Based Ocular Drug Delivery

Anjali Hirani

University of South Florida, USA & Virginia Tech-Wake Forest University, USA

Aditya Grover

University of South Florida, USA

Yong Woo Lee

Virginia Tech-Wake Forest University, USA

Yashwant Pathak

University of South Florida, USA

Vijaykumar Sutariya

University of South Florida, USA

ABSTRACT

Millions of people suffer from ocular diseases that impair vision and can lead to blindness. Advances in genomics and proteomics have revealed a number of different molecular markers specific for different ocular diseases, thereby optimizing the processes of drug development and discovery. Nanotechnology can increase the throughput of data obtained in omics-based studies and allows for more sensitive diagnostic techniques as more efficient drug delivery systems. Biocompatible and biodegradable nanomaterials developed through omics-based research are able to target reported molecular markers for different ocular diseases and offer novel alternatives to conventional drug therapy. In this chapter, the authors review the pathophysiology, current genomic and proteomic information, and current nanomaterial-based therapies of four ocular diseases: glaucoma, uveal melanoma, age-related macular degeneration, and diabetic retinopathy. Omics-based research can be used to elucidate specific genes and proteins and develop novel nanomedicine formulations to prevent, halt, or cure ocular diseases at the transcriptional or translational level.

DOI: 10.4018/978-1-5225-5195-9.ch017

OCULAR DISEASE

Approximately 140 million Americans over the age of 40 suffer from a variety of ocular diseases that impair vision and may lead to blindness (NEI, 2012). The prevalence of ocular disorders will continue to increase with the worldwide aging population. Although current treatments do exist, there is a need for better diagnostics and more efficient therapies that can arrest the progression and/or even reverse damage of ocular diseases. Currently, more information is needed to understand the pathogenesis of ocular disease as well as determining new drug targets to enhance ocular drug discovery or repositioning current drugs for more efficacious therapy.

Limitations in Treatment for Ocular Diseases

Currently, therapies exist to delay progression of some ocular diseases; however, a better understanding of pathogenic processes is needed to find more effective treatments. Some of the common ocular diseases presented later in this chapter possess a complex interplay of genetic factors that are challenging to treat. Discovery of genes responsible for ocular disorders can aid in the development of new therapeutic agents. Clinically, we are merely treating symptoms and not targeting the actual disease mechanisms. More research needs to be completed to elucidate these mechanisms.

A number of barriers for ocular drug delivery exist, such as nasolacrimal drainage and the blood-aqueous and blood-retinal barriers. This restricts administration of potential therapeutics. Drug can be delivered by a variety of routes including topical ocular, periocular injection, intravitreal injection, and systemic administration. The topical route is a convenient method of drug delivery to the anterior segment; however, a model of transient diffusion has shown that less than 5% of a lipophilic drug and 0.5% of a hydrophilic drug penetrate the cornea (W. Zhang, Prausnitz, & Edwards, 2004), and the remainder is cleared through nasolacrimal drainage and systemic absorption (Gambhire, Bhalerao, & Singh, 2013). The amount of available drug that permeates across the sclera is reduced with cationic and lipophilic solutes and the RPE has tight intercellular junctions for hydrophilic molecules (Urtti, 2006). Additionally, the lymphatic system, blood vessels and active transporters all work to clear drugs administered through transscleral routes. Systemic administration of drugs requires high doses that are potentially toxic to obtain a therapeutic concentration across the blood ocular barriers (Geroski & Edelhauser, 2000; Sigurdsson, Konraethsdottir, Loftsson, & Stefansson, 2007). Intravitreal injections circumvent physiological barriers and maintain therapeutic doses without damage to bystander tissues; however, frequent injections can lead to complications like retinal detachment, increase in ocular pressure, and hemorrhage (Peyman, Lad, & Moshfeghi, 2009). Given the presence of these physiological barriers, the development of therapies utilizing nanotechnology that efficiently deliver drugs and extend drug release to the eye would be beneficial to the progression of ocular disease treatment. Due to the lengthy pipeline in gaining FDA approval, newly repositioned drugs can be utilized to expand current disease therapy.

Omics-Based Nanotechnology

The goal of omics-based nanotechnology is to use nanoscale technology to enhance early detection, gain an understanding of pathophysiology, as well as find better treatments for eye disease. Nanogenomics refers to a new approach for medical diagnostics and therapy (Nicolini, 2006). Nanoproteomics allows us to evaluate expression of ocular proteins, identify novel therapeutic targets study the pharmacological

effects of therapeutics (Steely & Clark, 2000). These new techniques can improve the current understanding of ocular diseases and aid in the discovery of therapies targeting genes responsible for ocular disease.

APPLICATION TO OCULAR DISEASES

Glaucoma

Pathophysiology

Glaucoma causes blindness in about 7 million people every year, only 10% of the people affected by glaucoma worldwide (Quigley, 1996). A number of risk factors have been identified for glaucoma, including hypertension, family history, and age, among others (Abbot F Clark & Thomas Yorio, 2003). Glaucoma is caused by progressive damage to the trabecular meshwork, optic nerve head, and retinal ganglion cells; however, the exact mechanism behind the nerve damage is yet unknown (Abbot F Clark & Thomas Yorio, 2003; Frank S Ong et al., 2013). Glaucoma can usually be diagnosed as open- or closed-angle and primary or secondary based on the degree of ocular hypertension (Abbot F Clark & Thomas Yorio, 2003). Elevated intraocular pressure (IOP) is characteristic of primary open-angle glaucoma (POAG), the most common type of glaucoma, and is the most common target of treatment.

Current Genomic and Proteomic Information

A number of genetic markers that play a role in multiple different types of glaucomas have been identified.

MYOC was one of the first genes identified for juvenile and adult-onset POAG (Stone et al., 1997). Its associated protein, myocilin, has been associated with the trabecular meshwork and may be associated with increased outflow resistance, leading to an increase in IOP pressure (Fautsch, Bahler, Jewison, & Johnson, 2000; WuDunn, 2002; Z. Zhou & Vollrath, 1999).

Reiger syndrome is a genetic disorder which manifests itself in craniofacial and umbilical abnormalities (Amendt, Semina, & Alward, 2000). The varied phenotypes associated with Reiger syndrome are associated with different mutations in the *PITX2* gene and the *PITX2* transcription factor for which it codes. More than half of the individuals diagnosed with Reiger syndrome develop glaucoma, making the mutant *PITX2* gene a risk factor and molecular marker for glaucoma (WuDunn, 2002).

Primary congenital glaucoma has been traced to mutations in *CYP11B1* gene. *CYP11B1* codes for the CYP11B1 protein from the cytochrome P450 family, but its mechanism in ocular pathology is not yet fully understood (Stoilov, Jansson, Sarfarazi, & Schenkman, 2001). Studies of various ethnic populations affected with congenital glaucoma revealed multiple mutations of the *CYP11B1* gene responsible for the disease in Western- and Middle Eastern as well as Japanese populations (Michels-Rautenstrauss et al., 2001).

Six genes (*GLC1A-GLC1F*) have been identified through pedigree analysis of families affected by hereditary POAG. *PCOLCE2* has also been identified as a possible indicator of glaucoma because of its association with the trabecular meshwork and the *GLC1C* locus, but no mutations in *PCOLCE2* were identified in patients with *GLC1C*-induced POAG (WuDunn, 2002). Population studies in Estonian POAG patients also showed a significantly higher association between individuals positive for the

glutathione S-transferase (GSTM1) protein with POAG as compared to a control population. Smoking increased this risk (Juronen et al., 2000).

Reductions in the outflow of aqueous humor from the anterior chamber of the eye have been implicated in glaucoma pathology due to its association to IOP. Imbalances in the expression levels of matrix metalloproteinases (MMPs) and tissue inhibitors of MMPs (TIMPs), which remodel the extracellular matrix (ECM) of the trabecular meshwork, may account for the differences in aqueous humor outflow in patients with glaucoma (Wong et al., 2002). Disruption of trabecular meshwork ECM was also revealed as a result of increased TGF-beta levels in glaucoma patients (Zhao, Ramsey, Stephan, & Russell, 2004). Prostaglandins increase the activity of MMPs in ciliary smooth muscle cells, which effects the outflow of aqueous humor, and can lead to a decrease in the high IOP pressure characteristic of POAG (Weinreb, Kashiwagi, Kashiwagi, Tsukahara, & Lindsey, 1997). In addition, cochlin protein has been identified as an elevator of IOP pressure in glaucoma patients by disrupting the trabecular meshwork (Bhattacharya et al., 2005).

Current Therapies

A number of current nanomedicine therapies have been investigated in the treatment of glaucoma physiology. The benefits that nanomedicines offer are their biodegradability, sustained release of drugs, and targeting of necessary tissues and molecular pathways.

Chu et al. investigated the activity of 7-hydroxy-2-dipropylaminotetralin (7-OH-DPAT)-loaded calcium phosphate nanoparticles (CAP) in the reduction of IOP and aqueous flow rate in glaucomatous rabbits. 7-OH-DPAT in CAP showed a hypotensive, therefore therapeutic, effect in the glaucomatous model; however, raclopride, a dopamine D2/D3 receptor agonist, was shown to reduce the effect of 7-OH-DPAT in CAP. The data suggests that dopamine D2/D3 receptors may play a role in modulating IOP and that CAP may potentially be a therapeutic agent for glaucoma. In addition, further investigations of the role of the dopamine D2/D3 receptor in glaucoma may elucidate further directed therapies for the modulation of glaucomatous IOP (Chu, He, & Potter, 2002).

Wadhwa et al. revealed the IOP-reducing effects of hyaluronic acid (HA)-conjugated chitosan (CS) nanoparticles (CS-HP-NPs) loaded with dorzolamide hydrochloride and timolol maleate, 2 drugs used in glaucoma treatment. CS-NPs have been used as nanomedicine carriers due to their biodegradability and drug availability, but conjugation with HA synergistically increases the mucoadhesion of CS-NPs. *In vivo* studies in rabbits revealed a significant IOP reduction in rabbits treated with CS-HA-NPs as opposed to the free drug solution, suggesting its potential use against glaucoma (Wadhwa, Paliwal, Paliwal, & Vyas, 2010).

Jiang et al. reported the neuroprotective role of glial cell-line derived neurotrophic factor (GDNF) loaded into poly DL-lactide-co-glycolide (PLGA) microspheres in elevated IOP-induced rats. Intravitreal injections of the GDNF-PLGA microspheres were significantly better in the neuroprotection of retinal ganglion cells (RGCs) in chronically elevated IOP through the analysis of glial fibrillary acidic protein (GFAP) production compared to the blank PLGA microspheres and GDNF alone (Jiang et al., 2007). It is reasonable to believe that the nanomedicine administration of various other genes and RNA inhibitors of proteins may be able to provide further neuroprotection to RGCs after injury or surgery (Zarbin, Montemagno, Leary, & Ritch, 2013). Indeed, as a potential post-operative therapy to protect against scarring after glaucoma surgery, Dos Santos et al. investigated the role of nanosized complexes of antisense TGF-beta2 phosphorothiorate oligonucleotides (PS-ODN) with polyethylenimine (PEI)

encapsulated in PLGA microspheres. Subconjunctival injections in rabbits significantly improved bleb survival and increased the intracellular penetration of PS-ODN, revealing the microspheres' potential therapeutic role (Gomes dos Santos et al., 2006).

The incorporation of drugs, genes, or oligonucleotides into biodegradable and biocompatible nano-medicine vectors may provide novel therapeutic potentials in the prevention and treatment of glaucoma. The size range of nanomedicines make these vectors compatible for endocytosis into effected cells and also offer sustained release of the compounds associated with the vectors. These compounds may be able to directly influence the genetic and molecular pathways that influence the glaucoma phenotype.

Uveal Melanoma

Pathophysiology

Uveal melanoma (UM) is one of the most common ocular cancers in adults, with 7 cases per million each year and over 20 cases per million in those over the age of 70 (Ramasamy et al., 2014; Singh & Topham, 2003). Over ninety percent of UM cases arise in the choroid and have the worst prognosis, followed by the ciliary body and iris, with the best prognosis (Ramasamy et al., 2014). Over half of UM cases result in metastasis, 40% of which result in death even after primary tumor treatment (Bedikian, 2006). Close to 90% of UM metastatic cases result in metastasis to the liver; the skin, bones, and lungs are other common sites of metastasis following metastasis to the liver (Lorigan, Wallace, & Mavligit, 1991; Singh & Borden, 2005).

Current Genomic and Proteomic Information

Heat shock protein 27 (HSP-27) is a cytoplasmic protein involved in cell migration, cytoskeletal structure, cell survival, and tumor progression (Kostenko & Moens, 2009). It plays different roles in a number of different cancers; HSP-27 is over expressed in gastric, prostate, and node-negative breast carcinoma and indicates a poor prognosis in each, but over-expression of HSP-27 indicates good prognosis in non-small-cell lung- and ovarian carcinomas (Ramasamy et al., 2014). Proteomic analysis of primary UM tissue revealed a down regulation of HSP-27 in monosomy 3 tumors, with a significantly lower expression in monosomy 3 tumors as opposed to disomy 3 tumors (Coupland et al., 2010). In addition, Jmor et al. showed that a significantly reduced expression of HSP-27 in UM tissue correlated with a predicted survival of less than 8 years (Jmor, Kalirai, Taktak, Damato, & Coupland, 2012). Investigations in a human cutaneous melanoma cell line revealed that the over expression of HSP-27 inhibited cell proliferation and reduced cell invasiveness, which suggests that the under expression of HSP-27 might induce greater cell migration in UM (Aldrian et al., 2002).

Two-dimensional difference gel electrophoresis (2D DIGE) followed up by immunohistochemical studies in primary UM tumor samples also identified the over expression of fatty acid-binding protein heart type (FABP3) and triosephosphate isomerase (TPI1). In addition, siRNA knockdowns of these 2 proteins in a primary UM cell line revealed significantly reduced levels of cell invasion and migration (Linge et al., 2012). FABPs are thought to play a number of metabolic roles in cells, including growth, differentiation, and apoptosis (Lichtenfels et al., 2009). Investigation of the over expression of FABP in small cell lung cancer implicate its role in mitosis and cell growth (L. Zhang, Cilley, & Chinoy, 2000). FABP has also been linked with poor prognosis and tumor aggressiveness in human gastric carcinoma

(Hashimoto et al., 2004). TPI1 plays a role in the cell's glycolysis and gluconeogenesis pathways, high rates of which are required for tumor cells (Albery & Knowles, 1976; Bui & Thompson, 2006). TPI1 has been reported to be associated with the aggressiveness of breast cancer, and its under expression was found to induce apoptosis in the HeLa cell line (Lee et al., 2010; Selicharova et al., 2008). However, its over expression in lung cancer tissue, cell lines, and plasma, as well as in prostate cancer implicates its role in the progression of disease and as biomarkers (Chen et al., 2002; Kim, Koo, Kim, Sohn, & Park, 2008; Qian et al., 2010). The identification of these genetic markers in UM and their varied roles in a number of different types of cancers suggests that their over expression in primary UM tumors may contribute to the oncogeneity of the tissue. Further investigations of the roles of FABP3 and TPI1 in UM may reveal novel pathways for therapeutic intervention as well as screening techniques in preventing the progression of UM.

Proteomic analyses of primary tumors and cell lines have revealed the above-mentioned proteins as potential biomarkers for UM; however, further such studies are required to elucidate more proteins for the identification of UM. There is a lack of genomic and proteomic analysis of UM tissues in available literature, but such studies would greatly increase the understanding of the molecular mechanisms behind the induction and progression of the disease. The proteins and biomarkers identified by future studies would provide researchers with genomic and molecular pathways to target through nanotechnological intervention.

Current Therapies

The relatively low incidences of UM and the considerable lack of extensive genomic and proteomic studies of UM tissues contribute to low number of nanomedicines to target UM. However, the versatile nature of nanomedicines suggests its possible successes in treating UM.

Wang et al. investigated the role of dendrimer nanoparticle transfection therapy in the human choroidal melanoma cell line (OCM-1) as a potential treatment (Yingchih Wang, Mo, Wei, & Shi, 2013). The dendrimer nanoparticles were complexed with recombinant DNA plasmids of tumor necrosis factor- α (TNF α) and herpes simplex virus thymidine kinase (HSV-TK), both constructed with the promoter sequence of early growth response-1 (Egr1). Dendrimer nanoparticles are biocompatible and are formed from nanoparticle polymers with sizes of less than 100 nm, physiologically relevant when treating ocular diseases. The polymer is composed of amino groups which are protonated at physiological pH levels, allowing electrostatic interactions with oligonucleotides and their compaction and protection during transfection. The transfection complex is able to be endocytosed by the cell, allowing the oligonucleotide complex to be released into the cell and enter the nucleus for transcriptional regulation. Dendrimer-based nanoparticle transfection complexes offer biocompatibility and the protection of associated nucleic acids (Yingchih Wang et al., 2013).

Molecular studies in various tumors have identified the HSV-TK suicide gene as a promising and successful cancer treatment by killing infected cells and surrounding uninfected cells when administered in conjunction with other drugs or compounds (Rainov, 2000). Wang et al. administered HSV-TK with TNF- α due to the natural anti-tumor properties exhibited by TNF- α , including the ability to activate immune responses and cause hemorrhaging and necrosis in tumoric tissues (Ha Thi et al., 2013; Kearney et al., 2013). HSV-TK and TNF- α were complexed with Egr1 promoter due to Egr1's revealed anti-tumor properties when associated with target genes (Y. Zhou et al., 2010) and the hypothesis that irradiation

with ^{125}I may activate the Egr1 promoter complex and induce the transcription and translation of TNF- α and HSV-TK (Yingchih Wang et al., 2013).

Wang et al. radiated the successfully-transfected tissues with ^{125}I and found a significantly elevated expression of TNF- α and HSV-TK through western blot and ELISA analysis after radiation as compared to before, thought to be due to the activation of Egr1 transcription. Transmission electron microscopy (TEM) analysis of irradiated TNF-TK transfected tissues revealed an increased number of cells in the necrotic state along with the inhibition of cell growth and proliferation. The successful coupling of radiation with gene therapy revealed that targeted gene therapy through the Egr1 promoter and radiation could provide for a novel therapeutic route against UM (Yingchih Wang et al., 2013).

Future proteomic studies that reveal a number of other proteins involved in UM pathological pathways may also become similar targets for *in vitro* and *in vivo* experiments such as the one conducted by Wang et al. Coupling nanomedicine gene therapy with standard radiation therapy reveals a synergistic therapeutic effect in treated tissues, and may lead to clinical breakthroughs and better therapies.

Age-Related Macular Degeneration

Pathophysiology

Age-related macular degeneration (AMD) is a disease that destroys sharp, central vision. It affects the central region of the retina known as the macula, which is responsible for fine vision. It is characterized by the presence of drusen and area of hyperpigmentation on the retinal pigment epithelium (RPE). Advanced AMD is characterized by choroidal neovascularization (CNV), the growth of abnormal blood vessels beneath the RPE or between the RPE and the retina (Bylsma & Guymer, 2005). It is accompanied by fluid and blood rupturing Bruch's membrane into the subretinal space, leading to irregularities of the retina.

Current Genomic and Proteomic Information

Case studies have provided evidence for a variety of genetic markers involved in the occurrence of AMD, namely in the formation of drusen and degeneration of macula. Docosahexaenoic acid (DHA) is present in photoreceptor cell membranes in the retina. It is extremely sensitive to oxidative damage and cleavage results in the production of carboxyethylpyrrole (CEP), an oxidative protein (Gu et al., 2010). CEP has been found to be abundant in ocular tissue of patients presenting with AMD. While a genetic marker of oxidative damage, CEPs promote the growth of capillaries and can contribute to neovascularization (Lu et al., 2009).

Due to the neovascularization present in AMD, anti-angiogenic therapy is useful to slow the progression of the disease. Vascular endothelial growth factor A (VEGF-A) is the most potent promoter of angiogenesis and vascular permeability and its role in the pathogenesis of neovascular AMD is well recognized (Ferrara, Gerber, & LeCouter, 2003; Park, Rhu, Kang, & Roh, 2012; Verteporfin In Photodynamic Therapy Study, 2001). VEGF levels and vitreous levels are elevated in human CNV in compared to healthy controls (Sendrowski, Jaanus, Semes, & Stern, 2008). Due to the implication of VEGF in the progression of AMD, anti-angiogenic drugs have been recently pursued to block the development and leakage of new, abnormal blood vessels.

Current Therapies

Three anti-angiogenic drugs are currently being used in the treatment of AMD: ranibizumab (Lucentis), bevacizumab (Avastin), and pegaptanib (Macugen) (Bylsma & Guymer, 2005). Ranibizumab is a human recombinant antibody fragment that displays high binding affinity towards all VEGF isoforms. Clinical trials have shown that ranibizumab helps maintain stable vision without further progression of the disease; however, because of the high cost of the drug, the use of the drug worldwide is limited (Rosenfeld et al., 2006). Bevacizumab has been used more recently as an 'off label' therapy. It is a full-length human recombinant monoclonal antibody, which binds all VEGF isoforms. It is FDA approved for colorectal, lung, and breast cancer, but is used in clinical trials for AMD due to lower patient cost. Pegaptanib is a pegylated aptamer that acts as an anti-VEGF agent. It binds the VEGF₁₆₅ isoform and inhibits angiogenesis (Vadlapudi, Ashaben, Kishore, & Ashim, 2012). For these anti-angiogenic drugs, the biggest challenge is route of administration. Intravitreal injections allow for the most direct approach; however, the chronic nature of the disease requires consistent injections resulting in side-effects such as retinal detachment and cataract formation (Mudunuri, 2008). Recent studies using nanoemulsions and polymeric micelles containing anti-VEGF bevacizumab result in sustained delivery. Additional research has shown that pDNA encapsulated by micelles can ameliorate choroidal neovascularization in AMD (F. S. Ong et al., 2013). These nanoemulsions and polymeric micelles used for delivery offer more effective drug delivery by their ability to maintain therapeutic concentrations of the active drug molecule over a longer duration than previous methods.

Diabetic Retinopathy

Pathophysiology

Diabetic retinopathy (DR) is a consequence of diabetes, usually developing within 5-10 years. The disease is associated with progressive retinal ischemia (A. F. Clark & T. Yorio, 2003). It is characterized by loss of pericytes in retinal capillaries and subsequent thickening of capillary basement membranes and local ischemia. This induces the expression of VEGF, which can cause vessel leakage and formation of abnormal blood vessels, similar to AMD. The majority of vision loss from DR is due to macular edema. Other factors such as proliferation of fibrovascular membranes can lead to retinal detachment (A. F. Clark & T. Yorio, 2003).

Current Genomic and Proteomic Information

DR has been studied by proteomic analysis of the vitreous humor. Mass spectroscopy based studies have shown that elevated levels of extracellular carbonic anhydrase-I and kallikrein are present in patients with DR. This suggests that retinal hemorrhage contribute to the DR proteomic information. Studies displaying intravitreal injection of carbonic anhydrase-I in rats lead to increased retinal vessel leakage and edema (Gao et al., 2007).

Current Therapies

Current therapies include photocoagulation therapy and pharmacological agents that block VEGF signaling, such as ruboxistaurin mesylate which is a protein kinase C- β inhibitor. Additionally, corticosteroids are also being evaluated for their angiostatic, antipermeable and antifibrotic properties (Samudre, Lattanzio, Williams, & Sheppard, 2004; Y. Wang, Wang, & Chan, 2011). Triamcinolone acetonide and dexamethasone are used in combination with other treatments for posterior ocular disorders. They act by binding steroid receptors in cells to induce or repress targeted genes, thereby inhibiting inflammatory symptoms like edema and vascular permeability (Sherif & Pleyer, 2002). Corticosteroids act on VEGF by inhibiting VEGF secretion and inhibiting cytokine production (Wu, Wang, Yang, Huang, & Kuo, 2006). Corticosteroids can also inhibit basic fibroblast growth factor and ICAM-1 expression and decrease VEGF levels that are evident in neovascularization (Penfold et al., 2000; Y. S. Wang, Friedrichs, Eichler, Hoffmann, & Wiedemann, 2002). As with AMD, nanoparticles have gained attention as a drug delivery system to overcome the blood-retinal barriers. Recent studies have encapsulated current therapies in nanoemulsions to sustain drug delivery. Alternatively AuNPs alone have been shown to inhibit retinal neovascularization by suppressing VEGF receptor activation. It is believed that AuNP bind to the heparin-binding proteins of certain VEGF isoforms (Jo, Lee, & Kim, 2011).

CONCLUSION AND FUTURE PERSPECTIVES

Genomic and proteomic analyses consist of a number of different techniques to help identify the molecular basis behind diseases. Because the eyes act as our window to the world around us, measures taken to protect the eyes from damage would be of great benefit to all people.

We have described a number of different ocular diseases, ranging in severity from slight discomfort caused by IOP in glaucomatous patients, to partial blindness in AMD patients, leading to death in patients of UM. We have described a number of molecular markers, genomic and proteomic, that act as indicators for their respective diseases. These genes and proteins are involved in a multitude of pathways in ocular tissues and may play different roles in different diseases, but elucidating their role in ocular diseases helps in developing therapies against those diseases. However, the data obtained from genomic and proteomic analyses in ocular tissues available in current literature is not exhaustive; further research needs to be conducted to identify many more omics-related markers in all kinds of ocular tissues and diseases.

What has been reported so far in regards to genomic and proteomic biomarkers of ocular diseases have been useful in the development of nanomedicine for those diseases. Nanomedicine offers a number of advantages when compared to conventional drug therapy, including small sizes, tissue-targeting, sustained release of the drug, low toxicity, biocompatibility, and biodegradability. Nanomedicine is between 1-999 nm in size, but most are around 100-200 nm in size, sizes that are tolerated in ocular tissues. The sizes and targeting of tissues through surface conjugations of the nanomedicine vectors enable their endocytosis into the cell. Once in the cell, nanomedicine exhibits a steady and sustained release of the drug compound over days, weeks, and even months. Most nanomedicine vectors are made from organic compounds that are well tolerated in ocular tissues, such as PLGA, and can be broken down into harmless compounds by catabolism and eventually excreted. The ability to deliver novel drug, nucleic acid,

protein, and herbal compounds through complexing or encapsulating them within nanomedicine allows for the direct targeting of the molecular pathways indicated by omics analysis specific for that disease. Through directly targeting specific proteins, the disease can be prevented, arrested, or even cured at the transcriptional or translational level. Further and continued omics-based research will have a direct impact on the well-being and prognosis of degenerative ocular diseases through the development of novel nanomedicine formulations.

ACKNOWLEDGMENT

Anjali Hirani and Aditya Grover are equal authors to the manuscript.

REFERENCES

- Albery, W.J., & Knowles, J. R. (1976). Free-energy profile for the reaction catalyzed by triosephosphate isomerase. *Biochemistry*, 15(25), 5627–5631. doi:10.1021/bi00670a031 PMID:999838
- Aldrian, S., Trautinger, F., Fröhlich, I., Berger, W., Micksche, M., & Kindas-Mügge, I. (2002). Over-expression of Hsp27 affects the metastatic phenotype of human melanoma cells in vitro. *Cell Stress & Chaperones*, 7(2), 177. doi:10.1379/1466-1268(2002)007<0177:OOHATM>2.0.CO;2 PMID:12380685
- Amendt, B. A., Semina, E. V., & Alward, W. L. M. (2000). Rieger syndrome: A clinical, molecular, and biochemical analysis. *Cellular and Molecular Life Sciences CMLS*, 57(11), 1652–1666. doi:10.1007/PL00000647 PMID:11092457
- Bedikian, A. Y. (2006). Metastatic uveal melanoma therapy: Current options. *International Ophthalmology Clinics*, 46(1), 151–166. doi:10.1097/01.iio.0000195852.08453.de PMID:16365561
- Bhattacharya, S. K., Rockwood, E. J., Smith, S. D., Bonilha, V. L., Crabb, J. S., & Kuchtey, R. W. et al. (2005). Proteomics reveal Cochlin deposits associated with glaucomatous trabecular meshwork. *The Journal of Biological Chemistry*, 280(7), 6080–6084. doi:10.1074/jbc.M411233200 PMID:15579465
- Bui, T., & Thompson, C. B. (2006). Cancer's sweet tooth. *Cancer Cell*, 9(6), 419–420. doi:10.1016/j.ccr.2006.05.012 PMID:16766260
- Bylsma, G. W., & Guymer, R. H. (2005). Treatment of age-related macular degeneration. *Clinical & Experimental Optometry*, 88(5), 322–334. doi:10.1111/j.1444-0938.2005.tb06716.x PMID:16255691
- Chen, G., Gharib, T. G., Huang, C.-C., Thomas, D. G., & Shedden, K. A, Taylor, J. M.G., . . . Iannetoni, M. D. (2002). Proteomic analysis of lung adenocarcinoma identification of a highly expressed set of proteins in tumors. *Clinical Cancer Research*, 8(7), 2298–2305. PMID:12114434
- Chu, T.-C., He, Q., & Potter, D. E. (2002). Biodegradable calcium phosphate nanoparticles as a new vehicle for delivery of a potential ocular hypotensive agent. *Journal of Ocular Pharmacology and Therapeutics*, 18(6), 507–514. doi:10.1089/108076802321021054 PMID:12537677

- Clark, A. F., & Yorio, T. (2003). Ophthalmic drug discovery. *Nature Reviews. Drug Discovery*, 2(6), 448–459. doi:10.1038/nrd1106 PMID:12776220
- Clark, A. F., & Yorio, T. (2003). Ophthalmic drug discovery. *Nature Reviews. Drug Discovery*, 2(6), 448–459. doi:10.1038/nrd1106 PMID:12776220
- Coupland, S. E., Vorum, H., Mandal, N., Kalirai, H., Honoré, B., & Urbak, S. F. et al. (2010). Proteomics of uveal melanomas suggests HSP-27 as a possible surrogate marker of chromosome 3 loss. *Investigative Ophthalmology & Visual Science*, 51(1), 12–20. doi:10.1167/iovs.09-3913 PMID:19643972
- Dutt Vadlapudi, A., Patel, A., Cholkar, K., & K. Mitra, A. (2012, March 01). Recent Patents on Emerging Therapeutics for the Treatment of Glaucoma, Age Related Macular Degeneration and Uveitis. *Recent Patents on Biomedical Engineering*, 5(1), 83–101. doi:10.2174/1874764711205010083
- Fautsch, M. P., Bahler, C. K., Jewison, D. J., & Johnson, D. H. (2000). Recombinant TIGR/MYOC increases outflow resistance in the human anterior segment. *Investigative Ophthalmology & Visual Science*, 41(13), 4163–4168. PMID:11095610
- Ferrara, N., Gerber, H. P., & LeCouter, J. (2003). The biology of VEGF and its receptors. *Nature Medicine*, 9(6), 669–676. doi:10.1038/nm0603-669 PMID:12778165
- Gambhire, S., Bhalerao, K., & Singh, S. (2013). In situ hydrogel: Different approaches to ocular drug delivery. *Int. J. Pharm. Pharm Sci.*, 5(2), 27–36.
- Gao, B. B., Clermont, A., Rook, S., Fonda, S. J., Srinivasan, V. J., & Wojtkowski, M. et al. (2007). Extracellular carbonic anhydrase mediates hemorrhagic retinal and cerebral vascular permeability through prekallikrein activation. *Nature Medicine*, 13(2), 181–188. doi:10.1038/nm1534 PMID:17259996
- Geroski, D. H., & Edelhauser, H. F. (2000). Drug delivery for posterior segment eye disease. *Investigative Ophthalmology & Visual Science*, 41(5), 961–964. PMID:10752928
- Gomes dos Santos, A. L., Bochot, A., Doyle, A., Tsapis, N., Siepmann, J., & Siepmann, F. et al. (2006). Sustained release of nanosized complexes of polyethylenimine and anti-TGF- β 2 oligonucleotide improves the outcome of glaucoma surgery. *Journal of Controlled Release*, 112(3), 369–381. doi:10.1016/j.jconrel.2006.02.010 PMID:16644054
- Gu, J., Pauer, G. J., Yue, X., Narendra, U., Sturgill, G. M., & Bena, J. et al. (2010). Proteomic and genomic biomarkers for age-related macular degeneration. *Advances in Experimental Medicine and Biology*, 664, 411–417. doi:10.1007/978-1-4419-1399-9_47 PMID:20238042
- Ha Thi, H. T., Lim, H.-S., Kim, J., Kim, Y.-M., Kim, H.-Y., & Hong, S. (2013). Transcriptional and post-translational regulation of Bim is essential for TGF- β and TNF- α -induced apoptosis of gastric cancer cell. *General Subjects*, 1830(6), 3584–3592. doi:10.1016/j.bbagen.2013.03.006
- Hashimoto, T., Kusakabe, T., Sugino, T., Fukuda, T., Watanabe, K., & Sato, Y. et al. (2004). Expression of heart-type fatty acid-binding protein in human gastric carcinoma and its association with tumor aggressiveness, metastasis and poor prognosis. *Pathobiology*, 71(5), 267–273. doi:10.1159/000080061 PMID:15459486

- Jiang, C., Moore, M. J., Zhang, X., Klassen, H., Langer, R., & Young, M. (2007). Intravitreal injections of GDNF-loaded biodegradable microspheres are neuroprotective in a rat model of glaucoma. *Molecular Vision*, 13, 1783–1792. PMID:17960131
- Jmor, F., Kalirai, H., Taktak, A., Damato, B., & Coupland, S. E. (2012). HSP-27 protein expression in uveal melanoma: Correlation with predicted survival. *Acta Ophthalmologica*, 90(6), 534–539. doi:10.1111/j.1755-3768.2010.02038.x PMID:21114636
- Jo, D. H., Lee, T. G., & Kim, J. H. (2011). Nanotechnology and nanotoxicology in retinopathy. *International Journal of Molecular Sciences*, 12(12), 8288–8301. doi:10.3390/ijms12118288 PMID:22174664
- Juronen, E., Tasa, G., Veromann, S., Parts, L., Tiidla, A., & Pulges, R. et al. (2000). Polymorphic glutathione S-transferase M1 is a risk factor of primary open-angle glaucoma among Estonians. *Experimental Eye Research*, 71(5), 447–452. doi:10.1006/exer.2000.0899 PMID:11040079
- Kearney, C. J., Sheridan, C., Cullen, S. P., Tynan, G. A., Logue, S. E., & Afonina, I. S. et al. (2013). Inhibitor of apoptosis proteins (IAPs) and their antagonists regulate spontaneous and tumor necrosis factor (TNF)-induced proinflammatory cytokine and chemokine production. *The Journal of Biological Chemistry*, 288(7), 4878–4890. doi:10.1074/jbc.M112.422410 PMID:23275336
- Kim, J. E., Koo, K. H., Kim, Y. H., Sohn, J., & Park, Y. G. (2008). Identification of potential lung cancer biomarkers using an in vitro carcinogenesis model. *Experimental & Molecular Medicine*, 40(6), 709–720. doi:10.3858/emm.2008.40.6.709 PMID:19116456
- Kostenko, S., & Moens, U. (2009). Heat shock protein 27 phosphorylation: kinases, phosphatases, functions and pathology. *Cellular and Molecular Life Sciences*, 66(20), 3289–3307. doi:10.1007/s00018-009-0086-3 PMID:19593530
- Lee, W.-H., Choi, J.-S., Byun, M.-R., Koo, K.-, Shin, S., Lee, S.-K., & Surh, Y.-J. (2010). Functional inactivation of triosephosphate isomerase through phosphorylation during etoposide-induced apoptosis in HeLa cells: Potential role of Cdk2. *Toxicology*, 278(2), 224–228. doi:10.1016/j.tox.2010.02.005 PMID:20149834
- Lichtenfels, R., Dressler, S. P., Zobawa, M., Recktenwald, C. V., Ackermann, A., & Atkins, D. et al. (2009). Systematic comparative protein expression profiling of clear cell renal cell carcinoma a pilot study based on the separation of tissue specimens by two-dimensional gel electrophoresis. *Molecular & Cellular Proteomics*, 8(12), 2827–2842. doi:10.1074/mcp.M900168-MCP200 PMID:19752005
- Linge, A., Kennedy, S., O’Flynn, D., Beatty, S., Moriarty, P., & Henry, M. et al. (2012). Differential expression of fourteen proteins between uveal melanoma from patients who subsequently developed distant metastases versus those who did not. *Investigative Ophthalmology & Visual Science*, 53(8), 4634–4643. doi:10.1167/iovs.11-9019 PMID:22570344
- Lorigan, J. G., Wallace, S., & Mavligit, G. M. (1991). The prevalence and location of metastases from ocular melanoma: Imaging study in 110 patients. *AJR. American Journal of Roentgenology*, 157(6), 1279–1281. doi:10.2214/ajr.157.6.1950883 PMID:1950883

- Lu, L., Gu, X., Hong, L., Laird, J., Jaffe, K., & Choi, J. et al. (2009). Synthesis and structural characterization of carboxyethylpyrrole-modified proteins: Mediators of age-related macular degeneration. *Bioorganic & Medicinal Chemistry*, 17(21), 7548–7561. doi:10.1016/j.bmc.2009.09.009 PMID:19786352
- Michels-Rautenstrauss, K. G., Mardin, C. Y., Zenker, M., Jordan, N., Gusek-Schneider, G.-C., & Rautenstrauss, B. W. (2001). Primary congenital glaucoma: Three case reports on novel mutations and combinations of mutations in the GLC3A (CYP1B1) gene. *Journal of Glaucoma*, 10(4), 354–357. doi:10.1097/00061198-200108000-00017 PMID:11558822
- Mudunuri, K. (2008). *Intravitreal Delivery of Corticosteroid Nanoparticles*. (Ph.D. Dissertation). University of Florida, Gainesville, FL. Retrieved from <http://ufdc.ufl.edu/UFE0022065/00001>
- NEI. (2012). Prevalence of Adult Vision Impairment and Age-Related Eye Diseases in America. *Retrieved*, 11/20(13), 2013.
- Nicolini, C. (2006). Nanogenomics for medicine. *Nanomedicine (Lond)*, 1(2), 147–152. doi:10.2217/17435889.1.2.147 PMID:17716103
- Ong, F. S., Kuo, J. Z., Wu, W. C., Cheng, C. Y., Blackwell, W. L., & Taylor, B. L. et al. (2013). Personalized Medicine in Ophthalmology: From Pharmacogenetic Biomarkers to Therapeutic and Dosage Optimization. *J Pers Med*, 3(1), 40–69. doi:10.3390/jpm3010040 PMID:24624293
- Ong, F. S., Kuo, J. Z., Wu, W.-C., Cheng, C.-Y., Blackwell, W.-L. B., & Taylor, B. L. et al. (2013). Personalized Medicine in Ophthalmology: From Pharmacogenetic Biomarkers to Therapeutic and Dosage Optimization. *Journal of Personalized Medicine*, 3(1), 40–69. doi:10.3390/jpm3010040 PMID:24624293
- Park, Y. G., Rhu, H. W., Kang, S., & Roh, Y. J. (2012). New Approach of Anti-VEGF Agents for Age-Related Macular Degeneration. *Journal of Ophthalmology*, 2012. doi:10.1155/2012/637316 PMID:22496964
- Penfold, P. L., Wen, L., Madigan, M. C., Gillies, M. C., King, N. J., & Provis, J. M. (2000). Triamcinolone acetonide modulates permeability and intercellular adhesion molecule-1 (ICAM-1) expression of the ECV304 cell line: Implications for macular degeneration. *Clinical and Experimental Immunology*, 121(3), 458–465. doi:10.1046/j.1365-2249.2000.01316.x PMID:10971511
- Peyman, G. A., Lad, E. M., & Moshfeghi, D. M. (2009). Intravitreal injection of therapeutic agents. *Retina (Philadelphia, Pa.)*, 29(7), 875–912. doi:10.1097/IAE.0b013e3181a94f01 PMID:19584648
- Qian, Xiao-Long, Shi, Qing-Guo, Pang, Bo, Wu, Rui-Qin, Yu, Lan, Li, Shan-Hu, . . . Zhou, Jian-Guang. (2010). Identification and expression of two new secretory proteins associated with prostate cancer. *Yi chuan= Hereditas/Zhongguo yi chuan xue hui bian ji*, 32(3), 235–241.
- Quigley, H. A. (1996). Number of people with glaucoma worldwide. *The British Journal of Ophthalmology*, 80(5), 389–393. doi:10.1136/bjo.80.5.389 PMID:8695555
- Rainov, N. G. (2000). A phase III clinical evaluation of herpes simplex virus type 1 thymidine kinase and ganciclovir gene therapy as an adjuvant to surgical resection and radiation in adults with previously untreated glioblastoma multiforme. *Human Gene Therapy*, 11(17), 2389–2401. doi:10.1089/104303400750038499 PMID:11096443

- Ramasamy, P., Murphy, C. C., Clynes, M., Horgan, N., Moriarty, P., & Tiernan, D. et al. (2014). Proteomics in uveal melanoma. *Experimental Eye Research*, 118, 1–12. doi:10.1016/j.exer.2013.09.005 PMID:24056206
- Rosenfeld, P. J., Brown, D. M., Heier, J. S., Boyer, D. S., Kaiser, P. K., Chung, C. Y., & Kim, R. Y. (2006). Ranibizumab for neovascular age-related macular degeneration. *The New England Journal of Medicine*, 355(14), 1419–1431. doi:10.1056/NEJMoa054481 PMID:17021318
- Samudre, S. S., Lattanzio, F. A. Jr, Williams, P. B., & Sheppard, J. D. Jr. (2004). Comparison of topical steroids for acute anterior uveitis. *Journal of Ocular Pharmacology and Therapeutics*, 20(6), 533–547. doi:10.1089/jop.2004.20.533 PMID:15684812
- Selicharova, I., Sanda, M., Miadkova, J., Ohri, S. S., Vashishta, A., Fusek, M., . . . Vetvicka, V. (2008). 2-DE analysis of breast cancer cell lines 1833 and 4175 with distinct metastatic organ-specific potentials: comparison with parental cell line MDA-MB-231. *Oncology Reports*, 19(5), 1237–1244.
- Sendrowski, D. P., Jaanus, S. D., Semes, L. P., & Stern, M. E. (2008). *Anti-Inflammatory Drugs* (5th ed.). New York, NY: Elsevier Health Sciences.
- Sherif, Z., & Pleyer, U. (2002). Corticosteroids in ophthalmology: Past-present-future. *Ophthalmologica*, 216(5), 305–315. doi: 66189
- Sigurdsson, H. H., Konráðsdóttir, F., Loftsson, T., & Stefánsson, E. (2007). Topical and systemic absorption in delivery of dexamethasone to the anterior and posterior segments of the eye. *Acta Ophthalmologica Scandinavica*, 85(6), 598–602. doi:10.1111/j.1600-0420.2007.00885.x PMID:17645424
- Singh, A. D., & Borden, E. C. (2005). Metastatic uveal melanoma. [ix.]. *Ophthalmology Clinics of North America*, 18(1), 143–150. doi:10.1016/j.ohc.2004.07.003 PMID:15763199
- Singh, A. D., & Topham, A. (2003). Survival rates with uveal melanoma in the United States: 1973–1997. *Ophthalmology*, 110(5), 962–965. doi:10.1016/S0161-6420(03)00077-0 PMID:12750098
- Steely, H. T. Jr, & Clark, A. F. (2000). The use of proteomics in ophthalmic research. *Pharmacogenomics*, 1(3), 267–280. doi:10.1517/14622416.1.3.267 PMID:11256578
- Stoilov, I., Jansson, I., Sarfarazi, M., & Schenkman, J. B. (2001). Roles of cytochrome p450 in development. *Drug Metabolism and Drug Interactions*, 18(1), 33–55. doi:10.1515/DMDI.2001.18.1.33 PMID:11522124
- Stone, E. M., & Fingert, J. H. (1997). Identification of a gene that causes primary open angle glaucoma. *Science*, 275(5300), 668–670. doi:10.1126/science.275.5300.668 PMID:9005853
- Urtti, A. (2006). Challenges and obstacles of ocular pharmacokinetics and drug delivery. *Advanced Drug Delivery Reviews*, 58(11), 1131–1135. doi:10.1016/j.addr.2006.07.027 PMID:17097758
- Verteporfin In Photodynamic Therapy Study, Group. (2001). Verteporfin therapy of subfoveal choroidal neovascularization in age-related macular degeneration: two-year results of a randomized clinical trial including lesions with occult with no classic choroidal neovascularization--verteporfin in photodynamic therapy report 2. *Am J Ophthalmol*, 131(5), 541–560.

- Wadhwa, S., Paliwal, R., Paliwal, S. R., & Vyas, S. P. (2010). Hyaluronic acid modified chitosan nanoparticles for effective management of glaucoma: development, characterization, and evaluation. *Journal of Drug Targeting*, 18(4), 292–302. doi:10.3109/10611860903450023 PMID:19943753
- Wang, , Wei, W. B., Mo, L., & Shi, X.-H. (2013). Efficacy and safety of dendrimer nanoparticles with coexpression of tumor necrosis factor- α and herpes simplex virus thymidine kinase in gene radiotherapy of the human uveal melanoma OCM-1 cell line. *International Journal of Nanomedicine*, 8, 3805. doi:10.2147/IJN.S48950 PMID:24124368
- Wang, Y., Wang, V. M., & Chan, C. C. (2011). The role of anti-inflammatory agents in age-related macular degeneration (AMD) treatment. *Eye (London, England)*, 25(2), 127–139. doi:10.1038/eye.2010.196 PMID:21183941
- Wang, Y. S., Friedrichs, U., Eichler, W., Hoffmann, S., & Wiedemann, P. (2002). Inhibitory effects of triamcinolone acetonide on bFGF-induced migration and tube formation in choroidal microvascular endothelial cells. *Graefe's archive for clinical and experimental ophthalmology = Albrecht von Graefes Archiv für klinische und experimentelle Ophthalmologie*, 240(1), 42–48. doi:10.1007/s00417-001-0398-y PMID:11954780
- Weinreb, R. N., Kashiwagi, K., Kashiwagi, F., Tsukahara, S., & Lindsey, J. D. (1997). Prostaglandins increase matrix metalloproteinase release from human ciliary smooth muscle cells. *Investigative Ophthalmology & Visual Science*, 38(13), 2772–2780. PMID:9418730
- Wong, T. T.L., Sethi, C., Daniels, J. T., Limb, G. A., Murphy, G., & Khaw, P. T. (2002). Matrix metalloproteinases in disease and repair processes in the anterior segment. *Survey of Ophthalmology*, 47(3), 239-256.
- Wu, W. S., Wang, F. S., Yang, K. D., Huang, C. C., & Kuo, Y. R. (2006). Dexamethasone induction of keloid regression through effective suppression of VEGF expression and keloid fibroblast proliferation. *The Journal of Investigative Dermatology*, 126(6), 1264–1271. doi:10.1038/sj.jid.5700274 PMID:16575391
- WuDunn, D.WuDunn. (2002). Genetic basis of glaucoma. *Current Opinion in Ophthalmology*, 13(2), 55–60. doi:10.1097/00055735-200204000-00001 PMID:11880716
- Zarbin, M. A., Montemagno, C., Leary, J. F., & Ritch, R. (2013). Nanomedicine for the treatment of retinal and optic nerve diseases. *Current Opinion in Pharmacology*, 13(1), 134–148. doi:10.1016/j.coph.2012.10.003 PMID:23142104
- Zhang, L., Cilley, R. E., & Chinoy, M. R. (2000). Suppression subtractive hybridization to identify gene expressions in variant and classic small cell lung cancer cell lines. *The Journal of Surgical Research*, 93(1), 108–119. doi:10.1006/jsre.2000.5957 PMID:10945951
- Zhang, W., Prausnitz, M. R., & Edwards, A. (2004). Model of transient drug diffusion across cornea. *Journal of Controlled Release*, 99(2), 241–258. doi:10.1016/j.jconrel.2004.07.001 PMID:15380634
- Zhao, X., Ramsey, K. E., Stephan, D. A., & Russell, P. (2004). Gene and protein expression changes in human trabecular meshwork cells treated with transforming growth factor- β . *Investigative Ophthalmology & Visual Science*, 45(11), 4023–4034. doi:10.1167/iovs.04-0535 PMID:15505052

Zhou, Y., Song, X., Jia, R., Wang, H., Dai, L., Xu, X., . . . Fan, X. (2010). Radiation-inducible human tumor necrosis factor-related apoptosis-inducing ligand (TRAIL) gene therapy: a novel treatment for radioresistant uveal melanoma. *Pigment Cell & Melanoma Research*, 23(5), 661-674.

Zhou, Z., & Vollrath, D. (1999). A cellular assay distinguishes normal and mutant TIGR/myocilin protein. *Human Molecular Genetics*, 8(12), 2221-2228. doi:10.1093/hmg/8.12.2221 PMID:10545602

KEY TERMS AND DEFINITIONS

Age-Related Macular Degeneration: Ocular disease that usually affects older adults and results in loss of central, focused vision.

Diabetic Retinopathy: Damage to retina caused by diabetes and can lead to blindness.

Glaucoma: Eye condition that leads to damage of optic nerve due to intraocular pressure.

Nanogenomics: Nanotechnology utilized in the study of genomics.

Nanoproteomics: Nanotechnology utilized in the study of proteomics.

Nanotechnology: Engineering of functional systems at the molecular scale.

Omics: Refers to field of study such as proteomics and genomics.

Uveal Melanoma: Cancer of the eye involving the uvea.

This research was previously published in the Handbook of Research on Diverse Applications of Nanotechnology in Biomedicine, Chemistry, and Engineering edited by Shivani Soni and Amandeep Salhotra, pages 152-166, copyright year 2015 by Engineering Science Reference (an imprint of IGI Global).

Section 3

Visual Impairment

Chapter 18

Design Analytics of Complex Communication Systems Involving Two Different Sensory Disabilities

Gahangir Hossain

Texas A&M University-Kingsville, USA

ABSTRACT

The design of a robust communication among two different sensory disabilities (Deaf vs. Blind) remains an emerging field of research in disability healthcare communication system design. As an important part of modern technology, android and iPhone applications are frequently used in designing such communication systems. However, there is no 'one-size-fits-all' in case of different sensory disability health communication design. Hence, an in-depth understanding of their requirement, media preferences, similarity and difference and up-to-date technology usability are plausible towards universal and personalized communication system design. This research addresses such complex issues and performs a study involving two different types of disabilities (deaf and blind) communication. As a part of healthcare analytics, critical incidences are recorded and corresponding complexities are measured in order to evaluate communication protocol with social signal processing. Communication flow diagram, complexity analysis and critical incidence are quantified to improve communication protocols. Moreover, the uniqueness of disability can be personalized through this process which has valuable implications in rehabilitation and multi-purpose healthcare communication device development.

INTRODUCTION

According to a world report on disability (World Report, 2011; World Program of Action, 2007) over one billion people around the world have some type of disability. Twenty five percent of the population in a given country is adversely affected by the presence of some form of disability. Out of hundreds of millions of children who are not in school, thirty to forty million have sensory disabilities. Over fifty-

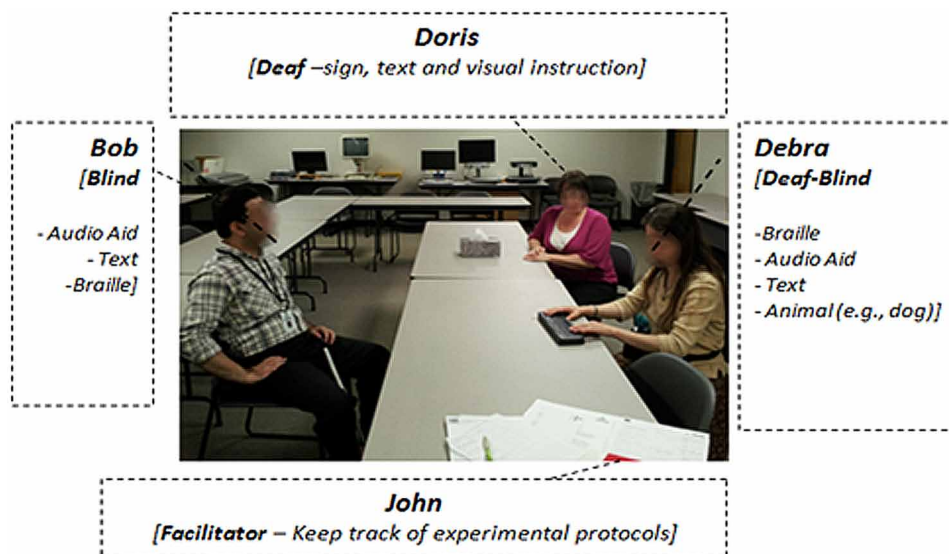
DOI: 10.4018/978-1-5225-5195-9.ch018

four million people in the US have some form of a disability. Out of seventy million families, twenty million have at least one family member who has a disability. Canada, Bangladesh, Pakistan, and Egypt reported to have four million, seventeen million, nine million and seven million people with sensory disabilities, respectively (People with Disabilities in India, 2007; Foulgers, 2004).

Since sensory disabilities are highly prevalent worldwide, it is necessary to design a robust and effective communication solution. Recent developments of communication technology within integrated technology devices (smart phone, tablet, pad etc.) may help to bridge the gap between people with and without sensory disabilities. People with disabilities are becoming more technologically aware and are adopting emerging applications with technology devices. With premium training and assistance, they can adopt modern technology for social networking as well as managing their daily lives. While assistive technology solutions are helpful, in many cases, they are not interoperable to bridge communication gaps between people with mutually exclusive types of sensory disabilities (for example, deaf vs. blind or deaf-blind). One viable solution to overcome this obstacle is to have technological devices with universal design. However, sensory disabilities are more personalized and there is no “one-size-fits-all”, which requires an in-depth study of their opinions in action (Aslaksen et al., 1995; Russell et al., 1993)

Let us consider the conversation among four assistive technology expert users (Figure 1): John, Bob, Doris, and Debra. John is an experiment designer for people with cross-disability. Bob is a blind instructor with ten years of experiences in teaching people who are blind or visually impaired. Doris, who is hearing impaired (deaf), works with Bob in the same school, teaching students who have hearing problems. Debra, who is both deaf and blind, also works with Bob and Doris. Their actual names are changed to preserve the confidentiality agreement. Bob can communicate through speech, audio feedback, and tactile communication methods (Braille), but prefers voiceover feedback. Doris favors sign language to other modes of communication. Debra loves the Braille communication tools. She also knows signing, animal behavior, auditory feedback, etc. The main theme of their conversation was to ascertain an optimal mode of communication between a deaf person and someone who is blind with the cutting-edge technology of smart phone applications. Naturally, their conversations are different from traditional inter

Figure 1. Communication between different sensory disabilities (Deaf, Blind, Deaf-Blind communication)



personal social coordination, the lacks some integral parts of social collaboration. However, there is no formal framework to evaluate the strength of collaboration and the integral components that makes the successful collaboration in such complex situation. Our research purpose was to identify analytics that are useful assessing the effectiveness in such complex communication design with modern technology application (e.g., mobile apps). Hence, the study was performed to gain a deeper understanding of the complex collaborative process among the people with three different sensory disabilities with assessment of their cognitive abilities and associated gaps. More details of the ability-demand gap and its mathematical modeling can be found from the authors' earlier works (Hossain et al., 2014).

The reminder of the paper is organized as follows. The second section explains some example of people with different sensory disabilities. Collaborative communication between such sensory disabilities is articulated with collaborative-sensemaking process. The third section explained the experimental design and case studies in deaf-blind communication system design. The fourth section discusses analytics results and the fifth section concludes the study.

DEAF-BLIND COMMUNICATION SYSTEMS

Traditionally, people with disability use hand-over-hand or hand-over-face communication techniques (e.g, hand-over-face; Figure 2). Hand-over-hand sign language, also known as tactile signing, is a form of communication utilized by people who are either deaf or blind (DB). It is a common technique for people with deafblindness and one does not have had visual abilities to learn this technique. The interpreter must put his or her hand on the client's hand and maintains contact with the client's hand throughout the duration of the communication process. Helen Keller was an American author who was both deaf and blind. Anne Sullivan who was Keller's tutor, was also visually impaired. Anne was able to teach Helen to speak using the 'Tadoma' method, which involved touching the lips and throats of others (Figure 2) as they spoke (Kim & Nielsen, 2004).

Figure 2. Hand over face-Helen Keller (left) "hears" her teacher Anne Sullivan by reading Sullivan's lips with her fingers. Source: AP/Wide World Photos Helen Keller/ Anne Sullivan.



Like Helen and Anne, Nuccio and A.J. Granda have a combination of hearing loss and an eye disorder called retinitis pigmentosa (RP) (Usher Syndrome). But both of them are successful in social and professional life. Nuccio was the first DeafBlind Director of the Seattle DeafBlind Service Center (DBSC) and Granda is a teacher, social justice activist, textile artist, and mom. Both Nuccio and Granda contributed a lot in developing curriculum on a national project for training SSPs and individuals who are Deaf-Blind (Report from Alabama Institute).

Towards successful social collaboration Deaf-Blind people value touch for purposes of communication, in the same way that Blind people value sound/voices and Deaf people value vision. This concept is introduced by Jelica Nuccio and Ajgranda and well known as “Pro-Tactile Communication”, where touch is the way of being present with one another in communication, coordination and collaboration. Back-channeling, a feedback cues that provides the communicators with information about each other, their responses to what is being communicated, and the environment - is used in Pro-Tactile Communication process. According to Jelica Nuccio it is an effective way to provide feedback to a Deaf-Blind presenter about the audience’s responses and reactions to their presentation in real time. Recently, Sharma et al. (2017) and his collaborators proposed a new prototype model with mobile phone based communication between marginalized communities like deaf-blind-dumb to faster, easier, and accurate message communication. Another new study shows that deaf-blind individuals outperformed blind participants in the spatial tactile task (Papagno et al., 2016). Anuradha proposed a refreshable Braille display for deaf-blind people (Anuradha, 2016).

Other earlier approaches are, TTY (TeleTYpe), TTD (Telecommunication Device for the Deaf), and TT (Text Telephone) all refer to the text-based telecommunications devices that people with auditory sensory disabilities, visual impairments, or both use to communicate on the telephone. The sighted person types a message on a small keyboard and the deaf/blind user receives the message on a Braille display. The deaf-blind responds by typing on a standard or Braille keyboard and the sighted person reads the message on the screen. Presently, TTY and TTD based communication systems are supported on android apps and are also available for other smart phones (Google play). In this work, such apps are demonstrated to see whether it makes sense for future communication design.

Successful communication requires robust understanding and exchanging of information among collaborative team participants. The sense-making process helps to connect novel information with both the unknown and known. This is used as a critical way for individuals to view and interpret the world and then act in the situation. It is the way in which people respond to uncertain events and construe their perceptions regarding goals, priorities, and problems they sense with their sensory organs (Weick, K. E. 1995). With strong communication among team participants, collaboration is defined as a process of joint decision-making among participants of a communication set-up and continuation toward successful accomplishment of a task (Gray, B., 1989). Sense-making is the working concept to investigate and improve interaction between participants’ from the simplest communication task to a more complex, social collaboration task. Essentially, collaborators play a significant role in adapting and responding to unexpected or unknown situations, as well as recognizing the known situations through the collaborative sense-making process (Paul et al., 2010).

Figure 3 Illustrates Dervin’s sense-making concept with a connection to the communication process in order to have the idea of collaborative sense-making. Taylor-Powell et al. (1998) showed that a true collaboration requires a seamless integration of four components: communication, contribution, coordination, and cooperation. These are considered to be essential steps toward collaboration (Figure 3C). The model structure and information integration properties are summarized in Table 1.

Figure 3. Collaborative sensemaking. (A) The sense-making metaphor (edited from the concept of Brenda Dervin, 1999). (B), (C) and (D) Construct of collaboration in sensemaking process.

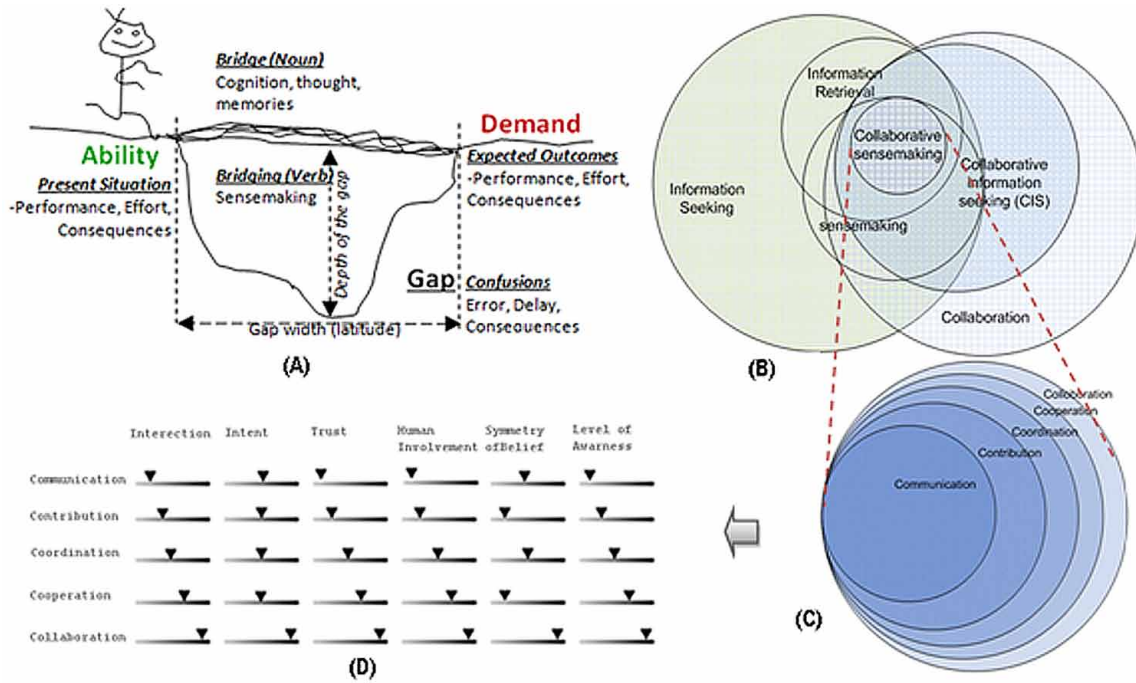


Table 1. Collaboration structure (Tailor-Powell et al., 1998)

Process	Structure	Information Integration
Communication	Network, round table	Very Low
Contribution	Support group	Low
Coordination	Task Force, council, alliance	Average
Cooperation	Partnership, coalition, consortium	High
Collaboration	Collaboration	Very High

Collaborative sense-making is evaluated by six criteria: interaction, intent, trust, symmetry of belief, and level of awareness (Shah, 2014), Figure 3D). Collaborative sense-making aims to support a group people, who are explicitly working together to accomplish a successful communication or sense-making task. In collaborative sense-making, collaborative systems should provide collaborators the capability “to infer some idea what they have, what they want, why they can’t get it, and why it may not be worth getting in the first place” (Weick, 1995). Collaborative sense-making can be thought of as the driving force of an individual’s cognitive processing of social interaction processes.

A collaborative system should satisfy some requirements to better support collaborative sense-making activities, including interpersonal social communications. Some essential requirements are summarized in Table 2.

Table 2. Collaborative sensemaking: essential requirements (Umapathy, 2010).

#	Requirement Description
1.	Creating explicit representation
2.	Co-existence of different representations
3.	Developing shared representation
4.	Creating representation using templates
5.	Providing workspace for developing shared representations
6.	Consensus building and reaching agreement
7.	Facilitating and moderating interactions
8.	Exchanging documents
9.	Retrieving and visualizing information

Individual sense-making should satisfy requirements 1, 2, 4 and 9, while collective sense-making should satisfy requirements 3, 4, 5, 6, 7, and 8 (Umapathy, 2010). The author also identified that, as a prerequisite, requirement number 2 depends on 1 and requirement 3 depends on 1, 5 and 6.

EXPERIMENTAL ANALYSIS AND CASE STUDY

The goal of this study was to make sense of complex collaboration processes between different sensory disabilities (deaf and blind). Understanding of how different disabilities communicate can help in designing effective assistive technology tools to leverage the synergy between smart phone apps (e.g., cross communication between people who are deaf and blind (Weick, 1995) and user with sensory disability. The finding aims to bridge the gaps in communication between different disabilities. Figure 4 captures a snapshot of the conversation scenario among the participants, John, Bob, Doris and Debra. The setup has some advantages of dividing information processing complexities among partners in the form of collective problem solving. Naturally, any collaboration aims to have an ideal shared goal among participants. Therefore, the participant's way of communication, coordination, cooperation and comprehension affects the cost of information processing. Furthermore, this causes a gap in collaboration.

In analyzing cross-disability collaborative experimental setting, the moderator initiates different ways of communication using android phone applications and other devices and then records the usability and critical incidences. Four different design options are discussed. Communication is analyzed with a data flow diagram along with cyclomatic complexities within the flow of communication. A snapshot of a conversation data flow is shown in Figure 5.

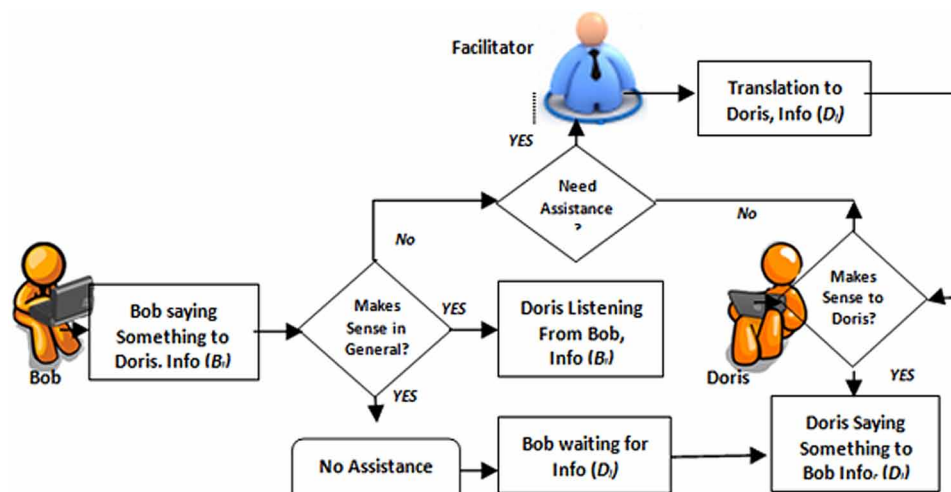
Communication Tasks

All participants were chosen to be experts in their own assistive technology operation and served as instructors in a local disability center, (Clovernook center for visual impaired and blind). Subjects are instructed to experiment with the four proposed communication designs with mobile phone applications and other devices (e.g., Braille display). These four designs are: speech-text-speech, Speech-sign-speech,

Figure 4. A snapshot of different disabilities sense-making through ability base collaborative information seeking scenario



Figure 5. A snapshot of partial conversation flow scenario among sensory disabilities with a facilitator: the flow diagram is constructed from a snap of the conversation in Figure 4



Braille-text-Braille and Braille-sign-Braille. The experiment was conducted without any time bound. Figure 6 illustrates a speech-sign-speech design, using a flow diagram.

- **Design Task ONE:** (Speech-text-speech) – Speech from Bob can be encoded and sent to Doris. Doris can read and text her reply that is decoded as speech to Bob.
- **Design Task TWO:** (Speech-Sign-Speech) - Speech from Bob can be encoded and sent to Doris and played by the avatar to mimic the sign (ASL) to Doris. Finally, Doris replies with a sign, which is encoded to speech and sent back to Bob. (Figure 11).
- **Design Task THREE:** (Braille-Text-Braille) - Braille from Bob can be encoded and sent to Doris as text and she can read and reply in a text to Bob that is decoded to Braille again.
- **Design Task FOUR:** (Braille-Sign-Braille) – Braille from Bob can be encoded and sent to Doris and played by the avatar to mimic the sign (ASL) to Doris. Finally, Doris replies with a sign, which is encoded to Braille and send back to B.
- **Other Preferable Design With Training:** Bob may text with audio feedback and Doris may text the reply. Bob may use the Braille display and Doris may use the Signing (ASL) display to understand the message. Due to the low popularity in the evaluation of other design strategies, these design tasks were skipped.

After each design discussion, subjects were asked to answer usability and cognitive load questionnaires. After each communication alternative, the facilitator collected cognitive load and usability scores based on Nielsen's usability questionnaires (strongly agree = 7 to strongly disagree = 0). Table 3 and Table 4 summarize all usability and cognitive load related questionnaires, respectively. All participants were interviewed (allowed to critique) on three cognitive load points (intrinsic load, extraneous load and germane load). These critical incidences are processed to find the inherent causes and were used to estimate the qualitative cost of sense-making.

Figure 6. Design TWO (speech-sign-speech): Bob and Doris conversation. All participants were interviewed after the completion of each design evaluation

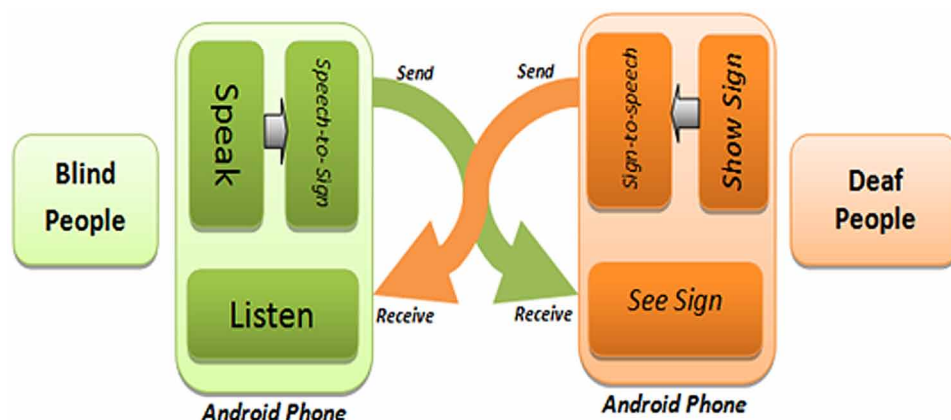


Table 3. Nielsen's five usability criteria with cognitive load

Question Category	Question
Memorability	How difficult was the experiment instruction content for you?
Learnability	How difficult was it for you to learn with the instruction format?
Efficiency	How much did you concentrate during experiment?
Errors	What do you think about the chances of errors during the experiment?
Satisfaction	How pleasant are you to participate in this experiment and to use the design?

Analysis Methods






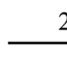
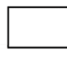
Usability Analysis

The rating results were considered to be quantitative data. The statistical mean and standard deviation was performed on that data set as a part of the usability measure. The user's critical behavior was considered to be qualitative data that was collected from conversation video and processed as conversation flow sequences using a data flow diagram (DFD) to find the sense and interest of communication activity.

Data Flow Analysis

Communication cues that are critical to its participants might create problem in successful communication - making a critical problem. Data flow diagrams (DFDs) are used to identify critical problems that the participant faces in the communication process while using experimental applications. Once the critical problems are identified it is adopted into the comparative analysis of the decision process. For instance, computation of cognitive load from qualitative analysis is compared with cognitive load that we have from subject's self reported rating. Some notations to construct a data flow diagram (DFD) are shown in Table 4.

Table 4. Basic data flow diagram (DFD) notations

Notation	Title	Description
	Transition States	Smallest unit of tasks in the communication process.
	Initial State	Starting point of assigned task in communication.
	End State	End point communication.
	Transition Line	Data flow / information flow in communication
	Bold line	Critical path – optimal communication path
	Weighted Line	Significance of the communication link between states
	Entity	Subject/Facilitator

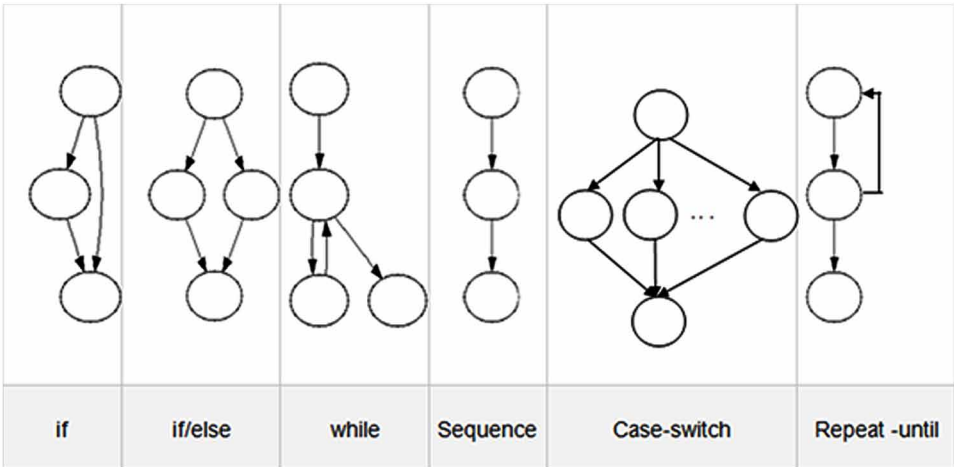
In such a critical problem, information flow assessment can be done using DFDs and their various patterns. Traditional dataflow diagram consists of a set of states and a set of transitions (labeled flows). States represent either the communication process as a concurrent process or a sequential process and are usually drawn as circles, ovals or boxes. Transitions or flows represents data paths and are drawn as arrows connecting to states. Transition flows coming to the state are called inflows and flows leaving a state are called outflows. The state processes its inflows and produces new information. In computability theory, a collection of data-manipulation rules (an instruction set, programming language, or cellular automaton) is said to be Turing complete if and only if such system can simulate any single-taped Turing machine. Classical Turing-complete systems include context-sensitive grammar, recursive functions, and lambda calculus. There are two types of flows: persistent and consumable flows. Persistent flows are like shared variables whose values are written by the source state and read by the destination state. Consumable flows are modeled as unbounded FIFO queues, with the source state enqueueing values on the queue and the destination states dequeuing values (Watson et al., 1996). Acceptability of a communication system can be assessed using the persistence of information flow between communicators. Some interesting patterns in data flow can indicate persistence or non-persistence of information flow, which is indispensable in communication design assessment. Figure 7 shows some data flow patterns.

A simple measure of flow persistence can be done using cyclomatic complexity assessment using DFD or flow graphs. Theoretically, DFD forms a graph of a particular communication protocol. The complexity of the communication is thus analyzed using cyclomatic complexity or McCabe’s complexity measure (McCabe, 1976). Cyclomatic complexity measures the amount of decision branches in the communication process. It gives the minimum number of paths that can generate from all possible ways of communication through the protocol. Cyclomatic complexity can defined as shown below:

$$CC = E - N + P \tag{1}$$

E is the number of edges of the graph, N is the number of nodes in the graph, and P is the number of connected components. In case of connected DFD:

Figure 7. Data flow patterns



$$CC = E - N + 2 \quad (2)$$

This can be simplified as shown below:

$$CC = D + 1 \quad (3)$$

D is the number of decision points in the graph. Again, let us consider a communication design represented with a flow diagram that consists of two sequential if-then-else statements similar to what is shown in Figure 8.

In the communication design shown in Figure 8, the red circle is the sender, and the blue circle represents the receiver. Data flow from the receiver to sender has been connected to create a feedback loop - improves communication strength. In this example, two test cases are sufficient to achieve complete branch coverage, while four cases are necessary for complete path coverage. The cyclomatic complexity of the design is 3 (as the strongly-connected graph for the program contains 9 edges, 7 nodes and 1 connected component). Decision weights can be done using cyclomatic complexity computation as shown in Table 5.

According to Miller (1956), the maximum limits of a one-dimensional, absolute judgment in the communication process is considered to be no more than 7 ± 2 , which is considered to be the cognitive limit. The limit has been recently redefined as 4 ± 1 (Cowan, 2002; 2001). In a cross-disability, collaborative, sense-making analysis, we proposed a sense-making cost bandwidth in terms of cyclomatic complexity scores. The standard ranges of collaborative complexity computation are shown in Table 6. DFD and cyclomatic complexity analysis are widely used in software engineering to analyze information

Figure 8. Example Communication Data Flow Diagram (DFD)

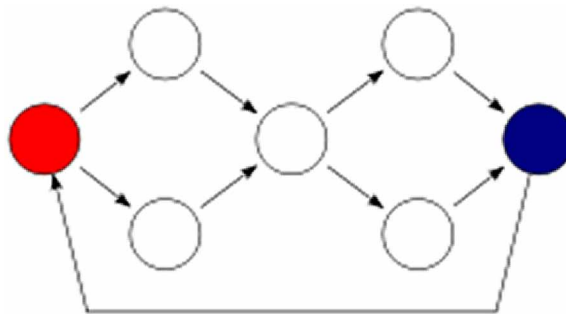


Table 5. Decision weighting in DFD (McCabe,1976)

Decision Types	Effect on CC
If..	+1
Elseif..	+1
Else	0
switch Case	+1 for each Case

Table 6. Cyclomatic complexity and gap in communication

Cyclomatic Complexity	Complexity Level and Gap
≤ 3	A simple communication task, low gap, and low sensemaking cost.
>3 but ≤ 5	More complex, moderate gap, moderate sensemaking cost.
> 5	Most complex, unacceptable gap, high sensemaking cost.

flow testing and dynamics analysis, which is used in this study to ability based communication flow and complexity analysis.

Critical Incidence Analysis

Critical incidence combines three components (What + Emotion + Why) of a given observation (Klein et al., 2006; Stevens et al., 1974). The word “What” represent to provide an in-depth description of the event without subjective judgment or interpretation? Emotion describe the feelings the subject ‘experienced’ with the incident. “Why” explains why the incident was meaningful to us, and then puts the observer in the position of the subject and explains from their perspective why the incident was meaningful. Since Critical Incident Analysis considers the position of observer, a couple of questions arise. What are some of his or her personal beliefs related to expert knowledge that he/she identified when reflecting on this incident? After considering this incident, what would he/she would do differently in light of new understanding? The matters that are under consideration are subjective experiences, functional states, task difficulty and time constraints. The ability-demand trade-offs for each weight (5-1) are shown in Table 7.

RESULTS AND DISCUSSION

We applied a one-way repeated measure ANOVA in Nielsen’s usability data. Usability scores are obtained based on Nielsen’s usability metrics (Table 8). The statistical mean and standard deviation are computed.

A one-way repeated measure ANOVA was conducted to compare the effect of design types on the usability scores. There was a significant effect of design type on a speech-based system ($\lambda = 0.10$, $F(2, 3) = 13.43$, $p = 0.032$). Four paired sample t-test were used to make post hoc comparisons between conditions. The first paired sample t-test indicated that there was a significant difference in the score of satisfaction ($M = 5.04$, $SD = 1.14$) and efficiency ($M = 9.15$, $SD = 1.24$) conditions ($t(4) = -5.67$, $p =$

Table 7. Critical Incidence Initial Index Table

Weight	Critical Incidence (Observed)
5	The subject is very much happy and responds quickly.
4	Subject asked question or responded very slowly.
3	Subject is confused about the rating.
2	Subject’s reply is not the relevant, facilitator need to ask him again.
1	Subject is sad.

Table 8. Usability scores

Nielsen's Usability Metrics	Design ONE		Design TWO		Design THREE		Design FOUR	
	M	SD	M	SD	M	SD	M	SD
Memorability	5.25	2.06	7.12	1.10	7.25	2.75	5	2.58
Learnability	5.75	2.06	5.4	1.15	8.3	1.82	5	2.16
Efficiency	8.25	2.36	9.15	1.24	8.01	1.41	6	2.16
Errors	6.75	1.5	9.45	1.104	7.2	1.41	6.25	1.5
Satisfaction	9.5	1.02	5.04	1.14	7.25	2.45	6.5	2.38

0.015). A second paired sample t-test indicated that there was a significant difference in the scores for learnability ($M = 5.4$, $SD = 1.15$) and memorability ($M = 7.12$, $SD = 1.10$) scores ($t(4) = -4.781$, $p = .009$). The third paired sample t-test indicated that there was no significance difference in the score of memorability ($M = 7.12$, $SD = 1.10$) and error ($M = 9.45$, $SD = 1.104$) scores ($t(4) = -3.75$, $p = .02$). The fourth paired sample t-test also indicated no significant difference on error ($M = 9.45$, $SD = 1.04$) and efficiency ($M = 9.15$, $SD = 1.14$) scores ($t(4) = -2.23$, $p = .024$).

User interaction (quantitative data) and critical incidence is peer reviewed by two cognitive scientists (experimenters) and logged in a format that facilitates analysis and interpretation. The reason of using two experimenters is to reduce the evaluator effect while maintaining a quick process – paired evaluation. The same qualitative logging template is maintained for both reviewers. The template contains the information shown in Table 9.

DFDs are designed with four key parts of a conversation: telling, asking, listening, and thinking. The ‘telling’ is considered as speaking, showing, sending or writing; listening as seeing, receiving; asking as requesting, questioning; thinking as understanding, waiting etc. Thus, processing modules can be considered as of four categories and indicated by different colors: telling (yellow), asking (red), listening (green) thinking (blue). In this research, participants’ CFDs are compared to understand problematic interactions. The critical incidences are identified from video data using DFD and Cyclomatic complexity. Figure 9 is the DFD representation of Figure 5, showing sample conversation between deaf and blind with the presence of a facilitator.

Table 9. Coding DFD with critical incidence

User #	Code	Design #	Task Completion Time(sec)	Critical Incidence	Problem Faced	Problem Classification	Design Recommendation
1	A1	ONE	154	The participant was placing a finger in different keys and wondering which to press while using the Braille display	The participant was not familiar with Braille display	Interaction	Access to the input method should be easy and multimodal
2	F128	TWO	97	Participant pressed “Menu” button when she was asked to press “Send” button	She expected to need explanation of the purpose of action.	Memory Load	Interface Should be designed with less extraneous load
...

Table 10. Design comparison in terms of gap model and cost model

DesignType	Communication Type (Bob-Doris-Bob)	Sensemaking Cost (Bob)	Sensemaking Cost (Doris)
ONE	Speech-text-speech	Moderate	Moderate
TWO	Speech-Sign-Speech	Low	Low
THREE	Braille-Text-Braille	Low	High
FOUR	Braille-Sign-Braille	Moderate	Low

CONCLUSION

Analytics of disability healthcare informatics can be one of the major determinants of effectiveness in disability communication design and assessment. Hence, individual sensory disabilities (deaf or blind) perceive the environment in a unique way; the communication framework becomes incompatible in terms of generalization or “one-size-fits-all”. As an important part of design analytics, it was observed that disability cognitive ability-demand gap analysis with DFDs and cyclomatic complexity gives a way to compare their discrepancies between cognitive ability and cognitive demand through mobile application based communication. This can also be used in mobile applications that are often used by healthcare professorial [35], to communicate with people with various sensory disabilities. In extension of this research, Miller’s magic number (Wilkinson, 2000), 7 ± 2 , and Cowan’s number, 4 ± 1 (Cowan, 2001) can be used in cognitive ability-demand gap estimation. (Hossain & Yeasin, 2014)

This study also uncovered the fact that people with sensory disabilities can communicate through multiple devices and translators even in health-related communication. Smartly integrated information system with multiple mobile apps may serve these functionalities including the role of a personal assistant. However, designing such integrated information system is challenging and strictly user-centric, which requires more universal and flexible design (Ventola, 2014).

Finally, the proposed healthcare analytics with DFD, cyclomatic complexity and critical component for decision-support system that will be useful in improving health care communication services among diversified community including different disabilities. The system can be useful not only for sensory disabilities, elderly people or people with special circumstance (example - sick for sometimes) might be benefited. More importantly, the proposed smart phone based systems will reduce difficulties in communication, improve health in community. The research is being conducted on limited targeted users due to the lack of access to such population. Future studies will be dedicated towards detailed usability and specific problems with distant communication.

REFERENCES

- Alabama Institute for Deaf and Blind (AIDB). (2007). People with disabilities in India: from commitment to outcomes. Retrieved from <http://aidb.org/2014/09/support-service-providerpro-tactile-communication-training-provided-by-aidb-adrs-and-troy-university/>
- Anuradha, P. G. (2016). A Refreshable Braille Display for the Interaction with Deafblind People. *Middle-East Journal of Scientific Research*, 24(Suppl. 1), 96–100.

- Aslaksen, F., Bergh, S., Bringa, O. R., & Heggem, E. K. (1995). *Universal Design - Planning and Design for All - 1995*. The Center for Universal Design, NC State University.
- Cowan, N. (2001). The magical number 4 in short-term memory: A reconsideration of mental storage capacity. *Behavioral and Brain Sciences*, 24(1), 87–114. doi:10.1017/S0140525X01003922 PMID:11515286
- Foulgers, D. (2004) Models of communication process.
- Gray, B. (1989). *Collaborating: Finding Common Ground for Multiparty Problems*. San Francisco, CA: Jossey-Bass.
- Hossain, G., & Yeasin, M. (2014). Cognitive Ability-Demand Gap Analysis With Latent Response Models. *IEEE Access*, 2, 711–724. doi:10.1109/ACCESS.2014.2339328
- Hossain, G., & Yeasin, M. (2014). Cognitive Ability-Demand Gap Analysis With Latent Response Models. *IEEE Access*, 2, 711–724. doi:10.1109/ACCESS.2014.2339328
- Kim, E., & Nielsen, H. J. (2004). *The radical lives of Helen Keller*. NYU press.
- Klein, G., Moon, B. & Hoffman, R. R. (2006). Making Sense of Sensemaking 2: A Macrocognitive Model. *IEEE Intelligent Systems*, 21(5), 88-92.
- Klein, G., Moon, B., & Hoffman, R. R. (2006). Making Sense of Sensemaking 1: Alternative Perspectives. *IEEE Intelligent Systems*, 21(4), 70–73. doi:10.1109/MIS.2006.75
- McCabe. (1976, December). A Complexity Measure. *IEEE Transactions on Software Engineering*.
- Miller, G. A. (1956). The magical number seven, plus or minus two: Some limits on our capacity for processing information. *Psychological Review*, 63(2), 81–97. doi:10.1037/h0043158 PMID:13310704
- Papagno, C., Cecchetto, C., Pisoni, A., & Bolognini, N. (2016). Deaf, blind or deaf-blind: Is touch enhanced? *Experimental Brain Research*, 234(2), 627–636. doi:10.1007/s00221-015-4488-1 PMID:26573575
- Paul, S. A., & Reddy, M. (2010). Understanding Together: Sensemaking in Collaborative Information Seeking. *Proc. of CSCW '10*. doi:10.1145/1718918.1718976
- Russell, D. M., Stefik, M. J., Pirolli, P., & Card, S. K. (1993). The cost structure of sensemaking. *Proc. of CHI '93* (pp. 269-276).
- Shah, C. (2014). Collaborative information seeking. *Journal of the Association for Information Science and Technology*, 65(2), 215–236. doi:10.1002/asi.22977
- Sharma, R., Bhateja, V., Satapathy, S. C., & Gupta, S. (2017). Communication Device for Differently Abled People: A Prototype Model. Proceedings of the International Conference on Data Engineering and Communication Technology (pp. 565-575). Springer Singapore. doi:10.1007/978-981-10-1678-3_54
- Stevens, W., Myers, G., & Constantine, L. (1974). Structured Design. *IBM Systems Journal*, 13(2), 115–139. doi:10.1147/sj.132.0115
- Taylor-Powell, E., Rossing, B., & Geran, J. (1998). *Evaluating collaborative: Reaching the potential. Technical report*. Madison, Wisconsin: University of Wisconsin-Extension.

- Umapathy, K. (2010) Requirements to support collaborative sensemaking. *Proceedings of CSCW CIS Workshop*.
- Ventola, C. L. (2014). Mobile devices and apps for health care professionals: Uses and benefits. *Pharmacy and Therapeutics*, 39(5), 356. PMID:24883008
- Watson, A. H., McCabe, T. J., & Wallace, D. R. (1996). Structured testing: A testing methodology using the cyclomatic complexity metric. NIST .
- Weick, K. E. (1995). *Sensemaking in Organizations*. Thousand Oaks, CA: Sage.
- Wilkinson, L. (2000). *Multidimensional scaling. SYSTAT 10*. Statistics II.
- World Program of Action, Global Partnerships on Disability and Development, United Nations, Cornell University Study. (2007).
- WHO. (2011). World Report on Disability. Retrieved from http://whqlibdoc.who.int/publications/2011/9789240685215_eng.pdf

This research was previously published in the International Journal of Healthcare Information Systems and Informatics (IJHISI), 12(2); edited by Joseph Tan, pages 65-80, copyright year 2017 by IGI Publishing (an imprint of IGI Global).

Chapter 19

Android-Based Visual Tag Detection for Visually Impaired Users: System Design and Testing

Hao Dong

University of Massachusetts, Amherst, USA

Jieqi Kang

University of Massachusetts, Amherst, USA

James Schafer

University of Massachusetts, Amherst, USA

Aura Ganz

University of Massachusetts, Amherst, USA

ABSTRACT

In this paper the authors introduce PERCEPT-V indoor navigation for the blind system. PERCEPT-V enhances PERCEPT system by enabling visually impaired users to navigate in open indoor spaces that differ in size and lighting conditions. The authors deploy visual tags in the environment at specific landmarks and introduce a visual tag detection algorithm using a sampling probe and cascading approach. The authors provide guidelines for the visual tag size, which is a function of various environmental, and usage scenarios, which differ in lighting, dimensions of the indoor environment and angle of usage. The authors also developed a Smartphone based user interface for the visually impaired users that uses Android accessibility features.

DOI: 10.4018/978-1-5225-5195-9.ch019

INTRODUCTION

The World Health Organization (2011) reported that 285 million people are visually impaired worldwide, of whom 39 million are blind and 246 have low vision (Pascolini & Mariotti, 2010). Based on data from the 2004 National Health Interview Survey, 61 million Americans are considered to be at high risk of serious vision loss if they have diabetes, or had a vision problem, or are over the age of 65 (Gordon, 2010). As documented by the American Diabetes Association, diabetes is the leading cause of new cases of blindness among adults aged 20–74 years. In 2005–2008, 4.2 million (28.5%) people with diabetes aged 40 years or older had diabetic retinopathy, and of these, almost 0.7 million (4.4% of those with diabetes) had advanced diabetic retinopathy that could lead to severe vision loss (“Data from the 2011 National Diabetes Fact Sheet”, 2011).

Since vision is the most important organ to sense the surroundings, its loss can significantly reduce the visually impaired individual orientation and mobility, especially in unfamiliar and complex indoor environments. Even with the help of a guide dog or cane, it is still a challenge for the visually impaired to independently navigate in such environments without help from sighted individuals. It is commonly accepted that the incapability of moving freely and independently can hinder the full integration of an individual into society (Golledge, Roberta & Jack, 1996).

We first introduced PERCEPT indoor navigation system, which was successfully tested with 24 blind and visually impaired users (Ganz et al., 2011). In PERCEPT system we deployed RFID tags (R-Tags) at specific landmarks in the environment and the user carried a Smartphone and a PERCEPT glove that included the RFID reader. When the user touched with his/her glove the R-tag navigation instructions were given to their desired destination. In this paper we introduce PERCEPT-V, which is an enhancement of PERCEPT system in two dimensions: use of visual tags (V-tags) and the user device is only a Smartphone. We deploy V-tags in the environment deployed above each R-tag. These V-tags will enable the blind user to find the R-tags from afar using the Smartphone without the necessity to trail the wall, making the system more convenient. In addition, we do not need to use the PERCEPT glove since the functionality of a RFID reader is incorporated in most Smartphones. The use of only a Smartphone as a user device significantly reduces the cost for the user since most of the visually impaired users will own a Smartphone with diverse helpful applications for the blind.

The paper is organized as follows. In the next section we introduce related work and. PERCEPT-V system overview is shown in Section III. In Section IV we introduce the User Interface and in Section V we summarize the visual tag and the detection algorithm. Section VI describes the testing scenarios and results and Section VII concludes the paper.

RELATED WORKS

There have been a number of research projects that can help the visually impaired navigate in unfamiliar indoor environments (Horowitz, 2003; Noor, HIsmael & Saaed, 2009; Chumkamon, Tuvaphanthaphiphat & Keeratiwintakorn, 2008; Ki Giampaolo, 2010; Ganz, Gandhi, Wilson & Mullett, 2010; Darvishy, Hutter, Früh, Horvath & Berner, 2008; Coughlan & Manduchi, 2009; Ivanov, 2010; Bostelman, Russo, Albus, Hong & Madhavan, 2006; Fernandes, Costa, Filipe, Hadjileontiadis & Barroso, 2010; Manduchi, Kurniawan & Bagherinia, 2010; Brilhault, Kammoun, Gutierrez, Truillet & Jouffrais, 2011). Most of these systems design and use new devices for their users, which mean extra cost. One of the prominent

projects that underwent user trials with 24 visually impaired subjects is the PERCEPT project (Ganz et al., 2011) funded by the National Institutes of Health/National Eye Institute. PERCEPT uses passive RFID tags (R-tags) deployed on different landmarks in the environment. PERCEPT user interacts with the environment using a glove and a Smartphone. Upon touching the R-tags using the glove, PERCEPT server through the Smartphone provides navigation instructions to the visually impaired users. More details on the system can be found in Ganz et al. (2011).

In this paper we introduce PERCEPT-V, which is an enhancement of PERCEPT system. In addition to the R-tags deployed in the environment we also deploy V-tags above each R-tag. These V-tags will facilitate the user access to these R-tags by using their Smartphone to find them. We developed a visual tag detection algorithm using a sampling probe and cascading approach. In the long history of the development of computer vision algorithms for object identification and localization, two approaches have been proposed: natural feature detection (Bay, Tuytelaars & Van Gool, 2006; Lowe, 1999; Mikolajczyk & Schmid, 2005; Rosten & Drummond, 2005; Lindeberg, 1998) and artificial feature detection (Belussi & Hirata, 2004; Szentandrási, Herout & Dubska, 2012; Shen & Coughlan, 2006; Olson, 2010; Miyaoku, Tang & Fels, 2007). In (Ali & Nordin, 2010) the authors use SIFT algorithm to calculate feature points in 3 dimensions, and then use them as reference points to locate the blind user. Their approach is computation intensive for handheld devices and requires the use of a database. In (Manduchi & Bagherrinia, 2011) the authors introduce multi-color markers as targets and detect them with a camera embedded cellphone. In this paper we also use a multi-color paper printed marker as targets but with a different detection algorithm which is more efficient as well as more robust considering the orientation of the phone by the blind users may not be precise. In addition, we have designed and implemented a visually impaired friendly user interface.

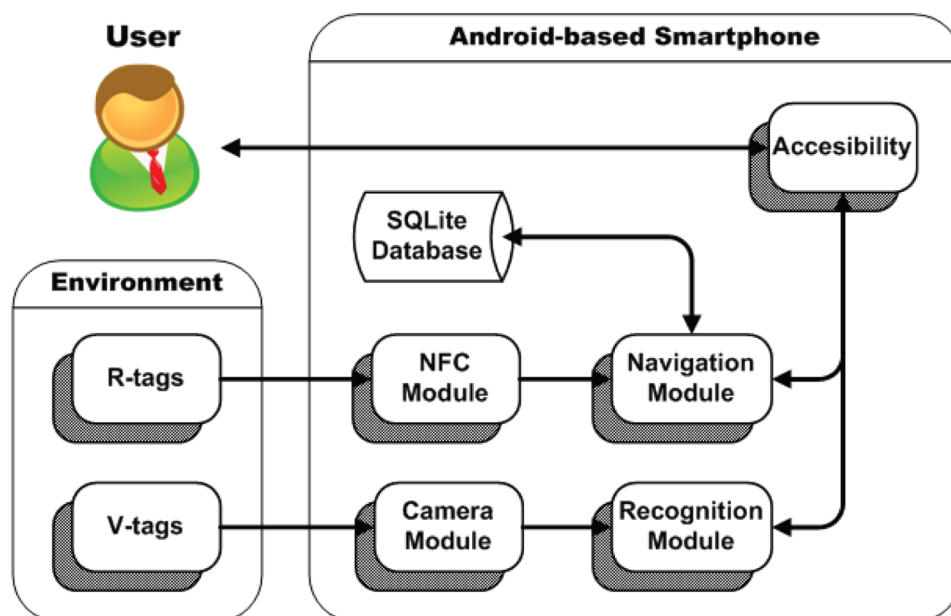
PERCEPT-V SYSTEM OVERVIEW

PERCEPT-V system architecture consists of the following system components: the Environment, and Android-based Smartphone, as seen in Figure 1.

Environment

- **R-Tags:** Passive RFID tags (R-tags) are deployed in the environment in strategic locations at eye-level height. Americans with Disabilities Act (ADA) Guidelines requires the signage to include high contrast raised letters between 1.6 cm and 5 cm, and embossed Braille (“ADA Accessibility Guidelines”, 2012). They are located on each possible destination (e.g. office doors, restrooms, emergency exits) and intermediate landmarks. Granularity was the main reason behind selecting this technology. Proximity of 2-3 cm is required to transfer data from the R-tag into the RFID reader. Other reasons for selecting these R-tags were their cost and the fact that they do not need any power source. On each R-tag we incorporate the room number in raised font and its Braille equivalent. R-tags were also used in PERCEPT system (Ganz et al., 2011);
- **V-Tags:** Paper printed visual tags (V-tags) are designed for remote detection through the camera embedded in the smartphone. V-tags are deployed above each R-tag and will allow the visually impaired users to find the R-tags from a distance. Using the V-tags, the users do not need to trail the walls to find the R-tags that help provide the navigation instructions. The users can find the

Figure 1. PERCEPT-V system architecture



R-tags from any place in the environment for up to 19 meters (65 feet) (testing regarding the distance between the user and the V-tag is reported in Section VI).

Android-Based Smartphone

PERCEPT-V Smartphone Application runs on the Android Platform. This application can run on any Android Smartphone that runs the Android Operating System 4.0 (Ice Cream Sandwich) or higher and that has an embedded Near Field Communication (NFC) Reader. Development and testing was performed on a Samsung Galaxy Nexus Smartphone.

The Smartphone App includes six modules:

- **NFC Module:** With the embedded NFC reader on the Smartphone, the Bluetooth connected PERCEPT glove is no longer needed (Ganz et al., 2011). Once the user puts the Smartphone close to the R-tag (near touch), the NFC reader will retrieve the R-tag unique ID;
- **Camera Module:** The embedded camera on the Smartphone captures the environment once the user pans the Smartphone running our application. The V-tag detection algorithm to find a V-tag will use this environment. More details are provided in Section V;
- **Accessibility:** Android operating system is designed to enable interaction with blind or visually impaired users. Accessibility features define new operation interface and voice feedback for this use;
- **SQLite Database:** The navigation instructions are stored locally on the Smartphone. One of the improvements from the original PERCEPT system described in Ganz et al. (2011) is the ability to use PERCEPT instructions without the need to be connected to the Internet at all times.

Therefore, in PERCEPT-V the navigation instructions that are generated on the server are stored on the Smartphone;

- **Navigation Module:** The navigation module receives the user's required destination using the accessibility features of the phone. Using the user current location obtained through the NFC Module, and the required destination, the application generates a query to the SQLite Database to obtain the navigation instructions. The resulting instructions are read out to the user using the Text-to-Speech module;
- **Recognition Module:** This module is responsible for detecting the V-tag and providing the instructions how to reach the V-tag. Details of the recognition module are provided in Section V.

USER INTERFACE

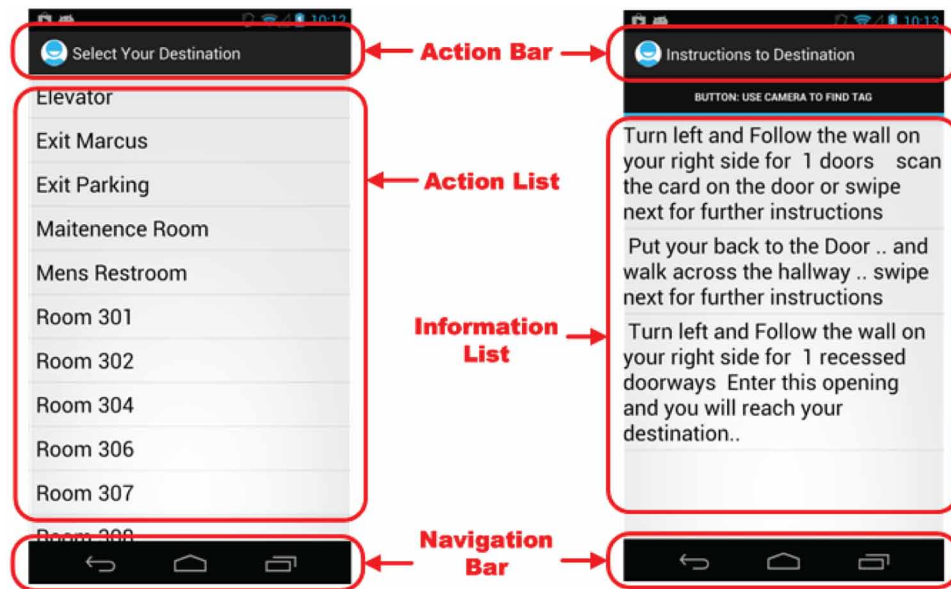
The two Android accessibility features we use are talkback and explore by touch. The touch features enable a visually impaired user to navigate the Smartphone through the use of gestures as follows:

- **Touch Gesture:** When a user touches the screen, if there is an item below their finger it will be focused. The focused item will then be read out to the user through text to speech output. This allows the user to first understand what they are touching through audio feedback and then they can make a decision if this is what they want to select by using a double tap gesture;
- **Double Tap Gesture:** When a user double taps anywhere on the screen the focused item is selected;
- **Swiping Gesture:** When a user swipes their finger in any direction they will focus on the next focusable item in the direction they swiped;
- **Two Finger Gesture:** If a user is presented a list of items that is too long to fit on the screen, they will need to scroll. When the list is first populated on the screen the user is told through Text-To-Speech how many items are in the list displayed on the screen out of the total number of items in the list. From this feedback the user knows they will need to scroll. In addition, when the user reaches the end of the list on the screen a chirp sound will inform the users that they are at the end of the list. By placing two fingers on the screen and making a swiping up gesture the following items are then displayed and by placing two fingers on the screen and swiping down the prior items in the list are displayed.

In our user interface the user either has to select a particular action or listen to the navigation instructions. These UI screens are made up of an Action Bar, a List, and Navigation Bar (see Figure 2):

1. **Action Bar:** This bar is located at the top of the screen. When a user navigates to any of the UI screens the Action Bar's title is spoken. This informs the user the purpose of the current UI. If the users are uncertain what is the functionality of the application, they can swipe or touch the top of the screen where the Action Bar is located. Then they are reminded the purpose of the current UI screen;
2. **List:** This represents the main content area of PERCEPT-V Application which includes two types of lists:

Figure 2. PERCEPT-V application screenshots



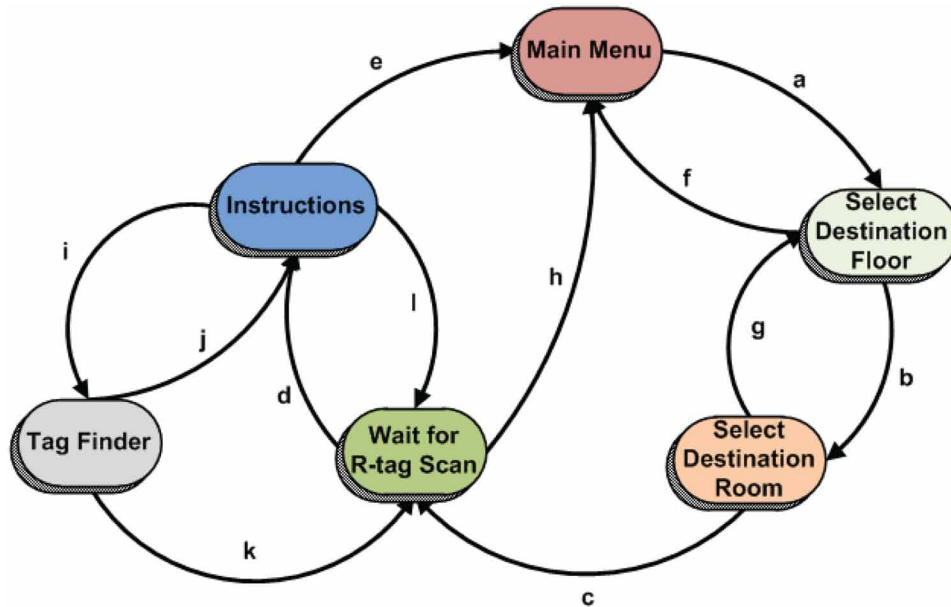
- a. **Action List:** The user has to select from the list a particular choice. The Action Bar Title describes the choice they have to make;
- b. **Information List:** The user is presented with step-by-step navigation instructions. The user follows these instructions to get to their destination;
3. **Navigation Bar:** This bar is part of the Android operating system. Using this bar the user can return to a prior part of the application. For example, if the user would like to return to the main menu in the App from any other screen in the application, all that is required is that they select the back button. The navigation bar also has buttons for the user to return to the home screen or select a recent application.

When using PERCEPT-V Smartphone Application, the users can navigate through 6 screens/states, whose state diagram shown in Figure 3.

The states and transitions shown in Figure 3 are:

- **Main Menu:** This is the first screen or menu shown, once the user opens PERCEPT-V application. The user can select the option of “set destination” in the Action List to switch into the next page of “select destination floor” (flow a);
- **Select Destination Floor:** The user is required to select one room as the destination from the list on the specific floor and the app will switch to the next page “select destination room”. (flow b). The user can double tap the “Back” button in Navigation Bar at the bottom of screen to return to the Main Menu (flow f);
- **Select Destination Room:** All rooms as potential destinations on the selected floor will be shown in the List. The destination will be selected and the application will move to wait for R-Tag Scan

Figure 3. State diagram



state (flow c). Another option is for the user to double tap the “Back” button in the Navigation Bar at the bottom of the screen to return and select another floor (flow g);

- **Wait for R-tag Scan:** This is a page that includes an Action Bar and a Navigation Bar. The user can scan an R-tag to get instructions (flow d) or double tap “Back” button to abort the navigation and return to the Main Menu (flow h);
- **Instructions:** In this page, navigation instructions will be shown in an Information List. In addition, another button will trigger the tag finder, which is right below the Action Bar. Several things are allowed at this state: double tap tag finder button to start tag finder (flow i), scan another R-tag for updated instructions (flow l & d), or double tap “Back” button in the Navigation Bar at the bottom of screen to return to Main Menu (flow e);
- **Tag Finder Interface:** Users can get directions, once a V-tag appears in camera view. Tag Finder assumes that the directions can get him or her to a V-tag, equivalent to a R-tag on location. Scanning a R-tag can update prior instructions (flow k & d). Or users can double tap the “Back” button in Navigation Bar at the bottom of screen to return to previous instruction (flow j).

VISUAL TAG AND DETECTION ALGORITHM

As described above, we will place the V-tags in the environment just above each R-tag. The user will look for these V-tags using pan and wait mode and the Tag Finder will provide voice feedback how to reach the specific V-tag that is within the camera view. These V-tag guiding instructions are designed as two parts. If the tag is not in the central area (we define it to be the middle 1/2 height and width area), the application will notify the user to pan the cell phone. Figure 4 shows the area partitions with their corresponding suggestions to user. For example, when the V-tag is located in the “Upper Left” tile, user

Figure 4. Tag finder interface



can hear the notification of “slide your phone to the left”. If the tag is in the central area, the guidance module will calculate the distance between the phone and the tag using geometric projections, and then notify the user an approximate distance in integer feet, like “go straight for 8 feet”.

V-Tag Determination

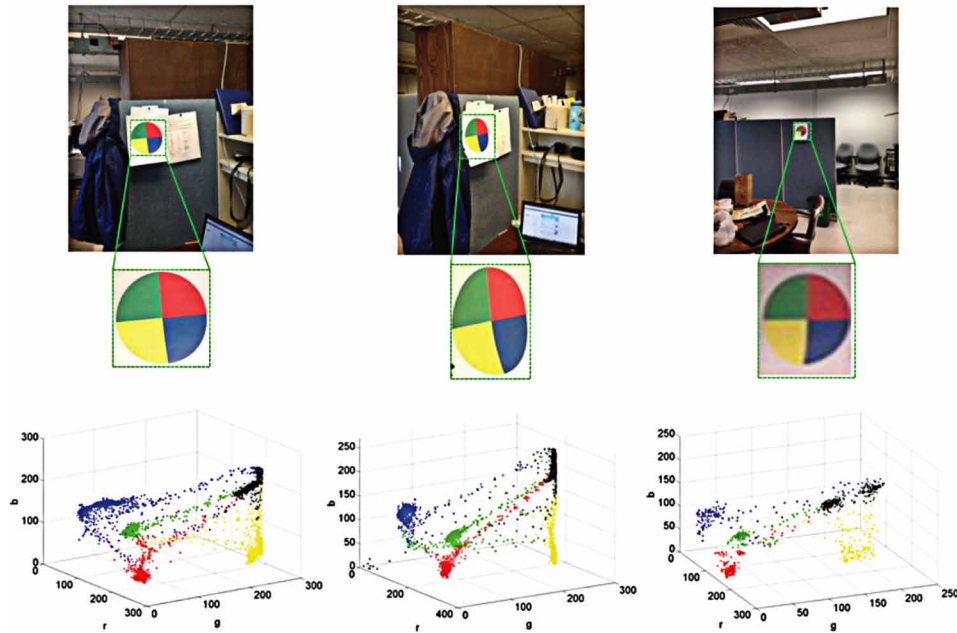
We use paper printed multi-color pie-shaped markers, similar to the visual markers proposed by Manduchi and Bagherrinia (2011). In Figure 5 we visualize the color distribution of 3 different marker variations.

These images, which contain color tags, are taken from real-world situations. From Figure 5, we can see that not only geometrical position will cause the visual marker to transform and distort the color, but also the illumination condition will lead to different output of color and geometrical structure of the V-tag on the screen. The three dimensional plots at the bottom illustrate colors of all the pixels on the plate by their RGB point in a 3D Euclidean space. Despite some transition pixels, most of the pixels in area with a certain color cluster pretty well. We also notice that the exact RGB values for certain areas in 3 different situations are not in the same range and the geometrical distances of pixels with different colors, and even the projection of such distances on 3 dimensions follow some obvious patterns. We can see that the difference of RGB values between pixels in distinct color areas still lay in certain intervals. The idea which we will utilize in the following detection algorithm is that despite the exact RGB values of the pixels change a lot in different conditions, even vary a lot inside the same tag area which should be very close theoretically, the distances between the RGB values of pixels in different color areas should maintain certain underlying restrictions for our V-tag compared to the background.

Detection Algorithm

The algorithm is based on sampling probe and a cascading algorithm (Goughlan, Manduchi & Shen, 2006):

Figure 5. Colour distributions of marker variations in real situations



- Down-Sampling Frame:** The first step of the algorithm is down-sampling to compress the frame from the original input into a much smaller representation in order to speed up the algorithm. Suppose the distance between two neighbouring “probe nodes” in such a grid network over the original frame is $2r$, thus the original frame is reduced by approximately $1/4r^2$ times in scale. After this step, the input frame is stored in a compressed version of itself with RGB values for each “probe pixel”;
- Cascading to Locate the V-Tag:** The next step is a cascading algorithm to detect the V-tag based on our compressed “probe pixel” data of the RGB values. The advantage of the cascading algorithm is that it can be implemented with very fast running time since it can break up the iteration anytime if one comparison fails. In Figure 6, we illustrate a cascading detection algorithm framework. In the algorithm, we scan the compressed image in 2 by 2 blocks. In each block, the algorithm compares the RGB values of probe 1 and 2 first, and if the result pass our criteria, the algorithm then compares the RGB values of probe 2 and 3, and so on so forth. If all four comparisons are successful, we conclude a successful detection of the V-tag. Suppose in each block, the RGB values are recorded as this formation: (r_i, g_i, b_i) for the i -th probe, we define our comparison function as the maximum absolute difference of R, G, and B component wise as (1):

$$dist_{ij} = \max \left\{ |r_i - r_j|, |g_i - g_j|, |b_i - b_j| \right\} \quad (1)$$

In our cascading algorithm, we simply request that the distance of two probes in each step in a certain pre-defined interval are computed by a stored distance of two pixels plus a certain threshold t (see Figure 6).

Technical Testing

In this section, we introduce the testing scenarios and associated performance results. Table 1 summarizes the testing common environment in terms of the Smartphone platform and detection algorithm parameters. We have tested the system performance for a number of parameters: luminance, distance between the camera phone and the V-tag, angle in which camera faces the V-tag, height from the floor to the center of the V-tag and tag size which is the V-tag diameter. The performance metrics are: 1) the detection speed which is measured from the time the V-tag is in the camera view and the time the

Figure 6. Cascading process to locate v-tag

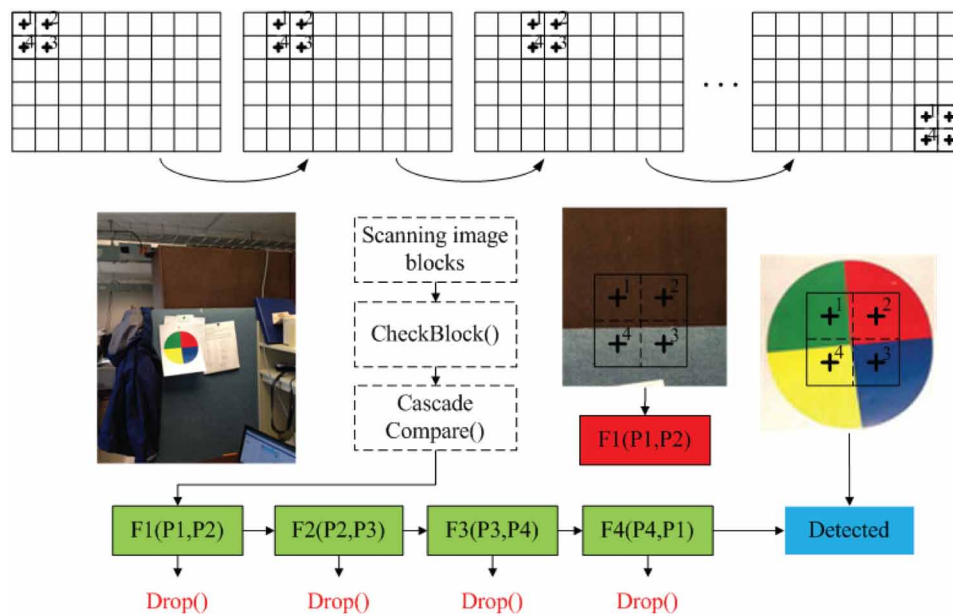


Table 1. Common test environment

Device: Samsung Galaxy Nexus	
CPU	Dual-core 1.2 GHz Cortex-A9
RAM	1 GB
Camera	1920*1280, Auto-focus, Auto-whitening
Algorithm Parameters	
Sampling radius	$r = 4$
Color threshold	$t = 55$
Pattern in (r, g, b)	(150, 131, 0), (78, 99, 36), (143, 31, 14), (43, 33, 74)

V-tag is detected, and 2) accuracy which is successful detection rate in a specific period of time. The successful detection rate will be calculated from 30 tests conducted under the same environment using the Smartphone on a tripod.

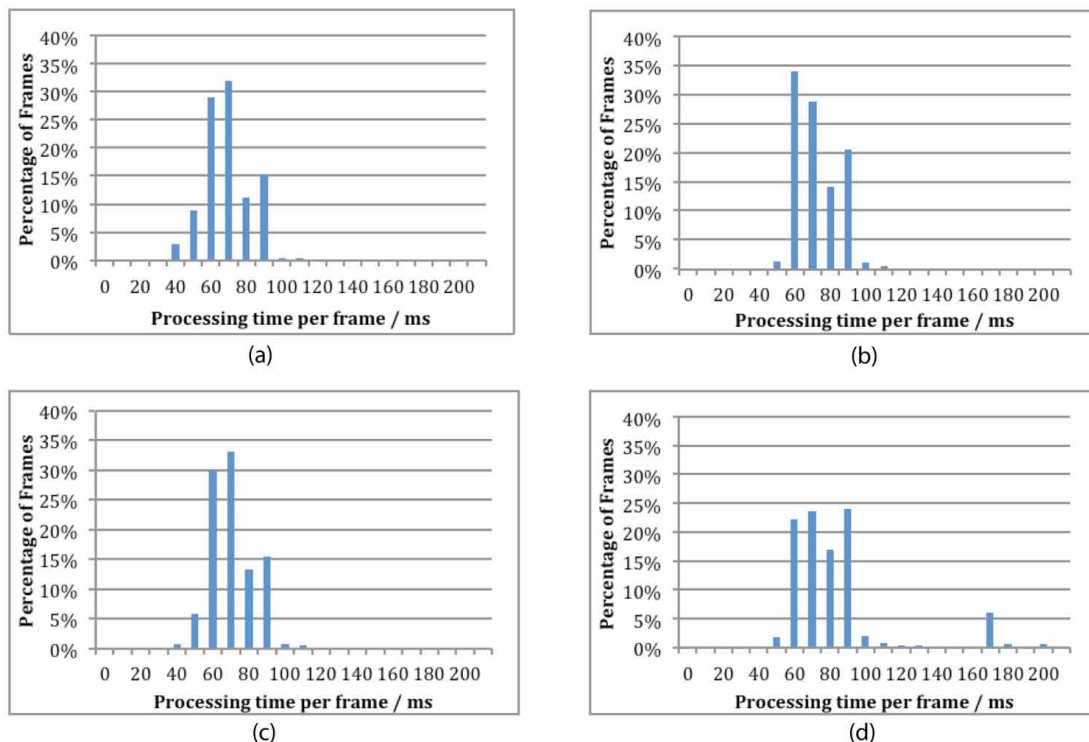
Our tests include different lighting conditions. In bright lighting, we turn on all the lights in the corridor; half of the lights are turned on for dim lighting; only doorway lights are on for dark lighting.

Real-Time Performance Test

As the Tag Finder is used in real-time mode, we first determine the processing time per frame, which is recorded by the application. Figure 7 depicts the frame processing time distribution for different scenarios. The performance is tested in two locations: a hallway on 3rd floor in KEB and room 312 in KEB. Room 312 has more complex color combinations than the hallway. We test two modes of the tag finder operation: Mode 1: the application is searching for the V-tag and Mode 2 in which the V-tag has been found and the user is directed to this V-tag.

From Figure 7 we observe that over 90% of frames; the frame processing time is between 50ms and 90ms, which results in a refresh rate of 11-20 fps. More than 10 frames can be processed in 1 second is fast enough to capture the surroundings and deal with the motion blur caused by hand shaking.

Figure 7. Distribution of processing time per frame for different scenarios: a) In a corridor - V-tag is found and user follows directions to approach the V-tag; b) In a corridor - searching for a V-tag; c) In a room - V-tag is found and user follows directions to approach the V-tag; d) In a room - searching for a V-tag

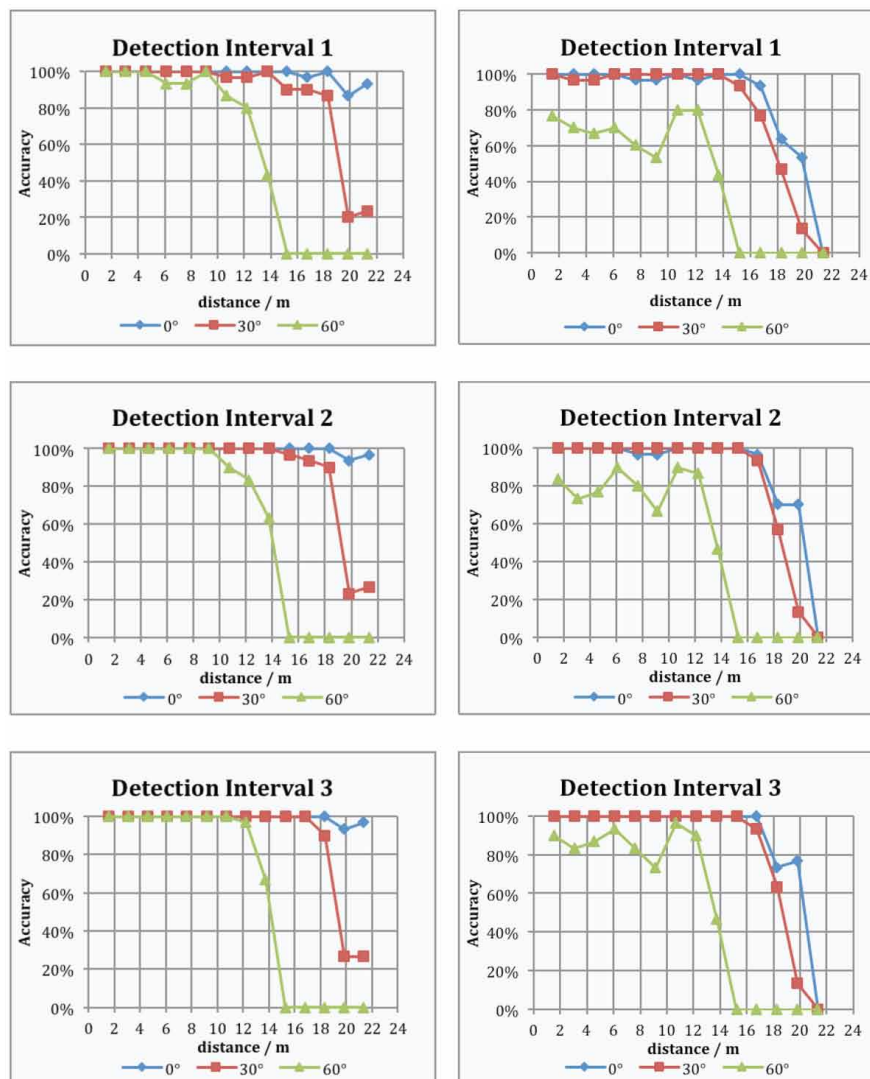


Lighting vs. Accuracy

Figure 8 displays the accuracy vs. the distance for different angles and detection times for bright lighting in left column. The V-tag is placed at 1.5meters (5 feet) height. In bright lighting, we observe that for 0 degrees angle we obtain 100% accuracy for up to 19.8meters (65 feet) distance and 2 seconds detection time. For a 0 degree angle we obtain over 95% accuracy for up to 21.3meters (70 feet). There is no improvement if we increase the detection time beyond 2 seconds. As expected, as the angle increases we observe that the accuracy is reduced. For example we can obtain 100% accuracy for up to 15.24 meters (50 feet) for 30 degree and 100% accuracy for up to 9.144 meters (30 feet) for 60 degrees.

Figure 8 displays the accuracy vs. the distance for different angles and detection times for dim lighting in the right column. Under dim lighting condition, we observe that for all angles we obtain 100%

Figure 8. Accuracy vs. distance for detection of a 7 inch v-tag with different angles, lighting condition and detection intervals. Left column: Bright lighting condition; Right column: Dim lighting condition.



accuracy for a shorter distance than in bright lighting conditions. It takes at least 3 seconds for the results to stabilize.

Figure 9 displays the accuracy vs. the distance for different angles and detection times for dark lighting. Under dark lighting condition, we observe that for all angles we obtain 100% accuracy for a shorter distance than in bright or dim lighting conditions (see Figure 8). In this case we need a scanning time longer than 4 seconds. The result shows that the detection performs well at 15.2 meters (50 feet) for 0 and 30 degrees angles; and 9.1 meters (30 feet) for 60 degrees angle. We observe that the accuracy drops off faster for 0 degrees than for 30 degrees. A possible reason is the uneven lighting in the testing environment, which can cause a better reflection on the tag placed in 30 degrees than 0 degrees. The clearer the image captured by the camera, the higher the probability of successful detection.

Tag Size vs. Accuracy

We tested the system performance for three tag sizes with diameters of 7.6 cm (3 inches), 12.7 cm (5 inches) and 17.8 cm (7 inches). As shown in Figure 10, the larger the tag the longer the detection distance.

Figure 11 depicts the distance vs. the tag diameter that can obtain 100% accuracy for different angles. The designers can use this figure as follows. For a specific setting (i.e., building) determine what is the maximum distance from a user to the wall on which the V-tags will be placed. From Figure 11 we can see that if the maximum distance is 4.6 meters (15 feet) we can chose a 3-inch (7.6 cm) V-tag that will

Figure 9. Accuracy vs. distance for different interval durations and angles (7 inch V-TAG and dark lighting)

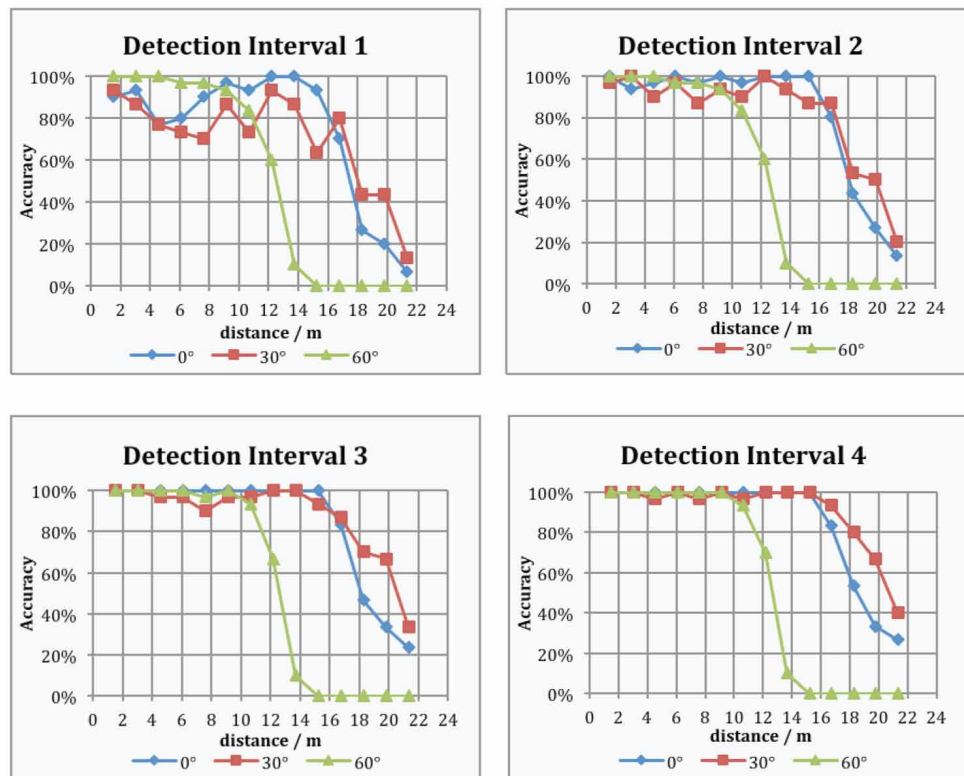


Figure 10. Accuracy vs. distance for different interval durations, v-tag sizes, angles (bright lighting and 2s detection interval)

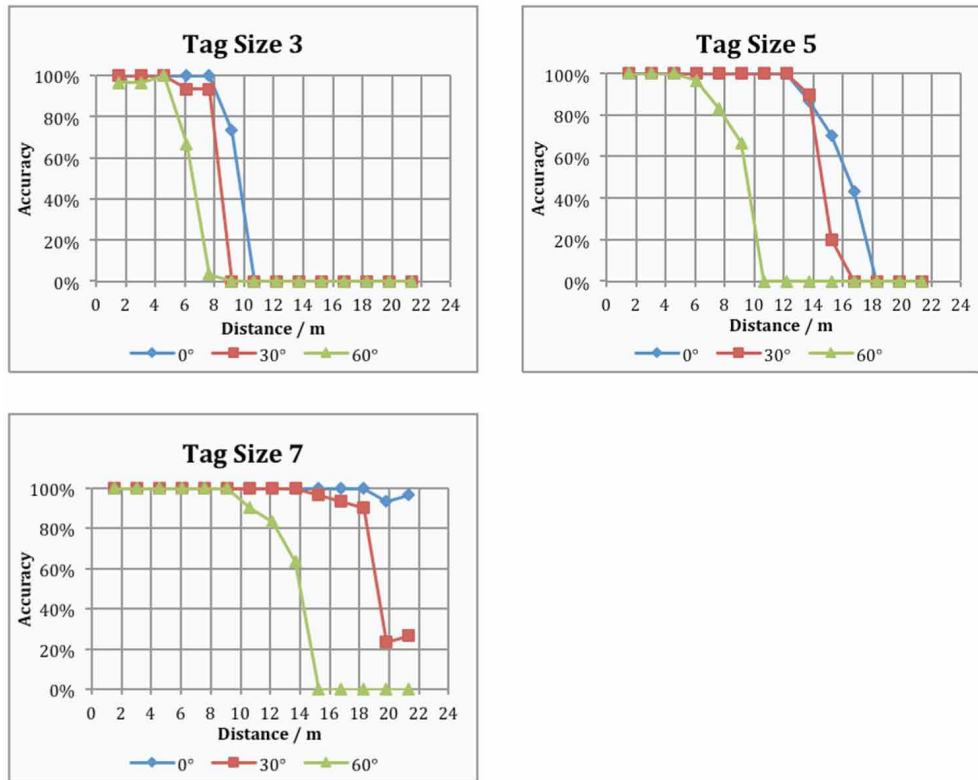
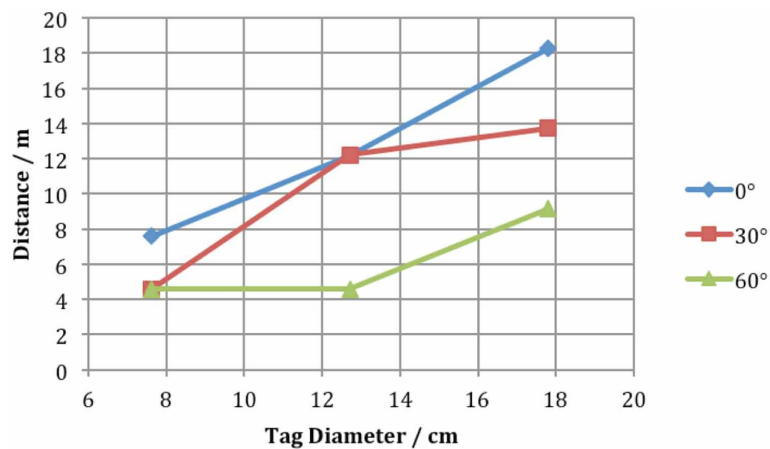


Figure 11. Detection distance vs. tag diameter that can obtain 100% accuracy for different angles



work for angles up to 60 degrees. On the other hand if the maximum distance is 9.1 meters (30 feet) we should choose a 7-inch (17.8 cm) tag that can work for angles up to 60 degrees.

Tag Height vs. Accuracy

Figure 12 depicts the accuracy vs. distance for different heights. We observe that up to 16.8 meters (55 feet) we obtain 100% accuracy for all heights. Above 16.8 meters (55 feet) the accuracy is worse especially for 1.8 meters (6 feet) height. This is due to the fact that as the tag gets close to the light source, it will cause the captured picture to turn dark.

CONCLUSION AND FURTHER WORK

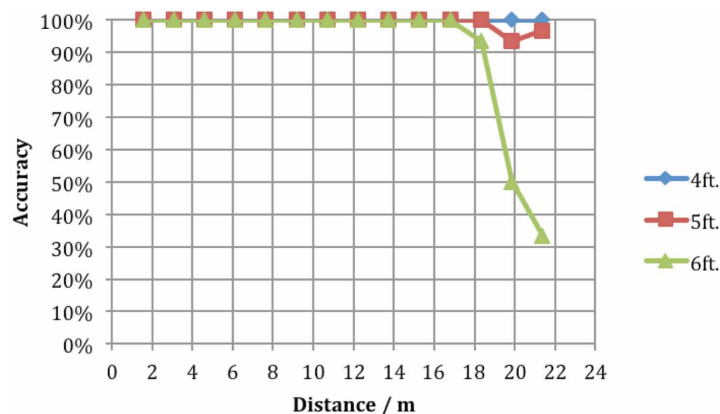
In this paper we introduced PERCEPT-V indoor navigation for the blind focusing on the visual tag detection and user interface. We introduced a reliable and robust visual tag detection algorithm, which was tested in multiple scenarios, which differ in environmental conditions such as lighting, and usage scenarios such as distance from the tag and angle. The performance results in terms of accuracy and detection time were excellent especially in good lighting conditions. We also provide guidelines for the visual tag size as a function of lighting, maximum distance, and angle. We have also developed a vision free user interface using Android accessibility features.

Our next steps are to test PERCEPT-V with blind and visually impaired users.

ACKNOWLEDGMENT

This project was supported in part by the following grants: DUE- 1003743 from the National Science Foundation, 1 R21 EY018231-01A1 from the National Eye Institute/ National Institutes of Health and New England University Transportation Center Program. The content is solely the responsibility of

Figure 12. Accuracy vs. distance for different heights (2s detection interval, 7 inch V-tag)



the authors and does not necessarily represent the official views of the National Science Foundation, National Eye Institute/National Institutes of Health or New England University Transportation Center.

REFERENCES

- ADA accessibility guidelines for buildings and facilities*. (2012). Retrieved March 2, 2013, from <http://www.access-board.gov/adaag/html/>
- Ali, A. M., & Nordin, M. J. (2010). Indoor navigation to support the blind person using true pathway within the map. *Journal of Computer Science*, 6(7), 740–747. doi:10.3844/jcssp.2010.740.747
- Baumberg, A. (2000). Reliable feature matching across widely separated views. In *Proceedings of IEEE Conference on Computer Vision and Pattern Recognition* (pp. 1774–1781).
- Bay, H., Tuytelaars, T., & Van Gool, L. (2006). SURF: Speeded up robust features. In *Proceedings of the 9th European Conference on Computer Vision: Springer LNCS*, (Vol. 3951, No. 1, pp. 404–417).
- Belussi, L. F. F., & Hirata, N. S. T. (2004). Fast QR code detection in arbitrarily acquired images. In *Proceedings of the 24th SIBGRAPI Conference on Graphics, Patterns and Images* (pp. 281–288).
- Bostelman, R., Russo, P., Albus, J., Hong, T., & Madhavan, R. (2006). Applications of a 3D range camera towards healthcare mobility aids. In *Proceedings of the IEEE International Conference on Networking, Sensing and Control* (pp. 416–421).
- Brilhault, A., Kammoun, S., Gutierrez, O., Truillet, P., & Jouffrais, C. (2011). Fusion of artificial vision and GPS to improve blind pedestrian positioning. In *Proceedings of the IFIP International Conference on New Technologies Mobility and Security (NTMS)* (pp. 1–5).
- Chumkamon, S., Tuvaphanthaphiphat, P., & Keeratiwintakorn, P. (2008). A blind navigation system using RFID for indoor environments. In *Proceedings of the 5th International Conference on Computer Telecommunications and Information Technology* (pp. 765–768).
- Coughlan, J., & Manduchi, R. (2009). A mobile phone wayfinding system for visually impaired users. *Assistive Technology Research Series*, 25, 849. PMID:21037932
- Coughlan, J., Manduchi, R., & Shen, H. (2006). Cell phone-based wayfinding for the visually impaired. In *Proceedings of the 1st International Workshop on Mobile Vision*.
- Darvisy, A., Hutter, H. P., Früh, P., Horvath, A., & Berner, D. (2008). Personal mobile assistant for air passengers with disabilities (PMA). *Computers Helping People with Special Needs*, 1129–1134.
- Data from the 2011 national diabetes fact sheet*. (2011). Retrieved March 2, 2013, from <http://www.diabetes.org/diabetes-basics/diabetes-statistics/>
- Di Giampaolo, E. (2010). A passive-RFID based indoor navigation system for visually impaired people. In *Proceedings of the 2010 3rd International Symposium on Applied Sciences in Biomedical and Communication Technologies* (pp. 1–5).

- Fernandes, H., Costa, P., Filipe, V., Hadjileontiadis, L., & Barroso, J. (2010). Stereovision in blind navigation assistance. In *Proceedings of the World Automation Congress (WAC)* (pp. 1-6).
- Ganz, A., Gandhi, S., Wilson, C., & Mullett, G. (2010). INSIGHT: RFID and bluetooth enabled automated space for the blind and visually impaired. In *Proceedings of the IEEE Engineering in Medicine and Biology Society 32nd Annual International Conference* (pp. 331-334).
- Ganz, A., Schafer, J., Gandhi, S., Singh, T., Wilson, C., Mullett, G., & Puleo, E. (2011). PERCEPT: Indoor navigation for the blind and visually impaired. In *Proceedings of the Engineering in Medicine and Biology Society (EMBC)*, 856-859.
- Golledge, R. G., Roberta, L. K., & Jack, M. L. (1996). Cognitive mapping and wayfinding by adults without vision. *The Construction of Cognitive Maps*, 33, 215-246. doi:10.1007/978-0-585-33485-1_10
- Gordon, A. R. (2010). *Prevalence of vision impairment. Lighthouse international*. Retrieved March 2, 2013, from <http://www.lighthouse.org/research/statistics-on-vision-impairment/prevalence-of-vision-impairment/>
- Horowitz, A. (2003). Depression and vision and hearing impairments in later life. *Generations (San Francisco, Calif.)*, 27(1), 32-38.
- Ivanov, R. (2010). Indoor navigation system for visually impaired. In *Proceedings of the 11th International Conference on Computer Systems and Technologies and Workshop for PhD Students in Computing on International Conference on Computer Systems and Technologies* (pp. 143-149).
- Lindeberg, T. (1998). Edge detection and ridge detection with automatic scale selection. *International Journal of Computer Vision*, 30(2), 117-154. doi:10.1023/A:1008097225773
- Lindeberg, T. (2012). Scale invariant feature transform. *Scholarpedia*, 7(5), 10491. doi:10.4249/scholarpedia.10491
- Lowe, D. G. (1999). Object recognition from local scale-invariant features. In *Proceedings of the International Conference on Computer Vision (Vol. 2, pp. 1150-1157)*.
- Manduchi, R., & Bagherrinia, H. (2011). Robust real-time detection of multi-color markers on a cell phone. *Journal of Real-Time Image Processing*, 8(2), 207-223.
- Manduchi, R., Kurniawan, S., & Bagherinia, H. (2010). Blind guidance using mobile computer vision: A usability study. In *Proceedings of the International ACM SIGACCESS Conference on Computers and Accessibility* (pp. 241-242).
- Mikolajczyk, K., & Schmid, C. (2005). A performance evaluation of local descriptors. *IEEE Transactions on Pattern Analysis and Machine Intelligence*, 10(27), 1615-1630. doi:10.1109/TPAMI.2005.188 PMID:16237996
- Miyaoku, K., Tang, A., & Fels, S. (2007). C-band: A flexible ring tag system for camera-based user interface. In R. Shumaker (Ed.), *Virtual reality* (pp. 320-328). Berlin, Heidelberg, Germany: Springer. doi:10.1007/978-3-540-73335-5_35

Noor, M. Z. HIsmaail., I., & Saaaid, M. F. (2009). Bus detection device for the blind using RFID application. CSPA 2009. In *Proceedings of the 5th International Colloquium on Signal Processing & its Applications* (pp. 247-249).

Olson, E. (2010). *AprilTag: A robust and flexible visual fiducial system*. University of Michigan, APRIL laboratory.

Pascolini, D., & Mariotti, S. P. M. (2010). Global estimates of visual impairment: 2010. *British Journal Ophthalmology Online First*. Retrieved July 13, 2013, from <http://bj.o.bmj.com/content/early/2011/11/30/bjophthalmol-2011-300539>

Rosten, E., & Drummond, T. (2005). Fusing points and lines for high performance tracking. In *Proceedings of the IEEE International Conference on Computer Vision* (Vol. 2, pp. 1508-1511).

Rosten, E., & Drummond, T. (2006). Machine learning for high-speed corner detection. In *Proceedings of the 9th European Conference on Computer Vision* (Vol. 3951, 430-443).

Shen, H., & Coughlan, J. (2006). Reading LCD/LED displays with a camera cell phone. In *Proceedings of the Computer Vision and Pattern Recognition Workshop* (Vol. 119).

Szentandrás, I., Herout A., & Dubska, M. (2012). Fast detection and recognition of QR codes in high-resolution images. In *Proceedings of the 28th Spring Conference on Computer Graphics (SCCG '12)* (pp. 129-136).

Tomasi, C., & Kanade, T. (2004). Detection and tracking of point features. *Pattern Recognition*, 37, 165–168.

This research was previously published in the International Journal of E-Health and Medical Communications (IJEHMC), 5(1); edited by Joel J.P.C. Rodrigues, pages 63-80, copyright year 2014 by IGI Publishing (an imprint of IGI Global).

Index

A

Adaptive Thresholding 18-19, 54, 155
 Age-Related Macular Degeneration 153-154, 170, 246-247, 283, 289, 298
 Android Smartphone 320
 Antibacterial 268, 272, 276, 281
 Antifungal 268, 272, 276, 281
 Anti-Inflammatory 268-269, 272, 279, 281
 Antioxidant 268, 272, 277-279, 282
 Antitubercular Treatment 115
 Argemone Mexicana 211-213
 Arnold Cat Map 190, 192-194, 207

B

Bacteria 268-269, 271, 281
 binocular vision 80, 83, 85, 91, 93
 Biometric 69, 217-218
 Blind 172, 174, 177, 186, 300-303, 305, 312, 314, 317-319, 331
 Blood Vessel 2, 4, 6-7, 9-10, 17-19, 22, 25, 34-36, 38-39, 44, 46-47, 49, 54, 69-72, 74, 123, 154-156, 158, 241, 251, 254, 257
 Blood Vessel Detection 22, 155
 Blood Vessel Extraction 17, 70
 Blood Vessel Pattern 69-71
 Blood Vessels Segmentation 9

C

Canny Operator 39, 52
 Ciliary 116, 218, 286-287
 Collarette 218
 Computer Vision 3, 66, 122, 319
 Contrast Limited Adaptive Histogram Equalization (CLAHE) 266

Cotton Wool Spots 3, 34-35, 37, 245, 266
 Critical Incidence 300, 311-312
 Cyclometric Complexity 310

D

Data Hiding 172-175, 186
 depth range 88-89, 91
 Diabetes 19, 34-36, 38, 48, 52, 54, 123, 220-221, 241-242, 245-247, 266, 268, 290, 298, 318
 Diabetic Macular Edema (DME) 242, 246, 266
 Diabetic Retinopathy 1, 18-19, 21, 34-38, 52-54, 63, 122-123, 138, 150, 189-191, 241, 245, 247, 249-250, 266, 283, 290, 298, 318
 Diabetic Retinopathy (DR) 18, 34-36, 123, 241, 245, 266, 290
 Disabilities 300-303, 305-306, 314
 Disability Communication 314

E

Encryption 189-197, 199, 201-203, 205, 207
 Epidemic Dropsy 211-214
 Exudates 3, 34-35, 37, 39-42, 44, 46-47, 49-50, 154, 158, 245-252, 254-257, 259-261, 266
 Eye Movement 100-102, 105-106, 110
 Eye Tracking 101, 110
 EYENET Model 153, 162, 166-168

F

Feature Extraction 12, 69-71, 106, 122, 124, 130, 134-135, 141, 147, 150, 159, 219, 221-222, 226, 239
 Fixation 100-101, 105
 Fovea 98, 100, 105, 154, 247-249, 252, 256-257, 260
 Free Radicals 279, 282

Fundus Image 3, 20, 38, 44, 69-71, 156, 192, 194-197, 199-204, 242-244, 247, 250, 252-256, 259
 Fundus Images 6, 21, 54, 61, 70, 153, 155, 170, 172-173, 175, 179, 189-192, 194, 197, 199-200, 202, 207-208, 241-242, 248, 251-253, 256
 Fundus Retinal images 18-19
 Fungi 268-269, 271

G

Gabor Filter 19, 53, 55-60, 62, 66, 133-134, 145, 149-150, 225, 228
 Gaussian Post Filter 57
 Genetic Algorithm 53, 55, 57-58, 60, 62, 65-66
 Geometric features 25, 217
 Glaucoma 1, 18-19, 35-37, 53-54, 189-191, 211-212, 214-215, 257, 283, 285-287, 298
 Gradient Descent 53, 57-58, 60, 62, 65
 Gray-Level Co-occurrence Matrix 6, 124, 128, 142, 217, 228
 Gray-Level Run Lengths 125, 141

H

Health Communication 300
 Hemorrhages 1, 11, 17, 34-35, 52, 212, 214, 245, 248
 horopter 92-93
 Hyperplane 41-42, 52, 107, 135-137

I

Image processing 2, 8, 11, 13, 37-38, 40, 53, 66, 124, 170, 182, 218-219, 223, 239, 241, 255-256
 Imaging 3, 13, 17, 19, 53-54, 78, 88, 155, 175, 242-243, 256
 India 34, 66, 110, 115, 119, 214, 268-269, 301
 Indoor Navigation 317-318, 331
 Intraocular Pressure (IOP) 211, 285
 Iris 118, 217-219, 221-229, 231-239, 282, 287
 Iris Diagnosis 218

K

Keratitis 268, 279, 282
 Kernel Function 52, 107, 137-138

L

Lesions 3, 11, 17, 20, 34-35, 116, 118, 154, 246, 251, 266, 268
 Local binary pattern 124, 130, 140, 150
 Lossless 172-174, 181, 184, 189-191, 207

M

Machine Learning Method 52
 Macula 2, 17, 70, 153-154, 241-242, 247-249, 252, 254, 256-257, 259-261, 289
 Macular Degeneration 1, 17, 54, 153-154, 170, 242, 246-248, 250, 261, 283, 289, 298
 Maculopathy 242-243, 249, 252, 256-257
 Magnetic Resonance Imaging 3, 17
 Matched Filter 6-7, 11, 19-20
 Medical Image Watermarking 173
 Microaneurysms 11, 34-35, 39, 52, 245, 247, 249, 252, 255, 257
 Model Based Approaches 11
 Monteux Positivity 115
 Morphological Processing 8-10, 159

N

Nanogenomics 284, 298
 Nanoproteomics 284, 298
 Nanotechnology 283-284, 298
 Neovascularization 19, 123, 154, 245, 248, 266, 289-291
 Neural Network 6-7, 17, 19, 62, 66, 123, 155, 164, 166, 221

O

Object Scanning 98
 Ocular Tuberculosis 115, 117, 119
 Omics 292, 298
 Ophthalmologist 5, 154, 191, 271
 Optic Disc 2-3, 9-10, 34, 36, 39-41, 44, 47, 49-50, 52, 70, 123, 154

Index

P

parallax angle 93, 96
Parallel 7, 11-13, 86, 88, 91
Pathology 285-286
perspective 80-81, 86-87, 116, 311
Phytochemicals 280, 282
Piece Wise Linear Chaotic Map 190, 193-194, 207
Probabilistic Neural Network 155, 166
Pupil 37, 99, 118, 138, 217-218, 220, 222-223, 239, 282

R

Radial Basis Function Neural Network 155, 166
Retina 2-3, 9, 19-21, 35, 37, 39-40, 44, 46, 48-49,
52-53, 69-72, 79-80, 91, 100, 103, 105, 109-110,
153-155, 158, 160, 217, 241-243, 245-248, 251,
266, 289, 298
Retinal Image 1-2, 6-10, 12, 18-19, 21, 23, 25-26, 34,
36, 53-54, 58, 62, 66, 70, 72, 79, 110, 154-156,
158, 170, 243, 248, 250, 261, 266

S

Saccade 101-102, 105-106
Soft Computing 34-35
Specificity 18, 27, 62, 66, 108, 119, 164-166, 168, 170
Supervised Method 5, 10
Support Vector Machine 6, 19, 34, 36, 52, 107, 123,
134-135, 154, 251
Systemic Tuberculosis 115

T

Tags 317-319, 324
Telemedicine 155, 190
Tele-Ophthalmology 175, 189-192, 207
texture based feature 124, 130, 150
Texture features 124, 217, 219, 221-222, 230-231,
233, 236-237, 239
Tuberculous Uveitis 115

U

Universal Design 301
Uveal Melanoma 283, 287, 298

V

Vesselness Enhancement Filter 18
visual perception 78, 80, 98-99, 102, 105, 109-110
Visually Impaired 301-302, 317-319, 321, 331

W

Watermarking 173-175, 199, 208